University of Engineering and Technology

Institute of Mechanics

Proceedings of the International Conference on Engineering Mechanics and Automation – ICEMA2 2012

PUBLISHING HOUSE FOR SCIENCE AND TECHNOLOGY

University of Engineering and Technology Institute of Mechanics

Proceedings of the International Conference on Engineering Mechanics and Automation – ICEMA2 2012

PUBLISHING HOUSE FOR SCIENCE AND TECHNOLOGY

Proceedings of the International Conference on Engineering Mechanics and Automation - ICEMA 2012

ISBN: 978-604-913-097-7

Published by
Publishing House for Science and Technology
18, Hoang Quoc Viet, Hanoi, Vietnam
Điện thoại: 04.22149034/40/41 Fax: 04 37910147
Email: nxb@vap.ac.vn; Website: http:// www.vap.ac.vn

Printed in Vietnam

The 2nd International Conference on Engineering Mechanics and Automation (ICEMA-2) will be organised at University of Engineering and Technology on August 16, 2012.

The aim of the conference is to provide an international forum for scientific researchers in the technologies and applications of Engineering Mechanics and Automation. The Conference also aims to provide a chance for exchange of experiences and international collaboration in these fields. The scope of the conference includes, but not limited to, the following topics:

- Fundamental Problems of Fluid Mechanics
- Mechanics with Climate Change and Environment
- Industrial and Environmental Fluid Mechanics
- River and Sea Dynamics
- Fundamental Problems of Mechanics of Solids
- Mechanics of Composite Materials and Structures.
- Fracture Mechanics and Fatigue
- Mechanics of Soil, Rocks and Porous Medium
- Technical Diagnostics
- Linear and Nonlinear Oscillations
- Dynamics of Multibody Systems
- Nonlinear Dynamics and Chaos
- Mechanics of Machines and Mechanism
- Computational Mechanics
- Industrial Automation
- CAD/CAM/CNC Systems
- Control Strategies and Algorithms
- Design Automation
- Intelligent Systems
- Machine Tools and Machinery
- Manufacturing Process Control
- Mechatronics Engineering
- Rapid Prototyping

Steering Committee

Chairman: Nguyen Ngoc Binh

Nguyen Dong Anh, Duong Ngoc Hai, Nguyen Van Hieu, Nguyen Hoa Thinh

Program Committee

Chairman: Nguyen Dong Anh

Vice Chairman: Nguyen Dinh Duc

Guy Bonnet (France), Dao Huy Bich, Ngo Huy Can, Doan Minh Chung, Truong Huu Chi, Dao Van Dung, D. Dufresne (France), Nguyen Kim Dan (France), Nguyen Van Diep, Pham Tien Dat, Cao The Huynh, Le Xuan Huynh, Nguyen Van Khang, Chun-Gon Kim (Korea), Nguyen Tien Khiem, Dang Van Ky (France), P. Le Tallec (France), D.J. Lee (Korea), Hoang Xuan Luong, Dinh Van Manh, Nguyen Cao Menh, Yoshihiro Ootao (Japan), Nguyen Van Pho, Dinh Van Phong, Pobedrya B.E. (Russia), Vu Duy Quang, Do Sanh, Nguyen Quoc Son (France), Pham Manh Thang, Tran Ich Thinh, Bui Dinh Tri, Nguyen The Truyen, Pham Anh Tuan, Pham Chi Vinh, Masayuki Yamaguchi (Japan), Jung Il Song (Korea), Shuo-Jen Lee (Taiwan), Hui-Shen Shen (China).

Organising Committee

Chairman: Nguyen Dinh Duc

Vice Chairman: Pham Manh Thang, Bui Dinh Tri, Tran Duong Tri

Dang The Ba, Dao Nhu Mai, Phan Quoc Nguyen, Nguyen Hoang Quan, Nguyen Cao Son, Jung Il Song (Korea), Masayuki Yamaguchi (Japan).

Secretariat

Chairman: Dao Nhu Mai

Nguyen Viet Anh, Nguyen Thi Cam Lai, Nguyen Thi Viet Lien, Phan Thi Cam Ly.

Table of Content

PLENARY SESSION

The 2nd International Conference on Engineering Mechanics and Automation (ICEMA2)
Hanoi, August 16-17, 2012
ISBN: 978-604-913-097-7

Duality in the Study of Responses to Nonlinear Systems

Nguyen Dong Anh

Institute of Mechanics, Vietnam Academy of Science and Technology
University of Engineering and Technology, Vietnam National University, Hanoi

Abstract

The main aim of the paper is to recommend the significant use of the dual approach to the study of scientific problems. A detailed analysis and examples are given in the following topics: equivalent linearization method, Boubnov-Galerkin method, global-local averaged values of functions, Duffing oscillator subjected to random excitations.

Keywords. Dual approach, global-local averaged values, dual criterion, Bubnov-Galerkin method.

1. Introduction

Natural phenomena and human activities exhibit often dual characters which reflect two side processes or/and the relative balance of two opposite sides. For illustration we may say attack – defense in a football match, one way and return in an excursion, day and night. When a problem is considered it is quite often that one its side is given too much attention while its other side is almost or completely forgotten. This usual approach doest not reflect the real essence of the problem in question and hence, in many cases, doest not yield an expected solution. The main aim of the paper is to recommend the significant use of the dual approach to the study of scientific problems. A detailed analysis and examples are given in the following topics: equivalent linearization method, Boubnov-Galerkin method, global-local averaged values of functions, Duffing oscillator subjected to random excitations.

2. Method of equivalent linearization

Equivalent linearization method of stochastic dynamical system is one of the common approaches to the approximate analysis. The original version of method was proposed by Caughey. This method is based on the replacement of a nonlinear oscillator under Gaussian excitation by a linear one under the same excitation for which the coefficients of linearization can be found from a mean-square criterion. Although the method of equivalent linearization has remained a popular tool over the many years new criteria need to be suggested to improve the accuracy and to understand the essence of the method. A dual criterion of the equivalent linearization method has been recently proposed in [1,2]. The obtained results show a significant accuracy of the method. Consider a non-linear stochastic oscillator with single degree of freedom governed by

$$\ddot{z} + 2h\dot{z} + \omega_0^2 z + g(z, \dot{z}) = f(t) \qquad (1)$$

where h, ω_0 are constants, $g(z, \dot{z})$ is a nonlinear function of $z, \dot{z}$, $f(t)$ is a zero mean Gaussian stationary process. Suppose that a stationary solution to Eq.(1) exists. Following the method of equivalent linearization Eq.(1) is to be linearized by the following form

$$\ddot{x} + (2h + \mu)\dot{x} + (\omega_0^2 + \lambda)x = f(t) \qquad (2)$$

where μ, λ are constant linearization coefficients that shall be determined by minimizing the error between the original non-linear Eq.(1) and the equivalent linearized Eq.(2) in some probabilistic sense. The error between Eq.(1) and Eq.(2) is

$$e(x, \dot{x}) = g(x, \dot{x}) - \mu\dot{x} - \lambda x \qquad (3)$$

The classical mean square error criterion requires

$$< e^2(x, \dot{x}) > \rightarrow \min_{\lambda, \mu} \qquad (4)$$

Using the dual conception one can suggest that the original nonlinear system can be replaced by an equivalent linearization system and then this equivalent system is replaced by a nonlinear system which belongs to the same class of the original nonlinear system. Thus, instead of (4) one can propose the dual criterion as follows [2]

$$\left\langle \left(g(x, \dot{x}) - \mu\dot{x} - \lambda x\right)^2 + \left(\mu\dot{x} - \lambda x - \beta g(x, \dot{x})\right)^2 \right\rangle \rightarrow \min_{\mu, \lambda, \beta} \qquad (5)$$

In [2] three typical nonlinear systems have been examined to show good accuracies of the dual conception. The approach has a large potential and it ought to be explored for wider nonlinear classes.

3. Bubnov-Galerkin method

Bubnov-Galerkin method is one of most popular approximate methods in many fields of applied mechanics since the method is general in scope and can be used for both conservative and nonconservative, both linear and nonlinear systems. The idea was apparently first suggested in 1913 by Bubnov [3], whereas the first paper along with elaborative examples was written in 1915 by Galerkin [4]. In 1937 Duncan [5] published the first comprehensive review of the method in the Western literature. For a given differential equation the Bubnov-Galerkin method approximates the sought solution as a linear combination of comparison functions and requires the orthogonality of the residual to each of comparison functions. In this context the Bubnov-Galerkin method is also known as a weighted residual method. Although the method can be used for both linear and nonlinear systems, it is known that the accuracy of the method decreases when the nonlinearity becomes larger. Elishakoff [6] connected the Bubnov-Galerkin method with the equivalent linearization method.

In [7] a representation of the Bubnov-Galerkin method in terms of the equivalent linearization method is presented and a dual approach is subsequently adopted to suggest a new method for solving nonlinear equations. This combined approach allows improving the accuracy when the nonlinearity is strong. Consider the following nonlinear differential equation

$$L(W) = 0 \qquad (6)$$

where L is a differential operator, W is an unknown function which satisfies specific boundary conditions. We replace approximately the function $L(W)$ by a linear term

$$L(W) \approx kW \qquad (7)$$

where the coefficient k is chosen from the condition of minimum mean square deviation criterion

$$\left\langle \left(L(W) - kW\right)^2 \right\rangle \rightarrow \min_{k} \qquad (8)$$

where $\langle \cdots \rangle$ is a functional which is usually taken in a form of integration operator over the domain of the operator $L(W)$. One gets from (8):

$$k = \frac{< L(W)W >}{< W^2 >} \tag{9}$$

Using Eq. (7) one obviously observes that Eq. (1) is satisfied approximately if

$$k=0 \tag{10}$$

Alternatively, from Eq. (9) we get another condition

$$< L(W)W >= 0 \tag{11}$$

The Eq. (11) is known as the orthogonality of the residual *L(W)* to the comparison function *W*. Hence, the Bubnov-Galerkin method can be employed in terms of the equivalent linearization method. Moreover, the accuracy of the method can be expected to be improved by using the dual approach developed recently by Anh [1,2]. Suppose that the operator *L(W)* can be expressed as a sum of two operators:

$$L(W) = M(W) + N(W) \tag{12}$$

where *M* is the linear operator and *N* is the nonlinear operator. We replace *N(W)* approximately by a linear term

$$N(W) \approx \alpha W \tag{13}$$

The difference can be minimized by the following dual expression:

$$\left\langle \left[N(W) - \alpha W \right]^2 \right\rangle + \left\langle \left[\alpha W - \beta N(W) \right]^2 \right\rangle \rightarrow \min_{\alpha,\beta} \tag{14}$$

which yields the dual form of Bubnov-Galerkin equation [7]

$$\langle L(W)W \rangle + \frac{\langle N(W)W \rangle^2 - \langle N(W) \rangle^2 \langle W^2 \rangle}{2\langle N(W) \rangle^2 \langle W^2 \rangle - \langle N(W)W \rangle^2} = 0 \tag{15}$$

It is seen that the equation (15) differs from the Bubnov-Galerkin equation (11). Moreover, in general the orthogonality of the residual *L(W)* to the comparison function *W* is not required anymore. For illustration of the effectiveness of the equation (15) we consider the well known Duffing oscillator under random excitation

$$L(W) \equiv \frac{d^2W}{dt^2} + 2h\frac{dW}{dt} + \omega_0^2 W + \mu W^3 - \sigma\dot{\xi}(t) = 0 \tag{16}$$

where $\dot{\xi}(t)$ is the white noise process with unit intensity. The comparison function *W* is taken as a solution of the corresponding linear equation:

$$\frac{d^2W}{dt^2} + 2h\frac{dW}{dt} + \omega_0^2 W + kW - \sigma\dot{\xi}(t) = 0 \tag{17}$$

Substituting (17) into (16) gives the residual

$$L(W) = \mu W^3 - kW \tag{18}$$

Thus by using the Bubnov-Galerkin method one gets

$$< L(W)W >=< (\mu W^3 - kW)W >= 0 \tag{19}$$

or

$$k = \mu\frac{< W^4 >}{< W^2 >} = 3\mu < W^2 > \tag{20}$$

where $< \cdot >$ is the mathematical expectation operator. The system of two equations (20) and (17) allows obtaining the unknown $<W^2>$. Using the present method one considers *L(W)* as a sum of two operators *M(W)* and *N(W)* where

$$M(W) = \frac{d^2W}{dt^2} + 2h\frac{dW}{dt} + \omega_0^2 W - \sigma\dot{\xi}(t), \quad N(W) = \mu W^3 \tag{21}$$

Substituting Eqs. (18), (21) into (15) gives

$$\left\langle (\mu W^3 - kW)W \right\rangle + \frac{\mu^2 \left\langle W^4 \right\rangle^2 - \mu^2 \left\langle W^6 \right\rangle \left\langle W^2 \right\rangle}{2\mu^2 \left\langle W^6 \right\rangle \left\langle W^2 \right\rangle - \mu^2 \left\langle W^4 \right\rangle^2} \mu \left\langle W^4 \right\rangle = 0 \quad (22)$$

one gets

$$3\mu \left\langle W^2 \right\rangle^2 - k \left\langle W^2 \right\rangle + \frac{(15-9)\left\langle W^2 \right\rangle^4}{(30-9)\left\langle W^2 \right\rangle^4} 3\mu \left\langle W^2 \right\rangle^2 = 0 \quad (23)$$

or

$$k = \frac{15}{7} \mu < W^2 > \quad (24)$$

It is remarkable that Eqs. (19) and (23) differ from each other. The results of mean-square response of Duffing oscillator obtained by the Bubnov-Galerkin method ($<W^2>_{GM}$) and present method ($<W^2>_{PM}$) are compared with the exact ones ($<W^2>_E$) in Table 1.

Table 1. Mean-Square Responses $<W^2>$ of Duffing oscillator for $\sigma^2/(4h) = 1, \omega_0 = 1$.

γ	$<W^2>_E$	$<W^2>_{GM}$	error %	$<W^2>_{PM}$	error %
0.1	0.8176	0.8054	1.4876	0.8465	3.5352
0.5	0.5792	0.5486	5.2861	0.6062	4.6670
1.0	0.4679	0.4343	7.1938	0.4885	4.4082
5.0	0.2543	0.2270	10.7384	0.2624	3.1708
10	0.1889	0.1667	11.7721	2.6697	2.6697
50	0.0904	0.0784	13.2721	1.8539	1.8539
100	0.0650	0.0561	13.6491	0.0660	1.6331

It is seen that the errors of mean-square responses determined by the present method are much less than the errors of mean-square response obtained by the straightforward Bubnov-Galerkin method for the case of strong nonlinearity.

4. Dual conception to averaged values

Averaged values play major roles in the study of dynamic processes. The use of those values allows transforming varying processes to some constant characteristics that are much easier to be investigated. In order to extend the use of averaged values one may apply the dual approach recently proposed and developed in [1-2]. One of significant advantages of the dual conception is its consideration of two different aspects of a problem in question allows the investigation to be more appropriate. New global and local averaged values of functions based on the dual conception have been proposed in [8]. The global average value (GAV) of an integrable deterministic function *x(t)* on a domain *D* : (*0,d*) is a constant value defined by

$$< x(t) > = \frac{1}{d} \int_0^d x(t)dt \quad (25)$$

In many cases when the function *x(t)* is periodic with period 2π the value d is taken as 2π and it leads to the averaged value of *x(t)* over one period. Using the dual approach to averaged values one may suggest a consideration respect two aspects, namely, to local and global levels. Thus, the following notations can be introduced.

Notation 1. The local averaged value (LAV) at level *r* of a deterministic integrable function *x(t)* is defined by

$$< x(t) >_r = \frac{1}{r} \int_0^r x(t)dt \quad (26)$$

It is seen from (26) that in stead of the constant global averaged value (25) one has local averaged values (26) as a function depending on level *r*. When *r* = *d*, LAV (26) leads to GAV (25). Thus, GAV is a particular value of LAV.

Notation (1) can be called LAV order 1, a particular case of LAV order n, defined by

$$\left\langle \cdots \left\langle \left\langle x(t) \right\rangle_{r1} \right\rangle_{r2} \cdots \right\rangle_{rn} = \frac{1}{r_n}\int_0^{r_n} \cdots \frac{1}{r_2}\int_0^{r_2} \frac{1}{r_1}\int_0^{r_1} x(t)dtdr_1dr_2 \cdots dr_{n-1} \tag{27}$$

Now the consideration of second aspect yields the notation 2.

Notation 2. The global-local averaged value (GLAV) of a deterministic integrable function *x(t)* is defined by

$$\left\langle \left\langle x(t) \right\rangle_r \right\rangle = \frac{1}{d}\int_0^d \left\langle x(t) \right\rangle_r dr = \frac{1}{d}\int_0^d \frac{1}{r}\int_0^r x(t)dtdr \tag{28}$$

It can be seen that in general GLAV (28) differs from GAV (25 since GAV (25) is the averaged value of original values of *x(t)* while GLAV is the averaged value of all local averaged values of *x(t)*. From the notation 2 it would be expected that GLAV (28) might express averaged characteristics that could not be obtained from GAV (25).

In the case of stationary random functions x(t) the following notations can be introduced.

Notation 3. The local mean value (LoMeV) at level *r* of a stationary random function *x(t)* is defined by

$$< x(t) >_r = \int_{-r}^{r} xp(x)dx \tag{29}$$

where *p(x)* is the stationary probabilistic density function of *x(t)*.

It is seen from (29) that the classical constant global mean value (GMeV) of *x(t)* is a particular value of LoMeV when $r = \infty$. It also noted that the local mean square error criterion (LOMSEC) was introduced in [9] and developed in [10].

Notation 4. The global-local mean value (GLoMeV) of a stationary random function *x(t)* is defined by

$$\left\langle \left\langle x(t) \right\rangle_r \right\rangle = \lim_{d\to\infty} \frac{1}{d}\int_0^d \left\langle x(t) \right\rangle_r dr = \lim_{d\to\infty} \frac{1}{d}\int_0^d \int_{-r}^{r} xp(x)dxdr \tag{30}$$

Same comments as above can be given to LoMeV and GLoMeV of a stationary random function. For illustration of possible uses of the proposed global-local averaged values consider the following equation

$$e(u(t,x)) = 0 \tag{31}$$

where *e* is a given operator, *u(t,x)* is unknown defined in the domain *D*: $t \in [0,d]$, $x \in [0,L]$. Let *u(a,t,x)* is an approximate solution of (11) which depends on a constant parameter *a*. The value of *a* can be determined from some conditions, for example, the mean square minimum criterion

$$< e^2(u(a,t,x)) > \to \min_a \tag{32}$$

where the averaging operator $< \cdot >$ is taken as follows

$$< \cdot > = \frac{1}{d}\int_0^d \frac{1}{L}\int_0^L (\cdot)dxdt \tag{33}$$

Using the dual conception the global averaged value (32) can first be replaced by local averaged values as follows

$$< e^2(a,t,x) >_{r,s} \equiv \frac{1}{r}\int_0^r \frac{1}{s}\int_0^s e^2(a,t,x)\,dxdt \to \min_a \tag{34}$$

The solution of (34) will be a function of *r* and *s*, *a = a(r,s)*. Thus, the expected value of *a* can be suggested as the global averaged value of *a(r,s)*, i.e.,

$$a = \frac{1}{d}\int_0^d \frac{1}{L}\int_0^L a(r,s)\,dsdr \tag{35}$$

Another possible use of the proposed global-local averaged values can be found in [11]. First, we recall the mean square error criterion. Consider a non-linear stochastic oscillator with single degree of freedom governed by Eq.(1) and its equivalent linear

one (2). The error between Eq.(1) and Eq.(2) is expressed in (3) and the classical mean square error criterion requires (4), or in the explicit form:

$$\int_{-\infty}^{+\infty}\int_{-\infty}^{+\infty} e^2(x,\dot{x})P(x,\dot{x})dxd\dot{x} \to \min_{\lambda,\mu} \qquad (36)$$

Since the integrations is taken over the entire coordinate space $(-\infty,+\infty)$, criterion (36) may be called as global mean square error criterion. In 1995 based on the assumption that the global integration domain taken in the mean square error criterion should be reduced to a local one where the response would be concentrated Anh and Di Paola [9] proposed a local mean square error criterion (LOMSEC):

$$\int_{-x_0}^{+x_0}\int_{-\dot{x}_0}^{+\dot{x}_0} e^2(x,\dot{x})P(x,\dot{x})dxd\dot{x} \to \min_{\lambda,\mu} \qquad (37)$$

where $x_0, \dot{x}_0$ are given positive values. The expected integrations in (37) can be transformed to a non-dimensional variable by $x_0 = r\sigma_x, \dot{x}_0 = r\sigma_{\dot{x}}$ with r is a given positive value, σ_x and $\sigma_{\dot{x}}$ are the normal deviations of displacement and velocity, respectively. Thus, criterion (37) leads to

$$[e^2(x,\dot{x})] = \int_{-r\sigma_x}^{+r\sigma_x}\int_{-r\sigma_{\dot{x}}}^{+r\sigma_{\dot{x}}} e^2(x,\dot{x})P(x,\dot{x})dxd\dot{x} \to \min_{\lambda,\mu} \qquad (38)$$

where [.] denotes the local mean values of random variables taken as follows

$$[.] = \int_{-r\sigma_x}^{+r\sigma_x}\int_{-r\sigma_{\dot{x}}}^{+r\sigma_{\dot{x}}} (.)P(x,\dot{x})dxd\dot{x} \qquad (39)$$

It is seen from (3) and (39) the linearization coefficients obtained by LOMSEC are to be functions of $r, \mu = \mu(r), \lambda = \lambda(r)$, and expressed as follows

$$\mu(r) = \frac{\left[g(x,\dot{x})\dot{x}\right]}{\left[\dot{x}^2\right]},\ \lambda(r) = \frac{\left[g(x,\dot{x})x\right]}{\left[x^2\right]}. \qquad (40)$$

The local mean values of $x, \dot{x}$ can be expressed in terms of conventional global mean values (see [11]). Formulas (40) indicates that the linearization coefficients are functions depending on parameter r and when r is determined they become constant values. In this sense the linearization coefficients $\mu(r), \lambda(r)$ can be called as local linearization coefficients. The most important advantage of LOMSEC is that it enables to obtain much more accurate solutions than the one of classical criterion [10]. The main disadvantage of LOMSEC, however, is that the local domain of integration, namely in our case the value of *r*, is unknown and the open question is of how to find it. Using the dual approach to LOMSEC it is suggested that instead of finding a special value of *r* one may consider its varying in all the global domain of integration. Thus, the constant linearization coefficients μ, λ can be suggested as global mean values of all local linearization coefficients as follows

$$\mu = <\mu(r)> = \lim_{s\to\infty}\left(\frac{1}{s}\int_0^s \mu(r)dr\right),$$
$$\lambda = <\lambda(r)> = \lim_{s\to\infty}\left(\frac{1}{s}\int_0^s \lambda(r)dr\right). \qquad (41)$$

For illustration we consider Duffing oscillator governed by

$$\ddot{z} + 2h\dot{z} + \beta z + \varepsilon z^3 = \sigma w(t) \qquad (42)$$

where w(t) is a Gaussian white noise with unit intensity; $\sigma, h, \beta, \varepsilon$ are positive parameters. Replace the non-linear stiffness element in (42) by λx, thus the equivalent linearized equation to (42) is described by

$$\ddot{x} + 2h\dot{x} + (\beta + \lambda)x = \sigma w(t) \qquad (43)$$

where λ is the linearization coefficient. The stationary solution to (43) is known

$$\left\langle x^2 \right\rangle = \frac{\sigma^2}{4h(\beta+\lambda)};$$

$$\left\langle \dot{x}^2 \right\rangle = \frac{\sigma^2}{4h} = (\beta+\lambda)\left\langle x^2 \right\rangle \tag{44}$$

The error between (42) and (43) is

$$e(x) = \varepsilon x^3 - \lambda x \tag{45}$$

Denote λ_C the linearization coefficient found by the classical criterion we obtain

$$\lambda_C = \varepsilon \frac{\left\langle x^4 \right\rangle}{\left\langle x^2 \right\rangle} = 3\varepsilon \left\langle x^2 \right\rangle \tag{46}$$

and the solution by the classical criterion

$$\left\langle x^2 \right\rangle_C = \frac{1}{6\varepsilon}\left(-\beta + \sqrt{\beta^2 + \frac{3\varepsilon\sigma^2}{h}} \right) \tag{47}$$

Denote $\lambda(r)$ the local linearization coefficient found by LOMSEC (40) then we obtain

$$\lambda(r) = \varepsilon \frac{\left[x^4 \right]}{\left[x^2 \right]} = \varepsilon \left\langle x^2 \right\rangle K(r) \tag{48}$$

where

$$K(r) = \frac{\int_0^r t^4 \eta(t)dt}{\int_0^r t^2 \eta(t)dt}; \eta(t) = \frac{1}{\sqrt{2\pi}} e^{\frac{-t^2}{2}} \tag{49}$$

Combine (48) with (41), the linearization coefficient obtained by GLOMSEC is to be

$$\begin{aligned} \bar{\lambda} &= \underset{s\to\infty}{Lim}\left(\frac{1}{s}\int_0^s \lambda_L(r)dr \right) \\ &= \varepsilon \left\langle x^2 \right\rangle \underset{s\to\infty}{Lim}\left(\frac{1}{s}\int_0^s K(r)dr \right) \\ &= 2,412\varepsilon \left\langle x^2 \right\rangle \end{aligned} \tag{50}$$

We obtain the solution by GLOMSEC

$$\left\langle x^2 \right\rangle_{GL} = \frac{1}{4.82378\varepsilon}\left(-\beta + \sqrt{\beta^2 + \frac{2.41189\varepsilon\sigma^2}{h}} \right) \tag{51}$$

Consider the system with parameters $h = 0.25, \beta = 1, \sigma = 1$ meanwhile ε varies. The results of $\left\langle x^2 \right\rangle_C$ and $\left\langle x^2 \right\rangle_{GL}$ are presented in Table2. The exact solution $\left\langle x^2 \right\rangle_E$ of system (43) exists which is used for evaluating the relative errors.

Table 2. The mean square responses of Duffing oscillator versus ε ($h = 0.25, \beta = 1, \sigma = 1$)

ε	$\left\langle x^2 \right\rangle_E$	$\left\langle x^2 \right\rangle_C$	error %	$\left\langle x^2 \right\rangle_{GL}$	error %
0.1	0.81756	0.80540	-1.487	0.83274	1.857
1	0.46792	0.43426	-7.194	0.46915	0.263
10	0.18890	0.16667	-11.768	0.18394	-2.626
100	0.06496	0.05609	-13.655	0.06235	-4.018

The relative errors indicate that for the considered Duffing system, the accuracy of solution given by GLOMSEC is much more improved than the one obtained by the classical criterion, especially when the non-linearity is strong, (for more detail see [11]) .

5. Conclusion

Natural phenomena and human activities exhibit often dual characters which reflect two side processes or/and the relative balance of two opposite sides. When a problem is considered it is quite often that one its side is given too much attention while its other side is almost or completely forgotten. This usual approach doest not reflect the real essence of the problem in question and hence, in many cases, doest not yield an expected solution. The main aim of the paper is to recommend the significant use of the dual approach to the study of scientific problems. One of significant advantages of the dual conception is its consideration of two different aspects of a problem in question allows the

investigation to be more appropriate. A detailed analysis and examples are given in the following topics: equivalent linearization method, Boubnov-Galerkin method, global-local averaged values of functions, Duffing oscillator subjected to random excitations. The dual conception is used to suggest new global and local averaged values for studying varying processes. These averaged values contain the global averaged value (GAV) as a particular case. It can be seen that GAV is obtained from original values of the process *x(t)* while global-local averaged value (GLAV) is obtained from all local averaged values of *x(t)*. It would be expected that GLAV might express averaged characteristics that could not be obtained from GAV The dual approach appears to have a certain potential; it ought to be explored for wider problems.

Acknowledgements

The research reported in this paper is supported by Vietnam National Foundation for Science and Technology Development under Project 107.04-2011.13 (09 – Mechanics).

References

Anh, N. D. (2010), Duality in the Analysis of Responses to Nonlinear Systems, *Vietnam Journal of Mechanics*, Vol. 32, N4, 263-266.

N. D. Anh, N. N. Hieu, N. N. Linh, (2012), A dual criterion of equivalent linearization method for nonlinear systems subjected to random excitation, *Acta Mechanica*, DOI 10.1007/s00707-011-0582-z.

Bubnov I. G. (1913) Reviews of Professor Kirpichev, Belzetskii, Bubnov and Kolosoff on Works of Professor Timoshenko, awarded the D. I. Zhuravskii Prize, *Sbornik St. Peterburgskogo Instituta Inzhenerov Putei Soobchenia* (Collection of St. Petersburg Institute of Transportation Engineering), Vol. 81, 1-40 (see also Bubnov I. G., 1956, *Selected Works*, Sudpromgiz Publishers, Leningrad, pp. 136-139, in Russian).

Galerkin B. G.,(1915), Rods and Plates, Series in Some Questions of Elastic Equilibrium of Rods and Plates, *Vestnik Inzhenerov i Technikov*, Vol. 19, 897-908, (English Translation, in W. P. Rodden, *Theoretical and Computational Aeroelasticity*, pp. 700-745, 2011, Crest Publishing).

Duncan W. J. (1937), Galerkin's Method in Mechanics and Differential Equations, *Aeronautical Research Committee Reports and Memoranda*, N 1848.

Elishakoff, I., (2000), Stochastic Linearization Technique: a New Interpretation and a Selective Review, *Shock and Vibration Digest*, Vol 32, 179-188.

N.D. Anh, I. Elishakoff, (2012), A new view on the Bubnov-Galerkin method in the linear context, *Vietnam Journal of Mechanics*, Vol. 34, N1, 1-6.

Anh, N. D. (2012), Dual approach to averaged values of functions, *Vietnam Journal of Mechanics*, Vol. 34, N3, (under publication).

Anh N. D., Di Paola M. (1995), Some extensions of Gaussian equivalent linearization. International Conference on Nonlinear Stochastic Dynamics, Hanoi, Vietnam, 5-16.

N.D. Anh, L.X. Hung, (2003), An Improved criterion of GEL for analysis of non-linear stochastic systems, J. Sound and Vibration, v.268, 177-200.

N.D. Anh, L.X. Hung, L.D. Viet, (2012), Dual approach to the local mean square error criterion, Acta Mechanica, (under review).

The 2nd International Conference on Engineering Mechanics and Automation (ICEMA2)
Hanoi, August 16-17, 2012
ISBN: 978-604-913-097-7

Material Reinforcement of Injection-Molded Polypropylene Having Plywood Structure

Masayuki Yamaguchi

Japan Advanced Institute of Science and Technology, 1-1 Asahidai, Nomi, Ishikawa 923-1292 JAPAN
m_yama@jaist.ac.jp

Abstract

Structure and properties of novel injection-molded plaques composed of isotactic polypropylene (PP) containing a specific nucleating agent have been studied. It is found that the nucleating agent employed exists as needle crystals in a molten PP. During the crystallization of PP from the surface of the nucleating agent, the chain axis of PP orients perpendicular to the long axis of the needle crystals. Because the needle crystals of the nucleating agent orient to the flow direction at processing, PP chains orient perpendicular to the flow direction in general. In case of injection-molding, PP chain orients perpendicular to the flow direction in the core layer, whereas that in the skin layer near the surface orients to the flow direction by the flow induced crystallization as similar to conventional injection-molded products. As a result, the direction of molecular orientation in the skin layer is perpendicular to that in the core layer in the injection-molded plaque. The anomalous molecular orientation like plywood is responsible for the improved mechanical toughness. Moreover, this unique structure can be applicable to control the shape of broken pieces, because the direction of the crack changes abruptly inside of the plaque owing to the crossing behavior of the molecular orientation.

Key Words: Plywood Structure; Injection-Molding; Polypropylene; Molecular Orientation

1. Introduction

Control of the crystalline state and molecular orientation is a key technology to enhance the material performance for crystalline polymers. In particular, crystalline form of PP as a polymorphic material has to be considered to a great extent, because β trigonal form exhibits marked toughness as compared to α monoclinic form.[1,2] Therefore, new types of efficient nucleating agents for β-modification are being developed.[3-6]

Generally, the molecular orientation is enhanced by adding a nucleating agent because of a rapid solidification. Since the degree of orientation decides the mechanical anisotropy, it is important for actual products.

In this paper, the crystallization kinetics of PP with a specific β nucleating agent is presented employing N,N'-dicyclohexyl-2,6-naphthalenedicarboxamide including the peculiar molecular orientation of injection-molded plaques.

2. Experimental

2.1. Materials

PP and N,N'-dicyclohexyl-2,6-naphthalene dicarboxyamide (New Japan Chemical, NJ Star^{TR} NU-100) as a β nucleating agent were mixed with/without N,N',N"-tris(2-methyl cyclohexyl)-1,2,3-propanetricarboxamide (New Japan Chemical, RiKA Clear^{TR} PC-1) as an α nucleating agent by a twin-screw extruder at 260 ºC. The amounts of the nucleating agents were 500/1500 ppm for the β nucleating agent and 0/500 ppm for the α nucleating agent. The obtained pellets were fed into an injection-molding machine to produce flat plaques. The barrel temperature was 200 ºC, and the mold temperature T_M was controlled at either 80 or 120 ºC.

2.2. Measurements

Shape of the β nucleating agent and crystallization behavior of PP were observed during cooling process using a polarized microscope equipped with a hot stage.

Crystalline form was characterized using an X-ray diffractmeter by a reflection mode. After the measurement of the surface, the surface area was removed by grinding the plaque in water. Then the grinded product was mounted again to evaluate the crystalline form of the inside of the plaque.

Orientation birefringence was measured by an optical microscope using a tilting compensator. Film specimens with 10 μm thickness were cut out from the injection-molded plaque by an ultra-microtome.

Impact tests were carried out by a Dupont impact tester following JIS K 5600. Various weighs were fallen onto the punch placed on the samples.

The warpage of the injection-molded plaques was evaluated. The plaque was placed on the flat table, and the average height of both edges was measured.

3. Results and Discussion

3.1. Crystallization

The crystallization behavior of PP as well as the nucleating agent was observed under crossed polars. Figure 1 shows the optical micrographs of the sample at a cooling process from 260 ºC at a rate of 5 ºC/min. Although nothing is detected at 260 ºC, the nucleating agent appears around at 220 ºC as needle crystals, in which the length of the long axis is about 100-200 μm. Further, the crystallization of PP is observed around at 135 ºC, which occurs on the surface of the needle crystals.

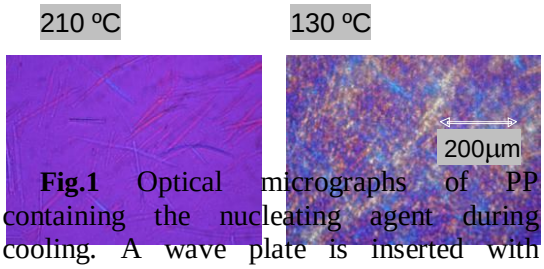

Fig.1 Optical micrographs of PP containing the nucleating agent during cooling. A wave plate is inserted with crossed polars

Crystalline form of the injection-molded plaques containing 500 ppm of the β nucleating agent is studied by WAXD measurements. Figure 2(a) shows WAXD profile of the surface of the plaque with 1.0 mm thickness. As seen in the figure, the peak ascribed to β trigonal crystals, i.e., 2θ = 16.1º, is significantly weak in the surface, i.e., skin layer, especially for the pure PP. The intense flow field would lead to α form crystallization at the current processing

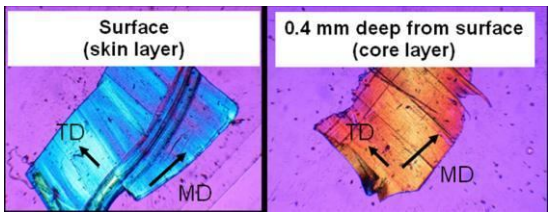

condition. On the contrary, β form is prevailing in the core layer for the sample containing the nucleating agent.

Molecular orientation is evaluated by the birefringence measurement employing thin sliced films cut out from the plaque for PP containing 500 ppm of the β nucleating agent, obtained at TM = 80 ºC.

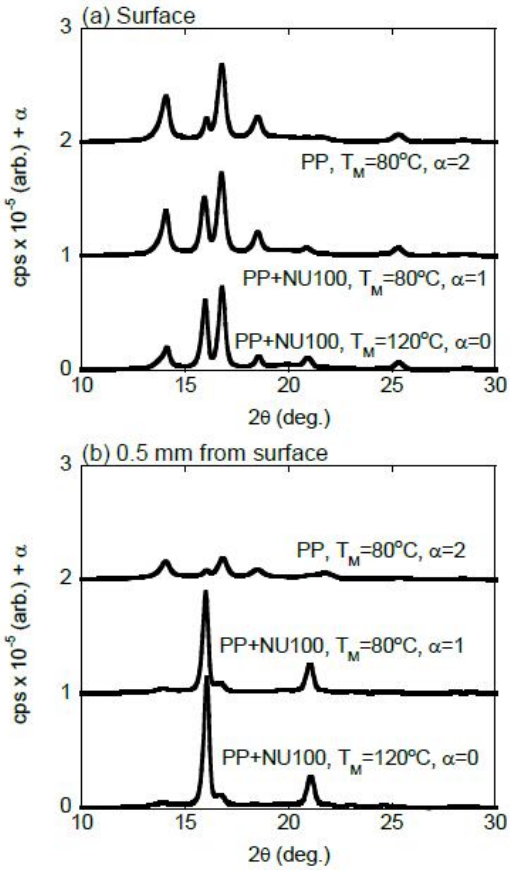

Fig.2 WAXD profiles for the injection-molded plaques of pure PP and PP with the β nucleating agent.

Figure 3 shows the optical micrographs under crossed polars inserting a full-wave plate. As seen in the figure, the thin slice at the surface is blue, demonstrating that MD is the direction of molecular orientation. This is attributed to the flow induced crystallization as observed in most injection-molded products. On the contrary, TD is the direction of molecular orientation in the core, which is perpendicular to the applied flow field.

Fig.3 Optical micrographs under crossed polars inserting a full-wave plate for the slices (MD-TD plane) from the plaque of PP containing 500 ppm of the β nucleating agent (TM = 80 ºC); (left) surface and (right) 0.4 mm deep from the surface.

The birefringences in Figure 3 are found to be 1.0 x 102 (left) and -1.0 x 102 (right). Further information is found in our paper.11,12)

The plywood structure of the injection-molded plaques is responsible for the enhanced toughness. Furthermore, it is well known that □ crystalline structure provides marked toughness due to the energy dissipation mechanism during yield process, where the phase transformation from □ to □ occurs.1-3) Consequently, the obtained plaque having plywood structure shows high level of toughness. For example, Dupont impact strength of the plaque for PP containing 500 ppm of the □ nucleating agent, obtained at TM = 80 ºC, is approximately 1.5 J, whereas that of the pure PP is lower than 0.6 J. Moreover, the plywood structure provides the extraordinary failure behavior, as shown in Figure 4.

Fig.4 Sample specimen after Dupont impact test using the plaque containing 500 ppm of the β nucleating agent (TM =120 ºC). The thickness of the plaque is 2 mm.

The crack propagation, initiating near the surface, is prohibited inside the plaque because of the abrupt change of the

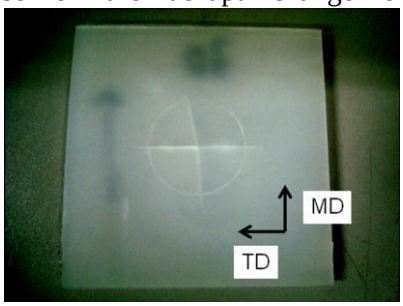

molecular orientation. The complicated crack propagation will be benefits for various

applications, because it changes the shape of broken pieces.

The injection-molded plaque containing the β nucleating agent, however, shows marked warpage. Recently, it is found that further addition of the specific α nucleating agent can improve it. As seen in the table, the warpage, which is defined as the average height of both edges divided by the length between the edges, can be reduced greatly by the addition of the α nucleating agent.

Table 1 Warpage of injection-molded plaques

β nucleating agent	α nucleating agent	Warpage (%)
0	0	0.0012
0.15	0	0.0166
0.15	0.05	0.0020

T_M = 80 ºC

4. Conclusion

The effect of the nucleating agent, N,N'-dicyclohexyl-2,6-naphthalenedicarboxamide, on the structureand the mechanical anisotropyisstudied. The nucleating agentexistsas needle crystals during cooling process. In the flow field, the needle crystals orient to the applied flow direction by hydrodynamic force. Furthermore, during crystallization, PP chains grow perpendicular tothe long axis of the needle crystals, leadingto extraordinary mechanical anisotropyinthecore layer of an injection-molded product.On the contrary, flow induced crystallization provides the MD orientation of PP chain in thesurface layer.Asaresult,plywood structure is attained in injection-molded products.Finally, the plywood structure of the injection-molded PP is responsible for the marked toughness as well as complicated crack propagation.

Acknowledgement

The author would like to express their gratitude to Mr. Yohei Uchiyama of New Japan Chemical Co., Ltd. for his valuable advice and the kind supply of the samples employed in this study.

References

J. Kargar-Kocsis; J. Varga, *J Appl Polym Sci*, **62**, 291 (1996) .

J. Karger-Kocsis, *Polym Eng Sci*, **36**, 203 (1996).

J. Varga, *J Macromol Sci*, **41**, 1121 (2002).

X. Li; K. Hu; M. Ji; Y. Huang; G. Ahou, *J Appl Polym Sci*, **86**, 633 (2002).

J. Kotek, I. Kelnar, J. Baldrian; M. Raab, *Eur Polym J*, **40**, 679 (2004).

B. Shentu; J. Li; G. Tan; Z. Weng, *Eur Polym J*, **43**, 3036 (2007).

T. Miyazawa, *J Polym Sci C*, **7,** 59 (1964).

B. E. Read, *Ultra-violet, Visible and Infra-ed Dichroism*; in *Structure and Properties of Oriented Polymers*, Chap.4, Ed. I. M. Ward, Applied Science Publishers, London, 1975.

M. Yamaguchi; T. Fukui; K. Okamoto; S. Sasaki; Y. Uchiyama; C. Ueoka, *Polymer*, **50**, 1497 (2009).

Y. Uchiyama; S. Iwasaki; C. Ueoka; T. Fukui; K. Okamoto; M. Yamaguchi, *J Polym Sci Polym Phys Ed*, **47**, 424 (2009).

M. Yamaguchi; Y. Irie; P. Phulkerd; H. Hagihara; S. Hirayama; S. Sasaki, *Polymer*, **51**, 5983 (2010).

P. Phulkerd, S. Nobukawa, Y. Uchiyama, M. Yamaguchi, *Polymer*, **52**, 4867 (2011).

The 2nd International Conference on Engineering Mechanics and Automation (ICEMA2) Hanoi, August 16-17, 2012 ISBN: 978-604-913-097-7

R-SAW Analysis on Single-Crystal AlN Substrate for Liquid Sensors

Tung Bui Duc, Thu-Hang Bui, Dat Nguyen Tien, and Trinh Chu Duc

University of Engineering and Technology, Vietnam National University, Hanoi

Abstract

Acoustic wave sensors are highly sensitive in detecting the properties of fluid materials in contact between solid and liquid. In this paper, a sensing systems using Rayleigh – Surface Acoustic Waves (R-SAWs) propagating on the Aluminum Nitride (AlN) piezoelectric substrate are described. Phase-shift and amplitude ratio between sample and reference channel are varied by density changes. Likewise, energy loss and output signal changes with static and stably flowing fluid are compared. The results indicate that R-SAW sensor with Aluminum Nitride substrate has suited for liquid measurements.

Key Words: Rayleigh - Surface Acoustic Wave sensor (R-SAW), liquid sensor, Aluminum Nitride

1. Introduction

SAW devices have been used for diverse telecommunication signal processing and filtering for many decades [1]. It may also be used for fluid manipulation including jetting, atomization, drop micromixing and drop translation [2][3][4]. Moreover, their sensitivity to very small changes on the surface due to resonant frequency shift, time delay has also enabled SAW devices used as micro sensors [5].

In a typical surface acoustic wave sensor, mechanical waves are generated and travel through the surface through the piezoelectric effect, either in compressional or shear waves. The shear wave is very attractive for liquid phase sensing applications [6]. The surface-normal wave causes an excessive attenuation in the liquid. On the other hand, when SAWs are in contact with the liquid, leaky SAWs, which are converted from SAWs, are excited and consequently their energy radiates into liquid [7][8]. The SAW velocity depends on some material properties such as elasticity, density, piezoelectricity and quality of substrate. Piezoelectric materials as Lithium Tantalate ($LiTaO_3$), Lithium Niobate ($LiNbO_3$) or quartz, have been commonly used in SAW sensors. Recently, the trend includes materials that are able to propagate SAWs more swiftly, have higher frequency and compatibility with micro-electromechanical systems (MEMS) [9]. Therefore, a new application for SAW sensor based on a piezoelectric thin film of AlN or ZnO becomes a promising device [10].

Piezoelectric Aluminum Nitride (AlN) is a attracting material in the surface acoustic wave technology. It possesses this type of mode along the surface with the high velocity, good temperature stability and large electromechanical coupling coefficient (K^2 =

47%) [11]. Compared to the leaky SAWs generated by piezoelectric materials like LiNbO3, LiTaO3 and quartz, they have larger K^2 values and better temperature stability for certain orientation [12][13][14].

This work presents finite element method (FEM) for the SAW device based on AlN which is implemented via commercial software COMSOL Multiphysics 4.2. Changes in propagation characteristics of SAWs, in terms of time delay of voltage, particle displacement and insertion loss due to the well existence in the middle of path and different density values of liquids are described.

2. Theoretical Background

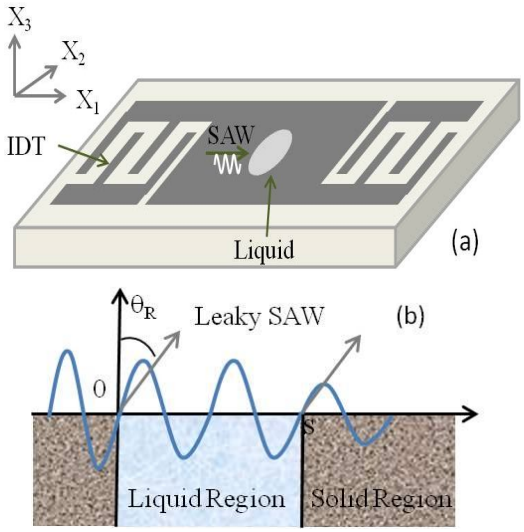

Figure 1. (a) The coordinate system is used in calculations. SAWs travel along X_1 axis.

(b) Ultrasonic radiation in the liquid-solid boundary by SAW.

It is assumed that there exists a liquid medium positioning in the propagation path with the coordinate system as shown in Fig. 1. While X_1 is the wave propagation direction, X_3 is the surface normal direction. The particle displacement and potential are considered to be independent of the X_2 coordinate. The wave propagation in a non-piezoelectric and piezoelectric media is described by the following equation [5][15]:

$$\rho \frac{\partial^2 u_i}{\partial t^2} = \sum_{j,k,l=1}^{3} c_{ijkl} \frac{\partial^2 u_k}{\partial x_j \partial x_l} \quad (1)$$

$$\sum_{i,k,l=1}^{3} e_{ikl} \frac{\partial^2 u_l}{\partial x_k \partial x_i} = \sum_{i,k=1}^{3} \epsilon_{ik} \frac{\partial^2 \emptyset}{\partial x_k \partial x_i} \quad (2)$$

where ρ is the mass density of material, c_{ijkl}, e_{ikl} and ϵ_{ik} are the elastic stiffness, the piezoelectric and the dielectric permittivity tensors (as shown in Appendix), respectively, u_i is the elastic displacement vector and $\emptyset$ is the electric potential.

Therefore, the travelling wave solutions are sought in the form:

$$u_1^f = W_1 \alpha e^{jb_f k x_3} e^{jk(lx_1 - vt)} \quad (3)$$

$$u_3^f = W_1 e^{jb_f k x_3} e^{jk(lx_1 - vt)} \quad (4)$$

$$\emptyset^f = W_2 e^{jb_f k x_3} e^{jk(lx_1 - vt)} \quad (5)$$

Here, u_i^f is the particle displacement, $\emptyset^f$ is the potential in the liquid media, $k = \omega/v$ is the wave number, k is the wave number, v is the velocity of the wave, $b_f = \pm\sqrt{\frac{\rho^f v^2 - c^f}{c^f}}$ is the decay constant of the wave in the X_3 direction and $\alpha = \frac{\rho^f v^2 - c^f b_f^2}{c^f b_f} = \frac{1}{b_f}$ is the relation coefficient. ρ^f is the fluid density and c^f is the elastic constant of the fluid. For Rayleigh waves, the value l equals to unit [16].

When SAWs propagate along the boundary between the liquid and solid medium, leaky waves appear and excite the longitudinal waves into solid at Rayleigh angle θ_R. The boundary conditions are:

$$u_1^f = u_1$$
$$u_3^f = u_3 \quad (6)$$
$$\emptyset^f = \emptyset$$

where the particle displacement u_1, u_3 and the potential $\emptyset$ are in the piezoelectric media.

From application of boundary conditions to Eq. (2), the relation between displacement and potential in the contact of AlN substrate can be illustrated by:

$$\frac{(e_{31}+e_{311})W_1\alpha b_f + e_{113}W_1 + e_{333}b_f^2 W_1}{e_{11}+e_{33}b_f^2} = W_2 \quad (7)$$

Hence, the effect of coupling between displacement and potential in the boundary showed that surface waveforms depend on the liquid density.

3. Design of Saw Liquid Sensing System

3.1. System configuration

The R-SAW liquid sensing system consists of two channels: a reference channel (Channel 1) and a sensing channel (Channel 2). Figure 2 shows the top view and cross-section of the R-SAW sensor.

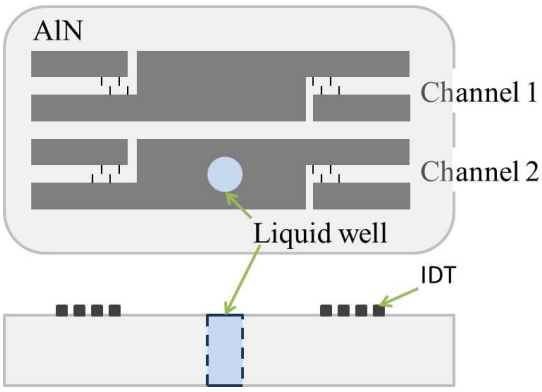

Figure 2: Schematic illustration of two-channel R-SAW sensor and liquid well position.

Table 1. Parameters of Interdigital Transducer

IDT period (acoustic wavelength), Λ (μm)	40
Number of finger pairs, N	3
Aperture length, L (mm)	80
AlN thickness, h (μm)	10
Center frequency f_0 (MHz)	143
SAW velocity (m/s)	5720

The SAW interdigital transducer (IDT) made of Al film is deposited on the surfaces. The measurement is performed using transducer with periodΛ, number of periods N, and aperture length (see Table I).

For the surface acoustic wave delay path, a cylinder well with a diameter of 30 μm is placed in the center of delay line between input and output IDTs. The used liquids are classified into two groups: Standing Group including fluids with density = 1, 2, 3, 4, 6, 8, 10, 11, 12 and 13 g/cm^3, and Moving Group consisting of fluids with velocity $v = 0$, $v = v_z$ =10 μm/s and $2t$ where t is the time.

The piezoelectric surfaces of the developed models are meshed with maximum element size of 32 μm and the IDT boundaries are meshed with a maximum element size of 8 μm. These parameters provided a much denser mesh at the top of the model which is essential to achieve a high accuracy in simulating the SAW propagation.

A sinusoidal voltage 10 V of frequency 143 MHz is applied to the input IDT to generate the needed SAWs. The output voltages in both cases are acquired at the alternating fingers of the output IDT.

3.2. Measurement Method

Therefore, the relation between input and output is given by frequency response function H which is the Fourier transformer of the unit impulse response function of the system. It can be calculated optimally from the input power spectrum density P_{XX} and the cross power spectral density P_{XY} as the following equation [17]:

$$H(f) = \sqrt{\frac{P_{XY}(f)}{P_{XX}(f)}} \quad (8)$$

The well insertion loss is measured with the first output IDT. Since it was long, a larger time window is used to avoiding scattering from substrate edges.

4. Results And Discussion

4.1. Investigating Standing Group

The sensing system is explored within 200 nsec and a time step is 0.09 nsec. The contour plot for total particle displacements of the reference channel and sensing channel with different liquid densities are shown in Figure 3. Total displacements of SAW device with well at almost densities are smaller than that of device without well excepting density equals 12 g/cm^3.And Figure 4 illustrates mode profile in Z coordinate. This mode is referred to as Rayleigh wave because it varies across thickness of devices and involves any change in the thickness of substrate. When SAW medium is contact by liquid, this component generates compressional wave [5]. Therefore, attenuation in the Z coordinate is mainly

reason of attenuation of total displacement. However, with 10 – 40 µm diameter well, the sensing system still detects small output differences.

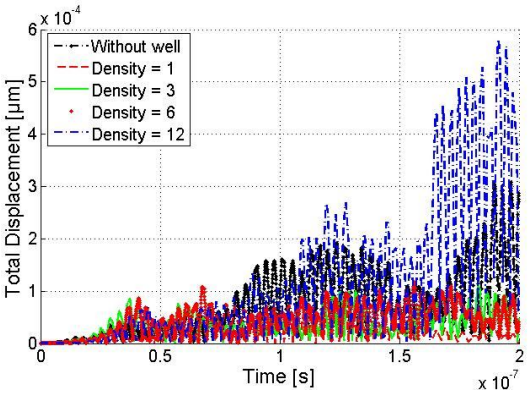

Figure 3: Total displacements of points placed behind the well for standing fluids

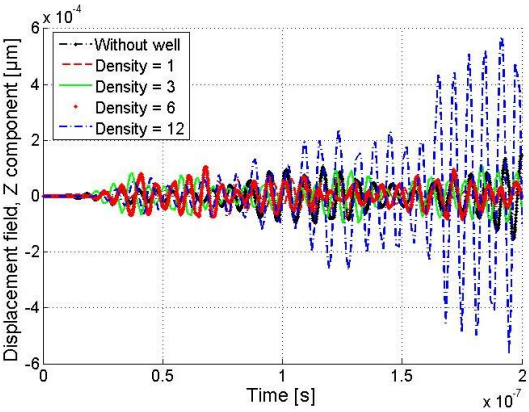

Figure 4: Cross-sectional displacement profiles for the compressional wave mode with different liquid densities.

Response peaks as following in Figure 5 show that amplitude ratio at center frequency of the reference channel reaches a peak whereas its phase shift ploughs to a bottom. In density range from 1 to 12 g/cm^3, the maximum amplitude ratio peak is achieved at 22.9 at density = 8 g/cm^3 and the maximum point of phase shift is at density = 3 g/cm^3.

For comparison, the attenuation response (like insertion loss) of two-port SAW sensor is shown in Figure 6. It is due solely to changes in density. The highest points are at density = 3, 12 g/cm^3 while the lowest peak is at density = 1 g/cm^3. However, amplitude reduction is major cause. It is clearly seen that changes in attenuation differs from one in time delay in Figure 7.

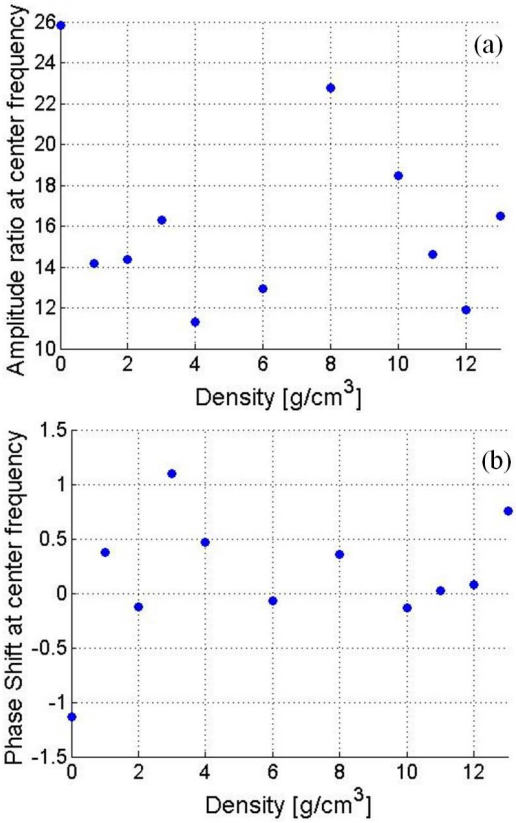

Figure 5: Frequency response at center frequency: (a) Amplitude ratio and (b) Phase shift.

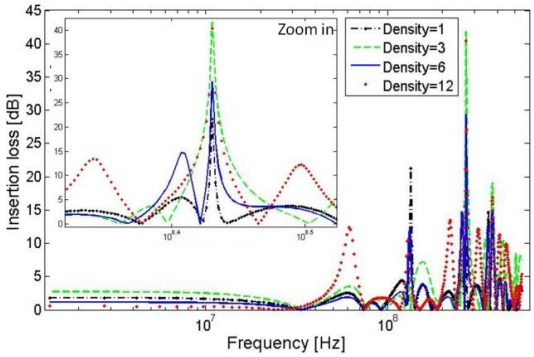

Figure 6: Attenuation response (shown as insertion loss) for the SAW device with liquid density = 1, 3, 6, 12 g/cm^3.

4.2. Investigating Moving Group

When the fluid travels across the well, dissipated power thus Rayleigh wave is less. The more velocity is, the less this mode generates compressional waves like Figure 8.

Nevertheless, it affects shear wave component, thus insertion loss of the moving liquid is higher than the standing liquid as

shown in Figure 9. When velocity is increased, insertion loss is also moved up

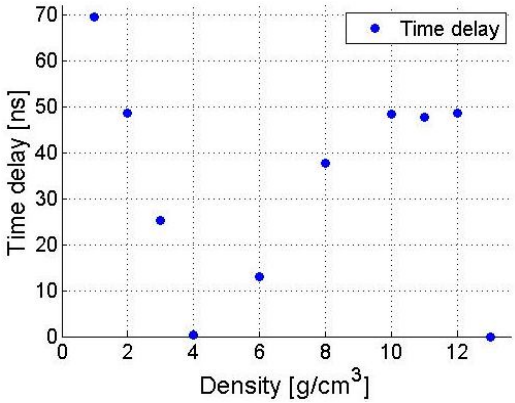

Figure 7: Compared to system without well, time delay of system with well having liquid with density in range 1– 13 g/cm^3.

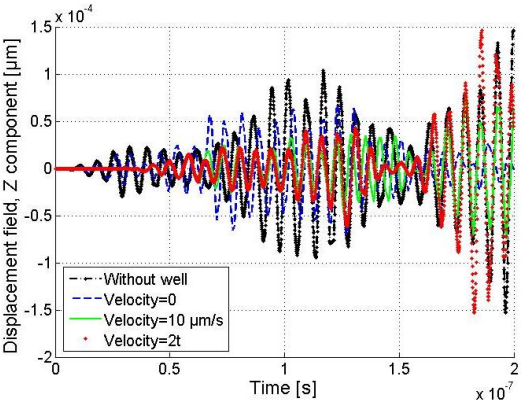

Figure 8: Cross-sectional displacement profiles for the compressional wave mode with moving fluid.

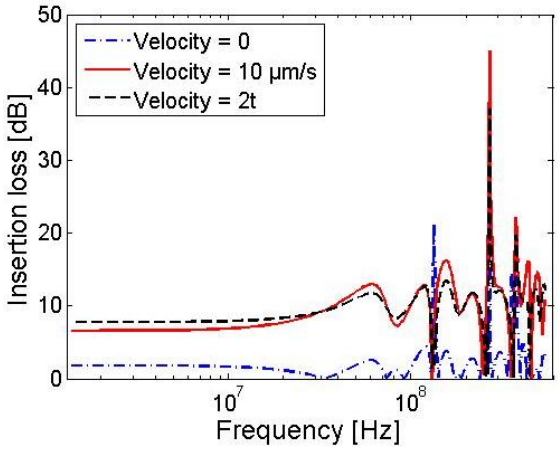

Figure 9: Attenuation response (shown as insertion loss) for the single-crystal AlN substrate when changing velocity.

In future work, more efficient ways of increasing the investigation points and the time, restraining noise from transverse waves as well as decreasing the error tolerance levels may provide more accurate analysis of the performance of the SAW sensors.

5. Conclusion

This paper reports a sensing system using Rayleigh wave mode for the standing liquid group and moving group. They are influenced much by the liquid density and achieve attenuation peak at density = 3 g/cm^3. Phase shift at density =3, 12 g/cm^3 roses to a peak. The 3D finite element analysis was performed to investigate the performance of R-SAW sensor for liquid. The response of SAW devices under alternating-current excitation proved that it is very sensitivity with small changes of the liquid placed in the middle of the two-port SAW delay-line device. This study provides a strong meaning for manufacturing and designing R-SAW sensor in practice.

6. Appendix

Material constants for a non-conducting, non-viscous liquid and Aluminum Nitride piezoelectric in class 6 mm symmetry in simulation [18]:

$$c^f = \begin{pmatrix} c^f & c^f & c^f & 0 & 0 & 0 \\ c^f & c^f & c^f & 0 & 0 & 0 \\ c^f & c^f & c^f & 0 & 0 & 0 \\ 0 & 0 & 0 & 0 & 0 & 0 \\ 0 & 0 & 0 & 0 & 0 & 0 \\ 0 & 0 & 0 & 0 & 0 & 0 \end{pmatrix}$$

$$c = \begin{pmatrix} c_{11} & c_{12} & c_{13} & 0 & 0 & 0 \\ c_{12} & c_{11} & c_{13} & 0 & 0 & 0 \\ c_{13} & c_{13} & c_{33} & 0 & 0 & 0 \\ 0 & 0 & 0 & c_{44} & 0 & 0 \\ 0 & 0 & 0 & 0 & c_{44} & 0 \\ 0 & 0 & 0 & 0 & 0 & \frac{c_{11}-c_{12}}{2} \end{pmatrix}$$

$$e = \begin{pmatrix} 0 & 0 & 0 & 0 & e_{15} & 0 \\ 0 & 0 & 0 & e_{15} & 0 & 0 \\ e_{31} & e_{31} & e_{33} & 0 & 0 & 0 \end{pmatrix}$$

$$\epsilon = \begin{pmatrix} \epsilon_{11} & 0 & 0 \\ 0 & \epsilon_{11} & 0 \\ 0 & 0 & \epsilon_{33} \end{pmatrix}$$

where c_{11} = 345 GPa, c_{33} = 395 GPa, c_{44} = 118 GPa, c_{12} = 125 GPa, c_{13} = 120 GPa, c^f= 2.25 GPa, e_{15} = -0.48 Cm^{-2}, e_{31} = -0.58 Cm^{-2},

e_{33} = 1.55 Cm^{-2}, $\square_{11}$ = 9, $\square_{33}$ = 11andρ = 4600 Kgm^{-3}.

Acknowledgement

This work is partly supported by VNU project QG.11.30

References

[1] D. Morgan, "*Surface Acoustic Wave Filters*", Elsevier, New York (1985).

[2] M. K. Tan, J. R. Friend and L. Y. Yeo, "*Microparticle collection and concentration via a miniature surface acoustic wave device*", Lab Chip 7- 618(2007).

[3] M. K. Tan, J. R. Friend and L. Y. Yeo, *Proceedings of the 16th AustralasianFluid Mechanics Conference*, Gold Coast, Queensland, Australia, 3–7December 2007, edited by P. Jacobs, P. McIntyre, M. Cleary, D. Buttsworth, D. Mee, R. Clements, R. Morgan, and C. Lemckert (Univer-sity of Queensland, Brisbane, 2007), pp. 790–793.

[4] A. Wixforth, C. Strobl, Ch. Gauer, A. Toegl, J. Scriba and Z. v. Gutten-berg, "*Acoustic manipulation of small droplets*", Anal. Bioanal. Chem. 379, 982 (2004).

[5] S. Shiokawa and J. Kondoh, "*Surface acoustic wave sensors*", Jpn. J. App. Phys., Part 1, 2004, 43, 2799-2802.

[6] D. S. Ballantine, R. M. White, S. J. Martin, A. J. Ricco and E. T. Zellers, G. C. Frye and H. Wohltjen, "*Acoustic wave sensors*", Academic Press, 1997.

[7] S. Shiokawa, Y. Matsui and T. Ueda, "*Liquid streaming and droplet formation caused by leaky Rayleigh waves*", IEEE Ultrasonics Symposium – 643, 1989.

[8] Thu-Hang B., Tung B. D., Dat N. T. and Trinh C. D., "*3-D Finite Element Modeling of SAW sensing system for liquids*", 2012 IEEE/ASME International Conference on Advanced Intelligent Mechatronics, p.782-787.

[9] A.N. Cleland, "*Foundations of Nanomechanics. From Solid-State Theory to Device Applications*" , Springer 2002, ISBN 3540436618.

[10] G. Chung, D. T. Phan, "*Finite Element Modeling of Surface Acoustic Waves in Piezoelectric Thin Films*", J. of Korean Phys. Society, Vol. 57, No. 3, 2010.

[11] G. Bu, D. Ciplys, M. Shur, L. J. Schowalter, S. Schujman and R. Gaska, "*Surface acoustic wave velocity in Single-Crystal AlN substrate*", IEEE Trans. on Ultrasonics, Ferroelectrics and Frequency Control, Vol. 53, No. 1.

[12] A. Takayanagi, K. Yamanouchi and K. Shibayama, "*Piezoelectric leaky surface wave in $LiNbO_3$*", Appl. Phys. Lett., Vol. 17, No. 5, 225-227(1970).

[13] K. Yamanouchi and M. Takeuchi, "*Application for piezoelectric leaky surface waves*", Ultrasonics Symposium, pp. 11-18(1990).

[14] S. Tonami, A. Nishikata and Y. Shimizu, "*Characteristics of leaky surface acoustic waves propagating on $LiNbO_3$ and $LiTaO_3$ substrates*", Jpn. J. Appl. Phys., Part 1, Vol. 34, No. 5B, 2664-2667(1995).

[15] J. J. Campell and W. R. Jones, "*A method for estimating optimal crystal cuts and propagation directions for excitation of piezoelectric substrate waves*", *IEEE Trans. on Sonics and* Ultrasonics, vol. SU-15, No. 4, 1968.

[16] G. Bu, D. Ciplys and M. S. Shur, L. J. Schowalter and S. B. Schujman, "*Leaky Surface Acoustic Waves in single-Crystal AlN Substrate*", International J. of High Speed Electronics and Sys., Vol. 14, No. 3 (2004) 837-846.

[17] A. Leon-Garcia, "*Probability and Random Processes for Electrical Engineering*", Addison-Wesley Publishing Company, 2nd Ed.

[18] J. G. Gualtiei, J. A. Kosinski and A. Ballato, "*Piezoelectric materials for acoustic wave applications*", IEEE Tran. on Ultrasonics, Ferroelectrics and Frequency control, vol. 41, No. 1, 1994.

[19] COMSOL Multiphysics Reference Guide, Ver. 3.5a, 2008.

[20] COMSOL Multiphysics Matlab interface Guide, Ver. 3.5a, 2008.

The 2nd International Conference on Engineering Mechanics and Automation (ICEMA2)
Hanoi, August 16-17, 2012
ISBN: 978-604-913-097-7

Nonlinear Modeling and Optimal Design Parameters of Hydraulic Engine Mounts

Do Van Diep[a]

[a] *Le Quy Don Technical University, 100 Hoang Quoc Viet St, Cau Giay District, Ha noi, Vietnam, dvdiepvcg@gmail.com*

Abstract

In this study, a typical nonlinear model of hydraulic engine mount (HEM) is developed to analyses the vibrations of the engine transmission unit mounted on the vehicle. A half-vehicle model is used to evaluate the optimization results, and to determine whether it is enough to optimize the HEM in the simplified models to achieve the desired performance, or it is required to precede the optimization for the vehicle model or even a more intricate model. The HEMs are optimized to improve the vehicle ride comfort using the Sequential Quadratic Programming (SQP) method. When embedded into the half-vehicle system, the HEMs efficiently provide high amplitude-sensitive damping and tune the engine bounce mode and to reduce the Noise, Vibration and Harshness perceived by driver and to improve the ride comfort.

Key Words: Vibration isolation, Hydraulic Engine Mount, Optimization

1. Introduction

The modern engine transmission unit (ETU) mounting systems have been successfully used to reduce the Noise, Vibration and Harshness (NVH) perceived by driver and to improve the ride comfort. The main vehicle NVH sources are low frequency road roughness and high frequency engine excitation force. To satisfy the requirements, ETU mounts should be capable of adequate isolation in a wide range of frequency. Different kinds of engine mounting system, from elastomeric to hydraulic, and from passive to active, have been develop to improve the mount performance. Almost constant stiffness and damping of rubber mounts with respect to frequency, leaded vehicle industries to develop hydraulic or pneumatic engine mounts.

Many recent studies have focused on studying and designing of hydraulic engine mount (HEM). A HEM equipped with inertia track and decoupler performs a desirable performance in a wide range of frequency "Geisberger, 2002". The unfavorable high stiffness in fluid resonance frequency motivated the development of bell plate. Equipping the HEM with bell plate provides a good performance in all working frequencies "Brach, 1993). These are inherently nonlinear devices and their steady-state characteristics are extensively reported and used for design, usually in the form of spectrally varying and amplitude sensitive

stiffness spectra based on non-resonant type sinusoidal testing methods.

In this study, hydraulic engine mounts are optimized to improve the vehicle ride comfort using the nonlinear optimization method called Sequential Quadratic Programming (SQP) method "Papalambros and Wilde, 1988". A half-vehicle model is used to evaluate the optimization results, and to determine whether it is enough to optimize the HEM in the models to achieve the desired performance, or it is required to precede the optimization for the vehicle model or even a more intricate model.

2. Mathematical models

Reference model of half-vehicle investigated in this study consists of an ETU body mounted to vehicle body, front and rear wheel bodies jointed to the vehicle body via suspension system, as demonstrated in Fig. 1.

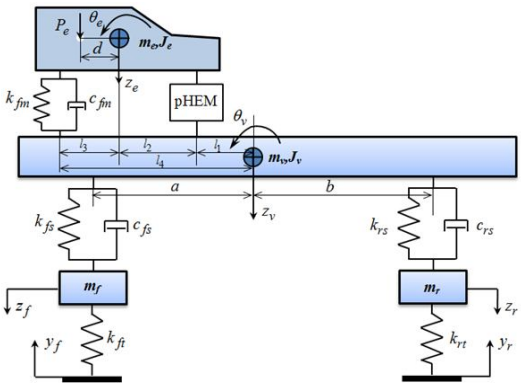

Figure 1. Half-vehicle model incorporating HEM system

In this system, ETU is modeled as a 2DOF rigid body, mounting to the vehicle body via a front rubber mount and a rear HEM. Vehicle body and chassis are modeled as a unified body capable to move in bounce and roll modes. Front and rear wheels are connected to it via suspension system; each is assumed as a rigid body travels in vertical direction and is connected to the ground through the tire. Suspension system and tires are modeled as linear springs and dampers.

The considered system has six degrees of freedom: z_e is the vertical displacement of the ETU; z_v is the vertical displacement of chassis mass; z_f and z_r are the vertical displacements of front and rear tires mass; θ_v and θ_e are the rotary angle of the chassis and ETU mass at the center of gravity.

An inline four-cylinder engine is studied whose engine force arises from the motion of engine inner bodies including piston, connecting rod, crankshaft, and balancing system. The engine force acting on the engine body is the only source of excitation. The engine excitation force can be expressed in the format "Ohadi, 2007":

$$P_e = m_0 \omega_d^2 \sin \omega_d t \tag{1}$$

The force transmitted to front and rear wheels from tires:

$$F_{ft} = k_{ft}\left(z_f - y_f\right), F_{rt} = k_{rt}\left(z_r - y_r\right). \tag{2}$$

where, y_f and y_r are the irregular excitations from the road surface; k_{ft} and k_{rt} are the spring stiffness of front and rear tires, respectively.

The force transmitted to vehicle body from suspension system:

$$\begin{aligned} F_{fs} &= k_{fs}\left(z_v - a\theta_v - z_f\right) + c_{fs}\left(\dot{z}_v - a\dot{\theta}_v - \dot{z}_f\right) \\ F_{rs} &= k_{rs}\left(z_v + b\theta_v - z_r\right) + c_{rs}\left(\dot{z}_v + b\dot{\theta}_v - \dot{z}_r\right), \end{aligned} \tag{3}$$

in which k_{fs}, c_{fs} and k_{rs}, c_{rs} are the spring stiffness and damping coefficient of the front and rear suspensions, respectively.

The force transmitted to vehicle body from front rubber mount:

$$\begin{aligned} F_{fm} = {} & k_{fm}\left(z_e - l_3\theta_e - z_v + l_4\theta_v\right) \\ & + c_{fm}\left(\dot{z}_e - l_3\dot{\theta}_e - \dot{z}_v + l_4\dot{\theta}_v\right) \end{aligned} \tag{4}$$

where k_{fm} and c_{fm} are the spring stiffness and damping coefficient of front rubber mount.

The HEM of interest is structurally similar to the conventional HEM, generally, consist of two chambers, main rubber and hydraulic part where create dynamic behavior in the system. In low amplitude and

high frequency excitation fluid flow through the decoupler, due to minimum of decoupler resistance this system acts as normal mount. In high amplitude excitations the decoupler stick to engine and flow go through inertia track. The cross section of a HEM with decoupler and inertia track shown in Figure 2(a) and the mathematical model is illustrated in Figure 2(b).

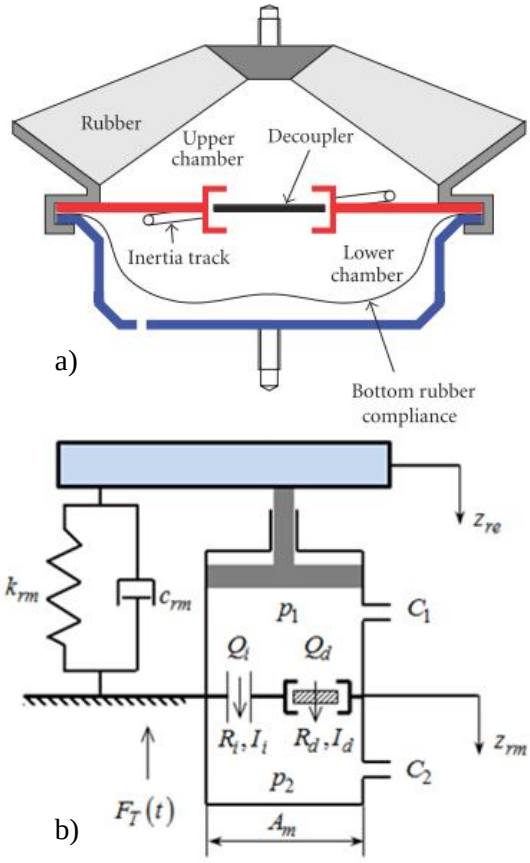

Figure 2. (a) HEM with inertia track and decoupler, (b) Lumped parameter system model of HEM

Excitation causes relative motion of the two ends of the HEM; thus pressure varies in the chambers which motivates the fluid to flow through the two passages. The fluid passing the inertia track, which is a long narrow passage, causes a high damping. But in high frequency behavior, low damping is required which motivated the creation of the decoupler "in Haddow and Brach (1993)". In high frequencies, the decoupler disk, which lies on one of its limits and blocks the decoupler passage in low frequencies, stands in the middle, and the pressure difference between the upper and lower chambers causes the fluid to flow through the decoupler - which is a short wide passage- instead of the inertia track.

Equations of this model consist of continuity equations of the upper and lower chambers and coupled momentum equations of two orifices of decoupler and inertia track, which are relatively indicated by equations

$$C_1 \dot{p}_1 = A_m \dot{X}_e - Q_i - Q_d \tag{5}$$

$$C_2 \dot{p}_2 = Q_i + Q_d \tag{6}$$

$$\begin{aligned} p_1 - p_2 = {} & I_i \dot{Q}_i + \left(R_{i1} + R_{i2}\left|Q_i\right|\right) Q_i \\ & + I_d \dot{Q}_d + \left(R_{d1} + R_{d2}\left|Q_d\right|\right) Q_d \end{aligned} \tag{7}$$

in which C_1 and C_2 are the compliances of upper chamber and lower chamber, respectively. p_1 and p_2 represent the pressure of upper chamber and lower chamber. Q_i and Q_d are the flow passing through inertia track and decoupler, respectively. I_i and I_d represents the inertia of track and decoupler passages. R_{i1}, R_{i2} and R_{d1}, R_{d2} represents the linear and nonlinear resistances of each passage due to laminar flow and turbulent flow through track and decoupler. A_m is the area of the HEM and X_e is the displacement of the upper end of the HEM.

Momentum equation is formed by considering inertia track and decoupler orifices as control volume simultaneously. The number of dynamic variables of system is 4 (Q_i, Q_d, p_1, p_2) and the number of equations is reduced to 3 because of the coupling of momentum equations for forming state space equations, another independent equation should be derived from internal operation of orifices.

The transmitted force equation as dynamic response of the model is defined as equation (8), in which A_d, the relation of nonlinear cross section of decoupler is added.

$$\begin{aligned} F_{rm} = {} & k_{rm}(z_{re} - z_{rm}) + c_{rm}(\dot{z}_{re} - \dot{z}_{rm}) \\ & + (A_m - A_d) p_1 + A_m p_2 + A_d R_d Q_d \end{aligned} \tag{8}$$

where k_{rm} and c_{rm} are the stiffness and viscous damping of elastomeric rubber element. z_{re} and z_{rm} are the displacement of ETU and chassis at the points associated with HEM.

$$\begin{aligned} z_{re} - z_{rm} &= z_e + l_2\theta_e - z_v + l_1\theta_v \\ \dot{z}_{re} - \dot{z}_{rm} &= \dot{z}_e + l_2\dot{\theta}_e - \dot{z}_v + l_1\dot{\theta}_v \end{aligned} \tag{9}$$

Clear that due to the nonlinear properties of the hydraulic flow so characteristic of the HEM is nonlinear.

Based on the model in Figure 1 and the equations from (2)-(4) and (8), the governing equations of motion for the half-vehicle system

$$\begin{cases} m_f \ddot{z}_f = F_{fs} - F_{ft} \\ m_r \ddot{z}_r = F_{rs} - F_{rt} \\ m_v \ddot{z}_v = F_{fs} + F_{rs} - F_{fm} - F_{rm} \\ J_v \ddot{\theta}_v = aF_{fs} - bF_{rs} - l_1 F_{rm} - l_4 F_{fm} \\ m_e \ddot{z}_e = P_e + F_{fm} + F_{rm} \\ J_e \ddot{\theta}_e = l_3 F_{fm} - l_2 F_{rm} - dP_e \end{cases} \tag{10}$$

where, m_f, m_r, m_v and m_e are mass of the front wheel, the rear wheel, the vehicle body and the ETU. J_v and J_e are the mass moment of inertia for the vehicle body and ETU with respect to the transverse axis passing through the gravity center.

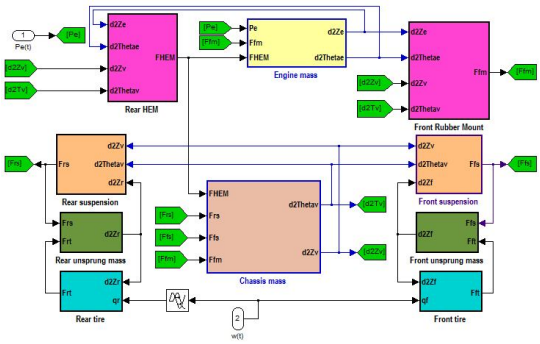

Figure 3. The simulation model of half-vehicle model incorporating HEM system by using Matlab-simulink software

Base on the equations system the nonlinear simulation model of half-vehicle model incorporating HEM system by using MATLAB/SIMULINK was developed and showed as in Fig.3. Except for the decoupler, nonlinear components can be modeled via continuous nonlinear functions.

3. Optimal Design Parameters of HEM

In this section, the parameters of the HEM are designed by using the model is built previous section.

The performance characteristics of the HEM can be better assessed in terms of the force transmissibility (the ratio of the force transmitted to the chassis with the engine excitation force) and the motion transmissibility (the ratio of the relative displacement between the ETU and the chassis with the road excitation). For the model shown in Figure 1, the ratios are defined as:

$$T_F = \frac{F_{fm} + F_{HEM}}{P_e} \tag{11}$$

$$T_D = \frac{z_e - [z_v - (l_1 + l_2)\theta_v]}{y_f} \tag{12}$$

The purpose of HEMs mount is to reduce the total force transmitted to the chassis structure and also to reduce the road excitation transmitted to the ETU. Thus, the criteria for choosing the optimum parameters of the HEM is minimize the force transmitted from the ETU through the mount. The force transmission of the HEM can be effectively evaluated in terms of the root mean square (RMS) values of the force transmissibility and motion transmissibility. The RMS value of force transmissibility and the motion transmissibility are defined as:

$$T_{Frms} = \sqrt{\frac{1}{T}\int_0^T T_F^2(t)dt} \tag{13}$$

$$T_{Drms} = \sqrt{\frac{1}{T}\int_0^T T_D^2(t)dt} \tag{14}$$

where T is the observation period. T_{Frms} and T_{Drms} are the RMS force transmissibility and the RMS motion transmissibility corresponding to the frequency.

HEM parameters including $k_{rm}, c_{rm}, C_1, C_2, I_i, R_i, I_d, R_d$ and A_m are studied to determine the design parameters. However, the parameters have a great influence on vibration behavior of the system "in Arai, 1993". Thus, the design parameters that greatly affect vibration isolation effectiveness were considered as design variables such as the effective piston area, inertia track, inertia of decoupler, inertia track resistance, decoupler resistance, rubber stiffness and compliance in upper and lower chambers. The vector of design parameters of the HEM is defined as:

$$\mathbf{x} = \left\{k_{rm}, A_m, I_i, R_i, I_d, R_d, C_1, C_2\right\}^T \tag{15}$$

The objective function is optimized:

$$f(\mathbf{x}) = T_{Frms} + T_{Drms} \tag{16}$$

In this paper, for the optimal design of the non-linear HEM with inertia track and decoupler they used sequential quadratic programming technique to minimize the transmitted vibration of the HEM. The SQP methods belong to the most powerful optimization algorithms we know today for solving differentiable nonlinear programs. The theoretical background is described for example "in Stoer, 1987". From a more practical point of view, the SQP method is also introduced in the books of "Papalambros and Wilde, 1988". Their excellent numerical performance has been tested and compared with other methods for many years, see "Edgar and Himmelblau, 1988", and they belong to the set of most frequently used algorithms for solving practical optimization problems.

We can be found $\mathbf{x}$ which minimizes $f(\mathbf{x})$ by using the SQP method. Here, computing procedure of the SQP method is shown as follows:

1. Initial solution $\mathbf{x}^{(0)}$, Hessian approximation $\mathbf{B}^{(0)}$ and penalty parameter $r > 0$ are set up. And k = 0.
2. Quadratic programming problem is defined by objective function and constrained condition. When it is solved, $\mathbf{d}^{(k)} = \mathbf{x}^{(k+1)} - \mathbf{x}^{(k)}$ and Lagrange multiplier $\mathbf{u}^{(k+1)}$ are determined.

$$\nabla f\left(\mathbf{x}^{(k)}\right)^T \mathbf{d} + \frac{1}{2}\mathbf{d}^T \mathbf{B}^{(k)} \mathbf{d} K \to \min \tag{17}$$

$$c\left(\mathbf{x}^{(k)}\right) + \nabla c\left(\mathbf{x}^{(k)}\right)^T \mathbf{d} \geq 0 \tag{18}$$

3. Penalty parameter is updated. Here $\sigma > 0$

$$r = \begin{cases} \max\left\{\left|u_i^{(k+1)}\right| : i = 1,2,...,m\right\} + \sigma \\ \text{if } r < \max\left\{\left|u_i^{(k)}\right| : i = 1,2,...,m\right\} \\ r, \text{ else} \end{cases} \tag{19}$$

4. Linear search is done, step width $t^{(k)} > 0$ is searched and $\mathbf{x}^{(k+1)} = \mathbf{x}^{(k)} + t^{(k)}\mathbf{d}^{(k)}$.
5. Hessian approximation B is updated by Broyden–Fletcher–Goldfarb–Shanno (BFGS) algorithm.
6. When convergence condition is fulfilled, this calculation is finished. Otherwise $k = k + 1$ and it returns to 2.

The flow chart of the optimization process is shown in Fig. 4.

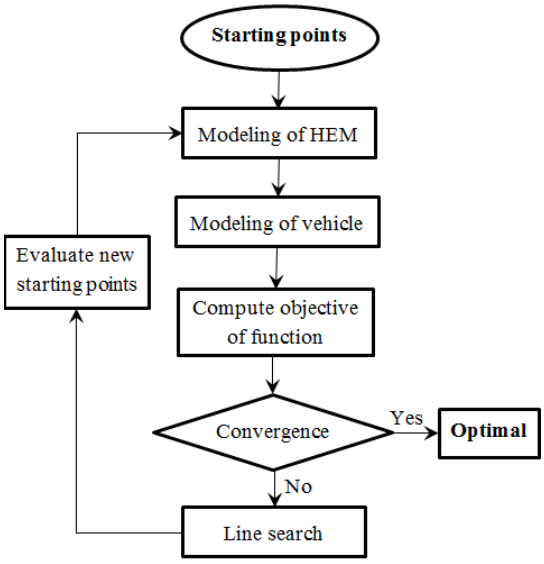

Figure 4. The flow chart of optimization process

Application model and the optimal method for the vehicle with parameters are as follows:

$m_v = 1410\text{kg}; m_e = 160\text{kg}; m_f = m_r = 74\text{kg};$

$J_v = 1620\text{kgm}^2; J_e = 81\text{kgm}^2; a = 1,25\text{m};$

$b = 1,2\text{m}; l_1 = 0,31\text{m}; l_2 = 0,833\text{m}; l_3 = 0,187\text{m};$

$k_{ft} = k_{rt} = 250000\text{N/m}; k_{fs} = 57300\text{N/m};$

$k_{rs} = 63600\text{N/m}; c_{fs} = c_{rs} = 4350\text{Ns/m};$

$k_{fm} = 650000\text{N/m}; c_{fm} = 4340\text{Ns/m}$

The frequencies used in the SQP for low frequency range model and high frequency range model were calculated from the simulation of the mathematical model. To obtain effective vibration for the high and low frequency range models the SQP was combined with low and high frequency range models. Obtain of the optimal parameters of the HEM with the parameters of the vehicle are as following:

$k_{rm} = 2,25.10^5\ \text{N/m}; A_m = 2,5.10^{-3}\ \text{m}^2;$

$I_i = 3,8.10^6\ \text{Ns}^2/\text{m}^5; R_i = 1,05.10^8\ \text{Ns/m}^5;$

$I_d = 7,5.10^4\ \text{Ns}^2/\text{m}^5; R_d = 1,17.10^7\ \text{Ns/m}^5;$

$C_1 = 3.10^{-11}\ \text{m}^5/\text{N}; C_2 = 2,5.10^{-9}\ \text{m}^5/\text{N}.$

The dynamic stiffness of the HEM with the design parameters is shown on Fig. 5. The force transmissibility and motion transmissibility through HEM is shown in Fig. 6 and Fig.7

Time histories of the relative displacement through HEM and the random disturbance roads when the vehicle is moving on the asphalt and gravel road with constant velocity v = 100 km/h and the engine speed at 4000 rpm as shown on Fig.8.

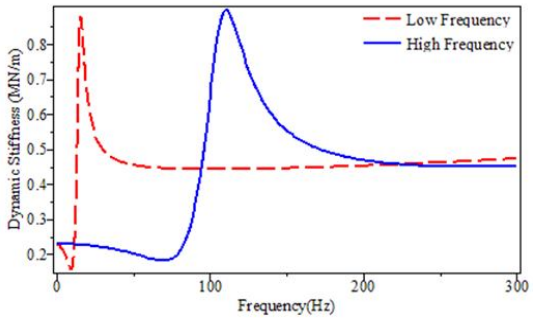

Figure 5. Dynamic stiffness of the HEM

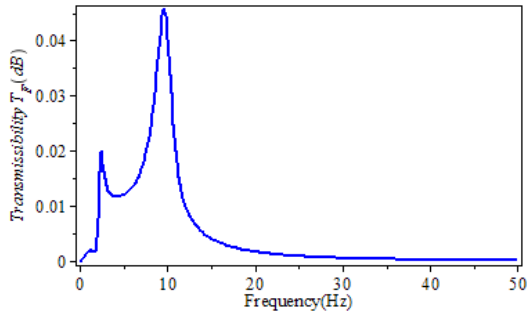

Figure 6. Force transmissibility

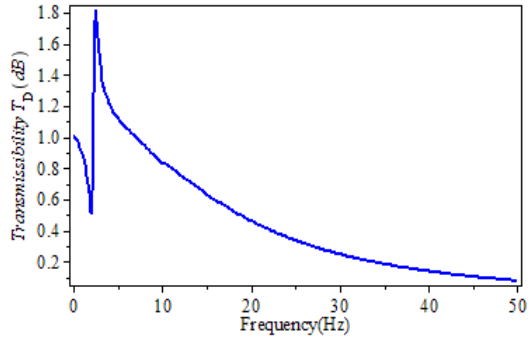

Figure 7. Motion transmissibility

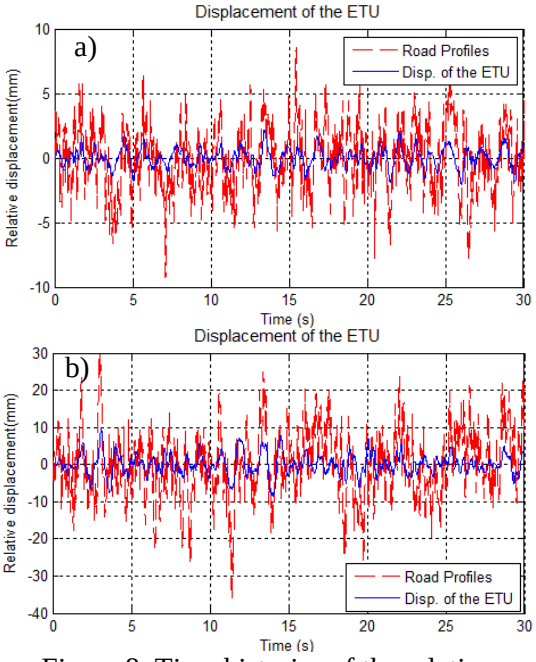

Figure 8. Time histories of the relative displacement through HEM and the random disturbance roads when moving on the asphalt (a) and gravel (b) road

4. Conclusion

Hydraulic engine mounts are important vehicle components to isolate the vehicle

structure from ETU vibration. A parameter optimization methodology for an HEM based on SQP optimization method is proposed in this study. A half-vehicle model incorporating HEM system is a nonlinear model with many degrees of freedom. The simulation results have proved effectively in reducing vibration and noise, improving the system under the engine excitation force and the excitement from the road.

Acknowledgements

This research is funded by Vietnam National Foundation for Science and Technology Development (NAFOSTED) under grant number: "107.04-2011.13".

References

A. Geisberger, A. Khajepour and F. Golnaraghi (2002). Non-linear modeling of hydraulic mounts: theory and experiment. *Journal of Sound and vibration*, 249(2), pp. 371-397.

Brach R. M. and Haddow A. (1993). On the dynamic response of hydraulic engine mounts. *SAE Technical Paper Series*, 931321.

Edgar T.F. and Himmelblau D.M. (1988). *Optimization of Chemical Processes*. Mc-Graw Hill.

Ohadi, A. and Fakhari, V. (2007). Effect of bell plate on vibration behavior of automotive engine supported by hydraulic engine mounts. *SAE 2007 Noise and Vibration Conference and Exhibition*, SAE paper 2007-01-2364.

Papalambros P.Y. and Wilde D.J. (1988). *Principles of Optimal Design*. Cambridge University Press.

Stoer J. and Tapia R.A. (1987). On the characterization of q-superlinear convergence of quasi-Newton methods for constrained optimization. *Mathematics of Computation*. Vol. 49 pp. 581-584.

T. Arai, T. Kubozuka and S. D. Gray (1993). Development of an angine mount optimization method using modal parameters. *SAE Technical Paper Series*, 932898.

The 2nd International Conference on Engineering Mechanics and Automation (ICEMA2)
Hanoi, August 16-17, 2012
ISBN: 978-604-913-097-7

Some types of dynamic vibration absorbers in pendulum structures

La Duc Viet[a], Nguyen Xuan Nguyen[b]

[a] *Institute of Mechanics, 264 Doi Can, Hanoi, Viet Nam*
[b] *Hanoi University of Science, 334 Nguyen Trai, Hanoi, Viet Nam*

Abstract

The dynamic vibration absorber (DVA) moving in the tangential or in the normal direction of a pendulum's orbit can reduce the free vibration of the pendulum. This paper discusses the analytical methods to design the DVA based on the stability maximization criterion. Moreover, two schemes of combination of two orthogonal DVA motions in a pendulum are presented. The numerical calculations are performed to show the effectiveness of each type of DVA.

Key Words: Vibration control, dynamic vibration absorber, pendulum structure

1. Introduction

Dynamic vibration absorber (DVA), which consists of a moving mass attached to the main structure through springs and dampers, is a well-known device to suppress vibration. In practice, some types of structures such as ropeway gondola, crane loads or floating structures (ships, tension leg platform) should be described by pendulum models. Using DVA was a mean for reducing the swing of pendulum structures [Anh et al 2007, Matsuhisa et al 2003,2005, Tondl et al 2000, Viet et al 2011a, 2011b, 2012]. However, the effect of DVA on a pendulum structure can be quite different from that on a spring-mass structure. Especially, the effects of DVA's locations and pendulum's nonlinearity are important. Some types of installation of DVA in a pendulum structure are shown in Fig.1.

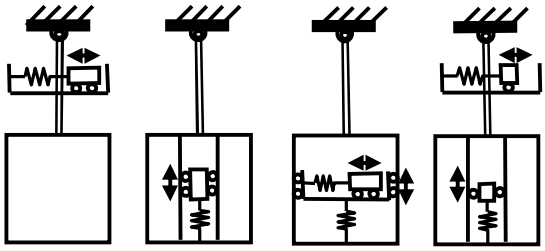

Figure 1. Some types of DVA attachments in a pendulum structure

This paper presents two types of DVA moving in two orthogonal directions and their combinations. The analytical analyses and numerical calculations are performed to show the effectiveness of each type of DVA.

2. DVA moving in tangential direction

2.1. Equations of motion

The DVA moves in the tangential direction of the pendulum's orbit as shown in Fig.2

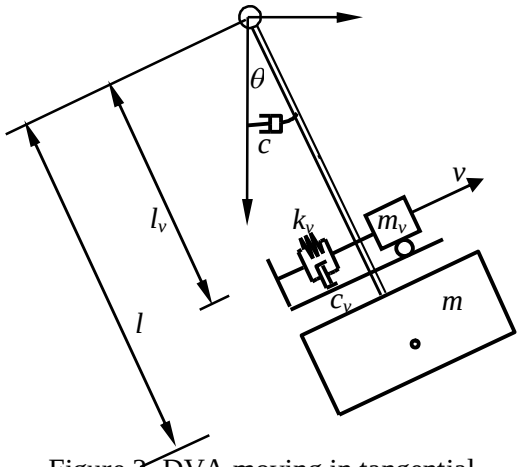

Figure 2. DVA moving in tangential direction

Consider a pendulum structure having a concentrated mass m and a pendulum length l. Denote c as the structural damping coefficient, θ is the rotational angle of the pendulum and g is the acceleration of gravity. The notation v is the DVA displacement in tangential direction, l_v is the distance between the fulcrum and the DVA in the static condition, m_v is the DVA mass, k_v is the DVA spring constant, c_v is the DVA damping coefficients.

To write the equations in non-dimensional forms, some parameters are introduced in Table 1.

The motion equations are derived as following non-dimensional form:

$$\begin{aligned}&\left(1+\mu_v\left(\gamma_v^2+z_v^2\right)\right)\ddot{\theta}+2\zeta_s\dot{\theta}+\left(1+\mu_v\gamma_v\right)\sin\theta\\&\quad+\mu_v\gamma_v\ddot{z}_v+\mu_v z_v\cos\theta+2\mu_v z_v\dot{z}_v\dot{\theta}=0\\&\ddot{z}_v+2\zeta_v\dot{z}_v+\alpha_v z_v+\gamma_v\ddot{\theta}-\dot{\theta}^2 z_v+\sin\theta=0\end{aligned} \tag{1}$$

in which the dot operator from now denotes the differentiation with respect to normalized time τ. The DVA moving in the tangential direction works in the linear zone. To the first order, ignore the structural damping ratio ζ_s, equations (1) are written in the state space form as:

$$\dot{\mathbf{p}}=\mathbf{A}\mathbf{p} \tag{2}$$

where the state vector $\mathbf{p}$ and the system matrix $\mathbf{A}$ are given by:

$$\mathbf{p}=\begin{bmatrix}\theta & \dot{\theta} & z_v & \dot{z}_v\end{bmatrix}^T;$$

$$\mathbf{A}=\begin{bmatrix}0 & 1 & 0 & 0\\ -1 & 0 & \mu_v\left(\gamma_v\alpha_v-1\right) & 2\mu_v\gamma_v\zeta_v\\ 0 & 0 & 0 & 1\\ \gamma_v-1 & 0 & \mu_v\gamma_v\left(1-\alpha_v\gamma_v\right)-\alpha_v & -2\zeta_v\left(1+\mu_v\gamma_v^2\right)\end{bmatrix} \tag{3}$$

Table 1. Symbols used for tangential DVA

Symbol	Description
$\omega_s=\sqrt{\frac{g}{l}};$ $\zeta_s=\frac{c}{2l^2m\omega_s}$	Natural frequency and structural damping ratio of the pendulum
$\tau=\omega_s t$	Non-dimensional time with time scale ω_s^{-1}
$\mu_v=\frac{m_v}{m}$	DVA mass ratio
$\alpha_v=\frac{k_v/m_v}{\omega_s^2}$	Square of DVA natural frequency ratio
$\zeta_v=\frac{c_v}{2m_v\omega_s}$	DVA damping ratio
$\gamma_v=\frac{l_v}{l}$	Location parameter specifying the DVA position
$z_v=\frac{v}{l}$	Non-dimensional form of the DVA displacement

2.2. Parameter optimization

It is well-known that there are many ways to determine the linear DVA parameters depending on the chosen criteria [Soong et al 1997, Krenk 2005, Warburton 1982]. In this paper, the double root condition is used. The characteristic polynomial of $\mathbf{A}$ is given by:

$$\begin{aligned}P_A(s)&=s^4+2\zeta_v\left(1+\mu_v\gamma_v^2\right)s^3\\&+\left(\alpha_v\left(1+\mu_v\gamma_v^2\right)+1-\mu_v\gamma_v\right)s^2\\&+2\zeta_v\left(1+\mu_v\gamma_v\right)s+\alpha_v\left(1+\mu_v\gamma_v\right)-\mu_v\end{aligned} \tag{4}$$

The optimal values of α_v and ζ_v are found such that the polynomial has four roots as

$$s_1=s_2=-a_1+\mathrm{i}a_2,\ s_3=s_4=-a_1-\mathrm{i}a_2 \tag{5}$$

in which a_1 and a_2 are positive numbers and "i" is the imaginary unit. The conditions (5) are called the double pole or repeated root conditions [Anh et al 2007, Krenk 2005, Viet 2012]. The problem has analytical solutions,

which were presented in detail in [Anh et al 2007]. Omit the detailed calculations, the optimal parameters can be obtained as:

$$\alpha_v^* = \frac{1+\mu_v\gamma_v}{\left(1+\mu_v\gamma_v^2\right)^2} + \frac{\mu_v}{1+\mu_v\gamma_v}$$
$$\zeta_v^* = \frac{\left|1-\gamma_v\right|\sqrt{\mu_v}}{\left(1+\mu_v\gamma_v^2\right)^{3/2}\left(1+\mu_v\gamma_v\right)^{1/2}} \quad (6)$$

where α_v^* and ζ_v^* respectively are the optimal values of α_v and ζ_v. Because the mass ratio μ_v is often small in many practical case, the optimal values α_v^* is near 1 to produce resonance. The disadvantage of the tangential DVA comes from the location parameter γ_v. As seen from (6), the absolute value $|\gamma_v$-1| should be as large as possible. This means the DVA located near the center of oscillation G has quite poor effect [Matsuhisa et al 2003]. In practice, the DVA should be located as high as possible, which can be not convenient in some cases.

3. DVA moving in normal direction

3.1. Equations of motion

The DVA moves in the normal direction of the pendulum's orbit as shown in Fig.3. Denote u as the DVA displacement in the normal direction, l_u is the distance between the fulcrum and the DVA in the static condition, m_u is the DVA mass, k_u is the DVA spring constant, c_u is the DVA damping coefficients.

To write the equations in non-dimensional forms, some parameters are introduced in Table 2.

The motion equations are derived as following non-dimensional form:

$$\left(1+\mu_u\left(\gamma_u-z_u\right)^2\right)\ddot{\theta} - 2\mu_u\dot{\theta}\left(\gamma_u-z_u\right)\dot{z}_u + 2\zeta_s\dot{\theta} + \left(1+\mu_u\left(\gamma_u-z_u\right)\right)\sin\theta = 0$$
$$\ddot{z}_u + 2\zeta_u\dot{z}_u + \alpha_u z_u + \dot{\theta}^2\left(\gamma_u-z_u\right) - \left(1-\cos\theta\right) = 0 \quad (7)$$

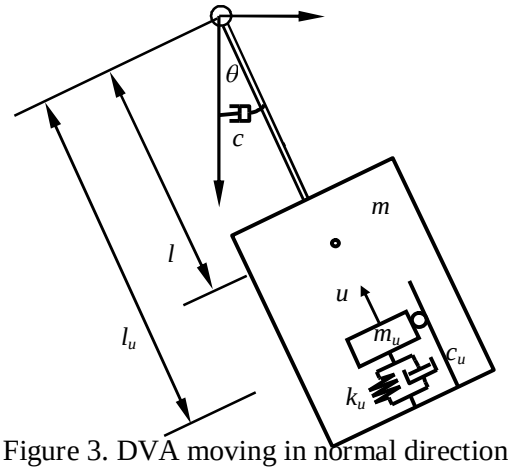

Figure 3. DVA moving in normal direction

Table 2. Symbols used for normal DVA (some other symbols are defined in Table 1)

Symbol	Description
$\mu_u = \frac{m_u}{m}$	DVA mass ratio
$\alpha_u = \frac{k_u/m_u}{\omega_s^2}$	Square of DVA natural frequency ratio
$\zeta_u = \frac{c_u}{2m_u\omega_s}$	DVA damping ratio
$\gamma_u = \frac{l_u}{l}$	Location parameter specifying the DVA position
$z_u = \frac{u}{l}$	Non-dimensional form of the DVA displacement

3.2. Parameter optimization

Unlike the DVA moving in the tangential direction, the DVA moving in the normal direction only has effect from the second order terms in (7). Because the Eqs. (7) are nonlinear, the effective damping approach is used to optimize the DVA. The effective damping of the DVA moving in the normal direction (c_e) are determined by:

$$c_e = \frac{-2\gamma_u\mu_u\left\langle\dot{z}_u\dot{\theta}^2\right\rangle}{\left\langle\dot{\theta}^2\right\rangle} \quad (8)$$

where the averaging operator defined as the infinite integral:

$$\left\langle g(\tau)\right\rangle = \int_0^\infty g(\tau)d\tau \quad (9)$$

By using the effective damping approach, to the second order, the Eqs (7) are rewritten by:

$$\begin{aligned}&\left(1+\mu_u\gamma_u^2\right)\ddot{\theta}+2\zeta_s\dot{\theta}+\left(1+\mu_u\gamma_u\right)\theta+c_e\dot{\theta}=0\\&\ddot{z}_u+2\zeta_u\dot{z}_u+\alpha_u z_u+\gamma_u\dot{\theta}^2-\theta^2/2=0\end{aligned} \quad (10)$$

An expanded state vector is defined as:

$$\mathbf{p}=\left[\theta \quad \dot{\theta} \quad z_u \quad \dot{z}_u \quad \theta^2 \quad \dot{\theta}^2 \quad \theta\dot{\theta}\right]^T \quad (11)$$

Eq.(10) are written in state space form as:

$$\dot{\mathbf{p}}=\mathbf{A}\mathbf{p} \quad (12)$$

where:

$$\mathbf{A}=\begin{bmatrix}\mathbf{A}_1 & \mathbf{0}_{2\times5}\\ \mathbf{0}_{5\times2} & \mathbf{A}_2\end{bmatrix},\qquad \mathbf{A}_1=\begin{bmatrix}0 & 1\\ \dfrac{-\left(1+\mu_u\gamma_u\right)}{1+\mu_u\gamma_u^2} & \dfrac{-\left(2\zeta_s+c_e\right)}{1+\mu_u\gamma_u^2}\end{bmatrix}$$

$$\mathbf{A}_2=\begin{bmatrix}0 & 1 & 0 & 0 & 0\\ -\alpha_u & -2\zeta_u & \dfrac{1}{2} & -\gamma_u & 0\\ 0 & 0 & 0 & 0 & 2\\ 0 & 0 & 0 & \dfrac{-2\left(2\zeta_s+c_e\right)}{1+\mu_u\gamma_u^2} & \dfrac{-2\left(1+\mu_u\gamma_u\right)}{1+\mu_u\gamma_u^2}\\ 0 & 0 & \dfrac{-\left(1+\mu_u\gamma_u\right)}{1+\mu_u\gamma_u^2} & 1 & \dfrac{-\left(2\zeta_s+c_e\right)}{1+\mu_u\gamma_u^2}\end{bmatrix} \quad (13)$$

in which $\mathbf{0}_{2\times5}$, $\mathbf{0}_{5\times2}$ denote the zero matrices with appropriate dimensions. Because the parameters α_u and ζ_u only appear in the matrix $\mathbf{A}_2$, the characteristic polynomial of $\mathbf{A}_2$ is determined by:

$$\begin{aligned}P_{A_2}(s)=&\left(s+\frac{2\zeta_s+c_e}{1+\mu_u\gamma_u^2}\right)\times\\&\left(s^2+\frac{2\left(2\zeta_s+c_e\right)}{1+\mu_u\gamma_u^2}x+\frac{4\left(1+\mu_u\gamma_u\right)}{1+\mu_u\gamma_u^2}\right)\\&\times\left(s^2+2s\zeta_u+\alpha_u\right)\end{aligned} \quad (14)$$

The quintic polynomial (14) has one real root and two pairs of roots of complex conjugate. By using the same approach above, the repeated roots conditions give the optimal values α_u^*,ζ_u^* of α_u and ζ_u:

$$\alpha_u^*=\frac{4\left(1+\mu_u\gamma_u\right)}{1+\mu_u\gamma_u^2};\quad \zeta_u^*=\frac{2\zeta_s+c_e}{1+\mu_u\gamma_u^2} \quad (15)$$

Substituting (15) into (13) will express the system matrix **A** in term of the effective damping c_e. Conversely, the effective damping c_{eu} in (8) depends on the response . Let us consider the initial condition $\theta(0)=\theta_0$. The infinite integral (9) gives a sextic equation of c_e [Viet 2012]. This sextic equation is somewhat involved. However, if the higher order terms of the parameters μ_u, c_e and ζ_s are ignored, the authors can obtain a quadratic equation to calculate c_e:

$$32c_e^2+64\zeta_s c_e-\mu_u\gamma_u\theta_0^2\left(2\gamma_u+1\right)=0 \quad (16)$$

The positive solution of (16) has form:

$$c_e=\sqrt{\zeta_s^2+\frac{1}{32}\mu_u\gamma_u\theta_0^2\left(2\gamma_u+1\right)}-\zeta_s \quad (17)$$

Formulas (15) and (17) give the optimal parameter of the DVA moving in normal direction. We have some remarks:

- Because the mass ratios μ_u is often small in many practical case, the optimal value α_u^* is near 4 to produce resonance.

- The optimal DVA damping ζ_u^* increases proportionally to the initial angle θ_0. That means the DVA moving in normal direction has only good effect for reducing large vibration. This phenomenon is the main difference between the linear and nonlinear DVAs. Moreover, as seen from (17) the DVA effective damping increases with the distance from the DVA to the fulcrum point. Therefore, in the opposite way of the tangential DVA, the normal DVA still has good effect when it locates at the center of oscillation.

4. Combinations of two DVAs

Because each type of DVA has advantages and disadvantages, the idea of combination of two types of DVA has recently studied [Viet et al 2011b, Viet 2012]. Two possible combinations are shown in Fig.4.

In Fig.4a, one DVA is allowed to move in two orthogonal directions. It is well-known that the DVA effectiveness depends on the DVA mass ratio and the DVA location. Because of using only one DVA, the scheme in Fig.4a has the advantage of the DVA mass ratio but the disadvantage of the DVA position. Conversely, if the single mass is divided into two smaller masses as shown in Fig.4b, the DVAs are located more freely but the mass ratios are reduced.

By using the above notations, the equations of motion of the combined DVAs can be derived as:

For the combined DVA in Fig.4a:

$$\begin{aligned}
&\left(1+\mu\left(\gamma-z_u\right)^2+\mu z_v^2\right)\ddot{\theta}+2\zeta_s\dot{\theta}+\\
&\left(1+\mu\left(\gamma-z_u\right)\right)\sin\theta+\mu\left(\gamma-z_u\right)\ddot{z}_v\\
&+\mu z_v\left(\ddot{z}_u+\cos\theta\right)-2\mu\dot{\theta}\left(\left(\gamma-z_u\right)\dot{z}_u-\dot{z}_v z_v\right)=0\\
&\ddot{z}_u+2\zeta_u\dot{z}_u+\alpha_u z_u+\ddot{\theta}z_v+2\dot{z}_v\dot{\theta}\\
&+\dot{\theta}^2\left(\gamma-z_u\right)-1+\cos\theta=0\\
&\ddot{z}_v+2\zeta_v\dot{z}_v+\alpha_v z_v+\ddot{\theta}\left(\gamma-z_u\right)\\
&-2\dot{z}_u\dot{\theta}-\dot{\theta}^2 z_v+\sin\theta=0\\
&\left(\mu_u=\mu_v=\mu;\qquad \gamma_u=\gamma_v=\gamma\right)
\end{aligned} \tag{18}$$

For the combined DVA in Fig.4b:

$$\begin{aligned}
&\left(1+\mu_u\left(\gamma_u-z_u\right)^2+\mu_v\left(\gamma_v^2+z_v^2\right)\right)\ddot{\theta}+2\zeta_s\dot{\theta}\\
&+\left(1+\mu_u\left(\gamma_u-z_u\right)+\mu_v\gamma_v\right)\sin\theta+\mu_v\gamma_v\ddot{z}_v\\
&+\mu_v z_v\cos\theta+2\mu_v z_v\dot{z}_v\dot{\theta}-2\mu_u\dot{\theta}\left(\gamma_u-z_u\right)\dot{z}_u=0\\
&\ddot{z}_v+2\zeta_v\dot{z}_v+\alpha_v z_v+\gamma_v\ddot{\theta}-\dot{\theta}^2 z_v+\sin\theta=0\\
&\ddot{z}_u+2\zeta_u\dot{z}_u+\alpha_u z_u+\dot{\theta}^2\left(\gamma_u-z_u\right)-\left(1-\cos\theta\right)=0
\end{aligned} \tag{19}$$

The optimal DVA parameters in the combination case can be found numerically [Viet et al 2011b, Viet 2012].

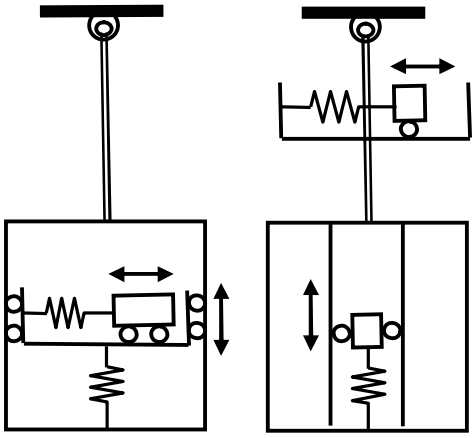

(a) (b)

Figure 4. Two schemes of combination of two orthogonal DVA motions in a pendulum
(a) Single large DVA, two directions,
(b) Two small DVAs, two directions.

5. Numerical simulations

5.1. First combined DVA

Let us consider the combined DVA in Fig.4a. The performance of this combined DVA is compared with those of two single DVAs moving in one direction. The following non-dimensional performance index is considered to be minimized:

$$J=\frac{1}{T_f}\int_0^{T_f}\left(\begin{array}{l}\left(1-\cos\theta\right)\left(1+\mu\left(\gamma-z_u\right)\right)+\\ \mu z_v\sin\theta+\frac{1}{2}\mu\left(\alpha_u z_u^2+\alpha_v z_v^2\right)\end{array}\right)dt \tag{20}$$

in which T_f is the total time of simulation and is taken as 100s. In fact, the performance index (20) expresses the total potential energy over time. Because the advantage and also the disadvantage of the DVA depend much on the location parameter γ and vibration initial angle θ_0, in the simulations, the mass ratio μ and the structural damping ratio ζ_s are fixed at 0.1 and 0.01, respectively.

Then the optimized performance indexes are plotted versus the initial angle θ_0 for various location parameter γ as shown in Figs.5a-d. In Figs.5a-d, J and J_u denote the performance indexes of the structures with and without DVA, respectively.

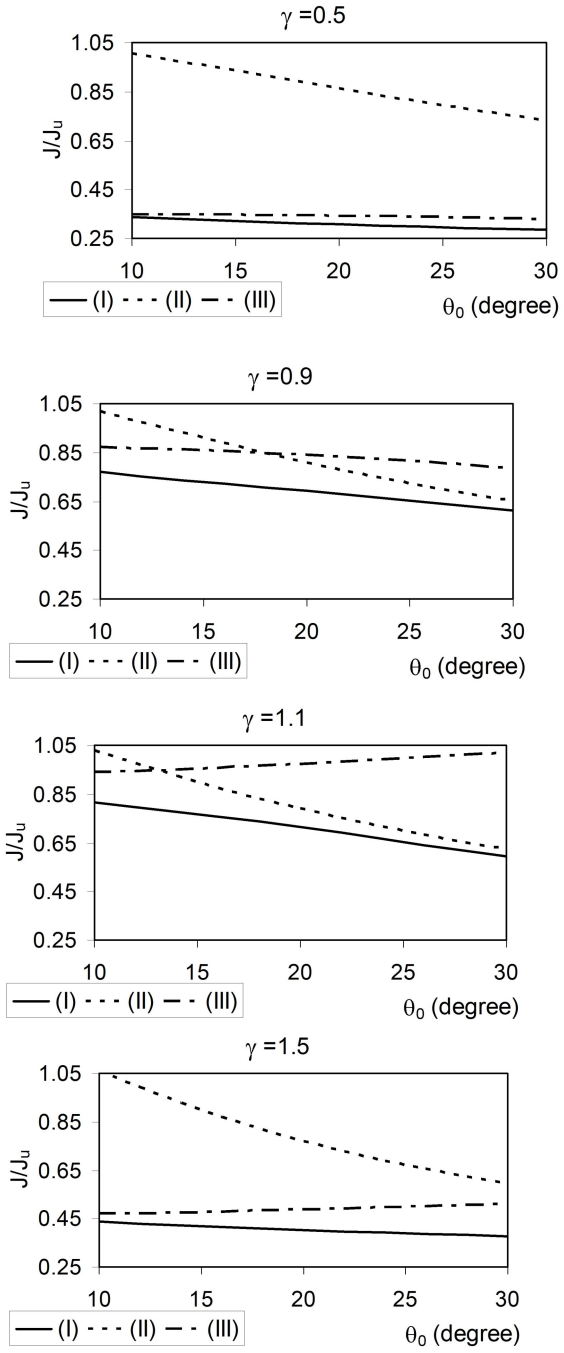

Figures 5a-d: J as functions of θ_0; Legends (I), (II), (III): DVA moving in two directions, normal direction and tangential direction, respectively.

Some remarks can be drawn from the plots:

- As seen from the lines with legend (II) in the Fig. 5, when location parameter γ increases, the effectiveness of DVA moving in normal direction also increases. However, these improvements are only significant for the large initial vibration angle.

- As seen from the lines with legend (III) in the Fig. 5, when the value of γ is far from 1 (Fig. 5a and Fig. 5d), the DVA moving in tangential direction has quite good effect. However, when the location of DVA is near to the center of oscillation (Fig 5b and Fig 5c), the effectiveness is quite poor.

- As seen from the lines with legend (I) in the Fig. 5, it is clear that the DVA moving in two directions at the same time has the best performance in comparison with two other types. When the value of γ is far from 1 (Fig. 5a and Fig. 5d), the DVA moving in two directions not only reduces vibration significantly as the DVA moving in tangential direction but also reduces better the large vibration as the DVA moving in normal direction. When the value of γ is near to 1 (Fig. 5b and Fig. 5c), although the motion in tangential direction has no effect, the DVA moving in two directions still has good effect due to the motion in normal direction.

5.2. Second combined DVA

Let us consider the combined DVA in Fig.4b. We compare the performances of two small DVAs moving orthogonally at the same time with one large DVA moving in only one direction. The total mass of the DVAs is fixed. The following performance index is considered to be minimized:

$$P_f = \frac{\int_0^{T_f} \left(\left(1+\mu_v+\mu_u\right)\dot{\theta}^2 + \mu_v \dot{z}_v^2 + \mu_u \dot{z}_u^2 \right) d\tau}{\theta_0^2 / \left(2\zeta_s\right)} \tag{21}$$

In fact, the integrand in (21) represents the kinetic energy while the denominator of (21) is the value of the integral in case of pendulum without DVAs. Some cases of system parameters used in simulation are summarized in Table 3.

In all cases, the structural damping ratio ζ_s is taken of 1%. The total time of simulation T_f is taken of 500s. The comparisons are shown in Figs.6a-d.

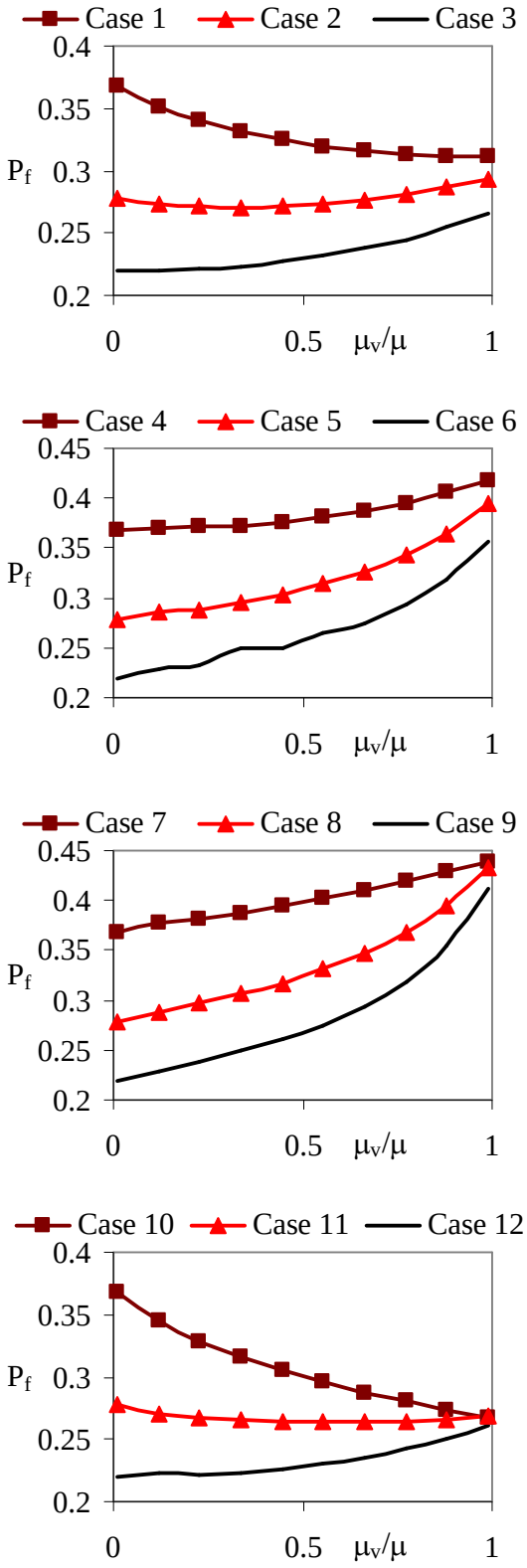

Figures 6a-d. DVA effectiveness versus mass ratio μ_v (cases are mentioned in Table 3)

Table 3. Parameter value used in numerical simulations

Case	$\mu=\mu_u+\mu_v$	γ_u	γ_v	θ_0
1	8%	1.3	0.8	15°
2	8%	1.3	0.8	25°
3	8%	1.3	0.8	35°
4	8%	1.3	0.9	15°
5	8%	1.3	0.9	25°
6	8%	1.3	0.9	35°
7	8%	1.3	1.1	15°
8	8%	1.3	1.1	25°
9	8%	1.3	1.1	35°
10	8%	1.3	1.3	15°
11	8%	1.3	1.3	25°
12	8%	1.3	1.3	35°

It is noted that when $\mu_v=0$, we have the DVA moving in normal direction. Conversely, when $\mu_v=1$, we have the DVA moving in tangential direction. It can be seen that there are no clear minima in all plots. That means the two-DVA scheme has no clear benefit. This negative conclusion, however, can be useful in practice because the two-DVA arrangement can be excluded in the design.

6. Conclusion

This paper consider two DVAs moving in the normal and tangential directions of the pendulum orbit and two of their combinations. By analytical and numerical analyses, we conclude that each type of single DVAs has advantages and disadvantages. The combined single DVA moving in normal and tangential directions at the same time has the best performance in comparison with the DVA moving only in normal direction or tangential direction. Conversely, the combined scheme using two small DVAs moving orthogonally has quite small benefit.

Acknowledgements

This work is supported by the Vietnam National Foundation for Science and Technology Development, under project number: 107.04-2011.14.

References

N.D. Anh, H. Matsuhisa, L.D. Viet, M. Yasuda, Vibration control of an inverted pendulum type structure by passive mass–spring-pendulum dynamic vibration absorber, *Journal of Sound and Vibration*, 307, 187–201, (2007).

S. Krenk, Frequency Analysis of the Tuned Mass Damper, *Journal of Applied Mechanics*, 72 (2005), 936-942.

H. Matsuhisa and M. Yasuda, Location effect of dynamic absorbers on rolling structures, *Proc. of Asia-Pacific Vibration Conference*, Gold Coast, Australia, pp.439-444, (2003).

H. Matsuhisa, H. Kitaura, M. Isono, H. Utsuno, J.G. Park and M. Yasuda, A new Coriolis dynamic absorber for reducing the swing of gondola, *Proc. of Asia-Pacific Vibration Conference*, Langkawi, Malaysia, 211-215, (2005).

T.T. Soong, G.F. Dargush, *Passive Energy Dissipation Systems in Structural Engineering*, John Wiley & Sons, Ltd. (UK), (1997)

A. Tondl, R. Nabergoj, Dynamic absorbers for an externally excited pendulum, *Journal of Sound and Vibration*, 234(4), (2000), 611-624

L.D.Viet, Sequential design of two orthogonal dynamic vibration absorbers in a pendulum based on stability maximization, *Journal of Mechanical Engineering Science*, (2012), http://dx.doi.org/10.1177/0954406212437302

L.D Viet, N.D. Anh and H. Matsuhisa, The effective damping approach to design a dynamic vibration absorber using Coriolis force, *Journal of Sound and Vibration*, 330, (2011a), 1904-1916

L.D Viet, N.D. Anh and H. Matsuhisa, Vibration control of a pendulum structure by dynamic vibration absorber moving in normal and tangential directions, *Proc. IMechE, Part C: J. Mechanical Engineering Science*, 225, (2011b), 1087-1095.

G.B. Warburton, Optimal absorber parameters for various combinations of response and excitation parameters, *Earthquake Engineering and Structural Dynamics*, 10, (1982), 381-401.

The 2nd International Conference on Engineering Mechanics and Automation (ICEMA2)
Hanoi, August 16-17, 2012
ISBN: 978-604-913-097-7

Vibration tests-based Stiffness Evaluation of Building

Le Thai Hoa [a,b], Akihito Yoshida [a] and Yukio Tamura [a]
Shinji Nakata [c], Shinichi Kiriyama [c], Shinichi Naito [d] and Ronjie Aquino [a]

[a] *Wind Engineering Research Center, Tokyo Polytechnic University, Kanagawa 243-0297, Japan*
[b] *University of Engineering and Technology, Vietnam National University at Hanoi 144 Xuan Thuy, Cau Giay, Hanoi, Vietnam*
[c] *Asahi Kasei Homes Corporation Co., Ltd, Shizuoka 461-8501, Japan*
[d] *Taku Structural Design Co. Ltd., Tokyo 167-0051, Japan*

Abstract

This paper estimates generalized stiffness of a steel building model under different erections using vibration tests. Contribution of nonstructural and structural components such as bare steel frame, autoclaved light concrete (ALC) walls, sealing joints between the wall panels, interior wooden frame and cover plate, interior separation wall, windows on the stiffness has been directly evaluated. Two analytical models have been built for the stiffness estimates, concretely are a simplified lumped mass model and comprehensive three-dimensional mass distributed model. Three-dimensional finite element models of the building models during erection have been carried out for a purpose of estimating three-dimensional mode shapes and mass distribution as well. Some vibration tests such as ambient vibration, free vibration, sweep vibration, white noise vibration and seismic base excitation have been applied to the building model. Natural frequencies and damping ratios have been identified from measured vibration responses of the vibration tests using logarithmic decrement technique, random decrement technique and frequency domain decomposition.

Key Words: Stiffness evaluation; Stiffness estimate; Modal parameters estimation; Vibration tests; Steel building; Autoclaved Light Concrete; During construction

1. Introduction

Both structural components and nonstructural ones of the light-gauge steel-framed buildings could significantly influence dynamic properties and global stiffness thanks to sensitive distribution of generalized masses, stiffness and damping on the buildings. However, such kind of investigations on influences of the structural and nonstructural components and their stiffness contribution on the light gauge steel-framed buildings are really rare so far, main reason is due to costly and time-consuming works for full-scale construction and vibration monitoring. Evaluation of the generalized stiffness and the contribution of structural and nonstructural components on the building stiffness can be carried out by vibration tests in an indirect approach via investigating changes of the dynamic properties of the buildings. Concretely, natural frequencies and damping ratios of

fundamental building modes in the three principle directions can be used for indirectly investigating the influences of structural and nonstructural components on the building stiffness. Memari et al.,1999 carried out an investigation on dynamic properties of a full-scale steel building during construction also using both ambient and forced vibration tests. Authors discussed on contribution of exterior walls on increases of the dynamic properties and building stiffness (Memari et al. 1999), however, construction stages were few and an effect of constructional joints was still not into the investigation. Le et al., 2010 investigated the influences of structural and nonstructural components and vibration amplitudes on the dynamic properties on the one-storey experimental building using ambient and forced vibration tests. They indicated the structural and nonstructural components such as ALC walls, sealing, mortar joints and interior cover plate, separation walls could significantly affect dynamic properties, consequently the building stiffness. Especially, the sealing joints between the exterior ALC walls have increased the natural frequency and the generalized stiffness of the investigated building (Le et al. 2010). In these studies, the generalized stiffness has been indirectly evaluated via changing of the dynamic properties, but on the generalized stiffness sill has not been directly estimated. Vibration tests and stiffness evaluation on a six-storey timber framed building under its construction also was studied by Ellis and Bougard, 2001, their test showed a decrease of building stiffness with an increase of building height and some nonstructural components provided considerable stiffening to translational dynamic behavior of the investigated building. They also estimated the generalized stiffness of the timber building using a simplified lumped mass model from identified natural frequencies, lumped masses and simplified two-dimensional mode shapes. This simplified approach cannot treat with the three-dimensional distribution of masses and mode shapes as a nature of dynamic behavior and stiffness of the low-rise building. More precise analytical model for directly estimating the generalized stiffness of building based on the vibration tests and three-dimensional distribution characteristic of the building must be pivoted. Furthermore, it is also generally agreed that excitation amplitude also affects on the dynamic properties which can considerably change with the large amplitude of excitation due to structural nonlinearity, non-stationary signals and system noises. Large-amplitude excitations might deteriorate material properties, structural joints, structural damages and so on, which reduce the contribution of structural components on the generalized stiffness of the buildings. Evaluation of the influence of excitation amplitudes on the dynamic properties of the steel buildings has been investigated somewhere, however, the effect of excitation amplitudes on the generalized stiffness of the building also requires to be further clarified.

This paper estimates generalized stiffness of a steel building model at the different erections using almost applicable vibration tests. Contribution of some structural and nonstructural components such as the main steel frame, ALC wall panels, sealing joints, interior wooden frame and cover plate, interior separation wall, windows on the generalized stiffness has been evaluated. The paper has established two analytical models for the stiffness estimates via (1) simplified lumped mass model and (2) three-dimensional mass distributed model. The natural frequencies and damping ratios have been extracted from the measured responses at the building erections and the vibration tests. The paper also has built up the three-dimensional FE models for estimating the mode shapes and mass distribution for the stiffness estimation. Most applicable vibration tests for engineering structures such as ambient vibration, free vibration, sweep vibration, white noise vibration and seismic base excitation have been applied to the building model during assembled stages.

2. Building model during erection

The light-gauge steel-framed one-storey building has been assembled on the shaking table for the vibration tests. The building model has its dimension of 3.66m (width) x 2.44m (depth) x 2.87m (height). Bare steel frame mainly comprises H-beams, steel columns, bracing system and floor slabs. Steel columns have special details at two ends for reducing ending moments of columns, while the bracing system has special bracing joints for strengthening friction damping. The building model is constructed into six assembled stages (coding as D1-D6) in which the structural and nonstructural components have been added onto the bare steel frame (D1) as the ALC wall panels in X-direction (D1); sealing joints between two ALC wall panels (D3); interior wooden frames and wooden cover plates (D4); interior separate walls of aluminum columns and wooden cover plates (D5); windows and exterior ALC wall panels in Y-direction as final assembled stage (D6) (see Figure 1)

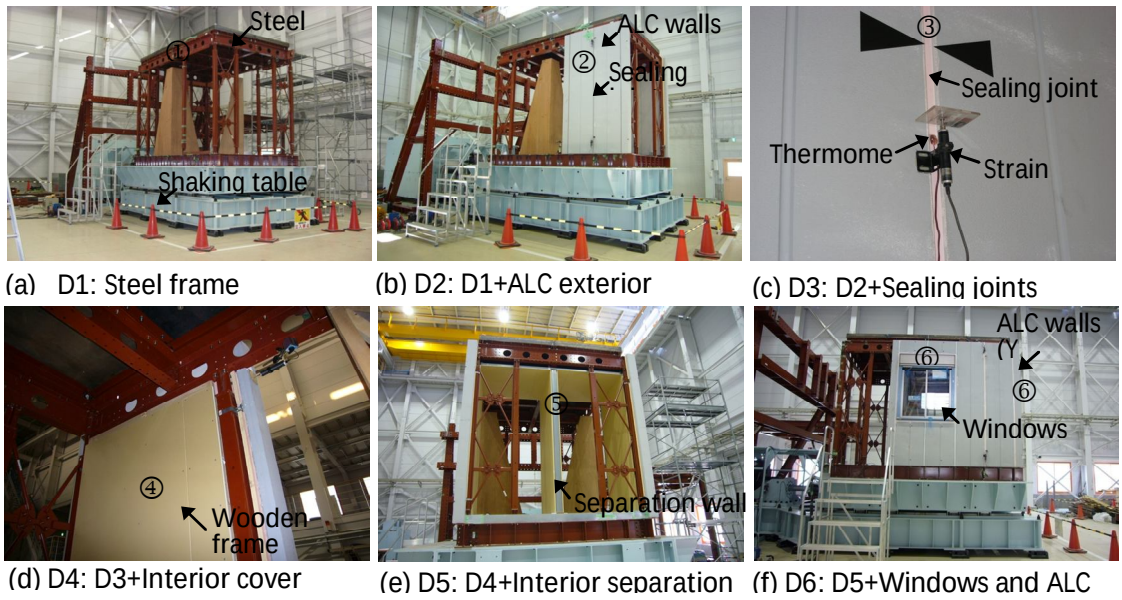

Figure 1. Building model during assembled stages D1-D6

3. Vibration tests

The most applicable vibration tests such as the ambient vibration, sweep vibration, free vibration, white noise vibration and seismic base excitation have been used for the assembled stages of the building model. Ambient vibration tests were carried out by constructional micro-tremors with 5-minute records of measured responses. Sweep vibration tests were generated by a shaker installed at top floor of the building model by which a linearly sinusoidal sweep force in the X-direction with a continuously-tuned frequency band between 2Hz and 6Hz, a sweep rate of 0.01Hz, 13-minute records have been generated. Response amplitude of the sinusoidal weep data has reached a peak when sweep excitations tuned resonantly at fundamental frequencies of the building model. Free vibration tests were created also using the shaker on the top roof in such a manner that an excitation frequency of the sinusoidal sweep force has tuned coincidently with the fundamental natural frequency, then moving mass of the shaker suddenly stopped. Measured responses at these resonant states were determined as free decay response data associated with a certain fundamental mode of the building model. White noise vibration and seismic bas excitation tests were simulated by using a dynamic servo exciter installed at a base of the building model. The dynamic servo

exciter has simulated the white noise forces and two mock seismic forces following specifications of the Japan Meteorological Agency (JMA)'s earthquake scenario and the Building Center of Japan (BCJ)'s earthquake one. In the JMA's earthquake scenario, the seismic excitations are shortly-concentrated seismic intensity like the real earthquakes, while the BCJ scenario develops longer-distributed seismic intensity. Two amplitude levels of excitations considered as relatively low and high amplitudes have been applied for the free vibration, sweep vibration and white noise vibration, while three large amplitude levels used for the seismic base excitation which are corresponding to 10%, 30% and 60% of peak acceleration intensity of the JMA and BCJ' earthquake scenarios. Dual-axial accelerometers were arranged in two X-, Y-directions at two corners and centers on the first and second floors of the building model. There are totally 8 sensors used are located on the floor 1 and the floor 2. Vibration responses have been measured at the sensor stations in every assembled stage and vibration test.

4. Estimates of natural frequency and damping ratio

Natural frequencies of the building model can be directly obtained from auto power spectral density (PSD) functions of measured responses from the ambient vibration and the free vibration tests. In cases of the forced vibration tests, the natural frequencies can be estimated alternatively via transfer functions or FRFs which are determined as a ratio between power spectral density functions of measured response at analyzing point and that of measured response at referred stationary one (Bendat and Piersol 1993).

Damping ratio can be estimated simply from the free decay responses by the logarithmic decrement technique (LDT). Free decay responses can be obtained from either the free vibration tests or resulted from other identification techniques in the time domain and in the frequency domain.

Random decrement technique (RDT) can apply directly to the ambient response data to obtain the free decay function or SDOF response function associated with certain building modes. In its theoretical basis, the output response subjected to random excitation consists of both the free decay response function and forced response function that RDT is applied to estimate the free decay response by removing the forced response from the measured output response. The RDT is implemented firstly by selecting crossing level of the measured response data, from which equally-spaced segments in $[t_0,t+t_0]$ interval are started at every crossing point between crossing line and response data. Then, averaging operation of these segments to estimate a random decrement function is carried out (Ibrahim 1977):

$$\delta_{XX}(\tau) = (1/N)\sum_{i=1}^{N} X(t_i + \tau) \mid X_0 \qquad (1)$$

where $\delta_{XX}(\tau)$: random decrement function of measured response $X(t+t_0)$; N: number of segments; X_0: crossing level (conditional value); τ: length of segments; t_i: starting time for i-th segment.

More complicated, but powerful output-only system identification technique to get the natural frequency and damping ratios is the frequency domain decomposition (FDD). The output power spectral density matrix is orthogonally decomposed using well-known singular value decomposition (SVD) to obtain both the singular values and the singular vectors (Brincker et al. 2001a):

$$S_{XX}(\omega) = \Phi(\omega)\Theta(\omega)\Phi(\omega)^{*T} = \sum_{k=1}^{M} \varphi_k(\omega)\theta_k(\omega)\varphi_k(\omega)^{*T} \qquad (2)$$

where $\Phi(\omega), \Theta(\omega)$: singular vectors and singular values matrices; k, M: index and number of singular vectors. Because the SVD is usually very fast-decaying, thus the output power spectral density matrix can be approximated by using the first singular value and associated singular vector:

$$S_{XX}(\omega) \approx \varphi_1(\omega)\theta_1(\omega)\varphi_1(\omega)^{*T} \qquad (3)$$

where $\varphi_1(\omega), \theta_1(\omega)$: the first singular vector and singular value.

One can be estimate the natural frequencies of the building via the first singular value, however the damping ratio estimation requires a further special treatment from the first singular value and singular vector. The EFDD has been extended the FDD just for a purpose of estimating the damping ratios. Due to the first singular vector contains information of terminated if a desirable limit of the MAC reached. From estimated auto power spectral density functions associated with building modes, the free decay functions can be obtained by converting the auto spectral density function in the frequency domain back to the time domain by inverse Fourier transform technique, from which the damping ratios are estimated by LDT of free

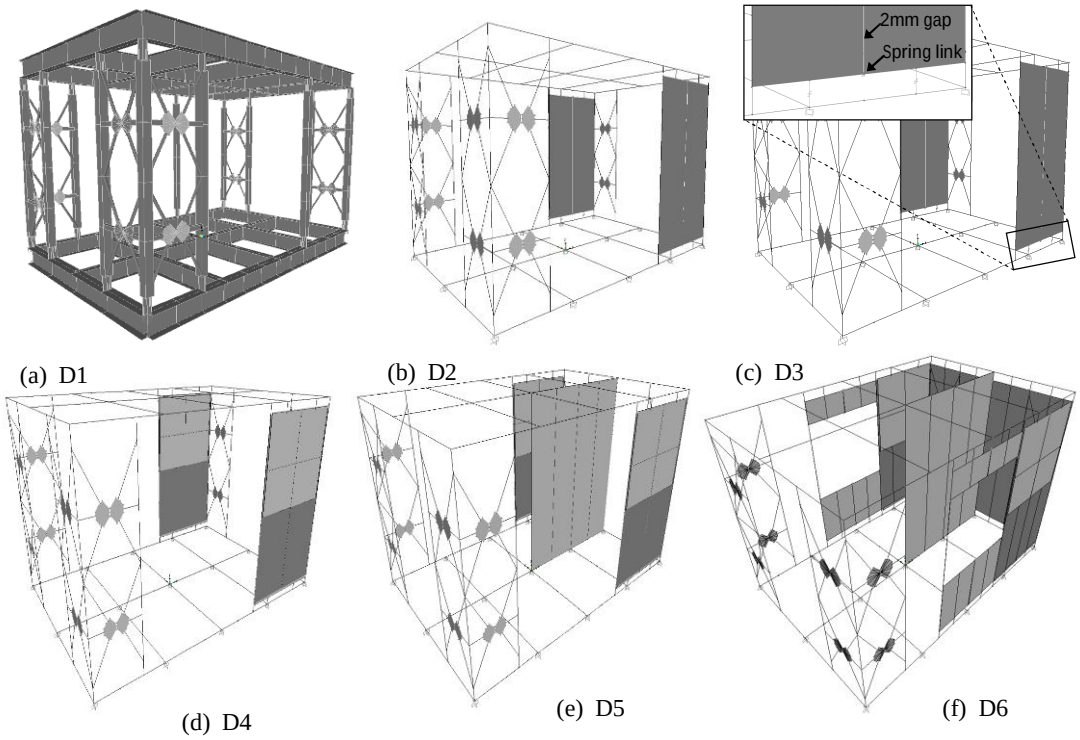

Figure 2. FEMs of assemble stages D1-D6

unscaled mode shapes at selected natural frequencies, thus prior knowledge of the natural frequencies is required for estimating the mode shapes and the damping ratios. Accuracy of estimated mode shapes from the first singular vector can be evaluated via correlation criteria between estimated mode shapes and analytical mode shapes. Here well-known the modal assurance criterion (MAC) is used. For the damping estimation, a key point is to identify the auto power spectral density function of the SDOF generalized coordinate of certain building mode from the first singular value. Tracking the auto power spectral functions of building modes is carried out on both sides of selected natural frequencies, and it would be decay functions (Brincker et al. 2001b).

Unscaled mode shapes can be identified as the FDD's first singular vectors. However, values of unscaled mode shapes are determined at sensor stations only. Correction factors for unscaled mode shapes can be estimated via scaling mode shapes obtained by the finite element models.

5. Stiffness estimates

One has a relationship between the global stiffness, global mass and mode shape from the eigen solution as follows:

$$M\Omega\Phi = K\Phi \quad (4)$$

where Ω : diagonalized eigenvalue matrix, which contains squared circular frequencies on its main diagonal.

We have other form of Eq.(13):

$$\Phi^T M \Omega \Phi = \Phi^T K \Phi = \overline{K} \quad (5)$$

where $\overline{K}$: dianonalized generalized stiffness matrix, containing the generalized stiffness of each structural mode in its main diagonal.

Finally, we can estimate the generalized stiffness of the i-th mode as follows:

$$k_i = M\phi_i^2\omega_i^2 = 2\pi^2 f_i^2 M\phi_i^2 \quad (6)$$

where f_i: i-th natural frequency.

mass and mode shape value at the floor level, measured natural frequency of the Y-translational mode (see Figure 3a). It is noted that $M_X = M_Y$ for the lumped mass model. When the effect of the damping ratio accounted into the generalized stiffness, the natural frequencies in the Eq.(7) are replaced as $f_X \Big/ \sqrt{1-\zeta_X^2}$; $f_Y \Big/ \sqrt{1-\zeta_Y^2}$, ζ_X, ζ_Y: measured damping ratios of the X-,Y-translational modes.

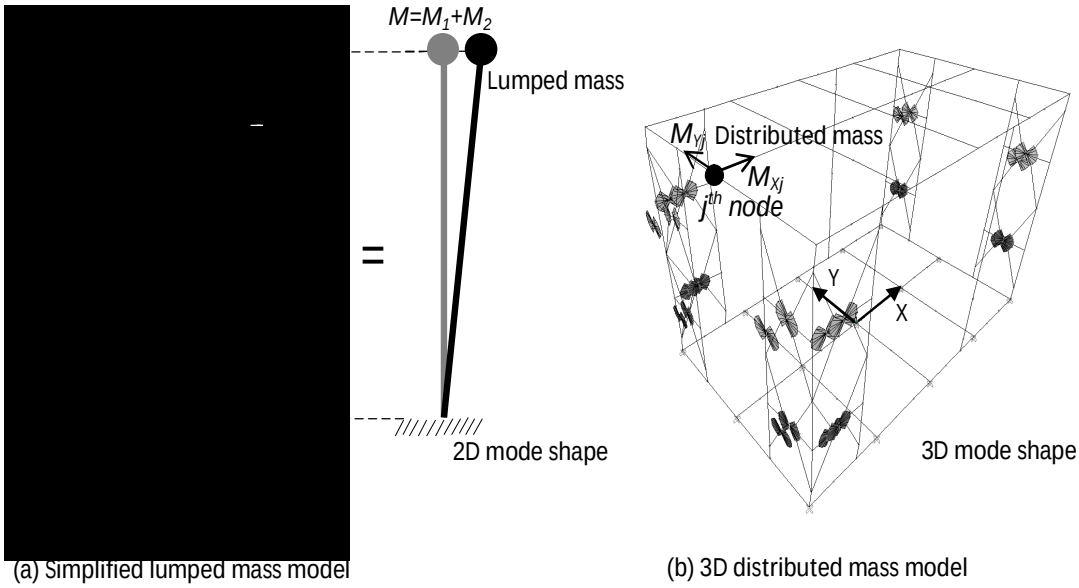

Figure 3. Proposed analytical models for estimates of generalized stiffness

For the generalized stiffness estimation from the vibration tests, the natural frequency will be estimated from the measurements. Basing on the way to determine the structural mass and the mode shapes in the Eq.(6), two analytical models can be proposed hereafter.

5.1. Lumped mass model

Masses have been lumped on two ends at the base and the roof levels. The generalized stiffness on two fundamental X-,Y-translations can be formulated as follows:

$$K_X = 4\pi^2 M_X \phi_{0X}^2 f_X^2 \quad (7a)$$

$$K_Y = 4\pi^2 M_Y \phi_{0Y}^2 f_Y^2 \quad (7b)$$

where M_X, ϕ_{0X}, f_X: Lumped mass and mode shape value at the floor level, measured natural frequency of the X-translational mode; M_Y, ϕ_{0Y}, f_Y: Lumped

5.2. Three-dimensional distributed mass model

Comprehensively, the generalized stiffness can be estimated by combination between the measured natural frequencies and theoretical mass distribution, theoretical mode shapes which are already determined from the FEMs. Here, the mode shapes and masses are spatially distributed at discrete structural nodes, thus the three-dimensional distributed mass model can be approached for the generalized stiffness estimation as follows (see Figure 3b):

$$K_X = 4\pi^2 f_X^2 \sum_{j=1}^{N_n} M_{Xj} \phi_{Xj}^2 \quad (8a)$$

$$K_Y = 4\pi^2 f_Y^2 \sum_{j=1}^{N_n} M_{Yj} \phi_{Yj}^2 \quad (8b)$$

where j: index of structural node; N_n: number of structural nodes; M_{Xj}, M_{Yj}: Distributed mass value at structural node j; ϕ_{Xj}, ϕ_{Yj}: mode shape value at structural node j. All three-dimensional distributed masses and mode shape values are determined via a support of the FEMs.

6. Results on estimated natural frequencies and damping ratios and generalized stiffness

Natural frequencies and damping ratios have been estimated firstly thanks to some presented methods, after that the generalized stiffnesses have been then determined. However, estimated natural frequencies and damping ratios have not discussed due to a sake of brevity.

Generalized stiffness has been estimated using two models: (1) Lumped mass model and (2) 3D distributed mass model presented in the section 5. Estimated generalized stiffnesses of the fundamental X-translational mode of the assembled stages D1-D6 (results of Y-translational mode not to show for purpose of brevity), the vibration tests and the amplitude levels with two recommended models are indicated in Figure 4. Here, the natural frequency, the damping ratio, the unscaled mode shapes have been already obtained thank to the modal parameter identification methods in the section 3, furthermore, the scaling factors of mode shapes have been estimated thanks to the finite element models indicated in Figure 2.

It is agreed that general tendency of estimated generalized stiffnesses is similar to that of estimated natural frequencies. These similar images can be explained due to the generalized stiffnesses are estimated proportionally to squared natural frequencies. The estimated stiffness on the fundamental X-translational mode based on the 3D distributed mass model is shown in Figure 4. The generalized stiffness from the ambient vibration data increases from 562kN/m of the original D1 to 559kN/m of the D2 (0.5% decrease), to 697kN/m of the D3 (24% increase), to 801kN/m of the D4 (42% increase), to 852kN/m of the D5 (51% increase), to 741kN/m of the D6 (31% increase) (see Figure 4). In comparison with adjacent stage, the generalized stiffness of the D2 decreases 0.5% from the D1, the D3 increases 24% from the D2, the D4 increases 14% from the D3, the D5 increases 6% from the D4, and D6 decreases 13% from the D5. Similar trends to such the ambient data can be observed with in some other vibration tests such as the free vibration data, sine sweep vibration data and white noise excitation data at their low amplitude level. Some reasons for these changes can be explained as follows. In the D2, the AAC wall panels are erected, they are just hinged to floor steel beams but not to be connected together, this D2 does not contribute to the stiffness. After the soften sealing joints between the AAC wall panels are constructed in the D3, there is dramatical increase in the stiffness. This observation is interesting because the sealing joint plays its main function to prevent the building against a moisture and environmental impact. In the following stages of D4, D5, D6, the investigated structural components such as the interior cover plates, interior separate walls and windows also contribute in their some extents to the building stiffness. Similar to the estimated natural frequency, the estimated stiffness at the high amplitude level of the seismic data does not follow described trends at the low amplitude level. There is just a little change in the estimated stiffness observed in the seismic data at the high amplitude levels. This means that the investigated structural components do not influence the generalized stiffness at the high amplitude level.

In comparison between the vibration tests, the estimated generalized stiffness of the X-direction trends to decrease from the ambient data to the free vibration data, sweep data, white noise data to the seismic data with respect to an increase in the amplitude levels. Concretely, the generalized stiffness of X-direction with the lumped mass model at the lowest amplitude levels of the D1 as an example changes 556kN/m of the ambient

data to 532kN/m of the free, sweep and white noise data (4% decrease), to 518kN/m of the JMA data (6% decrease), 504kN/m of the BCJ data (9% decrease). In the comparison between the vibration tests at adjacent stages, the generalized stiffness of the D6 with the lumped mass model for an example also change 0% decrease from the ambient vibration data (the maximum amplitude level 0.01m/s^2) to the free vibration data (the maximum amplitude 0.1m/s^2) and the sweep vibration data (the maximum amplitude 0.01m/s^2), 12% decrease from the sweep data to the white noise data (the maximum amplitude 0.15m/s^2), 21% decrease from the white noise data to the JMA seismic data (the maximum amplitude 2m/s^2), 15% increase from the JMA seismic data to the BCJ seismic data (the maximum amplitude 1.5m/s^2) (see Figure 4).

Figure 5 compares the estimated generalized stiffness between two recommended models of the lumped mass model and the 3D distributed mass model during the assembled stages D1-D6, with the ambient, free and sweep, white noise vibration data. It is observed that the generalized stiffness of the building model obtained by the lumped mass model generally exhibits higher than that by the 3D distributed mass model, however, there is no much difference in the estimated generalized stiffness between the two analytical models in this investigated building model. A reason for little difference between two recommended models is explained due to simple one-storey building model and specific mass distribution of the building model where the weighted roof panels contribute almost on the total mass of the building model. For actual low-rise buildings, however, the 3D mass model expects to perform its advantage over the simplified lumped mass model for estimating more accurately the generalized stiffness of the buildings from the vibration tests.

Contribution of the structural and non-structural on the generalized stiffness is shown in Figure 6.

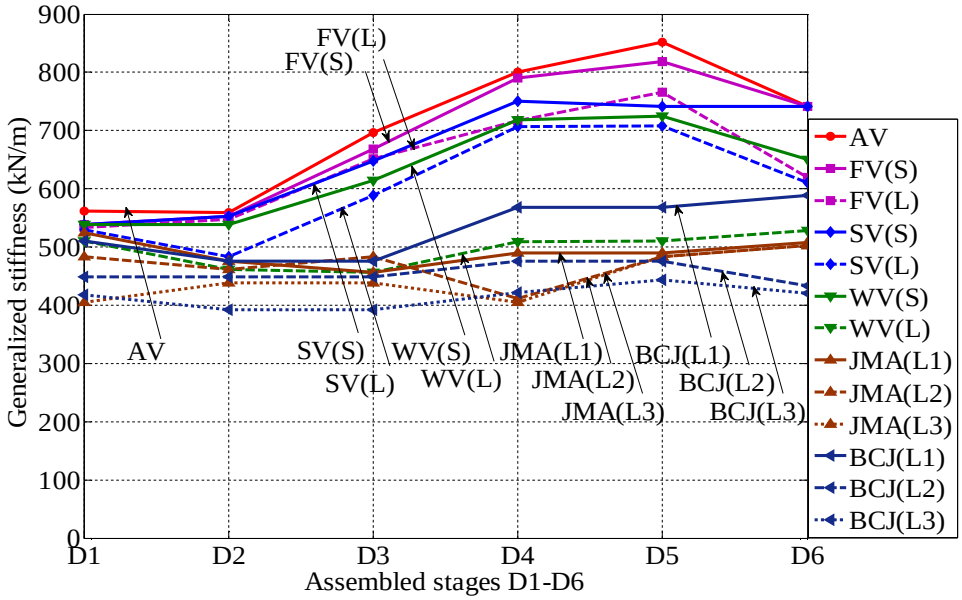

Figure 4. Generalized stiffness estimation of building of X-translational mode during assembled stages D1-D6 with 3D distributed mass model

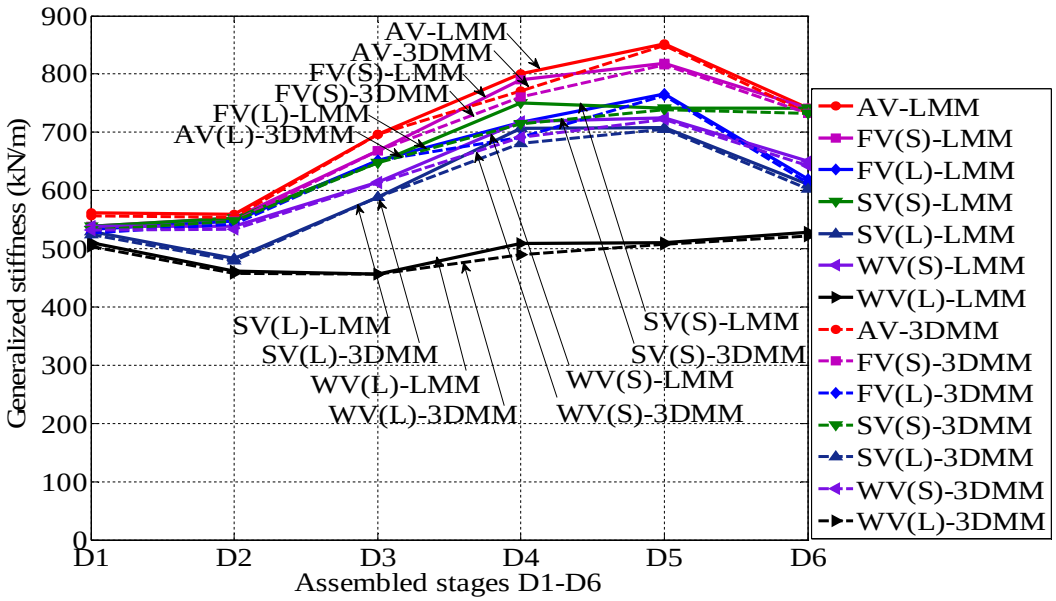

Figure 5. Comparison of generalized stiffness of building of X-translational mode during assembled stages D1-D6 between lumped mass model and 3D distributed mass model

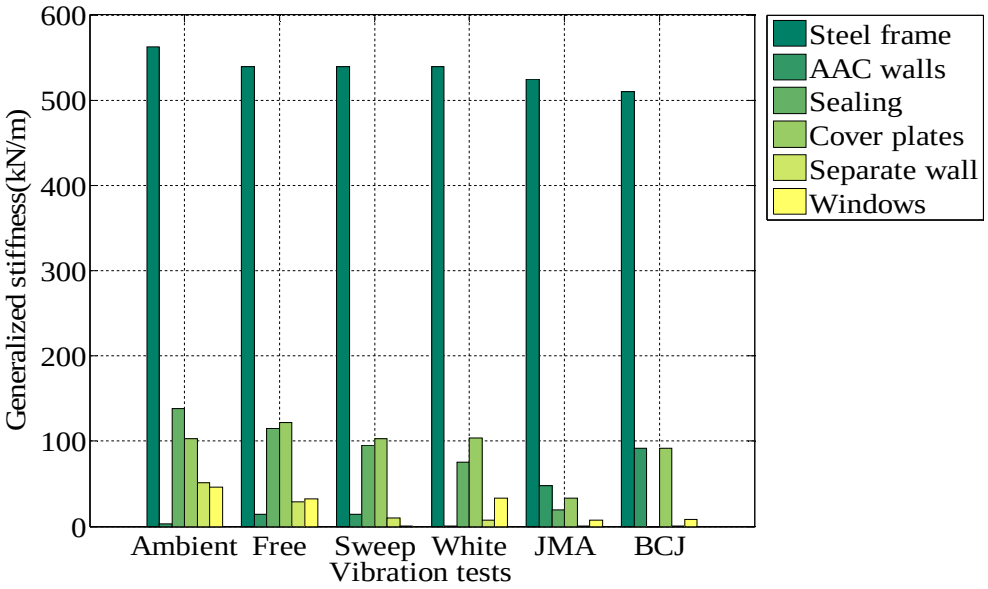

Figure 6. Influence of structural components on generalized stiffness of building model during assembled stages D1-D6 on X-translational mode in 3D distributed mass model

7. Conclusion

Generalized stiffness of the building model during the assembled stages has been estimated by the proposed analytical models. The influences of the structural and nonstructural components, the vibration tests, and amplitudes of excitation and response on the dynamic properties and the generalized stiffness of the building model have been investigated. Structural and nonstructural components such as the ALC exterior wall panels, soft sealing joints, interior cover plates, interior separate walls, windows significantly affect on the natural frequencies

and damping ratios of the building model. Especially, their contribution has been clearly observed at the low amplitude range of excitation and response. However, influence of these structural and nonstructural components is unclear to be clarified at the high amplitude range and strong motion. Importantly, effectiveness of the sealing between the ALC exterior wall panels on strengthening the global stiffness of the building model via the increase of its natural frequencies and the generalized stiffness as well have been observed in this study. Furthermore, the amplitudes of excitation and response have strongly influenced both the natural frequencies and the damping ratios of the building model. The natural frequencies and the generalized stiffness tendentiously reduce with the increase of excitation and response amplitudes, where the damping ratios increase with the increase of amplitudes

8. Acknowledgements

This study was funded by the Ministry of Education, Culture, Sport, Science and Technology, Japan through the Global Center of Excellence Program, 2008-2012.

9. References

A.M. Memari, A.A. Aghakouchak, M.G. Ashtiany, M. Tiv, Full-scale dynamic testing of a steel building during construction, Engineering Structures 21(1999) 1115-1127.

T.H. Le, S. Nakata, A. Yoshida, S. Kiriyama, S. Naito, Y. Tamura, Influence of vibration methods, structural components and excitation amplitudes on modal parameters of low-rise buildings, Proceedings of 5th World Conference on Structural Control and Monitoring, 2010, Tokyo Japan

B.R. Ellis, A.J. Bougard, Dynamic testing and stiffness evaluation of a six-storey timber frame building during construction, Engineering Structures 23(2001) 1232-1242.

A. Cunha, E. Caetano, Experimental model analysis of civil engineering structures, Sound and Vibration 40(2006) 12-22.

R. Brincker, L. Zhang, P. Andersen, Modal identification of output-only systems using frequency domain decomposition, Smart Materials and Structures 10(2001a) 441-445.

R. Brincker, C.E. Ventura, P. Andersen, Damping estimation by frequency domain decomposition, Proceedings of the 19th International Modal Analysis Conference, 2001b, 141-146.

S.R. Ibrahim, Random decrement technique for modal identification of structures, Journal of Spacecraft and Rockets 14(1977) 696-700.

M. Marchitti, Averaging spectral functions from in flight flutter signals, Mechanical System and Signal Processing 20(2006) 757-761.

J.S. Bendat, A.G. Piersol, Engineering applications of correlation and spectral analysis, John Wiley & Sons, 1993.

The 2nd International Conference on Engineering Mechanics and Automation (ICEMA2)
Hanoi, August 16-17, 2012
ISBN: 978-604-913-097-7

Ambient Modal Identification Based on Blind Source Separation

Le Thai Hoa[a,b] and Yukio Tamura[c]

[a] *Wind Engineering Research Center, Tokyo Polytechnic University, Japan, thle@arch.t-kougei.ac.jp*
[b] *University of Engineering and Technology, Vietnam National University, Hanoi, thle@vnu.edu.vn*
[c] *Department of Architectural Engineering, Tokyo Polytechnic University, Japan, yukio@arch.t-kougei.ac.jp*

Abstract

Modal analysis of operational civil and large structures exploits ambient vibration tests. All natural excitation sources such as wind, wave, traffic, micro tremors can be applied for the ambient vibration tests and modal parameter estimation using output-only system identification methods. Some well-known output-only system identification methods have been evolved in either the time domain, the frequency domain or the time-frequency plane with major assumption of Gaussian white noise excitations. One of difficulties is that there is no information on the input excitations because the input conditions cannot be measured, but just only output responses measured. So far, the output-only system identification methods estimate the modal parameters from the measured output responses without any knowledge and evaluation on the input conditions. Blind source separation as original statistical technique has been developed recently for various engineering applications including the modal analysis and modal identification of structures. The blind source separation could estimate the input sources of output-only measurements. This paper presents the use of blind source separation for the modal parameter identification from the ambient vibration data. Ambient vibration on five-storey steel building has been used for demonstration of the modal analysis using the blind source separation.

Key Words: Ambient vibration; Vibration tests; Modal estimation; Operation modal analysis; Blind source separation; Independent component analysis; Second-order blind identification

1. Main instructions

Ambient vibration test is the most recently applicable and reliable method to determine modal parameters of structures (e.g. natural frequencies, damping ratios and mode shapes) for operational structures due to its advantages on testing during traffics, time and cost benefits as well. Estimated modal parameters are served in multipurpose uses as dynamic assessment, model updating and validation, response prediction, structural control and damage detection. Generally, the vibration tests can be classified into forced vibration tests including free vibration test and ambient vibration tests. In the first testing type, the structures are excited by shaker or impulse hammer (the free vibration test is a special case of the forced vibration

tests when the exciting forces is suddenly removed). In the forced vibration tests, both input excitations and output responses are often measured. Accordingly, input-output identification techniques have been applied for estimating the modal parameters of structures via either frequency response function (FRF) or impulse response function (IRF). The ambient vibration tests use directly natural and environmental excitations such as traffic vehicles, human activities, wind and micro tremors for exciting the structures. Because only the output response can be measured without the input excitations in the ambient vibration tests, thus the output-only modal identification techniques have been applied to estimate the modal parameters.

Output-only modal parameter identification techniques have been evolved into some following three recent branches: (i) Nonparametric methods in the frequency domain; (ii) Parametric methods in the time domain and (iii) Time-frequency analysis methods in the simultaneous time-frequency plane. Generally, the output-only modal parameter identification techniques have no prior information and measurement on the input excitations, but based on some principal assumptions: (i) the input excitations are typed as Gaussian white noises in which their power spectral densities are constant; (ii) the input excitation sources are uncorrelated, thus their cross spectral components are negligible; and (iii) the system damping is small, thus relationship between the spectra of excitation and those of response or so-called frequency response function matrix can be decomposed in the simplified way. Furthermore, the output-only modal identification has its drawback on the closely-spaced modal separation and high-order modal identification as well due to only using the measured responses. Without such above-mentioned assumptions, the output-only modal parameter techniques cannot be satisfied. Furthermore, there are no consistent studies in effects of the assumptions of the input excitations on the accurate estimation of the modal parameters. However, it was generally agreed that uncertainties of the input excitations surely affect the accuracy of estimated modal parameters.

Recovering the input excitation sources from ambient vibration tests and the measured responses is required. Blind source separation (SSB) and Independent component analysis (ICA) have been invented firstly in the late of 90s for retrieving the speech signals from some simultaneously-spoken persons (Hyvarinen et al., 2001). So far, BSS and ICA techniques have been applied for various fields of studies, including the structural dynamics, system identification, damage detection and so on. In the modal parameter identification, BSS and ICA techniques have been used to estimate the input excitation sources from the measured responses. In the original idea of BSS, one can estimate unknown virtual source signals from the known observation signals or mixtures thanks establishing linear, convolutional or nonlinear relationship between the virtual sources and observed mixtures. Relationship between the sources and observations is expressed under so-called mixing matrix. BSS techniques enable to retrieve the virtual sources and mixing matrix. Estimates of the virtual sources and mixing matrix can be classified into some main branches: (i) Second-order blind identification techniques and (ii) Higher-order blind identification techniques (or Independent component analysis) (Poncelet, Kerschen and Golinval, 2010). Thus, ICA is a specific branch of the BSS for the higher-order blind source separation. ICA is ultimate extension of the well-known principal component analysis (PCI), also known as a proper orthogonal decomposition (POD). Figure 1 show a comparison in basic coordinate systems between PCI and ICA, while the PCA coordinates are fixed and orthogonal ones, the ICA coordinates more adaptive and independent. Thus, the independent coordinates seem better to capture characteristic of independent impacts but none of orthogonality. In the output-only modal identification, BSS techniques have been applied to retrieve the independent

excitation sources and mixing matrix in which the natural frequencies, damping ratios then are estimated from the sources and mode shapes from the mixing matrix. A principal framework for BSS-based modal parameter identification can be seen in Figure 2 (Zhou and Chelizde, 2007).

This paper presents a background theory and application of the blind source separation for the output-only modal parameter identification from the ambient vibration tests of structures. The difference between the PCA and ICA for the output-only modal identification is emphasized. Some BSS techniques are as the second-order blind identification and the independent component analysis used for the modal identification. Ambient vibration measurements have been carried out on a five-storey steel building.

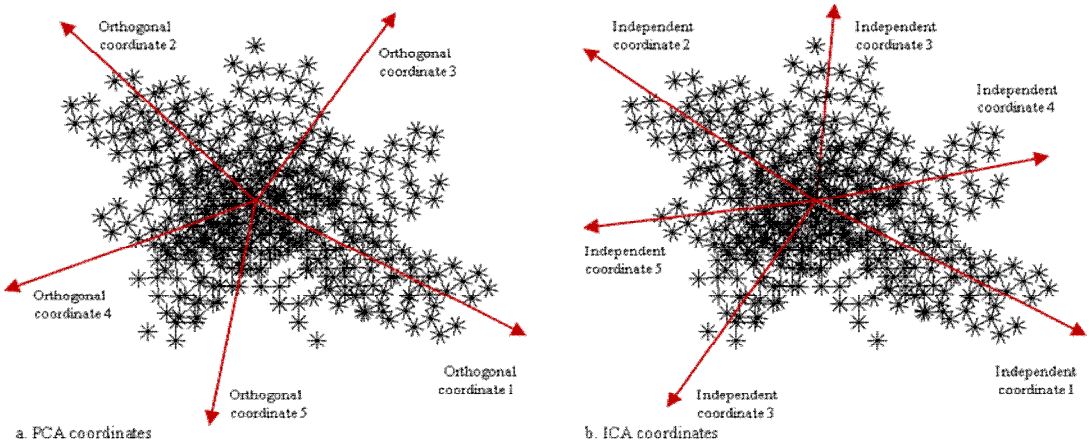

Figure 1. Comparison in basic coordinate systems between PCA and ICA

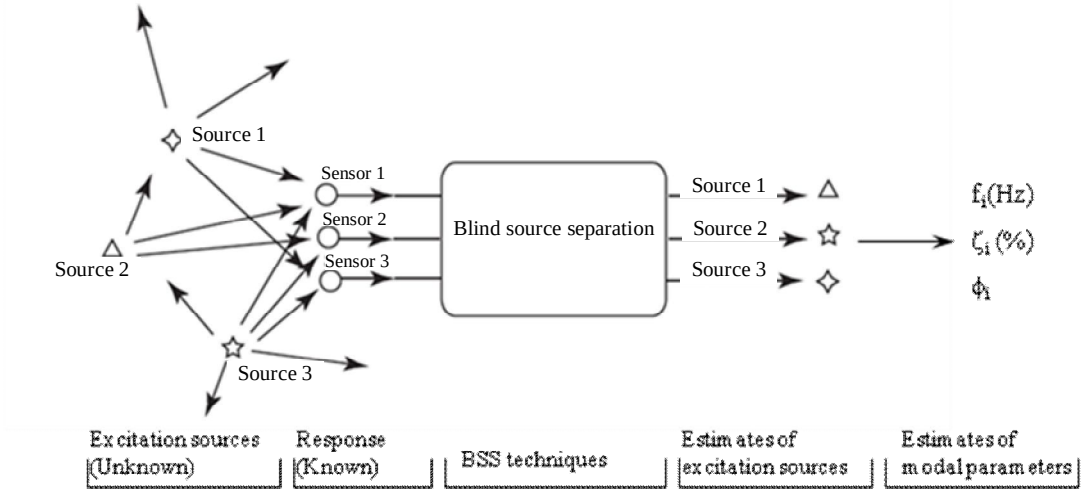

Figure 2. Framework for BSS-based modal parameter identification

2. From principal component analysis to blind source separation and independent component analysis

2.1. Principal component analysis

PCA of measured responses *y(t)* can be expressed in the time domain as follows:

$$y(t) = \Theta x(t) \quad (1)$$

where *x(t)*: orthogonal (principal) coordinates; Θ : mixing matrix

Mixing matrix is found as orthogonal eigenvectors of the eigen solution of the zero-time-lag covariance matrix $R_y(0)$ of measured responses *y(t)*:

$$R_y(0)\Theta = \Gamma_y\Theta \quad (2)$$

where Γ_y, Θ: covariance eigenvalue and eigenvector matrices $\Gamma_y = diag(\gamma_{y1}, \gamma_{y2}, ...\gamma_{yN})$ $\Theta = [\theta_1, \theta_2, ...\theta_N]$, respectively.

Principal coordinates *x(t)* can be determined from observed responses as:

$$x(t) = \Theta^{-1} y(t) = y(t)\Theta \approx \sum_{j=1}^{\hat{N}} y_j(t)\theta_j \quad (3)$$

However, the principal coordinates and mixing matrix are determined in the orthogonal basis as the eigen decomposition, thus no proof that they are related to the excitation sources and mode shapes.

In a similar way but in the frequency domain, Fourier transform and power spectral densities of the measured responses can be expressed by PCA as follows:

$$\hat{y}(f) = \Psi(f)\hat{x}(f) \quad (4a)$$

$$S_y(f) = \Psi(f)\Lambda(f)\Psi(f)^{*T} \quad (4b)$$

where $\hat{y}(f), S_y(f)$: Fourier transform coefficient and power spectrum of measured responses *y(t);* $\hat{x}(f)$: spectral principal coordinates as Fourier transform of principal coordinates *x(t);* $S_y(f)$: spectral mixing matrix as power spectra of mixing matrix.

The spectral mixing matrix can be determined as spectral eigenvectors of the power spectra $S_y(f)$ of measured responses thanks to the eigen solution as:

$$S_y(f)\Psi(f) = \Lambda(f)\Psi(f) \quad (5)$$

where $\Lambda(f), \Psi(f)$: spectral eigenvalue and eigenvector matrices, respectively.

Accordingly, the Fourier transform of principal coordinates can be estimated as follows:

$$\hat{x}(f) = \Psi(f)^{-1}\hat{y}(f) \approx \sum_{j=1}^{\hat{N}} \psi_j(f)\hat{y}_j(f) \quad (6)$$

It is also noted that the principal coordinates in the time domain as Eq.(3) and their Fourier transform coefficients as Eq.(6) in the frequency domain are orthogonal. There is no existing linkage between the principal coordinates and their Fourier transform with the input excitation sources, though the spectral eigenvalues and spectral eigenvectors of measured responses contain information of the modal properties.

2.2. Independent component analysis and blind source separation

A major aim of ICA and BSS is to recover the sources from measured responses, with own assumptions: (i) Sources are mutual independence of the sources; (ii) Sources are mixed in different types of linear or nonlinear manners; simultaneous or convolutive manners. Linear simultaneous mixture between the sources and measured responses can be expressed as:

$$y(t) = As(t) \quad (7)$$

where *y(t)*: measured responses $y(t) = [y_1(t), y_2(t), ...y_m(t)] \in R^m$; *s(t)*: unknown excitation sources $s(t) = [s_1(t), s_2(t), ...s_n(t)] \in R^n$, satisfied m>n; A: unknown mixing matrix $A \in R^{mxn}$. The purpose of BSS is to determine the mixing matrix first, then the sources as follows:

$$s(t) = A^{-1}y(t) \quad (8)$$

Recently, almost the BSS techniques use the second-order statistical quantity (ex., a variance) such as Second-order blind identification (SOBI), Algorithm for multiple unknown signal extraction (AMUSE), while the ICA technique uses higher-order statistical one (eg., kurtosis) such as Fourth-order blind identification (FOBI), Joint approximate diagonalization of eigenmatrices (JADE) to describe the components. Hereafter, two powerful BSS techniques are the SOBI and ICA to be presented.

2.3. Second-order blind identification (SOBI)

Similar to the PCA, the SOBI algorithm deals with the covariance matrix of the output responses. Eigenvalue decomposition (EVD) or singular value decomposition (SVD) then is applied to either the zero-time-lag covariance matrix $R_y(0)$ (AMUSE) or time-shifted covariance $R_y(\tau_i)$ (SOBI) of the measured responses. Time-shifted covariance matrix of responses *y(t)* can be calculated as:

$$R_y(\tau_i) = \frac{1}{N}\sum_{k=1}^{N} E[y[k]y[k+\tau_i]^T] \quad (9)$$

SVD is used to decompose the time-shifted covariance matrix as so-called whitening process:

$$R_y(\tau_i) = U_y \Sigma_y V_y^T = \Theta_s \Gamma_s \Theta_s^T + \Theta_N \Gamma_N \Theta_N^T \quad (10)$$

where $R_y(\tau_i)$: time-shifted covariance matrix; Θ_y, Γ_y: covariance eigenvectors and eigenvalues; $\Theta_s \in R^{mxn}$, $\Gamma_s \in R^{nxn}$: eigenvectors and eigenvalues related to the sources (taking first n eigenvalues and associated eigenvectors), $\Theta_N \in R^{mx(m-n)}$, $\Gamma_s \in R^{(m-n)x(m-n)}$: components related to noises that are emitted. Thus, we have:

$$R_y(\tau_i) \approx \Theta_s \Gamma_s \Theta_s^T \quad (11)$$

In the next step, the pre-whitening process for the measured responses with newly-established responses is carried out:

$$\bar{y}(t) \approx \Gamma_s^{1/2} \Theta_s^T y(t) = Qy(t) \quad (12)$$

The covariance matrix of newly-established responses is determined, then the SVD is applied once as follows:

$$R_{\bar{y}}(\tau_i) = U_{\bar{y}} \Sigma_{\bar{y}} V_{\bar{y}}^T \quad (13)$$

Finally, the mixing matrix and the input excitation sources can be estimated as (Chauhan et al., 2009):

$$A = QU_{\bar{y}} = \Gamma_s^{1/2} \Theta_s^T U_{\bar{y}} \quad (14a)$$

$$s(t) = U_{\bar{y}}^T \bar{y}(t) \quad (14b)$$

Modal parameters can be identified from the estimated mixing matrix and the retrieved sources.

2.4. Joint approximate diagonalization of eigenmatrices (JADE)

The JADE is extension of the FOBI, but uses fourth-order zero-time-lag quadricovariance matrix instead of the second-order covariance matrix in the FOBI. Then, the EVD is used for the quadricovariance matrix as follows:

$$C_y(E) = \Theta_y \Gamma_y \Theta_y^T \quad (15)$$

where $C_y(E)$: quadricovariance matrix; Θ_y, Γ_y : quadricovariance eigenvectors and eigenvalues, $\Gamma_y = diag(\gamma_1 \theta_1 \theta_1^T, ..., \gamma_n \theta_n \theta_n^T)$ and $\Theta_y = (\theta_1, ..., \theta_n)$, $\gamma_i = \kappa_4(s_i) = E[s_i^4] - 3E^2[s_i^2]$ as the kurtosis of i-th source.

The next steps are similar to the SOBI which has been previously presented to estimate the mixing matrix and the sources.

3. BSS and ICA-based modal parameter identification

The free decay response of the MDOF system can be expressed as follows:

$$y(t) = \Phi Z(t) \quad (16a)$$

$$y(t) = \sum_{r=1}^{N} \phi_r \xi_r(t) = \sum_{r=1}^{N} \phi_r a_r \exp(-\zeta_r \omega_{nr} t) \sin(\omega_{nr} t + \varphi_r) \quad (16b)$$

where $\Phi, Z(t)$: mode shape matrix and generalized modal coordinates; ϕ_r: r-th mode shape; a_r: r-th amplitude; ω_{nr}, ζ_r: r-th natural frequency and damping ratio; φ_r: r-th phase angle; N: number of combined modes.

Similarity between the expression of responses in the modal coordinates as Eq.(16a) and the BSS/ICA one in the independent coordinates as Eq.(7). Concretely, the maxing matrix is corresponding to the mode shapes, while the sources are similar to the modal coordinates. Thus, the framework for the BSS/ICA-based modal parameter identification from the measured responses is described as following procedures:

(1) Responses are measured at different sensing positions of the structure.
(2) BSS/ICA techniques are applied to the measured responses to estimate the mixing matrix and the sources.
(3) Mode shapes are obtained from the estimated mixing matrix.
(4) Natural frequencies and damping ratios are extracted from the estimated sources by fitting with the damped harmonic functions $a\exp(-\zeta\omega t)\sin(\sqrt{1-\zeta^2}\,\omega t + \varphi)$, where a, φ are constants obtained from initial conditions.

4. Ambient vibration measurements of five-storey steel building

Full-scale ambient measurements have been carried out on a 5-storey steel building at the test site of the Disaster Prevention Research Institute (DPRI), Kyoto University (see Figure 3). Ambient data were recorded at all 5 floor levels and ground as reference, by tri-axial velocity sensors with output velocity signals (VCT Corp., Models UP255S/UP252) with A/D converter, amplifier and laptop computer. All data were sampled for per iod of 30 minutes per floor (5 minutes per a set-up) with sampling rate of 100Hz. Sensors have been located to capture ambient motions in lateral X-direction and horizontal Y-direction from ground level to 5th floor, see Figure 3 (Kuroiwa and Iemura, 2007).

Only outputs sensors and modal parameters in the X direction have been discussed in this paper. It is noted that all outputs were velocity time series, thus a single integration in the time domain using a trapezoic integration approach has been required to obtain output displacements which are necessary for estimating mode shapes in next steps. An integration drift due to unknown initial condition of the displacements during the time integration have been treated through compensation to be zero-mean output displacements. Figure 4 shows the displacements as the output responses at all 5 floors and the ground level.

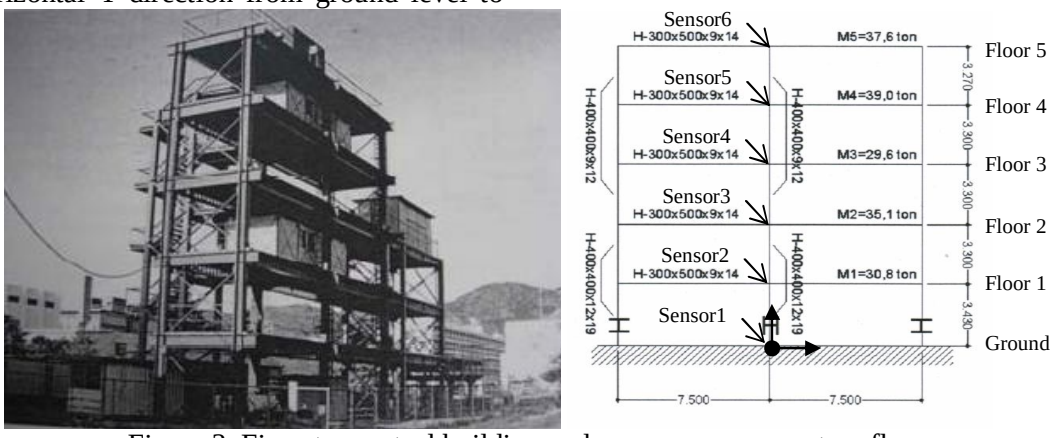

Figure 3. Five-storey steel building and sensor arrangement on floors

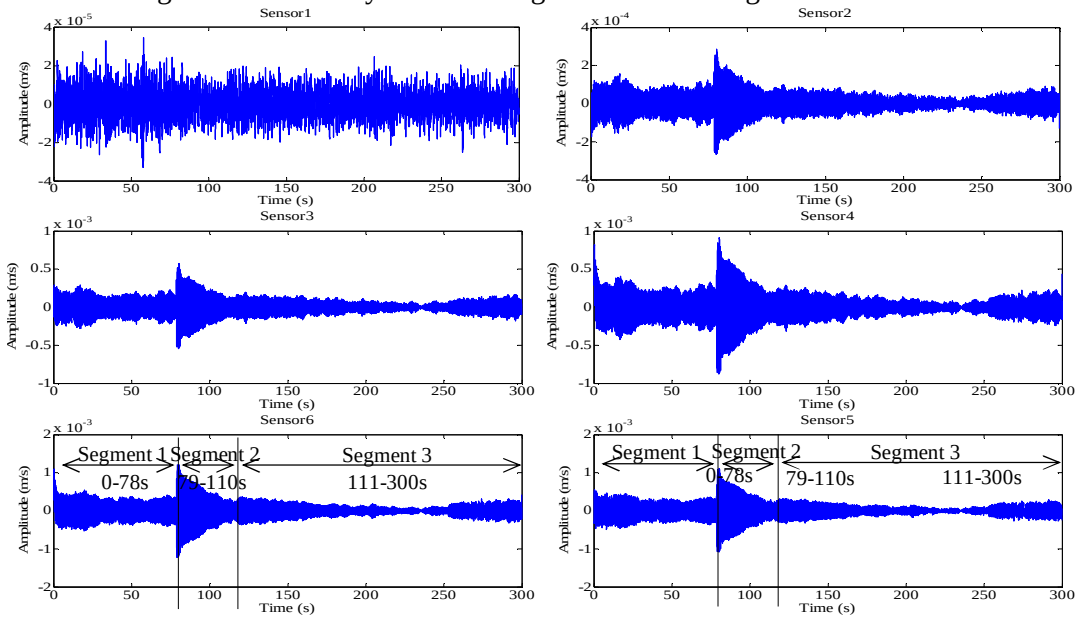

Figure 4. Measured displacements at building floors

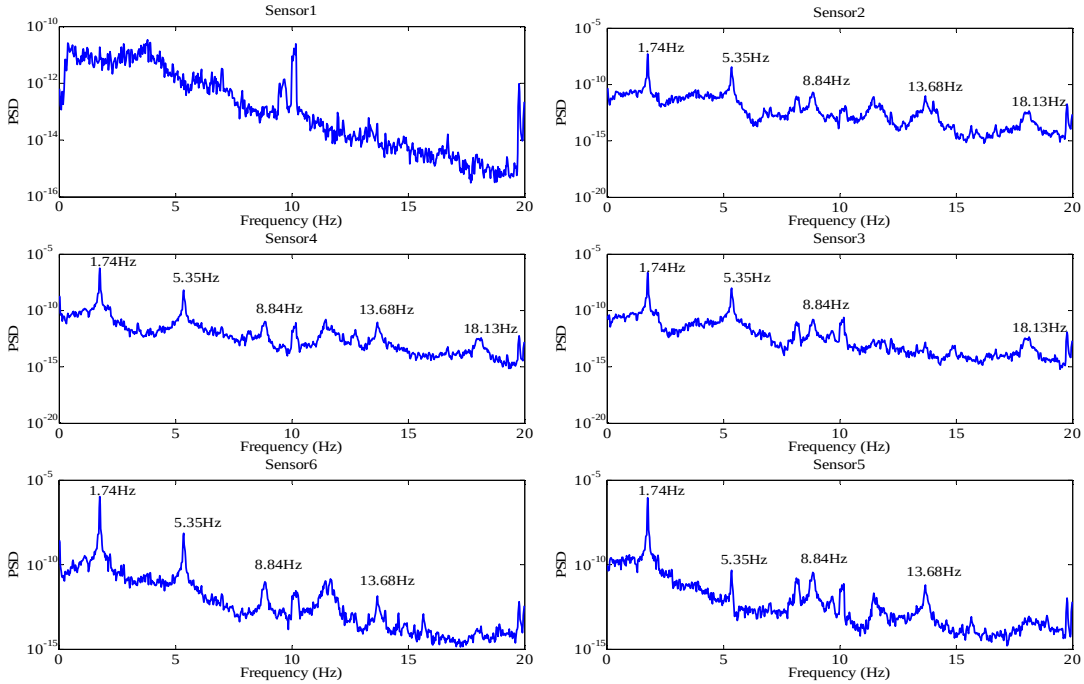

Figure 5. Power spectral density functions of measurements

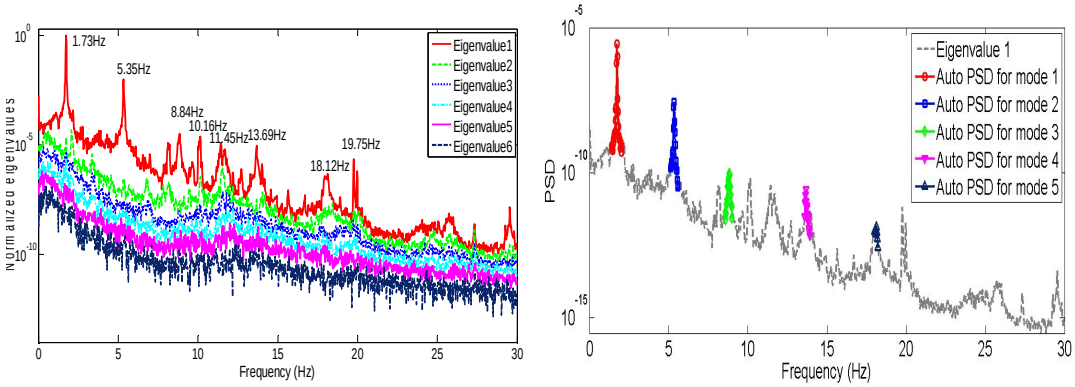

Figure 6. PCA-based modal parameter identification in the frequency domain:
(a) Normalized eigenvalues and (b) Auto power spectral density functions of first five modes

5. Results and discussions

Firstly, the PCA-based technique in the frequency domain has been applied for extracting the modal parameters. Figure 5 shows the power spectral density (PSD) functions of the measured displacements. The natural frequencies of the building can be observed as dominant peaks in the PSDs. First five natural frequencies have been extracted as 1.73Hz, 5.35Hz, 8.84Hz, 13.69Hz, 18.02Hz, respectively (see Figure 5).

Spectral eigenvalues and eigenvectors have been determined from the cross spectral matrix of the measured responses via Eq.(4b), Eq.(5). Some normalized spectral eigenvalues are indicated in Figure 6a, whereas auto power spectral functions of the first five modes are shown in Figure 6b, estimated from the first dominant eigenvalue for extracting the damping ratios. It is noted that the PCA-based modal parameter identification requires the prior information (here, the natural frequencies need to be known) to extract the damping ratios and the mode shapes as well.

In the application of BSS/ICA techniques for the ambient modal identification, the SOBI has been applied firstly (the background theory presented in section 3.6).

One divides measured responses into three segments (0-78s; 79-110s and 111-300s) in respect with waveform of the responses which the SOBI uses for each segment. Figures 7, 8 show the estimated virtual sources of excitations of the segments 1, 2. Figure 9 indicates the PSD functions of the virtual excitation sources of the segment 1 for example. Sources 1, 2 contain the first and second natural frequencies, while sources 3-6 do not contain, except spectral disturbances at low frequencies. Figure 10 shows the blind mode shapes from estimated mixing matrix of the segment 1.

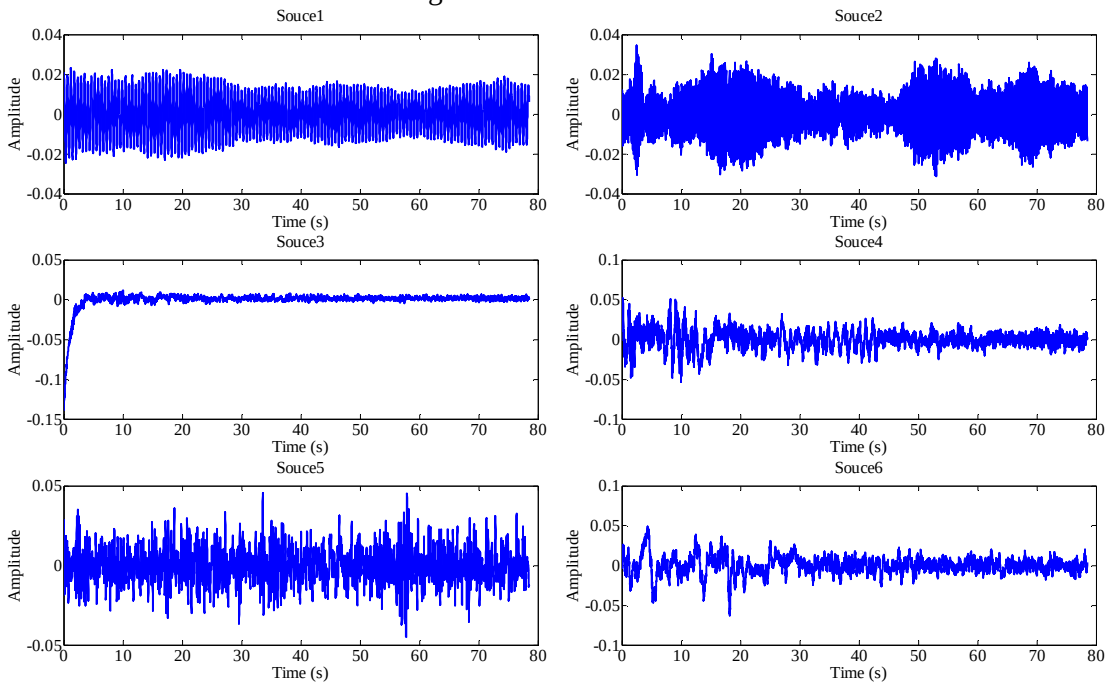

Figure 7. Identification of virtual sources of segment 1

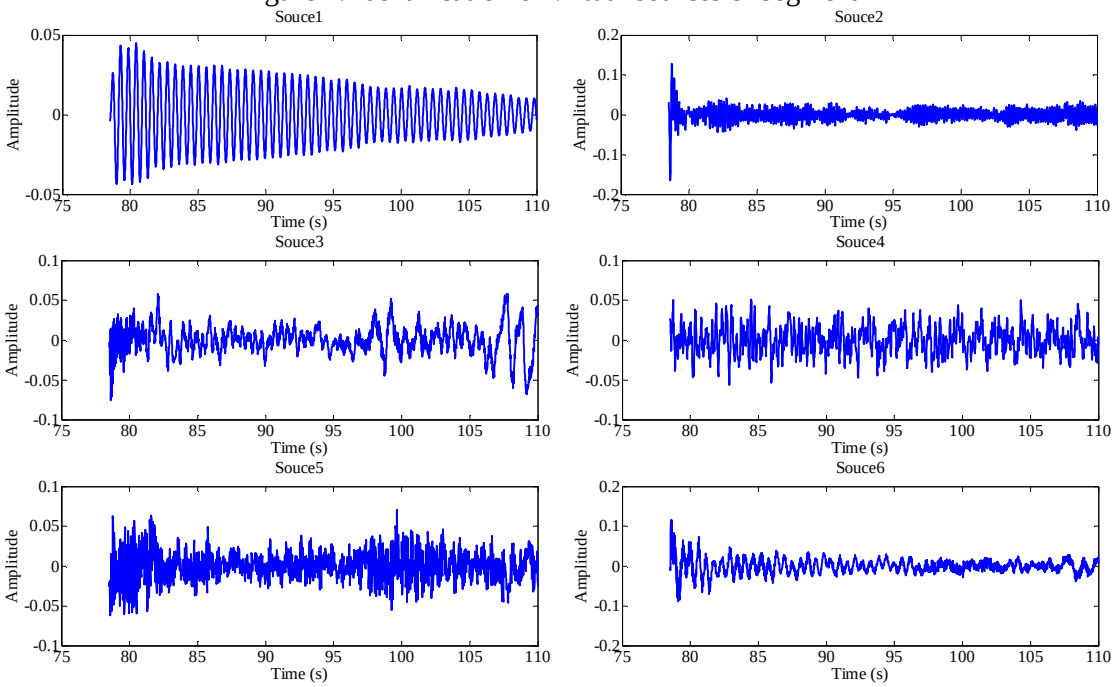

Figure 8. Identification of virtual sources of segment 2

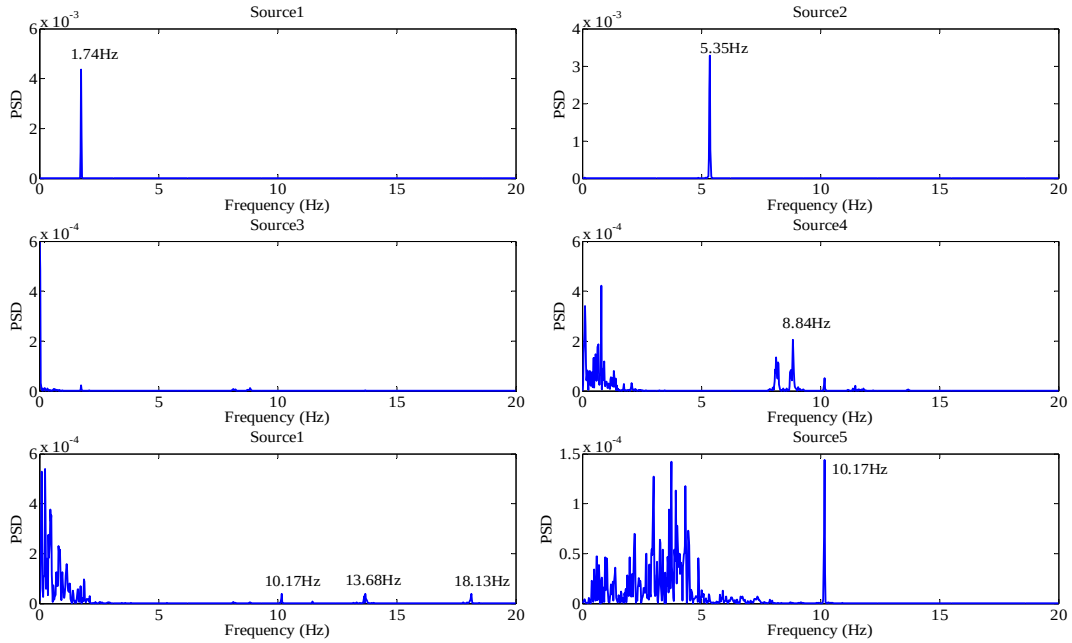

Figure 9. Power spectral density functions of estimated virtual sources of segment 1

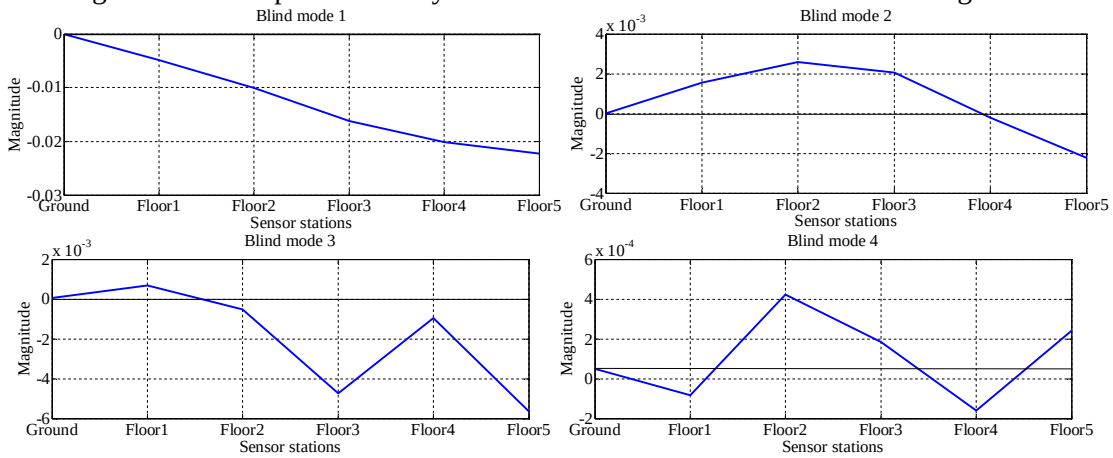

Figure 10. Blind mode shapes from identified mixing matrix of segment 1

5. Conclusion

The paper discusses the modal parameter identification from the ambient vibration data of the five-storey steel building using the advanced techniques of the blind source separation and the independent component analysis. The BSS/ICA techniques have estimated the virtual sources of excitations and the mixing matrix without any prior knowledge of the input excitations which are corresponding to the input excitation sources and the mode shapes of the building. The method has proved potentially due to obtaining directly and evaluating the sources of excitations, however, the BSS/ICA algorithms seems to be more complicated than other well-known output-only modal identification techniques. Further investigations must be required to be applicable for the ambient modal identification of practical structures.

6. Acknowledgements

This study was funded by the Ministry of Education, Culture, Sport, Science and Technology, Japan through the Global Center of Excellence Program, 2008-2012. Data have been provided for use by Dr. Tatiana Kuroiwa of Structural Dynamics Laboratory, Kyoto

University for which the first author would express the special thank.

7. References

Chauhan, S., Allemang, S.J., Martell, R., Brown, D.L. (2007). Application of independent component analysis and blind source separation techniques to operational modal analysis. *Proceedings of International Operational Modal Analysis Conference (IMACXXV)*, Florida USA.

Hyvarinen, A., Karhunen, J., Oja, E. (2001). *Independent component analysis*. John Willey and Sons, Inc.

McNeill, S.I., Zimmerman, D.C. (2008). A framework for blind modal identification using joint approximate diagonalization. *Mechanical Systems and Signal Processing*, 22, 1526–1548

Ponceleta, F., Kerschena, G., Golinvala, C., Verhelst, D. (2007. Output-only modal analysis using blind source separation techniques. *Mechanical Systems and Signal Processing*, 21, 2335–2358

Poncelet, F., Kerschen, G., Golinval, J.C. (2008). Operational Modal Analysis using Second-Order Blind Identification. *Proceedings of International Modal Analysis Conference (IMAC)*, Orlando, USA

Zhou,_W.L., Chelidze, D. (2007). Blind source separation based vibration mode identification. M*echanical Systems and Signal Processing*, 21, 3072–3087

The 2nd International Conference on Engineering Mechanics and Automation (ICEMA2)
Hanoi, August 16-17, 2012
ISBN: 978-604-913-097-7

Time-frequency Coherence for Multivariate Random Fields

Le Thai Hoa[a, b] and Yukio Tamura[c]

[a] *Wind Engineering Research Center, Tokyo Polytechnic University, Japan, thle@arch.t-kougei.ac.jp*
[b] *University of Engineering and Technology, Vietnam National University, Hanoi, Vietnam, thle@vnu.edu.vn*
[c]*Department of Architectural Engineering, Tokyo Polytechnic University, Japan, yukio@arch.t-kougei.ac.jp*

Abstract

Paper presents new approach of using some recent time-frequency analysis methods for investigating coherence and coherent structure of multi-variate random fields such as turbulent, wind-induced pressure, force fields and so on. Time-frequency analysis-based coherence of the multi-variate random fields advantages over their conventionally Fourier transform-based representation due to its broader capacity to investigate the specific hidden coherence events in the simultaneous time-frequency plane, while the Fourier transform-based coherence represents only dominant spectral coherence events in the frequency domain only but no information in the time domain could be observed. Especially, intermittent distribution and localized high coherence events in the time domain has been investigated and considered as a specific characteristic of the coherence. Most recent time-frequency analysis methods are the short-time Fourier transform, the wavelet transform and the Hilbert-Huang transform applied to establish the so-called time-frequency coherence. Influence and analysis of time-frequency resolution on the time-frequency coherence has been investigated. The physical data of surface pressures on some fundamental rectangular cylinders with slenderness ratios of B/D=1 and B/D=5 in turbulence flows have been used for investigation of proposed time-frequency coherence.

Key Words: Random fields; Coherence; Time-frequency analysis; Short-time Fourier transform; Wavelet transform; Hilbert-Huang transform; STFT coherence; Wavelet coherence; HHT coherence

1. Introduction

Characteristic of spatial distribution and coherence of multi-variate random fields such as wind turbulence, pressures and forces on the structures is essential for the gust response analysis of engineering structures immersed in the turbulence flows. So far, the Fourier transform-based coherence in the frequency domain (Fourier coherence for short) has been commonly used for investigating the coherence structures of wind turbulence, pressures and wind forces and used in a basic theory of the gust response prediction of structures. Recently, some physical measurements indicated that the force coherence is larger than the turbulence one (ex. Larose, 1996; Jakobsen, 1997; Kimura et al., 1997; Matsumoto et al., 2003). Higher coherence of the turbulence-induced forces may cause underestimation on the gust response prediction of structures. Moreover, practical formulae of the force

coherence have based on Davenport's formula containing parameters of spanwise separation and frequency (Jakobsen, 1997) or on modified von Karman's one adding parameter of turbulence conditions (Kimura et al., 1997). Mechanism of the higher force coherence and effects of the bluff body flow and temporal parameter still have not been investigated yet. Fourier coherence is applicable for purely stationary time series, moreover, no temporal information can be observed.

Time-frequency analysis methods have been devoted recently for series of topics and applications beside well-known Fourier transform-based tools due to its capacity to represent any signal into simultaneous time-frequency plane. It also advantages for analyzing non-stationary events as a nature of practical measurements. Short-time Fourier transform (STFT), known as Gabor transform has been extended from the original Fourier transform to represent the signals into the time-frequency plane thanks to adding windowed function to localize the time translation (Oppenheim and Schafer 1989). However, due to a fixed length of windowed function, thus STFT enable to analyze the signals at fixed time-frequency resolution at whole the time-frequency plane (see Figure 1). The most famous and applicable time-frequency analysis is known as wavelet transform (Daubechies 1992). The wavelet transform enables to represent the signals into the time-frequency plane with flexible time-frequency resolution (also known as multi-resolution analysis) thanks to using wavelet function (see Figure 1). Similar to the Fourier transform-based tools, beside the conventional short-time Fourier transform coefficient and the wavelet transform coefficient, high-order short-time Fourier transform-based tools like Gabor power spectrum, Gabor cross power spectrum, Gabor coherence and Gabor phase difference; as well as high-order wavelet transform-based tools such as a wavelet auto power spectrum, wavelet cross power spectrum, wavelet coherence and wavelet phase difference have been devoted. The most recent time-frequency analysis method has been developed by Huang et al. 1998, named as Hilbert-Huang transform or Hilbert spectrum which exploits a combination of empirical mode decomposition and Hilbert transform. The Hilbert-Huang transform analyzes the signals with concepts of instantaneous frequency, instantaneous time and instantaneous time-frequency resolution. For its applications, the wavelet transform coefficients have been applied for the wind turbulence and pressure (ex., Geurts et al., 1998), the wavelet coherence was used to detect cross correlation events between the turbulence and the pressure (Kareem and Kijewski, 2002; Gurley et al. 2003). In these studies, the traditional complex Morlet wavelet and no time-scale smoothing have been used, thus normalized coherence cannot be gained as expected. Fourier coherence and the wavelet coherence of wind turbulence and pressures also have been investigated with focus on effects of spanwise separations, the frequency and the intermittency of coherence structure of the pressure fields as well as comparison between the turbulence coherence and the pressure coherence (Le et al., 2009; Le et al., 2011). They have agreed from their studies that spanwise coherence of the pressures is larger than that of the wind turbulence due to effect of the bluff body flow on model surface, moreover, the spanwise coherence structures of wind turbulence and pressure would depend on the turbulence condition, the frequency, the spanwise separation, the bluff body flow. They also observed that the pressure coherence distributes intermittently in the time domain, and high coherence events distribute locally in the time-frequency plane. In these previous studies, localized high coherence events, intermittency and effect of time-frequency resolution on the spanwise coherence structure of pressures hasn't been clarified yet. Furthermore, second-order Gabor transform-based and Hilbert-Huang transform-based tools have not been developed yet for application.

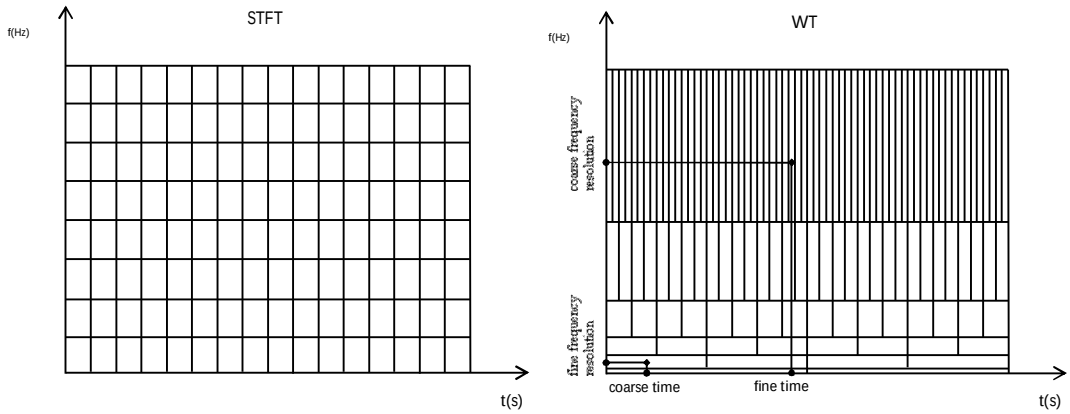

Figure 1. Time-frequency resolution diagram of Gabor and wavelet transforms

In this paper, the time-frequency coherence has been developed based on some most recent time-frequency analysis methods such as the short-time Fourier transform, the wavelet transform and the Hilbert-Huang transform. Then, the time-frequency coherence has been applied to investigate multi-variate random pressure fields. Physical measurements on the surface pressure on some typical rectangular cylinders with slender ratios B/D=1, B/D=5 under the turbulent flows. Finally, the time-frequency resolutions of the Gabor coherence, the wavelet coherence and the Hilbert-Huang coherence have been investigated.

2. Short-time Fourier coherence

The short-time Fourier transform (STFT) or the Gabor transform of a time series *X(t)* is defined as follows (Oppenheim and Schafer, 1989):

$$SF_X(\tau, f) = \int_{-\infty}^{\infty} X(\tau) w(t-\tau) \exp(-2j\pi f\tau) d\tau \quad (1)$$

where $SF_X(\tau, f)$: Short-time Fourier transform coefficient at translation τ and frequency *f*; *w(t)*: short time windowed function (shortly, the window). Practically, a harmonic Gaussian window is used in the short-time Fourier transform of the signals:

$$w(t) = \exp(-a\frac{t^2}{2}) \quad (2)$$

where *a*: length of window.

STFT auto power spectra and STFT cross power spectrum at/between two separated points, respectively are defined as:

$$SPS_X(\tau, f) = E[FT_X(\tau, f) FT_X(\tau, f)^{*T}]$$
$$SPS_Y(\tau, f) = E[FT_Y(\tau, f) FT_Y(\tau, f)^{*T}] \quad (3)$$
$$SCS_{XY}(\tau, f) = E[FT_X(\tau, f) FT_Y(\tau, f)^{*T}]$$

where E[]: expectation operator; *,T: complex conjugate and transpose operators; $FT_X(\tau, f)$, $FT_Y(\tau, f)$: STFT coefficients of time series $X(t), Y(t)$ respectively.

The STFT-based spectral coherence (shortly, STFT coherence or Gabor coherence) is approximately expressed as the normalized correlation coefficient of two spectral quantities of time series *X(t)* and *Y(t)* in the frequency domain (Zhou et al. 2005):

$$SCO_{XY}^2(\tau, f) = \frac{|\langle SCS_{XY}(\tau, f)\rangle|^2}{\langle|SPS_X(\tau, f)|\rangle\langle|SPS_Y(\tau, f)|\rangle} \quad (4)$$

where $|\ |$: absolute operator; $\langle\ \rangle$: smoothing; $SPS_X(\tau, f), SPS_Y(\tau, f)$: STFT auto spectra of *X(t)*, *Y(t)*; $SCS_{XY}(\tau, f)$: STFT cross spectrum between *X(t)* and *Y(t)*. The Gabor coherence is normalized between 0 and 1, thus if two time series *X(t)*, *Y(t)* are fully-correlated, coherence is unit, whereas coherence is zero if two time series are uncorrelated in the frequency domain. It is noted that the smoothing in both the time domain and the frequency must be applied to obtain the Gabor coherence.

3. Wavelet coherence

The continuous wavelet transform (WT) of a time series *X(t)* is defined as the convolution operation between *X(t)* and the wavelet function $\psi_{\tau,s}(t)$ (Daubechies, 1992):

$$WT_X^{\psi}(\tau,s)=\int_{-\infty}^{\infty}X(t)\psi_{\tau,s}^{*}(t)dt \quad (5)$$

where $WT_X^{\psi}(s,\tau)$: wavelet transform coefficient at translation τ and scale s in the time-scale plane; $\psi_{\tau,s}(t)$: wavelet function at translation τ and scale *s* of the basic wavelet function $\psi(t)$ (also called mother wavelet), expressed as follows:

$$\psi_{\tau,s}(t)=\frac{1}{\sqrt{s}}\psi\left(\frac{t-\tau}{s}\right) \quad (6)$$

The wavelet transform coefficients $WT_X^{\psi}(s,\tau)$ can be considered as a correlation coefficient and a measure of similitude between the wavelet function and the original time series in the time-scale plane. The wavelet scale has its meaning as an inverse of the Fourier frequency, thus relationship between the wavelet scale and the Fourier frequency can be consequently obtained:

$$s=\frac{f_0 f_c}{f} \quad (7)$$

where f_c: wavelet central frequency; *f*: Fourier frequency; f_0: sampling frequency of time series *X(t)*.

Complex Morlet wavelet is the most commonly used for the continuous wavelet transform due to its containing of harmonic component as analogous as the Fourier transform which is better adapted to capture oscillatory behavior in the time series.

$$\psi(t)=(2\pi)^{-1/2}\exp(i2\pi f_c t)\exp(-t^2/2) \quad (8a)$$

$$\hat{\psi}(sf)=(2\pi)^{-1/2}\exp\left(2\pi^2(sf-f_c)^2\right) \quad (8b)$$

where $\hat{\psi}(sf)$: Fourier transform coefficient of wavelet function; f_c: central frequency. It can be seen from Eq.(5) that adjustment of time-frequency resolution depending on only the central frequency.

Modified form of the complex Morlet wavelet has been applied here for more flexible analysis of time-frequency resolution (Yan et el., 2006):

$$\psi(t)=(\pi f_b)^{-1/2}\exp(i2\pi f_c t)\exp(-t^2/f_b) \quad (9a)$$

$$\hat{\psi}(sf)=(\pi f_b)^{-1/2}\exp(-f_b\pi^2(sf-f_c)^2) \quad (9b)$$

where $\hat{\psi}(sf)$: Fourier transform coefficient of wavelet function; f_b: bandwidth parameter. Fixed bandwidth parameter is used $f_b=2$ in traditional complex Morlet wavelet (Kareem and Kijewski, 2002; Gurley et al., 2003). Generally, the central frequency relates to number of waveforms to which relates to the wavelet scale or wavelet frequency, whereas the bandwidth parameter relates to the width of wavelet window.

Corresponding to the Fourier transform-based tools, one would like to develop wavelet transform-based tools such as a wavelet auto spectrum, a wavelet cross spectrum, a wavelet cross spectrum at time shift index *i* and scale *s* of two time series *X(t)* and *Y(t)*, based on their wavelet transform coefficients $WT_{X_i}(s)$, $WT_{Y_i}(s)$ which are defined with following formulae:

$$WPS_{XX_i}(s)=\left\langle WT_{X_i}(s)WT_{X_i}^{*T}(s)\right\rangle \quad (10a)$$

$$WPS_{YY_i}(s)=\left\langle WT_{Y_i}(s)WT_{Y_i}^{*T}(s)\right\rangle \quad (10b)$$

$$WCS_{XY_i}(s)=\left\langle WT_{X_i}(s)WT_{Y_i}^{*T}(s)\right\rangle \quad (10c)$$

where $WPS_{XX_i}(s), WPS_{YY_i}(s)$: wavelet auto spectra of *X(t)*, *Y(t)*; $WCS_{XY_i}(s)$: wavelet cross spectrum between *X(t)* and *Y(t)*; $\langle\ \rangle$: smoothing operator in both time and scale axes.

With respect to the Fourier coherence, the squared wavelet coherence of *X(t)*, *Y(t)* is defined as the absolute value squared of the smoothed wavelet cross spectrum, normalized by the smoothed wavelet auto spectra (Torrence and Compo, 1998):

$$WCO_{XY_i}^2(s)=\frac{\left|\left\langle s^{-1}WCS_{XY_i}(s)\right\rangle\right|^2}{\left\langle s^{-1}\left|WPS_{XX_i}(s)\right|\right\rangle\left\langle s^{-1}\left|WPS_{YY_i}(s)\right|\right\rangle} \quad (11)$$

where $WCO_{XY_i}(s)$: wavelet coherence of *X(t)* and *Y(t)*; s^{-1} is used to normalize unit energy density.

4. Hilbert-Huang coherence

Hilbert power spectrum or Hilbert-Huang transform combines the empirical mode decomposition (EMD) at first, then the Hilbert transform afterward. The EMD determines empirically so-called intrinsic mode functions (IMF) from the measured time series, in which the signal can be decomposed into a set of almost orthogonal mono-components in the time domain. The mono-component is conditional to obtain analytic time series with instantaneous amplitude, phase and instantaneous frequency. Algorithm of the empirical mode decomposition to obtain the intrinsic mode functions from measured time series can be found out somewhere (Huang et al. 1998). As a result, measured response can de decomposed into sum of the intrinsic mode functions and residue (constant or trend) as follows (Huang et al. 1998):

$$X(t) = \sum_{j=1}^{N} IMF_j(t) + R_N \qquad (12)$$

where IMF_j: i-th intrinsic mode function; R_N: residue; N: Level of decomposition.

Practically, only first few low-order intrinsic mode functions are meaningful due to containing of actual natural frequencies, other higher-order functions are pseudo-components which contain pseudo low frequencies. Thus, elimination of the higher-order intrinsic mode function from the response time series does the same as noise filtering.

In the next step, analytic signals Z(t) can be determined from the intrinsic mode functions by the Hilbert transform as follows:

$$Z(t) = X(t) + iY(t) = \mathrm{H}[X(t)] \qquad (13a)$$

$$Z(t) = \sum_{j=1}^{N} A_j(f,t)\exp(i\phi_j(f,t)) \qquad (13b)$$

where $A_j(f,t)$: instantaneous amplitude; $\phi(f,t)$: instantaneous phase.

Thus, the HHT auto spectra and HHT cross spectra of the signals *X(t)* or/and *Y(t)* can be defined as follows:

$$HPS_X(f,t) = \sum_{j=1}^{N} E[A_{Xj}(f,t)A_{Xj}(f,t)^T] \quad (14a)$$

$$HCP_{XY}(f,t) = \sum_{j=1}^{N} E[A_{Xj}(f,t)A_{Yj}(f,t)^T] \quad (14b)$$

where E[]: expectation operator

Finally, the HHT coherence between two signals *X(t)* and *Y(t)* can be developed obviously in the similar way as the Gabor coherence and the wavelet coherence:

$$HCO_{XY}^2(f,t) = \frac{|\langle HCP_{XY}(f,t)\rangle|^2}{\langle|HSP_X(f,t)|\rangle\langle|HSP_Y(f,t)|\rangle} \qquad (15)$$

where: $\langle\ \rangle$: smoothing operator; $HCO_{XY}(f,t)$: HHT coherence. Also, smoothing in both the time and frequency axes must be carried out for the HHT coherence.

5. Physical measurements

Physical measurements of the surface pressures were carried out on the fundamental rectangular cylinders with the slenderness ratios of B/D=1 and B/D=5 in an open-circuit wind tunnel. Cylinders B/D=1 and B/D=5 were selected due to their typical patterns of bluff body flows around the cylinder sections. Some previous studies indicated that the Karman vortices dominantly form in a wake of the cylinder B/D=1, where the cylinder B/D=5 creates a favorable condition for a formation of separation bubble and vortex reattachment on its surface. Isotropic turbulence flow was generated artificially using grid devices installed upstream of the cylinders. Turbulence intensities of two u-,w-wind fluctuations were I_u=11.56%, I_w=11.23%, respectively. Pressure taps were arranged on one surface of the cylinders. Cylinder B/D=1 consists of 10 pressure taps (named as from po1 to po10) in the chordwise direction, whereas the cylinder B/D=5 arranges 19 pressure taps (named as from po1 to po19) in

the chordwise direction. In the spanwise direction, the pressure taps were arranged apart at different spanwise separations y=25, 75, 125 and 225mm from a reference pressure line at y=0mm for the both cylinders B/D=1 and B/D=5 (see Figure 2). Surface pressures were measured on the cylinders by using multi-channel pressure measurement system at a sampling rate of 1000Hz in every 100-seconds period. Figure 3 shows the wind tunnel tests on the cylinders B/D=1 and B/D=5.

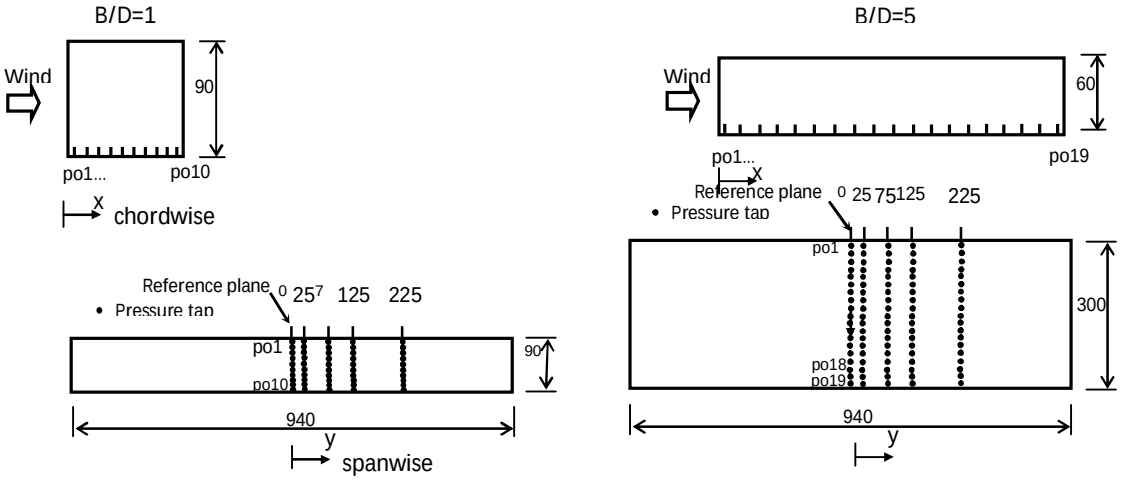

a. b.

Figure 2. Rectangular cylinders and pressure tapes: a. B/D=1, b. B/D=5

a. b.

Figure 3. Wind tunnel tests on cylinders: a. B/D=1 and b. B/D=5

6. Results and discussions

Coherence of the fluctuating multi-variate pressure fields on the cylinders B/D=1 and B/D=5 has been investigated using presented the time-frequency coherence. Figure 4 shows an example of the pressure time series and their corresponding Fourier transform-based power spectral density functions (PSD) at positions y=0 and y=25mm on the B/D=1, B/D=5 (see also Figure 2). One observes that it is impossible to reveal when in the time domain any coherence event in the frequency domain occurs. This is the reason for establishing the time-frequency coherence tools. Firstly, the wavelet coherence has been investigated. Figure 5 indicates the wavelet coherence for two pressure time series at y=0 and y=25mm (Δy=25mm) on the cylinder B/D=1 and B/D=5. Obviously, the wavelet coherence presents the coherence map in the simultaneous time-frequency plane. The high coherence events (bright color) and the low coherence ones (dark color) can be observed through the wavelet coherence maps. It is noted that the high coherence events have been locally and intermittently distributed in

the time-frequency plane. This reveals that the intermittency in the time-frequency plane is a natural characteristic of the pressure coherence. Moreover, the high coherence events can be observed at the high frequency band, but distributed in small time-frequency areas. Intermittency and localization of the pressure coherence have been clarified thanks to the wavelet coherence maps, but they cannot be observed by the conventional Fourier coherence. Figure 6 verifies results between the wavelet coherence and the Fourier coherence in the frequency domain at two different frequency resolutions. There are rather good agreement observed, however, difference between the wavelet coherence and Fourier coherence has been seen at the high frequency range and at higher analyzing frequency resolution (see Figure 6).

STFT coherences of pressure at the separation y=25mm on the cylinders B/D=1 and B/D=5 are shown in Figure 7. It can be seen from the Figure 7 that the high coherence events and the low coherence ones cannot be observed clearly in the time-frequency plane by the STFT coherence maps. It seems to us that the STFT coherences distribute more uniformly than the wavelet ones in the time-frequency plane. However, this unclear observation can be due to (i) smoothing and (ii) time-frequency resolution. Further investigation on influences of the time and frequency resolutions and smoothing techniques on the STFT coherence should be required.

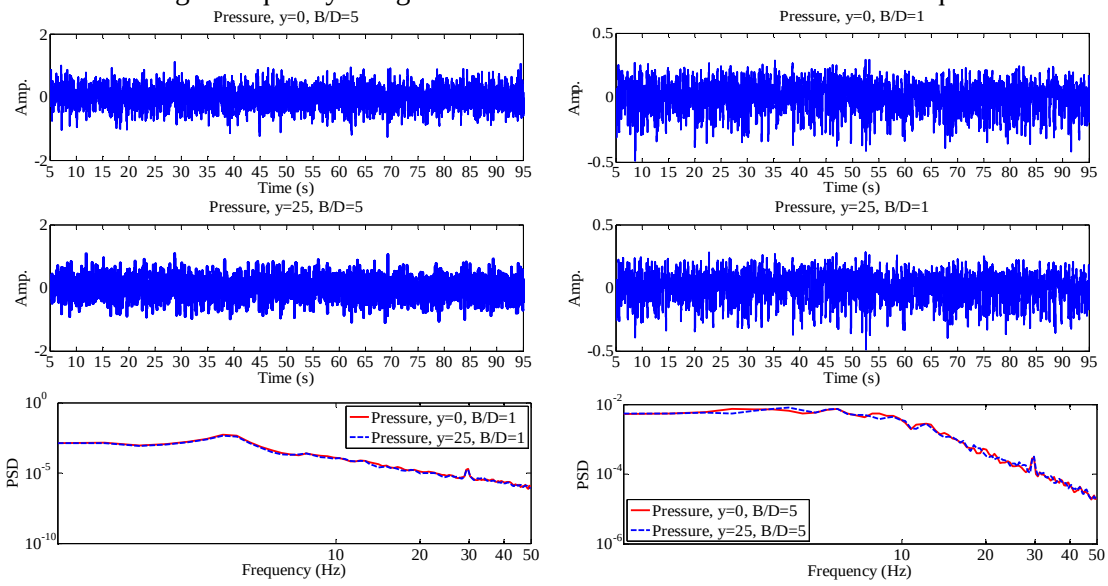

Figure 4. Examples of pressure time series and their PSD at y=0, y=25: a. B/D=1 and b. B/D=5

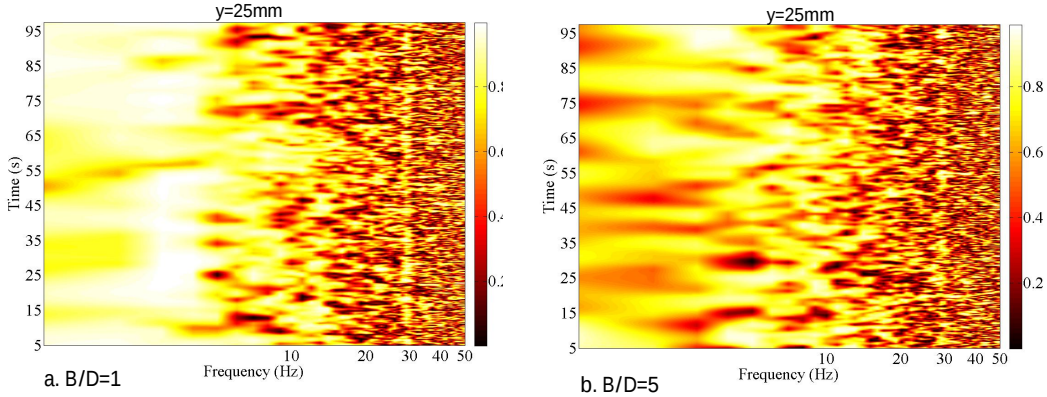

Figure 5. Wavelet coherences of pressure at separation Δy=25mm: a. B/D=1, b. B/D=5

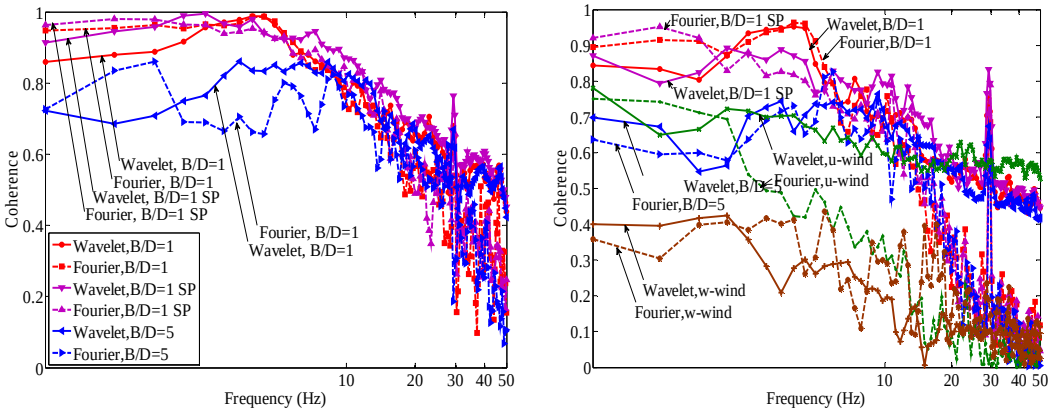

a. Δf=0.24 b. Δf=0.48

Figure 6. Comparison between wavelet coherence and Fourier coherence of pressures on cylinders at spanwise separation y=25mm, at the different analyzing frequency resolutions

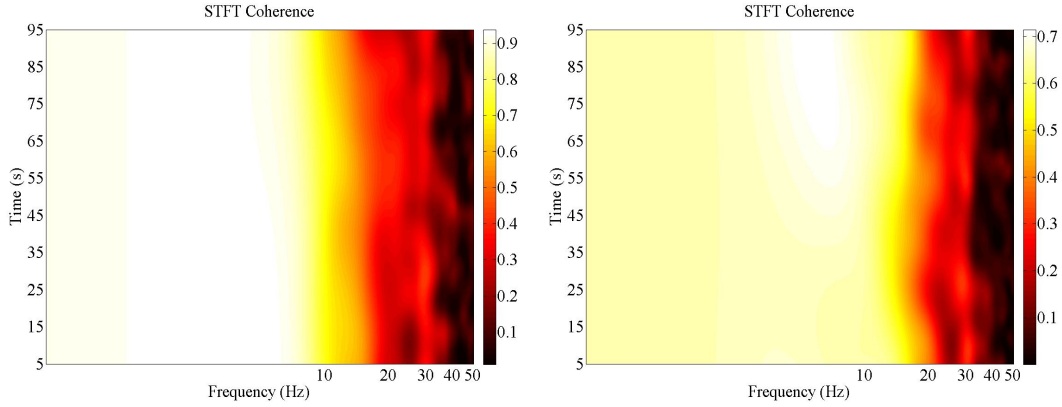

a. b.

Figure 7. STFT coherences of pressure at separation Δy=25: a. B/D=1, b. B/D=5

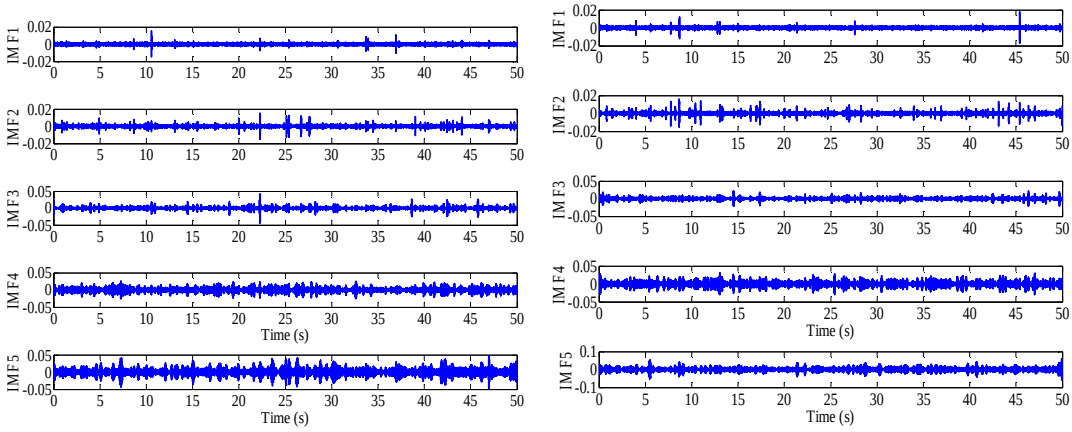

a. b.

Figure 8. First five intrinsic mode functions of pressures at y=0, y=25mm on B/D=1

In the HHT coherence of pressures, the EMD has been applied to obtain the IMFs, then Hilbert transform is used with IMFs to gain HHT spectra, HHT cross spectra and the HHT coherence. Figure 8 shows the first five IMFs of pressures at y=0 and y=25mm on the B/D=1, while the HHT coherences of the pressures at the spanwise separation Δy=25 on the cylinders B/D=1 and B/D=5 are indicated in Figure 9. Coherence events can

be seen through the HHT coherence maps at the simultaneous scale of the time and frequency axes. Though the HHT coherence enables to compute time series with simultaneous time and frequency, but similar to the STFT coherence, the time-frequency resolution analysis and the smoothing must be handled carefully and require further investigations.

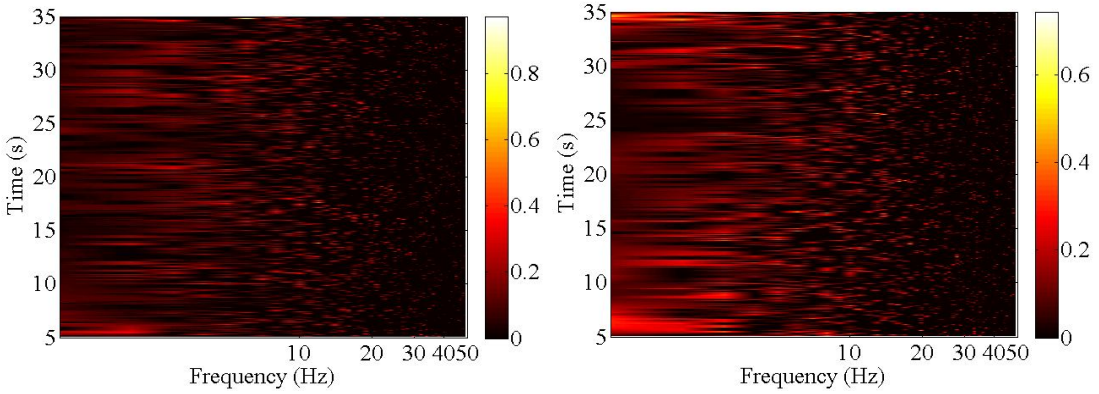

a. b.

Figure 9. HHT coherences of pressure at separation Δy=25mm: a. B/D=1 and b. B/D=5

7. Conclusion

Time-frequency coherence tools have been developed based on the most recent time-frequency analysis methods, concretely the short-time Fourier transform or Gabor transform, the wavelet transform and the Hilbert-Huang transform. Time-frequency coherence has been applied to investigate the multi-variate random pressure fields on some typical cylinders with slenderness ratios B/D=1 and B/D=5 which are measured physically in the wind tunnel. Time-frequency coherence enables to map the high coherence events of the multi-variate fields in the simultaneous time-frequency plane. It is indicated that the intermittency and the localized high coherence are intrinsic characteristics of the pressure coherence. It is noted that the time-frequency resolutions are very important to the time-frequency coherence and it should be carefully considered during computing the time-frequency coherence.

Acknowledgements

This study was funded by the Ministry of Education, Culture, Sport, Science and Technology, Japan through the Global Center of Excellence Program, 2008-2012. Wind tunnel tests have been carried out at the Wind and Bridge Engineering Lab., Kyoto University for which the first author would express his many thanks.

References

Bendat, J.S. and Piersol, A.G., 2000. *Random data: analysis and measurement procedures.* 3rd Edition, John Wiley and Sons.

Daubechies, I., 1992. *Ten lectures on wavelets.* Society of Industrial and Applied Mathematics, Philadelphia.

Gurley, K., Kijewski, T., Kareem, A., 2003. First- and high-order correlation detection using wavelet transform. *Journal of Engineering Mechanics* 129(2), 188-201.

Huang, N., Shen, Z., Long, S., Wu, M., Shih, H., Zheng, Q., Yen, N., Tung, C., Liu, C., 1998. The empirical mode decomposition and the Hilbert spectrum for nonlinear and non-stationary time series analysis. *Proceedings of the Royal Society of London Series A: Mathematical Physical and Engineering Sciences* No.454, 903–995.

Kareem, A., Kijewski, T., 2002. Time-frequency analysis of wind effects on structures. *Journal of Wind Engineering and Industrial Aerodynamics* 90, 1435-1452.

Kijewski, T.L., and Kareem, A. (2003). Wavelet transforms for system identification: considerations for civil engineering applications.

Journal of Computer-aided Civil and Infrastructure Engineering, 18, 341-357.

Larose, G.L.,1996. The span-wise coherence of wind forces on streamlined bridge decks. *Proceedings of the Third International Colloquium on Bluff Body Aerodynamics and Applications*, Blacksburg, USA.

Le, T.H., Matsumoto, M., Hiromichi, H., 2009. Spanwise coherent structure of wind turbulence and induced pressure on rectangular cylinders. *Wind & Structures*, 12(5), 441-455.

Le, T.H., Tamura, Y., Matsumoto, M., 2011. Spanwise pressure coherence on prisms using wavelet transform and spectral proper orthogonal decomposition based tools. *Journal of Wind Engineering and Industrial Aerodynamics* 99, 499-508.

Matsumoto, M., Shirato, H., Araki, K., Haramura, T., Hashimoto, T., 2003. Spanwise coherence characteristics of surface pressure field on 2-D bluff bodies. *Journal of Wind Engineering and Industrial Aerodynamics* 91,155-163.

Oppenheim, A.V. and Schafer, R.W., 1989. *Discrete time signal processing*. Prentice-Hall.

Torrence, C. and Compo, G.P., 1998. A practical guide to wavelet analysis. *Bulletin of the American Meteorological Society* 79(1), 61-78.

Zhan, Y., Halliday, D., Liu, X.,Feng, J., 2005. Detecting the time-dependent coherence between non-stationary electrophysiological signals: A combined statistical and time-frequency approach. *Research report*, 33pages.

The 2nd International Conference on Engineering Mechanics and Automation (ICEMA2)
Hanoi, August 16-17, 2012
ISBN: 978-604-913-097-7

On the equivalent linearization method using dual criterion

Nguyen Dong Anh[a], **Luu Xuan Hung**[b], **Nguyen Ngoc Linh**[c]

[a] *Institute of Mechanics, VAST, 264, Doi Can, Ba Dinh, Hanoi*
University of Engieneering Technology, VNU, Hanoi
[b] *Hanoi Metropolitan Rail Board, 8, Ho Xuan Huong, Hai Ba Trung, Hanoi*
[c] *Construction Technical College No. 1 , Trung Van, Tu Liem, Hanoi*

Abstract

The paper investigates equivalent linearization method using the dual criterion. Mean-square responses of nonlinear stochastic oscillator with nonlinear restoring force subjected to random excitation are considered in two type of linearized systems. The alternate approaches are discussed and compared with the exact solution and the one of the conventional criterion by asymptotic expansion technique. The results shown the significant improvement in the accuracy, especially for small nonlinearities.

Key Words: dual criterion, equivalent linearization, nonlinear stochastic oscillator

1. Introductions

The stochastic equivalent linearization method [5-8] has been proven quite successful in determining approximately the mean square response of nonlinear systems. The method is based on replacing the original nonlinear system by a linear one, that is equivalent to the original one in some probabilistic sense. Several criteria have been suggested in more than recent fifty years but the most popular one was proposed by Caughey [3], that usually called the conventional or classical criterion.

The dual conception has been proposed in [1] for the study of nonlinear vibrations. Based on this conception, Anh N.D. et al. [2] suggested a new criterion using the dual approach to the "replacing" problem. This criterion can be expressed in the following general form

$$E = \left\{ \left\langle \left(A - B(k_i) \right)^2 \right\rangle + \left\langle \left(B(k_i) - \mu A \right)^2 \right\rangle \right\} \to \min_{k_i, \mu} \quad (*)$$

where A represents an element of the nonlinear system that is linearized, $B(k_i)$ represents the linearized element of A in the equivalent linearized system in which the linearization coefficients k_i and μ are determined by a minimizing criterion. The authors used this criterion to investigate three typical nonlinear systems and obtained a significant improvement in the accuracy. However, their investigation has concentrated on the replacement of the only nonlinear stiffness or nonlinear damping element represented by A in (*).

Taking into account the versatility and accuracy of this criterion, it is desirable to extend to another replacement in which there is participation of the corresponding linear elements included in A.

2. Dual criterion of equivalent linearization method

Here, we consider a single-degree-of-freedom oscillator with the nonlinear restoring function

$$e(z) \equiv \ddot{z} + 2h\dot{z} + \omega_o^2 z + \varepsilon g(z) - f(t) = 0 \qquad (1)$$

where first element on the left hand side of equation (1) is acceleration, the second one is presented for the linear damping force, the third one is presented for the linear spring force and $g(z)$ is presented for the nonlinear spring force with coefficient ε. For the sake of simplicity, we assume that $g(z)$ is an old function. In the right hand side of (1), $f(t)$ is presented for the Gaussian white noise excitation with zero mean value,

$$\begin{aligned} &\langle f(t)\rangle = 0 \\ &\langle f(t) f(t+\tau)\rangle = \sigma\delta(t) \end{aligned} \qquad (2)$$

where $\langle . \rangle$ represents the expectation operator, σ is the intensity of white noise.

There exist mathematical difficulties in the derivation of a general solution to equation (1). The dual criterion of equivalent linearization method in [1,2] gives an approximate solution that can be achieved by an equivalent linearization system in which the nonlinear element $g(z)$ is replaced by the linear one. Let $z(t) \approx x_1(t)$ be a solution of the following linear equation:

$$\ddot{x}_1 + 2h\dot{x}_1 + \omega_o^2 x_1 + k_1 x_1 = f(t) \qquad (3)$$

where k_1 is the linearization coefficient. From (1) and (3) one has the equation error

$$\begin{aligned} e(x_1) &= \ddot{x}_1 + 2h\dot{x}_1 + \omega_o^2 x_1 + \varepsilon g(x_1) - f(t) \\ &= \varepsilon g(x_1) - k_1 x_1 \end{aligned} \qquad (4)$$

The coefficient k_1 is chosen so as to minimize the mean square errors between the nonlinear restoring force element in equation (1) and the linear restoring force element in equation (2) according to the dual criterion as following

$$\begin{aligned} E(x_1) = \Big\{ &\Big\langle \big(\varepsilon g(x_1) - k_1 x_1\big)^2 \Big\rangle \\ &+ \Big\langle \big(k_1 x_1 - \mu_1 \varepsilon g(x_1)\big)^2 \Big\rangle \Big\} \to \min_{k_1, \mu_1} \end{aligned} \qquad (5)$$

We can see that the first term of (5) derives from the conventional criterion which represents the forward replacement of the nonlinear element by the linear one, the second term is the mean square error between the linear element $k_1 x_1$ and the nonlinear one $\mu_1 g(x_1)$ which represents the backward replacement called the dual part of the first term. The coefficient μ_1 implies that the nonlinear element is changed in the backward replacement. When $\mu_1 = 1$, we receive the conventional criterion again. In other words, the dual criterion requires minimizing the arithmetic mean of two mean square errors of the forward and backward replacements. Let $g_1 = g(x_1)$, the coefficient k_1 and the mean square value of the displacement of the linearization system are

$$k_1 = \frac{1}{2 - \eta_1} \frac{\varepsilon \langle x_1 g_1 \rangle}{\langle x_1^2 \rangle} \qquad (6)$$

$$\langle x_1^2 \rangle = \frac{\sigma^2}{4h(\omega_o^2 + k_1)} \qquad (7)$$

where $\eta_1 = \dfrac{\langle x_1 g_1 \rangle^2}{\langle x_1^2 \rangle \langle g_1^2 \rangle}$ (8)

Let us take another approximate solution $z(t) \approx x_2(t)$ where $x_2(t)$ is a solution of the equivalent linearization system of following form

$$\ddot{x}_2 + 2h\dot{x}_2 + k_2 x_2 = f(t) \qquad (9)$$

in which the two both linear and nonlinear restoring force elements in the original system are replaced by the only one linear element.

From (1) and (9) one has the error of the two equation

$$\begin{aligned} e(x_2) &= \ddot{x}_2 + 2h\dot{x}_2 + \omega_o^2 x_2 + \varepsilon g(x_2) - f(t) \\ &= \omega_o^2 x_2 + \varepsilon g(x_2) - k_2 x_2 \end{aligned} \qquad (10)$$

The dual criterion in this case is expressed as

$$E(x_2)=\left\{\left\langle\left(\omega_o^2 x_2+\varepsilon g(x_2)-k_2x_2\right)^2\right\rangle + \left\langle\left(k_2x_2-\mu_2\left(\omega_o^2x_2+\varepsilon g(x_2)\right)\right)^2\right\rangle\right\}\to\min_{k_2,\mu_2} \quad (11)$$

Denote $g_2=g(x_2)$ for the convenience. Omitting the intermediate calculation, the linearization coefficient and the approximate solution are, respectively,

$$k_2=\frac{1}{2-\eta_2}\frac{\omega_o^2\langle x_2^2\rangle+\varepsilon\langle x_2g_2\rangle}{\langle x_2^2\rangle} \quad (12)$$

$$\langle x_2^2\rangle=\frac{\sigma^2}{4hk_2} \quad (13)$$

where

$$\eta_2=\frac{1}{\omega_o^4\langle x_2^2\rangle+2\omega_o^2\varepsilon\langle x_2g_2\rangle+\varepsilon^2\langle g_2^2\rangle}\times\frac{\left(\omega_o^2\langle x_2^2\rangle+\varepsilon\langle x_2g_2\rangle\right)^2}{\langle x_2^2\rangle} \quad (14)$$

We can see that the approximate solutions determined by (7) and (13) are different because the coefficient k_2 do not keep in form of $k_2=\omega_o^2+k_1$ when using dual criterion. Therefore, the replacement between the restoring force elements of the origin system and the one of the linearization system plays an important role in the dual criterion. For the convenience, we call the replacement of the only nonlinear restoring element by the linear one as dual criterion 1, and the replacement of the both nonlinear and linear restoring elements by the only one linear element as dual criterion 2. For evaluating the effectiveness of the dual 2 solution, we will compare it with the dual 1 solution, with the conventional and exact solutions by using asymptotic expansion method with small value of ε.

Let $\sigma^2/4h=1$, $\omega_o=1$, the well-known probability density function of the oscillator (1) is

$$W(z)=C\exp\left(-\frac{z^2}{2}-\varepsilon I\right) \quad (15)$$

where C is the normalization constant, $I=\int_0^z g(z)dz$. After expanding $W(z)$ with the approximation of third oder to ε, the result of the exact solution is:

$$\langle z^2\rangle=\frac{\int_{-\infty}^{\infty}z^2\left(1-I\varepsilon+\frac{I^2}{2}\varepsilon^2-\frac{I^3}{6}\varepsilon^3\right)\exp\left(-\frac{z^2}{2}\right)dz}{\int_{-\infty}^{\infty}\left(1-I\varepsilon+\frac{I^2}{2}\varepsilon^2-\frac{I^3}{6}\varepsilon^3\right)\exp\left(-\frac{z^2}{2}\right)dz} \quad (16)$$

Next step, one calculates the integrations in (16) and continues making the expansion, the exact solution will be found in the approximation in terms of ε that is correct to third oder

$$\langle z^2\rangle=a_o+a_1\varepsilon+a_2\varepsilon^2+a_3\varepsilon^3 \quad (17)$$

Similarly, from (6), (7), (8), the asymptotic expansion of the dual 1 solution will have the expected form

$$\langle x_1^2\rangle=b_o+b_1\varepsilon+b_2\varepsilon^2+b_3\varepsilon^3=\frac{1}{1+\varepsilon V\left(\langle x_1^2\rangle\right)} \quad (18)$$

where $V\left(\langle x_1^2\rangle\right)=\frac{\langle x_1g_1\rangle\langle g_1^2\rangle}{2\langle x_1^2\rangle\langle g_1^2\rangle-\langle x_1g_1\rangle^2}$ (19)

Because $\langle x_1^2\rangle$ is expressed by the asymptotic variable ε, so the Taylor expansion for $V\left(\langle x_1^2\rangle\right)=V\left(b_o+b_1\varepsilon+b_2\varepsilon^2+b_3\varepsilon^3\right)$ is

$$\begin{aligned}V\left(\langle x_1^2\rangle\right)&=V(b_0)+\frac{1}{1!}V'(b_0)\left(b_1\varepsilon+b_2\varepsilon^2+b_3\varepsilon^3\right)\\&+\frac{1}{2!}V''(b_0)\left(b_1\varepsilon+b_2\varepsilon^2+b_3\varepsilon^3\right)^2\\&+\frac{1}{3!}V'''(b_0)\left(b_1\varepsilon+b_2\varepsilon^2+b_3\varepsilon^3\right)^3\\&=V(b_0)+b_1V'(b_0)\varepsilon\\&+\left(\frac{b_1^2V''(b_0)}{2}+b_2V'(b_0)\right)\varepsilon^2\\&+\left(\frac{b_1^3V'''(b_0)}{6}+b_2V''(b_0)+b_3V'''(b_0)\right)\varepsilon^3\end{aligned} \quad (20)$$

Substituting $V\left(\left\langle x_1^2\right\rangle\right)$ from (20) to (18) and expanding the right hand side, one has

$$b_o + b_1\varepsilon + b_2\varepsilon^2 + b_3\varepsilon^3 = 1 - V(b_0)\varepsilon + \left(V^2(b_0) - b_1V'(b_0)\right)\varepsilon^2 + + \left(V(b_0)\left(b_1V'(b_0) - V^2(b_0)\right) - b_2V'(b_0) - \frac{b_1^2V''(b_0)}{2} + b_1V(b_0)V'(b_0)\right)\varepsilon^3 \quad (21)$$

Identifying the parts of (21) that do not involve ε leads to the result

$$b_o = 1 \quad (22)$$

$$b_1 = -V(b_0) \quad (23)$$

$$b_2 = V^2(b_0) - V'(b_0)V(b_0) \quad (24)$$

$$b_3 = -\left(V(b_0)V'^2(b_0) + 3V^2(b_0)V'(b_0) + V^3(b_0) + \frac{V''(b_0)V(b_0)}{2}\right) \quad (25)$$

Consider the solution achieved by using conventional criterion

$$\left\langle x_{cv}^2\right\rangle = \frac{1}{1 + \varepsilon\dfrac{\left\langle x_{cv}g\left(x_{cv}\right)\right\rangle}{\left\langle x_{cv}^2\right\rangle}} \quad (26)$$

If one takes $V\left(\left\langle x_{cv}^2\right\rangle\right) = \dfrac{\left\langle x_{cv}g\left(x_{cv}\right)\right\rangle}{\left\langle x_{cv}^2\right\rangle}$ (27)

it will be seen that the conventional solution in (26) has the same form as the dual 1 solution in (18), so it is possible to use the result from (22) to (25) applying for asymptotic expansion of $\left\langle x_{cv}^2\right\rangle$.

From (12), (13), (14), the dual 2 solution can be written as

$$\left\langle x_2^2\right\rangle = \left(\left\langle x_2^2\right\rangle + 2\left\langle x_2^2\right\rangle\left\langle x_2g_2\right\rangle\varepsilon + \left(2\left\langle x_2^2\right\rangle\left\langle g_2^2\right\rangle - \left\langle x_2g_2\right\rangle^2\right)\varepsilon^2\right) / \left(\left\langle x_2^2\right\rangle + 3\left\langle x_2^2\right\rangle\left\langle x_2g_2\right\rangle\varepsilon + \left(2\left\langle x_2g_2\right\rangle^2 + \left\langle x_2^2\right\rangle\left\langle g_2^2\right\rangle\right)\varepsilon^2 + \left\langle x_2g_2\right\rangle\left\langle g_2^2\right\rangle\varepsilon^3\right) \quad (28)$$

The expected approximation of the dual 2 solution has the following form

$$\left\langle x_2^2\right\rangle = c_0 + c_1\varepsilon + c_2\varepsilon^2 + c_3\varepsilon^3 \quad (29)$$

Substituting (29) into (28) and make the expansion of third oder to ε, gives

$$\begin{aligned} c_0 + c_1\varepsilon + c_2\varepsilon^2 + c_3\varepsilon^3 = {} & 1 - \left\langle x_2g_2\right\rangle\varepsilon + \left(\left\langle g^2\right\rangle - c_1\left\langle x_2g_2\right\rangle + \left(3\left\langle x_2g_2\right\rangle + 2c_1\right)^2 - 3\left\langle x_2g_2\right\rangle^2 - \left(2\left\langle x_2g_2\right\rangle + 2c_1\right)\left(3\left\langle x_2g_2\right\rangle + 2c_1\right)\right)\varepsilon^2 \\ & + \left(\left\langle g_2^2\right\rangle c_1 - \left\langle x_2g_2\right\rangle c_2 + \left(3\left\langle x_2g_2\right\rangle + 2c_1\right)\times \right. \\ & \times\left(2\left\langle x_2g_2\right\rangle^2 + 3\left\langle x_2g_2\right\rangle c_1 + c_1^2 + \left\langle g_2^2\right\rangle + 2c_2\right) \\ & - \left(3\left\langle x_2g_2\right\rangle + 2c_1\right)\left(-\left\langle x_2g_2\right\rangle^2 + 2\left\langle x_2g_2\right\rangle c_1 + c_1^2 + 2\left\langle g_2^2\right\rangle + 2c_2\right) - \left(2\left\langle x_2g_2\right\rangle + 2c_1\right)\left(\left\langle g_2^2\right\rangle + 2c_2\right. \\ & + 3\left\langle x_2g_2\right\rangle c_1 - \left(3\left\langle x_2g_2\right\rangle + 2c_1\right)^2 + 2\left\langle x_2g_2\right\rangle + 2c_1\Big) \\ & + \left(3\left\langle x_2g_2\right\rangle + 2c_1\right)\left(\left\langle g_2^2\right\rangle + 2c_2 + 3\left\langle x_2g_2\right\rangle c_1\right. \\ & \left. \left. - \left(3\left\langle x_2g_2\right\rangle + 2c_1\right)^2 + 2\left\langle x_2g_2\right\rangle + 2c_1\Big) - \left\langle g_2^2\right\rangle\left\langle x_2g_2\right\rangle\right)\varepsilon^3 \end{aligned} \quad (30)$$

Identifying the parts of (30) that do not involve ε leads to the result

$$c_o = 1 \quad (31)$$

$$c_1 = -\left\langle x_2g_2\right\rangle \quad (32)$$

$$c_2 = \left\langle g_2^2\right\rangle - \left\langle x_2g_2\right\rangle^2 \quad (33)$$

$$c_3 = -\left\langle g_2^2\right\rangle\left\langle x_2g_2\right\rangle \quad (34)$$

3. Duffing oscillator

Consider the following nonlinear system:

$$e(z) \equiv \ddot{z} + 2h\dot{z} + \omega_o^2 z + \gamma z^3 - \sigma\xi(t) = 0 \quad (35)$$

where $h, \omega_o, \gamma, \sigma$ are positive real constants, $\xi(t)$ is a Gaussian white noise process with

$$\left\langle \xi(t) \right\rangle = 0, \left\langle \xi(t)\xi(t+\tau) \right\rangle = \delta(t) \tag{36}$$

Base on the dual criterion 2 in (11) and using the formulas (12), (13), (14), the equivalent linear system of (35) can be written as

$$\ddot{x}_2 + 2h\dot{x}_2 + k_2 x_2 = \sigma\xi(t) \tag{37}$$

and the coefficients η_2, k_2 are

$$\eta_2 = \frac{\omega_o^4 + 6\gamma\omega_o^2\left\langle x_2^2 \right\rangle + 9\gamma^2\left\langle x_2^2 \right\rangle^2}{\omega_o^4 + 6\gamma\omega_o^2\left\langle x_2^2 \right\rangle + 15\gamma^2\left\langle x_2^2 \right\rangle^2} \tag{38}$$

$$k_2 = \frac{\omega_o^4 + 6\gamma\omega_o^2\left\langle x_2^2 \right\rangle + 15\gamma^2\left\langle x_2^2 \right\rangle^2}{\omega_o^4 + 6\gamma\omega_o^2\left\langle x_2^2 \right\rangle + 21\gamma^2\left\langle x_2^2 \right\rangle^2}\left(\omega_o^2 + 3\gamma\left\langle x_2^2 \right\rangle\right) \tag{39}$$

Note that in the above equation, $g(x_2) = x_2^3$ and we use the following formula for the normal processes

$$\left\langle x^{2n} \right\rangle = (2n-1)!!\left\langle x^2 \right\rangle^n \qquad n = 1,2,3,... \tag{40}$$

We obtain the approximate solution as

$$\left\langle x_2^2 \right\rangle = \frac{\omega_o^4 + 6\gamma\omega_o^2\left\langle x_2^2 \right\rangle + 21\gamma^2\left\langle x_2^2 \right\rangle^2}{\omega_o^4 + 6\gamma\omega_o^2\left\langle x_2^2 \right\rangle + 15\gamma^2\left\langle x_2^2 \right\rangle^2} \times \frac{\sigma^2}{4h\left(\omega_o^2 + 3\gamma\left\langle x_2^2 \right\rangle\right)} \tag{41}$$

Come back to the nonlinear system (34), its exact mean square solution reads (see [5])

$$\left\langle z^2 \right\rangle = \frac{\int_{-\infty}^{\infty} z^2 \exp\left(-\frac{4h}{\sigma^2}\left(\frac{1}{2}\omega_o^2 z^2 + \frac{1}{4}\gamma^2 z^4\right)\right)dz}{\int_{-\infty}^{\infty} \exp\left(-\frac{4h}{\sigma^2}\left(\frac{1}{2}\omega_o^2 z^2 + \frac{1}{4}\gamma^2 z^4\right)\right)dz} \tag{42}$$

Similarly to the equivalent linearization equation (3), the approximate mean square solutions corresponding to the dual criterion 1 and to the conventional criterion are (see [2,7]), respectively

$$\left\langle x_1^2 \right\rangle = \frac{7}{30\gamma}\left(-\omega_o^2 + \sqrt{\omega_o^4 + \frac{15}{7}\frac{\gamma\sigma^2}{h}}\right) \tag{43}$$

$$\left\langle x_{cv}^2 \right\rangle = \frac{1}{6\gamma}\left(-\omega_o^2 + \sqrt{\omega_o^4 + 3\frac{\gamma\sigma^2}{h}}\right) \tag{44}$$

For small γ, one can make the asymptotic expansion in comparing the accuracy of the approximate solutions in (41), (43), (44) against the exact solution in (42) with note that $\omega_o = 1$, $h = 0.5$, $\sigma = \sqrt{2}$.
From (16), one has

$$\left\langle z^2 \right\rangle = \frac{\int_{-\infty}^{\infty}\left(1 - \frac{x^4}{4}\gamma + \frac{x^8}{32}\gamma^2 - \frac{x^{12}}{384}\gamma^3\right)z^2\exp\left(-\frac{z^2}{2}\right)dz}{\int_{-\infty}^{\infty}\left(1 - \frac{x^4}{4}\gamma + \frac{x^8}{32}\gamma^2 - \frac{x^{12}}{384}\gamma^3\right)\exp\left(-\frac{z^2}{2}\right)dz} \tag{45}$$

Omitting the integrating and expanding processes of (45), the approximation of the exact solution in term of γ is [7]

$$\left\langle z^2 \right\rangle = 1 - 3\gamma + 24\gamma^2 - 297\gamma^3 \tag{46}$$

Applying (31), (32), (33), (34) when expanding the dual 2 solution, gives

$$\left\langle x_2^2 \right\rangle = 1 - 3\left\langle x_2^2 \right\rangle^2\gamma + \left(15\left\langle x_2^2 \right\rangle^3 - 9\left\langle x_2^2 \right\rangle^4\right)\gamma^2 - 45\left\langle x_2^2 \right\rangle^5\gamma^3 \tag{47}$$

Substituting $\left\langle x_2^2 \right\rangle$ from (29) into the left hand side of (47), obtains the result

$$\left\langle x_2^2 \right\rangle = 1 - 3\gamma + 24\gamma^2 - 243\gamma^3 \tag{48}$$

For expanding the dual 1 solution, determines $V\left(\left\langle x_1^2 \right\rangle\right)$ from (19) first

$$V\left(\left\langle x_1^2 \right\rangle\right) = \frac{15}{7}\left\langle x_1^2 \right\rangle \tag{49}$$

then substituting the expected form of $\langle x_1^2 \rangle$ from (18) into (49), the necessary values of $V\left(b_o + b_1\gamma + b_2\gamma^2 + b_3\gamma^3\right)$ are

$$V(b_o) = \frac{15}{7}; \qquad V'(b_o) = \frac{15}{7}; \qquad V''(b_o) = 0; \qquad V'''(b_o) = 0 \tag{50}$$

Using (50), (22) - (25), leads to the asymptotic expansion of the dual 1 solution

$$\langle x_1^2 \rangle = 1 - \frac{15}{7}\gamma + \frac{450}{49}\gamma^2 - \frac{16875}{343}\gamma^3 \tag{51}$$

With the same above procedure, the approximation of the conventional solution is

$$\langle x_{cv}^2 \rangle = 1 - 3\gamma + 18\gamma^2 - 135\gamma^3 \tag{52}$$

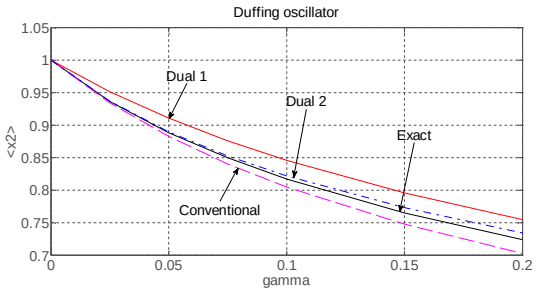

Fig 1. Comparison of mean square solutions with small value of γ, $\omega_o = 1$, $h = 0.5$, $\sigma = \sqrt{2}$

The results of asymptotic expansion in (46), (48), (51) and (60) show that the dual 2 solution agrees with the exact solution up to oder γ^2, the conventional solution is correct to oder γ and the dual 1 solution is only correct to the first term of the approximation. The above results are also shown in figure 1, when γ gets smaller 0.2.

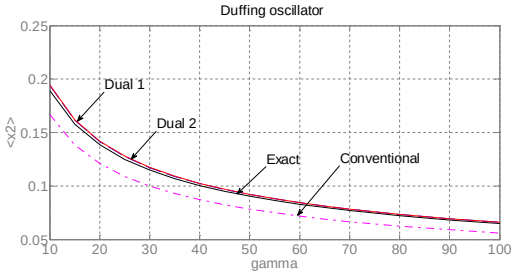

Fig 2. Comparison of mean square solutions with intermediate value of γ , $\omega_o = 1$, $h = 0.5$, $\sigma = \sqrt{2}$

Figure 2 compares the variation of the exact solution with intermediate value of γ against the corresponding approximate solutions, the conventional, the dual 1 and 2 solutions. When the nonlinearities increase, the two dual solutions are nearly coincident and close to the exact curve but the latter is a little closer, while the conventional criterion provides the worst.

For the larger value of γ, the displacement of Duffing oscillator (35) becomes smaller. The approximate form of exact mean square solution in (42) when $\gamma \to \infty$, $\omega_o = 1$, $h = 0.5$, $\sigma = \sqrt{2}$ is

$$\langle z^2 \rangle = \frac{\int_{-\infty}^{\infty} z^2 \exp\left(-\frac{h\gamma^2 z^4}{\sigma^2}\right) dz}{\int_{-\infty}^{\infty} \exp\left(-\frac{h\gamma^2 z^4}{\sigma^2}\right) dz} \tag{53}$$

Omitting the intermediate integrating, the asymptotic form of exact deviation has the form

$$\sigma_z = \frac{\beta}{\gamma^{1/4}} \tag{54}$$

where $\beta = 0.8222$ [6,7].

Obeys the approximation form in (54), the one of the dual 1, 2 and conventional deviations are, respectively

Table 1

Mean square solution	β	*% error*
Exact	0.8222	0
Conventional	0.7598	7.6
Minimization of difference between potential energies	0.7953	3.3
Equality of mean square system functions	0.7128	13.3
Equality of mean square potential energies	0.9036	9.9
Dual 1	0.8265	0.5
Dual 2	0.8265	0.5

$$\sigma_1 = \left(\frac{7}{30\gamma}\right)^{\frac{1}{2}} \left(\frac{60}{7}\gamma\right)^{\frac{1}{4}} \tag{55}$$

$$\sigma_2 = \left(\frac{7}{15}\right)^{\frac{1}{2}} \left(\frac{1}{\gamma\sigma_2^2}\right)^{\frac{1}{2}} \tag{56}$$

$$\sigma_{cv} = \left(\frac{1}{6\gamma}\right)^{\frac{1}{2}} (12\gamma)^{\frac{1}{4}} \tag{57}$$

One can make the comparison between the values of β in table 1. Again, the dual 1 and 2 solutions give the same result and almost coincide the exact solution while the error of conventional solution is 7.6%. Table 1 also presents the expanding results of three other linearization criteria [6], it can be seen that the dual solutions provide the best when compared with them.

4. Conclusions

The approach in this paper gives an extension for the dual criteron applied to a single - degree - of - freedom stochastic oscillator which considers the different replacements of the restoring force. The improvement of the accuracy is evaluated by asymptotic expansion. This approach has potential and it ought to be explored for wide nonlinear classes using the dual criterion.

Acknowledgments The paper is supported by the project *Optimize the parameter of energy hoarding or vanishing system in controlling and monitoring structures*, No 107.04-2011.14 of National Foundation for Science and Technology Development.

References

1. Anh N.D. (2010). *Duality in the anlysis of reponses to nonlinear systems.* Vietnam Journal of Mechanics, VAST, Vol. 32, No. 4, pp. 263 – 266

2. Anh N.D., Hieu N.N., Linh N.N.(2012). *A dual criterion of equivalent linearization method for nonlinear systems subjected to random excitation.* Acta Mechanica, Volume 223, p.645 Number 3

3. Anh N.D., Di Paola M. (1995). *Some extensions of Gaussian equivalent linearization.* International Conference on Nonlinear Stochastic Dynamics, Hanoi, Vietnam, pp. 5–16

4. Caughey TK. (1963) *Equivalent linearization techniques*. Journal of the Acoustical Society of America, 35:1706–1711

5. Crandall S.H. (2006). *A half-century of stochastic equivalent linearization.* Journal of structural control and health monitoring. John Wiley & Sons, 13:27–40

6. Proppe C., Pradlwarter H. J., and Schuëller G.I. (2003). *Equivalent linearization and Monte Carlo simulation in stochastic dynamics*. Probabilistic Engineering Mechanics, 18(1):1–15

7. Roberts J.B., Spanos P.D. (2003). *Random Vibration and Statistical Linearization*. Wiley, New York

8. Socha L. (2008). *Linearization methods for stochastic dynamic system.* Lecture Notes in Physics. Springer, Berlin

The 2nd International Conference on Engineering Mechanics and Automation (ICEMA2) Hanoi, August 16-17, 2012 ISBN: 978-604-913-097-7

Responses of a two-degree-of-freedom system under random excitation by the dual criterion of stochastic linearization method

Nguyen Dong Anh[a,*], Ninh Quang Hai[b], Nguyen Nhu Hieu[c]

[a]*Faculty of Engineering Mechanics and Automation, University of Engineering and Technology, Vietnam National University, email: ndanh@imech.ac.vn*
[b]*Hanoi Architectural University, Km 10, Nguyen Trai Str., Thanh Xuan, Hanoi, Vietnam, email: nqhai_hau@yahoo.com*
[c]*Institute of Mechanics, 264 Doi Can Str., Ba Dinh, Hanoi, Vietnam, email: nhuhieu@imech.ac.vn*

Abstract

In this study, mean-square responses of a two-degree-of-freedom system under random excitation are investigated using the dual criterion of stochastic linearization method. The obtained results are compared with those of two other methods including the conventional linearization technique and energy method. It is shown that there is a good prediction of the dual criterion for mean-square responses of the system in the case of large nonlinearity.

Key words: stochastic linearization, two-degree-of-freedom, mean-square-response, dual criterion

1. Introduction

The stochastic linearization is one of the most used approximate method for analyzing responses of nonlinear systems subjected to random excitation. It can be applied to investigate a wide class of problems of multi-degree-of-freedom (MDOF) systems in engineering. The first studies about the stochastic linearization method is independently introduced by Booton (1954), Kazakov (1954), and Caughey (1956, 1963). The basic idea of the method is that, the original nonlinear system under Gaussian random excitation is replaced by an equivalent linear one under the same excitation, for which coefficients of [illegible] be determined by [illegible] ce between two systems in some statistical sense. In Foster (1968), the method is generalized to random vibration of MDOF systems, and the later by Iwan and Yang (1972), Atalik and Utku (1976). The method of stochastic linearization is also generalized to the systems under both parametric and external excitations in Bruckner and Lin (1987). One can found some new ideas about method in Casciati and Faravelli (1993), Iyengar and Roy (1996), Colajanni and Elishakoff (1998).

Some survey papers reviewing the method of stochastic linearization method are presented by Spanos (1981), Roberts (1981), Socha and Soong (1991), Proppe et al. (2003), and in books by Roberts and Spanos (1990), Socha (2008). Those papers have provided an overview of stochastic

*Corresponding author

linearization method in analyzing responses of mechanical systems.

Recently, some approaches of stochastic linearization method have proposed in Fuijimura and Kiureghian (2007), Elishakoff et al. (2009). Fuijimura and Kiureghian (2007) presented a non-parametric linearization method for nonlinear random vibration analysis. They obtained the first-order approximation of the tail probability of the nonlinear system by using a discrete representation of the stochastic excitation and concept occurred from the first-order reliability method. Also, Elishakoff et al. (2009) developed a new setting for the stochastic linearization method suggested by Anh and Di Paola. Their approach is applied to study mean-square responses of some nonlinear system under random excitation.

In Anh (2010), Anh et al. (2012a), the author have proposed dual criteria of stochastic linearization method for single-degree-of-freedom systems under white noise random excitations. They show that the accuracy of the proposed method is significantly improved when the nonlinearity is increasing.

The dual approach are also generalized to multi-degree-of-freedom systems in Anh et al. (2012b). However, in that study, the authors only consider a particular case of the detuning parameter appearing in the second term of dual criterion. Some nonlinear systems are illustrated in this case. The aim of this study is to explore a wider range of the detuning parameter in order to understand the dual criterion in some specified sense of analyzing responses of nonlinear system subjected to random excitation.

2. Dual criterion applied to two-degree-of-freedom system with nonlinear stiffness

Consider the following two-degree-of-freedom oscillator with nonlinear stiffness

$$\begin{bmatrix}\ddot{x}_1\\ \ddot{x}_2\end{bmatrix}+\begin{bmatrix}h & 0\\ 0 & h\end{bmatrix}\begin{bmatrix}\dot{x}_1\\ \dot{x}_2\end{bmatrix}+\begin{bmatrix}\omega_1^2 & 0\\ 0 & \omega_2^2\end{bmatrix}\begin{bmatrix}x_1\\ x_2\end{bmatrix}+\begin{bmatrix}4\gamma_1 x_1^3+2\gamma_3 x_1 x_2^2\\ 4\gamma_5 x_2^3+2\gamma_3 x_1^2 x_2\end{bmatrix}=\begin{bmatrix}w_1(t)\\ w_2(t)\end{bmatrix}, \tag{1}$$

where $h, \omega_1, \omega_2, \gamma_1, \gamma_3, \gamma_5$ are positive constants, $\mathrm{w}(t)=\begin{bmatrix}w_1(t) & w_2(t)\end{bmatrix}^{\mathrm{T}}$ is a zero-mean Gaussian white noise stationary random vector process with the following correlation function $K_{ij}(\tau)$ $(i,\ j=1,2)$

$$K_{ij}(\tau)=E\left[w_i(t)w_j(t+\tau)\right]=2\pi S_i\delta_{ij}\delta(\tau), \tag{2}$$

where $\delta(\tau)$ is Direc delta function of time variable τ, δ_{ij} is the Kronecker symbol, the quantities S_1, S_2 are constant values of the spectral density of random excitations w_1, w_2, respectively.

Denote

$$\mathrm{C}=\begin{bmatrix}h & 0\\ 0 & h\end{bmatrix},\ \mathrm{K}=\begin{bmatrix}\omega_1^2 & 0\\ 0 & \omega_2^2\end{bmatrix},\quad \Phi=\begin{bmatrix}4\gamma_1 x_1^3+2\gamma_3 x_1 x_2^2\\ 4\gamma_5 x_2^3+2\gamma_3 x_1^2 x_2\end{bmatrix},\ \mathrm{x}=\begin{bmatrix}x_1\\ x_2\end{bmatrix}. \tag{3}$$

The linearized equation system of Eq. (1) takes the following matrix form

$$\begin{bmatrix}\ddot{q}_1\\ \ddot{q}_2\end{bmatrix}+\begin{bmatrix}h & 0\\ 0 & h\end{bmatrix}\begin{bmatrix}\dot{q}_1\\ \dot{q}_2\end{bmatrix}+\begin{bmatrix}\omega_1^2+k_{11}^e & k_{12}^e\\ k_{21}^e & \omega_2^2+k_{22}^e\end{bmatrix}\begin{bmatrix}q_1\\ q_2\end{bmatrix}=\begin{bmatrix}w_1(t)\\ w_2(t)\end{bmatrix}, \tag{4}$$

where

$$\mathrm{K}^{\mathrm{e}}=\begin{bmatrix}k_{11}^e & k_{12}^e\\ k_{21}^e & k_{22}^e\end{bmatrix} \tag{5}$$

is the linearization coefficient matrix found from a specified criterion of stochastic linearization method. There are many criteria for determining the matrix K^{e}, for example, the minimization mean-square criterion in Caughey (1963), Roberts and Spanos (1990),

energy criterion in Zhang et al. (1990), Zhang (2000). Responses of the system (1) are investigated by Jia and Fang (1992) and then by Anh and Hung (2003). Anh et al. (2012b), have employed the dual criterion approach to estimate mean-square responses of the original system (1). As shown in Anh (2010), Anh et al. (2012a, 2012b), the dual criterion appears from idea that, the nonlinear component of the original system is replaced by equivalent component one, in the first step. In the second step, the authors replaced the linearized system obtained by another nonlinear system which belongs to the same class of the original system. In the system (1), the nonlinear vector function Φ only depends on the displacement x. By applying the dual criterion for the original system (1), the nonlinear vector function Φ is replaced by the linear vector $\mathrm{K}^{\mathrm{e}}\mathrm{q}$, then this linear vector is replaced by another nonlinear vector function which is considered as a product of a matrix $\mathrm{D}=\left[d_{ij}\right]_{2\times 2}$ and the original nonlinear vector function Φ, where the matrices K^{e} and D are determined by the following dual criterion

$$E\left[\mathrm{e}^{\mathrm{T}}\mathrm{e}\right]+\rho E\left[\psi^{T}\psi\right]\rightarrow\min_{\mathrm{K}^{\mathrm{e}},\,\mathrm{D}}, \tag{6}$$

where

$$\mathrm{e}=\Phi\left(\mathrm{q}\right)-\mathrm{K}^{\mathrm{e}}\mathrm{q}, \tag{7}$$

$$\psi=\mathrm{K}^{\mathrm{e}}\mathrm{q}-\mathrm{D}\Phi\left(\mathrm{q}\right). \tag{8}$$

The vector e in Eq. (7) is the error between the original nonlinear system (1) and its linearized system (4). The vector ψ is the deviation between the linearized system (4) and the replaced nonlinear system appearing in the second step of replacement process as mentioned above. The parameter ρ attached in second term of the criterion (6) is known as a detuning one taken two values either 0 or 1 in Anh et al (2012b). When the parameter ρ is equal to zero, the criterion (6) will become the conventional mean-square criterion (Roberts and Spanos, 1990) of stochastic linearization method, and when the parameter ρ is equal to 1, the criterion (6) is so call the dual one. In the frame of this investigation, we extend to study a wider range of the parameter ρ of the dual criterion for analyzing responses of the system (1).

The criterion (6) leads the following system for determining two matrices K^{e} and D (Anh et al. (2012b))

$$\begin{bmatrix} E\left[\mathrm{q}\mathrm{q}^{\mathrm{T}}\right] & -\dfrac{\rho}{1+\rho}E\left[\mathrm{q}\Phi^{\mathrm{T}}\right] \\ E\left[\Phi\mathrm{q}^{\mathrm{T}}\right] & -E\left[\Phi\Phi^{\mathrm{T}}\right] \end{bmatrix}\begin{bmatrix} \mathrm{K}^{\mathrm{e}\mathrm{T}} \\ \mathrm{D}^{\mathrm{T}} \end{bmatrix} = \begin{bmatrix} \dfrac{1}{1+\rho}E\left[q\Phi^{\mathrm{T}}\right] \\ 0 \end{bmatrix}. \tag{9}$$

By solving Eq. (9), the following solution of K^{e} and D are obtained

$$\mathrm{K}^{\mathrm{e}\mathrm{T}}=\frac{1}{1+\rho}\mathrm{G}^{-1}E\left[\mathrm{q}\Phi^{\mathrm{T}}\right], \tag{10}$$

$$\mathrm{D}^{\mathrm{T}}=\frac{1}{1+\rho}E\left[\Phi\Phi^{\mathrm{T}}\right]^{-1}\times E\left[\Phi\mathrm{q}^{\mathrm{T}}\right]\mathrm{G}^{-1}E\left[\mathrm{q}\Phi^{\mathrm{T}}\right], \tag{11}$$

where the matrix G is given by

$$\mathrm{G}=E\left[\mathrm{q}\mathrm{q}^{\mathrm{T}}\right]-\frac{\rho}{1+\rho}E\left[\mathrm{q}\Phi^{\mathrm{T}}\right]E\left[\Phi\Phi^{\mathrm{T}}\right]^{\mathrm{T}}E\left[\Phi\mathrm{q}^{\mathrm{T}}\right], \tag{12}$$

and the following non-singular conditions are satisfied for the matrices G and $E\left[\Phi\Phi^{\mathrm{T}}\right]$

$$\det\left(\mathrm{G}\right)\neq 0, \tag{13}$$

$$\det\left(E\left[\Phi\Phi^{\mathrm{T}}\right]\right)\neq 0. \tag{14}$$

As shown in Atalik and Utku (1976), Roberts and Spanos (1990), one has the following property for Gaussian vector process q with zero-mean and sufficiently smooth vector

function $\Phi(\mathrm{q})$ having first partial derivative with respect to q

$$E\left[\mathrm{q}\Phi^{\mathrm{T}}\right]=E\left[\mathrm{qq}^{\mathrm{T}}\right]E\left[\nabla\Phi^{\mathrm{T}}\right], \tag{15}$$

where $\nabla=\left[\dfrac{\partial}{\partial q_1}\quad\dfrac{\partial}{\partial q_2}\right]$ is the nabla operator in two-dimension space. Using the property (15) for (10), (11), (12) yields the following expression for the equivalent stiffness matrix K^{e}

$$\begin{aligned}\mathrm{K}^{\mathrm{eT}}=&\frac{1}{1+\rho}\Big[\mathrm{I}_2\\&-\frac{\rho}{1+\rho}E\left[\nabla\Phi^{\mathrm{T}}\right]E\left[\Phi\Phi^{\mathrm{T}}\right]E\left[\nabla\Phi^{\mathrm{T}}\right]^{\mathrm{T}}\\&\times E\left[\mathrm{qq}^{\mathrm{T}}\right]\Big]^{-1}E\left[\nabla\Phi^{\mathrm{T}}\right].\end{aligned} \tag{16}$$

Here, we assume that all inverse matrices appearing in Eq. (16) exist, I_2 is the unit matrix of size 2. From Eq. (16), it is easy to see that the matrix K^{e} is a symmetry one. When ρ is equal to zero, the expression of K^{e} takes the form of conventional linearization

$$\mathrm{K}^{\mathrm{eT}}=E\left[\nabla\Phi^{\mathrm{T}}\right]. \tag{17}$$

When ρ differs from zero, different approximate responses of the original system (1) can be obtained corresponding to each value of ρ. In Anh et al. (2012), the authors have computed mean-square response of the system in the case of $\rho=1$ of dual criterion (6). In next sections, mean-square responses of the linearized system (4) are evaluated versus various values of ρ. It is observed that the matrix K^{e} in Eq. (16) also depends on responses of the linearized equation (4). To establish a closed equation system for K^{e}, D, one can use the frequency-response function matrix method for Eq. (4) based on spectral density of the random excitation (see (Roberts and Spanos, 1990) for details). In order to show the accuracy of the dual criterion method, in the following section, we also present two other methods, namely, the exact solution and energy methods.

3. System responses via exact solution and energy method

3.1. Exact solution

In the case of the same spectral density of random excitation, $S_1=S_2=S_0$, the Fokker-Planck equation corresponding to the system (1) has an exact solution for the stationary probability density function (Jia and Fang (1992), Anh and Hung (2003))

$$f\left(x_1,x_2\right)=C\exp\left\{-\frac{h}{\pi S_0}U\left(x_1,x_2\right)\right\}, \tag{18}$$

where the potential energy $U\left(x_1,x_2\right)$ and normalization constant C are determined as follows, respectively,

$$\begin{aligned}U\left(x_1,x_2\right)=&\frac{1}{2}\omega_1^2x_1^2+\frac{1}{2}\omega_2^2x_2^2\\&+\gamma_1x_1^4+\gamma_3x_1^2x_2^2+\gamma_5x_2^4,\end{aligned} \tag{19}$$

$$C^{-1}=\int_{-\infty}^{\infty}\int_{-\infty}^{\infty}\exp\left\{-\frac{h}{\pi S_0}U\left(x_1,x_2\right)\right\}dx_1dx_2. \tag{20}$$

The exact mean-square responses of x_1 and x_2 are given by the following expressions

$$E\left[x_i^2\right]=\int_{-\infty}^{\infty}\int_{-\infty}^{\infty}x_i^2\exp\left\{-\frac{h}{\pi S_0}U\left(x_1,x_2\right)\right\}dx_1dx_2. \tag{21}$$

$$(i=1,2)$$

3.2. Energy method

The energy method states that the mean-square difference between the potential energy, associated with the original nonlinear system (1) and its equivalent linear counterpart (4), to be minimal (Zhang et al. (1990), Zhang (2000)). That means

$$E\left[\left(U-U^e\right)^2\right]\to\min_{\mathrm{K}^{\mathrm{e}}}, \tag{22}$$

where U^e is the potential energy corresponding to the linearized system (4)

$$U^e = \frac{1}{2}\left(\omega_1^2 + k_{11}^e\right) q_1^2 + k_{12}^e q_1 q_2 + \frac{1}{2}\left(\omega_2^2 + k_{22}^e\right) q_2^2. \quad (23)$$

The energy criterion (22) yields the following system for determining the unknown matrix K^e (see Anh et al. (2012b))

$$\begin{bmatrix} \frac{1}{2}k_{11}^e \\ k_{12}^e \\ \frac{1}{2}k_{22}^e \end{bmatrix} = \begin{bmatrix} E\left[q_1^4\right] & E\left[q_1^3 q_2\right] & E\left[q_1^2 q_2^2\right] \\ E\left[q_1^3 q_2\right] & E\left[q_1^2 q_2^2\right] & E\left[q_1 q_2^3\right] \\ E\left[q_1^2 q_2^2\right] & E\left[q_1 q_2^3\right] & E\left[q_2^4\right] \end{bmatrix}^{-1} \times \begin{bmatrix} E\left[q_1^6\right] & E\left[q_1^4 q_2^2\right] & E\left[q_1^2 q_2^4\right] \\ E\left[q_1^5 q_2\right] & E\left[q_1^3 q_2^3\right] & E\left[q_1 q_2^5\right] \\ E\left[q_1^4 q_2^2\right] & E\left[q_1^2 q_2^4\right] & E\left[q_2^6\right] \end{bmatrix} \begin{bmatrix} \gamma_1 \\ \gamma_3 \\ \gamma_5 \end{bmatrix}. \quad (24)$$

For Gaussian process with zero-mean, one has a general expression for expectation as follows (Middleton (1960), Fang and Elishakoff (1995))

$$E\left[z_1 z_2 \ldots z_{2m}\right] = \sum_{\text{all independent pairs}} \left(\prod_{j \neq k} E\left[z_j z_k\right] \right), \quad (25)$$

where the number of independent pairs is equal to $(2m)!/\left(2^m m!\right)$. In view of the representation of expression (25), the following terms will appear in the right hand side of Eq. (24)

$$\begin{aligned} &E\left[q_i^4\right] = 3\left(E\left[q_i^2\right]\right)^2, \\ &E\left[q_i^3 q_j\right] = 3E\left[q_i^2\right]E\left[q_i q_j\right], \\ &E\left[q_i^2 q_j^2\right] = E\left[q_i^2\right]E\left[q_j^2\right] + 2\left(E\left[q_i q_j\right]\right)^2, \\ &E\left[q_i^6\right] = 15\left(E\left[q_i^2\right]\right)^3, \\ &E\left[q_i^5 q_j\right] = 15\left(E\left[q_i^2\right]\right)^2 E\left[q_i q_j\right], \\ &E\left[q_i^4 q_j^2\right] = 3\left(E\left[q_i^2\right]\right)^2 E\left[q_j^2\right] + 12E\left[q_i^2\right]\left(E\left[q_i q_j\right]\right)^2, \\ &E\left[q_i^3 q_j^3\right] = 6\left(E\left[q_i q_j\right]\right)^3 + 9E\left[q_i^2\right]E\left[q_j^2\right]E\left[q_i q_j\right]. \end{aligned} \quad (26)$$

By substituting expressions (26) into (24), we obtain the solutions k_{ij}^e $(i, j = 1, 2)$. However, these solutions also depend on responses of the system. Similar to the dual criterion method, a procedure for establishing a closed system of unknowns k_{ij}^e is obtained.

4. Numerical results and discussions

In this section, we present numerical results for estimating mean-square responses of the original system (1). These results are obtained using four approaches including exact solution (21), conventional linearization (17), energy method (24) and dual criterion method (16) with various values of the detuning parameter ρ. Results are presented in Tabs. 1, 2, 3 and 4, where $E\left[x_i^2\right]_{\text{ex}}$, $E\left[x_i^2\right]_{\text{co}}$, $E\left[x_i^2\right]_{\text{en}}$, $E\left[x_i^2\right]_{\text{du}}$ are mean-square responses of x_i $(i = 1, 2)$ obtained by the exact solution, conventional linearization, energy method and dual criterion method, respectively. The system parameters used for these calculations are $h = 1$, $\omega_1 = \omega_2 = 1$, $S_0 = 1$. The error between the results of the exact and approximate solutions is defined as follows

$$\text{error} = \frac{\left| E\left[x_i^2\right]_{\text{approx}} - E\left[x_i^2\right]_{\text{exact}} \right|}{E\left[x_i^2\right]_{\text{exact}}} \times 100\%. \quad (27)$$

A comparison between mean-square response $E\left[x_1^2\right]$ obtained from dual criterion (DC) method and other methods is presented in Tab. 1 with various values of the parameter γ_1 and the fixed values of γ_3, γ_5 ($\gamma_3 = \gamma_5 = 0.2$). It is seen that errors of the dual criterion are smaller than ones of the conventional linearization. For some values of γ_1, for example, $\gamma_1 = 0.5$, $\gamma_1 = 1.0$, $\gamma_1 = 2$, errors of the energy method is quite small, about 1%. When the linearity is creasing, the error of DC method is smallest, for example, 1.7578% for the case $\gamma_1 = 10$, whereas the error of the conventional linearization is largest, namely, 13.3457%.

Tab. 2 shows values of the mean-square response of x_2. It is also observed that the error of the conventional linearization is larger than that of energy and DC methods. In this table, the smallest error of conventional linearization is 8.3366% whereas the largest error of DC method is about 2 times less, namely, 3.9790%.

Tab. 3 and 4 present the error of mean-square responses of x_1 and x_2 for various values of the detuning parameter ρ appearing in the dual criterion (6). The range of ρ is taken from 0.1 to 1.5 ($\gamma_3 = \gamma_5 = 0.2$).

Table 1. Mean-square response of x_1 of the system versus parameter γ_1 with $\rho = 1$ ($\gamma_3 = \gamma_5 = 0.2$)

γ_1	$E\left[x_1^2\right]_{ex}$	$E\left[x_1^2\right]_{co}$	error (%)	$E\left[x_1^2\right]_{en}$	error (%)	$E\left[x_1^2\right]_{du}$	error (%)
0.1	1.2294	1.1457	6.8094	1.2860	4.6004	1.2782	3.9672
0.2	0.9737	0.8907	8.5213	0.9978	2.4835	1.0060	3.3238
0.5	0.6866	0.6166	10.2020	0.6904	0.5462	0.7055	2.7538
1.0	0.5146	0.4573	11.1469	0.5134	0.2392	0.5279	2.5738
2.0	0.3798	0.3343	11.9881	0.3764	0.9022	0.3887	2.3594
5.0	0.2498	0.2176	12.8658	0.2455	1.7275	0.2548	2.0004
7.0	0.2134	0.1854	13.1180	0.209	1.9866	0.2174	1.8753
10.0	0.1802	0.1562	13.3457	0.1762	2.2251	0.1834	1.7584

Table 2. Mean-square response of x_2 of the system versus parameter γ_1 with $\rho = 1$ ($\gamma_3 = \gamma_5 = 0.2$)

γ_1	$E\left[x_2^2\right]_{ex}$	$E\left[x_2^2\right]_{co}$	error (%)	$E\left[x_2^2\right]_{en}$	error (%)	$E\left[x_2^2\right]_{du}$	error (%)
0.1	0.9565	0.8735	8.6789	0.9716	1.5859	0.9866	3.1531
0.2	0.9737	0.8907	8.5213	0.9978	2.4836	1.0060	3.3238
0.5	0.9948	0.9119	8.3366	1.0313	3.6646	1.0319	3.7314
1.0	1.0084	0.9237	8.3999	1.0515	4.2710	1.0482	3.9467
2.0	1.0196	0.9321	8.5876	1.0655	4.4924	1.0602	3.9761
5.0	1.0309	0.9399	8.8329	1.0775	4.5219	1.0713	3.9145
7.0	1.0342	0.9420	8.9094	1.0808	4.5135	1.0744	3.8904
10.0	1.0371	0.9440	8.9813	1.0838	4.5031	1.0772	3.8679

Table 3. Error of mean-square response of x_1 for various values of the detuning parameter ρ

ρ / γ_1	error (%)							
	0.1	0.5	0.7	0.8	0.9	1.0	1.1	1.5
0.1	5.6163	1.1203	0.9794	1.9960	2.9917	3.9672	4.9235	8.5704
0.2	7.2233	2.3021	0.0124	1.1367	2.2402	3.3238	4.3881	8.4672
0.5	8.7933	3.4287	0.8918	0.3438	1.5588	2.7538	3.9297	8.4555
1.0	9.6545	3.9747	1.2886	0.0201	1.3073	2.5738	3.8205	8.6239
2.0	10.4289	4.4922	1.6828	0.3135	1.0335	2.3594	3.6648	8.6984
5.0	11.2540	5.1082	2.1954	0.7747	0.6236	2.0004	3.3567	8.5924
7.0	11.4934	5.2966	2.3585	0.9251	0.4858	1.8753	3.2442	8.5302
10.0	11.7099	5.4685	2.5083	1.0640	0.3580	1.7584	3.1383	8.4682

Table 4. Error of mean-square response of x_2 for various values of the detuning parameter ρ

γ_1 \ ρ	error (%)							
	0.1	0.5	0.7	0.8	0.9	1.0	1.1	1.5
0.1	7.3852	2.4742	0.1608	0.9638	2.0682	3.1531	4.2194	8.3107
0.2	7.2233	2.3021	0.0125	1.1368	2.2403	3.3238	4.3881	8.4672
0.5	7.0072	1.9831	0.3715	1.5134	2.6331	3.7314	4.8093	8.9314
1.0	7.0336	1.8849	0.5209	1.6861	2.8277	3.9467	5.0440	9.2335
2.0	7.1941	1.9501	0.4963	1.6804	2.8400	3.9761	5.0898	9.3378
5.0	7.4162	2.0914	0.3893	1.5893	2.7640	3.9145	5.0419	9.3389
7.0	7.4859	2.1380	0.3524	1.5568	2.7358	3.8904	5.0217	9.3323
10.0	7.5514	2.1818	0.3178	1.5265	2.7095	3.8679	5.0028	9.3265

In Tab. 3, it is seen that when the parameter ρ is far from 1, the error becomes larger, for example, 11.7099% for the case $\rho = 0.1$ and 8.4682% for the case $\rho = 1.5$ with the same value of γ_1 ($\gamma_1 = 10$). However, the error is quite small when ρ is near to 1, for example, 0.0201% for the case $\rho = 0.8$ with $\gamma_1 = 1$. We also obtained a similar result in Tabs. 4. In the case $\rho = 0.7$, the error of mean-square response $E\left[x_2^2\right]$ is smallest.

5. Conclusions

The stochastic linearization method is an effective tool for solving problems of multi-degree-of-freedom (MDOF) system subjected to random excitation. There are many criteria used for analyzing responses of MDOF system. In this study, we utilize the dual criterion approach with a wider range of the detuning parameter in order to calculate approximate mean-square responses of a two-degree-of-freedom system with nonlinear stiffness. For the considered system, there is an agreement between results obtained from the energy and dual criterion methods. Also, the results obtained from the dual criterion show that there is a good prediction on the response of the original nonlinear system when the nonlinearity is increasing and the detuning parameter is taken near to the value 1. The considerable improvement of the error obtained from the dual criterion method is recorded for the system (1).

Acknowledgement

This research is funded by Vietnam National Foundation for Science and Technology Development (NAFOSTED) under grant number: “107.04-2011.13”

References

Anh, N. D (2010). Duality in the analysis of responses to nonlinear systems. *VAST Vietnam Journal of Mechanics*, 32, pp. 263-266.

Anh, N. D., Hieu, N. N and Linh, N. N (2012a). A dual criterion of equivalent linearization method for nonlinear systems subjected to random excitation. *Acta Mechanica*, 223, pp. 645-654.

Anh, N. D., Zakovorotny, V. L., Hieu, N. N and Diep, D. V (2012b). A dual criterion of stochastic linearization method for multi-degree-of-freedom systems subjected to random excitation. *Acta Mechanica* (In Revision).

Anh, N. D and Hung, L. X (2003). An improved criterion of Gaussian equivalent linearization for analysis of nonlinear stochastic systems. *Journal of Sound and Vibration*, 268, pp. 177-200.

Atalik, T and Utku, S (1976). Stochastic linearization of multi-degree-of-freedom nonlinear system. *Earthquake Engineering & Structural Dynamics*, 4, pp. 411-420.

Booton, R. C (1954). The analysis of nonlinear control systems with random inputs. *IRE Trans. Circuit Theory*, 1, pp. 32-34.

Bruckner, A and Lin, Y. K (1987). Generalization of the equivalent linearization method for the nonlinear random vibration problems. *International Journal of Non-Linear Mechanics*, 22, pp. 227-235.

Caughey, T. K (1963). Equivalent linearization techniques. *J. Acoust. Soc. Am.*, 35, pp. 1906-1711 (Reference is made to presentations of the procedure in lectures delivered in 1953 at the California Institute of Technology).

Caughey, T. K (1956). Response of Van der Pol's oscillator to random excitations. *Trans. ASME Journal of Applied Mechanics*, 26, pp. 345-348.

Casciati, F and Faravelli, L (1993). A new philosophy for stochastic equivalent linearization. *Probabilistic Engineering Mechanics*, 8, pp. 179-185.

Colajanni, P and Elishakoff, I (1998). A new look at the stochastic linearization technique for hyperbolic tangent oscillator. *Chaos, Solitons & Fractals*, 9, pp. 1611-1623.

Elishakoff, I., Andrimasy, L and Dolley, M (2009). Application and extension of the stochastic linearization by Anh and Di Paola. *Acta Mechanica*, 204, pp. 89-98.

Fang, J and Elishakoff, I (1995). Nonlinear response of a beam under stationary random excitation by improved stochastic linearization method. *Applied Mathematical Modelling*, 19, pp. 106-111.

Foster, E (1968). Semi-linear random vibrations in discrete systems. *Trans. ASME Journal of Applied Mechanics*, 35, pp. 560-564.

Iwan, W. D and Yang, I (1972). Application of statistical linearization techniques to nonlinear multi-degree-of-freedom systems. *Trans. ASME Journal of Applied Mechanics*, 39, pp. 545-550.

Iyengar, R. N and Roy, D (1996). Conditional linearization in nonlinear random vibration. *ASCE Journal of Engineering Mechanics*, 122, pp. 197-200.

Kazakov, I. E (1954). An approximate method for the statistical investigation for nonlinear systems. Trudy VVIA im Prof. N. E. Zhukovskogo, 394, pp. 1-52 (in Russian).

Kazuya Fujimura and Armen Der Kiureghian (2007). Tail-equivalent linearization method for nonlinear random vibration. *Probabilistic Engineering Mechanics*, 22, pp. 63-67.

Middleton, D (1960). *An introduction to statistical communication theory*. McGraw-Hill, New York. pp. 343.

Proppe, C., Pradlwarter, H. J and Schueller, G. I (2003). Equivalent linearization and Monte-Carlo simulation in stochastic dynamics. *Probabilistic Engineering Mechanics*, 18, pp. 1-15.

Roberts, J. B (1981). Response of nonlinear mechanical systems to random excitation. Part 2: Equivalent linearization and other methods. *Sock. Vib. Dig.*, 13, pp. 15-29.

Roberts, J. B and Spanos, P. D (1990). *Random vibration and statistical linearization*. Wiley, New York.

Spanos, P. D (1981). Stochastic linearization in structural dynamics. *Applied Mechanics Review*, 34, pp. 1-8.

Socha, L and Soong, T. T (1991). Linearization in analysis of nonlinear stochastic systems. *Applied Mechanics Review*, 44, pp. 399-422.

Socha, L (2008). *Linearization methods for stochastic dynamic system*. Lecture Notes in Physics. Springer, Berlin.

Wen-Yao Jia, Tong Fang (1992). Error estimation of Gaussian closure for quasi-linear system. *Acta Mechanica Solida Sinica*, 5, pp. 27-33.

Zhang, X. T., Elishakoff, I and Zhang, R. C (1990). A stochastic linearization technique based on minimum mean-square deviation of potential energies. Stochastic Structural Dynamics. Y.K. Lin and I. Elishakoff. Springer-Verlag, Berlin, pp. 327-338.

Zhang, R. C (2000). Work/energy-based stochastic equivalent linearization with optimized power. *Journal of Sound and Vibration*, 230, pp. 468-475.

The 2nd International Conference on Engineering Mechanics and Automation (ICEMA2)
Hanoi, August 16-17, 2012
ISBN: 978-604-913-097-7

Periodic Parametric Vibration of a Two-Stage Gear System with Faulted Meshing

Nguyen Van Khang[a], Nguyen Phong Dien[a] and Markus Klug[b]

[a] *Dept. Applied Mechanics, Hanoi University of Science and Technology*
No 1. Dai Co Viet Road, Hanoi, nvankhang@mail.hut.edu.vn, dien@mail.hut.edu.vn
[b] *Karlsruhe Institute of Technology (KIT) - Germany, markus.klug@student.kit.edu*

Abstract

The present study deals with the problem of dynamic modeling to indentify sideband structures in vibration spectra of a two-stage gear system. The parametrically excited vibration of the system is investigated. A numerical procedure based on the well-known Newmark integration method is applied to calculate steady-state periodic vibrations. The modeling results provide a better understanding of the dynamic behavior of two-stage gear systems in presence of the distributed gear faults such as non-uniform tooth wear and tooth profile errors.

Key Words: parametric vibration, periodic solution, gear vibration, Newmark method

1. Introduction

Dynamic modeling of gear trains offers a better understanding of the vibration generation mechanisms as well as their dynamic behavior in the presence of gear tooth damage and profile errors. Since the main source of vibration in a geared transmission system is usually the meshing action of the gears, vibration models of the gear-pair in mesh have been developed, taking into consideration the most important dynamic factors such as time-varying mesh stiffness, friction in the meshing interface, gear backlash and static transmission errors. Over the last years there was a large variety of modeling suggestions and approaches to identify relevant effects in one-stage gear-pair systems, e.g. (Özgüven, 1991), (Parker et. al., 2000), (Theodossiades and Natsiavas, 2000), (Nguyen Van Khang et. al., 2009). However, it should be pointed out that the development on modeling and numerical methods for the vibration analysis of multi-mesh and multi-gear systems is still limited and only few papers on this respect have been published, (Lin and Parker, 2002), (Wang et. al., 2004) and (Walha et. al., 2006).

Besides, it is well known from previous experimental investigations that the most important components in steady-state gear vibration spectra are meshing frequencies and their harmonics, together with sideband structures due to the amplitude modulation effect. The increment in the number and amplitude of sidebands can be a symptom of distributed gear faults, and the spacing of the sidebands is related to their source, (Dalpiaz et. al, 2000).

The main objective of the present study is to indentify sideband structures of a two-stage gear system by means of dynamic modeling. The parametrically excited vibration of the system in mesh is investigated. In addition, a numerical procedure based on the well-known Newmark integration method is applied to calculate steady-state periodic vibrations.

2. Dynamic modeling

The considered dynamic model is displayed in Figure 1. This kind of modeling approach has already been investigated in Wang et. al. (2004) and Walha et. al. (2006). In contrast to those works, attention is especially paid to the calculation of steady-state periodic vibrations which generate modulation sidebands in vibration spectra. The two-stage gear system is modeled as two pairs of rigid disks connected by spring-dampers set along the lines of contact. The model takes into account influences of displacement excitation $e_1(t)$ and $e_2(t)$ along the lines of contact of two gear-pairs respectively. These excitations arise from several sources, such as tooth deflection under load, non-uniform tooth spacing, tooth profile errors caused by machining errors as well as pitting, scuffing of teeth flanks. Mesh stiffness $k_1(t)$ and $k_2(t)$ of two gear-pairs are expressed as time-varying functions. The gear-pairs are assumed to operate under high torque condition with zero backlash and the effect of friction forces at the meshing interface is neglected. The viscous damping coefficients of the gear meshes c_1 and c_2 are assumed to be constant. Gears 2 and 3 are connected by a stiff intermediate connecting shaft.

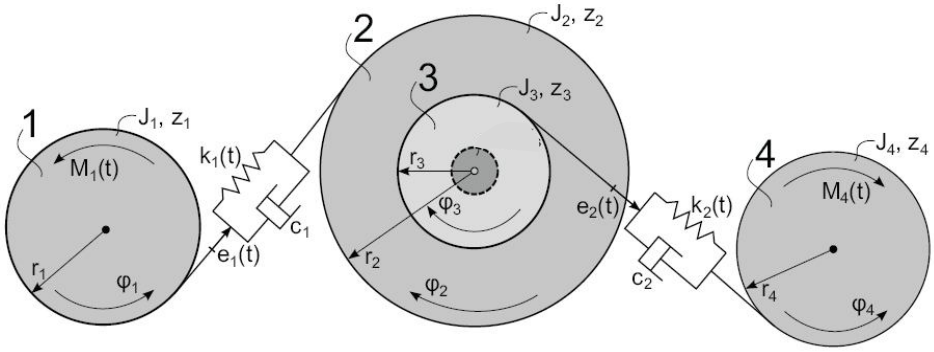

Figure 1. Dynamic model of a two-stage gear system

2.1. Derivation of equations of motion

The further notations shown in the model are as follows: φ_i $(i=1,...,4)$ are rotation angles, of the input pinion (gear 1), gear 2, gear 3 and the output wheel (gear 4) respectively; J_i $(i=1,...,4)$ are the mass moments of the corresponding gears; $M_1(t)$ and $M_4(t)$ denote the external torques applied on the system and r_i $(i=1,...,4)$ the base radii of the gears. Since the intermediate connecting shaft is considered as ideal stiff, it follows that $\varphi_2=\varphi_3$, $\omega_2=\omega_3=\dot{\varphi}_3$. The equations of motion for this system can be written in terms of φ_1, φ_3, φ_4 as

$$\begin{aligned} &J_1\ddot{\varphi}_1 + r_1k_1(t)\left[r_1\varphi_1 - r_2\varphi_3 + e_1(t)\right] \\ &+r_1c_1\left[r_1\dot{\varphi}_1 - r_2\dot{\varphi}_3 + \dot{e}_1(t)\right] = M_1(t), \end{aligned} \tag{1}$$

$$\begin{aligned} &\left(J_2+J_3\right)\ddot{\varphi}_3 - r_2k_1(t)\left[r_1\varphi_1 - r_2\varphi_3 + e_1(t)\right] \\ &-r_2c_1\left[r_1\dot{\varphi}_1 - r_2\dot{\varphi}_3 + \dot{e}_1(t)\right] \\ &+r_3k_2(t)\left[r_3\varphi_3 - r_4\varphi_4 + e_2(t)\right] \\ &+r_3c_2\left[r_3\dot{\varphi}_3 - r_4\dot{\varphi}_4 + \dot{e}_2(t)\right] = 0, \end{aligned} \tag{2}$$

$$\begin{aligned} &J_4\ddot{\varphi}_4 - r_4k_2(t)\left[r_3\varphi_3 - r_4\varphi_4 + e_2(t)\right] \\ &-r_4c_2\left[r_3\dot{\varphi}_3 - r_4\dot{\varphi}_4 + \dot{e}_2(t)\right] = -M_4(t). \end{aligned} \tag{3}$$

By introducing the following composite variables

$$q_1 = r_1\varphi_1 - r_2\varphi_3,\ q_2 = r_3\varphi_3 - r_4\varphi_4, \tag{4}$$

Eqs. (1-3) can be rewritten in the form

$$\begin{aligned} &m_{r1}\ddot{q}_1 + c_1\left[\dot{q}_1 + \dot{e}_1(t)\right] + k_1\left[q_1 + e_1(t)\right] \\ &= m_{r1}\left[\frac{r_1 M_1}{J_1} + \frac{r_2 r_3}{J_2 + J_3}\left(c_2\dot{q}_2 + c_2\dot{e}_2 + k_2 q_2 + k_2 e_2\right)\right] \end{aligned} \tag{5}$$

$$\begin{aligned} &m_{r2}\ddot{q}_2 + c_2\left[\dot{q}_2 + \dot{e}_2\right] + k_2\left[q_2 + e_2(t)\right] \\ &= m_{r2}\left[\frac{r_4 M_4}{J_4} + \frac{r_2 r_3}{J_2 + J_3}\left(c_1\dot{q}_1 + c_1\dot{e}_1 + k_1 q_1 + k_1 e_1\right)\right] \end{aligned} \tag{6}$$

where the reduced masses are defined by

$$\begin{aligned} m_{r1} &= \frac{J_1(J_2 + J_3)}{J_1 r_2^2 + (J_2 + J_3) r_1^2}, \\ m_{r2} &= \frac{(J_2 + J_3) J_4}{(J_2 + J_3) r_4^2 + J_4 r_3^2}. \end{aligned} \tag{7}$$

Note that in Eqs. (5-6) the rigid-body rotation from the original mathematical model is eliminated. The new coordinates $q_1(t)$ and $q_2(t)$ denote the dynamic transmission error for each gear-pair.

Eqs. (5-6) can then be expressed in the compact matrix form

$$\mathbf{M}(t)\ddot{\mathbf{q}} + \mathbf{C}(t)\dot{\mathbf{q}} + \mathbf{K}(t)\mathbf{q} = \mathbf{f}(t), \tag{8}$$

where matrices **M**, **C**, **K** and excitation vector **f** are given by

$$\mathbf{q} = \begin{bmatrix} q_1 \\ q_2 \end{bmatrix},\ \mathbf{M} = \begin{bmatrix} m_{r1} & 0 \\ 0 & m_{r2} \end{bmatrix},$$

$$\mathbf{K} = \begin{bmatrix} k_1 & -\dfrac{m_{r1} r_2 r_3 k_2}{J_2 + J_3} \\ -\dfrac{m_{r2} r_2 r_3 k_1}{J_2 + J_3} & k_2 \end{bmatrix},$$

$$\mathbf{C} = \begin{bmatrix} c_1 & -\dfrac{m_{r1} r_2 r_3 c_2}{J_2 + J_3} \\ -\dfrac{m_{r2} r_2 r_3 c_1}{J_2 + J_3} & c_2 \end{bmatrix},$$

$$\mathbf{f} = \begin{bmatrix} -c_1\dot{e}_1 - k_1 e_1 + m_{r1}\left[\frac{r_1 M_1}{J_1} + \frac{r_2 r_3}{J_2 + J_3}\left(c_2\dot{e}_2 + k_2 e_2\right)\right] \\ -c_2\dot{e}_2 - k_2 e_2 + m_{r2}\left[\frac{r_4 M_4}{J_4} + \frac{r_2 r_3}{J_2 + J_3}\left(c_1\dot{e}_1 + k_1 e_1\right)\right] \end{bmatrix}.$$

In steady-state motion of the gear system, the mesh stiffness $k_i(t)$ $(i = 1,2)$ can be approximately represented by a truncated Fourier series, (Theodossiades et. al., 2000)

$$k_i(t) = \bar{k}_i + \sum_{n=1}^{N_i} k_{i,n}\cos(n\omega_{zi}t + \gamma_{i,n}), \tag{9}$$

where ω_{zi} is the gear meshing angular frequency of stage i that is equal to the number of gear teeth times the shaft angular frequency and N_i is the number of terms of the series.

In general, the error components are no identical for each gear tooth and will produce displacement excitation that is periodic with the gear rotation (i.e. repeated each time the tooth is in contact). The excitation function $e_i(t)$ $(i = 1,2)$ can then be expressed in a Fourier series with the fundamental frequency corresponding to the rotation speed of the faulted gear (Jia and Howard, 2006). In the model, the gear mesh errors are simultaneously situated at the teeth of gear 1 and gear 3, functions $e_1(t)$ and $e_2(t)$ may be taken in the form

$$\begin{aligned} e_1(t) &= \sum_{i=1}^{I} e_{1i}\cos(i\omega_1 t + \alpha_{1i}) \\ e_2(t) &= \sum_{j=1}^{J} e_{2j}\cos(j\omega_3 t + \alpha_{2j}) \end{aligned} \tag{10}$$

Therefore, the vibration equations of gear-pair system according to Eq. (8) are differential equations with time-periodic coefficients.

2.2. Evaluation of the external torques

The external load conditions have an essential effect on the dynamical response of the considered system, but, in general, the external torques $M_1(t)$ and $M_4(t)$ are not prior-known exactly. In fact, constant values for these torques are only a rough assumptions. To treat this problem, the

approach using the static transmission error which is applied in (Nguyen Van Khang et. al., 2004) will be transferred to the two-stage gear system to evaluate the external torques. According to this approach, it is assumed that the rotating speeds of the gears can be nearly constant, and model parameters $k_i \approx \bar{k}_i$, $c_i \approx 0$. The dynamic transmission errors q_1 and q_2 are then equal to the static tooth deflection $\bar{q}_1$ and $\bar{q}_2$ under constant load. Eqs. (5-6) yield the following relations

$$\frac{r_1}{J_1} M_1(t) = \frac{\bar{k}_1}{m_{r1}}\left[\bar{q}_1 + e_1(t)\right] - \frac{r_2 r_3}{J_2 + J_3}\bar{k}_2\left[\bar{q}_2 + e_2(t)\right] \quad (11)$$

$$\frac{r_4}{J_4} M_4(t) = \frac{\bar{k}_2}{m_{r2}}\left[\bar{q}_2 + e_2(t)\right] - \frac{r_2 r_3}{J_2 + J_3}\bar{k}_1\left[\bar{q}_1 + e_1(t)\right] \quad (12)$$

When the static tooth deflection $\bar{q}_1$ and $\bar{q}_2$ are known, the time-varying torques can be evaluated using Eqs. (11) and (12).

3. Newmark procedure for calculating periodic vibrations of linear systems

The procedure presented below for finding the *T*-periodic solution of Eq. (8) is based on the Newmark direct integration method. Firstly, the interval $[0, T]$ is now divided into *m* equal subintervals with the step-size $h = t_i - t_{i-1} = T/m$. We use notations $\mathbf{q}_i = \mathbf{q}(t_i)$ and $\mathbf{q}_{i+1} = \mathbf{q}(t_{i+1})$ to represent the solution of Eq. (8) at discrete times t_i and t_{i+1} respectively. The *T*-periodic solution must satisfy the following conditions

$$\mathbf{q}(0) = \mathbf{q}(T),\ \dot{\mathbf{q}}(0) = \dot{\mathbf{q}}(T),\ \ddot{\mathbf{q}}(0) = \ddot{\mathbf{q}}(T). \quad (13)$$

Based on the single-step integration method proposed by Newmark, we obtain the following approximation formulas, (Newmark, 1959), (Géradin and Rixen, 1994):

$$\mathbf{q}_{i+1} = \mathbf{q}_i + h\dot{\mathbf{q}}_i + h^2\left(\frac{1}{2} - \beta\right)\ddot{\mathbf{q}}_i + \beta h^2 \ddot{\mathbf{q}}_{i+1}, \quad (14)$$

$$\dot{\mathbf{q}}_{i+1} = \dot{\mathbf{q}}_i + (1-\gamma)h\ddot{\mathbf{q}}_i + \gamma h\ddot{\mathbf{q}}_{i+1}, \quad (15)$$

Constants β, γ are parameters associated with the quadrature scheme. Choosing $\gamma = 1/4$ and $\beta = 1/6$ leads to linear interpolation of accelerations in the time interval $[t_i, t_{i+1}]$. In the same way, choosing $\gamma = 1/2$ and $\beta = 1/4$ corresponds to considering the acceleration average value over the time interval (Newmark, 1959).

From Eq. (8) we have the following iterative computational scheme at time t_{i+1}

$$\mathbf{M}_{i+1}\ddot{\mathbf{q}}_{i+1} + \mathbf{C}_{i+1}\dot{\mathbf{q}}_{i+1} + \mathbf{K}_{i+1}\mathbf{q}_{i+1} = \mathbf{f}_{i+1}, \quad (16)$$

where $\mathbf{M}_{i+1} = \mathbf{M}(t_{i+1})$, $\mathbf{C}_{i+1} = \mathbf{C}(t_{i+1})$, $\mathbf{K}_{i+1} = \mathbf{K}(t_{i+1})$ and $\mathbf{f}_{i+1} = \mathbf{f}(t_{i+1})$.

In the next step, substitution of Eqs. (14) and (15) into Eq. (16) yields

$$\begin{aligned}&\left(\mathbf{M}_{i+1} + \gamma h\mathbf{C}_{i+1} + \beta h^2\mathbf{K}_{i+1}\right)\ddot{\mathbf{q}}_{i+1} \\ &= \mathbf{f}_{i+1} - \mathbf{C}_{i+1}\left[\dot{\mathbf{q}}_i + (1-\gamma)h\ddot{\mathbf{q}}_i\right] \\ &-\mathbf{K}_{i+1}\left[\mathbf{q}_i + h\dot{\mathbf{q}}_i + h^2\left(\frac{1}{2} - \beta\right)\ddot{\mathbf{q}}_i\right].\end{aligned} \quad (17)$$

The use of Eqs. (14) and (15) leads to the prediction formulas for velocities and displacements at time t_{i+1}

$$\begin{aligned}\mathbf{q}^*_{i+1} &= \mathbf{q}_i + h\dot{\mathbf{q}}_i + h^2\left(\frac{1}{2} - \beta\right)\ddot{\mathbf{q}}_i, \\ \dot{\mathbf{q}}^*_{i+1} &= \dot{\mathbf{q}}_i + (1-\gamma)h\ddot{\mathbf{q}}_i.\end{aligned} \quad (18)$$

Eq. (18) can be expressed in the matrix form as

$$\begin{bmatrix}\mathbf{q}^*_{i+1} \\ \dot{\mathbf{q}}^*_{i+1}\end{bmatrix} = \mathbf{D}\begin{bmatrix}\mathbf{q}_i \\ \dot{\mathbf{q}}_i \\ \ddot{\mathbf{q}}_i\end{bmatrix}, \quad (19)$$

with

$$\mathbf{D} = \begin{bmatrix}\mathbf{I} & h\mathbf{I} & h^2(0.5-\beta)\mathbf{I} \\ \mathbf{0} & \mathbf{I} & (1-\gamma)h\mathbf{I}\end{bmatrix}, \quad (20)$$

where $\mathbf{I}$ denotes the $n \times n$ identity matrix, $\mathbf{0}$ represents the $n \times n$ matrix of zeros. Eq. (17) can then be rewritten in the matrix form as

$$\ddot{\mathbf{q}}_{i+1} = \left(\mathbf{S}_{i+1}\right)^{-1}\mathbf{f}_{i+1} - \left(\mathbf{S}_{i+1}\right)^{-1}\mathbf{H}_{i+1}\begin{bmatrix}\mathbf{q}^*_{i+1} \\ \dot{\mathbf{q}}^*_{i+1}\end{bmatrix}, \quad (21)$$

where matrices $\mathbf{S}_{i+1}$ and $\mathbf{H}_{i+1}$ are defined by

$$\mathbf{S}_{i+1} = \mathbf{M}_{i+1} + \gamma h \mathbf{C}_{i+1} + h^2 \beta \mathbf{K}_{i+1}, \quad (22)$$

$$\mathbf{H}_{i+1} = \left[\mathbf{K}_{i+1} \quad \mathbf{C}_{i+1}\right]. \quad (23)$$

By substituting relationships (19) into (21) we find

$$\ddot{\mathbf{q}}_{i+1} = \left(\mathbf{S}_{i+1}\right)^{-1} \mathbf{f}_{i+1} - \left(\mathbf{S}_{i+1}\right)^{-1} \mathbf{H}_{i+1} \mathbf{D} \begin{bmatrix} \mathbf{q}_i \\ \dot{\mathbf{q}}_i \\ \ddot{\mathbf{q}}_i \end{bmatrix} \quad (24)$$

From Eqs. (14), (15) and (18) we get the following matrix relationship

$$\begin{bmatrix} \mathbf{q}_{i+1} \\ \dot{\mathbf{q}}_{i+1} \\ \ddot{\mathbf{q}}_{i+1} \end{bmatrix} = \mathbf{T} \begin{bmatrix} \mathbf{q}^*_{i+1} \\ \dot{\mathbf{q}}^*_{i+1} \\ \ddot{\mathbf{q}}_{i+1} \end{bmatrix}, \quad (25)$$

where matrix $\mathbf{T}$ is expressed in the block matrix form as

$$\mathbf{T} = \begin{bmatrix} \mathbf{I} & \mathbf{0} & \mathbf{I}\beta h^2 \\ \mathbf{0} & \mathbf{I} & \mathbf{I}\gamma h \\ \mathbf{0} & \mathbf{0} & \mathbf{I} \end{bmatrix}. \quad (26)$$

The combination of Eqs. (25), (19) and (24) yields a new computational scheme for determining the solution of Eq. (8) at the time t_{i+1} in the form

$$\begin{bmatrix} \mathbf{q}_{i+1} \\ \dot{\mathbf{q}}_{i+1} \\ \ddot{\mathbf{q}}_{i+1} \end{bmatrix} = \mathbf{T} \begin{bmatrix} \mathbf{D} \\ -\left(\mathbf{S}_{i+1}\right)^{-1} \mathbf{H}_{i+1} \mathbf{D} \end{bmatrix} \begin{bmatrix} \mathbf{q}_i \\ \dot{\mathbf{q}}_i \\ \ddot{\mathbf{q}}_i \end{bmatrix} + \mathbf{T} \begin{bmatrix} \mathbf{0} \\ \mathbf{0} \\ \left(\mathbf{S}_{i+1}\right)^{-1} \mathbf{f}_{i+1} \end{bmatrix}. \quad (27)$$

In this equation, the iterative computation is eliminated by introducing the direct solution for each time step. Note that the matrices $\mathbf{T}$ and $\mathbf{D}$ are matrices of constants.

By setting

$$\mathbf{x}_i = \begin{bmatrix} \mathbf{q}_i \\ \dot{\mathbf{q}}_i \\ \ddot{\mathbf{q}}_i \end{bmatrix}, \quad \mathbf{A}_{i+1} = \mathbf{T} \begin{bmatrix} \mathbf{D} \\ -\left(\mathbf{S}_{i+1}\right)^{-1} \mathbf{H}_{i+1} \mathbf{D} \end{bmatrix},$$

$$\mathbf{b}_{i+1} = \mathbf{T} \begin{bmatrix} \mathbf{0} \\ \mathbf{0} \\ \left(\mathbf{S}_{i+1}\right)^{-1} \mathbf{f}_{i+1} \end{bmatrix}, \quad (28)$$

Eq. (27) can then be rewritten in the following form

$$\mathbf{x}_i = \mathbf{A}_i \mathbf{x}_{i-1} + \mathbf{b}_i \quad (i = 1, 2, ..., m). \quad (29)$$

Expansion of Eq. (29) for $i = 1$ to m yields

$$\mathbf{x}_1 = \mathbf{A}_1 \mathbf{x}_0 + \mathbf{c}_1$$
$$\mathbf{x}_2 = \mathbf{A}_2 \mathbf{A}_1 \mathbf{x}_0 + \mathbf{c}_2$$
$$\cdots\cdots\cdots\cdots\cdots\cdots$$
$$\mathbf{x}_m = \left(\prod_{i=m}^{1} \mathbf{A}_i\right) \mathbf{x}_0 + \mathbf{c}_m \quad (30)$$

where

$$\mathbf{c}_0 = \mathbf{0},\ \mathbf{c}_1 = \mathbf{A}_1 \mathbf{c}_0 + \mathbf{b}_1,\ \ \mathbf{c}_2 = \mathbf{A}_2 \mathbf{c}_1 + \mathbf{b}_2, ...,$$
$$\mathbf{c}_m = \mathbf{A}_m \mathbf{c}_{m-1} + \mathbf{b}_m.$$

Using the condition of periodicity, Eq. (13), the last equation of Eq. (30) yields a set of the linear algebraic equations

$$\left(\mathbf{I} - \prod_{i=m}^{1} \mathbf{A}_i\right) \mathbf{x}_0 = \mathbf{c}_m. \quad (31)$$

The solution of Eq. (31) gives us the initial value for the periodic solution of Eq. (8). Finally, the periodic solution of Eq. (8) with the obtained initial value can be calculated without difficulties using the computational scheme given by Eq. (27). Based on the proposed procedure, a computer program with MATLAB has been developed.

4. Numerical results

The major parameters of the gear-pairs given in Table 1 are used for numerical calculation.

The mesh stiffness of each gear-pair at particular meshing position is determined by means of a finite element model, and its time record is shown in Figure 2a. From the finite model, the static tooth deflection is estimated to be $\bar{q}_1 = 10^{-5}$ m and $\bar{q}_2 = 1.5 \times 10^{-5}$ m, in which an nominal load torque of 2000 Nm is applied. The mean value of the Lehr damping ratio used for the dynamic model is assigned to be 0.024.

Table 1. Parameters of the gear-pairs

Parameters	Gear 1	Gear 2	Gear 3	Gear 4
Gear type	helical, standard involute			
Material	steel			
Module (mm)	4.50		4	
Pressure angle (^{o})	20.00			
Helical angle (^{o})	14.56			
Number of teeth z_i	14	39	27	35
Face width (mm)	67	45	60	60
Radius r_i (mm)	30.46	84.86	52.22	83.17
J_i (kgm^2)	0.093	0.272	0.153	0.298
Rotating freq. f_i (Hz)	30	10.77	10.77	8.31
Meshing freq. f_{zi} (Hz)	420		290.8	

After z_3 rotations of the first gear or z_1 rotations of the third gear respectively, the gear system is positioned again in its initial state. Therefore, the time period T used for finding the periodic solution of Eq. (8) can be chosen as $T = z_3.f_1 = z_1.f_3$. The calculation interval is divided into 20000 subintervals or time steps. Using the numerical procedure based on Newmark method, the periodic solutions of Eq. (8) are then calculated for the case of the excitation functions $e_1(t)$ and $e_2(t)$ displayed in Figure 2b.

Figure 3 shows time-periodic curves of the dynamic transmission errors of the considered gear system as the calculation result. The frequency spectra of the first derivative of the dynamic transmission error $\dot{q}_1(t)$ and $\dot{q}_2(t)$ in Figure 4 show clearly the meshing frequencies and its harmonics with sideband structures. As expected, the sidebands are spaced by rotating frequency f_1 of gear 1 and rotating frequency f_3 of gear 3, and characterized by high amplitude. This sideband structure gives a clear indication of the presence of the distributed faults on the gears as indicated by a number of experimental results in Dalpiaz et. al (2000).

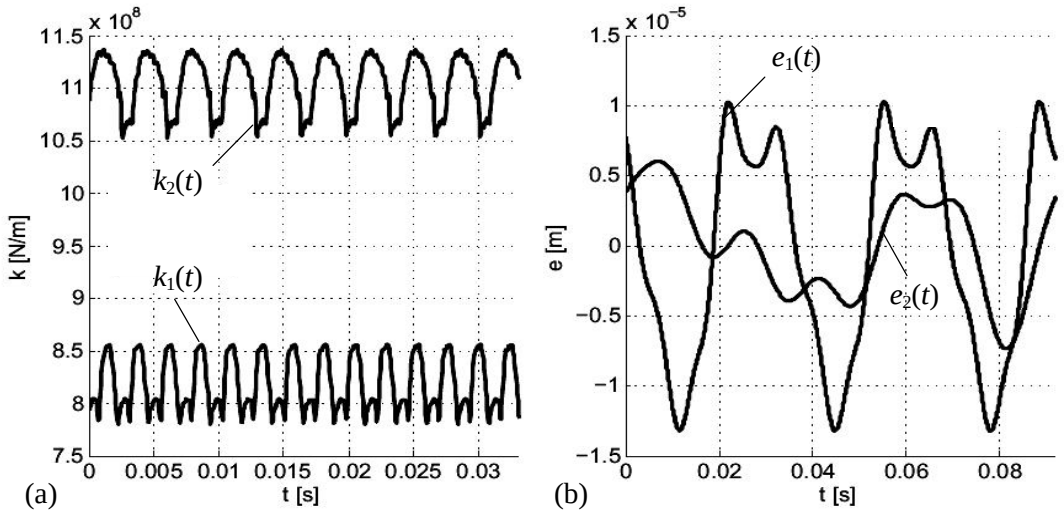

Figure 2. (a) Time records of mesh stiffness and (b) excitation functions

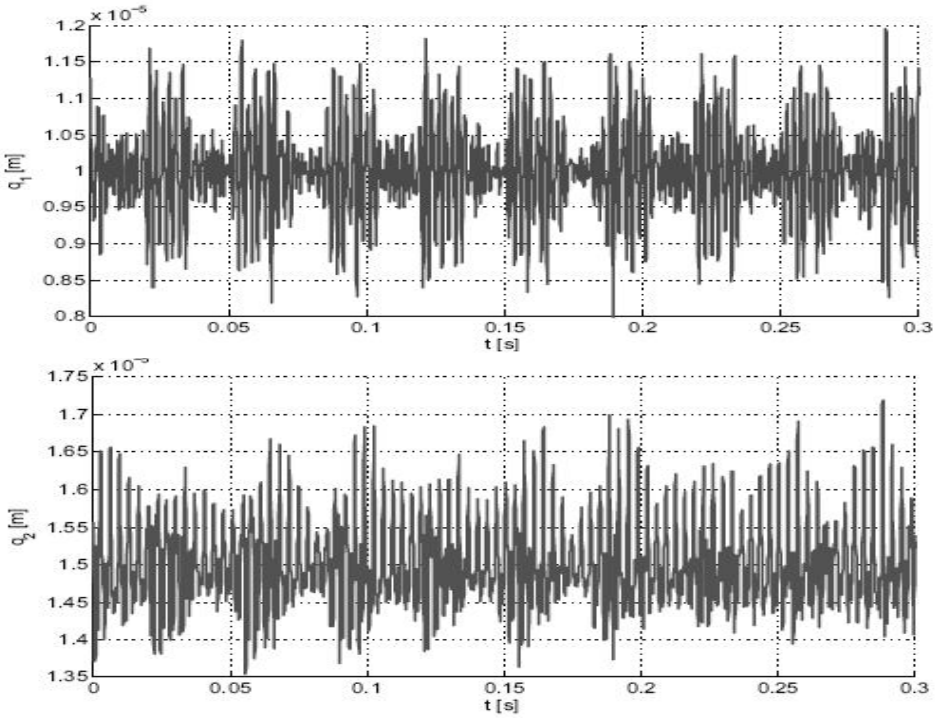

Figure 3. Calculation result for dynamic transmission errors $q_1(t)$ and $q_2(t)$

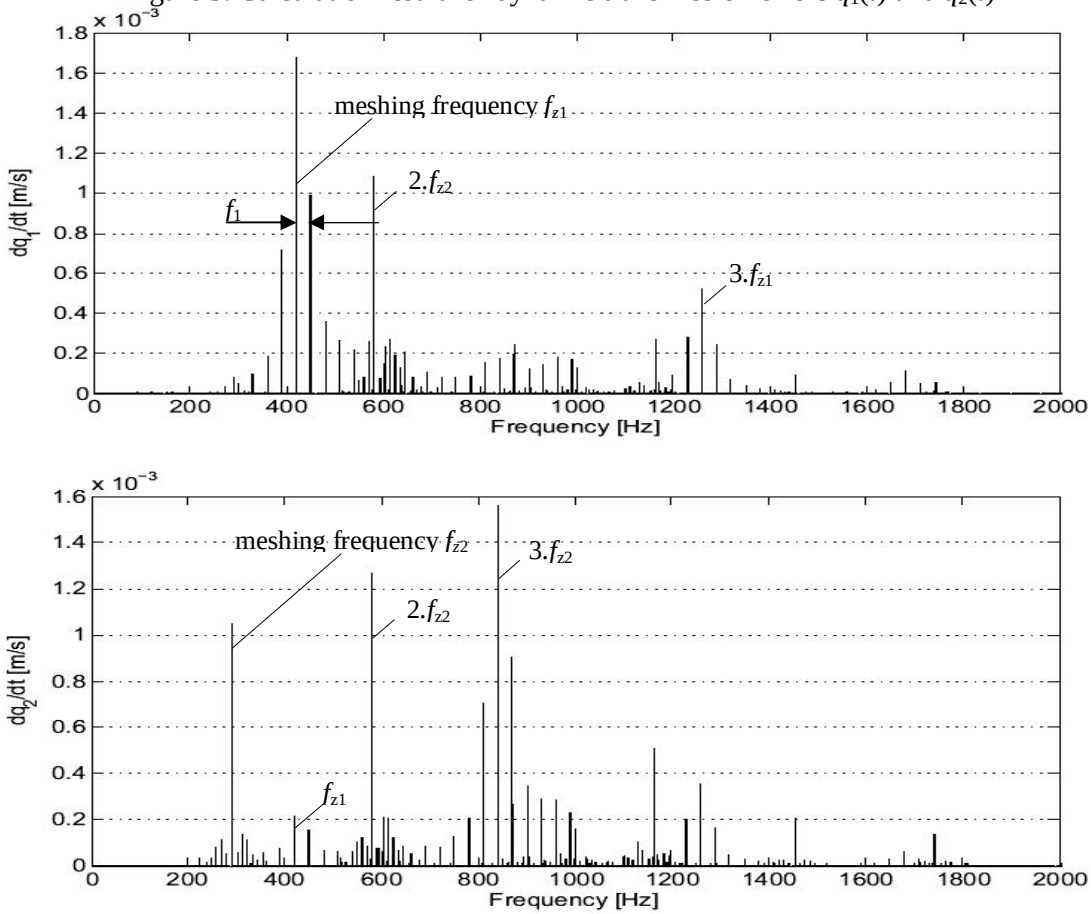

Figure 4. Frequency spectrum of $\dot{q}_1(t)$ and $\dot{q}_2(t)$

5. Concluding remarks

In the above sections, the parametrically excited vibration of a two-stage gear system in mesh was investigated. A numerical procedure based on Newmark integration method is applied to calculate steady-state vibration of the system governed by linear differential equations having time-periodic coefficients.

The study provided the fundamental understanding of the physical mechanism related to gear faults, which generate modulation sidebands in vibration spectra of the two-stage gear system. The modeling result can be used to predict sideband amplitude in presence of the distributed gear faults such as non-uniform tooth wear. Consequently, it may serve as a tool for aiding the gear fault diagnosis.

The vibration model can be able to reveal essential dynamic properties of the gear-pair in mesh. The obtained result could be extended to more complicated multi-mesh and multi-gear systems.

Acknowledgment

This paper was completed with the financial support by the Vietnam National Foundation for Science and Technology Development (NAFOSTED).

References

Dalpiaz, G., Rivola A. and Rubini, R. (2000). Effectiveness and sensitivity of vibration processing techniques for local fault detection in gears. Mechanical System and Signal Processing 14(3), pp. 387-412.

Géradin M., Rixen D. (1994). Mechanical Vibrations. Wiley, Chichester.

Lin J. and Parker G. R. (2002). Mesh stiffness variation instabilities in two-stage gear systems. ASME Journal of Vibration Acoustics 124, pp. 68-76.

Jia S., Howard I. (2006) Comparison of localised spalling and crack damage from dynamic modeling of spur gear vibrations. Mechanical Systems and Signal Processing 20, pp. 332–349.

Newmark N. M. (1959) A method of computation for structural dynamics. ASCE Journal of Engineering Mechanics Division 85, pp. 67-94.

Nguyen Van Khang, Thai Manh cau, Nguyen Phong Dien (2004). Modelling parameter vibration of gear-pair systems as a tool for aiding gear fault diagnosis. Technische Mechanik, 24, H.3-4 (2004), pp. 198-205.

Nguyen Van Khang, Nguyen Phong Dien, Hoang Manh Cuong (2009). Linearization and parametric vibration analysis of some applied problems in multibody systems. Multibody Systems Dynamics 22, pp. 163-180.

Özgüven H.N. (1991). A non-linear mathematical model for dynamic analysis of spur gears including shaft and bearing dynamics. Journal of Sound and Vibration 145, pp. 239–259.

Parker G.R., Vijayakar S.M., and Imajo T. (2000) Non-linear dynamic response of a spur gear pair: Modelling and experimental comparisons. Journal of Sound and Vibration 237, pp. 435-455.

Theodossiades, S. and Natsiavas, S. (2000). Non-linear dynamics of gear-pair systems with periodic stiffness and backlash. Journal of Sound and Vibration 229(2), pp. 287-310.

Walha L., Fakhfakh T. and Haddar M. (2006). Backlash Effect on dynamic analysis of a two-stage spur gear system. ASM International Journal of Failure Analysis and Prevention 6(3), pp. 60-68.

Wang S., Shen Y. and Zhang S. (2004). On nonlinear-dynamic behavior of a two-stage gear train with time-varying stiffness and backlashes. Proceedings of the 11th World Congress in Mechanism and Machine Science in Tianjin-China, China Machine Press.

The 2nd International Conference on Engineering Mechanics and Automation (ICEMA2)
Hanoi, August 16-17, 2012
ISBN: 978-604-913-097-7

Wavelet Based Technique for Detection of a Sudden Crack of a Beam-Like Bridge During Earthquake Excitation

Khoa Viet Nguyen, Quang Van Nguyen

Institute of Mechanics, Vietnam Academy of Science and Technology
18 Hoang Quoc Viet, Cau Giay, Hanoi, Vietnam

Abstract

This paper presents a wavelet spectrum technique for monitoring the sudden crack of a beam-like bridge structure during earthquake excitation. When there is a crack induced by earthquake excitation the stiffness of the structure is changed leading to the change in natural frequencies of the structure during vibration. It is difficult to monitor this change in frequency by using conventional approaches such as Fourier transform. Also, in Fourier transform the time information is lost and it is impossible to analyse short time events. To overcome this disadvantage of Fourier transform, wavelet spectrum which is time-frequency analysis is used to monitor the sudden change in frequency appeared during earthquake excitation. The structure is modeled by finite element method and the crack model is adopted from fracture mechanics. Numerical results showed that the occurrence of the crack during earthquake shaking is clearly detected by the sudden change in frequency in the time-frequency spectrum of the structural dynamic response. Experiment has been carried out to verify the efficiency of the proposed method.

Keywords: Earthquake, crack, crack detection, sudden crack, sudden crack detection, time-frequency.

1. Introduction

The cracks of certain structures such as a building, an oil-rig structure or a bridge which be catastrophic, therefore early detection of cracks in such structures is essential. Structural Health Monitoring (SHM) ensures early detection of such damages and, hence, prevention of catastrophic failure. Structural health monitoring is a system which comprises sensors, instrumentation and methods for in situ monitoring of the integrity of the structures [1]. Among methods for SHM, the vibration-based method has emerged as one possible approach to the problem of structural damage identification and localization. Under ambient excitation or applied loading the dynamic response of the structure is measured and analyzed for damage-induced changes to the dynamics. The structural dynamic characteristics such as frequencies, mode shapes, flexibility, etc. can be extracted from the dynamic response and analyzed to track the crack-induced

changes of these parameters [1–8]. Other non-modal-based methods have been applied such as auto-regressive approaches [9, 10], fuzzy logic and neural networks [11-13], time-series dimensionality [14, 15], wavelets [16–17] and genetic algorithms [18, 19]. Many studies conducted to focus on extracting the relevant information from a cracked structure. Information of the cracked structure is then analysed and compare to information of the intact structure to detect and estimate the existence, location and severity of the damage.

However, information of intact structures is not always met in practice for on-service structures. Also, in many cases the external excitations may not always be available for structures such as buildings, towers ect. The dynamic characteristics of these structures can be obtained when the structures are excited by natural calamities such as storms or earthquakes. Due to these natural calamities damages may appear after or even during the excitation lead to the change in dynamic parameters of the structure such as natural frequencies and mode shapes. The change in frequency is the most interest parameter for damage tracking because it is a global parameter of structure. By conventional approach, the natural frequency can be extracted by Fourier transform. However, the information of the time when the frequency changed is lost in this transform. Fortunately, there is another approach which can analyse the frequency change while the information of time is still kept called time-frequency analysis. Recently, some time-frequency based methods have been applied wildly for SHM such as Short Time Fourier transform (STFT), Wigner-Ville Transform (WVT), Auto Regressive (AR), Moving Average (MA), Auto Regressive Moving Average, and Wavelet Transform (WT) [20-21]. Among these methods, the WT has emerged as an effective method for tracking the change in natural frequency of structures.

The present study proposes a wavelet spectrum method to monitor the sudden crack of a beam-like bridge structure occurred during the earthquake excitation. The method is simple since only one transducer is needed and the use of wavelet analysis removes the need of the information of the intact structure. The change in frequency of the structure is analysed by the wavelet spectrum and the moment of appearance of the crack is detected by wavelet transform. The sudden cracked beam-like bridge subjected to earthquake excitation is modeled by finite element method and fracture mechanics. Theoretical background of the wavelet analysis is provided. Numerical simulation results are presented in this paper.

2. Vibration of the beam-like bridge subject to harmonic ground shaking

2.1. Intact beam like structure

We begin by considering the beam as an Euler–Bernoulli beam subject to the ground excitation shown in Fig. 1. The beam is

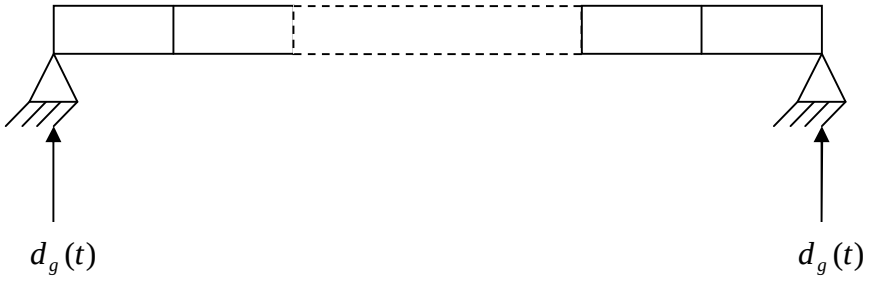

Fig 1. A beam-like bridge under moving vehicle

modeled as Q elements in finite element analysis. The ground excitation is assumed to be a harmonic function d_g. Under these assumptions and apply the finite element method the governing equation of motion of the beam can be written as follows [22]:

$$\mathbf{M}\ddot{\mathbf{d}}_{\mathbf{r}} + \mathbf{C}\dot{\mathbf{d}}_{\mathbf{r}} + \mathbf{K}\mathbf{d}_{\mathbf{r}} = -\mathbf{M}\mathbf{I}\ddot{d}_{\mathbf{g}} \quad (1)$$

Here **M**, **C**, **K** are structural mass, damping and stiffness matrices; **I** is a vector of order 2Q; d_g is the ground displacement time history; $\mathbf{d_r}$ is a beam vector which denotes the relative nodal displacement of the beam in comparison with the ground.

In practice, the absolute acceleration or displacement of the structures under the ground motion can be measured. Denote the absolute displacement vector of the beam as **d,** the relationship between the relative displacement and the absolute displacement of the beam can be expressed as:

$$\mathbf{d} = \mathbf{d_r} + \mathbf{I}d_g \quad (2)$$

Therefore, equation (1) can be rewritten in connection with (2) as the equation of the absolute motion of the beam as follows:

$$\begin{aligned} &\mathrm{M}(\ddot{\mathrm{d}}_{\mathrm{r}} + \mathrm{I}\ddot{d}_g) + \mathrm{C}(\dot{\mathrm{d}} - \mathrm{I}\dot{d}_g) \\ &+\mathrm{K}(\mathrm{d} - \mathrm{I}d_g) = 0 \end{aligned} \quad (3)$$

or

$$\mathbf{M}\ddot{\mathbf{d}} + \mathbf{C}\dot{\mathbf{d}} + \mathbf{K}\mathbf{d} = \mathbf{C}\mathbf{I}\dot{d}_g + \mathbf{K}\mathbf{I}d_g \quad (4)$$

The displacement of the beam u at the arbitrary position x can be obtained from the shape functions **N** and the nodal displacement **d** as:

$$u = \mathbf{N}\mathbf{d} \quad (5)$$

The shape function of an element can be obtained as:

$$\mathbf{N} = \begin{bmatrix} N_1 & N_2 & N_3 & N_4 \end{bmatrix} \quad (6)$$

where

$$N_1 = 1 - 3\left(\frac{x}{l}\right)^2 + 2\left(\frac{x}{l}\right)^3;$$

$$N_2 = x\left(\frac{x}{l} - 1\right)^2; N_3 = 3\left(\frac{x}{l}\right)^2 - 2\left(\frac{x}{l}\right)^3;$$

$$N_4 = x\left[\left(\frac{x}{l}\right)^2 - \frac{x}{l}\right] \quad (7)$$

with l is the length of the element.

2.2. Cracked beam like structure

Fig. 2 shows a uniform beam-like structure divided into Q elements with a crack situated at the distance L_c from the ground. It is

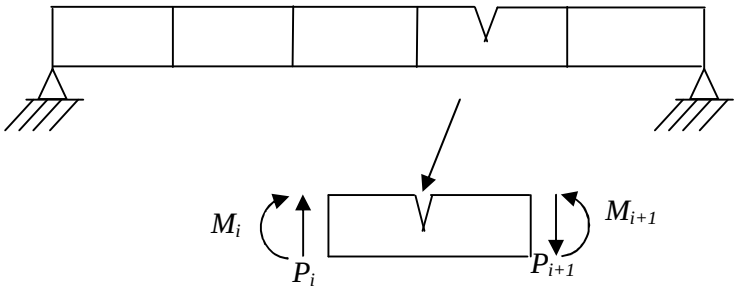

Fig. 2. Model of beam with a crack

assumed that the cracks only affect the stiffness, not affect the mass and damping coefficient of the beam. An element stiffness matrix of a cracked element can be obtained as following [23]:

$$W^{(o)} = \frac{1}{2EI}\left(M^2 l + MPl^2 + \frac{P^2 l^3}{3}\right) \quad (8)$$

where P and M are the shear and bending internal forces at the right node of the element (Fig. 2).

The additional stress energy of a crack has been calculated from fracture mechanics and the flexibility coefficients are obtained by a stress intensity factor in the linear elastic range, using Castigliano's theorem. For a rectangular beam with the thickness h, the

width *b*, and the additional energy due to the crack can be written as

$$W^{(1)} = b\int_0^a \left(\frac{\left(K_I^2 + K_{II}^2\right)}{E'} + \frac{(1+\nu)K_{III}^2}{E} \right) da \tag{9}$$

where $E' = E$ for plane stress, $E' = \dfrac{E}{1-\nu^2}$ for plane strain and a is the crack depth, and K_I, K_{II}, K_{III} are stress intensity factor for opening type, sliding type and tearing type cracks, respectively.

Taking into account only bending, equation (9) leads to

$$W^{(1)} = b\int_0^a \frac{\left(K_{IM} + K_{IP}\right)^2 + K_{IIP}^2}{E'} da \tag{10}$$

where

$$K_{IM} = \frac{6M\sqrt{\pi a}F_I(s)}{bh^2};\ K_{IP} = \frac{3Pl\sqrt{\pi a}F_I(s)}{bh^2};$$

$$K_{IIP} = \frac{P\sqrt{\pi a}F_{II}(s)}{bh} \tag{11}$$

$$F_I(s) = \sqrt{\frac{2}{\pi s}tg\left(\frac{\pi s}{2}\right)}\frac{0.923 + 0.199\left[1-\sin\left(\frac{\pi s}{2}\right)\right]^4}{\cos\left(\frac{\pi s}{2}\right)} \tag{12}$$

$$F_{II}(s) = \left(3s - 2s^2\right) \times \frac{1.122 - 0.561s + 0.085s^2 + 0.18s^3}{\sqrt{1-s}} \tag{13}$$

Where $s=a/h$; *a* is the crack depth and *h* is the beam height.

The generic component of the flexibility matrix $\tilde{\mathbf{C}}$ of the intact element can be calculated as

$$\tilde{c}_{ij}^{(o)} = \frac{\partial^2 W^{(o)}}{\partial P_i \partial P_j};\ i, j = 1,2\ ; P_1 = P; P_2 = M \tag{14}$$

The additional flexibility coefficient is

$$\tilde{c}_{ij}^{(1)} = \frac{\partial^2 W^{(1)}}{\partial P_i \partial P_j};\ i, j = 1,2\ ; P_1 = P; P_2 = M \tag{15}$$

Therefore, the total flexibility coefficient is:

$$\tilde{c}_{ij} = \tilde{c}_{ij}^{(o)} + \tilde{c}_{ij}^{(1)} \tag{16}$$

From the equilibrium condition the following equation can be derived

$$\begin{pmatrix} P_i & M_i & P_{i+1} & M_{i+1} \end{pmatrix}^T = \mathbf{T}\begin{pmatrix} P_{i+1} & M_{i+1} \end{pmatrix}^T \tag{17}$$

where

$$\mathbf{T} = \begin{bmatrix} -1 & -l & 1 & 0 \\ 0 & -1 & 0 & 1 \end{bmatrix}^T \tag{18}$$

By the principle of virtual work the stiffness matrix of the cracked element can be expressed as:

$$\mathbf{K}_c = \mathbf{T}^{\mathbf{T}}\tilde{\mathbf{C}}^{-1}\mathbf{T} \tag{19}$$

The stiffness matrix and mass matrix for an element without a crack can be obtained as:

$$\mathbf{K}_e = \frac{EI}{l^3}\begin{bmatrix} 12 & 6l & -12 & 6l \\ 6l & 4l^2 & -6l & 2l^2 \\ -12 & -6l & 12 & -6l \\ 6l & 2l^2 & -6l & 4l^2 \end{bmatrix} \tag{20}$$

$$\mathbf{M_e} = \frac{ml}{420}\begin{bmatrix} 156 & 22l & 54 & -13l \\ 22l & 4l^2 & 13l & -3l^2 \\ 54 & 13l & 156 & -22l \\ -13l & -3l^2 & -22l & 4l^2 \end{bmatrix} \tag{21}$$

where *I* is the moment of inertia; *E* is the Young's modulus; *m* and *l* are the mass and the length of the element.

Element mass matrices $\mathbf{M}_e$ are assembled to form the global mass matrix **M**, while matrices $\mathbf{K}_e$ and $\mathbf{K}_c$ are assembled to form the global stiffness matrix **K** of the cracked beam. Rayleigh damping in the form of

$\mathbf{C} = \alpha\mathbf{M} + \beta\mathbf{K}$ is used for the beam. Where ω_1 and ω_2 are the first two bending natural frequencies of the beam, and α and β are calculated as follows [24]:

$$\alpha = \frac{2\omega_1\omega_2\left(\xi_1\omega_2 - \xi_2\omega_1\right)}{\omega_2^2 - \omega_1^2}; \quad \beta = \frac{2\left(\xi_2\omega_2 - \xi_1\omega_1\right)}{\omega_2^2 - \omega_1^2} \tag{22}$$

Substituting global matrices **M**, **C**, and **K** of the cracked beam into equation (4) and solving this equation by Newmark method, the dynamic responses of the vehicle and the beam will be obtained.

2. Wavelet spectrum

The continuous wavelet transform is defined as follows [25]:

$$\mathrm{W}(a,b) = \int_{-\infty}^{+\infty} f(t)\psi_{a,b}\,dt \tag{23}$$

Where *a* and b are scale and position, *W(a,b)* are wavelet coefficients at scale *a* and position *b*, *f(t)* is input signal, $\psi_{\mathrm{a,b}}(\mathrm{t}) = \frac{1}{\sqrt{\mathrm{a}}}\psi^*\left(\frac{\mathrm{t}-\mathrm{b}}{\mathrm{a}}\right)$. Here $\psi\left(\frac{\mathrm{t}-\mathrm{b}}{\mathrm{a}}\right)$ is called wavelet function and $\psi^*\left(\frac{\mathrm{t}-\mathrm{b}}{\mathrm{a}}\right)$ is complex conjugate of $\psi\left(\frac{\mathrm{t}-\mathrm{b}}{\mathrm{a}}\right)$. Wavelet function must satisfy some mathematical requirements as:

1) A wavelet must have finite energy:

$$E = \int_{-\infty}^{+\infty} \left|\psi(t)\right|^2 dt < \infty \tag{24}$$

2) If $\hat{\psi}(\omega)$ is Fourier transform of $\psi(t)$, i.e.

$$\hat{\psi}(\omega) = \int_{-\infty}^{+\infty} \psi(t)e^{-i\omega t}\,dt \tag{25}$$

then the following condition must be satisfied:

$$C_g = \int_0^{\infty} \frac{\left|\hat{\psi}(\omega)\right|^2}{\omega} d\omega < \infty \tag{26}$$

This implies that the wavelet has no zero frequency component: $\hat{\psi}(0) = 0$,

$$\int_{-\infty}^{+\infty} \psi(t)e^{-j\omega t}\,dt = 0 \quad when\ \omega = 0 \tag{27}$$

or in other words, the wavelet must have a zero mean:

$$\int_{-\infty}^{+\infty} \psi(\mathrm{t})\mathrm{dt} = 0 \tag{28}$$

3) An additional criterion is that, for complex wavelets, the Fourier transform must both be real and vanish for negative frequencies.

In order to monitor the change in frequency, the wavelet power spectrum *S(a,b)*, which provides a measure of the time series variance at each time and each scale is used in this study. The wavelet power spectrum is defined as the square modulus of the wavelet transform [26]:

$$S(a,b) = \left|W(a,b)\right|^2 \tag{29}$$

Note that, if the signal *f(t)* is a vibration signal of a structure the scale *a* corresponds to the frequency of the structure. The small value of the scale corresponds to the large value of the frequency and vise versa.

3. Simulation results and discussions

A numerical simulation of a beam under earthquake excitation has been carried out. The earthquake excitation is assumed to be a ground harmonic process. Parameters of the beam are: Mass density is 7855 kg/m^3; modulus of elasticity E=2.1x10^{11} N/m^2; L=2 m; b=0.02 m; h=0.02 m. Modal damping ratios for all modes are equal to 0.01. It is assumed that in practice we can measure vibration signal in the durations of T/2 s before and T/2 s after the appearance of the crack. Therefore, for simulating the sudden crack we assume that during the first half of the excitation structure is modelled as an intact beam and in the second half of the excitation duration, a crack at location L_c=L/3 of the beam is made. The absolute displacement-time history at the top of the beam is obtained in the duration of T=10 s

for the monitoring purpose. The ground excitation function is chosen as F=0.05sin(35*t*). Due to this excitation, the beam vibrates mainly with its first natural frequency of 4.14 Hz. In this work, the continuous wavelet transform and wavelet power spectrum are applied for tracking the crack. After trying several differing wavelet functions for signal processing, the wavelet function "Symlet" is chosen as the most suitable for this study. Five levels of the crack from zero to 40% were examined. These five cases are numbered as in Table 1.

Table 1. Five cases with cracks of varying depths at crack position *Lc*=*L*/3

Case	Crack depth (%)
1	0
2	10
3	20
4	30
5	40

Fig. 3 presents the wavelet transform of the absolute displacement of the beam when the crack depth is zero. It is certainly that there is no sign of the crack appearance can be seen from this figure

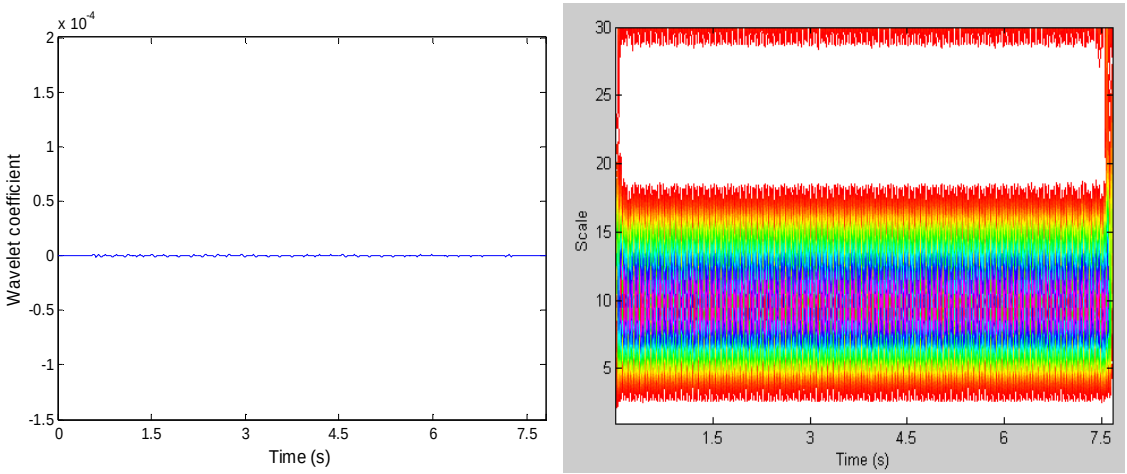

a) b)

Fig. 3. Crack depth 0%; a) Wavelet transform; b) Wavelet spectrum

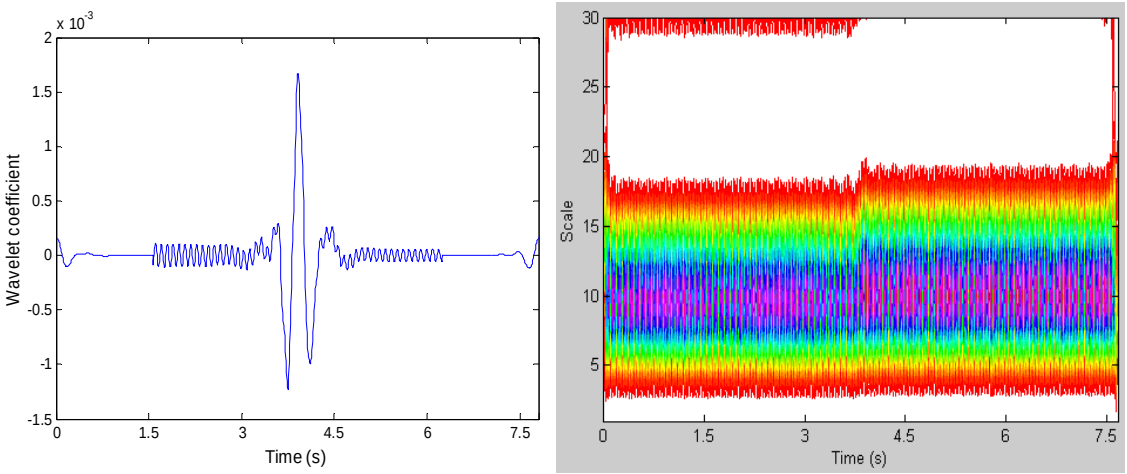

a) b)

Fig. 4. Crack depth 10%; a) Wavelet transform; b) Wavelet spectrum

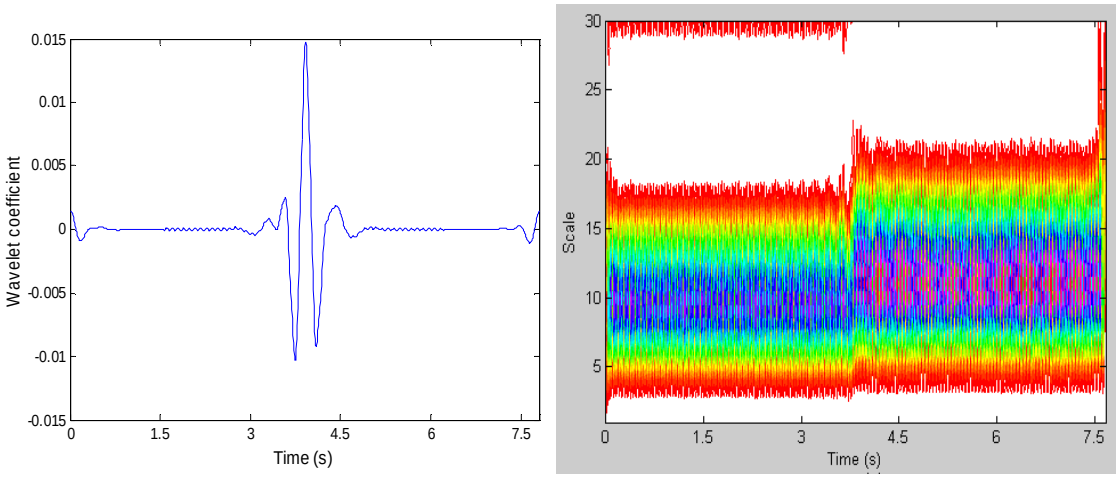

a) b)

Fig. 5. Crack depth 30%; a) Wavelet transform; b) Wavelet spectrum

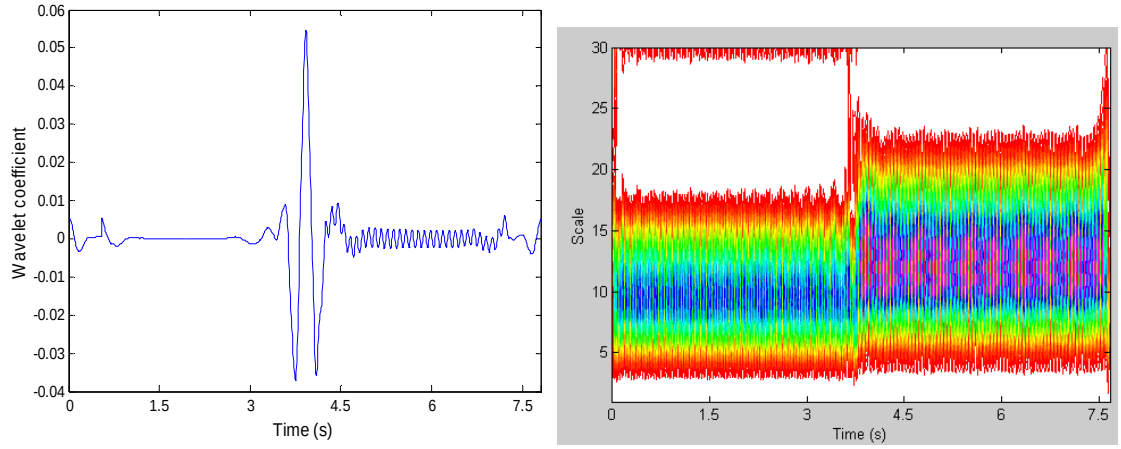

a) b)

Fig. 6. Crack depth 50%; a) Wavelet transform; b) Wavelet spectrum

However, when there is a small crack of 10% of the beam width appeared at t=T/2, there is a significant peak in the wavelet transform of the displacement at exact moment t=T/2 (graph a) Fig. 4). Meanwhile, the time varying spectrum estimated using wavelet power spectrum is illustrated as in the graph b) of Fig. 4. We can see that in the first half of the ground excitation duration, the energy of the displacement mainly distributes in the scale range centered at about a=10, while in the second half of the duration the wavelet spectrum moves slightly toward the larger scale (smaller frequency). This can be explained that in the first half of duration the beam was not cracked the beam vibrates at the main scale of a=10, while in the second half the beam was cracked leads to the reduction of the main scale (smaller frequency).

When the crack depth increases, as can be seen from the graph a) of Figs. 5-6 the wavelet transforms remain one significant peak at t=T/2 which imply the moment of crack appearance. In the meantime, it is interesting that the wavelet spectrums in the graphs b) of these figures show clearly two parts with two different main frequencies separated at exact moment t=T/2 when the crack occurs. In the first parts of the wavelet spectrum the main energy of the displacement distributes at the scale a=10 which corresponding to the case of intact beam. In contrast, the main energy

distribution in the second parts reduces to 12 as the crack depth increases up to 50%.

4. Summary and conclusion remarks

In practice, the damage in a structure may appear after a period of time in operation or may immediately occur during an external excitation. Therefore, monitoring the crack existence and whether there is a crack after sudden external excitations is of importance. In general, in order to monitor the crack the intact information of a structure is often required which is not always available for real structures. In this study a wavelet – time frequency based method to monitor the crack appeared during the ground excitation is presented and gives promising results.

For the case of harmonic ground excitation, the appearance of the crack can be detected by the significant peak in the wavelet transform of the dynamic displacement of the beam during excitation.

The existence of the crack is also confirmed by the movement of the main frequency distribution toward the smaller range of frequency in the wavelet power spectrum. The movement starts at the moment the crack occurs and remains consistently until the rest of the excitation duration.

The advantage of the proposed method is that it does not require any information of the intact structure since only one measured displacement signal is needed for monitoring the crack appearance. Another advantage of the proposed method is that it can be used to monitor the crack depth as small as 10% of the beam width, while other conventional frequency based methods can only detect the cracks with depth larger than 40%.

The efficient of the proposed method needs to be justified in the laboratory before applying to real structures. This is considered as a future work of the authors.

Acknowledgement

This work is supported by Vietnam Academy of Science and Technology, 2012-2013.

References

[1] Khoo L. M., Mantena P. R., and Jadhav P., Structural Damage Assessment Using Vibration Modal Analysis. Structural Health Monitoring 2004, Vol. 3(2), pp. 177-194.

[2] Pandey A. K., Biswas M. and Samman M. M., Damage Detection from Changes in Curvature Mode Shapes. Journal of Sound and Vibration 1991, Vol. 145(2), pp. 321-332.

[3] Pandey A. K. and Biswas M., Damage Detection in Structures Using Changes in Flexibility. Journal of Sound and Vibration 1994, Vol. 169(1), pp. 3-17.

[4] C.R. Farrar, T.A. Duffey, S.W. Doebling, D.A. Nix, A statistical pattern recognition paradigm for vibrationbased structural health monitoring, in: Structural Health Monitoring 2000, 1999, pp. 764–773.

[5] D Göge, M. Link, Results obtained by minimizing natural frequency and mode shape errors of a beam model, Mechanical Systems and Signal Processing 17 (1) (2003) 21–27.

[6] K. Bohle, C.-P. Fritzen, Results obtained by minimizing natural frequency and mac-value errors of a plate model, Mechanical Systems and Signal Processing 17 (1) (2003) 55–64.

[7] P. Verboven, E. Parloo, P. Guillaume, M. Van Overmeire, Autonomouss tructural health monitoring—part I: modal parameter estimation and tracking, Mechanical Systems and Signal Processing 16 (4) (2002) 637–657.

[8] S.W. Doebling, C.R. Farrar, M.B. Prime, A summary review of vibration-based identification methods, Shock and Vibration Digest 205 (5) (1998) 631–645.

[9] H. Sohn, C.R. Farrar, N.F. Hunter, K. Worden, Structural health monitoring using statistical pattern recognition techniques, Journal of Dynamic Systems, Measurement, and Control 123 (2001) 706–711.

[10] J.B. Bodeux, J.C. Golinval, Modal identification and damage detection using the data-driven stochastic subspace and armav methods, Mechanical Systems and Signal Processing 17 (1) (2003) 83–89.

[11] C.M. Bishop, Novelty detection and neural network validation, in: IEE Proceedings: Vision, Image, and Spectral Processing 141 (4) (1994) 217–222.

[12] Reda Taha M.M. and Lucero J., Damage Identification for Structural Health Monitoring using Fuzzy Pattern Recognition. Engineering Structures 2005, Vol. 27, pp. 1774-1783.

[13] K. Worden, G. Manson, D. Allman, Experimental validation of a structural health monitoring methodology— part I: novelty detection on a laboratory structure, Journal of Sound and Vibration 259 (2) (2003) 323–343.

[14] D. Logan, J. Mathew, Using the correlation dimension for vibration fault diagnosis of rolling element bearings—i. Basic concepts, Mechanical Systems and Signal Processing 10 (3) (1996) 241–250.

[15] W.J. Wang, Z.T. Wu, J. Chen, Fault identification in rotating machinery using the correlation dimension and bispectra, Nonlinear Dynamics 25 (2001) 383–393.

[16] A.C. Okafor, A. Dutta, Structural damage detection in beams by wavelet transforms, Smart Materials and Structures 9 (6) (2000) 906–917.

[17] Z. Hou, M. Noori, R.St. Amand, Wavelet-based approach for structural damage detection, Journal of Engineering Mechanics 126 (7) (2000) 677–683.

[18] J.S. Owen, B.J. Eccles, B.S. Choo, M.A. Woodings, The application of auto-regressive time series modelling for the time–frequency analysis of civil engineering structures. Engineering Structures 23 (2001) 521–536.

[19] A. Nag, D.R. Mahapatra, S. Gopalakrishnan, Identification of delamination in composite beams using spectral estimation and a genetic algorithm, Smart Materials and Structures 11 (2003) 899–908.

[20] C. Mares and C. Surace, An application of genetic algorithm to identify damage in elastic structures. Journal of Sound and Vibration 1996, 195(2), 195-215.

[21] J.S. Owen, B. J. Eccles, B. S. Choo, and M. A. Wooding, The Application of Auto-Regressive Time Series Modelling for the Time-Frequency Analysis of Civil Engineering Structures. Journal of Engineering Structures 2001, Vol. 23, pp. 521-536.

[22] A. K. Chopra, Dynamics of Strucutres, Theory and applications to earthquake engineering. Prentice -Hall Inc. Simson & Schuster Company 1995.

[23] Y.H. Lin, M.W. Trethewey, Finite element analysis of elastic beams subjected to moving dynamic loads, Journal of Sound and Vibration 136 (2) (1989), 323–342.

[24] G.L. Qian, S.N. Gu, J.S. Jiang, The dynamic behaviour and crack detection of a beam with a crack, Journal of Sound and Vibration 138 (2) (1990), 233–243.

[25] Daubechies I., Ten lectures on wavelets. CBMS-NSF Conference series, 61. Philadelphia, PA: SISAM, 1992.

[26] X. Jiang, S. Mahadevan., Wavelet spectrum analysis approach to model validation of dynamic systems. Mechanical Systems and Signal Processing 25(2011), 575–590.

The 2nd International Conference on Engineering Mechanics and Automation (ICEMA2)
Hanoi, August 16-17, 2012
ISBN: 978-604-913-097-7

Detection of a Breathing Crack of a Beam-Like Bridge Subjected to a Moving Vehicle Using Wavelet Technique

Khoa Viet Nguyen, Hoa Thi Mai Pham

Institute of Mechanics, Vietnam Academy of Science and Technology
18 Hoang Quoc Viet, Cau Giay, Hanoi, Vietnam

Abstract

In this paper a wavelet based technique for detection of a breathing crack of a beam- like bridge subjected to a moving vehicle is presented. The stiffness matrix of the beam is modeled as time dependent stiffness matrix using finite element method. The stiffness matrix of the cracked element at each moment is calculated from the curvature of the structure at the crack position. The time history displacement of the vehicle is obtained by solving simultaneously the dynamic equations of the vehicle-bridge system. Numerical simulation results show that natural frequencies of the system increase in comparison with the case of fully open crack. Meanwhile, the amplitude of the vibration in the case of breathing crack is smaller than the case of fully open crack. This is a warning that the small amplitude of the dynamic displacement does not necessarily corresponds to the small crack size. The wavelet technique for crack detection is then carried out by analysing the dynamic response. The result of the crack detection in the case of breathing crack is compared to the result in the case of fully open crack. It is concluded that the peaks in the wavelet transform of the displacement in case of breathing crack are larger in comparison with the case of non-breathing crack. This implies the wavelet method for crack detection is more efficient with the presence of the breathing crack.

1. Introduction

In practice, depending on loading conditions on the cracked structure (residual loads, body weight of a structure, etc.), and the vibration effect a crack may be fully or partly open, fully closed at all times, or it can open and close regularly. This crack which closes and opens during vibration was termed a ‘‘breathing crack’’ and was discussed by Chondros et al. [1]. The dynamic response to harmonic excitation of a beam with several breathing cracks was analyzed by Ruotolo and Surace [2], Rizzo and Scalea [3]. In their study, natural frequencies of a beam with a breathing crack are shown to be not constant during vibration but it is changing in time, and the relative decrease in natural frequencies found is much smaller than the decrease due to an open crack. Douka and Hadjileontiadis [4] proposed a method called empirical mode decomposition to analyse the instantaneous frequency. It is shown that the instantaneous frequency oscillates between frequencies corresponding to the open and closed states revealing the breathing of the crack. The presence of non-linear

phenomenon of a beam with breathing crack has been studied by Sundermeyer and Weaver [5]. In these studies, a response at a frequency that is different from the driving frequencies was discovered. This new response is due to the nonlinearity in the beam response. Bovsunovsky and Matveev [6] presented a concept of concomitant mode shapes that occur at the time the crack closes and opens was presented to explain the nonlinearity caused by the breathing crack. Qian et al [7] and Ariaei et al. [8] stated that the difference between the displacement response of the intact beam and the cracked beam due to breathing crack is smaller than that between an open-cracked beam and intact beam.

The analysis of continuous elastic systems subjected to moving subsystems has been a topic of interest in many diverse fields such as civil and aerospace engineering for well over a century. The problem arose in the design of railway bridges, roadways, tunnels and bridges ect. Especially in bridge engineering many applications have been developed from the study of this subject. Parhi and Behera [9] presented an analytical method along with experimental verification to investigate the vibration behavior of a cracked beam under a moving mass. The vehicle–bridge interaction system was calculated by Piombo et al [10] by considering it as a three-span orthotropic plate subject to a seven degrees-of-freedom multi-body system with linear suspensions and tires flexibility. In other studies, Mahmoud and Zaid [11] presented iterative methods for the effect of single transverse cracks on the dynamic behavior of simply supported and cantilever undamped Euler-Bernoulli beams subject to a moving mass. While Lee et al. [12] proposed a procedure for identification of the operational modal properties and the assessment of damage locations and their associated severities. Bilello and Bergman [13] studied beams with damages modeled by rotational springs subject to a moving load. Recently, Zhu and Law [14] analysed the cracked bridge subject to a moving vehicular load by analyzing the operational deflection time history of a bridge and used the wavelet transform for crack detection.

However, most of the current approaches for damage detection of the vehicle-bridge system used dynamic responses the bridge, only the authors of this paper recently used the dynamic responses obtained directly from the vehicle moving on bridge with fully open cracks [15]. To this end, this study will first investigate the effect of breathing crack on the response of the vehicle-bridge system measured directly from the vehicle and then consider its influence on the damage detection using the wavelet transform which is a very efficient tool for signal processing [16, 17, 18, 19, 20, 21, 22].

2. Intact beam like structure

Consider the bridge–vehicle system shown in Fig. 1. The vehicle is modelled as two DOFs system with sprung vehicle body and sprung tyre. The bridge is considered approximately as an Euler–Bernoulli beam. It is assumed that the surface unevenness of the bridge can be ignored and the tyre is always in contact with the supported beam.

Under these assumptions the governing equation of motion for the bridge–vehicle system in finite element method can be shown as follows:

$$m_1\ddot{y}_1 + c_1(\dot{y}_1 - \dot{y}_2) + k_2(y_1 - y_2) = 0 \quad (1)$$

$$\begin{aligned} &m_2\ddot{y}_2 - c_1(\dot{y}_1 - \dot{y}_2) - k_2(y_1 - y_2) \\ &+k_2(y_2 - w_0) + c_2(\dot{y}_2 - \dot{w}_0) = 0 \end{aligned} \quad (2)$$

$$\mathbf{M}\ddot{\mathbf{d}} + \mathbf{C}\dot{\mathbf{d}} + \mathbf{K}\mathbf{d} = \mathbf{f} = \mathbf{N}^{\mathrm{T}} f_o \quad (3)$$

$$f_o = -(m_1 + m_2)g - m_1\ddot{y}_1 - m_2\ddot{y}_2 \quad (4)$$

Where m_1, m_2, k, c are vehicle parameters; y is vertical deflection of the vehicle body m_1; u_o is the vertical deflection of m_2 and is equal to the deflection of the beam u at the contact position; **M**, **C**, **K** are structural mass, damping and stiffness matrices; $\mathbf{N}^{\mathbf{T}}$ denotes the transpose of the shape functions at the position x of the force; f_0 is the magnitude of the interaction force between the vehicle and

the beam; **d** is a nodal displacement column vector of the beam. The displacement of the beam u at the arbitrary position x can be interpolated from the shape functions **N** and the nodal displacement **d** as:

$$u=\mathbf{Nd} \tag{5}$$

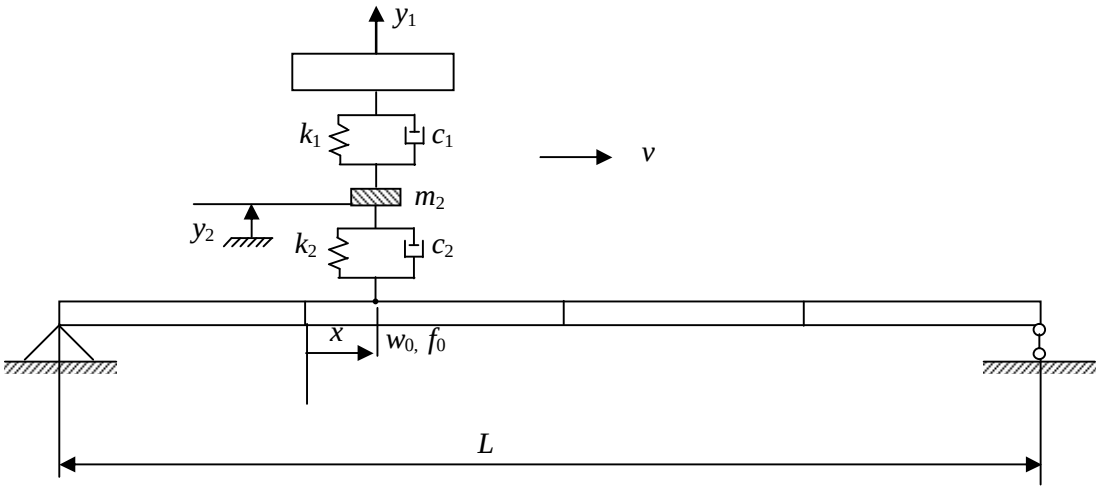

Fig. 1. A beam-like bridge subject to moving vehicle

The components of shape function of an element can be obtained as:

$$N_1 = 1-3\left(\frac{x}{l}\right)^2+2\left(\frac{x}{l}\right)^3 ; N_2 = x\left(\frac{x}{l}-1\right)^2 ;$$
$$N_3 = 3\left(\frac{x}{l}\right)^2-2\left(\frac{x}{l}\right)^3 ; N_4 = x\left[\left(\frac{x}{l}\right)^2-\frac{x}{l}\right] \tag{6}$$

with l is the length of the element.

The time derivatives of u_o are:

$$\dot{u}_o(x,t) = \frac{\partial u}{\partial x}\dot{x}+\frac{\partial u}{\partial t} \tag{7}$$

$$\ddot{u}_o(x,t) = \frac{\partial^2 u}{\partial x^2}\dot{x}^2+2\frac{\partial^2 u}{\partial x\partial t}\dot{x}+\frac{\partial u}{\partial x}\ddot{x}+\frac{\partial^2 u}{\partial t^2} \tag{8}$$

Because **N** is spatial function while **d** is time dependent, from (4) we have:

$$\frac{\partial^2 u}{\partial x^2} = \mathrm{N}_{xx}\mathrm{d} ; \ \frac{\partial u}{\partial x} = \mathrm{N}_x\mathrm{d} ;$$
$$\frac{\partial^2 u}{\partial x\partial t} = \mathrm{N}_x\dot{\mathrm{d}} ; \ \frac{\partial^2 u}{\partial t^2} = \mathrm{N}\ddot{\mathrm{d}} \tag{9}$$

where the subscript x implies the differentiation with respect to x. Substituting (7), (8) and (9) into equations (1), (2), and (3) yields:

$$\begin{pmatrix} \mathrm{M} & \mathrm{M}_1 \\ \mathrm{M}_2 & \mathrm{M}_3 \end{pmatrix}\begin{pmatrix} \ddot{\mathrm{d}} \\ \ddot{\mathrm{y}} \end{pmatrix}+\begin{pmatrix} \mathrm{C} & \mathrm{C}_1 \\ \mathrm{C}_2 & \mathrm{C}_3 \end{pmatrix}\begin{pmatrix} \dot{\mathrm{d}} \\ \dot{\mathrm{y}} \end{pmatrix}$$
$$+\begin{pmatrix} \mathrm{K} & \mathrm{K}_1 \\ \mathrm{K}_2 & \mathrm{K}_3 \end{pmatrix}\begin{pmatrix} \mathrm{d} \\ \mathrm{y} \end{pmatrix}=\begin{pmatrix} -\mathrm{N}^{\mathrm{T}}\left(m_1+m_2\right)g \\ \mathrm{O}^{\mathrm{T}} \end{pmatrix} \tag{10}$$

Here **O** is a row zero matrix, and:

$$\mathbf{y}=\begin{bmatrix} y_1 \\ y_2 \end{bmatrix} \qquad \mathbf{M_1}=\begin{bmatrix} \mathbf{N}^{\mathbf{T}}m_1 & \mathbf{N}^{\mathbf{T}}m_2 \end{bmatrix}$$
$$\mathbf{M_2}=\begin{bmatrix} \mathbf{O} \\ \mathbf{O} \end{bmatrix} \qquad \mathbf{M}_3=\begin{bmatrix} m_1 & 0 \\ 0 & m_2 \end{bmatrix} \tag{11}$$

$$\mathbf{C_1}=\begin{bmatrix} \mathbf{O}^{\mathbf{T}} & \mathbf{O}^{\mathbf{T}} \end{bmatrix} \qquad \mathbf{C_2}=\begin{bmatrix} \mathbf{O} \\ -\mathbf{N}c_2 \end{bmatrix}$$
$$\mathbf{C}_3=\begin{bmatrix} c_1 & -c_1 \\ -c_1 & c_1+c_2 \end{bmatrix} \tag{12}$$

$$\mathbf{K_1}=\begin{bmatrix} \mathbf{O}^{\mathbf{T}} & \mathbf{O}^{\mathbf{T}} \end{bmatrix}, \ \mathbf{K_2}=\begin{bmatrix} \mathbf{O} \\ \mathbf{N}k_2-\mathbf{N}_{\mathbf{x}}c_2\dot{x} \end{bmatrix}$$
$$\mathbf{K}_3=\begin{bmatrix} k_1 & -k_1 \\ -k_1 & k_1+k_2 \end{bmatrix} \tag{13}$$

2.2 Multi breathing cracks

Figure 2 shows a uniform beam-like structure divided into *Q* elements with *R* cracks situated in *R* different elements. It is assumed that the cracks only affect the stiffness, not affect the mass and damping coefficient of the beam. Neglecting shear action, the strain energy of an element without a crack can be written as [7]:

$$W^{(o)} = \frac{1}{2EI}\left(M^2 l + MPl^2 + \frac{P^2 l^3}{3} \right) \quad (11)$$

where *P* and *M* are the shear and bending internal forces at the right node of the element (Fig. 2). For a rectangular beam with the thickness *h*, the width *b*, and the additional energy due to the crack can be written as

$$W^{(1)} = b\int_0^a \left(\frac{\left(K_I^2 + K_{II}^2\right)}{E'} + \frac{(1+\nu)K_{III}^2}{E} \right) da \quad (12)$$

where $E' = E$ for plane stress, $E' = \frac{E}{1-\nu^2}$ for plane strain and a is the crack depth, and K_I, K_{II}, K_{III} are stress intensity factor for opening type, sliding type and tearing type cracks, respectively.

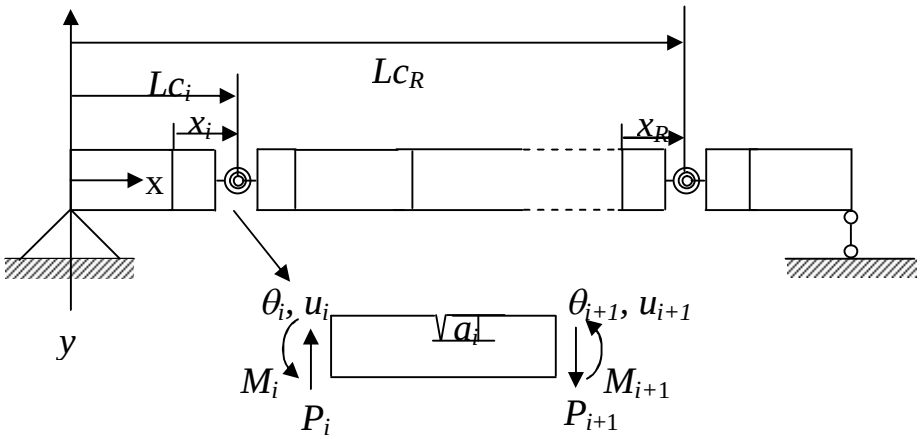

Fig. 2. Model of beam with *R* cracks

Taking into account only bending, equation (12) leads to

$$W^{(1)} = b\int_0^a \frac{\left(K_{IM} + K_{IP}\right)^2 + K_{IIP}^2}{E'} da \quad (13)$$

where

$$K_{IM} = \frac{6M\sqrt{\pi a}F_I(s)}{bh^2}; K_{IP} = \frac{3Pl\sqrt{\pi a}F_I(s)}{bh^2};$$

$$K_{IIP} = \frac{P\sqrt{\pi a}F_{II}(s)}{bh} \quad (14)$$

$$F_I(s) = \sqrt{\frac{2}{\pi s} tg\left(\frac{\pi s}{2}\right)} \frac{0.923 + 0.199\left[1 - \sin\left(\frac{\pi s}{2}\right)\right]^4}{\cos\left(\frac{\pi s}{2}\right)} \quad (15)$$

$$F_{II}(s) = \left(3s - 2s^2\right)\frac{1.122 - 0.561s + 0.085s^2 + 0.18s^3}{\sqrt{1-s}} \quad (16)$$

Where $s=a/h$; *a* is the crack depth and *h* is the beam height.

The generic component of the flexibility matrix $\tilde{\mathbf{C}}$ of the intact element can be calculated as

$$\tilde{c}_{ij}^{(o)} = \frac{\partial^2 W^{(o)}}{\partial P_i \partial P_j}; \quad i, j = 1,2 \; ; \; P_1 = P; \; P_2 = M \quad (17)$$

The additional flexibility coefficient is

$$\tilde{c}_{ij}^{(1)} = \frac{\partial^2 W^{(1)}}{\partial P_i \partial P_j}; \quad i, j = 1,2 \; ; \; P_1 = P; \; P_2 = M \quad (18)$$

Therefore, the total flexibility coefficient is:

$$\widetilde{c}_{ij} = \widetilde{c}_{ij}^{(o)} + \widetilde{c}_{ij}^{(1)} \quad (19)$$

From the equilibrium condition the following equation can be derived

$$\left(P_i \;\; M_i \;\; P_{i+1} \;\; M_{i+1}\right)^T = \mathrm{T}\left(P_{i+1} \;\; M_{i+1}\right)^T \quad (20)$$

$$\text{Where } \mathbf{T} = \begin{bmatrix} -1 & -l & 1 & 0 \\ 0 & -1 & 0 & 1 \end{bmatrix}^T \quad (21)$$

By the principle of virtual work the stiffness matrix of the cracked element can be expressed as:

$$\mathbf{K}_c = \mathbf{T}^{\mathbf{T}}\widetilde{\mathbf{C}}^{-1}\mathbf{T} \quad (22)$$

The stiffness matrix and mass matrix for an element without a crack can be obtained as:

$$\mathbf{K}_e = \frac{EI}{l^3}\begin{bmatrix} 12 & 6l & -12 & 6l \\ 6l & 4l^2 & -6l & 2l^2 \\ -12 & -6l & 12 & -6l \\ 6l & 2l^2 & -6l & 4l^2 \end{bmatrix} \quad (23)$$

$$\mathbf{M_e} = \frac{ml}{420}\begin{bmatrix} 156 & 22l & 54 & -13l \\ 22l & 4l^2 & 13l & -3l^2 \\ 54 & 13l & 156 & -22l \\ -13l & -3l^2 & -22l & 4l^2 \end{bmatrix} \quad (24)$$

where I is the moment of inertia; E is the Young's modulus; m and l are the mass and the length of the element.

Element mass matrices $\mathbf{M}_e$ are assembled to form the global mass matrix **M**, while matrices $\mathbf{K}_e$ and $\mathbf{K}_c$ are assembled to form the global stiffness matrix **K** of the cracked beam. Rayleigh damping in the form of $\mathbf{C} = \alpha\mathbf{M} + \beta\mathbf{K}$ is used for the beam.

When a breathing crack is presented in the bridge, the crack opens and closes gradually leading to the gradual change in the stiffness at the cross section of the crack during vibration. It is assumed that the effect of cracks depends on the curvature of beam at crack location and that range from 0 to 1 when the curvature ranges from negative maximum positive maximum. As a result, the stiffness matrix K of the element with breathing crack breathing crack can be modelled as follows [8]:

$$K_b = K_e + \frac{1}{2}(K_c - K_e)\left[1 + \frac{d''}{d''_{\max}}\right] \quad (25)$$

Where, $\mathbf{K_b}$ and $\mathbf{K_c}$ are the stiffness of the element with breathing crack, open crack and $\mathbf{K_e}$ is the stiffness of the intact element. d'' is the instantaneous curvature of the beam at the crack position and $d''_{\max}$ is the maximum curvature of the beam at the crack position during motion of the vehicle.

Substituting global matrices **M**, **C**, and **K** of the cracked beam into equation (9) and solving this equation by Newmark method, the dynamic responses of the vehicle and the beam will be obtained.

3. Wavelet transform

The continuous wavelet transform is defined as follows [23]:

$$W(a,b) = \int_{-\infty}^{+\infty} f(t)\psi_{a,b}\,dt \quad (28)$$

Where $\psi_{a,b}(t) = \frac{1}{\sqrt{a}}\psi^*\left(\frac{t-b}{a}\right)$, a is a real number called scale or dilation, b is a real number called position, $W(a,b)$ are wavelet coefficients at scale a and position b, $f(t)$ is input signal, $\psi\left(\frac{t-b}{a}\right)$ is wavelet function and $\psi^*\left(\frac{t-b}{a}\right)$ is complex conjugate of $\psi\left(\frac{t-b}{a}\right)$.

In order to be classified as a wavelet a function must satisfy the following mathematical criteria:

1) A wavelet must have finite energy:

$$E = \int_{-\infty}^{+\infty} |\psi(t)|^2\,dt < \infty \quad (29)$$

2) If $\hat{\psi}(\omega)$ is Fourier transform of $\psi(t)$, i.e.

$$\hat{\psi}(\omega) = \int_{-\infty}^{+\infty} \psi(t)e^{-i\omega t}\,dt \quad (30)$$

then the following condition must be satisfied:

$$C_g = \int_0^{\infty} \frac{|\hat{\psi}(\omega)|^2}{\omega} d\omega < \infty \quad (31)$$

This implies that the wavelet has no zero frequency component: $\hat{\psi}(0) = 0$,

$$\int_{-\infty}^{+\infty} \psi(t) e^{-j\omega t} dt = 0 \quad when\ \omega = 0 \quad (32)$$

or in other words, the wavelet must have a zero mean:

$$\int_{-\infty}^{+\infty} \psi(t) dt = 0 \quad 33)$$

3) An additional criterion is that, for complex wavelets, the Fourier transform must both be real and vanish for negative frequencies.

4. Simulation results

A numerical example of the beam with two cracks at locations of Lc_1=L/3 and Lc_2=2L/3 is carried out. The crack depths of two cracks are the same. Parameters of the beam are: mass density is 7855 kg/m^3; modulus of elasticity E=2.1x10^{11} N/m^2; L=50 m; b=0.5 m; h=1 m. Vehicle parameters are adopted from [24] as follows: m_1=m_2=50000 N; k_1=k_2=1.0x10^6 N/m; c_1=c$_2$=5.0x10^2 Ns/m. The displacement-time history of the moving vehicle is obtained to investigate the influence of the cracks.

4.1. Influence of the breathing crack on frequencies

When there are breathing cracks, the natural frequency of the system is larger than the case of fully open cracks which is in agreement with the discussion in the Introduction section. This is because the crack remains not fully open but it is changing between close and open states which cause the beam stiffer. Table 1 presents the comparison of the first two natural frequencies in two cases: fully open and breathing cracks with five levels of cracks. It can be seen from this Table and Figure 3 that the differences of the two natural frequencies increase when the depth of crack increase This suggests that when the crack depth is smaller than 20 %, the beam with breathing crack behaves similar to one with fully open crack.

Table 1. Difference of frequencies

Crack depth (%)	1st frequency			2nd frequency		
	Breathing crack	Open crack	Difference (%)	Breathing crack	Open crack	Difference (%)
10	0.90	0.90	0	3.38	3.36	0.60
20	0.90	0.90	0	3.36	3.26	3.07
30	0.90	0.88	2.27	3.32	3.04	9.21
40	0.90	0.84	7.14	3.28	2.64	24.24
50	0.90	0.80	12.50	3.26	2.16	50.93

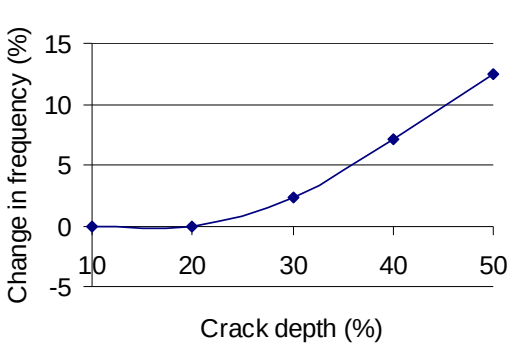

a) 1nd frequency

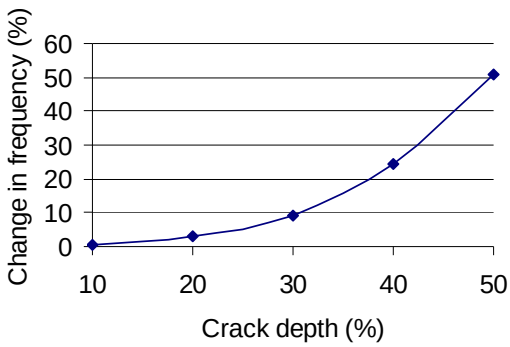

b) 2rd frequency

Fig. 3. Frequency difference vs. crack depth

4.2. Influence of the breathing crack on displacement

Figs from 4 to 8 show the dynamic displacements of the vehicle moving on the bridge without a crack, with a fully open crack, and with a breathing crack calculated from five different levels of the cracks. As can be seen from these Figs, the amplitude of the vertical displacement of vehicle moving on the bridge with breathing cracks is smaller than that with open cracks and larger than the case of intact beam. This means that it is more difficult when using the dynamic displacement to detect the crack if it behaves as a breathing crack.

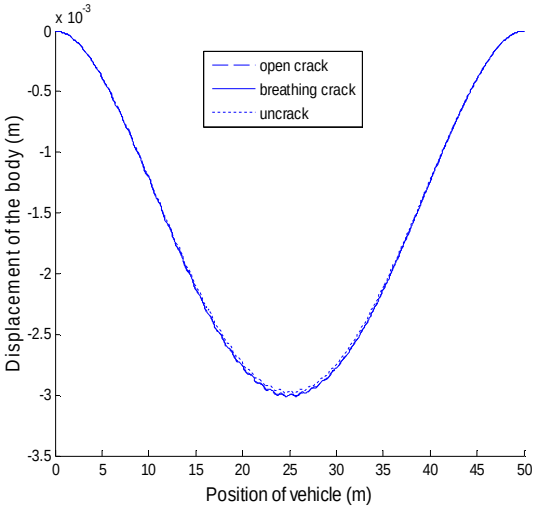

Fig. 4. Vertical displacement of the vehicle, crack depth is 10%

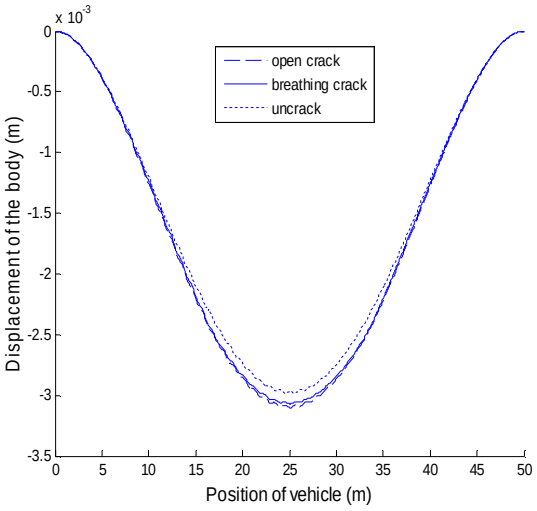

Fig. 5. Vertical displacement of the vehicle, crack depth is 20%

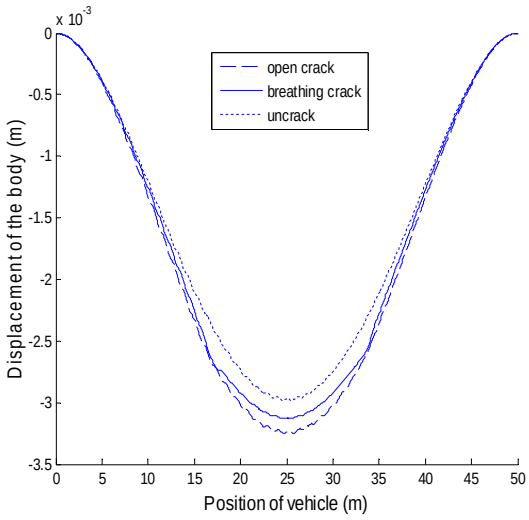

Fig. 6. Vertical displacement of the vehicle, crack depth is 30%

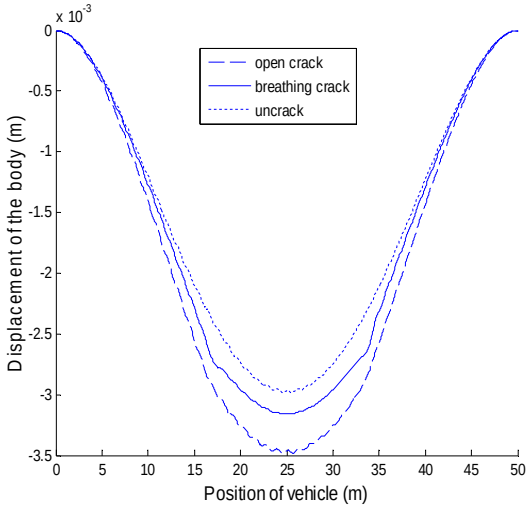

Fig. 7. Vertical displacement of the vehicle, crack depth is 40%

Another conclusion can be drawn from these Figs is that, when the crack depth is smaller than 30 %, the difference between the response of vehicle moving on the beam without a crack and beam with a breathing crack is smaller than that of the same beam and one with a fully open crack. However, when the crack depth increases, this difference decreases. This again suggests that the system with a breathing crack behaves similar to a fully open crack when the crack depth is small, but when the crack depth is larger the effect of the breathing crack can primitively be considered as the effect of a fully open crack with much smaller depth.

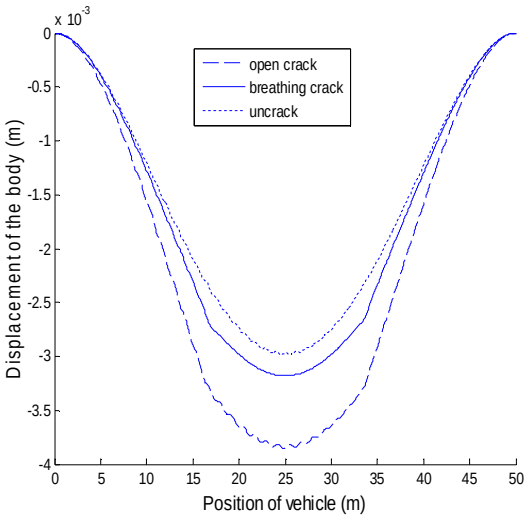

Fig. 8. Vertical displacement of the vehicle, crack depth is 50%

4.3. Influence of the breathing crack on crack detection

When the beam is cracked, there are distortions in the dynamic response of the vehicle at crack locations. However, these local distortions are generally small and difficult to be detected visually. Therefore, in this work the CWT with its special property is applied for data processing. After trying different wavelet functions for signal processing, the wavelet function "Symlet" is chosen as the most suitable one for this study.

Figs from 9 to 13 present wavelet transforms of the vehicle displacement in five levels of the crack depth. As can be seen in these Figs, there are clear peaks in the wavelet transform at crack positions. These peaks become more significant when the depth of crack is larger. Therefore, the peaks are indicators of the present of cracks. It is interesting that, although the amplitude of the displacement of the system with the breathing crack is smaller than that with open crack, peaks in the wavelet transform of the displacement in case of breathing crack are larger. This can be explained as follows: when moving on the beam the vehicle loading causes local maximum influences on the breathing crack phenomenon in the area adjacent to the cracks. This leads to the significant local changes in the displacement at crack positions. As a result, these local changes will be amplified as significant peaks in wavelet transform. This implies that the wavelet method for crack detection is more efficient with the present of the breathing crack.

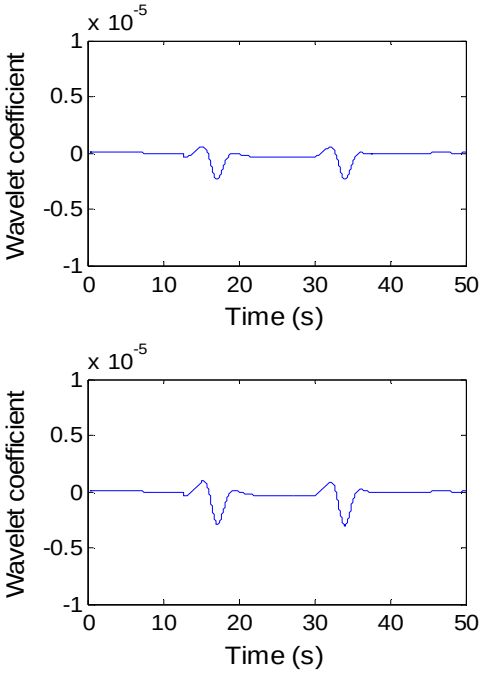

Fig. 9. Wavelet transform of y, crack depth is 10%: a) Open crack; b) Breathing crack

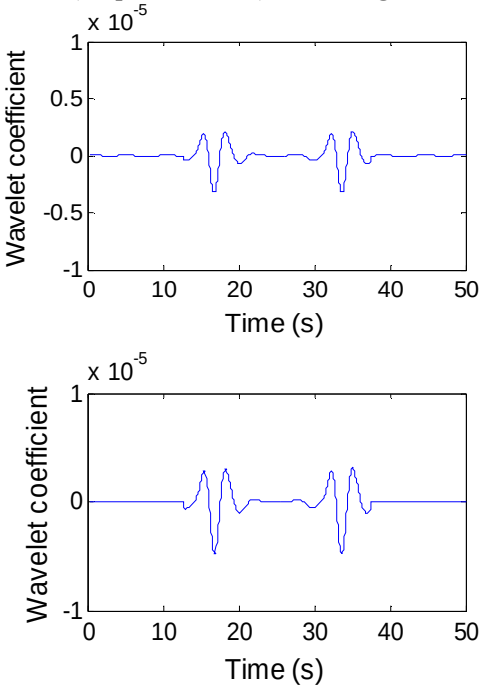

Fig. 10. Wavelet transform of y, crack depth is 20%: a) Open crack; b) Breathing crack

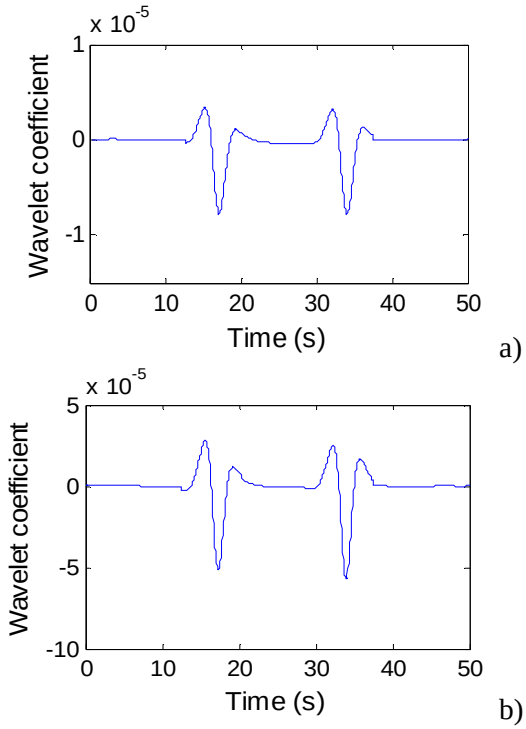

Fig. 11. Wavelet transform of y, crack depth is 30%: a) Open crack; b) Breathing crack

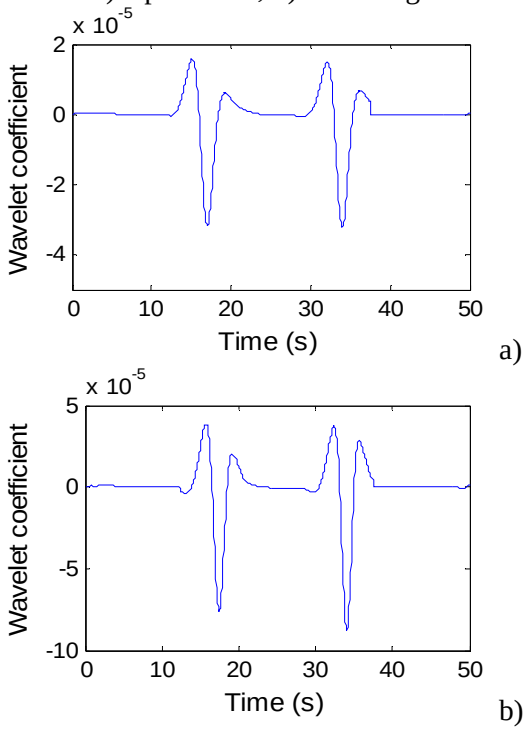

Fig. 12. Wavelet transform of y, crack depth is 40%: a) Open crack; b) Breathing crack

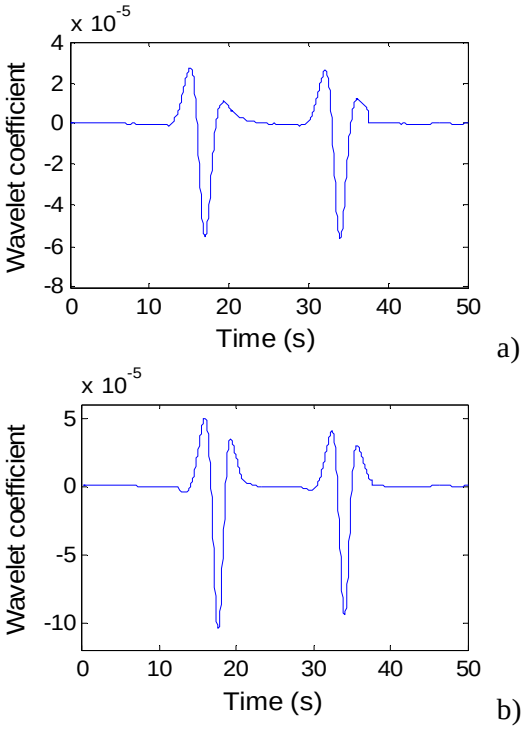

Fig. 13. Wavelet transform of y, crack depth is 50%: a) Open crack; b) Breathing crack

5. Conclusion

In this paper, effects of the breathing crack phenomenon on the dynamic response of a vehicle-bridge system obtained directly from the moving vehicle, and the influence of the breathing crack on crack detection have been investigated. The main conclusions can be drawn from this work as follows:

- Natural frequency of the vehicle-bridge with the breathing crack is larger in comparison with the case of open crack, which is in agree with other reports [2, 3, 8].

- The vertical displacement of the vehicle moving on the bridge with breathing cracks is smaller than that with open cracks. This is a warning when using the dynamic displacement to estimate the crack size: the small amplitude of dynamic response does not correspond to a small crack size if there is a presence of the breathing crack.

- When the crack depth is small the responses of vehicle moving on the beam with a breathing crack and beam with a fully open crack are close together. However, when the

crack depth increases, the beam with a breathing crack behaves similar to the beam without a crack in comparison with the case of open crack.

- Although the dynamic displacement of the system with the breathing crack is smaller than that of open crack, but it is interesting that the peaks in the wavelet transform of the displacement in case of breathing crack are larger. This implies that the wavelet method for crack detection is more efficient with the present of the breathing crack.

Acknowledgement

This work is supported by National Foundation for Science and Technology Development (NAFOSTED) 2012-2013.

References

[1] Chondros T.G., Dimarogonas A.D., and Yao J., *Vibration of a Beam with a Breathing Crack.* Journal of Sound and Vibration 2001, Vol. 239 (1), 57-67.

[2] Pugno N., Surace C., Ruotolo R., *Evaluation of the Non-Linear Dynamic Response to Harmonic Excitation of a Beam with Several Breathing Cracks.* Journal of Sound and Vibration 2000, Vol. 235(5), 749-762.

[3] Rizzo P. and Scalea F. L., *Feature Extraction for Defect Detection in Strands by Guided Ultrasonic Waves.* Structural Health Monitoring 2006, Vol. 5(3), pp. 297-308.

[4] Douka E. and Hadjileontiadis L.J., *Time-frequency Analysis of the Free Vibration Response of a Beam with a Breathing Crack.* NDT & E International 2005, Vol. 38, pp. 3-10.

[5] Sundermeyer J. N., and Weaver R. L., *On Crack Identification and Characterization in a Beam by Non-linear Vibration Analysis.* Journal of Sound and Vibration 1995, Vol. 183(5), pp. 857-871.

[6] Bovsunovsky A. P. and Matveev V. V., *Analytical Approach to the Determination of Dynamic Characteristics of a Beam with a Closing Crack*. Journal of Sound and Vibration 2000, Vol. 235(3), pp. 415-434.

[7] Qian G. L., Gu S. N., and Jiang J. S., *The Dynamic Behaviour and Crack Detection of a Beam with a Crack*. Journal of Sound and Vibration 1990, Vol. 138, pp. 233-243.

[8] Ariaei A., Ziaei-Rad S. and Ghayour M., Vibration analysis of beams with open and breathing cracks subjected to moving masses. Journal of Sound and Vibration 2009, Vol. 326, p. 709-724.

[9] Parhi D. R. and Behera A. K. *Dynamic Deflection of a Cracked Beam With Moving Mass.* Proc Instn Mech Engrs 1997, Vol. 211 Part C, 77-87.

[10] Piombo B.A.D., Fasana A., Marchesiello S., Ruzzene M. *Modelling and Identification of the Dynamic Response of a Supported Bridge*. Mechanical Systems and Signal Processing 2000, Vol. 14 (1), 75–89.

[11] Mahmoud M. A. and Abouzaid M. A., *Dynamic Response of a Beam with a Crack Subject to a Moving Mass*. Journal of Sound and Vibration 2002, Vol. 256 (4), 591-603.

[12] Lee J.W., Kim J.D., Yun C.B., Yi J.H., Shim J.M. *Health-Monitoring Method for Bridges under Ordinary Traffic Loadings.* Journal of Sound and Vibration 2002, Vol. 257 (2), 247–264.

[13] Bilello C., Bergman L.A. *Vibration of Damaged Beams under a Moving Mass: Theory and Experimental Validation.* Journal of Sound and Vibration 2004, Vol. 274, 567–582.

[14] Zhu X.Q., Law S.S. *Wavelet-based crack identification of bridge beam from operational deflection time history*. International Journal of Solids and Structures 2006, Vol. 43, 2299–2317.

[15] Khoa V. Nguyen, Hai T. Tran. *A Multi-cracks Detection Technique of a Beam-like Structure Based on the On-vehicle Vibration Measurement and Wavelet Analysis*. Journal of Sound and Vibration 2010, 329 (21), p.4455–4465.

[16] Lu CJ. and Hsu YT., *Vibration Analysis of an Inhomogeneous String for Damage Detection by Wavelet Transform*. International Journal of Mechanical Science 2002, Vol. 44, 745-754.

[17] Hong J.-C., Kim Y.Y., Lee H.C., and Lee Y.W., *Damage Detection Using the Lipschitz Exponent Estimated by the Wavelet Transform: Applications to Vibration Modes of a Beam.* International Journal of Solids and Structures 2002, Vol. 39, 1803-1816.

[18] Loutridis S., Douka E., and Trochidis A., *Crack Identification in Double-cracked Beam Using Wavelet Analysis.* Journal of Sound and Vibration 2004, Vol. 277, 1025–1039.

[19] Poudel U.P. and Fu G., and Ye J., *Structural Damage Detection Using Digital Video Imaging Technique and Wavelet Transformation.* Journal of Sound and Vibration 2005, Vol. 286, 869–895.

[20] Castro E., Garcia-Hernandez M. T., Gallego A., *Damage Detection in Rods by Means of the Wavelet Analysis of Vibration: Influence of the Mode Order*. Journal of Sound and Vibration 2006, Vol. 296, 1028-1038.

[21] Castro E., Garcia-Hernandez M. T., Gallego A., *Defect Identification in Rods Subject to Forced Vibration Using the Spatial Wavelet Transform.* Applied Acoustics 2007, Vol. 68, Issue 6, 699-715.

[22] Nguyen K. V. and Olatunbosun O. A., *A Proposed Method for Fatigue Crack Detection and Monitoring Using the Breathing Crack Phenomenon and Wavelet Analysis*. Journal of Mechanics of Materials and Structures 2007, Vol. 2 No 3, 400-420.

[23] Daubechies I., *Ten lectures on wavelets.* CBMS-NSF Conference series, 61. Philadelphia, PA: SISAM, 1992.

[24]. Majumder L. and Manohar C.S., *A time-domain approach for damage detection in beam structures using vibration data with a moving oscillator as an excitation source*. Journal of Sound and Vibration 268 (2003) 699–716.

The 2nd International Conference on Engineering Mechanics and Automation (ICEMA2)
Hanoi, August 16-17, 2012
ISBN: 978-604-913-097-7

Determine the Natural Frequencies of TLD by Experimental Method

Nguyen Ba Nghi[a], Bui Duc Tiep[b]

[a] *Msc, Institute of Mechanics, 264 Doi Can, Ha Noi, nbnghi@imech.ac.vn*
[b] *ME, Institute of Mechanics, 264 Doi Can, Ha Noi, budtiep@gmail.com*

Abstract

In Viet Nam, vibration reduction technology using TLD (tuned liquid damper) has studied by most of people. However, it is hardly applied in actual structures. To make TLD for actual structure we need to calculate all optimal parameters of TLD first. After TLD was manufactured, natural frequencies of TLD need to be determined to make sure it is the same as one was obtained by theory. In this paper, natural frequencies of TLD will be determined by two ways. The first way is measure acceleration of wave by sensor. Frequencies will be obtained by using signal processing methods. The second way is recording the wave by a camera. Frequencies are calculated by using image and signal processing methods.

Key Words: TLD experiment, frequency determination, image processing

1. Introduction

Sloshing of liquids has prompted numerous experimental studies in various disciplines due to the complexity of the problem and the difficulty in developing an analytical model. Some of the relevant work done in the area of liquid dampers is briefly reported here. The earliest experimental studies on TLDs are reported by Modi and Welt, 1987 and Fujino et al. 1988. Series of experimental studies, summarized in Modi et al. 1995, were conducted by using nutation dampers. These dampers covered different geometries like a toroidal ring, rectangular or circular cross-section cylinders, and in some situations may include baffles, screens, particle suspensions to manage liquid sloshing. Damper characteristics were determined by varying the amplitude and frequency of excitation. Fujino et al. 1988 carried out parametric studies of cylindrical containers by free-oscillation experiments. Effects of liquid viscosity, roughness of container bottom, air gap between the liquid and tank roof, and container size on the overall TLD damping were studied.

Experimental studies have been carried out for rectangular TLDs in the region of relatively small to medium vibration amplitudes, where the breaking of a wave does not occur, and the results have been found to be in good agreement with analytical results obtained by the shallow water theory (Fujino et al. 1992; Sun and Fujino, 1994; Sun et al. 1995). Similar experiments were done by Koh et al. (1994)

who considered earthquake type excitations as opposed to sinusoidal excitations utilized in previous studies.

2. Experimental Studies

Purpose of experiment is determined natural frequency of TLD. The TLD in experiment is a rectangular tank with dimension as in figure 1. The TLD was assigned on horizontal slip table of IMV vibration system. Wave surface of water in TLD will be recorded by a camera and acceleration sensor. The camera was fixed on horizontal slip table. The sensor was fixed on a buoy with a hole in middle. The buoy can only slide in vertical direction along a wire. Schematic of experiment as in figure 2 follow. In experiment water sloshing wave will be recorded by camera and acceleration sensor.

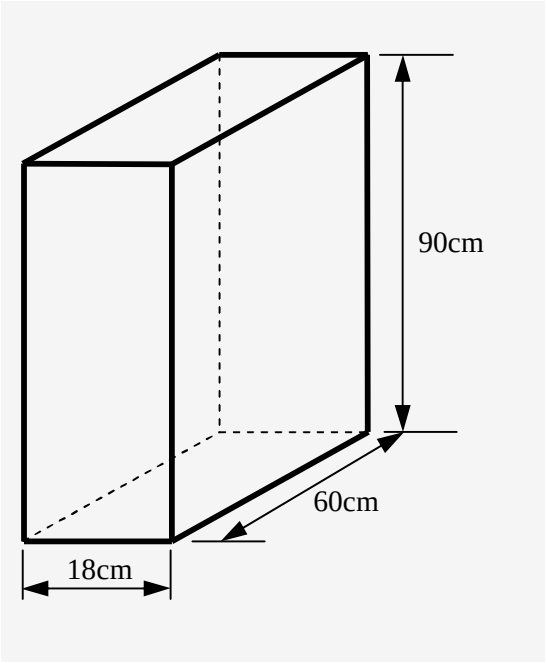

Figure 1. TLD was used in experiment

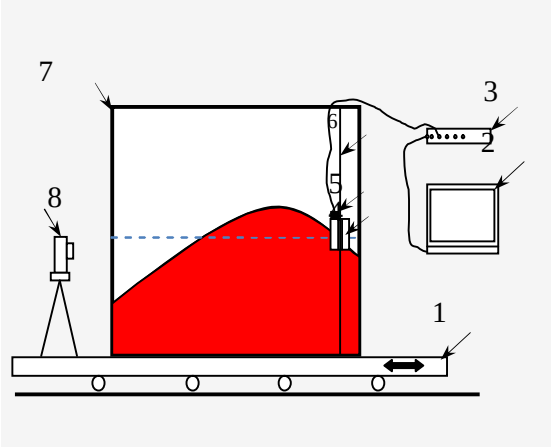

Figure 2. Schematic of the experimental setup.
1 – Shaking table; 2 – Computer;
3 – Signal conditioner; 4 – Buoy;
5 – Acceleration sensor; 6 – Wire;
7 – TLD; 8 – Camera

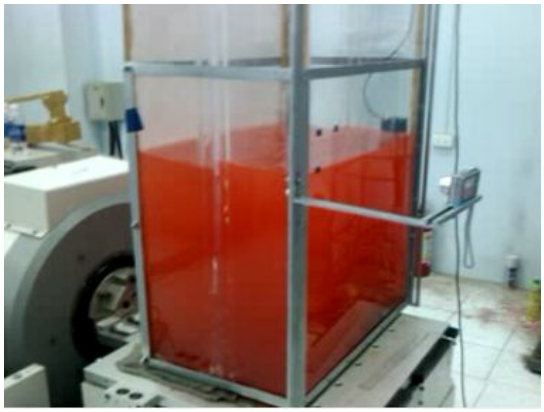

Figure 3. The TLD was assigned on horizontal slip table of IMV vibration system

The natural frequency of the TLD will be calculated from theory of liquid sloshing. A simplified model of sloshing in rectangular tanks is based on an equivalent mechanical analogy using lumped masses, springs and dashpots to describe liquid sloshing. The lumped parameters are determined from the linear wave theory (Abramson, 1966). The equivalent mechanical model is shown schematically in Fig. 2.1(a). The two key parameters are given by:

$$\omega_i^2 = \frac{g(2i-1)\pi \tanh[(2i-1)\pi r]}{a};\ i = 1,2,... \tag{1}$$

where i is the sloshing mode; m_i is the mass of liquid acting in that mode; ω_i is the frequency of sloshing; $r = h/a$ where h is the height of water in the tank; a is the length of the tank in the direction of excitation. From (1) the natural frequency of the first sloshing mode can compute as follow:

$$f = \frac{1}{2\pi}\sqrt{\frac{g\pi}{a}\tanh\left(\pi\frac{h}{a}\right)} \tag{2}$$

The TLD was used in experiment has length a = 0.18m. Using Eq. 1, the frequency of first sloshing mode is computed as in following table. The values of natural frequency depend on height of water in the TLD.

Table 1 Value of natural frequency of the first sloshing mode

Height of water h(m)	Natural frequency f(Hz)
0.1	2.02
0.2	2.0806
0.3	2.0825
0.4	2.0825
0.5	2.0825
0.6	2.0825

In table 1 value of natural frequency is almost unchanged when height of water in the TLD modify.

3. Determine natural frequency from experiment

In experiment, shaking table oscillated in harmonic rule. Frequency of oscillation was modified from 1.5Hz to 2.1Hz. During experiment, when frequency of shaking table increate the amplitude of sloshing wave increate too. As the frequency of shaking table increate to 2.0Hz the wave of sloshing was broken. This is resonance between frequency of shaking table and sloshing wave of water. In this case we had to reduce oscillation amplitude of shaking table. From that we can estimate that 2.0Hz is natural frequency of TLD. To obtain exactly value of natural frequency of TLD we have to process measured values from experiment.

3.1 Processing data measured from acceleration sensor

Sloshing wave of water in the TLD was recorded by vibration measurement system of IMV Corporation VM-5123/6. This System includes an acceleration sensor, signal conditioner and a laptop. This system was controlled by "Waveform Data Recording Software DS-5123R" software that was installed in laptop.

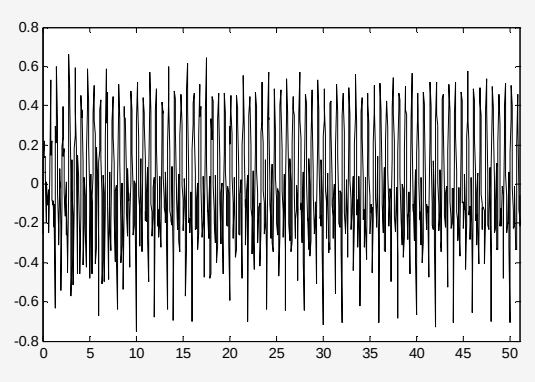

Figure 4. Acceleration of water sloshing wave in case of height of water is 0.2m and frequency of excitation 1.5Hz

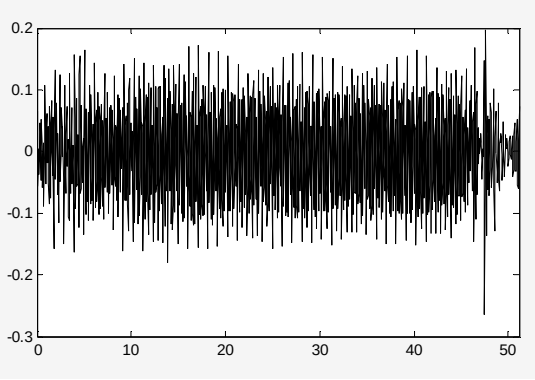

Figure 5 Acceleration of water sloshing wave in case of height of water is 0.4m and frequency of excitation 1.9Hz.

In this experiment, frequency of sloshing is around 2.0Hz. So we set sample frequency is 20Hz. The data measured is acceleration of water sloshing wave. In the following figures

showed acceleration of sloshing wave in some test case.

Using method of signal processing FFT(Fast Fourier Transform) to analyses the acceleration of water sloshing wave. We will obtain the natural frequency of the TLD. In Fig.6-7 are results of signal processing in some test case.

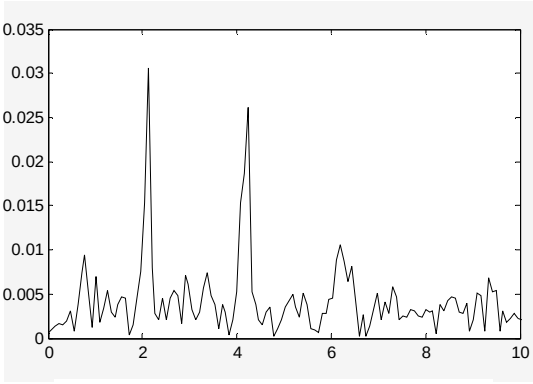

Figure 6 Result of frequency analysis in case height of water is 0.2m

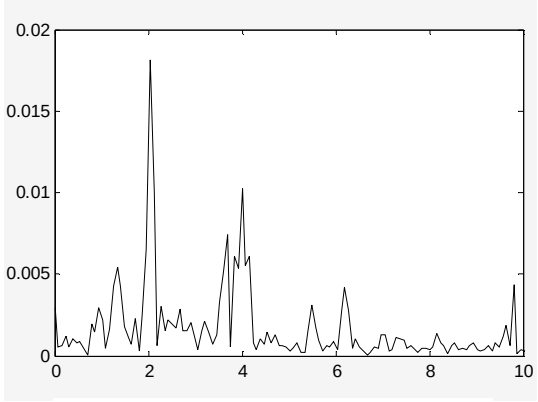

Figure 7 Result of frequency analysis in case height of water is 0.3m

From Fig.6 and Fig.7 we see that there is a tip around 2.0Hz . This mean that TLD has a natural frequency is around 2.0Hz.

3.2 Processing data measured from camera

With data recorded by camera, we have to use image processing method to convert data from video file to digital signal. In experiment, we put a mark at position of surface of water as in Fig.8. This mark will be used image processing process. The conversion include following step:

- Extract images from video file
- Using image processing method to identify wave surface and mark.
- Calculate distance from wave surface to mark as in Fig.9.
- Save all value distance to file (digital signal).

Figure 8. The mark was put on TLD before experiment

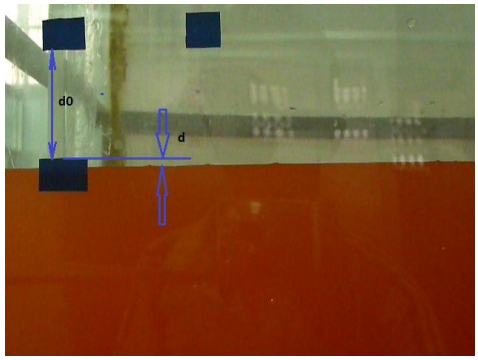

Figure 9. Distance from wave surface to mark

In the following figures are digital signal obtained in some case of experiment. One obtained from image processing method.

With digital signal obtained above. Using signal processing method we calculated natural frequency of TLD. Same as method of using acceleration sensor value of natural frequency is around 2.0Hz.

If see the results of frequency analysis in Fig. 6-7 and Fig. 13-15 we will find that in both method always exist a high pick around 2.0Hz. We also see that results in using camera method is look better. Results in Fig. 6-7 of method of using acceleration sensor

exist lost of small picks. The cause of these pick were noise in measurement process.

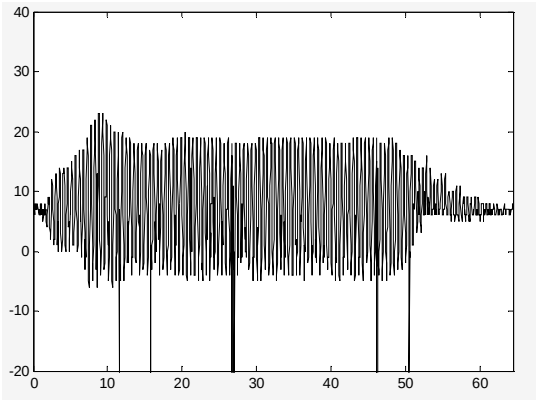

Figure 10 Displacement of water sloshing wave in case of height of water is 0.4m and frequency of excitation 1.9Hz

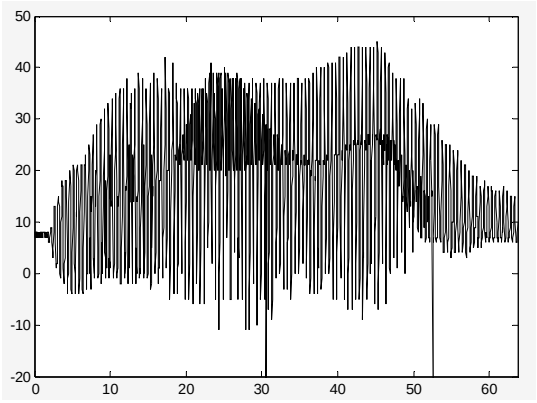

Figure 11 Displacement of water sloshing wave in case of height of water is 0.4m and frequency of excitation 2.0Hz

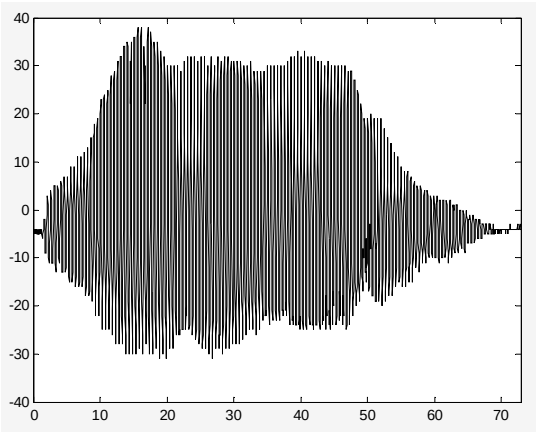

Figure 12 Displacement of water sloshing wave in case of height of water is 0.6m and frequency of excitation 2.0Hz

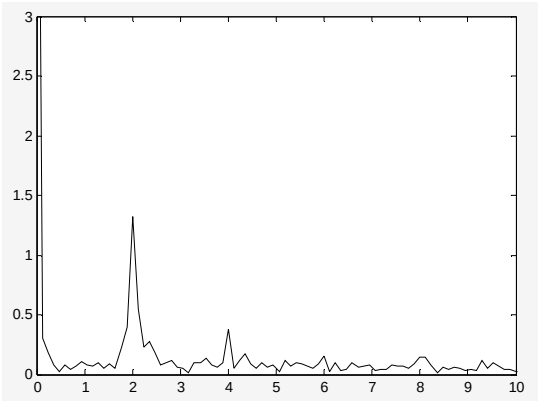

Figure 13. Result of frequency analysis in case height of water is 0.4m excitation frequency 1.9Hz

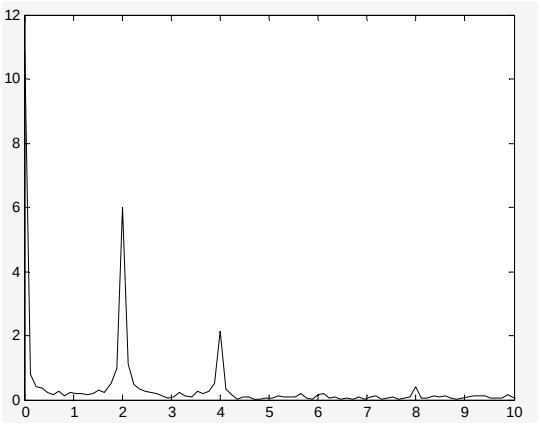

Figure 14. Result of frequency analysis in case height of water is 0.4m excitation frequency 2.0Hz

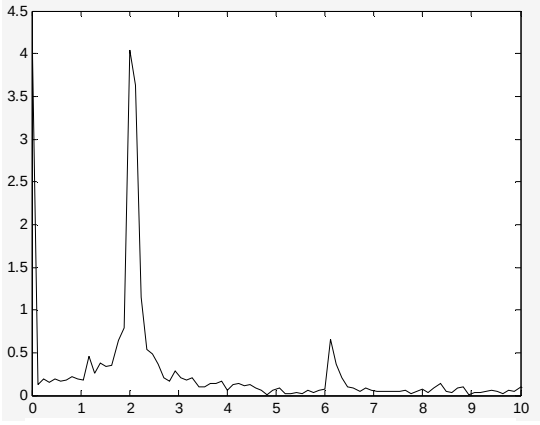

Figure 15. Result of frequency analysis in case height of water is 0.6m excitation frequency 2.0Hz

4. Conclusion

Paper has presented method of determine natural frequency of rectangular tank by experiment. The natural frequency determined by experiment is the same as result calculated by theory. So the experiment method is believable. Usually a camera is very cheap in compare with a vibration measurement system. Camera is easy to use. Method using sensor is affected by delay of the buoy. We also see that the result from two measurement method is quite similar. Thus we can say that the method of using camera has more advantage than using acceleration sensor.

5. Acknowledgement

The support from Vietnam Academy of Science and Technology, 18 Hoang Quoc Viet, Cau Giay, Hanoi, Vietnam is thankful.

6. References

[1] Abramson, H.N.(ed.)(1966), “The Dynamic Behavior of Liquids in Moving Containers”, NASA, SP-106.

[2] Fujino, Y., et al., "Fundamental Study of Tuned Liquid Damper (TLD) - A New Damper for Building Vibrations," Proceedings of the Symposium/Workshop on Serviceability of Buildings, 16-18 May 1988.

[3] Fujino,Y., Sun, L.M., Paceno, B. and Chaiseri, P. (1992), “Tuned Liquid Damper (TLD) for Suppressing Horizontal Motion of Structures,” ASCE Journal of Engineering Mechanics, 118(10), 2017-2030.

[4] Koh, C.G., Mahatma, S. and Wang, C.M. (1994) “Theoretical and experimental studies on rectangular liquid dampers under arbitrary excitations,” Earthquake Engng. and Struc. Dynamics. 23, 17-31.

[5] Modi, V. J. and Welt, F., "Damping of Wind Induced Oscillations Through Liquid Sloshing," Preprint vol. 5, Seventh International Conference on Wind Engineering, Aachen, W. Germany, July 6-10, 1987.

[6] Modi, V.J., Welt, F. and Seto, M.L. (1995), “Control of Wind-Induced Instabilities though application of Nutation Dampers: A brief overview,” Engineering Structures,17(9), 626-638.

[7] Sun, L.M. and Fujino, Y. (1994), “A Semi-analytical model for Tuned Liquid Damper (TLD) with wave breaking,” Journal of Fluids and Structures, 8, 471-488.

[8] Sun, L. M., Fujino,Y., Paceno, B. and Chaiseri, P. (1995), “The properties of Tuned Liquid Dampers using a TMD analogy,” Earthquake Engng and Struc. Dynamics, 24,967-976.

The 2nd International Conference on Engineering Mechanics and Automation (ICEMA2)
Hanoi, August 16-17, 2012
ISBN: 978-604-913-097-7

Passive Vibration Control of DKI Structure Using Tuned Liquid Damper

Nguyen Ba Nghi[a] and Phan Thi Tra My[b]

[a] *Msc, Institute of Mechanics, 264 Doi Can, Ha Noi, nbnghi@imech.ac.vn*
[b] *Msc, Institute of Mechanics, 264 Doi Can, Ha Noi, pttmy@imech.ac.vn*

Abstract

The DKI structures which were built at Truong Sa usually are excited by wind and wave load. Thus, vibrations of DKI structures are quite significant and lead to negative effects on DKI structures and solders who are living there. Hence, the research on the reduction of those vibrations is needed. This paper presents a method that used TLD (Tuned Liquid Damper) device for reducing vibration of DKI structures. Parameters of TLD are calculated in order to minimize vibrations as much as possible.

Key Words: reducing vibration, parameters of TLD

1. Introduction

TLDs were proposed in the late 1800s where the frequency of motion in two interconnected tanks tuned to the fundamental rolling frequency of a ship was successfully utilized to reduce this component of motion (Den Hartog, 1956). Initial applications of TLDs for structural applications were proposed by Kareem and Sun(1987); Modi *et al.* (1987) and Fujino *et al.* (1988). In the area of satellite applications, these dampers were referred to as *nutation dampers*.

Sakai *et al.* (1991) proposed a new type of liquid damper which was termed as a tuned liquid column damper (TLCD) and described an application for cable-stayed bridge towers. TLCDs were studied for wind excited structures by Honda *et al.* (1991); Xu *et al.*(1992) and Balendra *et al.* (1995). Studies were also made for determining certain optimal characteristics of these passive devices by Gao *et al.* (1997); Chang and Hsu (1999); and Gao *et al.* (1999). The performance of TLCDs for seismic applications has been studied by Won *et al.* (1996) and Sadek *et al.* (1998).

2. Calculate optimal parameters of TLD

2.1. Equivalent mechanical model of TLD

A simplified model of sloshing in rectangular tanks is based on an equivalent mechanical analogy using lumped masses, springs and dashpots to describe liquid sloshing. The lumped parameters are determined from the linear wave theory (Abramson, 1966). The equivalent

mechanical model is shown schematically in Fig.1. The two key parameters are given by:

$$m_i = M\left(\frac{8\tanh[(2i-1)\pi r]}{\pi^3 r(2i-1)^3}\right);\ i=1,2,...$$

$$\omega_i^2 = \frac{g(2i-1)\pi\tanh[(2i-1)\pi r]}{a};\ i=1,2,..$$

(1)

where i is the sloshing mode; m_i is the mass of liquid acting in that mode; ω_i is the frequency of sloshing; $r = h/a$ where h is the height of water in the tank; a is the length of the tank in the direction of excitation; M is the total mass of the water in the tank; and m_0 is the inactive mass which does not participate in sloshing, given by

$$m_0 = M - \sum_{i=1}^{\infty} m_i \qquad (2)$$

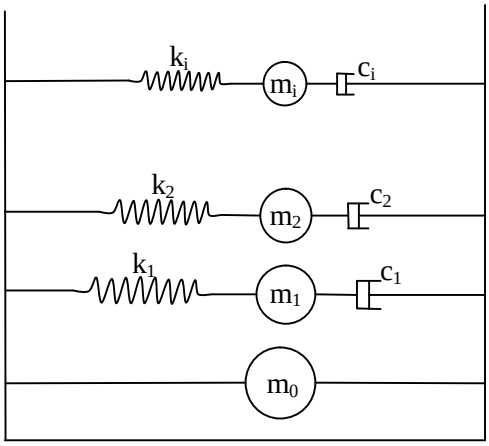

Figure 1. The equivalent mechanical model of TLD

Usually, only the fundamental mode of liquid sloshing (i.e., n = 1) is used for analysis. This model works well for small amplitude excitations, where the breaking wave and the influence of non-linearities do not influence the overall system response significantly. This model can also be used for initial design calculations of TLDs (Tokarcyzk, 1997).

2.2. Mechanical model of DKI structure and differential equations

The DKI structure can be modeled as inverted pendulum have concentrated mass m is connected with uniform bar length l, mass m_0, the stiffness of spiral spring is k, the damping of pendulum is c. The water tank on structure works as a TLD. This TLD can be converted to an equivalent TMD (tuned mass damper), which include concentrated mass m_d, spring with stiffness k_d and damping c_d, position of TMD is given by l_d.

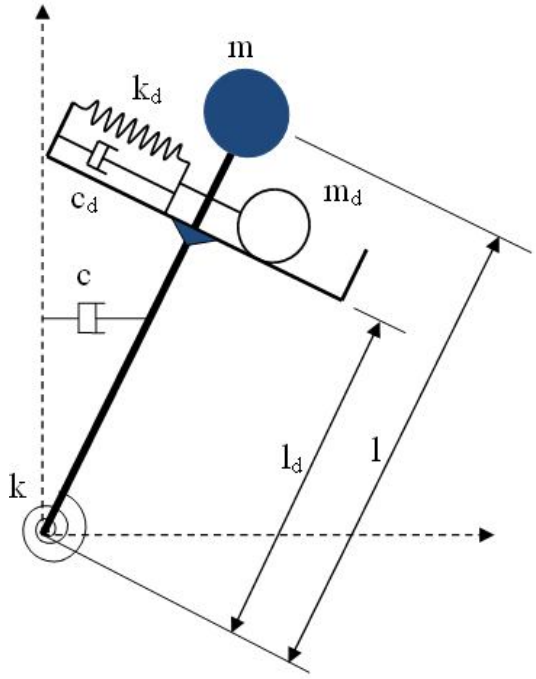

Figure 2. Mechanical model of DKI structure with TMD

The system of differential equations was established by using Lagrange's equation as follows:

$$\begin{bmatrix} ml^2+\frac{1}{3}m_0l^2+m_dl_d^2 & m_dl_d \\ m_dl_d & m_d \end{bmatrix}\begin{bmatrix}\ddot{\varphi}\\ \ddot{u}\end{bmatrix}+$$

$$+\begin{bmatrix} c & 0 \\ 0 & c_d \end{bmatrix}\begin{bmatrix}\dot{\varphi}\\ \dot{u}\end{bmatrix}+$$

$$+\begin{bmatrix} k-mgl-\frac{1}{2}m_0gl-m_dgl_d & -m_dg \\ -m_dg & k_d \end{bmatrix}\begin{bmatrix}\varphi\\ u\end{bmatrix}$$

$$= \begin{bmatrix} 0 \\ 0 \end{bmatrix} \tag{3}$$

By introducing dimensionless parameters:

$$\mu = \frac{m_d}{m + \frac{1}{3}m_0},\ \gamma = \frac{l_d}{l},\ \alpha = \frac{\omega_d}{\omega_s},$$
$$\xi = \frac{\gamma c_d}{2m_d\omega_d},\ \eta = \frac{\omega_0^2}{\omega_s^2} \tag{4}$$

where

$$\omega_s^2 = \frac{k - mgl - \frac{1}{2}m_0 gl}{ml^2 + \frac{1}{3}m_0 l^2},$$
$$\omega_0^2 = \frac{g}{l},\ \omega_d^2 = \frac{k_d}{m_d} \tag{5}$$

With supporting that damping of main structure is equal to zero (c = 0) and set $y = l\varphi$, the equation (3) can be rewritten as follows

$$\begin{bmatrix} 1+\mu\gamma^2 & \mu\gamma^2 \\ \mu\gamma^2 & \mu\gamma^2 \end{bmatrix}\begin{bmatrix} \dot{y} \\ \ddot{u} \end{bmatrix} + \omega_s \begin{bmatrix} 0 & 0 \\ 0 & 2\xi\mu\gamma\alpha \end{bmatrix}\begin{bmatrix} \dot{y} \\ \dot{u} \end{bmatrix}$$
$$+\omega_s^2 \begin{bmatrix} 1-\mu\gamma\eta & -\mu\gamma\eta \\ -\mu\gamma\eta & \mu\gamma^2\alpha^2 \end{bmatrix}\begin{bmatrix} y \\ u \end{bmatrix} = \begin{bmatrix} \frac{\gamma\gamma_1\mu}{m}P(t) \\ 0 \end{bmatrix} \tag{6}$$

The stability condition of (6) is that the mass and stiffness matrices are positive definite, damping matrix is semi-positive definite (***M***, ***K*** **>0**, ***D*** ≥ 0.)

From (6) we see that mass matrix is positive definite and the damping matrix is semi-positive definite, hence, the stability condition is that the stiffness matrix is positive definite:

$$\boldsymbol{K} = \begin{bmatrix} 1-\mu\gamma\eta & -\mu\gamma\eta \\ -\mu\gamma\eta & \mu\gamma^2\alpha^2 \end{bmatrix} > 0 \tag{7}$$

According to Hurwitz's criterion, the condition to stiffness matrix is positive definite is

$$\begin{cases} 1-\mu\gamma\eta > 0 \\ (1-\mu\gamma\eta)\mu\gamma^2\alpha^2 - \mu^2\gamma^2\eta^2 > 0 \end{cases} \tag{8}$$

2.3. Calculating optimal geometric parameter of TLD

Using the transformation of variables

$$x_1 = \varphi,\ x_2 = x,$$
$$x_3 = \dot{x}_1 = \dot{\varphi},\ x_4 = \dot{x}_2 = \dot{x}$$

Equation (6) can be rewritten in the form:

$$\dot{\boldsymbol{x}} = \boldsymbol{A}\boldsymbol{x} \tag{9}$$

where

$$\boldsymbol{A} = \begin{bmatrix} 0 & 0 & 1 & 0 \\ 0 & 0 & 0 & 1 \\ -1 & \mu\gamma\eta + \mu\gamma^2\alpha^2 & 0 & 2\xi\mu\gamma\alpha \\ \frac{\gamma+\eta}{\gamma} & -\mu\gamma\eta - \alpha^2 - \mu\gamma^2\alpha^2 & 0 & -\frac{2\left(1+\mu\gamma^2\right)\xi\alpha}{\gamma} \end{bmatrix};$$

$$\boldsymbol{x} = \begin{bmatrix} x_1 \\ x_2 \\ x_3 \\ x_4 \end{bmatrix} \tag{10}$$

Using the method of Lyapunov's equation (Anh, 2006), we obtain optimal parameters of equivalent TMD:

$$\alpha = \sqrt{\frac{1 - m^2\gamma^3\eta - 2\mu\gamma\eta}{\left(1+\mu\gamma^2\right)^2}},$$
$$\xi = \sqrt{\frac{\mu\gamma^2(\gamma+\eta)^2}{4(\mu\gamma^2+1)(\mu\gamma\eta-1)(\mu^2\eta\gamma^3 + 2\mu\eta\gamma - 1)}} \tag{11}$$

According to (4) and (11) we obtain:

$$\omega_d^2 = \alpha^2 \omega_s^2 = \frac{\left(1 - m^2\gamma^3\eta - 2\mu\gamma\eta\right)\alpha^2}{\left(1+\mu\gamma^2\right)^2} \quad (12)$$

On the other hand, according to (1) (with mode i = 1) we have:

$$\omega_d^2 = \frac{g\pi \tanh(\pi h/a)}{a} \quad (13)$$

By substituting (12) into (13) we obtain following equation:

$$\frac{g\pi \tanh(\pi h/a)}{a} = \frac{\left(1 - m^2\gamma^3\eta - 2\mu\gamma\eta\right)\alpha^2}{\left(1+\mu\gamma^2\right)^2} \quad (14)$$

With value of parameters of DKI structure as follows:

$$m = 145000,\ m_0 = 417000,$$
$$l_0 = 42.1,\ l = 39.4,\ g = 9.8,$$
$$m_d = 1000 \times 64 \times h,\ k = 73673802604 \quad (15)$$

Solving equation (14) we obtain optimal length of TLD according to value of depth of liquid inside TLD:

Table 1. Calculated Parameters of TLD and equivalent TLD

h(m)	a(m)	m_d	k_d
0.1	0.198	3003	430301
0.15	0.211	3399	485757
0.2	0.214	3520	502635
0.25	0.215	3551	507009
0.3	0.216	3558	508065
0.4	0.216	3560	508371
0.5	0.216	3560	508388
0.6	0.216	3560	508389
0.7	0.216	3560	508389
0.8	0.216	3560	508389

From result in the table above we see that if the level of water in TLD is higher than 0.3 the size of TLD, the concentrated mass and stiffness of equivalent TMD are virtually unchanged.

2.4. Numerical simulation

The effect of vibration reduction of TMD is determined according to the formula

$$h = \frac{\sum \hat{x}_k[i] - \sum \hat{x}_c[i]}{\sum \hat{x}_k[i]} \times 100\% \quad (16)$$

Where $\hat{\boldsymbol{x}}_k$ is the envelope of response of structure without TMD, $\hat{\boldsymbol{x}}_c$ is the vinculum of response of structure with TMD.

Numerical simulation was calculated for case of parameters of structure chosen as in (15). The damping value of DKI structure was chosen about 1.2%. With parameters as in (15), frequency of DKI structure is 2.0Hz.

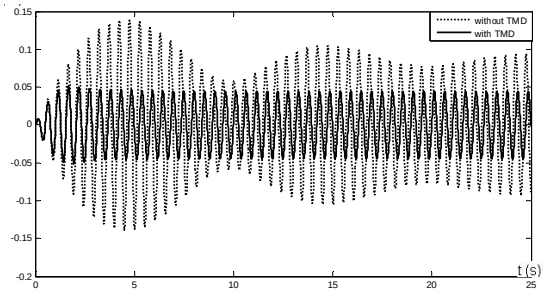

Figure 3. Response of structure with harmony excitation according to the level water h = 0.3, frequency of excitation is 1.9Hz

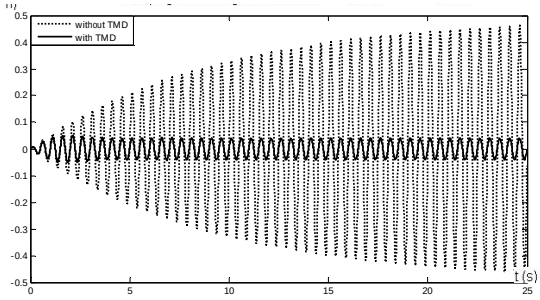

Figure 4. Response of structure with harmony excitation according to level water h = 0.3, frequency of excitation is 2.0Hz

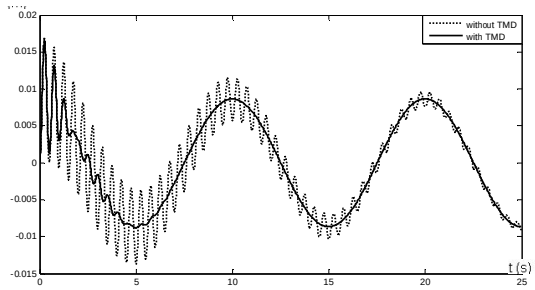

Figure 5. Response of structure with harmony excitation according to the level water h = 0.3, frequency of excitation is 0.1Hz

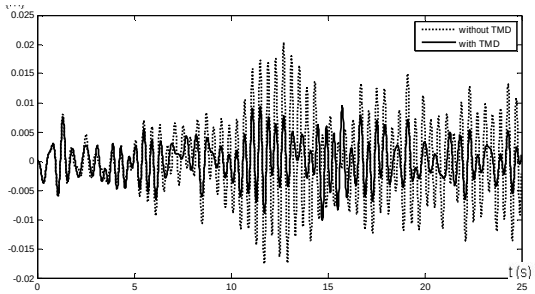

Figure 6. Response of structure with white noise excitation according to the level water h = 0.3

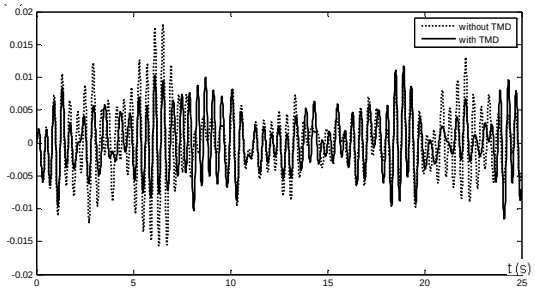

Figure 7. Response of structure with white noise excitation according to the level water h = 0.3

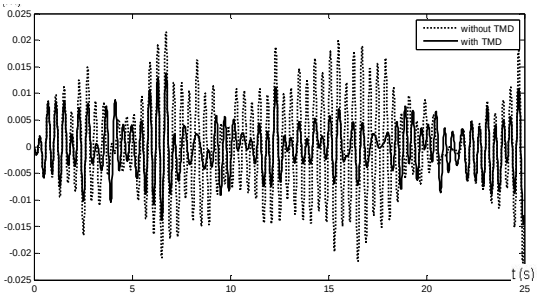

Figure 8. Response of structure with white noise excitation according to the level water h = 0.3

The results of numerical simulation are shown in figures 3-8 and indicate that the efficiency of vibration reduction is quite good. In the case of harmonic excitation, the vibration reduction efficiency is around 75%. If the frequency of excitation is approximate to the frequency of structure (resonance), TLD device reduces the force vibration of DKI structure, and reduced the free vibration in case when the frequency of excitation is different from the frequency of structure. In the case of white noise excitation the efficiency of vibration reduction is around 45%.

3. Conclusion

By converting the TLD into equivalent TMD, the calculation of optimal parameters of the TLD becomes simpler. With the results shown in Table 1, we see that when the level of water increases to a certain value, the parameters of the equivalent TMD will not change. Hence, we should take a note on the level of liquid when design TLD for a structure. If the level of liquid is higher than the limited value, it will not increase the efficiency of vibration reduction. On the contrary it will make the mass of system to be increased. The numerical simulation has proved that the TLD has a good effect on reducing the free vibration and forced vibration.

4. Acknowledgement

The support from Vietnam Academy of Science and Technology, 18 Hoang Quoc Viet, Cau Giay, Hanoi, Vietnam is thankful.

5. References

Abramson, H.N.(ed.) (1966). *The Dynamic Behavior of Liquids in Moving Containers*, NASA, SP-106

Anh, N.D and Nghi, N.B (2006). Design of TMD for Inverted Pendulum Type Structures to Reduce Free Vibration Components, *Proceeding of the National Conterence on Engineering Mechanics and Automation*, Bach Khoa Publishing House, Hanoi 1-8

Chang, C.C. and Hsu, C.T. (1999). Control performance of Liquid column vibration absorber. *Engineering Structures*, 20(7), 580-586

Den Hartog J.P. *Mechanical Vibrations.* McGraw-Hill, 1956

Fujino, Y., et al.. Fundamental Study of Tuned Liquid Damper (TLD) - A New Damper for Building Vibrations. *Proceedings of the Symposium/Workshop on Serviceability of Buildings*, 16-18 May 1988

Gao, H., Kwok, K.C.S. and Samali, B. (1997). Optimization of Tuned Liquid Column Dampers. *Engineering Structures*, 19, 476-486

Gao, H., Kwok, K.C.S. and Samali, B. (1999). Charcteristics of multiple Tuned Liquid Column Dampers in suppressing Structural Vibration. *Engineering Structures*, 21,316-331

Kareem, A. and Sun, W.-J. Stochastic Response of Structures with Fluid-Containing Appendages. *Journal of Sound and Vibration*, Vol. 119, No. 3, 1987

Modi, V. J. and Welt, F. Damping of Wind Induced Oscillations Through Liquid Sloshing. Preprint vol. 5, *Seventh International Conference on Wind Engineering*, Aachen, W. Germany, July 6-10, 1987

Sadek, F., Mohraz, B. and Lew, H.S. (1998) Single- and Multiple-Tuned Liquid Column Dampers for Seismic Applications. *Earthquake Engng. and Struc. Dyn.*, 27, 439-463

Sakai, F.,and Takaeda. S. (1991). *Tuned Liquid Column Damper (TLCD) for cablestayed bridges.* Innovation in Cable-stayed Bridges, Fukonova, Japan

Tokarcyzk, B.L. (1997), *The Mathematical Modeling of a Tuned Liquid Damper*. M.S. Thesis, Department of Civil Engineering, Texas A&M University, College Sta-tion, TX

Won, A.Y.J., Pires, J.A. and Haroun, M.A. (1996) Stochastic seismic performanceevaluation of tuned liquid column dampers. *Earthquake Engng & Structural Dynam-ics*, 25, 1259-1274

Xu, Y.L, Samali, B. and Kwok, K.C.S. (1992). Control of Along-wind Response of Structures by Mass and Liquid Dampers. *Journal of Engineering Mechanics*, 118(1),20-39

The 2nd International Conference on Engineering Mechanics and Automation (ICEMA2)
Hanoi, August 16-17, 2012
ISBN: 978-604-913-097-7

An Automatic Car License Plate Recognition Algorithm for Controlled Outdoor Environment

Manh Thang Pham[a], Tran Hiep Dinh[b]

[a] *Falcuty of Mechanics and Automation, University of Engineering and Technology, thangpm@vnu.edu.vn*
[b] *Falcuty of Mechanics and Automation, University of Engineering and Technology ,tranhiep.dinh@vnu.edu.vn*

Abstract

The paper presents a research on an automatic car license plate recognition system (ALPR), an important part in the building management system (BMS) project conducted by the Faculty of Mechanics and Automation (FEMA), University of Engineering and Technology, Hanoi National University. The system is supposed to take pictures of visiting and leaving cars of a building and to be able to recognize the license plates from the car images. In order to segment the plate regions from raster images, the morphology based method was employed. First, from the gray scale version of the original image, a vertical edge map was detected using the Sobel filter. Morphological operators were then applied to find the plate candidate regions. Based on ratio of the plate width and height as well as number of pixels in a plate area, the license plate region will be extracted. This extracted plate region was sent to an OCR engine for character recognition. Before passing to OCR module for character recognition, median filter and connected component labeling are applied on extracted region to remove unwanted areas such as plate boundary and nearby areas. The results show an average of 100% successful license plate localization in a total of 200 images from controlled outdoor environment.

Key Words: ALPR, BMS, Connected Component Labeling, OCR

1. Introduction

Automatic license plate recognition has a wide range of applications such as controlling access to parking lots, collecting automatic toll, identifying vehicles that violates traffic laws or finding stolen cars. As an important part of the building management system project conducted by FEMA, an algorithm to recognize license plates from car images was studied. Recognition algorithms are generally composed of three processing steps: license plate region extraction, character segmentation and character recognition. In this paper, the focus is on the localization algorithm of license plates from car images. The image of the extracted area was processed through an OCR engine to convert the license plate number to an ASCII string.

Several approaches to dealing with the localization algorithm of cars license plates have been published, namely the combination of Hough transform and contour algorithm (Tran, 2004), an approach based on the region of candidate areas (Wenjing, 2007) and morphology based approach (Suryanarayana, 2005). Each approach has its own advantages and disadvantages. The first method has a high accuracy rate and fast detection speed. However, it could produce many candidate regions due to the parallel lines that they detect, which adds challenges to the segmentation step. The second approach uses a mean shift in the spatial range domain of color images and shows a reliable accuracy in LPR. It, nevertheless, cannot produce accurate results when the car and the car plate have the same color. Lastly, the approach in (Suryanarayana, 2005) applies morphological operators on edge map of original images to locate candidate regions and segment the plate area based on characteristic features. Its main advantage is the execution speed and simple implementation. The recognition accuracy rate can be affected by quality of input images which are the result of such factors as the speed of passing cars, the distance from camera to car or light condition. In this paper we only present a study on controlled outdoor environment. It means that all the images are taken at close shot at good light condition and cars are not moving. The study worked with *200* car images at resolution *320 x 240* containing Vietnamese license plates.

Within the scope of the research, an morphology based algorithm was developed to make sure that the output images of extracted license plates can be easily processed through the OCR engine for character recognition. Our approach consists of two modules, license plate segmentation module and enhancement module. In the first module, we made use of the Sobel filter to get the vertical edge map of original car images, which helps to reduce the extra information of a car image. Morphological operators were then applied to find the candidate license plate regions. The segmentation step was processed based on the ratio of the plate width and height as well as the number of the contained pixel in the candidate region. In the enhancement module, median filter and connected component labeling algorithm were used to remove the plate boundary as well as unwanted nearby areas.

The paper is organized as follows. Section 2 presents the proposed method, section 2.1 describes segmentation of license plate region and section 2.2 presents enhancement steps on the extracted plate area. The experimental results and conclusions are discussed in section 3 and 4 respectively.

2. The proposed method

2.1. License plate detection

In this section, the main steps of the license plate localization algorithm will be introduced. Flowchart of the proposed method is shown in Figure 1. The color image was first converted into gray scale image using following equation:

$$x = 0.3r + 0.59g + 0.11b \qquad (1)$$

Where *r*, *g*, *b* are *R*, *G*, *B* spectrum of color image respectively, *x* is grayscale weight average. All parameters *r*, *g*, *b*, *x* are integers between 0 and 255.

The corresponding edge map of the car image was obtained using Sobel mask because the edge image that contains both horizontal and vertical edges is too complex to process and most of vehicles have more horizontal lines than vertical lines.

In this study, we applied a fixed threshold to obtain the binary images where vertical edges were highlighted in a black background. Experiment results showed that with a threshold higher than 0.2, it was only possible to obtain very strong edges which is, in practice, not very helpful. The chosen threshold in this project is *T = 0.12*. The obtained binary image is represented as follows:

$$B_{i,j} = \begin{cases} 1, & if \quad E_{i,j} > T \\ 0, & otherwise \end{cases} \quad (2)$$

Where $E_{i,j}$ is vertical edge intensity function of the input image at pixel *(i,j)* while $B_{i,j}$ denotes the corresponding binary vertical edge map.

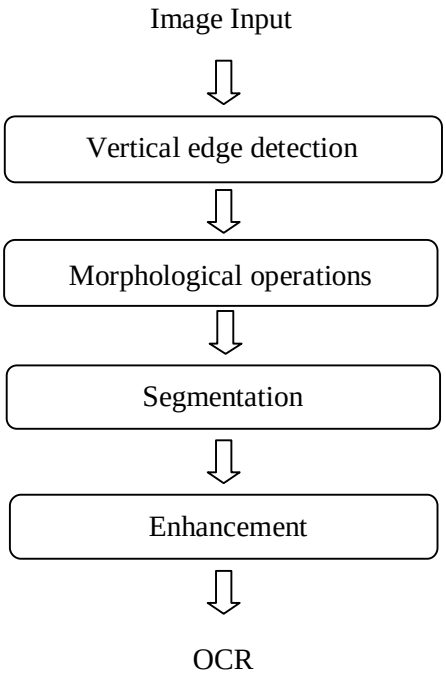

Figure 1. Flowchart of proposed method

Morphological operations were then performed on the obtained binary images to locate the candidate plate regions. The obtained vertical edges on the binary image was firstly shrunk (thinned) using erosion operation, during which short and thin edges were eliminated (Eq. 3). Closing operation was then applied on the remaining edges to remove holes and gaps between neighbouring vertical edges (Eq. 4). After this step, a set of candidate plate areas was generated.

$$B_e = B \ominus S_e \quad (3)$$

$$B_c = B \bullet S_c \quad (4)$$

Equations (3) and (4) represents erosion and closing steps where B_e, B_c are eroded and closed binary images generated from B while S_e and S_c are 3*1 and 15*25 structure element respectively. Rectangular structure element is here used to get plate-like shape of candidate regions.

(a)

(b)

Figure 2. Grayscale version (a) and edge map (b) of input image

The task now was to determine the region that consists of the license plate. Therefore, connected components algorithm using eight-neighborhood-definition was applied on the obtained image from Equation 4. From each candidate region, min and max coordinates of boundary pixel in vertical and horizontal direction were calculated (X_{max}, X_{min}, Y_{max}, Y_{min}). These parameters were used to evaluate if the current candidate region is the plate one. First, the number of contained pixels in each area was compared with the defined thresholds T_{Smin}, T_{Smax} and all areas with consisted pixels lower or higher than these thresholds were eliminated.

$$T_{S\min} <= W * H <= T_{S\max}$$

Where W, H are width and high of candidate regions respectively $W=X_{max} - X_{min}$, $H=Y_{max} - Y_{min}$.

(a)

(b)

Figure 3. Erosion (a) and Closing (b) operations on edge map

Since there are two main types of Vietnamese plate, the candidates that satisfied the above condition were recognized as license plate if its height and width ratio meets one of these two demands:

$$3.5 < W/H < 4.5 \quad \text{(1 row plate)}$$
$$0.6 < W/H < 0.9 \quad \text{(2 rows plate)}$$

2.2 License plate enhancement

The extracted image plate region obtained from last step often includes unwanted areas such as plate boundary or nearby regions. Processing steps to remove unwanted areas from plate region is described as follows. Otsu's method (N. Otsu, 1979) was applied to compute suitable threshold on grayscale image of the plate region, which is used to convert extracted image to binary. A 8 by 8 median filter was then applied to the current binary image to remove the boundary noise. Bounding box of connected component would be calculated to get the final coordination of the plate region.

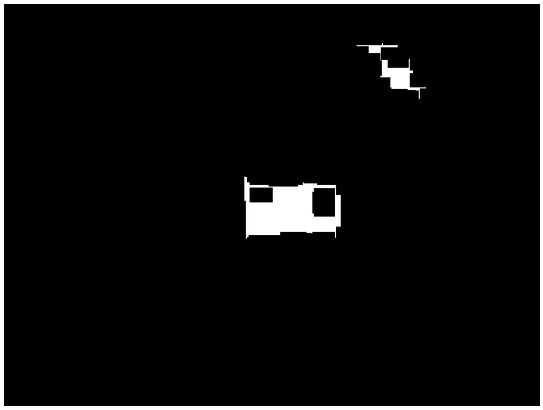

(a)

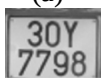

(b)

Figure 4. Candidate regions that satisfied the size condition (a) and segmented plate region (b)

Figure 5. Enhancement steps

3. Results

The method presented in this paper was first tested in MATLAB then implemented in C# to be made compatible with other modules in our developed BMS. In a fixed condition that all images of standing cars are taken at close shot with good light condition, the accuracy rate on 200 images containing Vietnamese license plate was 100%. Figure 6 presents some example of car images with extracted license plate.

4. Conclusions

In this paper, an morphology based approach to extract Vietnamese license plates from car

Figure 6. Car images and extracted license plate

images was presented. Morphology operations were applied on the vertical edge map obtained from input images. The plate region was then segmented from the candidate ones based on such characteristic features as the width and high ratio and the area size. Extracted region often consists of unwanted zone such as plate boundary and nearby areas, which were removed after enhancement steps thanks to the use of median filter and connected component analysis. The approach was tested successfully on 200 car images and will be used in our developed BMS.

5. Acknowledgement

This work is supported by the research project No. KC03.DA12/11-15 granted by Ministry of Science and Technology of Vietnam

6. References

Richard Szeliski (2011). *Computer Vision: Algorithms and Applications.* Springer, London.

N. Otsu (1979). A threshold selection method from grey-level histograms. *IEEE Transactions on Systems, Man, and Cybernetics*, vol. SMC-8, pp. 62-66

P. V. Suryanarayana, Suman K. Mitra, Asim Baneree and Anil K. Roy (2005). A Morphology Based Approach for Car License Plate Extraction. *IEEE Indicon 2005 Conference*, pp. 24-27

S. Hamidreza Kasaei, S. Mohammadreza Kasaei, S. Alireza Kasaei (2010). New Morphology-Based Method for Robust Iranian Car Plate Detection and Recognition. *International Journal of Computer Theory and Engineering, Vol. 2, No. 2 April, 2010*, pp. 264-268

Tran Duc Duan, Duong Anh Duc, Tran Le Hong Du (2004). Combining Hough transform and contour algorithm for detecting vehicle license-plates.*Proceedings of 2004 International Symposium on Intelligent Multimedia, Video and Speech Processing*, pp. 747-750

Wenjing Jia, Huaifeng Zhang, Xiangjian He (2007). Region-based license plate detection. *J. Network and Computer Applications*, pp. 1324-1333

The 2nd International Conference on Engineering Mechanics and Automation (ICEMA2)
Hanoi, August 16-17, 2012
ISBN: 978-604-913-097-7

Design and Implementation of Automatic Energy Meter Reading System Using GSM/GPRS Network

Manh Thang Pham[a], Van Manh Hoang[b], Minh Nghia Nguyen[c]

[a] *Faculty of Mechanics and Automation, University of Engineering and Technology, thangpm@vnu.edu.vn*
[b] *Faculty of Mechanics and Automation, University of Engineering and Technology, manhhv87@vnu.edu.vn*
[c] *Faculty of Mechanics and Automation, University of Engineering and Technology, nghianm.90@gmail.com*

Abstract

This paper presents the development of a fully GSM/GPRS Automatic Energy Meter (GAEM) which has ability to monitor an energy meter. The GAEM consists of a GSM/GPRS Digital Energy Meter (GDEM) and a Web Server. The GDEM uses Energy Metering ICs (MCP3905) and GSM/GPRS Sim900 module which is compliance with single phase digital energy meter standard IEC62053. GAEM continuously monitors the energy meter and send data on request of Web Server through GPRS. The energy meter can also be retrieved and verified on mobile phone through SMS. Once the GDEM receive the SMS it will compose the current meter reading and reply to customer's mobile phone. With this feature customers can monitor the power usage anytime and anywhere.

Key Words: AEMF (Automatic Energy Meter Reading), GSM (Global System Mobile), GPRS (General Packet Radio Service), SMS (Short Messaging System)

I. Introduction

GSM/GPRS Automatic Energy Meter (GAEM) is the technology of automatically collecting consumption, status data from metering devices (such as water, electric) and transferring that data to a central database for further processing. This remote reading technique has many advantages. It saves time to read data from any location. The GAEM system in this paper is primarily used for measurement of electrical energy consumption.

The complete system is made up of GSM/GPRS Digital Energy Meter (GDEM) and the Web Server. The system works in conjunction with the Web Server to retrieve power meter reading using GPRS technology. The GDEM is the integration of a single phase, IEC62053 standard compliance digital kWh power meter reading and GPRS/GSM module. The customer can also use their mobile phone to verify current power consumption value. This can be achieved by just sending a SMS to the owner GDEM. Once the GDEM receives the SMS, it will immediately response by composing its consumption reading in SMS format and

revert it to the customer mobile phone through SMS.

II. The Proposed Method

To introduce the concept of GEAM system, a model of wireless GEAM using GPRS/GSM technology has been developed. GPRS is quite often used for meters that need to transmit a lot of data or for meters that needs to communicate as a point to point link. Often this is called point to point so it is more secure than broadcast technique. The desired GEAM system has the following requirements:

a. Scalability: It should be able to be used for many meters without altering the architectural principles.

b. Security: It should be based on state-of-the-art security methods that offer confidentiality and integrity of the measurement data.

III. System Design

The design of the GAEM system is an integration of two main parts: GSM/GPRS Digital Energy Meter (GDEM) and Web Server as shown in Figure.1.

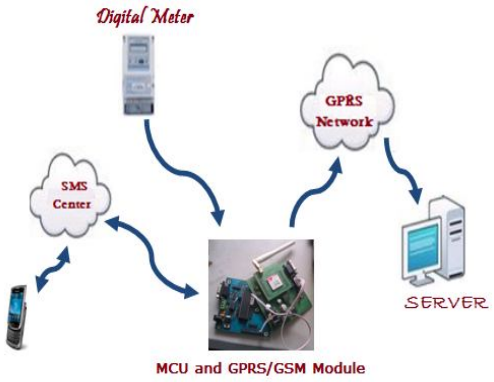

Figure.1. GAEM system architecture

1. GPRS/GSM Digital Energy Meter (GDEM) design

The meter is constructed using an Energy Metering ICs (MCP3905) which is compliance with single phase digital energy meter standard IEC62053, a Microcontroller Microchip (dsPIC30F4011) and GPRS/GSM module as shown in Figure.2.

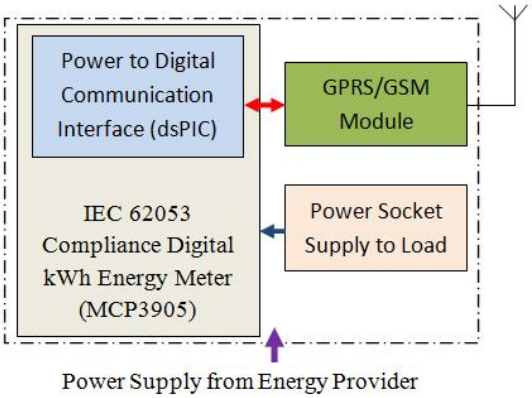

Figure.2. Block diagram of the GDEM

Energy Metering ICs (MCP3905) works in conjunction with the PIC Microcontroller to calculate consumed energy by sensing the load connected to it and saving the readings in the Microcontroller memory. The GPRS/GSM module will send data to Web Server and reply SMS to owner mobile phone.

a. The MCP3905 and Microcontroller design

The MCP3905 and Microcontroller were used to build a digital energy meter base on Microcontroller. The circuit has jumpers to configure its inputs/outputs. There are two prototype areas. The input prototype area, a current sensing element, such as shunt resister, has to be installed with the proper AC line and load connection to it. The shunt resistor is used to monitor the current in a circuit and translate the amount of current in that circuit into a voltage that can be easily measured and monitored. The output prototype area has an optocoupler to couple the impulse count without direct contact to the microcontroller. On the communication side, the microcontroller is used to communicate with the GPRS/GSM module using RS232 UART serial communication protocol and the AT command. The serial communication protocol operates at the baud rate of 9600 bps, one-bit start, eight-bit data, no parity and one-bit stop.

b. GPRS/GSM circuit design

General Packet Radio Service (GRPS) is the technology used the GSM network to connect mobile to the Internet. The GPRS/GSM SIM900 module from SIMCOM was chose to be used in the prototype implementation. The SIM900-QUAD modules are a product family that is easy-to-integrate for many industrial applications. The GPRS/GSM has quad-band cellular capabilities (850 / 900/ 1800 / 1900 MHz).

The GPRS/GSM communication circuit consists of GPRS/GSM SIM900 module, LM2576S-ADJ adjustable voltage regulator and other components.

The data is sent from ICs MCP3905 to microcontroller. The dsPIC will analyze the data, before sending AT commands to SIM900 module. These commands send data to Web Server and they provide updated power consumption readings.

2. Web Server Implementation

The server has much benefit. To decrease the cost of the proposed GAEM system, in house software was developed using PHP and MySQL server and used to control the central server. The implemented data management system has the following functions:

a) Remote metering: The server automatically receives the automatic meter reading that sent to the server from the meter using GPRS technology, place the reading in the database and customers can remotely get their consumption by logging to the server.

b) Consumption statistic: The system provides a consumption statistic for anytime chosen by customer.

c) Send email: The server can send power consumption to customer's email.

IV. Conclusion

The complete working prototype of GEAM system was built to demonstrate an automatic energy meter reading using GPRS/GSM network. The GAEM system consists of a meter digital, a GPRS/GSM based transmitter and a Web Server. A Web Server with data management system implemented using PHP and MySQL. Successful demonstration of the system prototype has made it possible to be implemented for meter reading applications. The GEAM system is proven to provide effective, reliable wireless automatic energy meter reading and data management by using the GPRS/GSM technology, thus reduce human operator energy meter reading operation cost.

V. References

Ali Abdollahi, Marjan Dehghani, and Negar Zamanzadeh (Oct. 2007). *SMS–based reconfigurable automatic meter reading system.* IEEE International Conference on Control Applications, pp. 1103-1107.

Abhinandan Jain, Dilip Kumar, and Jyoti Kedia (May. 2012). *Smart and Intelligent GSM base Automatic Meter Reading System.* International Journal of Engineering Research & Technology (IJERT).

H. G. Rodney Tan, C. H. Lee, and V. H. Mok (2007). *Automatic Power Meter Reading System Using GSM Network.* The 8th International Power Engineering Conference, pp. 465-469.

Terry Chandler (Nov. 2005). *The Technology Development of Automatic Metering and Monitoring Systems.* The 7th International Power Engineering Conference, pp. 147-150.

Saysoth Keoduangsine and Robert Goodwin (June 2012). *A GPRS-Based Data Collection and Transmission for Flood Warning System: The Case of the Lower Mekong River Basin.* International Journal of Innovation, Management and Technology, pp. 217-220.

The 2nd International Conference on Engineering Mechanics and Automation (ICEMA2)
Hanoi, August 16-17, 2012
ISBN: 978-604-913-097-7

Adaptive control for Tracking Trajectory

Pham Manh Thang, NguyenVan Quyen

Faculty of Engineering Mechanics and Automation-College of Technology-Viet nam Nation University
Faculty of Engineering Mechanics and Automation-College of Technology-Viet nam Nation University

Abstract

As we know, Robot has been important in many fielts in our life. It gradually becomes a vital part of industry. One of most crucial applications of Robot is controlling the robot end effector to track a trajectory which was known or not. There have been a lot of researches involving the tracking controller, such as PID controller, model based controller, and so on. The fact shows that almost robots have some parameters which are uncertain. This is the trouble for the controller. As a result, above controllers can not bring a good respond for system, which is a dynamic for researchs on the adaptive and robust controllers.

In this paper, an adaptive method for tracking control will be introduced. We derive the adaptive controller based on inverted model for trajectory tracking of robot with uncertain kinermatics and dynamics. With the controller used, the end effector is able to converge to a desired trajectory with the model uncertainties being updated online by parameter update laws. Experimental results are presented to show the performance of the proposed controller. A case of study is Two-link planar manipulator where analytical works and simulation results show a good performance of the control system.

Keywords. adaptive control, model based control

1. Introduction

People can respond intelligently and suitably to the world, despite not having accurate knowledge about it. For examble, with the help of our eyes, we are able to pick up a large number of new tool or objects with different and unknown kinematic and dynamic grasping point and orientations, and use it without any difficulty. In addition, humans can learn and adapt to the uncertainties from previous experience. We hope that the robot also can do that. This is our dynamic to find the adaptive controllers.

As we know, the kinermatics and dynamics of robot manipulators are highly nonlinear, and it is difficult to know those exactly. If we have an exact model, a precisely calibrated model-based robot controller may give good performance. Admitedly, it is very difficult to gain the exact knowledge about robot. This means the quality of respond depen on how accurate the model is. This controller can

* Corresponding author.

not equip the robot an adaptive ability to changes and uncertainties in model and environment.

In this paper, we present an adaptive controller for trajectory tracking control of robot manipulators. The proposed controller does not require exact knowledge of either kinematics or dynamics. The trajectory tracking control problem in the presence of kinematic and dynamic uncertainties is formulated and solved based on a Lyapunov-like analysis. The main new point is the adaptation to kinematic uncertainty in addition to dynamics uncertainty, which is something ”human-like” as in tool manipulation. This gives the robot a high degree of flexibility in dealing with unforseen changes and uncertainties in its kinematics and dynamics. The adaptive controller based on the inverted model Robot is designed to reject totally the non-linear in model and the uncertainties in model. In this controller, the parameters which is used to calculate the control signal will be estimated exactly by a online identifing regime

Section II formulates the robot kinematics and presents an adaptive tracking controllers; Section III presents some experimental results and shows that the robot's shadow can be used to control the robot; Section IV offers brief concluding.

2. Materials and methods

2.1. Dynamics of Robot Manipulator in the Joint Space

The joint space dynamics of an n - link rigid-body robot manipulator can be described by the following second order nonlinear vector differential equation, so-called Euler-Lagrange equation is given as follows [2]:

$$M = D(q)\ddot{q} + V(q,\dot{q})\dot{q} + G(q) \quad (1)$$

Where :

q denotes the joint angles of the manipulator

$\dot{q}$ and $\ddot{q}$ are the vectors of joint velocity and joint acceleration,respectively.

$D(q,\theta) \in R^{nxn}$ is the inertia matrix which is symmetric and positive definite

$V(q,\dot{q})\dot{q} \in R^n$ is a vector function containing coriolis and centrifugal forces

$G(q,\theta)$ is a vector function consisting of gravitational forces

M is the vector function consisting of applied generalized torques.

Several important properties of the dynamic equation described by equation (1) are given as follows [1]:

Property 1:

The inertia matrix M(q) is symmetric and positive definite for all $q \in R^n$ and M(q) is uniformly bounded above and below. That is

$$\mu_1 I \le M(q) \le \mu_2 I \text{ or } \mu_1 \le |M(q)| \le \mu_2 \quad (2)$$

Where $\|o\|$ stand for the Euclidean norm, μ_1 and μ_2 are positive constant.

Property 2:

The matrix $\dot{M} - 2V(q,\dot{q})$ is skew-symmetric. That is

$$y^T \dot{M} y = 2y^T V(q,\dot{q})y, \forall y, q, \dot{q} \in R^n \quad (3)$$

Property 3:

$V(q,\dot{q})\dot{q}$ is quadratic in $\dot{q}$

$$\|V(q,\dot{q})\dot{q}\| \le v_b \|\dot{q}\|^2$$

Property 4:

The left side of (1) can be linearly parameterized. This property may be expressed as

$$D(q)\ddot{q} + V(q,\dot{q})\dot{q} + G(q) = W(q,\dot{q},\ddot{q})P \quad (4)$$

Where $P \in R^m$ is a parameter vector and $W(q,\dot{q},\ddot{q})$ is a known matrix of robot function depending on the joint variables, joint velocities and joint accelerations.

2.2. Adaptive controller

We define θ is the uncertain parameters in model. In this case, Euler-Largrang equation is unexact. That is:

$$M = D(q,\theta)\ddot{q} + V(q,\theta,\dot{q}) + G(q,\theta) \quad (5)$$

Adaptive controller which is based on the invert model, is presented as following:

$$M = D(q,\mu)(\ddot{w} + K_1 e + K_2 \dot{e}) + V(q,\mu,\dot{q}) + G(q,\mu) \quad (6)$$

Where μ is a function of the estimated kinertic parameter θ.As we know, if we do not adjust μ, the respond output will not track the desired trajectory.

Let us rewrite some definitions in Euler-Largrang equation:

$$D = D(q,\theta)$$
$$V = V(q,\theta,\dot{q})$$
$$G = G(q,\theta)$$
$$\hat{D} = D(q,\mu)$$
$$\hat{V} = V(q,\mu,\dot{q})$$
$$\hat{G} = G(q,\mu)$$

Equation (6) is substituted into equation (5), we have:

$$D\ddot{q} + V + G = \hat{D}(\ddot{w} + K_1 e + K_2 \dot{e}) + \hat{V} + \hat{G} \quad (7)$$
$$\Leftrightarrow$$
$$(D - \hat{D})\ddot{q} + (V - \hat{V}) + (G - \hat{G}) = \hat{D}(\ddot{e} + K_1 e + K_2 \dot{e})$$

According to the Property 4, Euler-Largrang satisfy the following condition:

$$(D - \hat{D})\ddot{q} + (V - \hat{V}) + (G - \hat{G}) = F(q,\dot{q},\ddot{q})(\theta - \mu) \quad (8)$$

From equation (8), Equation (7) can be expressed as:

$$\hat{D}(\ddot{e} + K_1 e + K_2 \dot{e}) = F(q,\dot{q},\ddot{q})(\theta - \mu) \quad (9)$$
$$\Leftrightarrow$$
$$\frac{d}{dt}\begin{pmatrix} e \\ \dot{e} \end{pmatrix} = \begin{pmatrix} 0 & I \\ -K_1 & -K_2 \end{pmatrix}\begin{pmatrix} e \\ \dot{e} \end{pmatrix} + \begin{pmatrix} 0 \\ I \end{pmatrix}\hat{D}^{-1}F(\theta - \mu) \quad (10)$$
$$\Leftrightarrow \dot{x} = Ax + B\hat{D}^{-1}F(\theta - \mu) \quad (11)$$

Stability Proof:

To prove the stability of system (11), the Lyapunov function candidate is presented as:

$$V(x) = x^T P x + (\theta - \mu)^T T(\theta - \mu) \quad (12)$$

Where:

$P = P^T$, P is a positive definite matrix

T is also a positive definite matrix

The derivative of equation (12) respect to time can be written as:

$$\dot{V} = \dot{x}^T P x + x^T P \dot{x} - 2(\theta - \mu)^T T\dot{p} \quad (13)$$

$$\dot{V} = x^T (A^T P + PA)x + 2(\theta - \mu)^T [\,(B\hat{D}^{-1}F)^T P x - T\dot{\mu}] \quad (14)$$

In order that $\dot{V}$ is negatively definite, we chose the parametes as:

P satisfy equation:

$$(A^T P + PA) = -Q \quad (14)$$

Where Q is a symatric and positive definite matrix

μ satisfy condition:

$$\dot{\mu} = T^{-1}\,(B\hat{D}^{-1}F)^T P x \quad (15)$$

With chosen parameters, we have: $\dot{V} = -x^T Q x$ consequently the closed loop system is globally asymptotically stable in the presence of structure uncertanties. Hence, adative controller is presented as:

$$M = D(q,\mu)(\ddot{w} + K_1 e + K_2 \dot{e}) + V(q,\mu,\dot{q}) + G(q,\mu)$$
$$\dot{\mu} = T^{-1}\,(B\hat{D}^{-1}F)^T P x$$

3. Results and discussion

Case study of Two-link Elbow robot manipulator

In order to verify the performance of proposed control schemes, as an illustration, we will apply the above presented controllers to a two-link enbow robot manipulator as shown in Fig.1

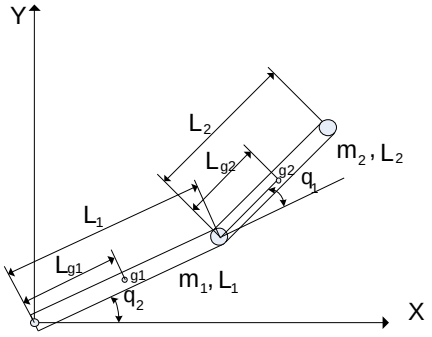

Fig.1 Two-link Elbow Robot

The dynamic of the two-link elbow robot manipulator can be described in the following differential equation:

$$\begin{bmatrix} D_{11} & D_{12} \\ D_{21} & D_{22} \end{bmatrix}\begin{bmatrix} \ddot{q}_1 \\ \ddot{q}_2 \end{bmatrix}+\begin{bmatrix} V_1 \\ V_2 \end{bmatrix}+\begin{bmatrix} G_1 \\ G_2 \end{bmatrix}=\begin{bmatrix} M_1 \\ M_2 \end{bmatrix}$$

$$D_{11}=\left(m_1 l_{g1}^2+J_1+m_2\left(l_1^2+l^2{}_{g2}+2l_1 l_{g2}\cos(\theta_2)\right)+J_2\right)$$

$$D_{12}=D_{21}=\left(m_2\left(l^2{}_{g2}+l_1 l_{g2}\cos(\theta_2)\right)+J_2\right)$$

$$D_{22}=\left(m_2 l^2{}_{g2}+J_2\right)$$

$$V_1=-m_2 l_1 l_{g2}\sin(\theta_2)\dot{\theta}_2^2-2m_2 l_1 l_{g2}\sin(\theta_2)\dot{\theta}_1\dot{\theta}_2$$

$$V_2=m_2 l_1 l_{g2}\sin(\theta_2)\dot{\theta}_1^2$$

$$G_1=m_1 g l_{g1}\cos(\theta_1)$$
$$+m_2 g\left[l_1\cos(\theta_1)+l_{g2}\cos(\theta_1+\theta_2)\right]$$

$$G_2=m_2 g l_{g2}\cos(\theta_1+\theta_2)$$

Where,

- ✓ l_1, l_2 are lengths of the first and second links respectively
- ✓ m_1, m_2 are masses of the first and second links respectively
- ✓ g is the gravitational force

Robot parameters which have been used in this simulation are given in table.1

Table.1: Parameters of robot

m_1 =1.4 kg	l_1 =2 m	l_{g1} =1 m	J_1 =1 kg.m2
m_2 =0.8 kg	l_2 =2 m	l_{g2} =1 m	J_2 =3 kg.m2

Table.2: Parameters of controller

$\hat{m}_1$ =0.7 kg	l_1 =2 m	l_{g1} =1 m	$\hat{J}_1$ =0.5 kg.m2
$\hat{m}_2$ =0.3 kg	l_2 =2 m	l_{g2} =1 m	$\hat{J}_2$ =2 kg.m2

Assuming that the uncertain parameters in model are m_1, m_2, J_1, J_2

Desired path in the task space and intial condition are expressed :

Xd=1+0.5sin(t/3)+0.3cos(t/2)
Yd=t/20

Simulation resulting from application of model based controller without adaptive regime:

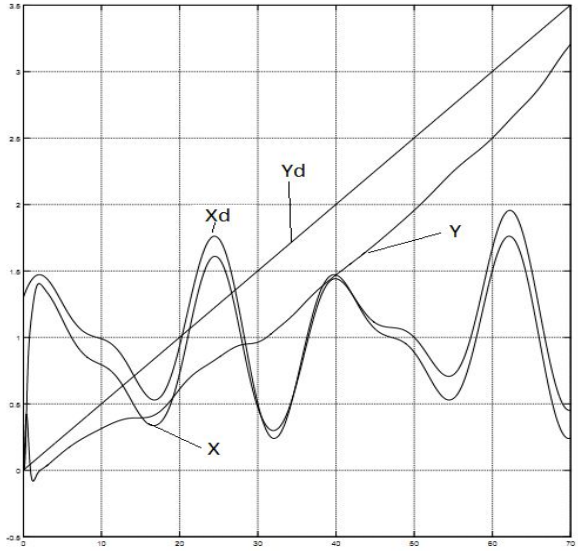

Fig.2 Tracking outputs of Xd and Yd in task space (controller without adaptive regime)

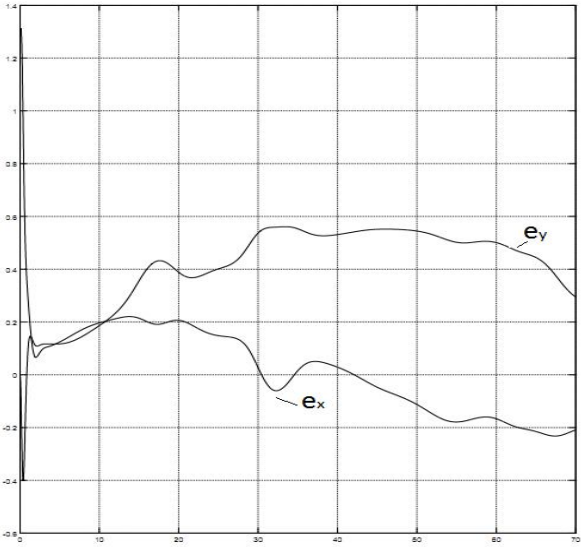

Fig.3 Tracking errors of Xd and Yd in the task space (controller without adaptive regime)

Simulation resulting from application of the adaptive control:

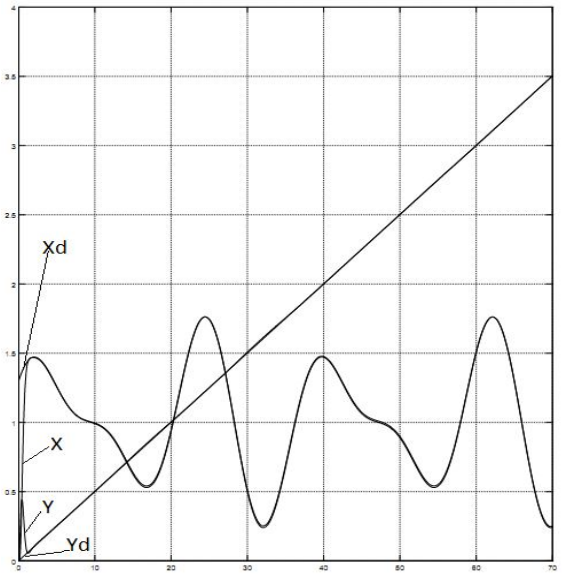

Fig.4 Tracking outputs of Xd and Yd in task space (controller with adaptive regime)

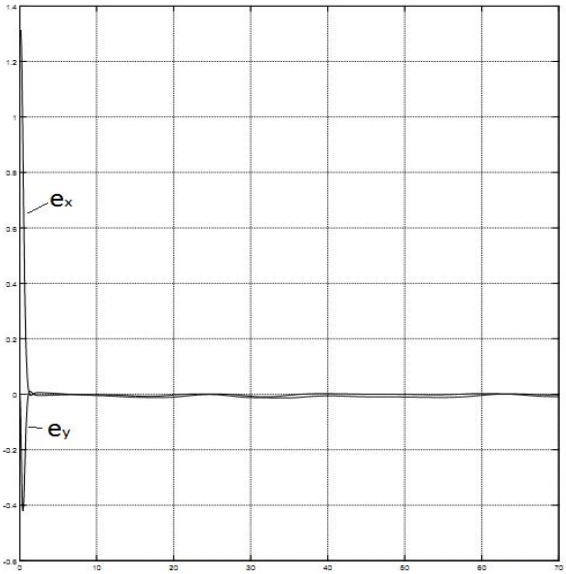

Fig.5 Tracking errors of Xd and Yd in the task space (controller with adaptive regime)

4. Conclusion

We have introduced an adaptive model based controller for tracking robot with uncertain dynamics and kinermatics. The paramaters of the adaptive controller is changed suitably by an online update law, which provides system with ability to track desired path. Experimental result shows the good performent of the proposed controller. The robot end effector track to the reference trajectory rapidly. Equally important, the overshoot in respond is slight.

By virtue of good performents, robots with adaptive controller are likely to be applied in many manufactures, such as: line weilding, fitting shops, cutting machines, and so on.

References

[1] Ph.D Frank L.Lewis, Darren M.Dawson, Chaouki T.Abdallah , *Robot manipulator control theory and practise*, Prentice-Hall inc,2006

[2] F. L. Lewis, C. T. Abdallah, and D. M. Dawson, *Control of Robot Manipulators*. New York: Macmillan Publishing Company, 1993.

[3] W. Li, *Adaptive control of robot manipulators*, Doctoral Thesis, MIT Dept. of Mechanical Engineering, June 1990.

[4] J. J. E. Slotine and W. Li, *Applied nonlinear control.* Englewood Cliffs, New Jersey: Prentice Hall, 1991.

[5] Nguyen Doan Phuoc, Phan Xuan Minh, Han Thanh Trung, *Ly thuyet dieu khien phi tuyen*, NXB Khoa hoc va ky thuat, 2006

[6] Nguyen Manh Tien, *Dieu khien robot cong nghiep*, NXB khoa hoc va cong nghe, 2007

The 2nd International Conference on Engineering Mechanics and Automation (ICEMA2)
Hanoi, August 16-17, 2012
ISBN: 978-604-913-097-7

Experimental Study of Various Effects of Pilot Diesel Fuel on Compression Ignition Engine Using Liquefied Petroleum Gas

Tran Van Nam[a], Tran Thanh Hai Tung[b] and Nguyen Van Phung[c]

[a] *University of Danang, 41 Le Duan St., Danang City Vietnam, tvntran@gmail.com*
[b] *University of Danang, 41 Le Duan St., Danang City Vietnam, haitungdng@gmail.com*
[c] *Quangnam Vocational College, 224 Huynh Thuc Khang St., Tamky City, phungtamky@gmai.com*

Abstract

This paper presents the results of various effects of pilot diesel fuel on an automotive dual fuel compression ignition engine (CIE) using liquefied petroleum gas (LPG) at medium and high loads. The dual fuel engine is WL-TURBO 2.5 engine (a 4-stroke, 4-cylinder and water cooled diesel engine with indirect-injection combustion chamber). The pilot fuel is diesel, and LPG is used as a main fuel. The experiments show that different masses of pilot diesel fuel can limit the engine's knock. Through the experiments, we could also determine the following parameters: technical and economic indicators, concentration of exhaust fumes components such as NO_x, HC, CO_2, and soot emissions. These results will form a basis for designing the organization and control LPG supply for CIE in order to limit the engine's knock, diversifying the fuel sources as well as reducing environment pollution.

Keywords: *Liquefied petroleum gas-air blend, pilot diesel fuel, electronic control, knocking phenomenon, combustion characteristics, combustion ignition engine*

1.Introduction

Nowadays, reducing the pollution of automobile emission and studying the application of an automobile alternative fuel are crucial subjects in the field of automobile. An increase in the number of vehicles is causing many economical, ecological and environmental problems. It is especially worried that buses and trucks equipped with diesel engines have caused a lot of harmful emissions in most urban centers around the world. Moreover an excessive increase in energy use is speeding up the depletion of fossil fuels [1], [11], [13]. The principal objectives of engine designers are to achieve a double goal: good performance and low levels of emission. Furthermore, the price of crude oil continues to increase rapidly and the Laws of Environmental protection oblige researchers in the internal combustion engines (ICE) domain to reexamine all possibilities of energy expenditure reduction of new engines and those which are already in use [21]. Towards the effort of reducing pollutant emissions, especially smoke and nitrogen oxides from diesel engines, many various solutions have been proposed. The use of liquefied petroleum gas (LPG) as an

alternative fuel and a partial supplement for liquid diesel fuel is a promising solution.

Figure 1. *Automobile exhaust is a major pollutant causing of environment pollution.*

Presently, the main interest for gaseous fuels lies with liquefied petroleum gas (LPG), compressed natural gas (CNG), biogas, hydrogen and so on which are used in the ICE. Among the alternative gaseous fuels now available on the market, LPG and CNG are most widely used. These gaseous fuels have economical and environmental benefits (in terms of price advantage and different physical and chemical properties which gives them a good chance for lower production of the exhaust pollutants). LPG has been primarily a by-product of the refining processes of crude oil.

Recently, more LPG has been being produced as a by-product of natural gas. In addition, as LPG is excellent regarding exhaust emission and performance, LPG-consuming vehicles are being rapidly developed as economical and less polluting cars. Some pieces of research were made public through the Science and Technology Journals, Science Research Literatures show that when LPG is used for vehicles, especially as fuel for duel fuel engines, knocking phenomenon occurs easily under increasing load or operating at high speeds [5], [14], [15], [16], [17], [18]. Thus, it is necessary to adjust the different masses of pilot diesel fuel in order to limit the engine's knock with increasing load or operating at high speeds.

2. Theoretical background

2.1. Combustion in dual-fuel engines

The combustion process in a dual-fuel engine is different from that in a normal diesel engine. The difference stems from the presence of the premixed fuel-air charge in the cylinder during the compression stroke. The dual-fuel combustion system features essentially a homogeneous gas-air mixture compressed rapidly below its auto-ignition conditions, and ignited by the injection of pilot liquid fuel near the top dead center position. This process is analogous to a typical spark ignition engine, with the spark plug replaced by the fuel injector as an ignition source. Dual-fuel engine is an engine in which energy release in its operating cycle comes from two fuels [8], [11], [20]. The blend of main fuel and purified air is absorbed in an inlet manifold and then it is ignited by the pilot diesel fuel injection. The primary fuel is generally gaseous at atmospheric conditions and controls the power output. The pilot liquid fuel, which is injected through the conventional diesel injection equipment, normally contributes only a small fraction (less than 10%) of the maximum power output [6]. The cause of the knock is usually considered to be auto-ignition of the end gas. Compression of the end gas as the flame front moves propagates away from the ignition point, and raises the end gas temperature and pressure. When the end gas reaches the auto-ignition point, a rapid evolution of energy occurs, producing a knock [2], [8], [9], [19]. This phenomenon is known as spark knock in SI engines, and this type of behavior has been observed in a dual-fuel engine. LPG conversion systems are classified into three main groups, as follows:

- Mechanically controlled LPG mixer systems (1st generation);
- Electronically controlled LPG mixer systems (2nd generation);
- LPG injection systems (3rd generation)[4].

2.2. Fuels used in diesel dual fuel engines

LPG is a petroleum-derived, colorless gas, typically comprised of main propane,

butane or a combination of these two constituents. LPG is a by-product of natural gas production and of refineries. It can be seen that LPG is in a gaseous state at room temperature and pressure, and it must be pressurized to about 5 [bar] at 25[ºC] to keep it liquefied. LPG fuel for vehicles is actually a mixture of various hydrocarbons which are gases at atmospheric pressure and temperature, but liquefies in a low pressure range of 7÷8 [bar] at atmospheric temperatures [4], [7].

Table 1. *Properties of LPG and some alternative fuels [1], [12], [16], [20]*

N°	Properties [Unit]	LPG		Diesel
		Propane	Butane	
1	Chemical formula	C_3H_8	C_4H_{10}	CxHy
2	Molecular mass [g]	44.10	58.12	198
3	Low heating value [MJ/kg]	47.85	45.87	42.53
4	Stoichiometric air fuel ratio [kg/kg]	15.7	15.4	14.6
5	Liquid density [g/m³]	1.81	2.41	0.85
6	Boling point [ºC], @ 1[atm]	- 42.3	- 0.5	180÷ 370
7	Vapour pressure [atm], @20[ºC]	8.4	2.1	<10-³
8	Ignition temperature [ºC]	470	365	254
9	Viscosity [cP] @20[ºC]	0.11	0.18	2-4
10	Octane number	112	94	
11	Composition[wt%]			
	C	81.8	109.1	86
	H	18.2	22.75	14

Some important advantages of LPG in comparison with the conventional fuels are as follows:

- Higher thermal efficiency, so improved fuel economy can be obtained from ICE using on LPG as opposed to unleaded rating.
- Emissions from LPG vehicles are significantly lower than those from conventionally fueled vehicles. In comparison with conventional liquid fuels, these engines lie in their relatively low carbon content, causing them to burn cleanly with lower emissions of CO, CO_2, HC and NOx.
- On an energy basis, LPG has lower carbon content than gasoline or diesel fuel and produces less CO_2, which plays a major role in global warming during combustion.
- In terms of safety, despite its volatile behavior, LPG has an excellent safety record. The fuel tank is much stronger than conventional fuel tanks as proved in crash and fire tests. When the engine is switched off or if the fuel pipe is damaged, an electronic shut-off valve operates. Such systems are constantly being improved. Therefore, it may be expected that a more stable supply of LPG is possible. There are mainly two solutions: the first is to convert diesel engines into gas fuelled engines and the second is to optimize the combustion process [3], [10].

3. Experimental apparatus and proceduce

3.1. Test engine

The test engine used is a 4-stroke 4-cylinder water cooled, indirect injection, high speed WL-TURBO 2.5 diesel engine. The basic data of the engine used are given in Table 2.

Table 2. *Engine WL-TURBO2.5 Specifications*

Parameters	Value [Unit]
Bore x stroke	93 x 92 [mm²]
Compression ratio	19.8:1
Type of cooling	Water cooled
Power rates	85/3500[kW/rpm]
Torque	280/2000[Nm/rpm]
Injection timing	10[°ATDC]
Injector opening pressure	116÷124[bar]

For liquid fuel injection, a high pressure fuel WL 84 pump is used. The injector nozzle is located in the center of the combustion chamber, and has an opening pressure of 116 [bar].

3.2.A dual –fuel engine using LPG diagram

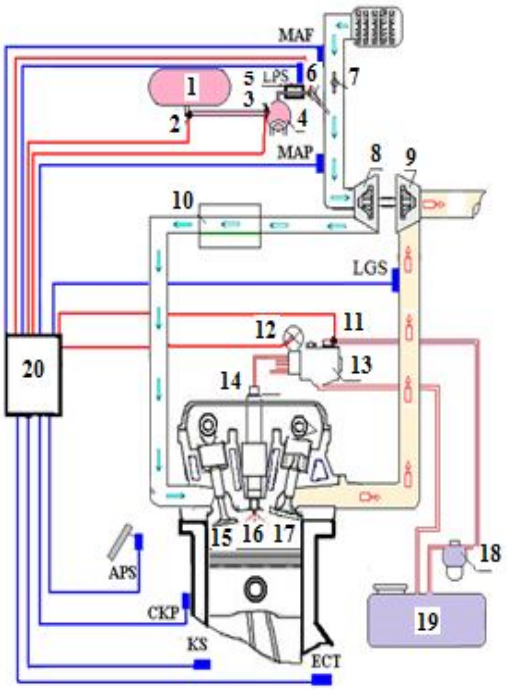

Figure 2. *Diagram of LPG injection system on the compression TURBO WL-2.5 engine.*
1. LPG tank; 2. Solenoid valve; 3. Solenoid vaporizer valve; 4. LPG vaporizer; 5. Pressure stabilisation and storage equipment; 6. LPG injector; 7. The inlet manifold throttle and servo motor; 8+9.Turbocharger; 10. Air cooller ; 11. Diesel solenoid valve; 12. DC motor; 13. High pressure pump; 14. Diesel nozzle injector; 15. Inlet soupape; 16. Engine combustion chamber; 17.Outlet soupape; 18. Diesel filter; 19. Diesel tank; 20. ECU. Electronic controller unit.
MAF. Mass air flow sensor; LPS. Liquefied petroleum gas *pressure sensor; MAP. Manifold Absolute Pressure sensor; IAT. Intake air temperature sensor; LGS. LPG gas known sensor; APS. Accelerator pedal sensor; CKP. Engine speed sensor; KS. Knock sensor; ECT. Engine temperature sensor.*

3.3. Experimental instruments

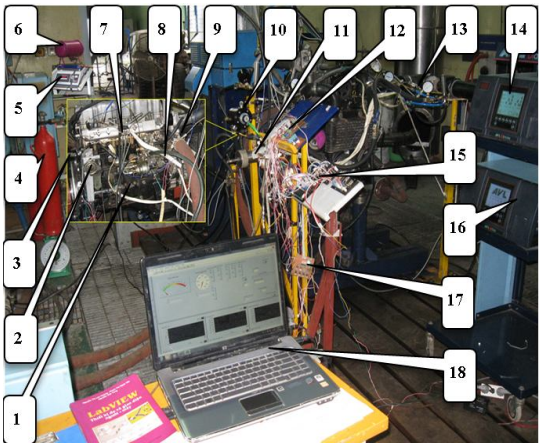

Figure 3. *Arrangement of the test engine and APA 204/8 power dynamometer.*

1.Knock sensor; 2.DC motor; 3.Crankshaft Position Sensor; 4.CO_2 tank; 5.AVL-Dispeed 6.LPG tank; 7.Manifold Absolute sensor; 8. High pressure WL84 fuel pump; 9. CO_2 injector; 10 LPG vaporizer; 11.Pressure stabilisation and storage equipment; 12. Microcontroller devices communicated with your PC; 13.LPG injector; 14.AVL-Digas 4000; 15.Electronic LPG injection control unit; 16. AVL-DiSmoke 4000; 17. Speed pulse board; 18.Computer PC.

To perform these tasks, the following instruments which are available at the Internal Combustion Engine and Automobile Research Center of the Danang University.

The dynamometer and control unit of test cell were produced by AVL List GmbH, Austria. The APA 204/8 power dynamometer is used in order to measure brake power and brake moment of test engine. Other modern pieces of equipment such as AVL-442 Blow by meter, AVL-DiSpeed, AVL-553, AVL-554, AVL-733S are also used in this experiment. Smoke is measured by AVL Dismoke 4000, Gaseous emissions are measured by AVL Digas 4000.

A high precision electronic JSC-TSC balance with 0.5 gramme instrumental error is used to measure LPG mass.

Figure 4. *LPG tank and electronic balance.*

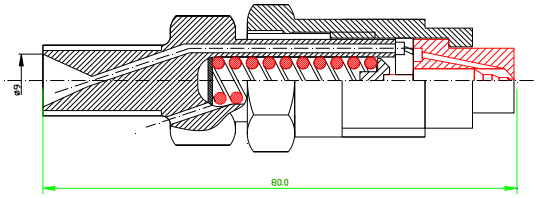

Fugure 5. *A diesel nozzle injector in test.*

3.4. Mathematical equations

** The flow of diesel fuel pintle nozzle injector*

Diesel injection duration is the period between these two instants. The start of injection of liquid fuel into the combustion chamber is the instant at which the needle starts to lift its seat. The end of injection is the instant at which it moves back and locates properly in the seat. Experimental tests of high pressure WL- 84 pump and the diesel nozzles on test engine, indicating the flow of diesel fuel depend on x (location of diesel shaft). The pilot fuel mass on the combustion data may be indicated by Eq. (1)

$$G_D = 1{,}4703e^{(0{,}0425.X)} [kg/h] \quad (1)$$

The engine is converted to run on dual fuel by the introduction of the gaseous fuel. In the present work the gaseous fuel is LPG, being injected into the inlet manifold by a relevant nozzle as shown in Fig 6 [3].

** Basic LPG injection timing*

Basic LPG injection timing in dual fuel engine was calculated is shown in Eq. (2)

$$t_{inj} = \frac{Q_{air}}{\lambda \times L_o \times S_{inj} \times \sqrt{2 \times \Delta p \times \rho_L}}; [sec]; (2)$$

Where Q_{air} is the air mass flow; λ is relative air/fuel ratio; L_o is the necessary air mass that engine can be used for best efficiency and stoicheiometric mixtures; S_{ij}: surface of nozzle; Δp: pressure deviation; ρ_L: density of liquefied petroleum gas.

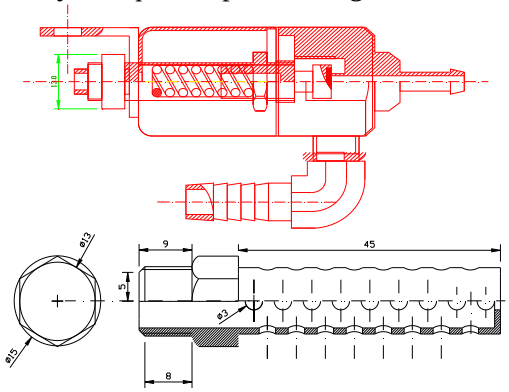

Figure 6. *LPG injector and nozzle used in test.*

** The mass of pilot fuel ratio (m%)*

The mass of pilot fuel ratio is the fraction of pilot fuel mass and LPG-diesel mixture:

$$m\% = \frac{m_d}{m_d + m_L} \times 100\%; \quad (3)$$

Where m_d is diesel mass; m_L is liquefied petroleum gas mass.

**Sensors test and preparation process*

Figure 7. *ECT sensor is conducted in test*

Sensors and electronic equipments have inspected carefully before being used in test. This engine coolant temperature sensor and some sensors are surveyed in Chemistry laboratory and Transportation mechanics laboratory of Technical College of Danang University. Their parameters are used to create computer and microcontroller program of experiment.

3.5. Schematic layout of operating system

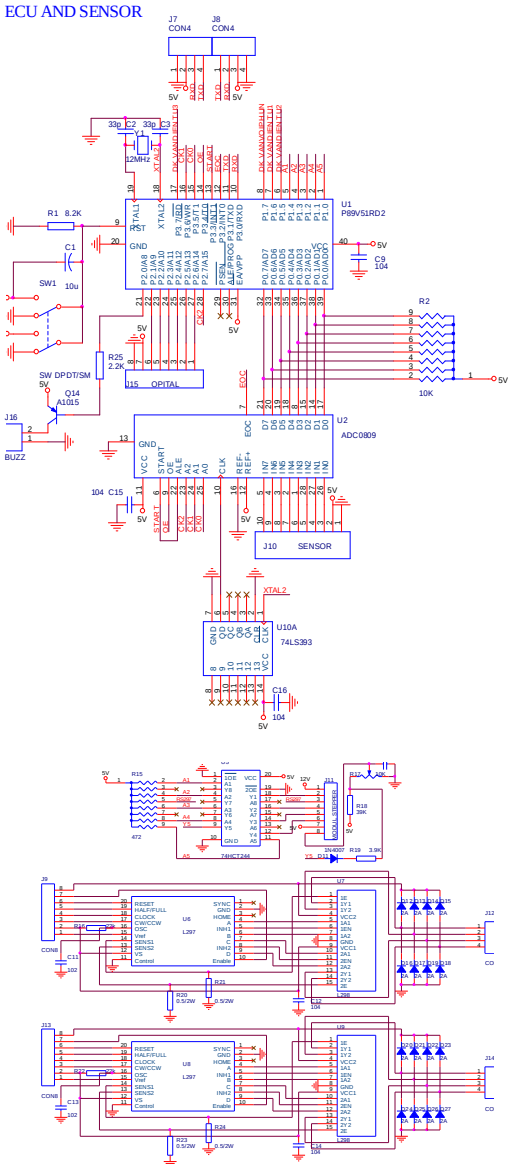

Figure 8. *Schematic layout of operating system.*

4. Results and discussion

In this section, the results of brake power output, fuel consumption efficiency, and concentration of exhaust fumes components when an experimental engine uses pure diesel as a single fuel and diesel-LPG as dual fuel are presented for the following cases in all figures for comparison.

4.1. Brake power output

The energy conversion efficiency in LPG –diesel modes is always lower than that of diesel mode at all the test points. The effect of engine speed, compression ratio, pilot diesel fuel mass, and pilot fuel injection timing on the output brake power is seen in Fig. 9 to Fig.11.

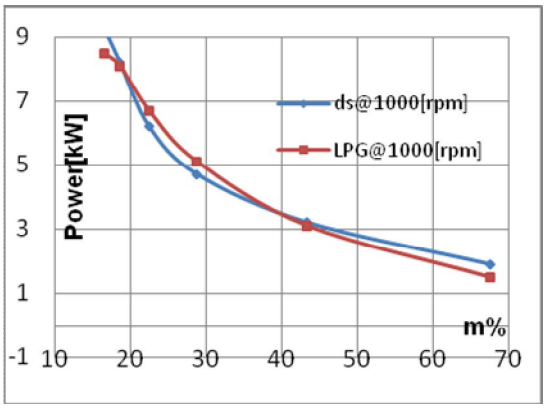

Figure 9. *Brake power output in n=1000[rpm]*

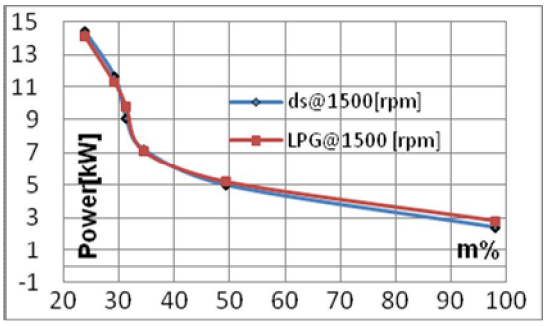

Figure 10. *Brake power output in n=1500[rpm]*

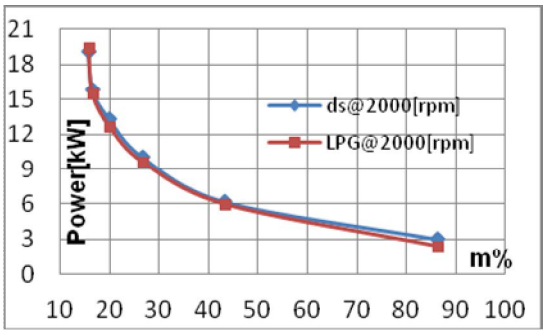

Figure11. *Brake power output in n=2000[rpm]*

Due to a larger size of pilot mixture envelope with a greater engagement of the

gaseous fuel, there were a larger number of ignition centers requiring shorter fame travels, higher rates of heat transfer to the unburned gaseous fuel-air mixture, and increased contribution of hot residual gases.

The brake power output generally increases with the increase in mass of pilot fuel. A rise in the pilot fuel mass causes more heat to be released, increasing the power output as more fuel is injected. The advance in fuel injection timing causes the pressure rise rate and maximum pressure to increase during the compression stroke, which tends to decrease the effective pressure and output. The comparison of brake power output pure diesel as single fuel, dual fuel of diesel as pilot and LPG as main fuel may be seen in Fig. 9 through Fig. 11.

4.2. Fuel consumption efficiency

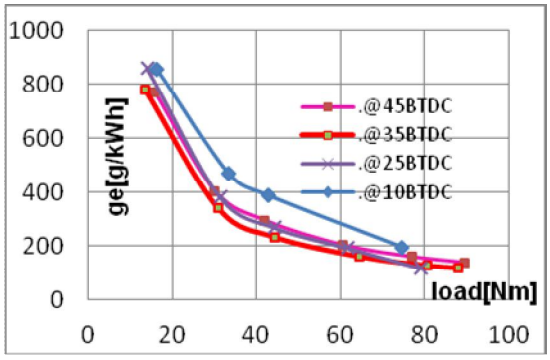

Figure 12. *Effect of pilot fuel mass, injection timing, and load on fuel consumption on efficiency for LPG- diesel fuels n=1750[rpm].*

The injection timing of the pilot fuel is an important factor that influences the combustion characteristics of dual-fuel engines. Fuel consumption of engine is least at 30÷35º BTDC. Combustion noise has increased with the increase in the mass of pilot fuel. The employment of a large pilot fuel quantity can lead to successful flame propagation. This consequently leads to the pressure rise rate increasing, which also leads to the early knocking.

4.3. Exhaust emissions

The effect of engine pilot fuel mass, pilot injection timing, and torque and the emission of smoke, hydrocarbons, and the oxides of nitrogen may be seen in Fig.13, 14, 15, 16. As can be seen from the figures, HC and NO_x emission is reduced when the mass of pilot fuel is increased due to the initial flame becoming bigger in size and thus able to burn most of the gaseous fuel. It can be seen that advancing the pilot fuel injection timing reduces the unburned hydrocarbons emissions. It is believed that a longer ignition delay is promoted with the increased timing advance. The longer ignition delay could have allowed a fuller spray penetration and development, creating a larger amount of the pilot fuel-air gaseous fuel mixture prior to ignition.

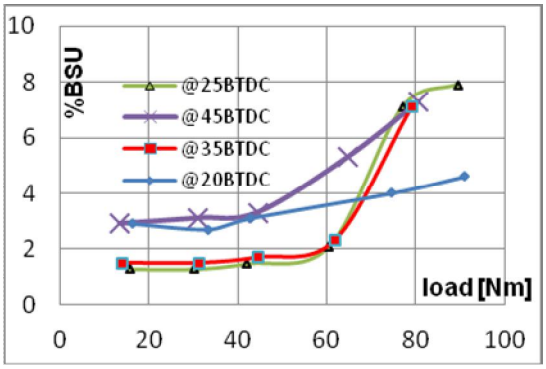

Figure 13. *Effect of pilot fuel mass, injection timing, and load on smoke emissions for LPG-diesel fuels n=1750[rpm].*

Advancing the injection timing likewise caused an earlier start of combustion relative to TDC. Because of this, the cylinder charge, being compressed as the piston moves to TDC, has relatively higher temperatures and the unburned hydrocarbons emissions are lowered. Better overall combustion may also have been due to the lower period of high temperatures within the cylinder and the activity of the partial oxidation reactions with bigger injection advance, which led to the reduction of the dioxide carbon emissions as shown in Fig. 14.

Effect of pilot diesel fuel injection timing on HC emissions in dual-fuel engines may be seen in Fig.15. Hydrocarbon emissions are decreased when pilot diesel fuel injection timing increases and their emissions are least valued at 35ºBTDC.

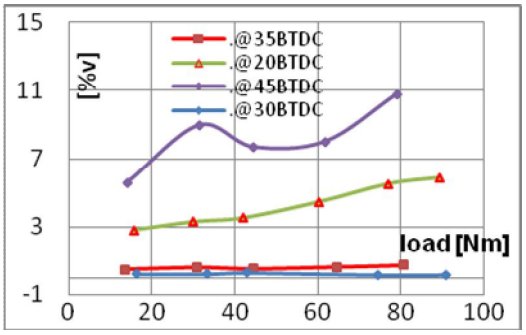

Figure 14. *Effect of pilot fuel mass, injection timing, and load on CO_2 emissions for LPG-diesel fuels n=1750[rpm].*

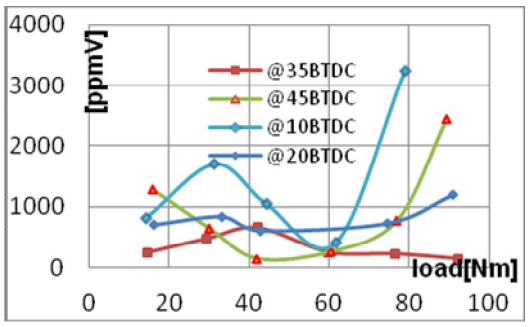

Figure 15. *Effect of pilot fuel mass, injection timing, and torque on HC emissions for LPG-diesel fuels n=1750[rpm].*

Fig. 16 illustrates the variations of the oxides of nitrogen in the cylinder as the pilot diesel fuel injection timing is increased. The production of the oxides of nitrogen depends on the maximum temperature in the cycle and the oxygen concentration in cylinder.

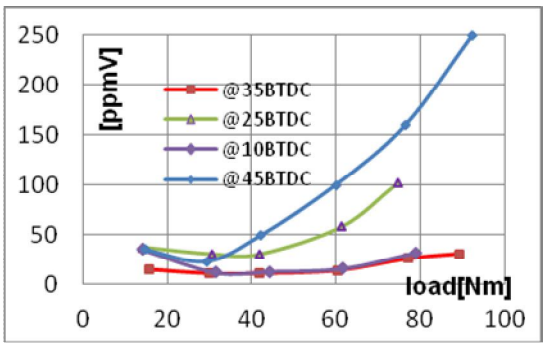

Figure 16. *Effect of pilot fuel mass, injection timing, and torque on NOx emissions for LPG-diesel fuels n=1750[rpm].*

5. Conclusions

From the experimental investigation carried out in the present work on using diesel as the pilot fuel and using LPG as the main fuel in a dual-fuel engine, the following may be concluded:

- The brake power output and brake specific fuel consumption are almost comparable for different fuels studied in the dual-fuel engine.
- The energy conversion efficiency in LPG –diesel modes is always lower than that in diesel mode at all the test points.
- The use of LPG at high amount of the gas in a dual-fuel engine with high compression ratio increases the possibility of engine knocking.
- Hydrocarbon (HC) and smoke emissions decrease as the pilot diesel fuel injection timing increases.
- Advancing the injection timing at medium and high load led to early knocking. Therefore it is not effective in improving exhaust emissions in dual-fuel operation at medium and high loads.
- The amount of diesel fuel increases in a dual fuel engine using LPG overcomes knock and ensures stable operation with the different speeds at medium and high loads, whereas this engine running LPG combined with CO_2 gas or EGR only operates at low and medium load but engine power is reduced.

6. Acknowledgements

The Authors would like to express our appreciation to the University of Danang for creating the advantages for our research and supporting experimental facilities to thanks to which the current investigation has been completed. Also, I (N.V.Phung) wish to express my gratitude to my supervisors, Associate Professor Tran Van Nam - President of the University of Danang and Associate Professor Tran Thanh Hai Tung - Chair of Department of equipment management for their enthusiastic support and guidance during the time I was studying in the University of Danang.

7. References

[1]. Donghui Qi, Longbao Zhou, Shenghua (2005). Experimental studies on the combustion characteristics and performance of a naturally aspirated, direct injection engine, *Pro Quest Science Journals*, pp.253-261.

[2]. Heywood J.B.(1988). *Internal Combustion Engine Fundamentals*, McGraw-Hill, New York.

[3]. Jemni M.A., Kantchev Gueorgui (2011). Influence of intake manifold design on in-cylinder flow and engine performances in a bus diesel engine converted to LPG gas fuelled, using CFD analyses and experimental investigations, *Energy*,36, pp.2701-2715.

[4]. Karamangil M. Ihsan (2007), Development of the auto gas and LPG-powered vehicle sector in Turkey: A statistical case study of the sector for Bursa, *Energy Policy*, 35, pp. 640–649.

[5]. Karim G.A., Liu Z.(1994). Knock in Dual-Fuel Engines, *International Symposium Comodia*, 94, pp. 171-175.

[6]. Karim G.A. (1980). A Review of combustion processes in the dual fuel engine- the gas diesel engine, *Prog. Energy Combustion Science*, Vol. 6, pp. 277-285.

[7]. Kowalewicz A., Wojtyniak M. (2005). Alternative fuels and their application to combustion engines, *Pro Quest Science Journals*, 219 (1) pp. 103-125.

[8]. Kubesh John, Brehob Diana D. (1997). Analysis of Knock in a Dual-Fuel Engine, *SAE Paper* 922367.

[9]. Litzinger Thomas A. (1990). A review of experimental studies of knock chemistry in engines, *Prog. Energy Combustion Science*, Vol. 16, pp. 155-167.

[10]. Papagiannakis R.G., (2008). Theoretical study of the effects of pilot fuel quantity and its injection timing on the performance and missions of a dual fuel diesel engine, *Energy Conversion and Management*, 48 pp. 2951–2961.

[11]. Phan Minh Duc (2006). A study on the LPG dual ffuel combustion characteristics of an indirect injection compression ignition engine, *Thesis of the Engineering Philosophy Doctor, Chulalongkom University, Thailand*.

[12]. Saleh H.E. (2008). Effect of variation in LPG composition on emissions and performance in a dual fuel diesel engine, *Fuel*, 87, pp. 3031–3039.

[13]. Sim Hansub, Lee Kangyoon, Chung Namhoon, Sunwoo Myoungho (2005). A study on the injection characteristics of a liquid-phase liquefied petroleum gas injector for air-fuel ratio control, *Pro Quest Science Journals*, pp. 1037-1045.

[14]. Tran Thanh Hai Tung, Nguyen Van Phung, (2009). Application of microcontroller in a regulator to automatically supply liquefied petroleum gas for SI engines, *Journal of Science and Technology of Danang University* 01(30), pp. 31-37.

[15]. Tran Thanh Hai Tung, Tran Van Nam, Nguyen Van Phung, (2010). Knocking in the compression ignition engine using gaseous fuels, *Journal of Science and Technology of Danang University*, 4(39), pp. 279-285.

[16]. Tran Van Nam, Tran Thanh Hai Tung, Nguyen Van Phung, (2010). A study on the manufacture of exhaust gas recirculation system on diesel engines using LPG/diesel dual-fuel, *Scientific research Theme of Danang University, code SDH 10-01-03-NCS, Official Acceptance agreement Dec. 29th 2010.*

[17]. Tran Van Nam, Tran Thanh Hai Tung, Nguyen Van Phung, (2011). A study on the manufacture of an automatic controller for LPG injection into the intake manifold of compression ignition engines, *Collection of National Scientific research Conference on aero-hydrodynamics Mechanic*, pp. 343-350.

[18]. Tran Van Nam, Tran Thanh Hai Tung, Nguyen Van Phung, (2012). Researches using microcontroller for LPG gas injection into the inlet manifold of dual fuel engines, *Collection of National Scientific research Conference on aero-hydrodynamics Mechanic*, pp. 357-367.

[19]. Lata D.B., Misra A. (2011). Analysis of ignition delay period of a dual fuel diesel engine with hydrogen and LPG as secondary fuels, *International Journal of hydrogen Energy 36*, pp. 3746-3756.

[20]. Zhihao Ma, Zuohua Huang, Chongxiao Li, Xinbin Wang, Haiyan Miao (2008). Combustion and emission characteristics of a diesel engine fuelled with diesel–propane blends, *Fuel 87*, pp. 1711–1717.

[21]. Alla G.H. Abd, Soliman H.A., adr O.A., Rabbo M.F. Abd (2004). Effect of injection on the performance of a dual-fuel engine, *Energy Conversion and Management 43* pp. 269–277.

The 2nd International Conference on Engineering Mechanics and Automation (ICEMA2)
Hanoi, August 16-17, 2012
ISBN: 978-604-913-097-7

Sliding mode control of a dual clutch during launch

V.N.Tran[a,b], J. Lauber[b] and M.Dambrine[b]

[a] *University of Transport and Communication, Hanoi, Vietnam, nhutrv@gmail.com*
[b]*LAMIH – University of Valenciennes and Haunait Cambresis, Le Mont Houy, 59300 Valenciennes, France*
{vannhu.tran, jimmy.lauber, michel.dambrine}@univ-valenciennes.fr

Abstract

The Automated Manual Transmission was introduced in vehicles to improve driving comfort, performances and fuel efficiency compared with manual transmissions. In this system, the management of the clutch is a key point especially when considering driving comfort. In this paper, we propose a control law for clutch engagement based on sliding mode control. The goal is to ensure a smooth clutch engagement while limiting slip clutch and avoiding engine no-stall. To achieve this goal, the speed of clutch slip and engine speed are controlled in order to track reference trajectories. In addition, some parametric variations of the model are also considered. Several simulations are provided to show the effectiveness of proposed control law.

Key Words: Dual clutch, Clutch slip control, Non-linear models, Trajectory tracking, Sliding control

1. Introduction

Recently, with the increasing use of Automated Manual Transmissions (AMT), the control of a clutch has become an important challenge. Nowadays, there exist two technologies for automated lay-shaft gearing transmissions. One uses a single clutch and is basically a manual transmission with an added-on control unit that automates the clutch and shift operations. The other one, using a Dual Clutch Transmission (DCT), consists of two independents sub-boxes, each one activated by separate clutches: on-coming clutch and off-going clutch. A shift process involves the engagement of the on-coming clutch and the release of the off-going clutch to ensure a shift without traction interruption.

The problems associated with AMT in literature, are the engagement of the clutch, the strategy of gearshift, and also the control of the actuator. The goal is to reduce the jerk in standing start and gearshift and thus ensure a good driveability and also reduce fuel consumption and emission of CO_2. Specifically, the dry clutch engagement must be controlled to satisfy conflicting objectives such as minimizing the slip energy and preservation of driving comfort.

To achieve these goals, many different approaches based on an optimal problem can be found in the literature. For example in (Dolcini 2006), (Dolcini, Canudas de Wit, and Bechart 2007), (Dolcini, Canudas de Wit, and Bechart 2008), (Garofalo et al. 2002), (Wu et al. 2010), they use an optimal control of dry clutch engagement in the standing start, or in (Heijden et al. 2007),

(Lucente, Montanari, and Rossi 2007) they use a hybrid optimal control of dry clutch engagement. The cost function takes into account the clutch slip speed and the jerk, to minimize the jerk and the dissipated energy.

Another family of approach is based on the use of tracking reference for the clutch slip speed (Ni, Lu, and Zhang 2009), (Gao et al. 2009), (Dassen 2003), (Amari, Alamir, and Tona 2008), and for engine speed (Ni, Lu, and Zhang 2009), (Dassen 2003), or for the vehicle acceleration (Lucente, Montanari, and Rossi 2007), or for the position of the clutch pedal (Horna et al. 2003), or finally a reference trajectory for the clutch pressure. Optimized clutch pressure profiles have been created for the best possible shift quality based on model simulation (Kulkarni, Shim, and Zhang 2007). The reference trajectory for clutch slip speed is pre-defined to satisfy the conditions no-lurch (Glielmo and Vasca 2000).

Based on sliding mode (Kim and Choi 2010) proposing the control architecture that consists of the speed control for synchronization and the output torque control for reducing jerk during launch.

The aim of this paper is to develop a control law based on the second family of approaches, i.e., using tracking trajectories for the clutch slip speed and the engine speed during the standing start. The trajectory reference is pre-defined to reduce the jerk and the oscillations during and after the synchronization, and to avoid the dead zone of the engine. Thus, a robust control law coming from sliding control methodology is proposed to ensure the desired tracking. Some simulations are provided to show the efficiency of the proposed controller.

2. Vehicle powertrain dynamic model

If we neglect the motion of the engine on its suspension and supposing that the drive train is symmetric, the powertrain model is one-dimensional mechanical system in which each element is a lumped mass model and a spring-damper model as show in Figure 1.

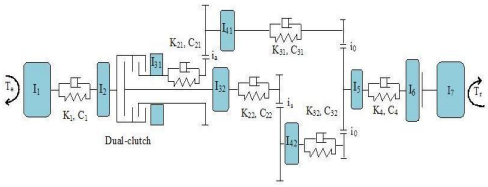

Figure 1. Dynamic models of powertrain with Dual clutch

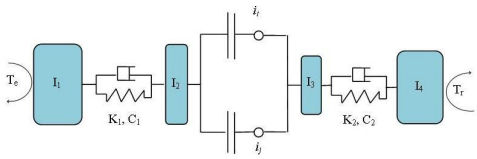

Figure 2. Simplified model of powertrain with Dual clutch

where: $I_1, I_2, I_{31}, I_{32}, I_{41}, I_{42}, I_5, I_6, I_7$ are the mass moment of inertia of the engine and flywheel, of the dual clutch drum, of the clutch disc, the gears and the input shaft of two sub-gearboxes, of the gears and the output shaft of two sub-gearboxes, of the final drive, of the half-shaft and wheels and of the vehicle mass, respectively; $K_1, C_1, K_{2i}, C_{2i}, K_{3i}, C_{3i}, K_4, C_4, (i = 1, 2)$ are the stiffness and damping coefficient of the flywheel, of the input shaft of two sub-gearboxes, of the output shaft and of the half-shaft, respectively; i_a, i_s are the gear ratios of the current and next rapport involved in the shift, respectively; i_0 is the final drive ratio; T_e is the engine torque; T_r is the load torque.

Considering the following assumptions: the tires have a perfect adherence and no transitory effects on tire-ground contact; the input shafts and output shafts of the two sub-gearboxes are infinitely rigid, then a simplified model with four states is obtained as shown Figure 2, with

$$I_3 = I_5 + \left(I_{41} + I_{42}\right) i_0^2 + I_{31}\left(i_0 i_a\right)^2 + I_{32}\left(i_0 i_s\right)^2,$$
$$I_4 = I_6 + I_7 = n_w I_w + m_v r_w^2, \qquad (1)$$
$$i_i = i_0 i_a,\ i_j = i_0 i_s.$$

Where: n_w is the number of wheels; I_w is the mass moment of inertia of one wheel; m_v is the vehicle mass; r_w is the radius of the wheel.

The differential equations describing the dynamics of the simplified model are given by

$$I_1\dot{\omega}_1 = T_e - K_1(\theta_1 - \theta_2) - C_1(\omega_1 - \omega_2), \quad (2)$$

$$I_2\dot{\omega}_2 = K_1(\theta_1 - \theta_2) + C_1(\omega_1 - \omega_2) - T_{c1}(.) - T_{c2}(.), \quad (3)$$

$$I_3\dot{\omega}_3 = i_i T_{c1}(.) + i_j T_{c2}(.) - K_2(\theta_3 - \theta_4) - C_2(\omega_3 - \omega_4), \quad (4)$$

$$I_4\dot{\omega}_4 = K_2(\theta_3 - \theta_4) + C_2(\omega_3 - \omega_4) - T_r, \quad (5)$$

$$\dot{\theta}_i = \omega_i i, \quad (i = 1..4). \quad (6)$$

Where: ω_i, θ_i are the angular velocities and angular displacements of the engine crankshaft, clutch drum, final drive and wheel, respectively; T_{c1}, T_{c2} are the clutch off-going and clutch on-coming torque, respectively.

When standing start, using only a single clutch is used, we assume that it is the first clutch, so $T_{c2} = 0$. Now we note T_c instead of T_{c1}.

2.1 Engine model

This part concerns the simplified model of the engine. As an assumption, the engine is modeled as a mean value torque generator that does not include the engine transients. Engine output torque is considered as a function of engine speed ω_1 and throttle position p

$$T_e = T_e(\omega_1, p).$$

Engine output torque is interpolated corresponding to engine speed and throttle position from an engine map modeled as a look-up table.

2.2 Clutch model

The torque transferred by the clutch in slip phase is the friction torque. In the literature, most of the models use classical friction models, such as static friction, Coulomb friction (dynamic friction), viscous friction, Stribeck friction (with Stribeck effect). Another model is developed by Carlos de Wit et al (Canudas de Wit et al. 1995). This solution provides a dynamic continuous model of the friction. In our study, a static model with Stribeck effect is considered as

$$T_c = 2n_d r_c \mu(\Delta\omega)\,\mathrm{sign}(\Delta\omega) F_n. \quad (7)$$

Where: n_d is the number of clutch discs; r_c is the friction radius of the clutch disc; F_n is the normal force applied on clutch face and $\mu(\Delta\omega)$ is the coefficient of friction that can be formulated as a function of clutch slip

$$\mu(\Delta\omega) = \mu_c + (\mu_s - \mu_c) e^{-\left(\frac{\Delta\omega}{\omega_s}\right)^2}.$$

Where: μ_c, μ_s are the Coulomb friction and the Stribeck friction; ω_s is the Stribeck angular velocity; $\Delta\omega$ is the sliding speed,

$$\Delta\omega = \omega_2 - i_i\omega_3.$$

When the vehicle is running in a particular speed with the clutch fully closed, $\omega_2 = i_i\omega_3$ and $\dot{\omega}_2 = i_i\dot{\omega}_3$, the torque applied on the clutch is obtained by combining the differential equations (3) and (4),

$$T_c = (T_{in} I_3 + T_{out} i_i I_2) / (I_2 i_i^2 + I_3).$$

Where:

$$T_{in} = K_1(\theta_1 - \theta_2) + C_1(\omega_1 - \omega_2);$$

$$T_{out} = K_2(\theta_3 - \theta_4) + C_2(\omega_3 - \omega_4).$$

2.3 Vehicle resistance

The vehicle resistance force includes rolling resistance force F_r, the aerodynamic resistance force F_a, and the uphill driving force caused by gravity when driving on non-horizontal roads F_g. The aerodynamic resistance force is approximated by

$$F_a = 0.5\rho_a A_f C_a \left(v_v + v_a\right)^2.$$

Where: A_f is the frontal area of vehicle; C_a is the aerodynamic drag coefficient; v_v is the vehicle speed; v_a is the wind speed; ρ_a is the density of the ambient air.

The rolling resistance force is often modeled as

$$F_r = m_v g \cos\left(\beta\right) c_r\left(.\right).$$

Where: m_v is the vehicle mass; g is the acceleration due to gravity; c_r is the rolling friction coefficient; β is the slope angle of road.

Uphill driving force induced by gravity when driving on a non-horizontal road

$$F_g = m_v g \sin\left(\beta\right).$$

The torque of resistance to forward is

$$T_r\left(.\right) = \left(F_a + F_r + F_g\right) r_w.$$

3. Dual clutch actuator model

The simplified diagram of a dual clutch actuator is show Figure 3. It consists in the pump (1), the three-way pressure controlled servo valve (2), the accumulator (3), the clutch actuator (4), the disc springs (5) and the dual clutch (6). The gearbox selectors and pressure modulating valves are not shown.

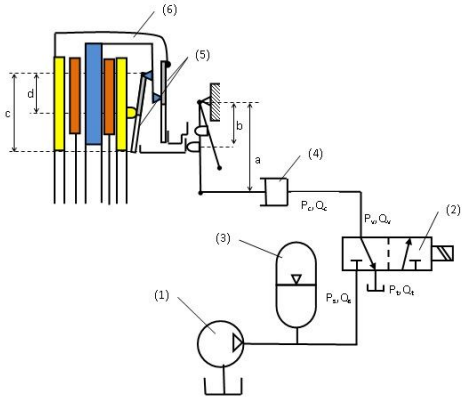

Figure 3. Simplified diagram of a dual clutch actuator

The simplified model of servo valve presented by (Owen 2001)

$$\dot{x}_v = -\frac{1}{\tau_v} x_v + \frac{K_v}{\tau_v} V. \qquad (8)$$

Where: K_v is the valve position gain; τ_v is the time constant of the valve; and V is the control voltage.

The following equations determine the flow rate through the servo valve

$$Q_v = Q_s - Q_t.$$

Where, Q_s, Q_t are flow rate in and out, respectively. They can be written according to the Bernoulli equation

$$Q_s = C_d \sqrt{\frac{2}{\rho}} A_f\left(x_v\right) \sqrt{|\, p_s - p_v\,|}\,\mathrm{sign}\left(p_s - p_v\right),$$

$$Q_t = C_d \sqrt{\frac{2}{\rho}} A_d\left(x_v\right) \sqrt{|\, p_v - p_t\,|}\,\mathrm{sign}\left(p_v - p_t\right).$$

Where: ρ is the oil density; C_d is the discharge coefficient; A_f, A_d are the filling and dumping orifice areas la surface; p_s, p_t are the oil pressures of the power supply and of the reservoir, they are assumed constant; and p_v is the oil pressures at the outlet.

$$A_f = \arccos\left(1 - \frac{x_v - L_d}{r_o}\right) r_o^2 - \left(r_0 - x_v + L_d\right)\sqrt{r_0^2 - \left(r_0 - x_v + L_d\right)^2}$$

if $x_v \in \left[L_d, 2r_o + L_d\right]$, else $A_f = 0$.

$$A_d = \arccos\left(1 + \frac{x_v + L_d}{r_o}\right) r_o^2 + \left(r_0 + x_v + L_d\right)\sqrt{r_0^2 - \left(r_0 + x_v + L_d\right)^2}$$

if $x_v \in \left[-L_d, -2r_o - L_d\right]$, else $A_d = 0$.

Where: r_o is the radius of the orifice; L_d the amplitude of the dead-zone;

$$x_v \in \left[-2r_o - L_d, 2r_o + L_d\right].$$

If we neglect the loss of pressure in the pipe. The pressure dynamic equation is written as follow

$$\dot{p}_c = \dot{p}_v = \frac{\beta}{V_0 + x_p A_p}\left(Q_v - \dot{x}_p A_p\right).$$

Where: β is the bulk modulus of the oil; V_0 is the minimum volume of the chamber; x_p is the actuator position; and A_p is the actuator cross-sectional area.

Finally, the dynamic equation of the actuator position is written as follow

$$\ddot{x}_p = \frac{1}{m_p}\left(p_c A_p - F_f(\dot{x}_p) - \frac{1}{i_1 i_2} F_n(x_p) \right).$$

Where: m_p is the equivalent mass of the actuator and the pressure plate; $i_1 = b/a$, $i_2 = d/c$ are the leverage ratios; F_n is the disc spring force (normal force on clutch face); and F_f is the force friction. In our study, a model of classical friction force with Stribeck effect is considered

$$F_f\left(\dot{x}_p\right) = \left(F_c + \left(F_s - F_c\right) e^{-\left(\frac{\dot{x}_p}{v_s}\right)^2} \right) \operatorname{sign}\left(\dot{x}_p\right).$$

Where: F_c, F_s is the Coulomb and Stribeck friction force, respectively; v_s is the Stribeck velocity.

The disc spring force F_n is determined by the formula of Almen and Láaszló (Almen and Laszlo 1936)

$$F_n\left(s\right) = \frac{4E}{\left(1-\mu^2\right) K D_e^2} s\left((h-s)(h-\frac{s}{2})t + t^3 \right).$$

With

$$K = \frac{1}{\pi} \frac{\left(\frac{\delta - 1}{\delta}\right)^2}{\frac{\delta+1}{\delta-1} - \frac{2}{\ln\delta}}, \quad \delta = \frac{D_e}{D_w}.$$

Where: E is the Young's modulus, [**N/m^2**]; D_e, D_w are the outside diameter and the diameter at the root of slots, [**mm**]; h is the cone height, [**mm**]; t is the thickness of individual, [**mm**]; μ is the Poisson's ratio; s is the axial deformation of the cone respective to its unconstrained height, [**mm**]. If we neglect the deformation of the lever

$$s = 1000 \frac{1}{i_1 i_2} x_p \,[\textbf{mm}].$$

4. Launch control design

In this section, the control law for clutch during engagement is developed based on sliding control methodology (Slotine and Li 1991). The goal of the control is to minimize the jerk, the oscillations during and after synchronization and to avoid the dead zone of the engine, while limiting the clutch slip time. In addition, the control law allows to take into account both road conditions and model parametric variations.

4.1 Reference trajectory of engine speed

The normal force applied to the clutch disk, and consequently the engine speed could drop too severely resulting in engine stall. To avoid the dead zone of the engine, the engine speed must be controlled. The reference trajectory of the engine during clutch engagement is presented in some works (Ni, Lu, and Zhang 2009), (Dassen 2003), (Amari, Alamir, and Tona 2008). Dassen et al (Dassen 2003) define the reference trajectory for the engine speed as a decreasing linear function satisfying the no-kill condition, $\omega_1 > \omega_1^{idle}$.

In the standing start and gear shifting phase, Amari et al (Amari, Alamir, and Tona 2008) define the reference speed of the engine at least at the idle speed set-point, unless the desired torque exceeds the maximum torque. This ensures that the engine is no-kill during standing start.

To avoid sudden change of engine speed, the initial values of the reference trajectory for engine speed and its differential must be equal to the real one

$$\omega_1^{ref}\left(t_0\right) = \omega_1\left(t_0\right), \tag{9}$$

$$\dot{\omega}_1^{ref}\left(t_0\right) = \dot{\omega}_1\left(t_0\right). \tag{10}$$

Where, t_0 is the time to begin launch.

The clutch slipping time is limited to a sufficiently short time, we propose the hypothesis that during the engagement, the

throttle position $p(t)$, which is controlled by the driver, increases linearly. With this hypothesis, we can determine the throttle position at the time of the lock-up point t_f

$$p\left(t_f\right) = p\left(t_0\right) + \dot{p}\left(t_0\right)\left(t_f - t_0\right).$$

The engine speed at that time $\omega_1^{ref}\left(t_f\right)$ is chosen so that the torque is stored for the maximum possible acceleration and so that the reference trajectory for the engine speed is always above the engine idle speed ω_1^{idle}

$$\omega_1^{ref}\left(t_f\right) = \left\{ \begin{array}{l} T_e^{-1}\left(\max\left\{T_e\left(\omega_1, p\left(t_f\right)\right)\right\}, p\left(t_f\right)\right) \\ \left| \min\left\{\omega_1^{ref}\left(t\right)\right\} > \omega_1^{idle} \right. \end{array} \right\}. \quad (11)$$

Ideally, at the time of lock-up point, there are no difference of acceleration between the flywheel and the clutch drum, and between the final drive and the wheel

$$\dot{\omega}_1\left(t_f\right) = \dot{\omega}_2\left(t_f\right) = i_i\dot{\omega}_3\left(t_f\right) = i_i\dot{\omega}_4\left(t_f\right). \quad (12)$$

Combining equations (2), (3), (4), (5) and (12) with the engine torque control $T_e^c(t_f) = 0$, we have

$$\dot{\omega}_1^{ref}\left(t_f\right) = \frac{T_e^d\left(t_f\right) - T_r\left(t_f\right)}{I_1 + I_2 + \left(I_3 + I_4\right)/i_i^2}. \quad (13)$$

Where, $T_e^d(t_f)$ is the engine torque coming from the driver request

$$T_e^d\left(t_f\right) = T_e\left(\omega_1\left(t_f\right), p\left(t_f\right)\right).$$

To pre-calculate the trajectory for the engine speed, the resistant torque T_r and the equivalent moment of inertia of the vehicle I_4 are needed. The resistant torque is a nonlinear function which depends on a priori unknown parameters such as the number of passengers, vehicle speed, tire pressure, and road surface conditions.

In normal conditions, those coefficients are bounded

$$c_r^{min} \le c_r \le c_r^{max},$$

thus,

$$T_r^{min} \le T_r \le T_r^{max}.$$

With

$$T_r^{min} = 0.5\rho_a A_f C_d \left(v_v + v_a\right)^2 r_w + m_v^{min} g\cos\left(\beta\right)c_r^{min} r_w + m_v^{min} g\sin\left(\beta\right)r_w,$$

$$T_r^{max} = 0.5\rho_a A_f C_d \left(v_v + v_a\right)^2 r_w + m_v^{max} g\cos\left(\beta\right)c_r^{max} r_w + m_v^{max} g\sin\left(\beta\right)r_w.$$

We consider, the average value defined by

$$\hat{T}_r = 0.5\left(T_r^{min} + T_r^{max}\right).$$

On the other hand, the moment of inertia of the vehicle I_4 depends on the vehicle mass. The vehicle mass is an uncertain parameter but also bounded

$$m_v^{min} \le m_v \le m_v^{max},$$

thus

$$I_4^{min} \le I_4 \le I_4^{max}.$$

With

$$I_4^{min} = n_w I_w + m_v^{min} r_w^2,$$

$$I_4^{max} = n_w I_w + m_v^{max} r_w^2.$$

As previously, we define the average moment of inertia of the vehicle as

$$\hat{I}_4 = 0.5\left(I_4^{max} + I_4^{min}\right).$$

Then, $\hat{T}_r$ and $\hat{I}_4$ instead of T_r and I_4 are used to compute $\dot{\omega}_1^{ref}\left(t_f\right)$

$$\dot{\omega}_1^{ref}\left(t_f\right) = \frac{T_e^d\left(t_f\right) - \hat{T}_r\left(t_f\right)}{I_1 + I_2 + \left(I_3 + \hat{I}_4\right)/i_i^2}. \quad (14)$$

Different choices are possible to define a trajectory satisfying the constraints (9), (10), (11) and (14). In this study, a polynomial of degree 3 is chosen to deal with the requirements.

4.2 Reference trajectory of the clutch slip speed

The clutch engagement process should ensure driving comfort and minimize the dissipated friction energy. In general, if engagement duration is limited in a suitable short time, the dissipated energy will not be too important. As to the driving comfort, because the sudden change of torque due to clutch lock-up tends to cause an undesired vehicle jerk just after the synchronization of

clutch, the clutch engagement should satisfy the so called no-lurch condition introduced by Glielmo and Vasca (Glielmo and Vasca 2000). This condition can be characterized as the rotational acceleration of clutch input shaft should be equal to the one of the output shaft at the lock-up point, $\dot{\omega}_2 - i_i\dot{\omega}_3$.

Therefore, the reference trajectory for the clutch slip speed must satisfy the following requirements: the clutch slipping should be finished after the selected time $\Delta t = t_f - t_0$

$$\Delta\omega_{ref}(t_f) = \omega_2(t_f) - i_i\omega_3(t_f) = 0;$$

at the lock up point, sliding acceleration must equal to zero

$$\Delta\dot{\omega}_{ref}(t_f) = \dot{\omega}_2(t_f) - i_i\dot{\omega}_3(t_f) = 0;$$

and under the initial conditions

$$\Delta\omega_{ref}(t_0) = \omega_2(t_0) - i_i\omega_3(t_0) = \omega_2(t_0),$$

$$\Delta\dot{\omega}_{ref}(t_0) = \dot{\omega}_2(t_0) - i_i\dot{\omega}_3(t_0) = \dot{\omega}_2(t_0).$$

Similarly to above, a polynomial of degree 3 is chosen.

4.3 Engine speed control

The engine torque is divided into two parts, the first part which is the one coming from the driver request T_e^d and the second part which is considered as a control input T_e^c. Rewriting the dynamic equation of the engine speed, (equation (2)), the following equation is obtained

$$\dot{x}_1 = f_1(.) + g_1.u_1. \qquad (15)$$

With

$$x_1 = \omega_1, \quad g_1 = \frac{1}{I_1}, \quad u_1 = T_e^c,$$

$$f_1(.) = \frac{1}{I_1}\left(T_e^d - K_1(\theta_1 - \theta_2) - C_1(\omega_1 - \omega_2)\right).$$

In order for the engine speed to track the reference trajectory x_{1r}, a sliding surface S_1 is defined by the following integral structure

$$S_1(t) = \left(\frac{d}{dt} + \lambda\right)\int_0^t e_1(\tau)\,d\tau$$

$$= e_1(t) + \lambda\int_0^t e_1(\tau)\,d\tau.$$

Where: λ is a strictly positive constant; e_1 is the tracking error, $e_1(t) = x_1(t) - x_{1r}(t)$.

The derivative of the sliding surface is given by

$$\dot{S}_1(t) = \dot{e}_1(t) + \lambda e_1(t)$$

$$= f_1(.) + g_1u_1(t) - \dot{x}_{1r} + \lambda e_1(t).$$

If the sliding regime is perfect, the operating point moves on the sliding surface $S_1 = 0$ and satisfies $\dot{S}_1 = 0$ as the function S_1 is constant. The best approximation $\hat{u}_1$ a continuous control law that would achieve $\dot{S}_1 = 0$ is thus,

$$\hat{u}_1(t) = g_1^{-1}\left(-f_1(.) + \dot{x}_{1r} - \lambda e_1(t)\right).$$

We add to $\hat{u}_1$ a term discontinuous across the surface $S_1 = 0$. The control law is defined as

$$u_1(t) = \hat{u}_1(t) - g_1^{-1}k\,\mathrm{sign}(S_1).$$

Where, k is a strictly positive constant.

4.4 Clutch slip control

By combining equations (3) and (4), the dynamic equation for the clutch slip control is

$$\dot{x}_2 = \frac{1}{I_2}T_{in}(.) + \frac{i_i}{I_3}T_{out}(.) - (\frac{1}{I_2} + \frac{i_i^2}{I_3})T_c. \qquad (16)$$

Where, $x_2 = \Delta\omega$.

By combining equations (7) and (16), we have

$$\dot{x}_2 = \frac{1}{I_2}T_{in}(.) + \frac{i_i}{I_3}T_{out}(.)$$

$$-2n_dr_c\left(\frac{1}{I_2} + \frac{i_i^2}{I_3}\right)\mathrm{sign}(x_2)F_n(x_p)\mu(x_2).$$

To develop a control law, the dynamic model of the valve is simplified. The time constant of the valve (τ_v) is very small compared with the time constants of other components of the control system. Therefore, the dynamic of the valve is neglected, the dynamic equation (8) becomes the algebraic equation,

$$x_v = K_vV. \qquad (17)$$

The main differential equations to develop the control law are

$$\dot{x}_2 = \frac{1}{I_2} T_{in}(.) + \frac{i_i}{I_3} T_{out}(.) - 2n_d r_c \left(\frac{1}{I_2} + \frac{i_i^2}{I_3} \right) \text{sign}(x_2) F_n(x_p) \mu(x_2), \quad (18)$$

$$\ddot{x}_p = \frac{1}{m_p} \left(p_c A_p - F_f(\dot{x}_p) - \frac{1}{i_1 i_2} F_n(x_p) \right), \quad (19)$$

$$\dot{p}_c = \frac{\beta}{V_0 + x_p A_p} \left(Q_v(V, p_v) - \dot{x}_p A_p \right). \quad (20)$$

We derive the equation (18) three times, then the control $u_2 = V$ appear on the dynamic equation of the clutch slip.

So neglecting the dead zone of the valve ($2L_d = 0$) and limiting $x_v \in [-2r_o, 2r_o]$, the function $Q_v = Q(V, p_v)$ is monotonically increasing function of V. So, it exists an inverse function $V = Q^{-1}(Q_v, p_v)$. The dynamic equation of the clutch slip can be rewritten as follow

$$\overset{(4)}{x}_2 = f_2(.) + g_2(.)v. \quad (21)$$

With v is the new input,

$$v = Q_v(V, p_v).$$

In order to have the engine speed track the reference trajectory x_{2r}, a sliding surface S_2 is defined by

$$S_2(t) = \left(\frac{d}{dt} + \lambda \right)^{(3)} e_2(t) = \overset{(3)}{e}_2(t) + 3\lambda \ddot{e}_2(t) + 3\lambda^2 \dot{e}_2(t) + \lambda^3 e_2(t).$$

Where: λ is a strictly positive constant; e_2 is the tracking error x_2,

$$e_2(t) = x_2(t) - x_{2r}(t).$$

The dynamic of the sliding surface is

$$\dot{S}_2(t) = \overset{(4)}{e}_2 + 3\lambda \overset{(3)}{e}_2 + 3\lambda^2 \ddot{e}_2 + \lambda^3 \dot{e}_2.$$

As previously, a control law of that form is introduced

$$v(t) = \hat{v}(t) - g(.)^{-1} k \text{sign}(S_2).$$

With

$$\hat{v}(t) = g(.)^{-1} \begin{pmatrix} \overset{(4)}{x}_{2r}(t) - f_2(.) - 3\lambda \overset{(3)}{e}_2(t) \\ -3\lambda^2 \ddot{e}_2(t) - \lambda^3 \dot{e}_2(t) \end{pmatrix}.$$

Where k is a strictly positive constant.

$$u_2(t) = V(t) = Q^{-1}(v(t), p_v(t)).$$

4.5 Control strategy

The reference trajectory for the engine speed is calculated with the previous hypotheses and taking into account parameter uncertainties. Therefore, the engine torque control is not zero at the lock-up point. To ensure that the driver take control of the vehicle, after closing, it is controlled to zero by another strategy. After synchronization, the normal force is also controlled by a strategy to a set value. The set value ensures the complete closure of the clutch and allows avoiding an over load in the powertrain.

To show the effectiveness of the proposed control law in the engagement phase, the dynamic model of the powertrain is implemented in Matlab/Simulink and simulated. Different tests with parametric m_v variations have been realized and are presented in Figure 4 to Figure 8. Begin of standing starts at 1 second and duration is limited to 2.5 seconds. The simulation results show that the engine speed is well tracking the reference trajectory (Figure 4) while the parameters are variables (9.4% of the vehicle mass), the clutch slip time about 2.5 second (Figure 7). Figure 6 show the behavior of the engine with and without engine controller. In the case without engine controller, the engine speed drops quickly to the dead zone. The vehicle jerk is shown in Figure 8, it depends on the engagement time but does not depend on driver behavior during the engagement.

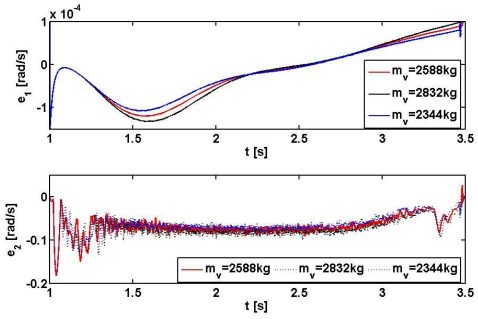

Figure 4. Trajectory tracking error e_1 and e_2

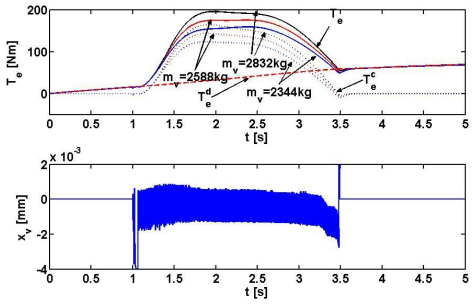

Figure 5. Engine torque driving T_e^d , engine torque control T_e^c and position of valve x_v

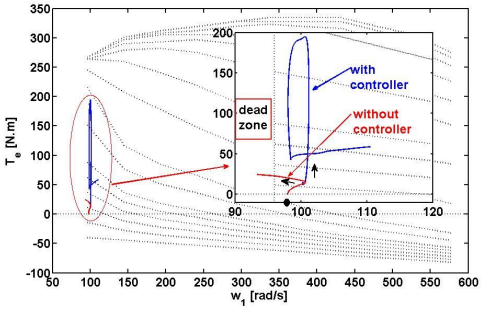

Figure 6. Engine behavior with engine control and without engine control

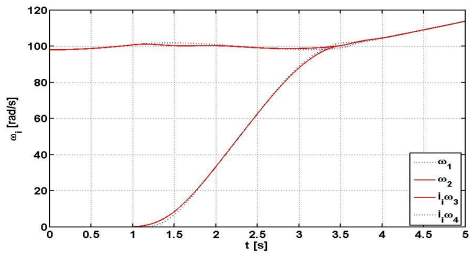

Figure 7 Angular speed of each element of the simplified model

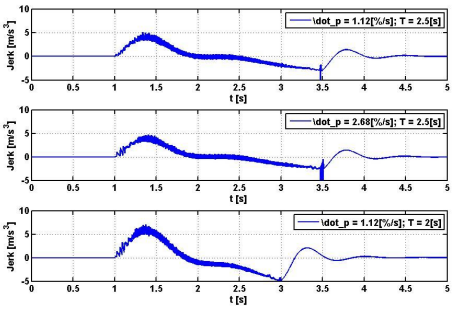

Figure 8. Vehicle jerk

5. Conclusion

A nonlinear model of the powertrain has been proposed. From the simplified model, a control law based on the sliding mode control methodology to ensure robust with respect to model parametric variations and road condition, has been developed. Finally, the simulation results applied in the case of standing start showed the efficiency of the proposed approach.

References

Almen, J.O., and A. Laszlo. 1936. "The Uniform-Section Disk-Spring." *Transactions of the American Society of Mechanical Engineers* 58, S: 305/314.

Amari, R., M. Alamir, and P. Tona. 2008. "Unified MPC Strategy for Idle-speed Control, Vehicle Start-up and Gearing Applied to an Automated Manual Transmission." In *Proceedings of the 17th World Congress, The International Federation of Automatic Control, Seoul, Korea, July 6-11.*

Canudas de Wit, Carlos, H.Olsson, K.J.Astrom, and P.Lischinsky. 1995. "A New Model for Control of Systems with Friction." *IEEE Transactions on Automatic Control* 40: 419–424.

Dassen, M.H.M. 2003. *Modelling and Control of Automotive Clutch Systems*. Department of mechanical engineering TU/e Eindhoven.

Dolcini, Pietro. 2006. "Contribution Au Confort De L'embrayage". Universite de Grenoble.

Dolcini, Pietro, Carlos Canudas de Wit, and H Bechart. 2007. "Observer-Based Optimal Control of Dry Clutch Engagement." *Oil*

& Gas Science and Technology 62: 615–621.

Dolcini, Pietro, Carlos Canudas de Wit, and Hubert Bechart. 2008. "Lurch Avoidance Strategy and Its Implementation in AMT Vehicles." *Mechatronics* 18: 289–300.

Gao, Bingzhao, Hong chen, Yan Ma, and Kazushi Sanada. 2009. "Clutch Slip Control of Automatic Transmission Using Nonlinear Method." In *Joint 48th IEEE Conference on Decision and Control And.*

Garofalo, Franco, Luigi Glielmo, Luigi Iannelli, and Francesco Vasca. 2002. "Optimal Tracking for Automotive Dry Clutch Engagement." In *IFAC, 15th Triennial World Congress, Barcelona, Spain.*

Glielmo, L., and F. Vasca. 2000. "Optimal Control of Dry Engagement." *SAE* 2000-01-0837.

Heijden, A. C. Van Der, A. F. A. Serrarens, M. K. Camlibel, and H. Nijmeijer. 2007. "Hybrid Optimal Control of Dry Clutch Engagement." *International Journal of Control* 80: 1717–1728.

Horna, Joachim, Joachim Bamberger, Peter Michau, and Stephan Pindl. 2003. "Flatness-based Clutch Control for Automated Manual Transmissions." *Control Engineering Practice* 11: 1353–1359.

Kim, Jinsung, and Seibum B. Choi. 2010. "Control of Dry Clutch Engagement for Vehicle Launches via a Shaft Torque Observer." In *American Control Conference, Marriott Waterfront, Baltimore, MD, USA.*

Kulkarni, Manish, Taehyun Shim, and Yi Zhang. 2007. "Shift Dynamics and Control of Dual-clutch Transmissions." *Mechanism and Machine Theory* 42: 168–182.

Lucente, G., M. Montanari, and C. Rossi. 2007. "Hybrid Optimal Control of an Automated Manual Transmission System." In *Seventh IFAC Symposium on Nonlinear Control Systems.*

Ni, Chunsheng, Tongli Lu, and Jianwu Zhang. 2009. "Gearshift Control for Dry Dual-clutch Transmissions." *Issn* 8: 1109–2777.

Owen, William Scott. 2001. "An Investigation into the Reduction of Stick-slip Friction in Hydraulic Actuators". The University of British Columbia.

Slotine, Jean-Jacques E., and Weiping Li. 1991. *Applied Nonlinear Control*. Printice Hall, Inc.

Wu, M. X., J. W. Zhang, T. L. Lu, and C.S. Ni. 2010. "Research on Optimal Control for Dry Dual-clutch Engagement During Launch." *Proceedings of the Institution of Mechanical Engineers, Part D: Journal of Automobile Engineering* 224: 749 –763.

The 2nd International Conference on Engineering Mechanics and Automation (ICEMA2)
Hanoi, August 16-17, 2012
ISBN: 978-604-913-097-7

Simple Model for Linear Permanent Magnet Generator in Wave Energy Conversion

Dang The Ba, Nguyen Hoang Quan and Le Trung Tien

University of Engineering and Technology - Vietnam National University, Hanoi
144 Xuan Thuy-Cau Giay- Hanoi-Vietnam

Abstract

Ocean wave energy is a renewable energy source with a large potential to contribute to the world's electricity production. The work presented in this article focuses on the first steps in the device types that represent current wave energy converter (WEC) technology and introduces the general status of wave energy. A simple simulation approche for the linear permanent magnet converter are presented and their responses are compared to previous results.

Keywords: Wave power, direct driven linear generator, power-take-off, electrical systems.

1. Introduction

To day, the focus on generating electricity from renewable sources is an important area of research. It is estimated that the potential worldwide wave power resource is 2TW (Thorpe, 1999), with the UK's realistic potential being 7– 10GW (Duckers, 2004) and Vietnam's examined potential indicated in Figs. 1, 2, 3. There are many wave energy devices investigated, tested and deployed in the oceans.

Figure 1: Estimated average annual power density of ocean waves (kW/m).

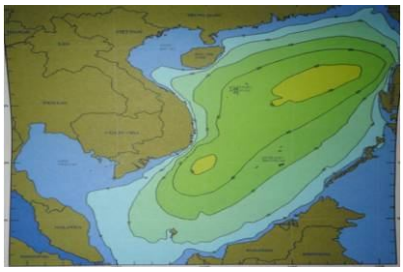

Figure 2: Estimated average annual power density of ocean waves in Vietnam.

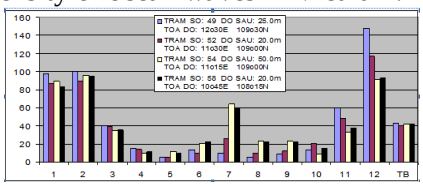

Figure 3: Estimated average annual ocean energy in Nam Trung Bo region

Despite there is a large number of concepts for wave energy conversion (Salter, 1974; Duckers, 2004; Previsic, 2004), WECs are generally categorized by location, type and modes of operation. Following we will introduce different WECs types.

For the location, WECs can be classified into following devices.

Shoreline devices have the advantage of being close to the utility network, are easy to maintain, and as waves are attenuated as they travel through shallow water they have a reduced likelihood of being damaged in extreme conditions. This leads to one of the disadvantages of shore mounted devices, as shallow water leads to lower wave power (Fig. 4).

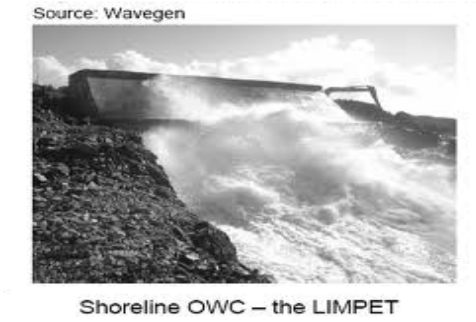

Figure 4: Shoreline device.

Nearshore devices are defined as devices that are in relatively shallow water (there is a lack of consensus of what defines 'shallow' water, but it has been suggested that this could be a depth of less than onequarter wavelength (Fig. 5).

Figure 5: UK's first nearshore (Internet)

Offshore devices are generally in deep water the advantage of siting a WEC in deep water is that it can harvest greater amounts of energy because of the higher energy content in deep water waves (Fig. 6).

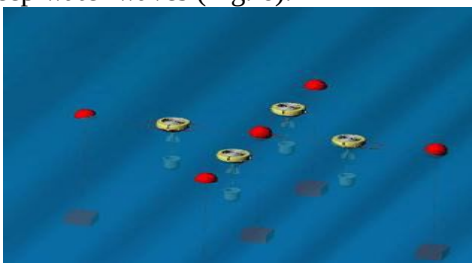

Figure 6: Offshore devices (Internet)

It is useful to note that wave energy occurs in the movements of water near the surface of the sea (Callaghan, 2006). Up to 95 per cent of the energy in a wave is located between the water surface and one-quarter of a wavelength below it (Duckers, 2004).

For the types, WECs can be classified into three predominant.

Attenuator device lies parallel to the predominant wave direction and 'rides' the waves (Fig. 7).

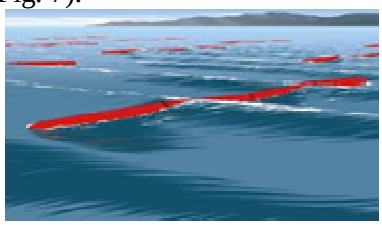

Figure 7: Pelamis wave farm.
(Source: http://ocsenergy.anl.gov)

Terminator device has their principal axis parallel to the wave front (perpendicular to the predominant wave direction) and physically intercept waves (Fig. 8).

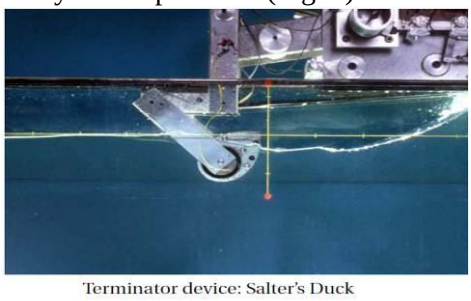

Figure 8: Terminator device (Internet).

Point absorber is a device that possesses small dimensions relative to the incident wavelength (Fig. 9).

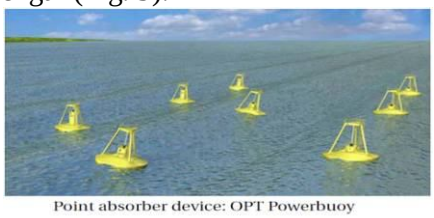

Figure 9: Point absorber (Internet).

For the mode of operation, WECs can be classified into following devices.

The submerged pressure differential device is a submerged point absorber that uses the pressure difference above the device between wave crests and troughs (Fig. 10).

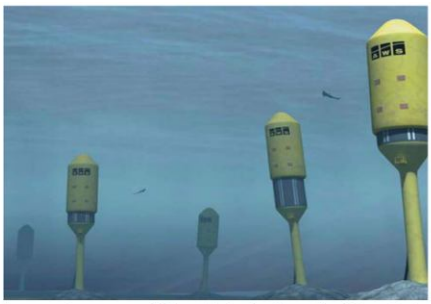

Figure 10: Submerged pressure differential device (Internet).

An oscillating wave surge converter is generally comprised of a hinged deflector, positioned perpendicular to the wave direction (a terminator), that moves back and forth exploiting the horizontal particle velocity of the wave (Fig. 11).

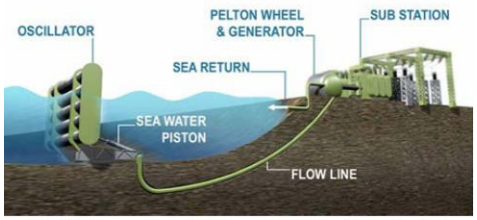

Figure 11: Oscillating wave surge converter (Internet).

An Oscillating water column (OWC) consists of a chamber with an opening to the sea below the waterline. As waves approach the device, water is forced into the chamber, applying pressure on the air within the chamber. This air escapes to atmosphere through a turbine. As the water retreats, air is then drawn in through the turbine (Fig. 12).

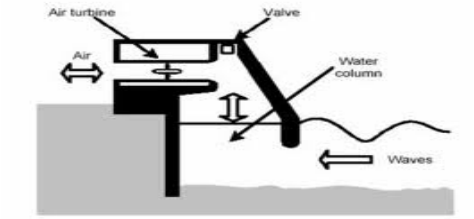

Figure 12: Oscillating water column (Internet).

An overtopping device captures sea water of incident waves in a reservoir above the sea level, then releases the water back to sea through turbines (Fig. 13).

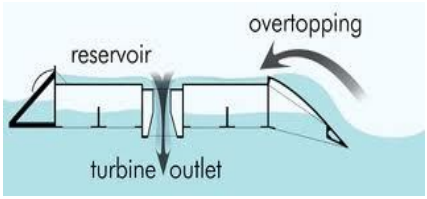

Figure 13: Overtopping device (Internet).

One of the major challenges of WECs is concerned with how to drive generators. During early wave power research, the possibility of using electrical linear generators was investigated. A linear SG offers the possibility of directly converting mechanical energy into electrical energy.

The basic concept of a linear generator is to have a translator on which magnets are mounted with alternating polarity directly coupled to a heaving buoy, with the stator containing windings, mounted in a relatively stationary structure. As the heaving buoy oscillates, an electric current will be induced in the stator. In this article we will present a simple simulation approche for the linear permanent magnet converter and compare their responses with previous results.

2. Simple analysis models

In the design process of the generator which can be modelled differently, it is important to have a model where the physical dimensions and the electric and magnetic behaviour can be set and studied.

The fundamental and governing equations in electromagnetics is Maxwell's equations:

$$\nabla \times \boldsymbol{E} = -\frac{\partial \boldsymbol{B}}{\partial t} \quad (1)$$

$$\nabla \times \boldsymbol{H} = \boldsymbol{J}_f + \frac{\partial \boldsymbol{D}}{\partial t} \quad (2)$$

$$\nabla . \boldsymbol{B} = 0 \quad (3)$$

$$\nabla . \boldsymbol{D} = \rho_f \quad (4)$$

Where **E** is the electric field, **D** is the electric flux density, **H** is the magnetic field, and **B** is the magnetic flux density. **J** and ρ are current and charge density respectively. In addition to Maxwell's equation material properties is needed, these can be formulated by the following constitutive equations:

$$\boldsymbol{B} = \mu \boldsymbol{H} \quad (5)$$

$$\boldsymbol{J} = \sigma \boldsymbol{E} \quad (6)$$

Where μ is the permeability and σ the conductivity, which is a scalar constant.

The first equation, Eq.1, can be seen as a vector formula of Faraday's law of induction. If the circuit consists of a tightly-wound N-turn coil of wires, the induced voltage, e, is given by:

$$e = -N\frac{d\emptyset}{dt} \quad (7)$$

Where ϕ can be expressed in terms of the electric and the magnetic field:

$$\emptyset = \int_S \boldsymbol{B} da \quad (8)$$

$$\frac{d\emptyset}{dt} = -\oint_c \boldsymbol{E} ds \quad (9)$$

The second equation, Eq.2, can be seen as a vector formula of Biot-Savart-Laplace law. It is used to compute the resultant magnetic field **B** at position **r** generated by an electric current I:

$$\boldsymbol{B} = \frac{\mu_0 \mu}{4\pi}\frac{I\boldsymbol{dl}\times \boldsymbol{r}}{|\boldsymbol{r}|^3} \quad (10)$$

Where $\mu_0 = 4\pi 10^{-7}(T.m/A)$ is the permeability of free space (or the magnetic constant) and μ is the permeability of a specific medium. $\boldsymbol{dl}$ is a vector whose magnitude is the length of the differential element of the wire.

In this model the electric system, generator and load, is translated into a mechanical damping function (Fig. 14). The forces acting on the generator can be expressed with Newton's second law:

$$m_b \ddot{s}_b(t) = F_{e,b}(t) + F_{r,b}(t) + F_{b,b}(t) + F_{b,v}(t) + F_{b,f}(t) + F_{b,u}(t) \quad (11)$$

Where m_b is the mass of the buoy and the translator and $\ddot{s}$ is the acceleration of the translator. $\left(F_{e,b}(t) + F_{r,b}(t)\right)$ is the lifting force from the buoy. This is the driving force in the system. $F_{b,b}(t)$ is the hydrostatic force of the buoy. $F_{b,v}(t)$ is the damping force. $F_{b,f}(t)$ is the friction force. The electromagnetic force, $F_{b,u}(t)$, is a consequence of the damping from the electrical system and has an influence on the WEC's ability to absorb energy.

To simplify the hydrodynamic model (Eq. 11), the complete equation of motion is given in the form of a simple mass, spring, damper model, with various expressions for the coefficients of displacement, velocity and acceleration:

$$m_b \ddot{s}_b(t) + R_b \dot{s}_b(t) + S_b s_b(t) = F_{e,b}(t) + F_{b,u}(t) \quad (12)$$

Here, R_b is the sum of damping coefficient and S_b is the sum of the hydrostatic stiffness of the buoy. $F_{e,b}(t)$ is the excitation force of incident wave. $F_{b,u}(t)$ is the electromagnetic force.

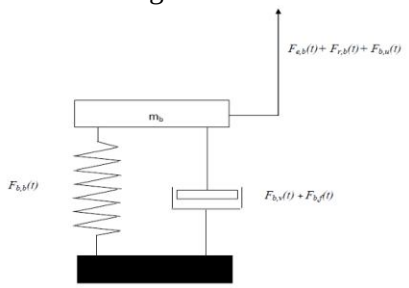

Figure 14: Schematic of force excitation system.

In a power system, the generator is usually represented by its equivalent circuit model. The generator can be replaced by resistances, inductances and voltage sources.

In Fig. 15, e_i is the internal EMF (electromotive force) of the generator, R_i is the resistance in the armature winding and L is the synchronous inductance. The terminal voltage, V_L, for the circuit can be written under any load condition. In this paper, the simplest load studied to connect the generator is a purely resistive load, R_e.

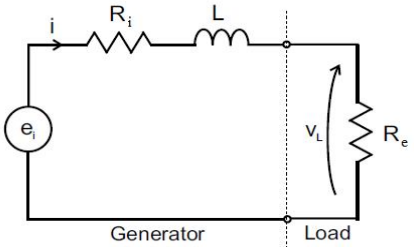

Figure 15: Equivalent circuit of a generator

The terminal voltage, V_L, over the load, R_e, can according to KVL be expressed as:

$$V_L(t) = e_i(t) - i(t)R_i - L\frac{di(t)}{dt} \quad (13)$$

The expression of the current, $i(t)$, is derived from Ohm's law:

$$i(t) = \frac{V_L(t)}{R_e} \quad (14)$$

The terminal voltage can be rewritten as:

$$V_L(t) = e_i(t) - \frac{V_L(t)}{R_z} R_i - \frac{L}{R_z}\frac{dV_L(t)}{dt} \quad (15)$$

From Faraday's law, the phase emf e_i may be written as:

$$e_i(t) = -N\frac{d\Phi(t)}{dt} = -nlB\frac{dS(t)}{dt} \quad (16)$$

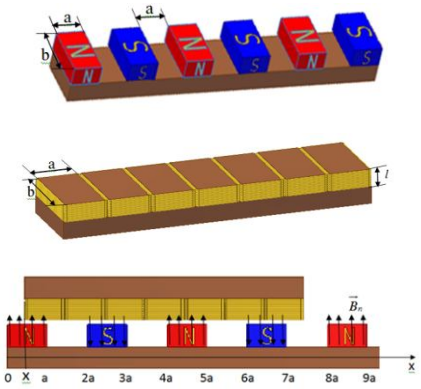

Figure 16: Stator and rotor

$$B\frac{dS(t)}{dt} = (-1)^{\left[I+\frac{x(t)}{2a}+1\right]} bB\frac{dx(t)}{dt} =$$
$$= (-1)^{\left[I+\frac{x(t)}{2a}+1\right]} bBv(t) \quad (17)$$

The synchronous inductance, L, is proportional to the magnetic flux, Φ_I, and the current, I, flowing in the circuit:

$$L = \frac{\Phi_I}{I} = \frac{nlB_c S}{I} \quad (18)$$

Here B_c, the magnetic flux density on the coil axis, is calculed as following expression (Fig. 17):

$$B_z = \mu_0\mu\frac{n.h.a}{4\pi} I\int_{-\frac{l}{2}}^{\frac{l}{2}} \frac{a}{\sqrt{a^2+\frac{a^2+b^2}{4}}}\left(\frac{a}{a^2+\frac{b^2}{4}}+\frac{a}{a^2+\frac{b^2}{4}}\right)dx \quad (19)$$

Substituting Eq. 19 into Eq. 18 we obtain an expression of the synchronous inductance:

$$L = \mu_0\mu\frac{n.h.a}{4\pi}\int_{-\frac{l}{2}}^{\frac{l}{2}} \frac{a}{\sqrt{a^2+\frac{a^2+b^2}{4}}}\left(\frac{a}{a^2+\frac{b^2}{4}}+\frac{a}{a^2+\frac{b^2}{4}}\right)dx \quad (20)$$

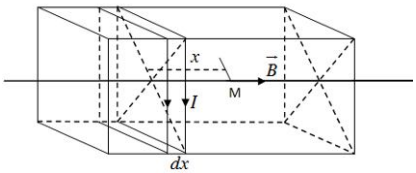

Figure 17: Magnetic flux density **B** on the coil axis

Substituting Eqs. 16, 17, 20 into Eq. 15 we obtain a different equation that presents the relation between voltage V_L and translator velocity $v(t)$:

$$\left(1+\frac{R_i}{R_z}\right)V_L(t) = -\left[(-1)^{\left[I+\frac{x(t)}{2a}+1\right]} nlbB.v(t) + \frac{L}{R_z}\frac{dV_L(t)}{dt}\right] \quad (21)$$

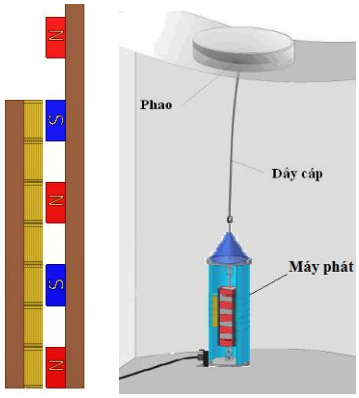

Figure 18: To the left a structure of stator and rotor, to the right an illustration of the wave energy converter

3. Simulation results and discussion

In this section we design and calculate parameters of the linear PM convecter (induced voltage, current, power) by analysing a detail converter model (see fig. 16, 18) and assuming harmonic translator displacement $x(t) = \cos(2\pi ft + \varphi)$, with $f = 1/7$, $\varphi = \pi$.

The characteristics of the simulated linear PM generator are given in the Table 1.

Table 1: Simulated Linear PM Generator

Generator Characteristic	**Value**
Size of turn coil block axbxl	0.04x0.25x0.04(m^2)
Number of turn coil of wires n	8000(rounds/m)
Wire cross-section area r_d	5×10^{-4}(m)
Wire resistance ρ	1.72×10^{-8} (Ωm)
Magnetic flux density **B**	1.8(T)
Load resistance R_z	100(Ω)
Resistance in the armature winding R_i	$\rho\frac{2n(a+b)}{\pi r_d^2}$

Basing on simple model presented in the previous section, we obtained following results. In Fig. 19, the value terminal voltage V_L has a harmonic shape related to harmonic waves that creates the translator displacement.

Similar Fig. 20 indicates that the voltage and current have a linear relation and its maximum amplitude corresponds to the

maximum value of translator velocity. Fig. 21 shows the generator power obtained.

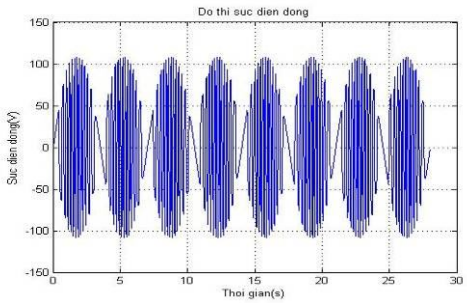

Figure 19: Terminal voltage V_L of the generator over resistive load R_e

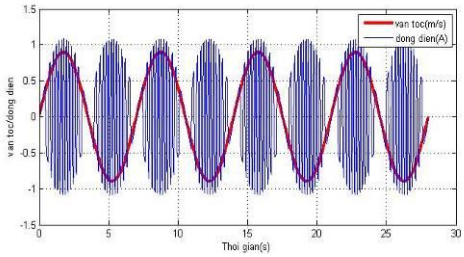

Figure 20: Translator velocity and current

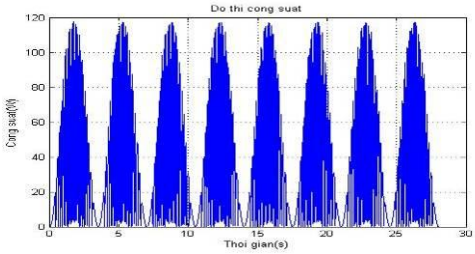

Figure 21: Instantaneous generator power

The result shown in Fig. 19 compared to the three-phase voltage case from the generator connected to resistive load and based on experimental data shown in Fig. 22. It indicates that voltage shapes are homologous and simple model studied is significant.

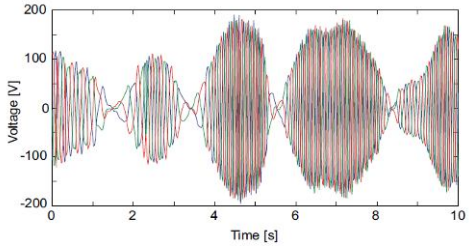

Figure 22: Three-phase voltage from the generator connected to resistive load (Boström, 2011)

Following we examine and estimate the influence of stator parameters on the generator power. Basing on the presented model in previous section, we show that average generator power is a function of stator parameter: $P_{av} = f(a, b, n)$. Fig. 23 shows that the change of number of turn coil varies the generator power. Using previous characteristics of the simulated linear PM generator, we obtained the highest average power ($P_{av} = 35(W)$) by $n = 8500(r/m)$. In Fig. 10, when turn coil sizes is changed ($a = 0.0833m, b = 0.12m$), maximum power is achieved by $n = 15000(r/m)$. This result indicates that when the turn coil size is determined, generator power will have a maximum at one determied number of turn coil.

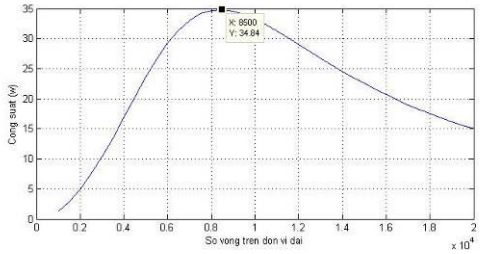

Figure 23: Average power function of the number of turn coil n

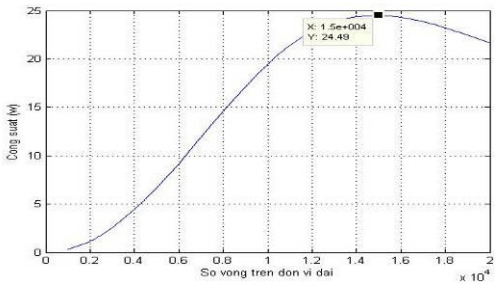

Figure 24: Average power function of the size of turn coil, $a = 0.0833m, b = 0.12m$

Similar Fig. 25 shows that generator power is dependent on turn coil size assuming number of turn coil determined. This result indicates that when the number of turn coil is determined, generator power will have a maximum at one determied turn coil size.

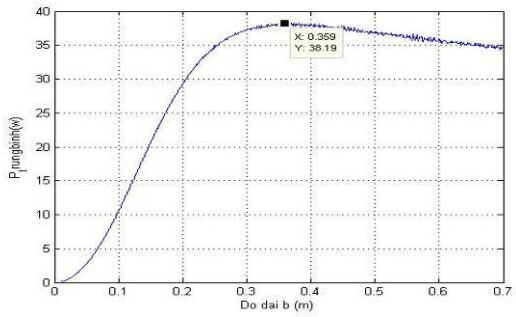

Figure 25: Maximum average power corresponds to turn coil size.

4. Conclusions

The concept of wave energy has been outlined and some different device types of WEC technology presented. The results from all of the papers show that the studied technology can convert the energy in the waves into electric energy.

The results show that the stator parameters of the WEC has influence on the power production. Comparisons with previous experimental results show significant, and indicate that the model is well suited for the design of wave energy converters of the studied type.

5. References

Boström, C. (2011). *Electrical Systems for Wave Energy Conversion*, Uppsala Dissertion, Acta Universitatis Upsaliensis

Callaghan, J. and Boud, R. (2006). *Future marine energy: results of the marine energy challenge: cost competitiveness and growth of wave and tidal stream energy*, Technical report, The Carbon Trust.

Drew, B., Plummer, A. and Sahinkaya, M. (2009). *A review of wave energy converter technology*. Proceedings of the Institution of Mechanical Engineers, Part A: Journal of Power and Energy, 223 (8). pp. 887-902. ISSN 0957-6509

Duckers, L. (2004). *Renewable energy* (Ed. G. Boyle), 2nd edition, Oxford University Press, Oxford, UK.

Duckers, L. (2004). *Wave energy. In Renewable energy*, 2nd edition, Oxford University Press, Oxford, UK.

Báo cáo đề tài KC.09.19/06-10. *Nghiên cứu đánh giá tiềm năng các nguồn năng lượng biển chủ yếu và đề xuất các giải pháp khai thác*, Bộ Khoa học và Công Nghệ.

Previsic, M. (2004). *Offshore wave energy conversion devices*, Technical report E21 EPRI WP-004-US-Rev 1, Electrical Power Research Institute.

Salter, S. H. (1974). *Wave power*. Nature, 49(5459), 720–724.

Thorpe, T. W. (1999). *A brief review of wave energy*, Technical reportno. R120, Energy Technology Support Unit (ETSU), A report produced for the UK Department of Trade and Industry.

The 2nd International Conference on Engineering Mechanics and Automation (ICEMA2)
Hanoi, August 16-17, 2012
ISBN: 978-604-913-097-7

ANSYS FLUENT and a preliminary application for simulation of Taylor-Couette flow

Dang Thi Hoa[a], Nguyen Tat Thang[a,c], Duong Ngoc Hai[a,b], Bui Dinh Tri[a,b] and Ha Tien Vinh[a]

[a] *Institute of Mechanics, Vietnam Academy of Science and Technology*
[b] *University of Engineering and Technology, Vietnam National University, Ha Noi, Viet Nam*
[c] *Tokyo Institute of Technology, Tokyo, Japan*
E-mail:ntthang@imech.ac.vn; ntthang_imech@yahoo.com

Abstract

ANSYS FLUENT is a fluid dynamics component software of ANSYS WORKBENCH. ANSYS FLUENT solver is basically based on the finite volume method (FVM) for general turbulent flows using various turbulence simulation techniques. It is capable of simulation of a wide range of research and engineering flows at high accuracy and reliability such as: general turbulent flows in fluid dynamics, thermodynamics, reacting flows in highly complicated geometries. ANSYS FLUENT is very flexible and powerful for complicated geometry modeling and mesh generation. It is capable of generating and treating both structured and unstructured mesh types. Boundaries of complicated geometries therefore can be adapted well in to simulation models. Many research and training institutions and engineering companies in Vietnam have applied this software. The Department for Industrial and Environmental Fluid Dynamics, Institute of Mechanics, Vietnam Academy of Science and Technology (VAST) has deployed this software under an academic license. This paper will present about the preliminary implementation of this software in research in Institute of Mechanics. Some simulation results using this software for the well-known Taylor-Couette flow will be given as a practical application of FLUENT in both research and engineering calculations.

Key Words: ANSYS FLUENT, Taylor-Couette flow, numerical simulation, CFD

1. Giới thiệu về phần mềm Ansys Fluent

Phần mềm Ansys Fluent thuộc dòng sản phẩm Ansys CFD có bộ giải CFD tiên tiến được ứng dụng rộng rãi trong mọi lĩnh vực công nghiệp, giải quyết các vấn đề về các dòng chảy rối tổng quát bao gồm: dòng chảy chất lưu, truyền nhiệt, truyền khối, dòng chảy cùng các phản ứng hóa học với các dạng mô hình hình học phức tạp. Ansys Fluent cung cấp sự linh hoạt và tự động trong cách chia lưới: lưới có cấu trúc, lưới không cấu trúc, lưới hỗn hợp, lưới trượt, lưới biến dạng…

Cách thiết lập các điều kiện biên, định nghĩa thuộc tính chất lưu, phương pháp giải, tinh chỉnh lưới, xử lý và biểu diễn kết quả đều được thực thi trong phần mềm Ansys Fluent. Ansys Fluent cho phép thay đổi cách thiết lập mô hình dễ dàng, xử lý kết quả nhanh nên đỡ tốn thời gian tính toán. Cho

phép ta xem được kết quả tính toán cũng như ứng xử của mô hình từ đó tiết kiệm thời gian,công sức, giảm chi phí cho thực nghiệm.

Ansys Fluent mô phỏng dựa trên cơ sở toán học bằng việc giải số hệ các phương trình Navier-Stokes dạng tổng quát bao gồm các phương trinh sau:

- phương trình bảo toàn khối lượng (phương trình liên tục),
- phương trình bảo toàn năng lượng,
- phương trình bảo toàn động lượng,
- phương trình bảo toàn chất,
- phương trình truyền tải,
- các phương trình mô tả các tác động của lực tương tác giữa các vật, lực khối,
- …

Các phương trình vi phân, đạo hàm này sẽ được rời rạc hóa và giải thông qua việc sử dụng các phương pháp số với các điều kiện biên, điều kiện ban đầu. Phương pháp số được sử dụng trong Fluent là phương pháp thể tích hữu hạn. Rất nhiều các kỹ thuật tính toán, mô phỏng và đóng kín rối khác nhau được áp dụng trong bộ giải của phần mềm Ansys Fluent.

Trong giao diện sử dụng của Ansys Fluent cho phép ta lựa chọn một trong hai bộ giải sau: bộ giải dựa trên áp suất (Pressure Based) hoặc bộ giải dựa trên mật độ (Density Based). Cả hai bộ giải này đều dựa trên một nguyên lý chung như sau:

- Phân chia miền tính toán thành hữu hạn tập hợp các thể tích điều khiển (control volume) hay còn gọi là các ô lưới tính toán.
- Tích phân các phương trình chủ đạo dựa trên các thể tích điều khiển đơn lẻ để xây dựng các phương trình đại số đối với các biến rời rạc phụ thộc như vận tốc, áp suất, nhiệt độ và bảo toàn các đại lượng vô hướng.
- Các phương trình vi phân từng phần liên tục (các phương trình chủ đạo) được rời rạc hóa thành hệ các phương trình sai phân dưới dạng hệ các phương trình đại số tuyến tính mà máy tính có thể giải được sử dụng các phương pháp giải hệ đại số tuyến tính thông thường (các phương pháp lặp hoặc giải trực tiếp).

Hai bộ giải trên đều thực hiện quá trình rời rạc hóa giống nhau (dựa trên phương pháp thể tích hữu hạn) nhưng cách tiếp cận sử dụng để tuyến tính hóa và giải quyết các phương trình rời rạc là khác nhau.

Bộ giải dựa trên áp suất coi động lượng và áp suất (hoặc áp suất hiệu chỉnh) là các biến chính. Hai thuật toán dùng trong bộ giải dựa trên áp suất đó là thuật toán độc lập và thuật toán liên kết.

- Thuật toán độc lập: giải áp suất hiệu chỉnh và động lượng một cách liên tục;
- Thuật toán liên kết: giải áp suất và động lượng đồng thời với nhau.

Sơ đồ thuật toán của bộ giải dựa trên áp suất được đưa ra như sau:

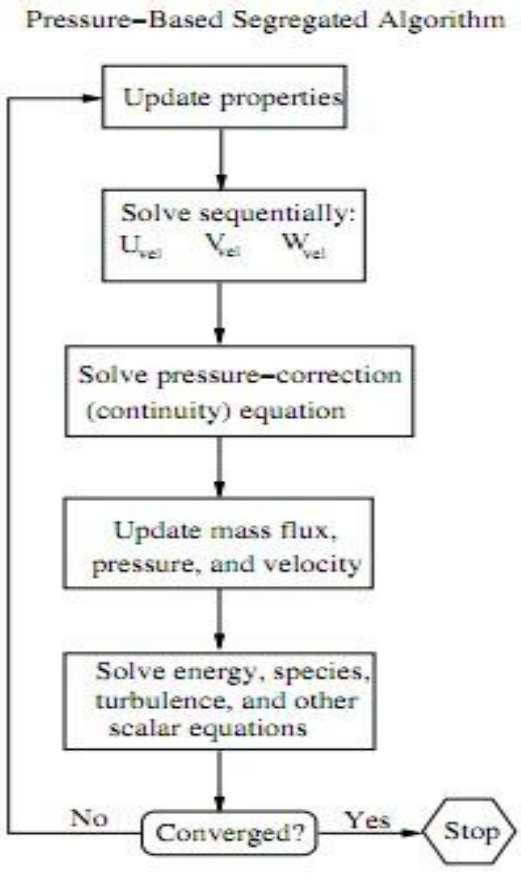

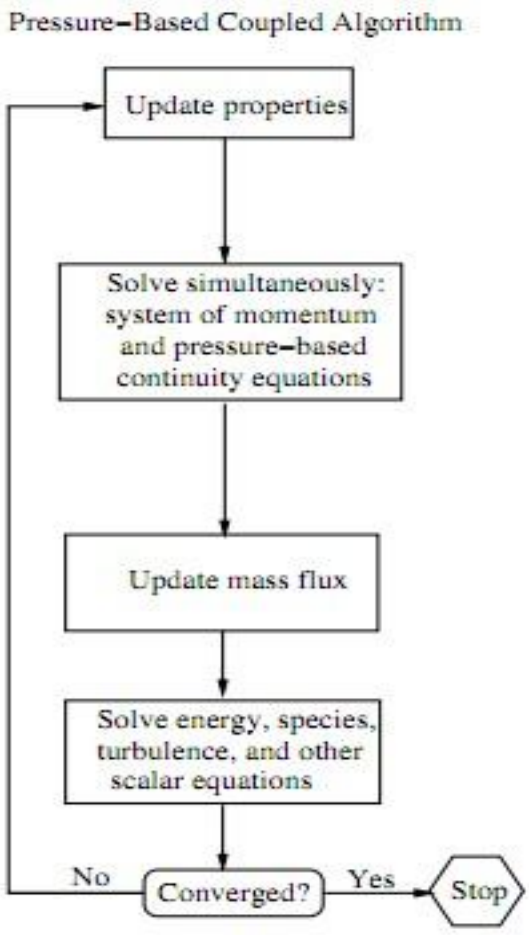

Hình 1 Sơ đồ thuật toán Pressure Based

Bộ giải dựa trên mật độ thì các phương trình liên tục, động lượng, năng lượng và truyền chất (nếu có) đều được giải dưới dạng vector. Áp suất đạt được qua phương trình trạng thái, các phương trình vô hướng bổ sung được giải theo cách riêng. Bộ giải dựa trên mật độ có thể giải tường minh hoặc giải ẩn (Explicit hoặc Implicit)

- Sơ đồ Implicit: dùng phương pháp điểm-ẩn Gauss-Seidel đối xứng để giải cho các biến;
- Sơ đồ Explicit dùng phương pháp tích phân tường minh thời gian đa bước Runge-Kutta.

Sơ đồ khối của thuật toán bộ giải dựa trên mật độ như sau:

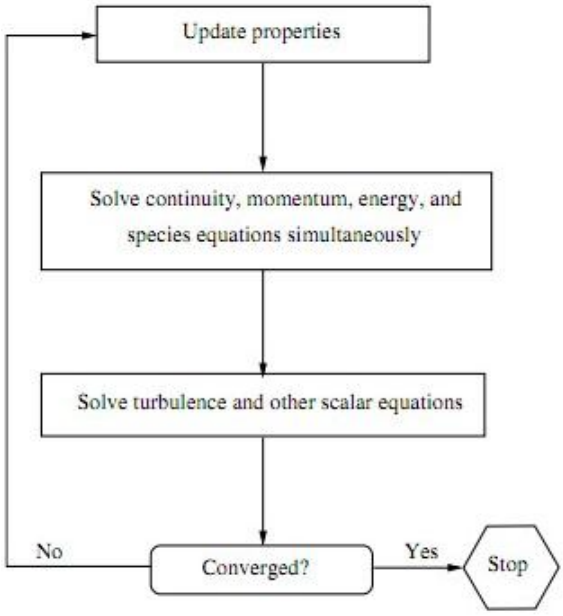

Hình 2 Sơ đồ khối của bộ giải Density Based

Trình tự của mô phỏng CFD (Computational Fluid Dynamics) sử dụng phần mềm Ansys Fluent bao gồm các bước như sau:

Nhận diện bài toán:

- Xác định mục tiêu;
- Nhận dạng miền tính toán.

Tiền xử lý (Pre-processing):

- Hình học;
- Lưới;
- Các mô hình vật lý;
- Thiết lập trình giải;
- Thiết lập tất cả các tham số có liên quan.

Giải:

- Giải số các phương trình.

Hậu xử lý (Post-processing):

- Xem xét kết quả.

Đối với mọi bài toán mô phỏng (trong nghiên cứu hay trong các ứng dụng công nghệ, kỹ thuật công nghiệp) sử dụng Ansys Fluent, các bước trên đều phải được tuân thủ. Ansys Fluent là phần mềm tính toán CFD có

khả năng mạnh và được hỗ trợ đầy đủ từ khâu chuẩn bị số liệu, mô hình hình học, chia lưới, thiết lập, lựa chọn các tham số tính toán cho đến việc biểu diễn đồ họa 3D các kết quả tính toán đầu ra [1,2].

2. Ứng dụng phần mềm Ansys Fluent tính toán mô phỏng dòng chảy Taylor Couette

2.1. Định nghĩa về dòng chảy Taylor Couette và các chế độ dòng chảy của nó

Trong động lực học chất lưu, dòng chảy Taylor Couette là dòng chảy quen thuộc trong cả nghiên cứu lý thuyết (tính ổn định và bất ổn định trong cơ học chất lỏng) và các ứng dụng thực tiễn trong công nghiệp (các thiết bị phân tách ly tâm, nghiên cứu giảm lực cản v.v.). Dòng Taylor-Couette được định nghĩa là dòng chảy chất lỏng nhớt giới hạn trong vùng giữa hai ống trụ quay đồng trục (Hình 3). Trong dòng chảy Taylor-Couette, số Reynolds được định nghĩa như sau:

$$\mathrm{Re} = \frac{\omega_1 R_1 (R_2 - R_1)}{\nu}$$

Trong đó ω_1 là vận tốc góc quay của trụ trong; R_1 và R_2 lần lượt là bán kính của trụ trong và trụ ngoài; ν là hệ số nhớt động học của chất lỏng.

Khi vận tốc góc tăng dần từ 0, dòng Taylor-Couette sẽ trải qua các chế độ dòng chảy khác nhau phụ thuộc vào vận tốc góc như sau. Với vận tốc góc nhỏ, thể hiện bởi số Reynold (Re) nhỏ, dòng chảy là phân tầng, dừng. Trạng thái cơ bản này được gọi là dòng chảy Taylor-Couette tròn (Circular Couette Flow - CCF). Khi tăng vận tốc góc của ống trụ trong lên một giá trị nào đó thì dòng Couette trở nên mất ổn định và xác lập trạng thái dừng thứ hai được mô tả bởi các xoáy tròn đối xứng trục và được gọi là dòng Taylor Vortex Flow (TVF). Tiếp tục tăng vận tốc góc của ống trụ trong, hệ thống trải qua một quá trình bất ổn định dẫn đến trạng thái không gian - thời gian phức tạp hơn, trạng thái tiếp theo này được gọi là dòng Wavy Vortex Flow (WVF - trạng thái mà các xoáy tròn đối xứng trục trong chế độ TVF bắt đầu có dao động sóng trong mặt phẳng ngang với một tần số sóng). Khi số Re vượt qua một giá trị nào đó thì có sự xuất hiện dạng tiếp theo của dao động sóng được gọi là Modulated Wavy Vortex (MWV - dao động sóng có nhiều tần số). Cuối cùng khi Re tiếp tục tăng thì dòng chảy phát triển đến chế độ bất ổn định hỗn loạn (chaos) và thường được xem là dòng rối.

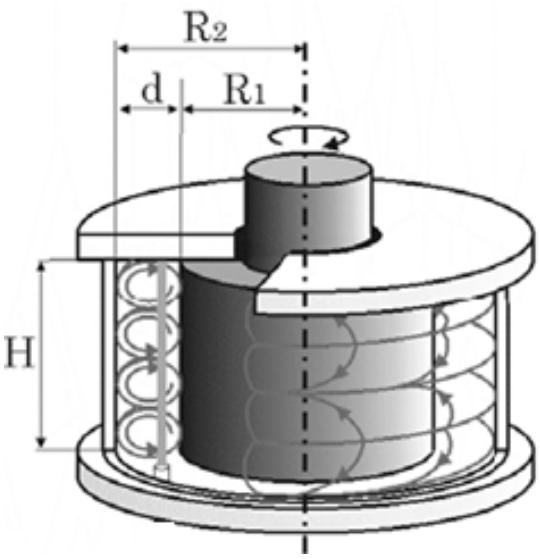

Hình 3 Dòng Taylor-Couette trong miền đóng kín

2.2. Điều kiện ổn định của dòng chảy Taylor Couette

Dòng chảy Taylor-Couette trong mô hình hai ống trụ đồng trục với ống trụ ngoài cố định và ống trụ bên trong quay thì dòng chảy Taylor-Couette trở nên mất ổn định khi số Re vượt ngưỡng một giá trị nào đó và được gọi là giá trị số Reynold tới hạn Re_{crit}. Tương ứng với Re_{crit} có số Taylor tới hạn Ta_{crit}. Theo Wei *et al*. (1992), số Taylor (Ta) được định nghĩa như sau:

$$Ta = \frac{\omega_1^2 R_1 (R_2 - R_1)^3}{\nu^2} \text{ hay}$$

$$Ta = \mathrm{Re}^2 \left(\frac{1}{\eta} - 1 \right) \text{ trong đó } \eta = \frac{R_1}{R_2} \text{ được}$$

gọi là hệ số tỷ lệ bán kính. Số Taylor tới hạn: Ta_{crit} =1712 [3,4].

2.3. Mô hình tính toán ứng dụng phần mềm Ansys Fluent

2.3.1. Mô tả bài toán

Xét bài toán chất lỏng nhớt chuyển động trong vùng không gian giới hạn bởi hai ống trụ đồng tâm có trụ trong quay và trụ ngoài cố định (bài toán dòng chảy Taylor-Couette). Kích thước của hai ống trụ lần lượt là R_1 = *50 mm*, R_2 = *75 mm*, H = *75* mm được mô tả như trong Hình 4.

Các thuộc tính của chất lỏng được sử dụng:

- Glyxerol 68 % khối lượng (glyxeryl);
- Mật độ khối lượng ρ = 1.17313 g/ml;
- Độ nhớt động học ν = 15.149 mm^2/s;

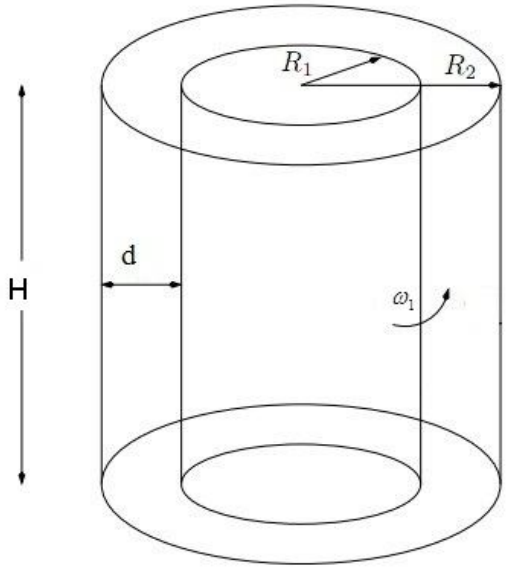

Hình 4 Mô hình hai ống trụ đồng tâm

2.3.2. Một số kết quả tính toán

2.3.2.1. Mô phỏng dòng Taylor Couette ở chế độ CCF

Thiết lập tính toán cho mô hình dòng chảy Taylor-Couette chế độ CCF:

Mô hình hình học dòng chảy Taylor-Couette được trình bày trong Hình 3,4. Trong đó trụ trong quay, trụ ngoài cố định. Hai biên trên và dưới là các biên cố định. Như vậy dòng chảy được giới hạn (đóng kín bởi các biên cứng) trong đó có biên bên trong chuyển động:

- Tỷ lệ bán kính (radius ratio): ξ = 3;
- Tỷ lệ phân bố (aspect ratio) Γ =3;

trong đó $\xi = \frac{R_2}{R_1}$, $\Gamma = \frac{H}{d}$; với H thông thường được định nghĩa là chiều cao cột chất lỏng (trong trường hợp dòng Taylor-Couette có biên trên đóng kín, H cũng chính bằng chiều cao hình học của các trụ quay).

Lưới tính toán có cấu trúc gồm các phần tử dụng hình hộp tổng quát. Các thông số của lưới tính toán bao gồm:

- Số phần tử chia theo phương bán kính (Radial number divisions): 25
- Số phần tử chia theo chu vi của hai trụ (Angular number divisions): 34
- Số phần tử chia theo hướng trục (Axial number divisions): 80
- Tổng số phần tử tính toán của toàn mô hình (Total number of elements): 68000

Thiết lập lời giải cho bài toán như sau:

Bộ giải (Solver):

- Steady
- Absolute Velocity
- Pressure Based

Các tham số mô hình được lựa chọn (Models):

- Energy Model: On
- Viscous Model: Laminar

Vật liệu (Material): Glyxerol 68% khối lượng

với các tính chất như sau:

- ρ = 1.17313 g/ml
- μ = 0.017772 g/(mm.s)

Miền tính toán (Cell Zone Conditions):

- Fluid: Glyxerol

Các điều kiện biên (Boundary Condition):

- Biên trên và dưới (Top and Bottom): Biên cứng (Wall, symmetry);
- Biên trụ trong (Inner Wall): biên quay tương đối với các phần tử xung quanh; có tính đến nhiệt (Moving Wall, Relative to Adjacent Cell Zone); Vận tốc góc quay (Rotational speed): ω_1 = 5 (rpm); Nhiệt (Thermal): nhiệt độ (Temperature) xác định theo đo đạc: 22^0C.
- Biên trụ ngoài cố định (Outer Wall): cố định (Stationary Wall); Nhiệt (Thermal): nhiệt độ (Temperature): 22^0C.

Các thiết lập sơ đồ tính toán nghiệm số (Solution Methods):

- Pressure–Velocity Coupling
  - Scheme: SIMPLE
- Spatial Discretization:
  - Gradient: Least Squares Cell Based
  - Pressure: Standard
  - Momentum: QUICK
  - Energy: QUICK

Trường hợp này ứng với dòng chảy Taylor-Couette phân tầng ổn định (CCF - Circular Couette Flow). Các kết quả mô phỏng tính toán sử dụng Ansys Fluent được trình bày trong các hình dưới đây.

Kết quả tính toán:

Hình 5 và 6 lần lượt trình bày contour vận tốc trong mặt cắt thẳng đứng và phân bố vector vận tốc trong mặt cắt ngang. Kết quả tính toán cho thấy hình ảnh dòng chảy phân tầng CCF trong trường hợp dòng chảy có số Re nhỏ.

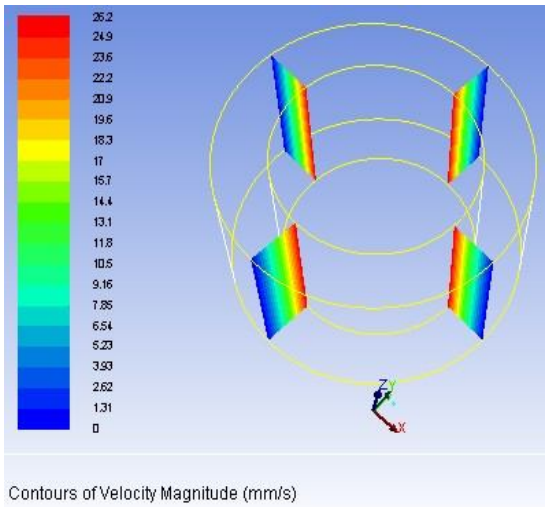

Hình 5 Contour vận tốc với ω_1 = 5 rpm

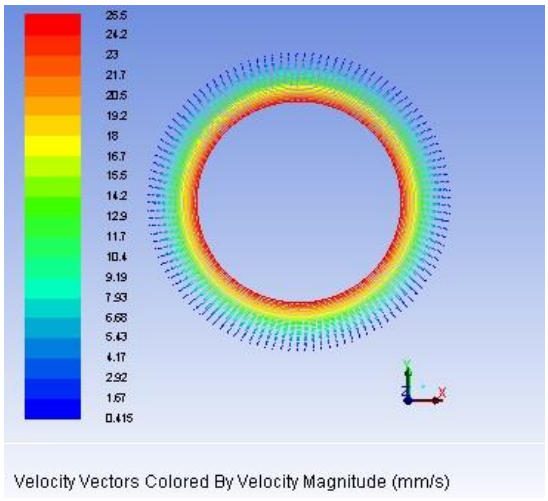

Hình 6 Vector vận tốc tại mặt Z = 37.5 mm

2.3.2.2. Mô phỏng dòng Taylor Couette ở chế độ TVF

Thiết lập mô hình và các tham số tính toán cho mô hình dòng chảy Taylor Vortex Flow chế độ TVF:

Về mô hình hình học (Geometry model), lưới tính toán (Grid), bộ giải (Solver), và các lự chọn khác như: Models, Material, Cell Zone Conditions, về cơ bản hoàn toàn tương tự như trường hợp mô phỏng dòng Taylor-Couette chế độ CCF.

Điều kiện biên Boundary Condition:

- Biên trên và dưới (Top and Bottom boundaries): Symmetry

- Biên trụ quay bên trong (Inner Wall): biên quay (Moving Wall, Relative to Adjacent Cell Zone); vận tốc góc quay (Rotational speed): ω_1 = 12 (rpm); Nhiệt (Thermal Temperature): 22^0C.
- Biên ngoài (Outer Wall): biên trụ cố định (Stationary Wall); Nhiệt (Thermal Temperature) 22^0C.

Phương pháp giải (Solution Methods):

- Pressure-Velocity Coupling
  - Scheme: PISO
- Rời rạc hóa không gian (Spatial Discretization):
  - Gradient: Least Squares Cell Based
  - Pressure: PRESTO
  - Monetum: QUICK
  -
  - Energy: QUICK

Kết quả tính toán:

Khi số Re tăng lên và vượt giá trị Re tới hạn, các bất ổn định xuất hiện trong dòng chảy và chế độ dòng chảy Taylor Couette chuyển từ chế độ CCF sang chế độ TVF. Trong chế độ này, dòng chảy đặc trưng bởi hai chuyển động: chuyển động theo hướng quay của trụ trong và chuyển động trong mặt phẳng thẳng đứng dưới dạng các xoáy Taylor (Taylor Vortex). Kết hợp của cả hai chuyển động này sẽ có dạng các ống trụ xoáy còn gọi là các vortex ring. Các Hình 7 và 8 dưới đây trình bày kết quả tính toán mô phỏng sử dụng Ansys Fluent ứng với trường hợp dòng chảy TVF.

Các kết quả tính toán trong trường hợp này cho thấy tồn tại 4 xoáy Taylor trong mặt phẳng thẳng đứng. Các tính toán của chúng tôi cho thấy quá trình hình thành của các xoáy và số lượng của chúng trong mô phỏng số có quan hệ tới mô hình mô phỏng được thiết lập gồm: tính chất của lưới tính toán (ảnh hưởng của lưới tới kết quả tính toán mô phỏng CFD), gia tốc góc quay của trụ trong được sử dụng. Trong các tính toán của chúng tôi được thực hiện ở đây, vận tốc góc của trụ trong được cho bằng hằng số ngay từ khi bắt đầu tính toán do đó ảnh hưởng của gia tốc đến quá trình hình thành các xoáy không được xem xét.

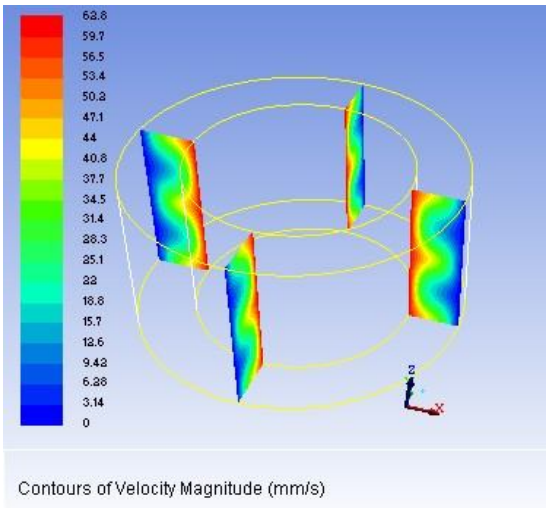

Hinh 7 Contour vận tốc dòng chảy TVF ứng với ω_1 = 12 rpm

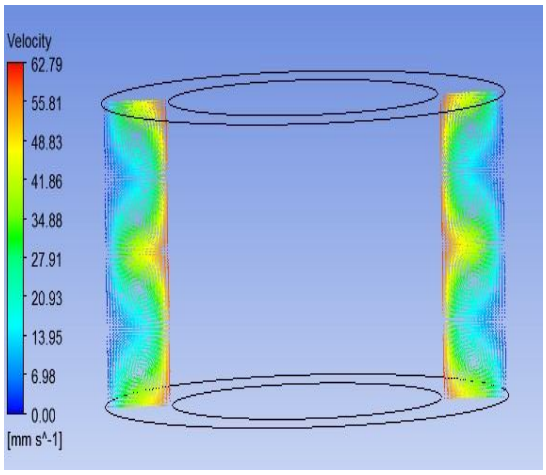

Hinh 8 Vector vận tốc theo phương tiếp tuyến (vận tốc trong mặt phẳng thẳng đứng)

So sánh với kết quả đo đạc:

Để đảm bảm mô hình tính toán mô phỏng CFD sử dụng Ansys Fluent cho kết quả chính xác, các kết quả tính toán được so sánh với số liệu đo đạc thực nghiệm dòng chảy Taylor-Couette [5]. Bước đầu kết quả thực nghiệm về quan sát trường vận tốc dòng chảy trong mặt phẳng thẳng đứng sử dụng kỹ thuật

quang học (camera và mặt phẳng sáng laser) được sử dụng.

Kết quả thực nghiệm cho thấy ứng với mỗi chế độ dòng chảy (TVF, WVF, MWV), còn có các chế độ dòng chảy thứ cấp căn cứ trên số lượng xoáy được hình thành [5]. Sự hình thành các chế độ dòng chảy thứ cấp phụ thuộc vào trạng thái bất ổn định hình thành trước đó trong chất lỏng. Trong thực nghiệm các chế độ dòng chảy thứ cấp được tạo ra bằng cách điều chỉnh gia tốc của trụ quay bên trong. Kết quả so sánh được được trình bày trong Hình 9 cho trường hợp dòng chảy có 2 xoáy (mode N2 - còn gọi là mode sơ cấp hay normal mode, [5]). Hiện tại trong kết quả mô phỏng chúng tôi mới thu nhận được các mode N2 và N4.

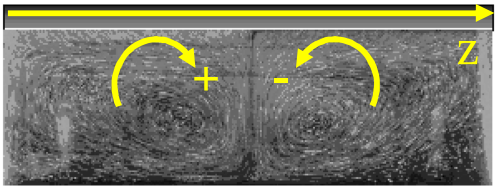

a)

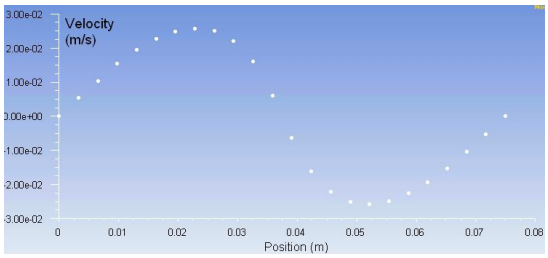

b)

Hinh 9 So sanh trường vận tốc trong chế độ dòng chảy 2 xoáy (a: kết quả quan sát đo đạc trường dòng chảy, b: kết quả tính toán)

Hình 9 a và b tương ứng trình bày kết quả đo đạc và tính toán dòng chảy Taylor-Couette chế độ TVF ứng với mode N2. Hình 9 b trình bày kết quả tính toán profile vận tốc hướng trục dọc theo đường vàng trong Hình 9 a. Hai xoáy được thể hiện chi tiết trong kết quả tính toán.

Kết quả so sánh cụ thể độ lớn vận tốc tính toán và đo đạc của cùng 1 profile sẽ được trình bày trong các báo cáo khoa học tiếp theo khi chế độ dòng chảy trong tính toán được thiết lập trùng khớp với chế độ dòng chảy có số liệu đo đạc.

3. Nhận xét và kết luận

Việc triển khai áp dụng phần mềm CFD Ansys Fluent tại Phòng Thủy khí Công nghiệp và Môi trường Lục địa, Viện Cơ học, Viện Khoa học và Công nghệ Việt Nam đã bước đầu được thực hiện cho kết quả tốt. Đây là một bộ chương trình CFD đồ sộ và phức tạp, việc tìm hiểu sử dụng chương trình đã bắt đầu được thực hiện. Kết quả áp dụng cho tính toán dòng chảy Taylor-Couette đã cho một số kết quả ban đầu. Đây là hướng áp dụng có ý nghĩa trong cả nghiên cứu (lý thuyết) lẫn trong tính toán dòng chảy kỹ thuật - công nghiệp, tự động hóa thiết kế v.v.

Các kết quả thu được từ mô phỏng CFD sử dụng phần mềm Ansys Fluent trong 2 chế độ của dòng chảy Taylor Couette là Circular Couette Flow (CCF) và Taylor Vortex Flow (TVF) cho thấy kết quả tính toán thu được là hoàn toàn phù hợp về mặt định tính với lý thuyết dòng chảy Taylor Couette. Các mô phỏng với số Re cao hơn hoàn toàn dễ dàng được thực hiện trong mô phỏng CFD (thay đổi vận tốc góc trong mô hình). Tuy nhiên việc trình bày dạng đồ họa các chế độ dòng chảy tương ứng với WVF, MWV và chế độ dòng rối (turbulent) sẽ được chúng tôi thực hiện và báo cáo trong một báo cáo khoa học tiếp theo.

Với trường hợp so sánh dòng chảy Taylor Couette ở chế độ TVF với kết quả thực nghiệm cho thấy kết quả mô phỏng sử dụng phần mềm Ansys Fluent đã thể hiện được kết quả đo đạc thí nghiệm. Các tính toán đang được chúng tôi tiếp tục thực hiện cho nhiều mode khác nhau của dòng Taylor-Couette nhằm nghiên cứu các hiệu ứng cụ thể của lưới tính toán và gia tốc góc quay của trụ trong tới chế độ dòng chảy và kết quả tính toán. Theo đó các so sánh cụ thể về độ lớn của các tham số tính toán (profile vận tốc) sẽ được thực hiện giữa 2 mode tương đương

nhau giữa thực nghiệm và mô phỏng số. Hiện tại trong tính toán chúng tôi mới thu nhận được các mode N2 và N4 của dòng chảy.

Đặc biệt qua các kết quả bước đầu áp dụng phần mềm CFD trong tính toán dòng chảy Taylor-Couette cho thấy vai trò rất quan trọng của tính toán trong việc định hướng, thiết kế và hiệu chỉnh phương pháp đo đạc phù hợp. Kết quả đo đạc đối chiếu với kết quả mô phỏng sẽ góp phần hoàn thiện phương pháp và kết quả đo. Ngược lại kết quả đo đạc cung cấp số liệu tin cậy để hiệu chỉnh mô hình CFD.

4. Tài liệu tham khảo

1. Ansys Fluent 12.0 (2009), Getting Started Guide, April 2009
2. Ansys Fluent 12.0 (2009), Theory Guide, April 2009
3. S. Dong (2007), Direct numerical simulation of turbulent Taylor Couette fow, *J. Fluid Mech.*, Vol. 587, pp. 373 – 393.
4. Frank M. White (1992), Viscous Fluid Flow, pp. 110-114.
5. D. Ito, S. Kishikawa, H. Kikura, H. Kawai, M. Aritomi and H. Takahashi (2004), UVP measurement of Taylor-Couette vortex flow with small aspect ratio, *Proc. 4th International Symposium on Ultrasonic Doppler Method for Fluid Mechanics and Fluid Engineering*, Sapporo, 6.-8. September, 2004, pp. 149-152.

The 2nd International Conference on Engineering Mechanics and Automation (ICEMA2)
Hanoi, August 16-17, 2012
ISBN: 978-604-913-097-7

On a Coupling Numerical Model for Calculating Tide, Surge and Waves in Stormy Condition for Nam Dinh Coastal Area

Thu Ha D. T.[a] and Manh D. V. [b]

[a] *Institute of Mechanics, VAST, 264 Doi can, Ba dinh, Hanoi, dtthuha@imech.ac.vn*
[b] *University of Engineering and Technology, VNU, 144 Xuan Thuy, Cau Giay, Hanoi*

Abstract

This paper presents some results of WST12 model applied for calculating storm tide and wave in stormy condition in Nam Dinh coastal area. The WST12 model was developed and improved by Department of Marine Mechanics and Environment, Institute of Mechanics on the basis of combination of CHB10 and the Simulating WAves Neashore (SWAN) models. The CHB10 model is based on a system of nonlinear shallow water equations, using the finite difference method, patching and wet/dry technique, and This SWAN model is a third-generation stand-alone (phase-averaged) wave model for the simulation of waves in waters of deep, intermediate and finite depth, using unstructured grids. The WST12 coupling model can be applied to simulate tide, surge and wave in coastal areas in which it may have a significant nonlinear interaction between the phenomena.

In order to apply for the Nam Dinh coastal area, a grid system with several different grid size (down to grid size of 200 m) have been was established. Several historical typhoons and calculating scenarios were carried out, then major characteristics of nonlinear interaction of tide, surge and wave during typhoons' acting were estimated.

Keywords: numerical model, tide, surge, wave, patching technique, swan

1. Introduction

In the Department of Marine Mechanics and Environment, Institute of Mechanics, the numerical modeling of tide and storm surge is developed and applied to the Viet Nam coastal area by using the CHB10 model. The effort of these researches has been concerned and determined with the accurate forecast of tides and storm surges [abc]. Manh, D.V.et al. (2007, 2008) developed a detailed database of tide and storm surge along the Vietnamese Coast to provide for sea dyke designing and coastal engineering activities. Thu Ha, D.T. and Manh, D.V. (2011) also applied the CHB10 model with several grids, in which the finest grid size is 300m, to simulation of inundation caused by storm surges in the coastal zone Thua Thien –Hue.

The generation of waves and storm surges is closely related, as they are both generated by wind. There exist strong nonlinear interactions between waves, tides and storm surges in shallow water. In the recent years, various studies have considered tide-surge-wave interaction mechanisms during typhoons and there have achieved some success.

This paper focuses on the application of a tide-surge-wave coupling model (WST12) for simulating tides, storm surges and waves during some typhoons in the Nam Dinh coastal area, and specifically investigates the effects of tides on wave field during typhoons. The WST12 model was developed by the Department of Marine Mechanics and Environment, Institute of Mechanics. This model is composed of the surge-tide model (CHB10) and the Simulating WAves Neashore model (SWAN). For some typical typhoon conditions, the coupling model simulation results are compared with those from an uncoupled model to give qualitative estimates and an appraisal of the effects of tides on typhoon waves in the Nam Dinh coastal area. In addition, for the these typical typhoons supposed that it hits the Nam Dinh coastal area at the same phases in the period tidal to estimated the effects of the tidal phase on typhoon waves. .

2. Mathematical models

Following models are incorporated to a coupling model to calculate surge, tide and wave during typhoons.

2.1. CHB10 model

Hydrodynamic and Environmental CHB10 model developed by Manh, D.V. at al. is modified to predict storm surges and tides. This model is based on the system of nonlinear shallow water equations, using the finite different method with patching technique. It allows detail simulated transmission and evolution of surges due to typhoons from ocean to the coastal areas with several nested grids scheme. This model is validated and calibrated with a low spatial resolution for almost typical typhoons which hit the Vietnam coastal zone. The results of surges due to typhoons simulation shows a good agreement with the observation.

2.2. SWAN model

A third-generation numerical wave model (SWAM) to computer random, short-crested waves in coastal regions with shallow water and ambient current was developed and verified by Booij et al. This model is applied to coastal regions with shallow water, islands, tidal flat and local wind as well as with horizontal scales less than 20-30km and water depths less than 20-30km. In addition, SWAN can be used on any scale relevant for wind generated surface gravity waves.

This model accounts for shoaling, refraction, generation by wind, whitecapping, triad and quadruplet wave-wave interactions, and bottom and depth-induced wave breaking. The basic equation in SWAN is the wave action balance equation.

2.3.Coupling process

Implementation of the coupling between wave and storm-tide models follows the procedure below:

i) The two models are initialized separately. Thus, the wave model is warmed up for 12 h, and the tide-surge model for 2 days. Initialization is performed in a manner permitting the synchronized coupling of two models.

ii) The wave model is run (in 5-min intervals) for 3 time intervals using the computed change in depth (mean water depth plus tide-surge elevation) and inhomogeneous unsteady currents from the two-dimensional tide-surge model to obtain wave parameters, such as the wave spectrum.

iii) The wave-dependent surface wind strees…. Back to the tide-surge model.

iv) The tide-surge model is run (in 15-min intervals) using the calculated …stress. This gives newly computed elevation and currents, which are passed back to the wave model to repeat the sequence of computation.

3. Application to Nam Dinh coastal area

3.1. Set up grid domain

A numerical model with 7 difference resolution nested girds has been set up and used to simulate tides, surges and waves during typhoons in the Nam Dinh coastal area. The different girds is nested from the coarse grids to the fine girds respectively from ocean to the Nam Dinh coastal area. Table 1 shows the parameters of 7 grids.

Table 1 Computational Grids

Grid	Num. grids	Grid size (°)	Long. (°)	Lat. (°)
1	67×71	0.1152	104.4022	13.92870
2	56×42	0.0576	104.6326	18.53670
3	70×54	0.0288	105.2086	19.11270
4	82×56	0.0144	105.7846	19.68870
5	102×60	0.0072	106.0726	19.97670
6	140×88	0.0036	106.2166	20.04870
7	200×122	0.0018	106.3066	20.12070

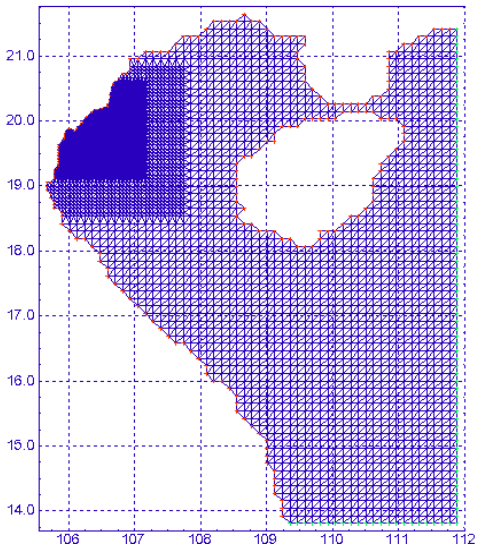

Fig.1 The scheme of the framework of nested grids

3.2. The typical typhoons is selected for the simulation

Historical typhoon data: All typhoons with their parameters acted in the South China Sea and landed on Vietnam coast are collected. The typhoon parameters are time, typhoon center's location, speed and direction of center movement, air pressure depression at center, maximum wind speed and its radius from the center and landed point. From 1957 to 2007, there are 313 typhoons occurred in the study area (in annual average, about 6 typhoons per year) as shown Fig2.

The five typical typhoons is selected from the lists of 67 typhoons hits or strongly effects to the Nam Dinh coastal area. The track of these typhoon is shown in Fig.2

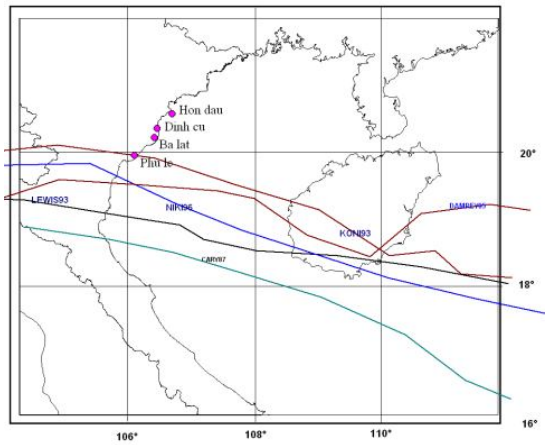

Fig.2 Track of typical typhoons for simulation

Typhoons Name	Landing Long. (°)	Landing Lat. (°)	Landing time	Vmax (m/s)
CARY.87	105.6	18.9	22-8-1987	36.0
LEWIS.93	105.8	19.3	12-7-1993	31.0
NIKI.96	105.9	19.7	22-8-1996	33.0
KONI.03	106.2	20.0	22-7-2003	31.0
DAMREY.05	105.8	19.6	27-9-2005	41.0

3.3. Calculating results

During the simulation, computed results of interest, such as significant wave heights, the directional wave spectrum, water surface elevations and velocities, with and without waves and storm tide interaction, can be output by the tide-surge-wave model, as described.

As mentioned before, tide and typhoon supposed are two natural independent phenomena. A typhoon can hit the coast at any tidal moment of high or low or in between. Therefore, a typhoon surge can combine incidentally any tide level.

With each historic typhoon, comparision of computed results of significant wave heights in with or without waves and storm tide interaction.

3.3.1. The history typical typhoon's calculating results

a) Cary87

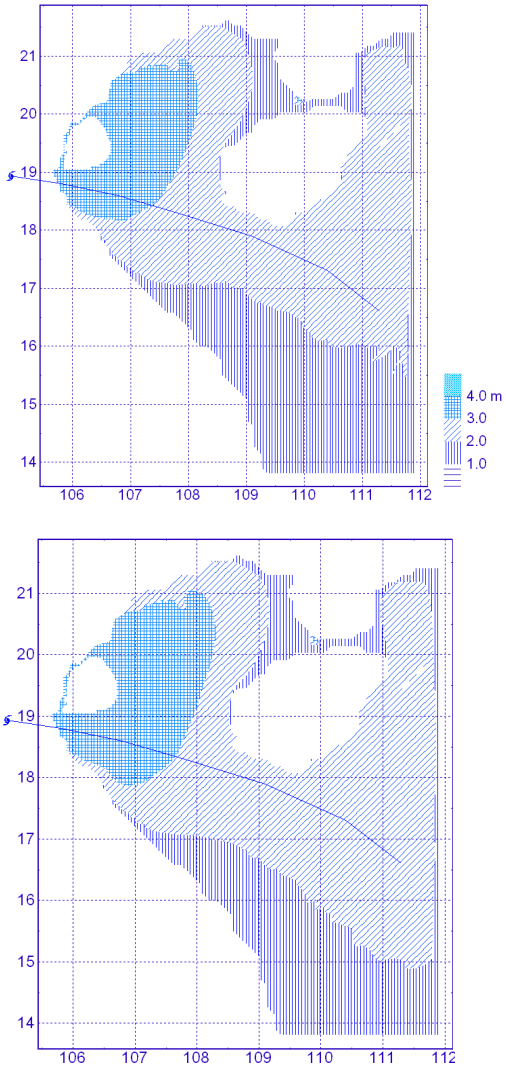

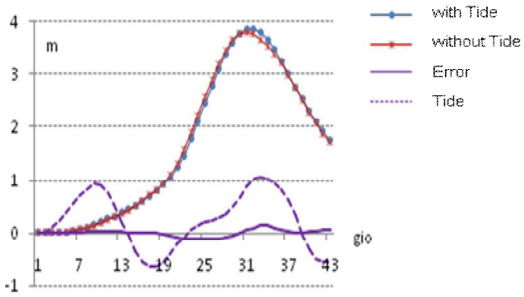

b) Lewis93

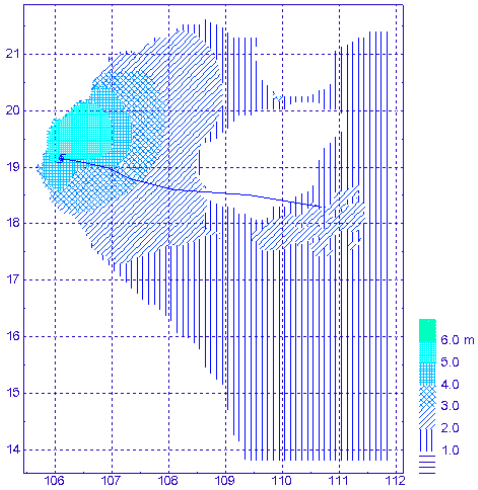

Abc

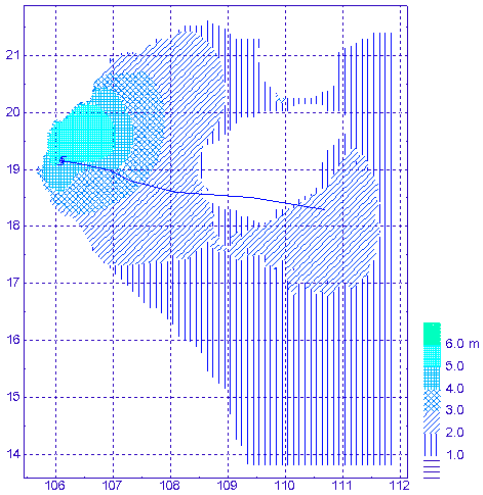

Abc

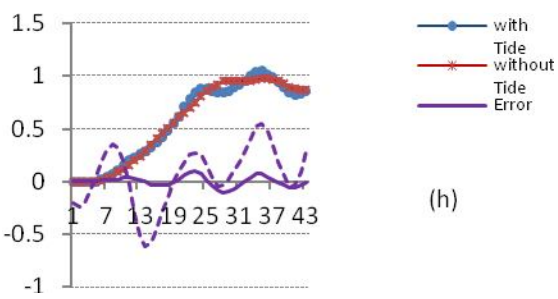

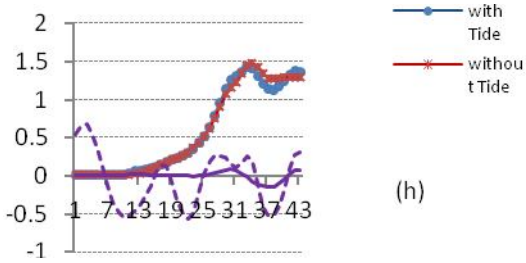

c) Niki96

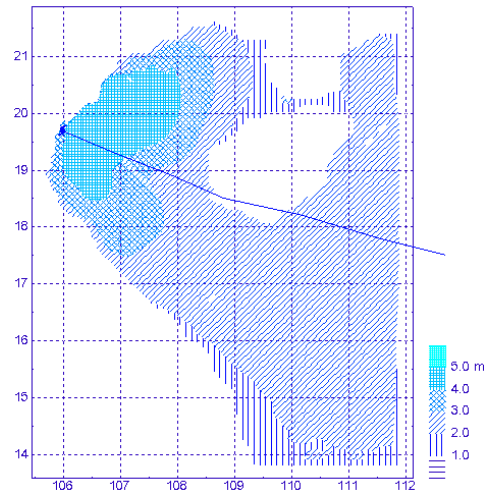

Abc

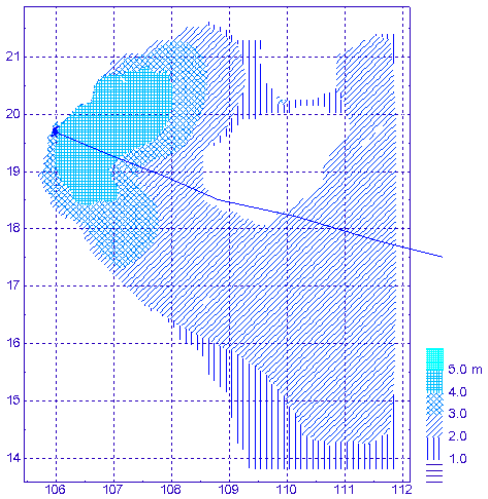

Abc

d) Koni03

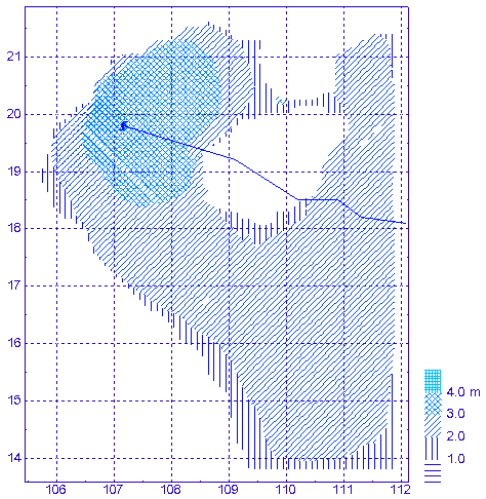

Abc

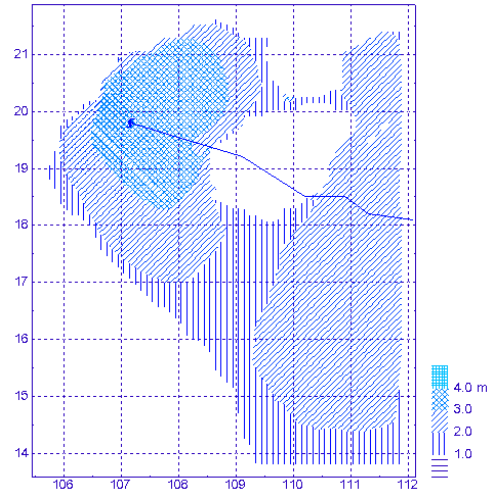

Abc

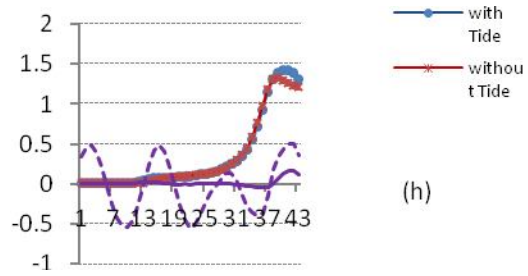

abc

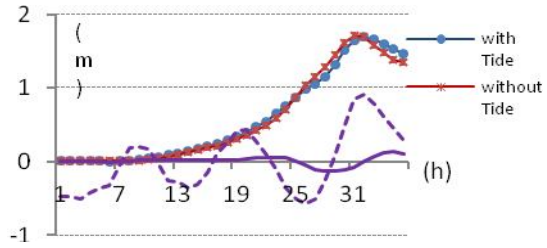

abc

e) Damrey05

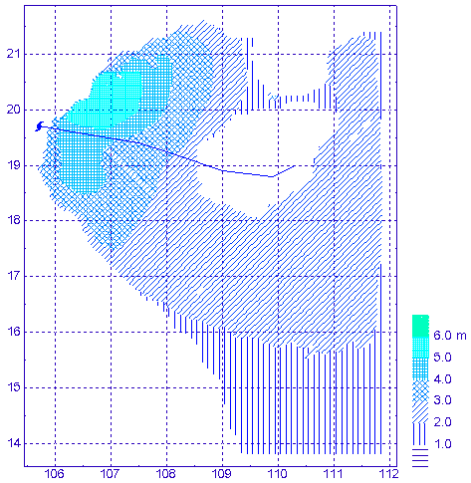

Abc

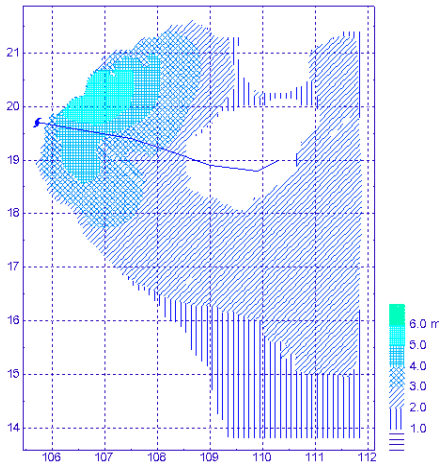

Abc

3.3.2. The calculating scenario results

As mentioned before, tide and typhoon supposed are two natural independent phenomena. A typhoon can hit the coast at any tidal moment of high or low or in between. Therefore, calculating scenarios were carried out to estimate the effect of any tide level on the wave filed during typhoon

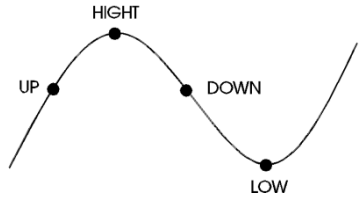

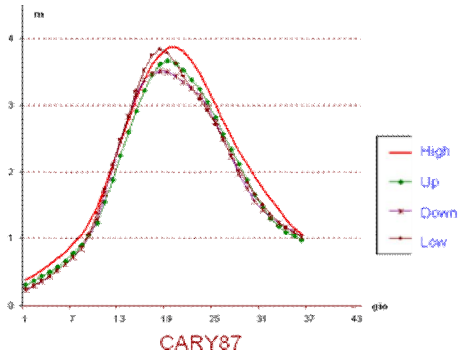

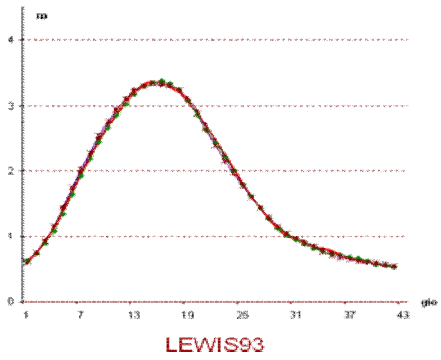

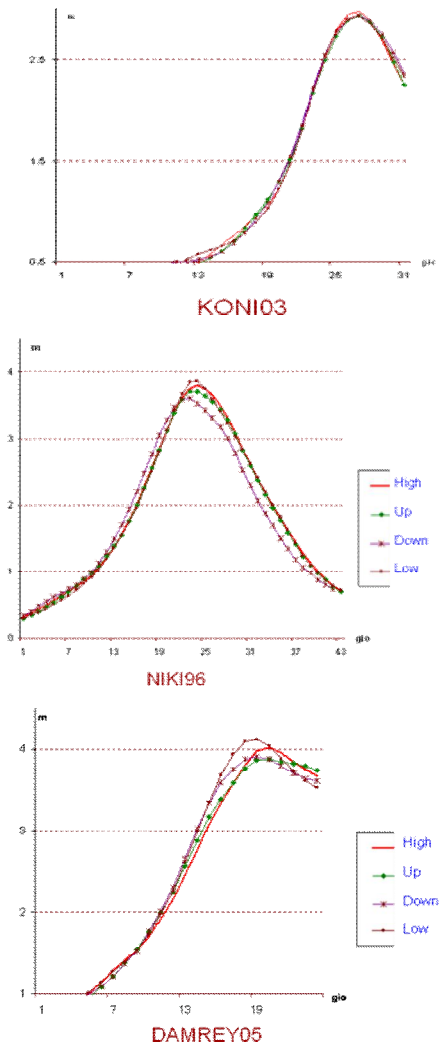

4. Conclusions

On the basis of the results on typhoon parameters and sea water levels mearured at tide gauges from 1957 to 2007 in the South China Sea, specially in the coast zone from Quangninh to Quangnam Provinces, as well as applying various models in statistic, hydrodynamics, the returned period curves (and annual exceedance probability) of storm surge plus tide at 96 points in distance of about 10km along the coast are produced. These curves are appropriate to use as the boundary condition in the design of sea dike as well as of other coastal constructions

- Calculating scenarios were carried out to show that there are differrently effect of any tide level on the wave filed during typhoon.
- With almost of typhoons, the Significant wave heights is higher at the high and down than at the low and up of tide level, Time of maximum of Significant wave heights is faster at the high and down than at the low and up of tide level

5. References

Do Ngoc Quynh and et al. (2001). *The Technology of forecast for surges due to typhoons*. Report of the National Project KT.03.06

Pham Van Ninh and et al. (1991). *The typhoon surges and Monsoons*. Report of the National Project 48B.02.02. Hanoi, Vietnam

Pham Van Ninh and et al. (1998). *The typhoon surges in Vietnam: the Regime Characteristics and Prediction*. Proceedings of the 5th Asian Science and Technology Week, Hanoi

Thu Ha D. T. and et al. (2009). *Mô phỏng số sóng thần do động đất trên biển Đông và vùng biển ven bờ Đà Nẵng*. Tuyển tập công trình Hội nghị khoa học Cơ học Thuỷ Khí Toàn quốc

Thu Ha D. T. and et al. (2009). *Mô phỏng số nước dâng do bão vùng ven biển Thừa Thiên – Huế*. Tuyển tập công trình Hội nghị khoa học Cơ học Thuỷ Khí Toàn quốc năm 2011. Cửa lò, Nghệ An

Thu Ha D. T. and et al. (2009). *Mô phỏng số nước dâng do bão vùng ven biển Thừa Thiên – Huế*. Tuyển tập công trình Hội nghị khoa học Cơ học Thuỷ Khí Toàn quốc năm 2011. Cửa lò, Nghệ An

Dinh Van Manh and et al. (2009). *A numerical model for calculating tide and typhoon surges in the coastal zone from Quangninh to Quangnam*. Proceedings of the National Conference on Fluid Mechanics

Dinh Van Manh and et al. (2007). *Preliminarily numerical simulations of Tsunamis caused by earthquakes in the East Sea*. Fluid Mechanics conference

Le Nhu Nga and Dinh Van Manh (2009*). Artificial Typhoon for calculating typhoon surge characteristics in the coastal zone from Quangninh to Quangnam*. Proceedings of the National Conference on Fluid Mechanics

Iwasaki T. and A. Mano (1979). *Numerical computation of two dimensional tsunami run-up based on Eulerian coordinate*. 26th coastal engineering conference, 70-74

The 2nd International Conference on Engineering Mechanics and Automation (ICEMA2)
Hanoi, August 16-17, 2012
ISBN: 978-604-913-097-7

The Theory of PIV-3D System and Some Experiment Results

Hà Tiến Vinh[a], Bùi Đình Trí[a,b] and Nguyễn Tất Thắng[a]

[a] *Institute of mechanic, Vietnam Academy of Science and Technology, 264, Doi Can, Hanoi*
[b] *University of Engineering and Technology, Vietnam National University, Ha Noi, Viet Nam*

Abstract

Measurement velocity area of flow via analysis images, such as LDV- Laser Doppler Velocity, PIV – Particle Image Velocity, is a process which was used in very long time ago. This result has a good quality and visually. The PIV works non- intrusive (don't use sense) so this method doesn't take any affect in the flow and allow in high speed flow measurement. Furthermore, PIV experiment provides velocity vector of an area and data of most of all place inside the flow (versus one point when used sense). By used high rate and high solution camera, PIV allows to research quick change behavior of flow such as turbulence, vortex….One Dantec PIV-3D system have been equipped in the lab of Department for Industrial and Environment Dynamics, Institute of Mechanic, Viet Nam Academy of Science and Technology. In this report, we want to provide introducing of PIV-3D on theory and experiment fact of our system. Beside, some first result, which we achieved, will be presented, in which will show many prospect using this experiment for theory research, experiment research and moreover application for production industrial. And more than everything, we hope to make, as much as possible, change to collaborate on research and exploit all ability of this system from interesting people.

Key words: PIV-3D, Flow dynamic

I INTRODUCE

I.1 Principle of PIV and PIV-3D

PIV had been first used by Ludwig Prandtl in 1904. At the moment with the development of computer science and camera, PIV has been used wildly on research and industrial to study behavior and action of flow.

Figure 1 shows the basis structure of a PIV system. Fundamental of PIV system is taking two frames in a short time interval of tracer particles. The tracer particles had been mixed in flow and flow was illuminated by a blinking laser source. At a pulse of laser source, an image had been taken. The displacement of particle between two pulses of laser source had been determined by the evolution PIV recording [1].

Quality of PIV result depends most on quality of laser source, adequate of tracer particles and resolution of camera.

Tracer particles can reflex light which it was illuminated. It has to distribute homogenous in flow. Moreover, the influence of gravitational forces when the densities of the fluid and the tracer particles do not adequate can recount unfaithfully the behavior of flow. Furthermore, the size of tracer particles can be a problem. The particle has to be very small to reflect good the flow motion. However, too small particles cannot recordable by camera.

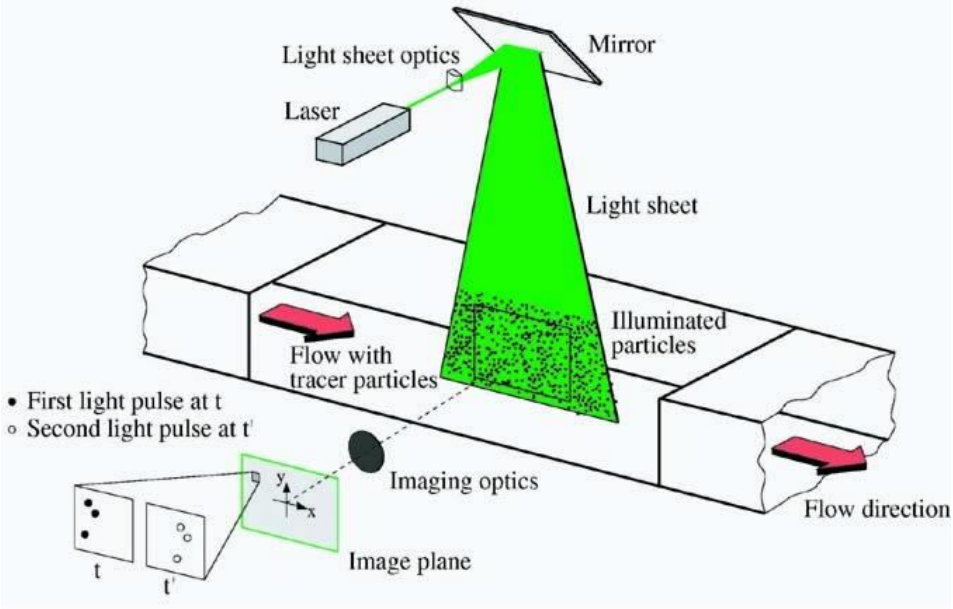

Figure 1: Basis arrangement of a PIV experiment

PIV experiment can use most of light even the nature light. However, the small particles need higher power light and to avoid the optical phenomena which can act on quality of image, the laser usually has been used. Laser source provides high power, changeable thickness and high frequency form to kHz so it can satisfies most of experiments requirement

Images were analyzed by software. The software will evaluated two images to distingue the displacement of particles between two images. The final result is a vector field of the illuminated field of the flow. We can calculate mean vector of the behavior of flow in case the flow have repeating ability or make a movie of the process of the behavior.

Fundamentally, the PIV-3D has same principles with the basic PIV but it use two, three and sometime four camera to record the flow in multi-dimensions. At the same time, these cameras take images of the flow in different angles and the three-component velocity vector will be reconstruct from. The PIV-3D method has many advantages with the PIV method. First of all, the three-component velocity vector allows study flow more exactly, more visually and multi-dimensions. Secondly, the problem of the thinness of laser sheet has been removed. In fact, the light sheet of PIV-3D was thick to measuring the third dimension. Besides, the calibration these cameras images can be a big problem and sometime provide unfaith result.

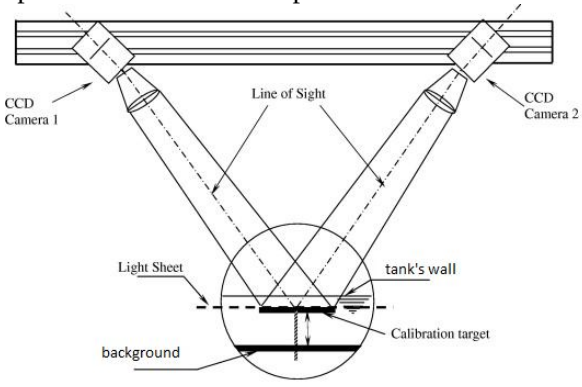

Figure 2: Model of a PIV 3D system

Calibration these cameras images can be a big problem and sometime provide unfaith result.

I.2 Advantage of PIV-3D method (Particle Image Velocity 3 Dimension)

The result of PIV has good quality and visually because of:

- PIV is a non-instructed method. So, properties of flow were not changed anything.
- PIV based on taking continuously images of flow and then images was analyzed by software. The final result is a vector field of whole flow.
- Moreover, with the power of computer and high velocity of CCD sense, PIV can provide the movie of the process
- PIV allows us to study all of point inside the laser sheet instead of one point of other method

Furthermore, with PIV-3D system in laboratory of department of Department for Industrial and Environment Dynamics, Institute of Mechanic, Viet Nam Academy of Science and Technology allows us recording and description flow in 3 dimensions. Based on that, flow can be studied more exactly, more visually.

II EXPERIMENT AND RESULT

II.1 PIV system

With the proposed to study the PIV and PIV-3D method, we have done experiments with two methods PIV and PIV-3D. Figure 3 shows the arrangement of the PIV experiment and so on figure 5 shows the arrangement of PIV-3D experiment. The laser used for both experiments is a Dantec dual power Nd-Yag laser. The pulse duration are approximately minimum 4 ns giving a max peak power of 1200 mJ. 80x80 high power light-sheet series was used to make a light sheet in range 200mm to 4000mm.

The position of the cameras is carefully aligned. The CCD allows one to take the picture with the limited exposure time is 141 µs. The video signal from the CCD sensor is transmitted to a PC and analyzed by Dantec dynamics studio software.

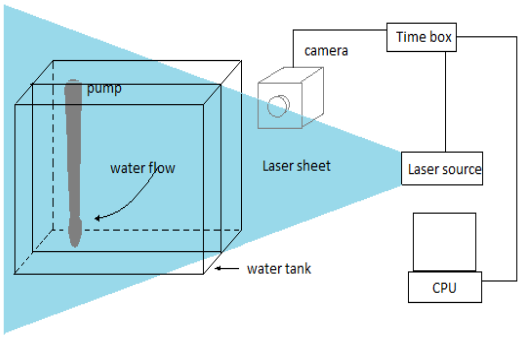

Figure 3: Arrangement of PIV experiment

The CCD camera and Laser source has been synchronized by a time box.

The completed system including laser, light sheet optics and camera is mounted on a traversing system that allows easy displacement to the position of interest.

II.2 Experiment and result

II.2.1 PIV experiment

Ours experiment, which used PIV method, show in the figure 3. A pump was placed in a water tank. The pump adsorbed water in the water tank at the bottom. The laser sheet and camera were orthogonal. The time between two frames of PIV image was 500 µs. 100 PIV images had been captured and the mean vector was calculated from. The adsorbent of pump was recorded and shown on the figure 4. The calibration was done with the calibration target.

We can easily realize that near the top of pump, the flow have tendency going forward the pump. Because of the power of the pump is only 15W, so the water in the right corner moved turbulent.

Some place in the figure 4, the velocity vector of the trace particle is only one very small point even points around having very large velocity. This is because of the moving of them is not in the same direction but in the PIV we only calculated the velocity of the

two dimension so the result is only the component of velocity in two dimension belong the lighter sheet.

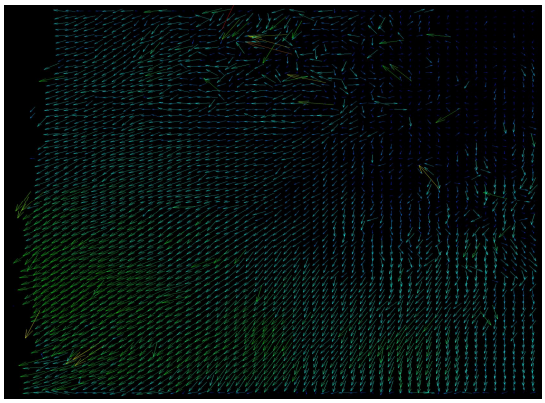

Figure 4: Vector field of the water tank

However, PIV shown that it is a very useful method to study directional flow such as Wind tunnel velocity experiments for testing aerodynamics of e.g. Cars, trains, aircraft, buildings and other objects/structures

II.2.2 PIV-3D experiment

In the idea studying PIV in two main flow, liquid and air, we arranged a PIV-3D experiment with the flow is air. A fan had been used, the fan made a vortex flow after. The laser sheet was placed orthogonal with the flow. The laser sheet was a centimeter thick.

The Flow tracker 700CE pump was used to make the trace particles from liquid. In this case, the oil was used. The trace particles had been mixed in the air which came from a pressure pump and leaded to a box after the fan. When the fan was running, the air in the box was pulled belong the flow and captured by cameras.

Two CCD cameras were placed in other sides of laser sheet. Two PIV result of the flow was taken. The software had used them to analysis the third-component.

A two side calibration target was used for calibration. The calibration was done with 3 status of calibration target (straight, inclined to the right and inclined to the left). The calibration for PIV-3D was very important in order to reconstruct the local displacement vector the viewing direction and magnification factor for each camera must be known at each point in the respective images [2]

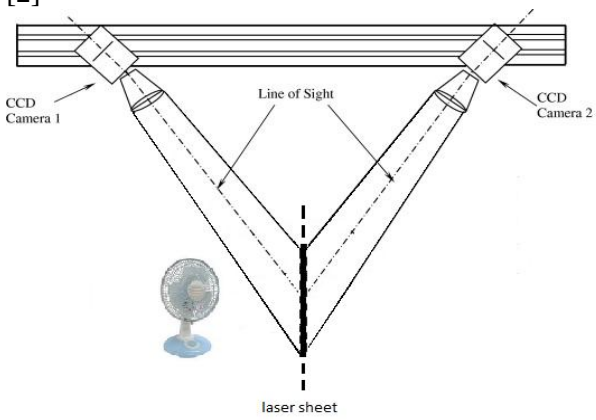

Figure 5: Arrangement for PIV-3D experiment

Two frames of PIV images were taken between 200µs. 250 PIV images had taken from each camera. The result, which was shown in the figure 6, is the mean vector of them. In figure 6, it is the stereo PIV-3D result of this experiment. Two dimension x and y were shown in velocity vector. The third component was shown in the color. The color of a point showed the magnitude of Z component at this place.

The horizontal vortex was shown in the circle A. The direction of vortex related with the rotation direction of the fan. Because we didn't use wind tunnel so the flow had been acted by the external effects. The Z velocity was not same in any place and not symmetric.

Although, this is simple experiment but the advantage of PIV-3D method cannot be deny. Moreover, it extended the application of PIV method and reduced the error to a minimum [1]

III DISCUSSION

PIV technique is one of the most powerful and non-intrusive measurement in hydro-sciences as well as fluid engineering

community [3]. The application of PIV method is wide in research and industry. Moreover, the development of PIV-3D extended the application of PIV.

In our experiment, the advantage of PIV method was shown and compared with the other methods. PIV shown the velocity of the whole flow at many point inside while other method only shown the average velocity of flow (Ultrasonic Velocimetry) or 1 point (Laser Doppler Anemometry). Furthermore, most of other methods have to act on the flow. It take the flow properties had been changed.

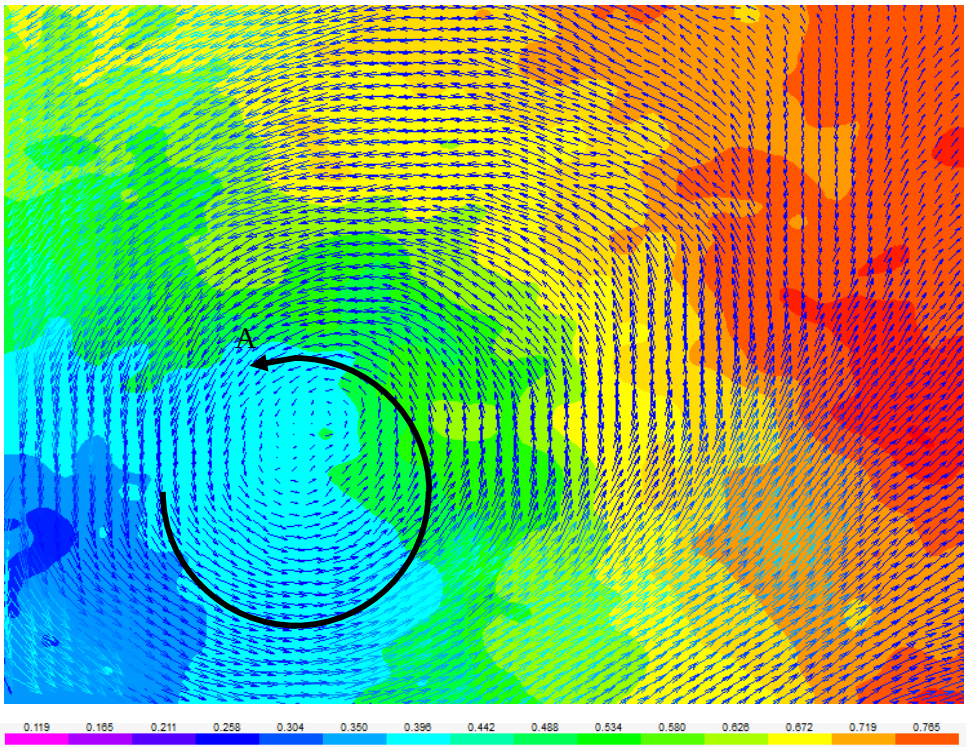

Figure 6: Vector field of flow after the fan.

The most advantage of PIV method is the ability to deconstruct the quick behavior of flow such as vortex, turbulent….

PIV-3D improved ability of PIV method when it can measure three dimension x, y, z. the behavior of flow has been studied deeper and multi-dimension.

Furthermore, the result of PIV can be used to compare with the theory result which can be calculated from CFD software.

Two experiment had recounted that PIV-3D system has good quality when was used to study in different experiment environments.

References

1. Markus Raffel, Christian E. Willert, Steve T. Werely, Jürgen Kompenhan: *Particle Image Velocimetry. A practical guide*

2. Dracos Th., ed. (1996): *Three-dimensional Velocity and Vorticity Measuring and Image Analysis Techniques*

3. Iehisa Nezu and Michio Sanjou, Journal of Hydro-environment Research *PIV and PTV measurement in hydro-sciences with focus on turbulent open-channel flows*

The 2nd International Conference on Engineering Mechanics and Automation (ICEMA2)
Hanoi, August 16-17, 2012
ISBN: 978-604-913-097-7

Comparison of Hydrodynamic Coefficients of a Ship Moving in Waves Obtained from Direct Rankine Panel Method and Indirect Rankine Panel Method

Nguyen Gia Thang[a] and Pham Van Thu[b]

[a] *Faculty of Ship Design and Shipbuilding Technology, Vietnam Maritime University*
Address: No 484, Lach Tray Street, Ngo Quyen District, Haiphong City, Vietnam
Email: ngthang@vimaru.vn
[b] *Institute of Post Graduate Education, Vietnam Maritime University*
Address: No 484, Lach Tray Street, Ngo Quyen District, Haiphong City, Vietnam
Email: pvthusdd.dhhh@gmail.com

Abstract

Based on the ways of describing the velocity potentials, there are two approaches for the Rankine panel method namely the Direct Rankine panel method and the Indirect Rankine panel method. In the Indirect Rankine panel method, the velocity potential at a field point is calculated based on the source strengths of all other source points distributed on the boundary surfaces of the fluid domain, whiles in the Direct Rankine panel method the velocity potential is illustrated through the velocity potentials at all other source points on the boundary surfaces of the fluid domain. In this paper, the author introduces the methodologies, and algorithm corresponding to those two approaches of the Rankine panel method. The free stream is used as the basic flow for both methods. The perturbation of the steady flow due to the ship is neglected. On the free surface, the derivative of velocity potential respect to x-axis is calculated by using a upwind differential scheme. In order to demonstrate the methodologies, a wigley hull model has been chosen for calculation. Results obtained from those two methods are compared to each other and compared to experimental data. It is showed that the Indirect Rankine panel method gives a very good prediction in both value and tendency of the hydrodynamic coefficients in both symmetric and anti-symmetric modes in comparison to the experimental data. But the Direct Rankine panel method does not give a good prediction. In conclusion, the Indirect Rankine panel method should be used for solving the hydrodynamic problem of a ship moving in waves.

Key Words: Direct, Indirect, Rankine panel method, Hydrodynamic coefficients, Upwind differential scheme.

1. Introduction

There are many approaches for solving the hydrodynamic problem of a moving ship in waves in frequency domain. The most popular approach may be the Green function method (Inglis and Price [1982]). In that method, the form of the Green function satisfies all the boundary conditions but only the one on the body wetted surface, therefore, only the body wetted surface is required for this approach. Due to the complexity of the form of the Green

function, it takes a lot of time and effort for this calculation.

Another approach is the Rankine panel method (Nakos and Sclavounos [1991], Bertram [1998]). The simple form of the Green function is used in this method. Since this simple form of the Green function does not satisfy the free surface boundary conditions, both the body wetted surface and the free surface are required for this approach. In comparison to the Green function method, the Rankine panel method does not have to calculate the complicated form of the Green function, however, it has to solve a bigger matrix that includes the free surface idealization.

In this paper, the Direct and Indirect Rankine panel methods based on the ways of describing the velocity potentials have been introduced. Calculated results obtained from two methods for a Wigley hull model are compared to each other and to experimental data.

2. Mathematical model

2.1. Linearization of the problem

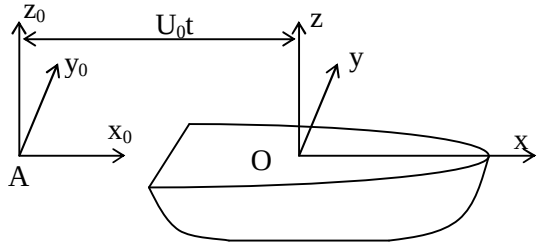

Figure 1. Coordinate system used in Seakeeping problems

Let $Ax_0y_0z_0$ be the space fixed coordinate system and Oxyz be the coordinate system moving with the ship in the same steady forward speed U in x-direction. The origin O lies in the calm water surface and has the same abscissa with the centre of gravity as in the Figure 1.

In the linear approach, it is assumed that the incident wave height and magnitude of the steady and unsteady flow due to steady translation and oscillation of the ship are small, the total velocity potential of the fluid flow can be represented as (see Lewis, Edward V. [1989])

$$\Phi(x_0, y_0, z_0) = U\bar{\phi}(x, y, z) + \varphi(x, y, z, t) \quad (1)$$

where $U\bar{\phi}(x,y,z)$ is the velocity potential of steady translation and $\varphi(x,y,z,t)$ is the velocity potential of the unsteady motions and deformations of the ship in waves.

The velocity vector of the steady flow in the moving coordinate system is

$$\mathbf{W} = U.\nabla(\bar{\phi} - x) \quad (2)$$

The free surface boundary condition can be found from Newman[1978] as follow

$$\frac{\partial^2\varphi}{\partial t^2} + 2\mathbf{W}.\nabla\frac{\partial\varphi}{\partial t} + \frac{1}{2}\mathbf{W}.\nabla(\mathbf{W}^2) + \mathbf{W}.\nabla(\mathbf{W}.\nabla\varphi) +$$

$$\frac{1}{2}\nabla\varphi.\nabla(\mathbf{W}^2) + gU\frac{\partial\bar{\phi}}{\partial z} + g\frac{\partial\varphi}{\partial z} = 0 \text{ on } z = \zeta \quad (3)$$

Neglecting the perturbation of the steady flow due to the ship, $\mathbf{W} = -U.\mathbf{i}$, then the linear free surface boundary condition will be

$$\frac{\partial^2\varphi}{\partial t^2} - 2U\frac{\partial^2\varphi}{\partial x\partial t} + U^2\frac{\partial^2\varphi}{\partial x^2} + g\frac{\partial\varphi}{\partial z} = 0 \text{ on } z = 0 \quad (4)$$

The unsteady potential for a sinusoidal wave excitation with encounter frequency takes the form (Bishop et al [1986])

$$\varphi(x,y,z,t) = [\phi_I(x,y,z) + \phi_D(x,y,z) + \sum_{r=1}^{6}\bar{p}_r\phi_r(x,y,z,t)]e^{i\omega_e t} \quad (5)$$

where ϕ_I, ϕ_D, ϕ_r are the amplitude of incident, diffraction, and radiation wave potentials respectively, $\bar{p}_r$ is the complex amplitude of ship's response in the r^{th} direction.

The amplitude of incident wave potential can be calculated as follow

$$\phi_I(x,y,z) = \frac{iga}{\omega}e^{k(z - ix\cos\chi - iy\sin\chi)} \quad (6)$$

where χ is the angle of incident between the phase velocity of waves and the forward velocity of the ship, k is the wave number $(k = 2\pi/\lambda)$ λ is the wave length, and ω_e is the encounter frequency such that

$$\omega_e = \omega - Uk\cos\chi \quad (7)$$

From equation (4) and (5), the linear free surface boundary condition is

$$-\omega_e^2\phi - 2Ui\omega_e\frac{\partial\phi}{\partial x} + U^2\frac{\partial^2\phi}{\partial x^2} + g\frac{\partial\phi}{\partial z} = 0 \text{ on } z = 0 \quad (8)$$

where ϕ stands for ϕ_D, ϕ_r in equation (5).

For diffraction problem, the body boundary condition is

$$\frac{\partial\phi_D}{\partial n} = -\frac{\partial\phi_I}{\partial n} \qquad \text{on } S_b \quad (9)$$

For radiation problem, the boundary condition is

$$\frac{\partial\phi_r}{\partial n} = i\omega_e n_r + Um_r \quad \text{on } S_b \quad (10)$$

Here the components n_r, m_r are defined as

$$\begin{cases}(n_1, n_2, n_3) = \mathbf{n}\\ (n_4, n_5, n_6) = \mathbf{x}\times\mathbf{n}\end{cases} \quad (11)$$

and

$$\begin{cases}(m_1, m_2, m_3) = -(\mathbf{n}.\nabla)\mathbf{W}\\ (m_4, m_5, m_6) = -(\mathbf{n}.\nabla)(\mathbf{x}\times\mathbf{W})\end{cases} \quad (12)$$

where $\mathbf{x}(x,y,z)$ is the position vector with respect to the origin of the coordinate system.

Neglecting the perturbation of the steady flow due to the ship, $\mathbf{W} = -U\mathbf{i}$, then

$$m_r = \{0, 0, 0, 0, n_3, -n_2\} \quad (r = \overline{1,6}) \quad (13)$$

2.2. Indirect Rankine panel method

Assuming waves created by the ship will decay when they reach to the see bottom surface and the surface of the cylinder with infinitive radius. Therefore, in the Indirect Rankine panel method, the velocity potential at each field point **x** is determined through the source strength of all other source points $\boldsymbol{\xi}$ on the body wetted surface (S_b) and the free surface (S_f) as follow

$$\phi(\mathbf{x}) = \frac{1}{4\pi}\iint_{S_b+S_f} G(\mathbf{x},\boldsymbol{\xi})\sigma(\boldsymbol{\xi})dS \quad (14)$$

here the Green's function takes the simple form

$$G(\mathbf{x},\boldsymbol{\xi}) = \frac{1}{R} \quad (15)$$

where R is the distance between the field point $\mathbf{x}(x, y, z)$ and the source point $\boldsymbol{\xi}(\xi, \eta, \zeta)$.

The normal derivative of the velocity potential of field point **x** will be

$$\frac{\partial\phi(\mathbf{x})}{\partial n(\mathbf{x})} = -\frac{1}{2}\sigma(\mathbf{x}) + \frac{1}{4\pi}\iint_{S_b+S_f}\frac{\partial G(\mathbf{x},\boldsymbol{\xi})}{\partial n(\mathbf{x})}\sigma(\boldsymbol{\xi})dS \quad (16)$$

The normal derivative of the Green's function at field point **x** on the right hand side of Eq. (16) can be calculated as

$$\frac{\partial G(\mathbf{x},\boldsymbol{\xi})}{\partial n(\mathbf{x})} = \frac{\partial G(\mathbf{x},\boldsymbol{\xi})}{\partial x}n_1(\mathbf{x}) + \frac{\partial G(\mathbf{x},\boldsymbol{\xi})}{\partial y}n_2(\mathbf{x}) + \frac{\partial G(\mathbf{x},\boldsymbol{\xi})}{\partial z}n_3(\mathbf{x}) \quad (17)$$

where

$$\frac{\partial G(\mathbf{x},\boldsymbol{\xi})}{\partial x} = \frac{\xi - x}{(\sqrt{(x-\xi)^2 + (y-\eta)^2 + (z-\zeta)^2})^3} \quad (18)$$

$$\frac{\partial G(\mathbf{x},\boldsymbol{\xi})}{\partial y} = \frac{\eta - y}{(\sqrt{(x-\xi)^2 + (y-\eta)^2 + (z-\zeta)^2})^3} \quad (19)$$

$$\frac{\partial G(\mathbf{x},\boldsymbol{\xi})}{\partial z} = \frac{\zeta - z}{(\sqrt{(x-\xi)^2 + (y-\eta)^2 + (z-\zeta)^2})^3} \quad (20)$$

and $n_1(\mathbf{x})$, $n_2(\mathbf{x})$,$n_3(\mathbf{x})$ are three cosine vectors respected to x, y, z respectively at field point **x**.

The normal derivative of velocity potential at field point **x** on the left hand side of Eq. (16) can be found by using the boundary conditions. For field points on the body wetted surface, the normal derivatives of velocity potential for diffraction waves and radiation waves can be found using Eq. (9) and (10) respectively. For field points on the free surface, using the linear free surface boundary condition Eq. (8) and the following condition

$$\frac{\partial\phi(\mathbf{x})}{\partial n(\mathbf{x})} = -\frac{\partial\phi(\mathbf{x})}{\partial z} \; on \; z = 0 \quad (21)$$

gives

$$\frac{\partial\phi(\mathbf{x})}{\partial n(\mathbf{x})} = -\frac{1}{g}[\omega_e^2\phi(\mathbf{x}) + 2Ui\omega_e\frac{\partial\phi(\mathbf{x})}{\partial x} - U^2\frac{\partial^2\phi(\mathbf{x})}{\partial x^2}] \quad (22)$$

In this Eq. (22), the first and second derivatives of the velocity potential respected to x for k^{th} panel of each longitudinal strip (see Figure 2) can be found using the upwind differential schemes as follows

$$\frac{\partial\phi_k}{\partial x} = \frac{\phi_{k-1} - \phi_k}{x_{k-1} - x_k} \quad (23)$$

and

$$\frac{\partial \phi_k}{\partial x} = \frac{\frac{\partial \phi_{k-1}}{\partial x} - \frac{\partial \phi_k}{\partial x}}{x_{k-1} - x_k} \tag{24}$$

With the initial boundary condition at the first panel of each longitudinal strip are (Nakos et al [1991])

$$(i\omega_e - U\frac{\partial}{\partial x})\phi = 0 \tag{25}$$

and $$(i\omega_e - U\frac{\partial}{\partial x})^2 \phi = 0 \tag{26}$$

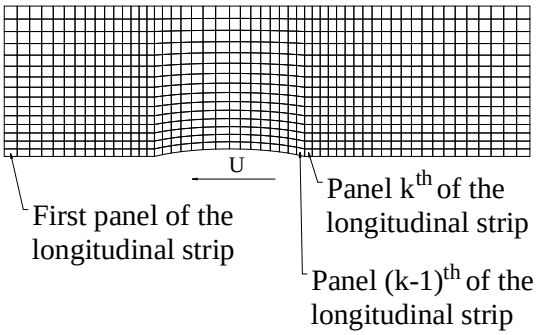

Figure 2. Free surface idealisation

According to the traditional approach of hydrodynamics, the general hydrodynamics fluid forces for k^{th} mode (k=1→6) can be decomposed as follows

$$F_{H_k}(t) = (F_k^{EX} + F_k^R + R_k)e^{i\omega_e t} \tag{27}$$

Here F_k^{EX}, F_k^R, R_k are the generalised wave exciting force, radiation force, and restoring force respectively.

The generalised wave exciting force can be decomposed as follows

$$F_k^{EX} = F_k^I + F_k^D \tag{28}$$

Here F_k^I is the Froude-Krylov exciting force which can be expressed as

$$F_k^I = -\rho \iint_{S_b} n_k (i\omega_e - U\frac{\partial}{\partial x})\phi_I \, dS \tag{29}$$

and F_k^D is the diffraction force

$$F_k^D = -\rho \iint_{S_b} n_k (i\omega_e - U\frac{\partial}{\partial x})\phi_D \, dS \tag{30}$$

The radiation force can be expressed as

$$F_k^R = \sum_{r=1}^{6} (\omega_e^2 A_{kr} - i\omega_e B_{kr})\overline{p}_r = \sum_{r=1}^{6} T_{kr}\overline{p}_r \tag{31}$$

where

$$T_{kr} = -\rho \iint_{S_b} n_k (i\omega_e - U\frac{\partial}{\partial x})\phi_r \, dS \tag{32}$$

The added mass and damping coefficients are given by

$$A_{kr} = \mathrm{Re}(\frac{T_{kr}}{\omega_e^2}) \tag{33}$$

$$B_{kr} = \mathrm{Im}(\frac{T_{kr}}{\omega_e}) \tag{34}$$

Here Re(A) and Im(A) denote the real and imaginary parts of A.

The generalised restoring force can be written in the form

$$R_k = -\sum_{r=1}^{6} p_r . C_{kr} \tag{35}$$

where C_{kr} are the restoring force coefficients

2.3. Direct Rankine panel method

In the Direct Rankine panel method, the velocity potential of a field point is evaluated by the velocity potential and the normal velocity of other source points on the body wetted surface and the free surface as follow

$$\phi(\mathbf{x}) = \frac{1}{2\pi} \iint_{S_b + S_f} \left(\phi(\xi)\frac{\partial G(\mathbf{x},\xi)}{\partial n(\xi)} + G(\mathbf{x},\xi)\frac{\partial \phi(\xi)}{\partial n(\xi)} \right) dS \tag{36}$$

here the Green function takes the simple form as in Eq. (15)

In Eq. (36), the normal derivative of the Green function at a source point ξ can be calculated as follow

$$\frac{\partial G(\mathbf{x},\xi)}{\partial n(\xi)} = \frac{\partial G(\mathbf{x},\xi)}{\partial \xi} n_1(\xi) + \frac{\partial G(\mathbf{x},\xi)}{\partial \eta} n_2(\xi) + \frac{\partial G(\mathbf{x},\xi)}{\partial \zeta} n_3(\xi) \tag{37}$$

where

$$\frac{\partial G(\mathbf{x},\xi)}{\partial \xi} = \frac{x-\xi}{(\sqrt{(x-\xi)^2 + (y-\eta)^2 + (z-\zeta)^2})^3} \tag{38}$$

$$\frac{\partial G(\mathbf{x},\xi)}{\partial \eta} = \frac{y-\eta}{(\sqrt{(x-\xi)^2 + (y-\eta)^2 + (z-\zeta)^2})^3} \tag{39}$$

$$\frac{\partial G(\mathbf{x},\xi)}{\partial \zeta} = \frac{z=\zeta}{(\sqrt{(x-\xi)^2 + (y-\eta)^2 + (z-\zeta)^2})^3} \tag{40}$$

and $n_1(\xi)$, $n_2(\xi)$,$n_3(\xi)$ are three cosine vectors respected to x, y, z respectively at source point ξ.

The normal velocity of a source point on the body wetted surface can be calculated using Eq. (9) and Eq. (10) for diffraction waves and radiation wave respectively.

For source points on the free surface, the normal velocity potential can be calculated using Eq. (22).

3. Calculated results for Direct and Indirect Rankine panel methods

Wigley hull model has been used widely in hydrodynamics study due to its convenience to generate. Therefore, in order to demonstrate these methodologies, the Wigley hull model III (see Journee [1992]) have been chosen. It is mathematically defined by

$$y = \frac{B}{2}\left[1-\left(\frac{z}{d}\right)^2\right]\left[1-\left(\frac{2x}{L}\right)^2\right]\left[1+0.2\left(\frac{2x}{L}\right)^2\right] \quad (41)$$

where L, B, d are the length, breadth, and draught of the model respectively, while x, y, z are the three coordinates of a point on the hull with the origin locates at half ship length, amidships, and on the still water surface.

The model has the length of 3(m), breadth of 0.3(m), and draught of 0.1875(m). The mean wetted surface of the Wigley hull is idealized by 400 panels (25 panels in longitudinal direction, 8 panels in transverse direction at each side) (see Figure 3).

The free surface size and idealization has been chosen such that the upstream distance from the bow to the front end of the free surface is a quarter of the hull length, the downstream distance from the stern to the back end of the free surface is half of the hull length, while the distance in y-direction is equal to one hull length. (see Figure 4).

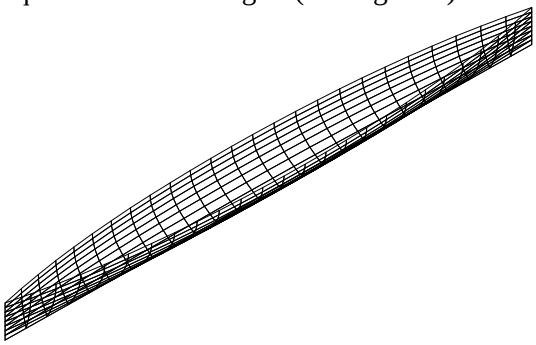

Figure 3. Idealisation of the Wigley hull model

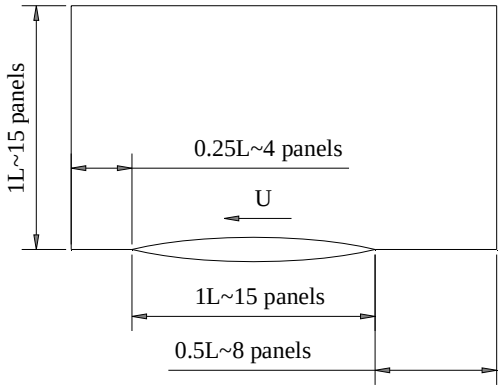

Figure 4. Size and Idealisation of the free surface

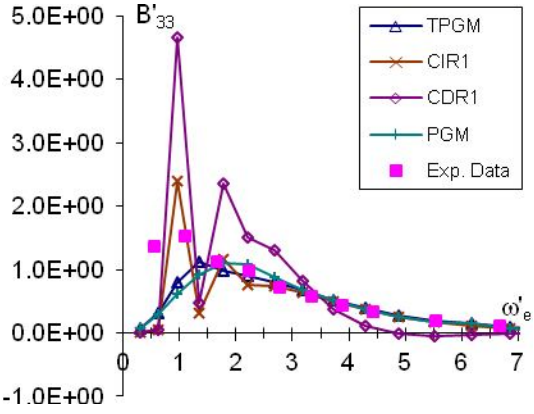

Figure 5. Non-dimensional damping coefficient for heave mode

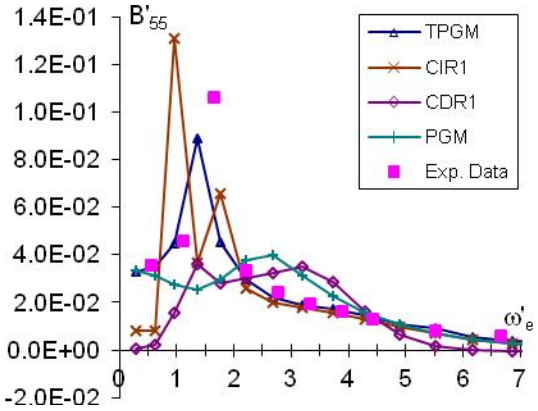

Figure 6. Non-dimensional damping coefficient for pitch mode

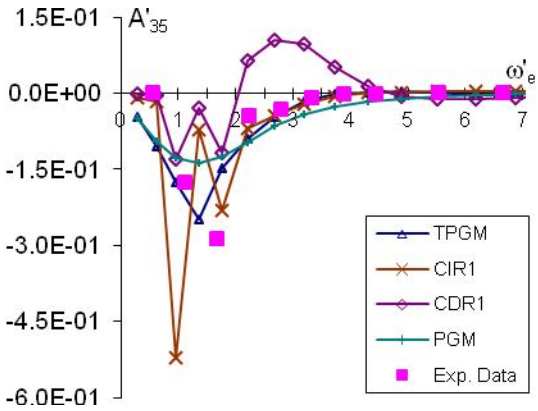

Figure 9. Non-dimensional added mass coefficient for heave-pitch coupling mode

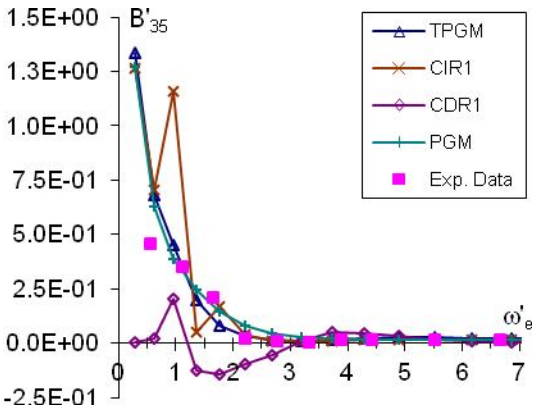

Figure 7. Non-dimensional damping coefficient for heave-pitch coupling mode

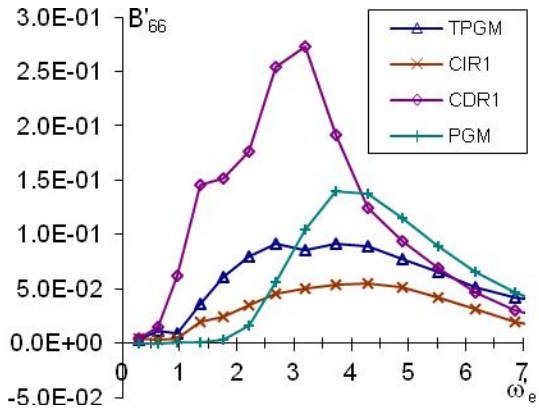

Figure 10. Non-dimensional damping coefficient for yaw mode

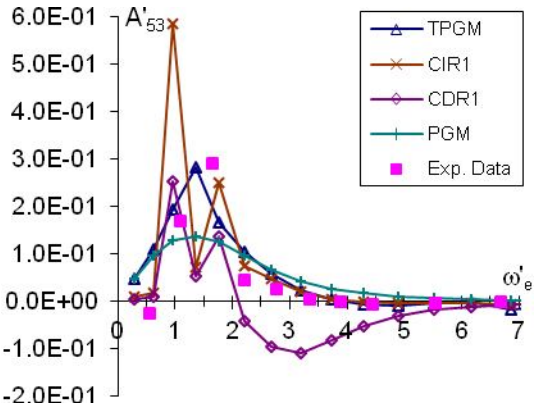

Figure 8. Non-dimensional added mass coefficient for pitch-heave coupling mode

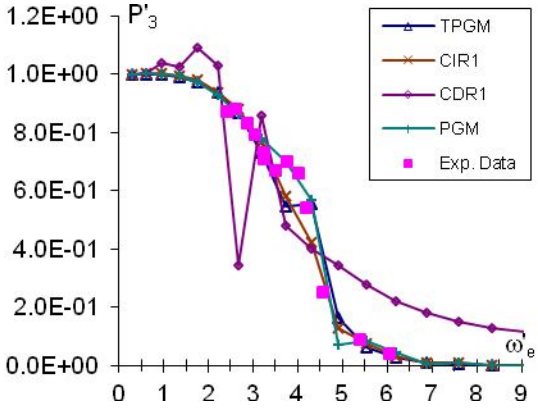

Figure 11. Non-dimensional response for heave mode

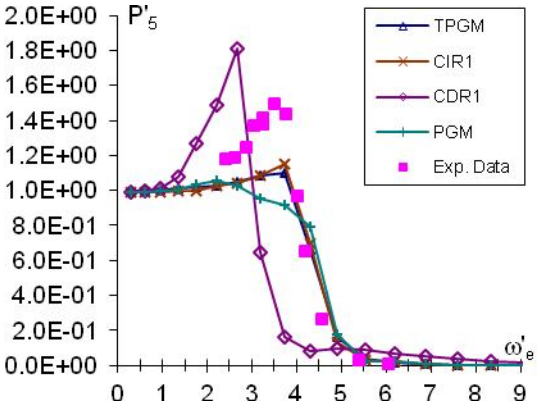

Figure 12. Non-dimensional response for pitch mode

Figures from 5 to 12 show the non-dimensional added mass, damping coefficients, and responses obtained from the Indirect and Direct Rankine panel methods (denoted as CIR1 and CDR1 respectively), Translating and Pulsating Green function method (TPGM), Pulsating Green function method (PGM), and experimental data (Exp. Data).

It can be seen that the Direct Rankine panel method's results are not as good as the ones's obtained from the Indirect Rankine panel method in both value and tendency.

Among the four methods, the Indirect Rankine panel method gives the best prediction of the added mass and damping coefficients as well as the responses in comparison to the experimental data.

For symmetric modes (k=1,3,5), the added mass and damping coefficients as well as the responses obtained from the Indirect Rankine panel method agree very well with experimental data.

For anti-symmetric modes (k=2,4,6), there is not available experimental data for this Wigley hull. Therefore, more calculation for other models with available anti-symmetric experimental data will be needed.

4. Conclusions

In summary, the Indirect Rankine panel method gives the best prediction among all the theoretical methods for this case of study. For symmetric modes, Indirect Rankine panel method's results agree very well with experimental data. The Direct Rankine panel method does not give a good prediction in comparison to the Indirect Rankine panel method, therefore the Indirect Rankine panel method should be chosen for further investigation.

5. References

Bertram, V. (1998). Numerical investigation of steady flow effects in three-dimensional seakeeping computations. *In Proceedings of the 22nd Symposium on Naval Hydrodynamics*, pages 417{31, Washington, DC.

Bishop, R.E.D., Price, W.G., and Wu, Y. (1986). A general linear hydroelasticity theory of foating structures moving in a seaway. *Philosophical Transactions of the Royal Society London*, 316:375-426.

Inglis, R. B. and Price, W. G. (1982). A three-dimensional ship motion theory: Comparison between theoretical predictions and experimental data of the hydrodynamic coefficients with forward speed. *Transactions of RINA*, 124:141-157.

Journee, J. M. J. (1992) Experiments and calculations on four Wigley hull forms in head waves. *Report 0909*, Delft University of Technology, Ship Hydromechanics Laboratory, The Netherlands

Lewis, Edward V. (1989). *Principle of Naval Architecture*. The Society of Naval Architects and Marine Engineers, 2nd Revision, Volume III.

Nakos, D. E. and Sclavounos, P. D. (1991). Ship motions by a three-dimensional rankine panel method. *In Proceedings of the 18th Symposium on Naval Hydrodynamics*, pages 21-40.

Newman, J. N. (1978). Theory of ship motions. *Advances in Applied Mechanics*, 18:221-283.

The 2nd International Conference on Engineering Mechanics and Automation (ICEMA2)
Hanoi, August 16-17, 2012
ISBN: 978-604-913-097-7

The Water Pollution Problem and Application of Data Assimilation Method

Tran Thu Ha[1,2] and Francois-Xavier Le Dimet[3,4]

1 Institute of Mechanics, VAST --18 Hoang Quoc Viet, Hanoi, Vietnam
2. University of Engineering and Technology, VNU, 144 Xuan Thuy, Hanoi, Vietnam
3. Laboratoire Jean-Kuntzmann, 51 rue des Maths, 38400 Saint Martin, France
4. Department of Mathematics, Florida State University, 414 Milton Carothers Hall, Tallahassee, FL 32306-4510, USA

Abstract

In calculation of fluid problems the initial condidtions are supposed. In water pollution model with the measurements on some places at some moments and using Data Assimilation by Optimal Differential Variation method the initial conditions can be corrected so that the simulation results are closed to the measurements. In this paper this method is applied to correct the initial conditions of water flow and pollution substance. In this model data of Thanh Nhan lake in Hanoi is used to simulate. The comparision of simulation results with or without correction of initial conditions is presented. The finite volume method, adjoint method and Gateaux derivatives are used in this problem.

1 INTRODUCTION

Worldwide water pollution is an important problem for agriculture and also for men's health. Preventing water pollution requires knowing the exact situation of lakes, rivers, ocean in order to be able to predict their evolution. To study the water pollution problems there are many mathematical methods and models are used. The linear 2D water pollution water is studied by semi group method in [1]. The nonlinear 2D-Imech water pollution model is studied in [3]. Mathematical models of water pollution exist since several decades they are necessary for prediction but they are not sufficient for at least three reasons:

- The prediction will be produced by an integration of the model starting from the initial condition. This initial condition must be obtained from observations and has to be in agreement with the general of the fluid.
- The mathematical models contain coefficients which cannot be directly measured because they parameterize complex physics at a scale smaller than grid size.
- In many situation sources of pollution are unknown both in location and also in intensity.

All these difficulties can be settled in the framework of a variation approach but in this paper we will concentrate our study on the initial conditions of the state and concentration values for the water pollution problem. In the second section we will describe the abstract definition of a variation problem. In the 3-rd section we will formulate the problem of water pollution we will work on.The 4-th section will be devoted to the application of variation methods to the identification of the initial conditions of the state and concentration values $X_0=(z_0, u_0, v_0)$, C_0. The 5-th section will be on application to the case of Thannhan Lake in Vietnam.

2 DERIVATION OF THE METHOD

2.1. Identification of the fields. Let us assume that the flow, described by the state variable *X*, satisfies, between time *0* and time *T* the differential system :

$$\begin{cases} \dfrac{dX}{dt} = F(X) \\ X(0) = U \end{cases} \tag{1}$$

The pollutant, considered as a passive tracer, is described by its concentration whose evolution is described by the following equations :

$$\begin{cases} \dfrac{dC}{dt} = G(X, C) \\ C(0) = V \end{cases} \tag{2}$$

C is the pollutant's concentration.

The first task is to retrieve the fields from observations $X_{obs} \in \chi_{obs}$ of the state variable $C_{obs} \in \zeta_{obs}$ of the concentration *C* of the pollutant. We introduce a cost function *J* defined by :

$$J(U,V) = \frac{1}{2}\int_0^T \left\| EX - X_{obs} \right\|^2 dt + \frac{1}{2}\int_0^T \left\| DC - C_{obs} \right\|^2 dt \tag{3}$$

E is an operator from the space of the state variable toward the space of observations and *D* from the space of concentration toward the space of observations of concentration. For sake of simplicity, we do not introduce regularization terms in the cost function, In practice they are of crucial importance. For retrieving the state variable and the concentration, we have to determine *U** and *V** which minimize *J*. They are solutions of the Optimality System which is the Euler-Lagrange equation involving the gradients of *J* with respect to *U* and *V*. To do so, we introduce *h* and *k*, two directions in the space of the state variable and the space of the concentration. We compute the Gateaux derivatives $\hat{X}, \hat{C}, \hat{J}$ by these directions. From the state equation, we deduce that they are solutions of :

$$\begin{cases} \dfrac{d\hat{X}}{dt} = \dfrac{\partial F}{\partial X}\hat{X} \\ \hat{X}(0) = h \end{cases} \tag{4}$$

And

$$\begin{cases} \dfrac{d\hat{C}}{dt} = \dfrac{\partial G}{\partial X}\hat{X} + \dfrac{\partial G}{\partial C}\hat{C} \\ \hat{C}(0) = k \end{cases} \tag{5}$$

Also we have:

$$\hat{J}(U,V,h,k) = \int_0^T \left\langle EX - X_{obs}, E\hat{X} \right\rangle dt + \int_0^T \left\langle DC - C_{obs}, D\hat{C} \right\rangle dt \tag{6}$$

where <.,.> is the dot product associated with the norm operator ||.||. Let us introduce *P* and *Q* as adjoint variables. We multiply equation 4 by *P* and equation 5 by *Q* and integrate between *0* and *T*, which yields :

(7)

$$\int_0^T \left\langle \frac{d\hat{X}}{dt}, P \right\rangle dt + \int_0^T \left\langle \frac{d\hat{C}}{dt}, Q \right\rangle dt = \int_0^T \left\langle \frac{\partial F}{\partial X}.\hat{X}, P \right\rangle dt + \int_0^T \left\langle \frac{\partial G}{\partial X}.\hat{X} + \frac{\partial G}{\partial C}\hat{C}, Q \right\rangle dt \tag{7}$$

Integrating by parts we get:

$$\left\langle \hat{X}(T), P(T) \right\rangle - \left\langle \hat{X}(0), P(0) \right\rangle$$
$$+ \left\langle \hat{C}(T), Q(T) \right\rangle - \left\langle \hat{C}(0), Q(0) \right\rangle =$$
$$\int_0^T \left\langle \hat{X}, \frac{dP}{dt} + \left[\frac{\partial F}{\partial X}\right]^T .P + \left[\frac{\partial G}{\partial X}\right]^T .Q \right\rangle dt \quad (8)$$
$$+ \int_0^T \left\langle \hat{C}, \frac{dQ}{dt} + \left[\frac{\partial G}{\partial C}\right]^T .Q \right\rangle dt$$

Whew the superscript ^{t} indicates the transpose of the matrix. If $P(T)=0$ and $Q(T)=0$ then it becomes:

$$-\left\langle h, P(0) \right\rangle - \left\langle k, Q(0) \right\rangle =$$
$$\int_0^T \left\langle \hat{X}, \frac{dP}{dt} + \left[\frac{\partial F}{\partial X}\right]^T .P + \left[\frac{\partial G}{\partial X}\right]^T .Q \right\rangle dt \quad (9)$$
$$+ \int_0^T \left\langle \hat{C}, \frac{dQ}{dt} + \left[\frac{\partial G}{\partial C}\right]^T .Q \right\rangle dt$$

Therefore if P and Q are defined as the solutions of:

$$\begin{cases} \dfrac{dP}{dt} + \left[\dfrac{\partial F}{\partial X}\right]^t .P + \left[\dfrac{\partial G}{\partial X}\right]^t .Q = E^t(EX - X_{obs}); \\ P(T) = 0; \end{cases} \quad (10)$$

$$\begin{cases} \dfrac{dQ}{dt} + \left[\dfrac{\partial F}{\partial C}\right]^t .Q = D^t(DC - C_{obs}); \\ Q(T) = 0; \end{cases} \quad (11)$$

then the linear dependence of the Gateaux derivatives of J with respect to the directions h and k are made explicit, and the components of the gradient ∇J can be deduced as follows:

$$\nabla J_U = -P(0) \quad (12)$$

$$\nabla J_V = -Q(0) \quad (13)$$

Equations (1), (2), (10), (11) and the condition for the gradient to be null is the Optimality System (O.S). It worthwhile to point out that it contains all the available information.

In practice, the resolution of the adjoint model permits the computation of the gradient which is used in the algorithm of optimization: Newton-Type methods, L-BFGS, etc. The optimal initial system state and initial pollutant concentration, with respect to observed data, are estimated.

3 FORMULATION OF THE 2D WATER POLLUTION PROBLEM

2D pollution water model consists of hydraulic model and transport - diffusion of pollution substances. In hydraulic model the Sain-Vernant equation is used as follows [2]:

$$\frac{\partial z}{\partial t} + \frac{\partial (uh)}{\partial x} + \frac{\partial (vh)}{\partial y} = 0, \qquad in\ \Omega. \quad (14)$$

$$\frac{\partial u}{\partial t} + u\frac{\partial u}{\partial x} + v\frac{\partial u}{\partial y} + g\frac{\partial z}{\partial x} = -\frac{gu(u^2+v^2)^{1/2}}{K_x^2 h^{4/3}}, \quad in\ \Omega. \quad (15)$$

$$\frac{\partial v}{\partial t} + u\frac{\partial v}{\partial x} + v\frac{\partial v}{\partial y} + g\frac{\partial z}{\partial x} = -\frac{gv(u^2+v^2)^{1/2}}{K_y^2 h^{4/3}}, \quad in\ \Omega. \quad (16)$$

Here,

- Ω is a bounded domain of R^2 with a boundary Γ ,
- z is the free surface elevation,
- $h = z - z_{bottom}$ is the water depth,
- u is the average velocity in the x direction,
- v is the average velocity in the y direction,
- g is the gravity acceleration,
- K_x is the Strickler coefficient in the x direction,
- K_y is the Strickler coefficient in the y direction.

We suppose that there are m substances dissolved in water. Then the transport and diffusion processes of pollution substances are described by the following equation [4].

$$\frac{\partial C}{\partial t} + u\frac{\partial C}{\partial x} + v\frac{\partial C}{\partial y} - \eta \Delta C = f(C), \quad in\ \Omega, \quad (17)$$

Here,

- $\Delta = \left(\dfrac{\partial^2}{\partial x^2} + \dfrac{\partial^2}{\partial y^2} \right)$
- C is the concentration of the substance,

- f(C)=KC is the conversion pollution function of the substance,
- K is the conversion coefficient,
- η is the diffusion coefficient of the substance.

Denoting $X = (z, u, v)^T$ we have the initial conditions:

$X_0 = (z(x, y,0), u(x, y, 0, v(x, y, 0))^T = U$

$C(x, y, 0) = V$

In the slow changing process for water pollution problem the boundary conditions are:

$$U.\vec{n} = \overline{U}_{in}(t),\ \mathrm{C(x,y,t)} = C_{in}(t)$$

on inflow boundary Γ_1,

$$z(x, y, t) = \bar{z}(t),\ \frac{\partial C}{\partial n} = 0$$

on outflow boundary Γ_2,

$$U.\vec{n} = 0, \frac{\partial C(x, y, t)}{\partial n} = 0$$

on solid wall $S_{w,}$

Where: U = *(u(x, y, t), v(x, y, t))*, S_w is the solid wall of Ω, Γ_2 and Γ_1 respectively are the outflow and inflow boundaries of the Ω domain, $\Gamma = \Gamma_1 \cup \Gamma_2 \cup S_W$ is the boundary of the region Ω, $\vec{n}$ is the unit normal vector onto Γ;

3.1. Equation for 2D flow system

To solve the above model equations, a cell centrednite volume method is used (see [2]). The type of mesh employed in this method is anunstructured triangulation of the solution domain enabling arbitrary shaped geometries to be accomodated more easily than a square grid system (see [2]). The mesh points of the grid are numbered in some given but arbitrary way.

To apply the finite volume method, the equations (13)-(15) are rewritten as follows:

$$\frac{\partial X}{\partial t} + \frac{\partial A(x)}{\partial x} + \frac{\partial B(x)}{\partial x} = F(X), \qquad (18)$$

Where

$$A(X) = \begin{pmatrix} uh \\ \frac{1}{2}u^2 + gz \\ uv \end{pmatrix},\ B(X) = \begin{pmatrix} vh \\ uv \\ \frac{1}{2}v^2 + gz \end{pmatrix}$$

$$F(X) = \begin{pmatrix} 0 \\ -gu\frac{\sqrt{u^2+v^2}}{K_x^2 h^{4/3}} + u\frac{\partial v}{\partial y} \\ -gv\frac{\sqrt{u^2+v^2}}{K_y^2 h^{4/3}} + v\frac{\partial u}{\partial x} \end{pmatrix}$$

The flow domain Ω is divided into *N* small cells Ω_j (j=1… N). In this small cell Ω_j integrating two sides of equation system (18) with respect to the spatial variables *x* and *y* we get the formula:

$$\int_{\Omega_j} \frac{\partial X}{\partial t} dxdy + \int_{\Omega_j} \vec{\nabla}.(A(X), B(X))dxdy = \int_{\Omega_j} F(X)dxdy$$

Here, $\vec{\nabla} = \left(\frac{\partial}{\partial x}, \frac{\partial}{\partial y}\right)$.

We assume that in small cell Ω_j the variables *(z,u,v)*, h and *F* can be approximated as constant values. Therefore, using Green formula the above formula can be rewritten as follows:

$$\frac{dX}{dt} S + \oint_{\gamma_j} (A(X), B(X)).\vec{n} d\gamma_j = F(X)S \qquad (19)$$

In formula (19) *S* is the cell's area, $\vec{n}$ is the unit normal vector onto γ_j with components in *x* and *y* directions denoted by n_x and n_y respectively. In the slow changing process problem to calculate the integrals we can use the average values for the functions in the cell. Using equation (19) the value of (*z, u, v*) at the cell center of Ω_j in the current step can be solved by the following equations:

$$z = z_t - \frac{\Delta t}{S}\oint_{\gamma_j}\left(hun_x + hvn_y\right)d\gamma_j \qquad (20)$$

$$u = u_t + \left[u_t\frac{\partial v_t}{\partial y} - \frac{gu_t\sqrt{u_t^2+v_t^2}}{K_x^2h^{4/3}}\right]\Delta t - \frac{\Delta t}{S}\oint_{\gamma_j}\left[\left(\frac{u^2}{2}+gz\right)n_x + uvn_y\right]d\gamma_j \qquad (21)$$

$$v = v_t + \left[v_t\frac{\partial u_t}{\partial y} - \frac{gv_t\sqrt{u_t^2+v_t^2}}{K_x^2h^{4/3}}\right]\Delta t - \frac{\Delta t}{S}\oint_{\gamma_j}\left[\left(\frac{v^2}{2}+gz\right)n_x + uvn_y\right]d\gamma_j \qquad (22)$$

Here z_t, u_t, v_t and z, u, v are called the values of z, u, v at cell center of Ω_j in the previous and in current steps.

3.2. Algorithm for transport-diffusion equations.

In pollution model the pollution process is depending on the combination of substances and number of them. In this paper we will study only one substance BOD_5 then the conversion pollution function f can be written by the formula $f=KC$.

By the same way as in paragraph 3.1 integrating two sides of quation (17) with respect to the spatial variable x and y then using Green formula, we get:

$$\int_{\Omega_j}\frac{\partial C}{\partial t}d\mathrm{x}d\mathrm{y} - \int_{\Omega_j}C\vec{\nabla}.Ud\mathrm{x}d\mathrm{y} + \oint_{\gamma_j}(UC\vec{n} - \eta\vec{\nabla}.C\vec{n})d\gamma_j = \int_{\Omega_j}KCd\mathrm{x}d\mathrm{y} \qquad (23)$$

Then the equation (23) can be rewriten as following:

$$\oint_{\gamma_j}\left[\left(u.n_x + v.n_y\right)C - \eta\left(\frac{\partial C}{\partial x}n_x + \frac{\partial C}{\partial y}n_y\right)\right]d_{\gamma_j} + \frac{\partial C}{\partial t}S + C\frac{1}{h}\frac{\partial z}{\partial t}S = KCS \qquad (24)$$

Thus in small cell Ω_j C can be calculated by the formula:

$$C = KC_t\Delta t + C_t\left(1 - \frac{z-z_t}{h}\right) - \frac{\Delta t}{S}\oint_{\gamma_j}\left[\left(u.n_x + v.n_y\right)C - \eta\left(\frac{\partial C}{\partial x}n_x + \frac{\partial C}{\partial y}n_y\right)\right]d_{\gamma_j} \qquad (25)$$

where: z, C and z_t, C_t are the water levels and concentrations in cell's center at the current and previous steps, $\frac{z-z_t}{h}$ is obtained when z is calculated by formula (20), (z,u,v) are getting from formulas (20)-(22).

4 THE INITIAL CONDITION'S CORRECTION BY DIFFERENTIAL OPTIMAL VARIATION METHOD

4.1. Model and notations.

To study the sensitivities of respect to source we do the same way as in paragraph 2.2 with the cost function J defined by the formula (3). Then, the Gateaux derivatives of X and C are $\hat{X} = (\hat{u}, \hat{v}, \hat{z})$, $\hat{C}$ obtaining by formulas (4) and (5) for 2D model with equations (17) and (18) are the solutions of equations:

$$\begin{cases} \dfrac{d\hat{X}}{dt} + \dfrac{\partial A(\hat{X})}{\partial x} + \dfrac{\partial B(\hat{X})}{\partial y} = F(\hat{X}) \text{ in } \Omega, \\ \hat{u}n_x + \hat{v}n_y = 0 \text{ on } \Gamma_1 \cup S_W, \\ \hat{z} = 0 \text{ on } \Gamma_2, \\ \hat{X}(0) = h. \end{cases} \qquad (26)$$

$$\begin{cases} \dfrac{\partial \hat{C}}{\partial t} + u\dfrac{\partial \hat{C}}{\partial x} + v\dfrac{\partial \hat{C}}{\partial y} + \hat{u}\dfrac{\partial C}{\partial x} + \hat{v}\dfrac{\partial C}{\partial y} - \eta\Delta\hat{C} \\ = K\hat{C} \quad in \quad \Omega, \\ \hat{C} = 0 \text{ on } \Gamma_1, \\ \dfrac{\partial \hat{C}}{\partial \vec{n}} = 0 \text{ on } \Gamma_2 \cup S_W, \\ \hat{C}(0) = k. \end{cases} \qquad (27)$$

Multiplying equation (27) by function vector P = (P_1; P_2; P_3) and integrating by t and Ω we have:

$$\int_0^T \left\langle \hat{X}, \frac{\partial P}{\partial t} - \frac{\partial A^*(X,P)}{\partial x} - \frac{\partial B^*(X,P)}{\partial y} + F^*(X,P) \right\rangle dt = \left\langle \hat{X}(T), P(T) \right\rangle - \left\langle \hat{X}(0), P(0) \right\rangle \tag{28}$$

Here:

$$A^*(X,P) = \begin{bmatrix} -gP_2 - uP_1 \\ -uP_2 - hP_1 - vP_3 \\ -uP_3 \end{bmatrix}$$

$$B^*(X,P) = \begin{bmatrix} -gP_3 - vP_1 \\ -vP_2 \\ -uP_2 - vP_3 - hP_1 \end{bmatrix}$$

$$F^*(X,P) = -\begin{bmatrix} P_1\dfrac{\partial u}{\partial x} + P_1\dfrac{\partial v}{\partial y} \\ \left[\dfrac{g\left(u^2+v^2\right)+u^2+uv}{K_x^2 h^{4/3}\sqrt{u^2+v^2}} + \dfrac{\partial u}{\partial x}\right]P_2 + \dfrac{\left(v^2+uv\right)P_3}{K_x^2 h^{4/3}\sqrt{u^2+v^2}} + \dfrac{\partial\left(vP_3\right)}{\partial x} + P_3\dfrac{\partial v}{\partial x} + P_1\dfrac{\partial z}{\partial x} \\ \left[\dfrac{g\left(u^2+v^2\right)+v^2+uv}{K_x^2 h^{4/3}\sqrt{u^2+v^2}} + \dfrac{\partial v}{\partial y}\right]P_3 + \dfrac{\left(u^2+uv\right)P_2}{K_x^2 h^{4/3}\sqrt{u^2+v^2}} + \dfrac{\partial\left(uP_2\right)}{\partial x} + P_2\dfrac{\partial v}{\partial y} + P_1\dfrac{\partial z}{\partial y} \end{bmatrix}$$

Multiplying equation (27) by function Q and integrating by t and Ω we have

$$\begin{aligned} &\int_0^T \left\langle \hat{C}, \frac{\partial Q}{\partial t} + \vec{\nabla}.(UQ) + \eta\Delta Q + KQ \right\rangle dt = \\ &\int_0^T \int_\Omega \left[\hat{u}Q\frac{\partial C}{\partial x} + \hat{v}Q\frac{\partial C}{\partial y} \right] d\Omega dt \\ &+ \left\langle \hat{C}(T), Q(T) \right\rangle - \left\langle \hat{C}(0), Q(0) \right\rangle \\ &+ \left\langle \hat{X}(T), P(T) \right\rangle - \left\langle \hat{X}(0), P(0) \right\rangle \end{aligned} \tag{29}$$

Adding equations (29) and (28) we have:

$$\begin{aligned} &\int_o^T \left(\widehat{X}, \frac{\partial P}{\partial t} - \frac{\partial A^*(X,P)}{\partial x} - \frac{\partial B^*(X,P)}{\partial y} + F^*(X,P) \right) \mathrm{dt} \\ &+ \int_o^T \left(\hat{C}, \frac{\partial Q}{\partial t} + \vec{\nabla}.(UQ) + \eta\Delta Q + KQ \right) \mathrm{dt} = \\ &\int_0^T \int_\Omega \left[\hat{u}Q\frac{\partial C}{\partial x} + \hat{v}Q\frac{\partial C}{\partial y} \right] d\Omega dt + \left(\hat{C}(T), Q(T) \right) - \\ &- \left(\hat{C}(0), Q(0) \right) + \left(\widehat{X}(T), P(T) \right) - \left(\widehat{X}(0), P(0) \right) \end{aligned}$$

Then if P and Q are the solutions of the following equations:

$$\begin{cases} \dfrac{\partial P}{\partial t} = \dfrac{\partial A^*(X,P)}{\partial x} + \dfrac{\partial B^*(X,P)}{\partial y} \\ -F^*.(X,P) + F_0.(Q,C) + E^T\left[EX - X_{obs}\right] \\ P_2 n_x + P_3 n_y = 0 \text{ on } S_W \\ P_2 = -\dfrac{U_{in}}{g} P_1 n_x \text{ on } \Gamma_1 \\ P_3 = -\dfrac{U_{in}}{g} P_1 n_y \text{ on } \Gamma_1 \\ P_2 = -\dfrac{h}{U\vec{n}} P_1 n_x \text{ on } \Gamma_2 \\ P_3 = -\dfrac{h}{U\vec{n}} P_1 n_y \text{ on } \Gamma_2 \\ P(T) = 0 \end{cases} \tag{30}$$

$$\begin{cases} \dfrac{\partial Q}{\partial t} = -\vec{\nabla}.(UQ) - \eta \Delta Q - KQ + D^T(DC - C_{obs}) \\ \dfrac{\partial Q}{\partial \vec{n}} = 0 \text{ on } S_W \\ U\vec{n}Q + \eta \dfrac{\partial Q}{\partial \vec{n}} = 0 \text{ on } \Gamma_2 \\ Q = 0 \text{ on } \Gamma_1 \\ Q(T) = 0 \end{cases} \qquad (31)$$

Where: $X_{obs} = \begin{bmatrix} z_{obs} \\ u_{obs} \\ v_{obs} \end{bmatrix}$; $\mathrm{F}_0(Q,C) = \begin{bmatrix} 0 \\ Q\dfrac{\partial C}{\partial x} \\ Q\dfrac{\partial C}{\partial y} \end{bmatrix}$

the gradient of cost functions $\nabla J = (\nabla J_U; \nabla J_V)$ can be deduced as followed:

$$\nabla J_U = -P(0) \qquad (32)$$

$$\nabla J_V = -Q(0) \qquad (33)$$

By the same way as solving *(z; u; v)* in section 3 P_1, P_2, P_3 are solved by the following formulas:

$$P_1 = P_{1,t} - \frac{dt}{S}\oint_{\gamma j}\left(gP_2n_x + gP_3n_y + uP_1n_x + vP_1n_y\right)d\gamma_j + \left[P_{1,t}\frac{\partial u_t}{\partial x} + P_{1,t}\frac{\partial v_t}{\partial y}\right]dt + I_1E^T\left[EX - X_{obs}\right]$$

$$P_1(T) = 0$$

$$P_2 = P_{2,t} - \frac{dt}{S}\oint_{\gamma j}\left[\left(uP_{2,t} + hP_{1,t} + vP_{3,t}\right)n_x + vP_{2,t}n_y\right]d\gamma_j + \left[\frac{g\left(u^2+v^2\right)+u^2+uv}{K_x^2h^{4/3}\sqrt{u^2+v^2}} + \frac{\partial u}{\partial x}\right]P_{2,t}$$

$$+\left[\frac{\left(v^2+uv\right)P_{3,t}}{K_x^2h^{4/3}\sqrt{u^2+v^2}} + \frac{\partial\left(vP_{3,t}\right)}{\partial x} + P_{3,t}\frac{\partial v}{\partial x} + P_{1,t}\frac{\partial z}{\partial x}\right] + Q\frac{\partial C}{\partial x} + I_2E^T\left[EX - X_{obs}\right]$$

$$P_2(T) = 0$$

$$P_3 = P_{3,t} - \frac{dt}{S}\oint_{\gamma j}\left[\left(uP_{2,t} + hP_{1,t} + vP_{3,t}\right)n_y + uP_{3,t}n_x\right]d\gamma_j + \left[\frac{g\left(u^2+v^2\right)+v^2+uv}{K_x^2h^{4/3}\sqrt{u^2+v^2}} + \frac{\partial v}{\partial y}\right]P_{3,t}$$

$$+\left[\frac{\left(u^2+uv\right)P_{2,t}}{K_x^2h^{4/3}\sqrt{u^2+v^2}} + \frac{\partial\left(uP_{2,t}\right)}{\partial y} + P_{2,t}\frac{\partial u}{\partial y} + P_{1,t}\frac{\partial z}{\partial y}\right] + Q\frac{\partial C}{\partial y} + I_3E^T\left[EX - X_{obs}\right]$$

$$P_3(T) = 0$$

Here: I_1, I_2 and I_3 are the projection operators to the spaces of variables *z*, *u* and *v*.
By the similar way as above Q can be calculated by the following formula:

$$Q = -KQ_t dt + Q_t - \frac{dt}{S}\oint_{\gamma_j}\left[\left(\eta\frac{\partial Q_t}{\partial x} + uQ_t\right)n_x + \left(\eta\frac{\partial Q_t}{\partial y} + vQ_t\right)n_y\right]d\gamma_j + D^T(DC - C_{obs})$$

5. SIMULATION EXPERIMENT FOR THANH NHAN LAKE.

Thanh Nhan Lake is located behind Thanh Nhan hospital. Its area, water capacity are about 8.1 ha and 162000 m^3 respectively. In this paper we study transport of BOD_5's indicator in this lake. BOD_5's indicator shows the oxygen quantity needing for bacterium in oxygen reactions of organic substances in water. The chemical process of conversion

indicator is described by the formula: $f(BOD_5) = K. BOD_5$.

On the collected data, we establish input data for the model. Geographical data is divided into the boundary and inside area of lake by the unstructured net with 1964 triangular cells and 1058 nodes. This unstructured net is described in figure 1, left panel.The velocity field and measurement positions are shown in the right panel of this figure

The data of discharges and substance contents at the gate into the lake are as follow:

- The discharges into the gate in of lake are 2100 m3 per day-night.
- The water depth is 4m in the gate out.
- The content of BOD5 at the gate into lake is the same as the measurement value 24 mg/l.

On the gate out there are the conditions of concentration: $\partial C / \partial n = 0$.

5.1. Simulation setup and results.

Let the model run 100h. Tthe initial conditions *X(0) = U* and *C(0) = V* wiil be the values at time t=100h and then let model run for 24 hours more. This model with this initial conditions will be called reference. Let the model run with the initial initial water velocity and concentration *X(0)=U+0.05*U* and *C(0)=V+0.05*V* . Let the model run 24h with correction algorithm with the measurements at some points and some time steps getting from reference model. It is called initial condidtion's correction model. The last one is the model running in 24h with this new initial velocity and concentration *X(0) = U + 0.05*U* and *C(0) = V + 0.05*V* without correction. Then we have 3 models running:

- The reference model with initial conditions X(0) = U and C(0) = V ;
- The model with new initial velocity and concentration X(0) = U +0.05* U and C(0) = V + 0.05*V and then using correcting initial condition module.
- The model with new initial velocity and concentration X(0) = U +0.05* U and C(0) = V + 0.05*V without corection; .

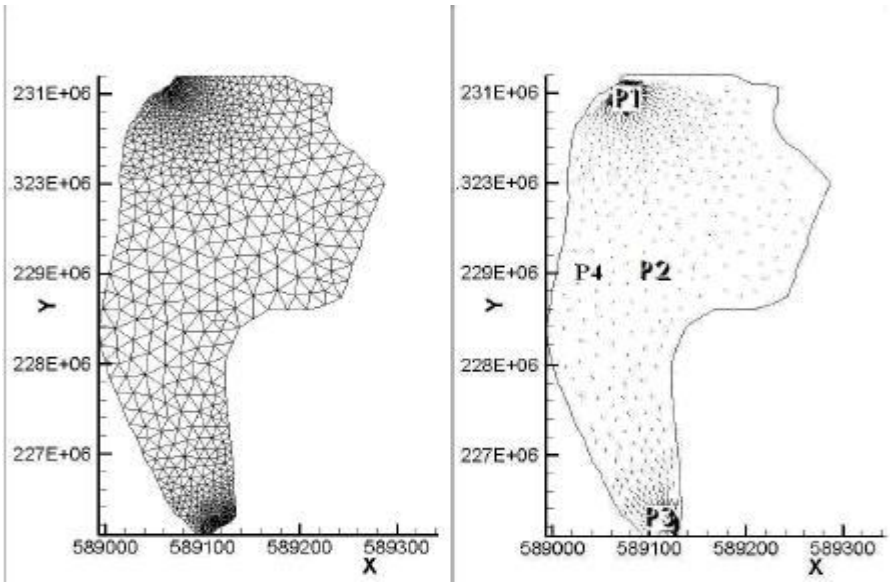

Figure 1: Unstructured net with triangular cells (left) and velocity field with measurement positions P1, P2, P3, P4 shown (right).

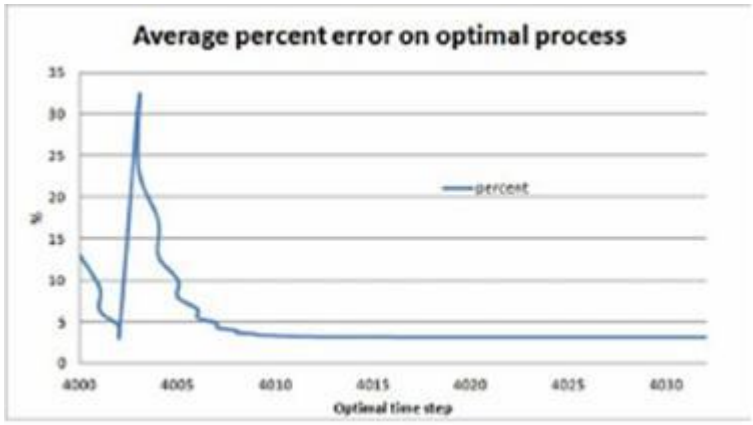

Figure 2: The Average error percent in the optimal process correcting initial conditions

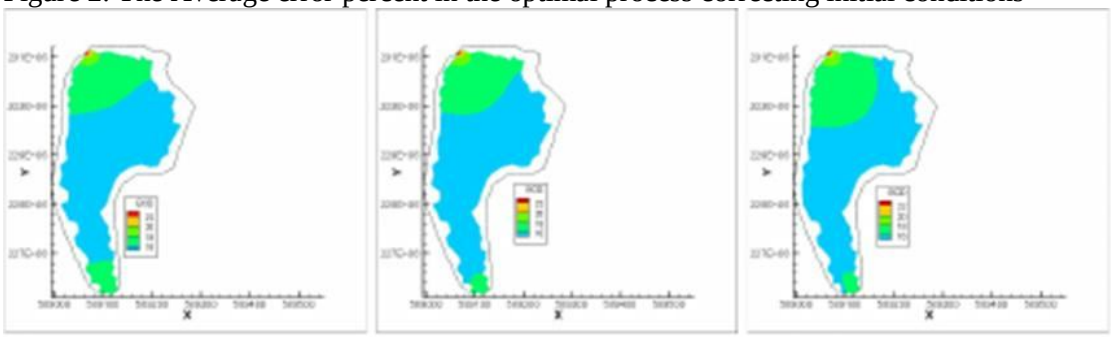

Figure 3: The concentration in the initial moment: In the reference model (left); In the correction model (middle); In the not correction model

The average error percent in the optimal process correcting the initial conditions in the lake is presented in figure 2.

The concentrations of reference model and the one with or without correcting initial condition are presented in figure 3. By this figure it is clear that the concentrations of the model with initial condition's correction are closer to reference than the other one without correction.

CONCLUSION

Simulation results suggest the good performance of the method. The Data Assimilation method correcting initial conditions by optimal variation is working well with 2D pollution model. Then the model can be the one of the tools to study water pollutant processes.

ACKNOWLEDGEMENTS

The authors are grateful to the Vast's pollution project and NAFOSTED's funds and for their supports forthis research.

REFERENCES

[1] Licht, C., Tran, T.H., and Vu, Q.P. (2009) On some linearized problems of shallow water ows. *Differential and Integral equations* 22, No 3-4, 275-283.

[2] Sleigh, P.A., Gaskell,P.H., Berzins M. and Wright, N.G. (1998) An unstructured Finite Volume Algorithm for predicting Flow in Rivers and Estuaries, *Computers & Fluids* 27, 479-508.

[3] Tran, T.H. and Nguyen, H.P. (2010) 2D-Model of contaminant water transmission processes and numerical simulation on a natural lake. *J. of Mechanics* 32, No 3, 157-166.

[4] W. Rauch, M. Henze, L. Koncsos, P. Shanahan, L. Somlyody and Vanrolleghem. (1998) *River water quality modlling*: *I. State of the art, Wat. Sci. Tech.* , 38, No. 11, 237-244

The 2nd International Conference on Engineering Mechanics and Automation (ICEMA2)
Hanoi, August 16-17, 2012
ISBN: 978-604-913-097-7

The Diffusion Coefficient of Water Pollution and Application of Data Assimilation Method

Tran Thu Ha[1,2] and Nguyen Ba Hung [1]

1 Institute of Mechanics, VAST --18 Hoang Quoc Viet, Hanoi, Vietnam
2. University of Engineering and Technology - VNU, 144 Xuan Thuy, Hanoi, Vietnam

Abstract

In this paper the Data Assimilation by Optimal Differential Variation method is apllied to correct the parameters so that the simulation results are closed to the measurements in water pollution model. The corrected parameter is diffusion parameter η. This corrected parameter is changing by simulation space. In this model data of Thanh Nhan lake in Hanoi is used to simulate. The comparision of simulation results with or without parameter correction is presented.

1. INTRODUCTION

Worldwide water pollution is an important problem for agriculture and also for men's health. Preventing water pollution requires knowing the exact situation of lakes, rivers, ocean in order to be able to predict their evolution. To study the water pollution problems there are many mathematical methods and models are used. The linear 2D water pollution water is studied by semi group method in [1]. The nonlinear 2D-Imech water pollution model is studied in [4]. In this paper 2D hydraulic and pollution models are used to describe the transport of the pollution substances. This model has been developed to simulate the transport of the pollution substance and thus can be used to estimate the pollution level if the initial values for the model equations are known and the model parameters are adequately specified. Since the model parameters for the model are not exactly known by all points of space , the estimates will not be exact and the model can be imperfect or not adequately specified, pollution estimation from the model will contain some errors. Data assimilation method presented in the section 2 permits to combine the available limited number of measurements and the model to obtain more precise estimate of model parameters and then evaluation of of the pollutant system state. We will concentrate our study on the identification of diffusion coefficient for the water pollution problem. In the second section we will describe the abstract definition of a variation problem. In the 3-rd section we will formulate the problem of water pollution we will work on.The 4-th section will be devoted to the application of variation methods to the identification of diffusion coefficient η. The

5-th section will be on application to the case of Thannhan Lake in Vietnam.

2. GENERAL VARIATIONAL APPROACH

In simulation model calculated contanminant transport process, the coefficients are defined so that simulation results are closed to measurements on some places. In this paper the parameter is corrected by Data Assimilation method using the adjoint problem. In this process the coefficients are found by Differential variation method. This method is described in many papers and a formalism closer to computational applications can be found in ([2]) and presented as follows:

Let C(t) a concentration variable describing the evolution of a system governed by the abstract equation

$$\begin{cases} \dfrac{dC}{dt} = F(C,E) \\ C(0) = C_0 \end{cases} \tag{1}$$

E is unknown parameter system. If we have some observation belonging to a space and if H is a linear mapping from the space of the state variable to the space of observation we define the so-called cost function.

$$J(E) = \frac{1}{2}\int_0^T \left\| HC - C_{obs} \right\|^2 dt + \frac{1}{2}\left\| E - E_0 \right\|^2 \tag{2}$$

H is an operator from the space of the state variable toward the space of observations and E_0 , are approximate values of E. The problem is to determine E* minimizing J. The second term in the definition of J are regularization term in the sense of Tykhonov to have a well posed problem. The optimal solution are characterized by $\nabla .J_E$, that is the gradient of J. To compute this gradient we introduce a direction in the space of E and we compute the Gateaux derivatives of $\hat{C}, \hat{J}$ in the directions of e.

We get

$$\begin{cases} \dfrac{d\hat{C}}{dt} = \dfrac{\partial F}{\partial C}.\hat{C} + \dfrac{\partial F}{\partial E}.e \\ \hat{C}(0) = 0 \end{cases} \tag{3}$$

Also we have:

$$\hat{J}(e) = \int_0^T \langle HC - C_{obs}, H\hat{C} \rangle \, dt + \langle E - E_0, e \rangle \tag{4}$$

where <.,.> is the dot product associated with the norm operator ||.||. To compute the gradient of J we need to exhibit the linear dependence $\hat{J}$ with respect to e and w. Let us introduce P as adjoint variable in the same space as X. We multiply equation 3 by P by and integrate between 0 and T, which yields :

$$\int_0^T \langle \frac{d\hat{C}}{dt}, P \rangle \, dt = \int_0^T \langle \frac{dF}{dt}.\hat{C}, P \rangle \, dt + \int_0^T \langle \frac{dF}{dE}.e, P \rangle \, dt \tag{5}$$

Integrating by parts we get:

$$\left\langle \hat{C}(T), P(T) \right\rangle - \left\langle \hat{C}(0), P(0) \right\rangle =$$

$$\int_o^T \left\langle \hat{C}, \frac{dP}{dt} + \left[\frac{\partial F}{\partial C} \right]^t .P \right\rangle \, dt + \int_o^T \left\langle e, \left[\frac{\partial F}{\partial E} \right]^t .P \right\rangle \, dt \tag{6}$$

Whew the superscript ^{t} indicates the transpose of the matrix. If *P(T)=0* then it becomes:

$$\int_o^T \left\langle \hat{C}, \frac{dP}{dt} + \left[\frac{\partial F}{\partial C} \right]^t .P \right\rangle \, dt + \int_o^T \left\langle e, \left[\frac{\partial F}{\partial C} \right]^t .P \right\rangle \, dt = 0 \tag{7}$$

Therefore if P is defined as the solutions of:

$$\begin{cases} \dfrac{dP}{dt} + \left[\dfrac{\partial F}{\partial C} \right]^t .P = H^t (HC - C_{obs}); \\ P(T) = 0; \end{cases} \tag{8}$$

$$\int_o^T \left\langle H^t (HC - C_{obs}), \hat{C} \right\rangle \, dt = -\int_o^T \left\langle \left[\frac{\partial F}{\partial C} \right]^t .P, e \right\rangle \, dt \tag{9}$$

then the linear dependence of the Gateaux derivatives of *J* with respect to the directions *h* is made explicit, and the components of the gradient ∇J can be calculated.

$$\hat{J}(e) = -\int_0^T \left\langle \left[\frac{\partial F}{\partial E} \right]^t P, e \right\rangle dt + \langle E - E_0, e \rangle \tag{10}$$

or $\hat{J}(e) = \langle \nabla J, e \rangle$ (11)

where ∇J is satisfied the following equation:

$$\nabla J = -\int_0^T \left[\frac{\partial F}{\partial E} \right]^t P dt + E - E_0 \tag{12}$$

Equations (1),(8) and the condition for the gradient to be null is the Optimality System (O.S). It worthwhile to point out that it contains all the available information.

In practice, the resolution of the adjoint model permits the computation of the gradient which is used in the algorithm of optimization: Newton-Type methods, L-BFGS, etc. The optimal initial system state and initial pollutant concentration, with respect to observed data, are estimated.

3. FORMULATION OF THE 2D WATER POLLUTION PROBLEM

2D pollution water model consists of hydraulic model and transport - diffusion of pollution substances. In hydraulic model the Sain-Vernant equation is used as follows [3]:

$$\frac{\partial z}{\partial t} + \frac{\partial (uh)}{\partial x} + \frac{\partial (vh)}{\partial y} = 0, \qquad in\ \Omega. \tag{13}$$

$$\frac{\partial u}{\partial t} + u\frac{\partial u}{\partial x} + v\frac{\partial u}{\partial y} + g\frac{\partial z}{\partial x} = -\frac{gu(u^2+v^2)^{1/2}}{K_x^2 h^{4/3}}, \quad in\ \Omega. \tag{14}$$

$$\frac{\partial v}{\partial t} + u\frac{\partial v}{\partial x} + v\frac{\partial v}{\partial y} + g\frac{\partial z}{\partial x} = -\frac{gv(u^2+v^2)^{1/2}}{K_y^2 h^{4/3}}, \quad in\ \Omega. \tag{15}$$

Here,

- Ω is a bounded domain of R^2 with a boundary Γ ,
- z is the free surface elevation,
- h is the water depth,
- u is the average velocity in the x direction,
- v is the average velocity in the y direction,
- g is the gravity acceleration,
- Kx is the Strickler coefficient in the x direction,
- Ky is the Strickler coefficient in the y direction.

We suppose that there are m substances dissolved in water. Then the transport and diffusion processes of pollution substances are described by the following equation [5].

$$\frac{\partial C}{\partial t} + u\frac{\partial C}{\partial x} + v\frac{\partial C}{\partial y} - \eta \Delta C = f(C),\ in\ \Omega, \tag{16}$$

Here,

- $\Delta = \left(\frac{\partial^2}{\partial x^2} + \frac{\partial^2}{\partial y^2} \right)$
- C is the concentration of the substance,
- f(C)=KC is the conversion pollution function of the substance,
- K is the conversion coefficient,
- η is the diffusion coefficient of the substance.

Denoting $X = (z, u, v)^T$ we have the initial conditions:

$X_0 = (z(x, y,0), u(x, y, 0, v(x, y, 0))^T$
$C(x, y, 0) = C_0$

In the slow changing process for water pollution problem the boundary conditions are:

$U.\vec{n} = \overline{U}_{in}(t),\ \mathrm{C(x,y,t)} = C_{in}(t)$
on inflow boundary Γ_1,

$z(x, y, t) = \bar{z}(t),\ \frac{\partial C}{\partial n} = 0$
on outflow boundary Γ_2,

$U.\vec{n} = 0, \frac{\partial C(x, y, t)}{\partial n} = 0$
on solid wall $S_{w,}$

where: U = *(u(x, y, t), v(x, y, t))*, S_w is the solid wall of Ω, Γ_2 and Γ_1 respectively are the outflow and inflow boundaries of the Ω domain, $\Gamma = \Gamma_1 \cup \Gamma_2 \cup S_W$ is the boundary of the region Ω, $\vec{n}$ is the unit normal vector onto Γ;

3.1. Equation for 2D flow system.

To solve the above model equations, a cell centrednite volume method is used (see [3]). The type of mesh employed in this method is an unstructured triangulation of the solution domain enabling arbitrary shaped geometries to be accomodated more easily than a square grid system (see [3]). The mesh points of the grid are numbered in some given but arbitrary way.

To apply the finite volume method, the equations (13)-(15) are rewritten as follows:

$$\frac{\partial X}{\partial t}+\frac{\partial A(x)}{\partial x}+\frac{\partial B(x)}{\partial x}=F(X), \qquad (17)$$

$$A(X)=\begin{pmatrix} uh \\ \frac{1}{2}u^2+gz \\ uv \end{pmatrix},\ B(X)=\begin{pmatrix} vh \\ uv \\ \frac{1}{2}v^2+gz \end{pmatrix}$$

$$F(X)=\begin{pmatrix} 0 \\ -gu\dfrac{\sqrt{u^2+v^2}}{K_x^2h^{4/3}}+u\dfrac{\partial v}{\partial y} \\ -gv\dfrac{\sqrt{u^2+v^2}}{K_y^2h^{4/3}}+v\dfrac{\partial u}{\partial x} \end{pmatrix}$$

With N_{point} mesh points ow domain is divided into N small cells Ω_j, that have boundary γ_j (j = 1,…,N). In this small cell Ω_j integrating two sides of equation system (178) with respect to the spatial variables x and y we get the formula:

$$\int_{\Omega_j}\frac{\partial X}{\partial t}dxdy+\int_{\Omega_j}\vec{\nabla}.(A(X),B(X))dxdy$$
$$=\int_{\Omega_j}F(X)dxdy$$

Here, $\vec{\nabla}=\left(\frac{\partial}{\partial x},\frac{\partial}{\partial y}\right)$.

We assume that in small cell Ω_j the variables (z,u,v), $h = z - z_{bottom}$ and F can be approximated as constant values. Therefore, using Green formula the above formula can be rewritten as follows:

$$\frac{dX}{dt}S+\oint_{\gamma_j}(A(X),B(X)).\vec{n}\,d\gamma_j=F(X)S. \qquad (18)$$

In formula (18) S is the cell's area, $\vec{n}$ is the unit normal vector onto γ_j with components in x and y directions denoted by n_x and n_y respectively. In the slow changing process problem to calculate the integrals we can use the average values for the functions in the cell. Using equation (18) the value of (z, u, v) at the cell center of Ω_j in the current step can be solved by the following equations:

$$z=z_t-\frac{\Delta t}{S}\oint_{\gamma_j}\left(hun_x+hvn_y\right)d\gamma_j \qquad (19)$$

$$u=u_t+\left[u_t\frac{\partial v_t}{\partial y}-\frac{gu_t\sqrt{u_t^2+v_t^2}}{K_x^2h^{4/3}}\right]\Delta t$$
$$-\frac{\Delta t}{S}\oint_{\gamma_j}\left[\left(\frac{u^2}{2}+gz\right)n_x+uvn_y\right]d\gamma_j \qquad (20)$$

$$v=v_t+\left[v_t\frac{\partial u_t}{\partial y}-\frac{gv_t\sqrt{u_t^2+v_t^2}}{K_x^2h^{4/3}}\right]\Delta t$$
$$-\frac{\Delta t}{S}\oint_{\gamma_j}\left[\left(\frac{v^2}{2}+gz\right)n_x+uvn_y\right]d\gamma_j \qquad (21)$$

Here z_t, u_t, v_t and z, u, v are called the values of z, u, v at cell center of Ω_j in the previous and in current steps.

3.2. Algorithm for transport-diffusion equations.

In pollution model the pollution process is depending on the combination of substances and number of them. In this paper we will study only one substance BOD_5 then the conversion pollution function f can be written by the formula $f=KC$.

By the same way as in paragraph 3.1 integrating two sides of quation (16) with respect to the spatial variable x and y then using Green formula, we get:

$$\int_{\Omega_j} \frac{\partial C}{\partial t} d\text{x}d\text{y} - \int_{\Omega_j} C\vec{\nabla}.U d\text{x}d\text{y} + \oint_{\gamma_j} (UC\vec{n} - \eta\vec{\nabla}.C\vec{n}) d\gamma_j = \int_{\Omega_j} KCd\text{x}d\text{y} \quad (22)$$

The equation (22) can be rewriten as following:

$$\oint_{\gamma_j} \left[\left(u.n_x + v.n_y \right) C - \eta \left(\frac{\partial C}{\partial x} n_x + \frac{\partial C}{\partial y} n_y \right) \right] d_{\gamma_j} + \frac{\partial C}{\partial t} S - C\vec{\nabla}.US = KCS \quad (23)$$

where: C and C_t are the concentrations in cell's center at the current and previous steps, $\vec{\nabla}.U$ is obtained when (u,v) is calculated by the formula (20) - (21).

Equation (23) can be discretized as follows:

$$\frac{C - C_t}{\Delta t} S - C_t \vec{\nabla}.U \; S + I_c = KC_t S \quad (24)$$

Thus in small cell Ω_j C can be calculated by the formula:

$$C = C_t + \left(K + \vec{\nabla}.U \right) C_t \Delta t - \frac{\Delta t}{S} \oint_{\gamma_j} \left[\left(u.n_x + v.n_y \right) C - \eta \left(\frac{\partial C}{\partial x} n_x + \frac{\partial C}{\partial y} n_y \right) \right] d_{\gamma_j}$$

4. THE DIFFUSION COEFFICIENT'S CORRECTION BY DIFFERENTIAL OPTIMAL FINDING THE IN POLLUTION EQUATION .

4.1. Diffusion coefficient .

We have an approximation η_0 of η and measurement Cobs of the concentration. Using the cost function from formula (2) the continuous problem is to determine C* minimizing

$$J(\eta) = \frac{1}{2} \int_0^T \left\| HC - C_{obs} \right\|^2 dt + \frac{1}{2} \left\| \eta - \eta_0 \right\|^2 \quad (26)$$

C_{obs} is a function of *x,y* and *t*. H is an operator, that is Diracts matrix, from the space of the variable C(x,y,t) to the space of observation with point wise measurement.

Therefore, we have an optimal control problem with respect to the coefficient η. An extension in this problem concern the frequent case when sources of pollution are unknown the problem being to identify source of pollution we will develop this problem later. The first step is to exhibit the Euler-Lagrange equation- necessary equation for an optimum in order to exhibit the gradient of J with respect to η, then we will be able to carry out some optimization algorithm.

– Computing Gateaux derivative of cost function J. Let $\bar{\eta}$ (x, y) being some function in the space of the control . We write (16) with the term $\eta + \alpha\bar{\eta}$ then we get the following equation:

$$\frac{\partial C_{\eta+\alpha\bar{\eta}}}{\partial t} + U\nabla C_{\eta+\alpha\bar{\eta}} - (\eta + \alpha\bar{\eta})\Delta C_{\eta+\alpha\bar{\eta}} = KC_{\eta+\alpha\bar{\eta}}, \quad in\ \Omega, \quad (27)$$

The Gateaux derivative of C is the function $\hat{C}$ satisfied the formula:

$$\hat{C} = \lim_{\alpha \to 0} \frac{C_{\eta+\alpha\bar{\eta}} - C}{\alpha}$$

Subtract equation (27) by equation (16) then divided by α we take the limit when $\alpha \to 0$ we get as the solution of:

$$\begin{cases} \dfrac{\partial \hat{C}}{\partial t} + U\nabla\hat{C} - \bar{\eta}\Delta C - \eta\Delta\hat{C} = K\hat{C} \ in\ \Omega, \\ \hat{C} = 0 \text{ on } \Gamma_1, \\ \dfrac{\partial \hat{C}}{\partial \vec{n}} = 0 \text{ on } \Gamma_2 \cup S_W, \\ \hat{C}(0) = 0 \end{cases} \quad (28)$$

The G-derivative of J is verifying:

$$\hat{J}(\bar{\eta}) = \int_0^T \left\langle HC - C_{obs}, H^T \hat{C} \right\rangle dt + \left\langle \eta - \eta_0, \bar{\eta} \right\rangle \quad (29)$$

To get the gradient we need to exhibit the linear dependant of J with respect to the direction $\bar{\eta}$. We introduce p(x,y) and adjoin

variable in the space of C. P will be later defined for convenience. Multiplying (28) by p and integrate on Ω and between 0 and T we have:

$$\int_0^T\int_\Omega \frac{\partial \hat{C}}{\partial t}p\mathrm{d}\Omega dt+\int_0^T\int_\Omega Up\nabla\hat{C}\mathrm{d}\Omega dt-\int_0^T\int_\Omega \bar{\eta}\,p\Delta C\mathrm{d}\Omega dt$$
$$-\int_0^T\int_\Omega \eta\,p\Delta\hat{C}\mathrm{d}\Omega dt=\int_0^T\int_\Omega K\hat{C}p\mathrm{d}\Omega dt, \quad (30)$$

Let us consider separately each term (30) is integrated by part with respect to time we get:

$$\int_0^T\int_\Omega \frac{\partial \hat{C}}{\partial t}p\mathrm{d}\Omega dt$$
$$=\int_\Omega\left[\hat{C}p\big|_{t=T}-\hat{C}p\big|_{t=0}-\int_0^T\hat{C}\frac{\partial p}{\partial t}dt\right]d\Omega \quad (31)$$

If the adjoint function p is satisfying the condition $p(T) = 0$ then equation (31) can be rewritten as follows:

$$\int_0^T\int_\Omega \frac{\partial \hat{C}}{\partial t}p\mathrm{d}\Omega dt=-\int_0^T\int_\Omega \hat{C}\frac{\partial p}{\partial t}d\Omega dt \quad (32)$$

Using the boundary condition $U\vec{n}\big|_{S_W}=0$ the second term of the left side of equation (30) can be rewritten as follows:

$$\int_0^T\int_\Omega U\nabla.\hat{C}p\mathrm{d}\Omega dt=\int_0^T\int_{\Gamma_2}\hat{C}Up\vec{n}d\Gamma_2 dt$$
$$-\int_0^T\int_\Omega \hat{C}\nabla.(Up)\,d\Omega dt \quad (33)$$

The third term of equation (30) is rewritten as follows:

$$-\int_0^T\int_\Omega p\eta\Delta\hat{C}\mathrm{d}\Omega dt=-\int_0^T\int_{\Gamma_1}\eta\,p\frac{\partial\hat{C}}{\partial\vec{n}}d\Gamma_1 dt$$
$$+\int_0^T\int_{\Gamma_2\cup S_W}\eta.\hat{C}\frac{\partial p}{\partial\vec{n}}d\left(\Gamma_2\cup S_W\right)dt-\int_0^T\int_\Omega \eta.\hat{C}\Delta p d\Omega dt, \quad (34)$$

The 4-th term of (30) can be written as following:

$$-\int_0^T\int_\Omega p\bar{\eta}\Delta C\mathrm{d}\Omega dt=-\int_0^T\int_{\Gamma_1}\bar{\eta}\,p\frac{\partial C}{\partial\vec{n}}d\Gamma_1 dt$$
$$+\int_0^T\int_\Omega \bar{\eta}.\nabla C\nabla p d\Omega dt \quad (35)$$

If p is satisfied following homogeneous boundary conditions and time condition:

$$\begin{cases} U\vec{n}p+\eta\dfrac{\partial p}{\partial\vec{n}}=0 \text{ on } \Gamma_2, \\ \dfrac{\partial p}{\partial\vec{n}}=0 \text{ on } S_W \\ p=0 \text{ on } \Gamma_1 \\ p(T)=0 \end{cases},$$

using equations (32) - (35) and the homogeneous boundary conditions of $\hat{C}$ (see equation (28)) we can write equation (30) as follows:

$$\int_0^T\int_\Omega \hat{C}\left[\frac{\partial p}{\partial t}+\nabla(Up)+\eta\Delta p+Kp\right]\mathrm{d}\Omega dt$$
$$=\int_\Omega\bar{\eta}\int_0^T\nabla p\nabla C dt d\Omega \quad (36)$$

Then if p is the solution of the following equation:

$$\begin{cases} \dfrac{\partial p}{\partial t}+\nabla.(Up)+\eta\Delta p+Kp=H(HC-C_{obs}), \\ U\vec{n}p+\eta\dfrac{\partial p}{\partial\vec{n}}=0 \text{ on } \Gamma_2, \\ \dfrac{\partial p}{\partial\vec{n}}=0 \text{ on } S_W, \\ p=0 \text{ on } \Gamma_1, \\ p(T)=0 \end{cases}, \quad (37),$$

using (27), (36) we have:

$$\hat{J}(\eta,\bar{\eta})=\left\langle\int_0^T\nabla p\nabla C dt,\bar{\eta}\right\rangle+\left\langle\eta-\eta_0,\bar{\eta}\right\rangle$$

Therefore, we have shown the linearity of $J(\eta,\eta^*)$ with respect to η^* and function $\hat{J}(\eta,\bar{\eta})=\left\langle\nabla J,\bar{n}\right\rangle$

with $\nabla J = \int_0^T \nabla p \nabla C dt + (\eta - \eta_0)$ (38)

- To summarize the computation schema of the cost funtion J there are 3 steps:
  - Solve the model:

$$\begin{cases} \dfrac{\partial C}{\partial t} + U\nabla.C - \nabla.(\eta\nabla.C) = KC \\ \mathrm{C(x,y,t)} = C_{in}(t) \text{ on } \Gamma_1, \\ \dfrac{\partial C}{\partial n} = 0 \text{ on } \Gamma_2 \cup S_w, \\ C(x,y,0) = C_0 \end{cases}$$

  - Solve the adjoin model (equation (37)) from T to 0 backward integration in time.
  - Deduce the gradient ∇J by formula (38)

SIMULATION EXPERIMENT FOR THANH NHAN LAKE.

Thanh Nhan Lake is located behind Thanh Nhan hospital. Its area, water capacity are about 8.1 ha and 162000 m^3 respectively. In this paper we only study transport of BOD_5's indicator in this lake. BOD_5's indicator shows the oxygen quantity needing for bacterium in oxygen reactions of organic substances in water. The chemical process of conversion indicator is described by the formula: $f(BOD_5) = K. BOD_5$

On the collected data, we establish input data for the model. Geographical data is divided into the boundary and inside area of lake by the unstructured net with 1964 triangular cells and 1058 nodes. This unstructured net is described in figure 1, left panel. The velocity field and measurement positions are shown in the right panel of this figure.

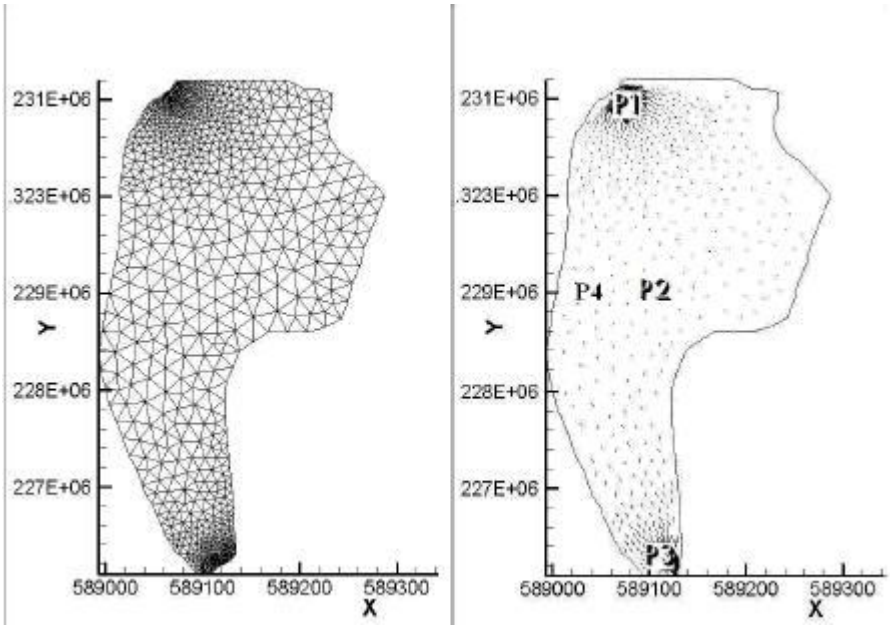

Figure 1: Unstructured net with triangular cells (left) and velocity field with measurement positions P_1, P_2, P_3 and test position P_4 shown (right).

The data of discharges and substance contents at the gate into the lake are as follow:

- The discharges into the gate in of lake are 2100 m^3 per day-night.
- The water depth is 4m in the gate out.
- The content of BOD_5 at the gate into lake is the same as the measurement value 24 mg/l.

On the gate out there are the conditions of concentration: $\partial C_1 / \partial n = 0$.

5.1. Simulation setup and results.

Let the model run 100h with the experimetal coefficient system η_0 for one substance such as BOD_5 in order to get the initial state and concentration X_0 and C_0. Then let it run for 24 hours more. This model with this coefficient η_0 will be called reference. The other model is running in 24 hours with initial state and concentration X_0 and C_0 but the new coefficient η is different than the old one 3 times ($\eta = 4\eta_0$). For this model the coefficient correction module with the measurements at 3 points (P_1-P_3) and some time steps getting from reference model is used. It is called correction coefficient model. The last one is the model running in 24 hours with initial state and concentration X_0 and C_0 and the new coefficient η but without coefficient correction process. Then we have 3 models running:

- The reference model with coefficient $\eta = \eta_0 = 1.7e^{-6}$ in all the lake area;
- The model with new coefficient $\eta = 4*\eta_0 = 4*1.7e^{-6}$ in all the lake area and using coefficient corection module;
- The model with new coefficient $\eta = 4*\eta_0 = 4*1.7e^{-6}$ in all the lake area and without coefficient corection;

The correction process of the coefficient in test position P_4 is presented in the left side of figure 2. The average error percent in the optimal process finding diffusion coefficient in the lake is presented in the right side of figure 2.

The concentration of the reference model and the one with or without correction coefficients are presented in the left side of figure 3. By this figure it is clear that the concentration distribution of the model with coefficient correction are closer to the one of reference than the other one without coefficient correction process.

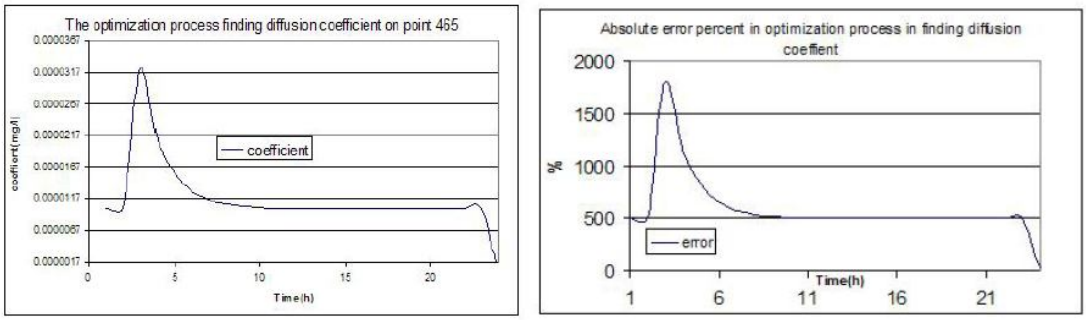

Figure 2. The optimal process finding diffusion coefficient on test point (P_4) in the lake (Left), The average error percent in the optimal process finding diffusion coefficient in the lake (Right)

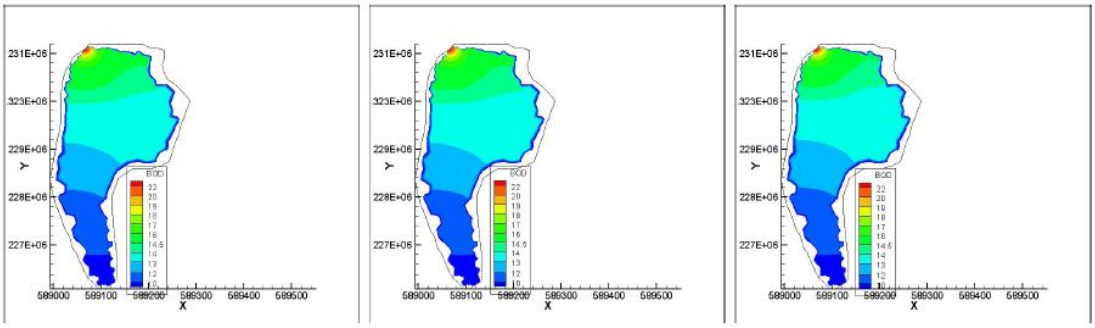

Figure 3. The concentration in the reference model (Left); The concentration in the model with diffusion coefficient's correction module (Middle); The concentration in the model without diffusion coefficient's correction module (Right).

It is easily to see that in figure 2 the diffusion coefficient comes to the one of reference model and the average error percent comes to zero by time. Figure 3 shows that the concentration in the model with diffusion coefficient's correction module is closer to the reference's concentration than the one in the model without diffusion coefficient's correction module.

CONCLUSION

Simulation results suggest the good performance of the method.. The Data Assimilation method correcting coefficients by optimal variation is working well with 2D pollution model. Then the model can be the one of the tools to study water pollutant process.

ACKNOWLEDGEMENTS

The authors are grateful to the Vast's pollution project and NAFOSTED's funds and for their supports forthis research.

REFERENCES

[1] Licht, C., Tran, T.H., and Vu, Q.P. (2009) On some linearized problems of shallow water ows. *Differential and Integral equations* 22, No 3-4, 275-283.

[2] Sleigh, P.A., Gaskell,P.H., Berzins M. and Wright, N.G. (1998) An unstructured Finite Volume Algorithm for predicting Flow in Rivers and Estuaries, *Computers & Fluids* 27, 479-508.

[3] Tran, T.H. and Nguyen, H.P. (2010) 2D-Model of contaminant water transmission processes and numerical simulation on a natural lake. *J. of Mechanics* 32, No 3, 157-166.

[4] W. Rauch, M. Henze, L. Koncsos, P. Shanahan, L. Somlyody and Vanrolleghem. (1998) *River water quality modlling*: *I. State of the art, Wat. Sci. Tech.* , 38, No. 11, 237-244

The 2nd International Conference on Engineering Mechanics and Automation (ICEMA2) Hanoi, August 16-17, 2012 ISBN: 978-604-913-097-7

Frequency Optimization of Corrugated Laminate Plate with Respect to Fiber Orientations

Bui Van Binh[a], Tran Ich Thinh[b] and Tran Minh Tu[c]

[a] *University of Power Electric, Hoang Quoc Viet Str. 235, Tu Liem Dist. Hanoi, Vietnam; binhphuongduc@yahoo.com*
[b] *Hanoi University of Science & Technology, Dai Co Viet Str. 1, Hai Ba Trung Dist. Hanoi, Vietnam; tranichthinh@yahoo.com*
[c] *University of Civil Engineering, Giai Phong Str. 55, Hai Ba Trung Dist. Hanoi, Vietnam; tpnt2002@yahoo.com*

Abstract

In this study, frequency optimization of corrugated laminate plate is investigated with respect to fiber orientations by using genetic algorithm (GA). The finite element code based on the first order shear deformation theory is developed to calculate natural frequencies of the corrugated plate. In this, an eight-nodded rectangular isoparametric element with five degrees of freedom per node is used. The optimal fiber orientations are obtained that maximized the first frequency of the plate under different boundary conditions. The standard modulus of selection, crossover and mutation are used to solve the optimal problems. The transient responses of the plate are investigated to see the effects of obtained optimal fiber orientations, folding angles of corrugated laminate plates. It is shown that optimal fiber orientations and folding angles are high-efficiency on bending corrugated composite plate.

Key Words: frequency optimization, transient responses, corrugated laminate plate, finite element method, genetic algorithm, Mindlin plate theory.

1. Introduction

Composite corrugated plates are found in all branches of engineering practice. The corrugations reinforce the plates and improve their strength to weight ratio. Thus, corrugated plates are popular in decking, roofing and sandwich plate core structures.

Many solutions of corrugate plate structures are treated as equivalent orthotropic plates. Once the equivalent rigidities are determined, corrugated plates can be analyzed as orthotropic plates either by theoretical methods or by numerical methods [1-6].

Mangetal [7] have formulated an equivalent orthotropic model of folded sheets for the analysis of the doubly corrugated shells by the finite element method. The majority of papers have deal with the stability analysis. Comparisons of flexural rigidity of the equivalent orthotropic plate have also been made [1, 8]. Shimansky and Lele [9] derived an analytical model for the initial transverse stiffness of sinusoidally corrugated plates. They found that for most corrugated plates, the transverse stiffness is dramatically less than it is for an uncorrugated plate of the same thickness, and that transverse stiffness is not negligible for

thick plates with a small degree of corrugation. Semenyuk and Neskhodovskaya [10] and Machimdamrong et al. [11] took into account the transverse shear stresses, and gave the equivalent expression of the transverse shear modulus for thick corrugated plates. Semenyuk and Neskhodovskaya [12] also presented the conditions under which a corrugated shell should not be treated as an orthotropic circular shell. All these investigations are focus on corrugated sheet equivalent orthotropic plates based on Seydel's flexural rigidity only. All of those analyses only investigated for plates made of by isotropic material. The plates made of by laminate composite are not readily available.

Moreover, there is very limited information regarding the analysis of corrugated composite structures. Basher et al [13] presented behaviour of horizontally curved composite plate girders with trapezoidally corrugated webs for different types of girders in terms of ultimate load carrying capacity, load–deflection and buckling patterns. Sokolinsky et al [14] presented a numerical simulation of the crushing response of a carbon–epoxy fabric corrugated plate specimen using the Abaqus/Explicit finite element code according to the geometry and lay-up of the corrugated plate. It was stated that the model accounts for both intralaminar (in-plane) and interlaminar (delamination) failure mechanisms. All of those analyses only investigated for a given fiber configuration. The optimal problem is not readily available.

Therefore, in this study frequency optimization of corrugated laminate composite plate is investigated to fill this gap. The fundamental frequencies of the corrugated plates are maximized with respect to fiber orientations. The first-order shear deformation theory is used for vibration analysis of the corrugated plate. The GA method is used for this optimization analysis.

2. Theory and formulation

2.1. Displacement and strain field

According to the Reissner-Mindlin plate theory, the displacements (u, v, w) are referred to those of the mid-plane (u_0, v_0, w_0) as:

$$\begin{Bmatrix} u \\ v \\ w \end{Bmatrix} = \begin{Bmatrix} u_0 + z\theta_x \\ v_0 + z\theta_y \\ w_0 \end{Bmatrix} \text{ and } \begin{Bmatrix} \theta_x \\ \theta_y \end{Bmatrix} = \begin{Bmatrix} \frac{\partial w}{\partial x} + \phi_x \\ \frac{\partial w}{\partial y} + \phi_y \end{Bmatrix} \quad (1)$$

Here, θ_x and θ_y are the total rotations, ϕ_x and ϕ_y are the constant average shear deformations about the y and x-axes, respectively.

The z-axis is normal to the xy-plane that coincides with the mid-plane of the laminate positive downward and clockwise with x and y.

The generalized displacement vector at the mid- plane can thus be defined as

$$\{d\} = \{u_0, v_0, w_0, \theta_x, \theta_y\}^T$$

2.2 Finite element formulations

The Hamilton variation principle is used here to derive the laminate equations of motion (see [15]). In laminated plate theories, the membrane $\{N\}$, bending moment $\{M\}$ and shear stress $\{Q\}$ resultants can be obtained by integration of stresses over the laminate thickness. The stress resultants-strain relations expressed in the form:

$$\begin{Bmatrix} \{N\} \\ \{M\} \\ \{Q\} \end{Bmatrix} = \begin{bmatrix} [A_{ij}] & [B_{ij}] & [0] \\ [B_{ij}] & [D_{ij}] & [0] \\ [0] & [0] & [F_{ij}] \end{bmatrix} \begin{Bmatrix} \{\varepsilon^0\} \\ \{\kappa\} \\ \{\gamma^0\} \end{Bmatrix} \quad (2)$$

Where

$$[F_{ij}] = \sum_{k=1}^{n} f \int_{h_{k-1}}^{h_k} \left([C'_{ij}]_k \right) dz; \quad f = 5/6; \; i, j = 4, 5 \quad (3)$$

$$\left([A_{ij}], [B_{ij}], [D_{ij}] \right) = \sum_{k=1}^{n} \int_{h_{k-1}}^{h_k} \left([Q'_{ij}]_k \right) (1, z, z^2) dz \quad (4)$$

with i, j=1,2,6

n: number of layers, h_{k-1}, h_k : the position of the top and bottom faces of the k^{th} layer.

$[Q'_{ij}]_k$ and $[C'_{ij}]_k$: reduced stiffness matrices of the k^{th} layer (see [16]).

In the present work, eight nodded isoparametric quadrilateral element with five degrees of freedom per nodes is used. The displacement field of any point on the mid-plane given by:

$$u_0 = \sum_{i=1}^{8} N_i(\xi,\eta).u_i;\ v_0 = \sum_{i=1}^{8} N_i(\xi,\eta).v_i$$
$$w_0 = \sum_{i=1}^{8} N_i(\xi,\eta).w_i;\ \theta_x = \sum_{i=1}^{8} N_i(\xi,\eta).\theta_{xi} \quad (5)$$
$$\theta_y = \sum_{i=1}^{8} N_i(\xi,\eta).\theta_{yi}$$

Where: $N_i(\xi,\eta)$ are the shape function associated with node i in terms of natural coordinates (ξ,η).

The element stiffness matrix are given by:

$$[k]_{e(40\times40)} = \int_{A_e} \left([B]^T\right)_{40\times8} [H]_{8\times8} [B]_{8\times40}\, t dA_e \quad (6)$$

The element mass matrix are given by:

$$[m]_e = \int_{A_e} \rho \left[N_i\right]^T \left[\overline{m}\right] \left[N_i\right] dA_e \quad (7)$$

Where $[H]$ is the material stiffness matrix; ρ is mass density of material; $\left[\overline{m}\right]$ is geometric inertia matrix (see [17]).

Nodal force vector is expressed as:

$$\{f\}_e = \int_{A_e} \left[N_i\right]^T q dA_e \quad (8)$$

Where q is the intensity of the applied load.

For free and forced vibration analysis, the damping effect is neglected; the governing equations are [15]:

$$[M]\{\ddot{u}\} + [K]\{u\} = \{0\} \text{ or}$$
$$\left\{[M] - \omega^2[K]\right\} = \{0\} \quad (9)$$

And $$[M]\{\ddot{u}\} + [K]\{u\} = f(t) \quad (10)$$

In which $\{u\}, \{\ddot{u}\}$ are the global vectors of unknown nodal displacement, acceleration, respectively. $[M], [K], f(t)$ are the global mass matrix, stiffness matrix, applied load vectors, respectively.

Where

$$[M] = \sum_1^n [m]_e ; [K] = \sum_1^n [k]_e ;$$
$$\{f(t)\} = \sum_1^n \{f_e(t)\}$$

With n is the number of element.

In the Reissner–Mindlin model, it is necessary to introduce a new unknown for the in-plane rotation called drilling degree of freedom, θ_z. The rotation θ_z at a node is not measured and does not contribute to the strain energy stored in the element. The technique is used here: Before applying the transformation, the 40×40 stiffness and mass matrices are expanded to 48×48 sizes, to insert sixth θ_z drilling degrees of freedom at each node of a finite element. The off-diagonal terms corresponding to the θ_z terms are zeroes, while a very small positive number, we taken the θ_z equal to 10^{-4} times smaller than the smallest leading diagonal, is introduced at the corresponding leading diagonal term. The load vector is similarly expanded by using zero elements at corresponding locations. So that, for a folded element, the displacement vector of each node [17] (see Fig.1):

$$\{u\} = [T]\{u'\}$$

$u = [u,v,w]^T$; $u' = \left[u',v',w'\right]^T$ are the displacement of any generic point in global and local coordinate system, respectively.

$[T]$ is the transformation matrix (see [17]).

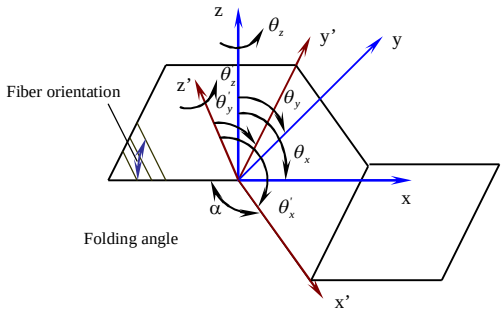

Fig.1. Global (*x*,*y*,*z*) and local (*x*',*y*'*z*') axes system for folded plate element, folding angle α.

2.3. Genetic algorithm

A genetic algorithm (GA) is an evolutionary optimization technique using Darwin's principal of survival of the fittest to improve a population of solutions. If the population size is suitably large, GA is not at the risk of being stuck in a local optimum. However, finding a global solution is not necessarily guaranteed to be successful unless an infinite number of iterations are performed. Despite the high computational cost, GA has been the most popular method for optimizing the stacking sequence of a laminated composite [18]. Its simple coding, which escapes gradient calculations, and its flexibility of being applied to a large variety of problems with different types of variables and objective functions make GA particularly useful for problems with multimodal functions, discrete variables, and functions with costly derivatives. The working principle of a GA is shown in Fig. 2.

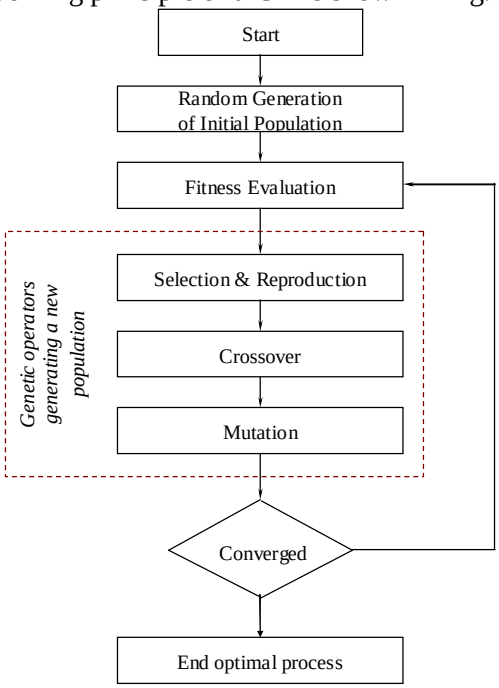

Fig.2. Flow chart of genetic algorithm

When GA is applied to solve a practical problem, the parameter set of the problem first needs to be coded as a finite-length string (an individual). These to fall strings is known as a population. Each string represents one possible solution to the problem. GA begins by randomly generating an initial population of strings. Then, the fitness of individuals is evaluated using a cost function and each solution is ranked based on its fitness value. Selection, crossover and mutation are known as genetic operators through which new solutions to the problem are reproduced. A selection criterion is imposed to determine which solution should be kept and which should be discarded. According to the fitness of chromosomes the selection process chooses solutions to be advanced to the next generation. A crossover operator is applied to a pair of solution strings (parents) by exchanging a part of one string with another part of the other string to create two new solution strings (children). A mutation operator operates on only one string, thus creating a new string (a child). These three steps are repeated until a termination criterion is satisfied. The stopping criterion might be a maximum number of generations or it might be that the score of a potential solution must lie within a certain boundary (Tavakolpour et al [19], 2010).

In optimal problem of this paper, the GA is applied to determine optimal fiber orientation that the first frequency of the problem maximized. So that, the objective of optimization problem is formulated as:

Maximization: $\omega_1 = \omega_1(\theta_i)$: i=1,2,3,4

Subjected to $0^0 \le \theta_1, \theta_2, \theta_3, \theta_4 \le 90^0$

The natural frequency ω_1 for a given fiber orientation is determined from the finite element program given by Eq. (10).

The parameters of the GA are given in Table 1 for all cases.

Table1. Parameter of genetic algorithm.

Parameter	Value
Number of individuals	10
Number of generations	100
Generation gap	0.9
Precision of variables	5
Number of variables	4 (for θ_i: i=1- 4)

3. Numerical results

3.1. Validation examples

Firstly, to observe the accuracy of the present Matlab code and applied GA, the optimal fiber orientations of one fold and two folds folded laminate plate which plotted in Fig.3 are recalculated, which is a previously reported by Topal et al [20], 2008. Dimension parameters of the plate are illustrated in Fig 3 with L = 1m, thickness of h = 0.01L; for one-fold folded laminate plate: b_1=b_2=L/2; for two-folds folded laminate plate: b_1=b_2=b_3=L/3. Material properties (T300/5208 graphite/epoxy): E_1 = 181 GPa, E_2 = 10.3 GPa, G_{12} = 7.17 GPa, υ_{12} =0.28, density ρ = 1600kg/m^3. The symmetrically laminates folded plate is constructed of four layers with θ_1= -θ_2 = -θ_3= θ_4 = θ. The thickness of each lamina is the same and not varied during the optimization. The results are compared with numerical results given by [20].

The first natural frequencies obtained from the present code and the results obtained by [20] are present in Table2 for comparison. It is observed that the optimal fiber orientations and non-dimensional frequencies are in good agreement with other authors results.

Table2. First five natural frequencies of isotropic stiffened flat plate.

BC's	[20]		Present (GA)	
	One-fold			
	θ^0_{opt}	$\bar{\omega}$	θ^0_{opt}	$\bar{\omega}$
CCFF	0	27.7	0	27.4
CCCC	90	76.2	90	74.6
	Two-folds			
CCFF	0	29.2	0	28.9
CCCC	74.3	129.8	74.6	127.8

The non-dimensional frequency is defined as $\bar{\omega} = \omega L^2 \sqrt{\rho / E_2} / h$

The boundary conditions are:

(CCFF): Two edges clamped and two edges free: At y=0 and y= L: clamped; At straight lines: free.

(CCCC): Four edges clamped: At y=0 and y= L: clamped; At straight lines: clamped.

The geometry parameters are taken as: L=1m; total thickness t= 0.01L; folding angle α = 150^0.

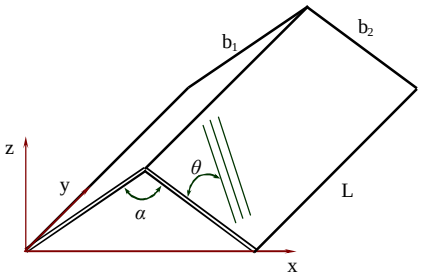

Fig.3. One fold folded plate

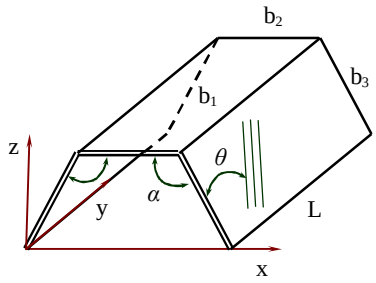

Fig.4. Two folds folded plate

In the following subsections, several new numerical examples have been analyzed.

3.2 Study case: Corrugated laminate plate

3.2.1. Free vibration analysis and frequency optimization.

Consider a corrugated composite plate is shown in Fig.6 with dimensions W=0.8m; F= L=0.1m, total thickness t =0.005m, folding angle α, the material properties: E_1 = 60.7 GPa, E_2 = 24.8 GPa, G_{12} = G_{13} = 12.0 GPa, υ_{12} =0.23, density ρ = 1300kg/m^3.

The boundary conditions are:

+ Clamped at edge 1 and edge 2: u = v = w= θ_x = θ_y = θ_z = 0 (denoted as FCFC case)

+ Clamped at edges x=0: u = v = w= θ_x = θ_y = θ_z = 0 (denoted as CFFF case)

+ Clamped all edges: u = v = w= θ_x = θ_y = θ_z = 0 (denoted as CCCC case)

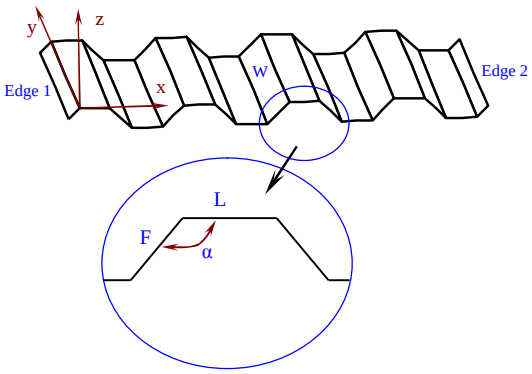

Fig.5. Corrugated composite plate.

In this section, firstly, we calculated natural frequencies of the plate made of symmetric off-axis configuration [45^0/-45^0/45^0/-45^0/-45^0/45^0/-45^0/45^0] and in-axis configuration [0^0/90^0/0^0/90^0/90^0/0^0/90^0/0^0] for different boundary conditions.

Secondly, the optimization procedure involves the stages of evaluating the natural frequencies and improving the fiber orientation θ_i to maximize the first frequency ω_1 using genetic algorithm. The configurations of the folded laminate plates for optimal design is [θ_1^0/-θ_2^0/θ_3^0/-θ_4^0/-θ_4^0/θ_3^0//-θ_2^0/θ_1^0]. The first three natural frequencies of the given symmetric configurations and obtained optimal frequencies of the plates are compared in Table 3 for different boundary conditions.

Fig. 4-6, Fig. 7-9 and Fig.10-12 plotted the variations of the population distribution as generations proceed in order to maximize the first fundamental frequency for various boundary conditions of folding angle $\alpha=135^0$, $\alpha=120^0$ and $\alpha=90^0$, respectively.

Fig.4- Fig.6 shown that the optimal values were determined around the generation of 60.

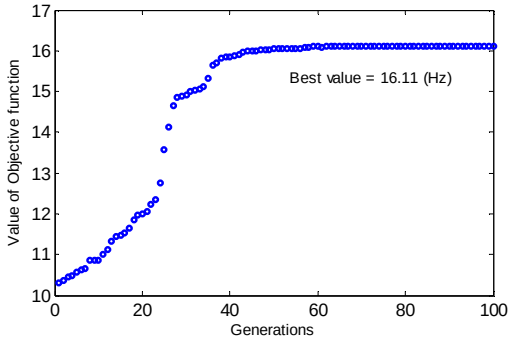

Fig.4. The variation of the objective function value with generation: FCFC case, $\alpha=135^0$

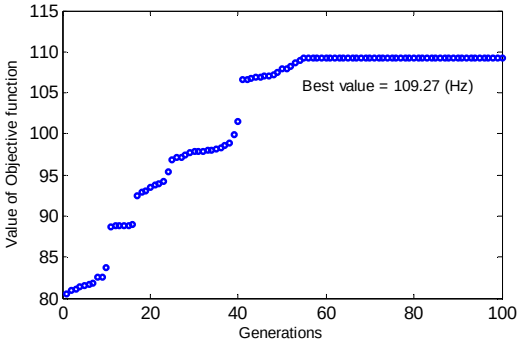

Fig.5. The variation of the objective function value with generation: CFFF case, $\alpha=135^0$

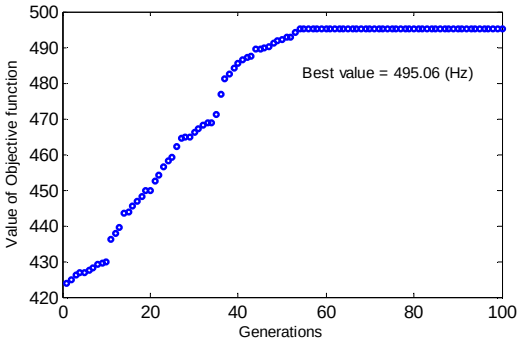

Fig.6. The variation of the objective function value with generation: CCCC case, $\alpha=135^0$

Fig.7- Fig.9 shown that the optimal values were determined around the generation of 50.

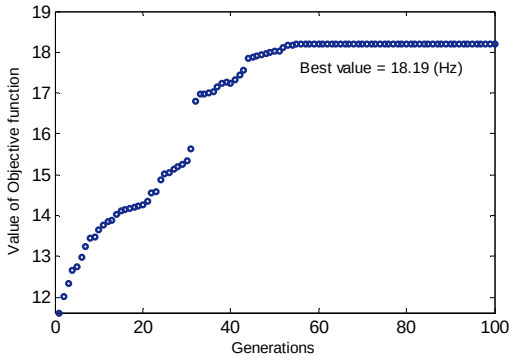

Fig.7. The variation of the objective function value with generation: FCFC case, $\alpha=120^0$

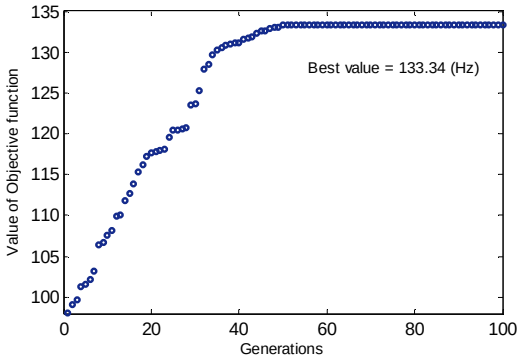

Fig.8. The variation of the objective function value with generation: CFFF case, $\alpha=120^0$

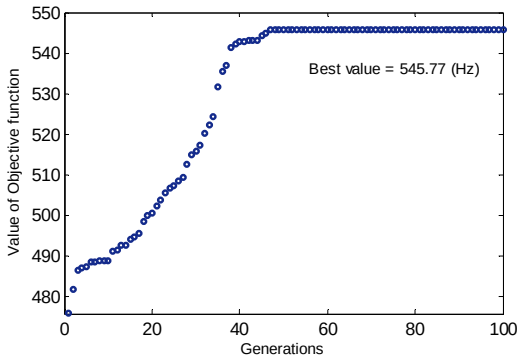

Fig.9. The variation of the objective function value with generation: CCCC case, $\alpha=120^0$

Fig.10- Fig.12 shown that the optimal values were determined around the generation of 55 for FCFC and CFFF cases; around the generation of 60 for CCCC case.

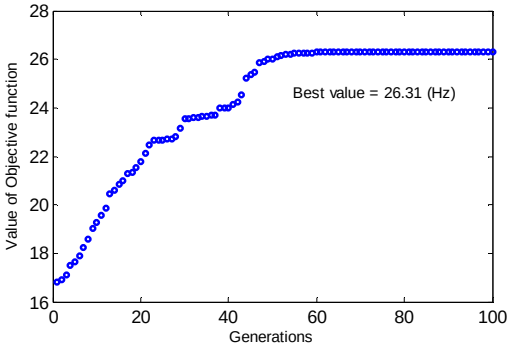

Fig.10. The variation of the objective function value with generation: FCFC case, $\alpha=90^0$

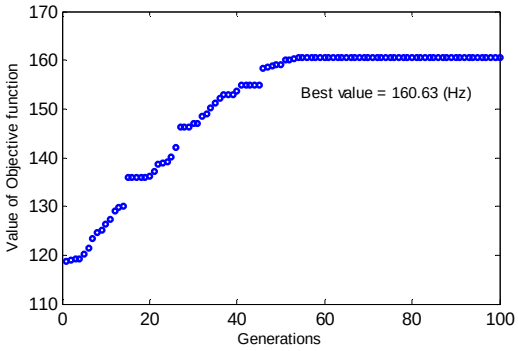

Fig.11. The variation of the objective function value with generation: CFFF case, $\alpha=90^0$

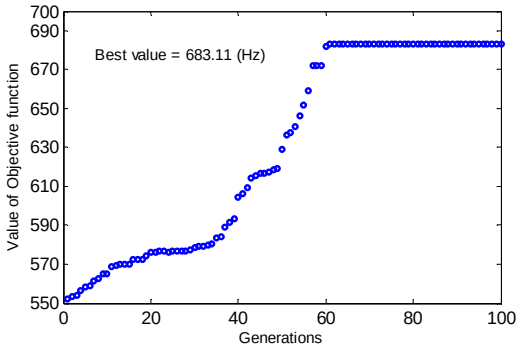

Fig.12. The variation of the objective function value with generation: CCCC case, $\alpha=90^0$

The Fig. 13 to Fig.15 shows the first three mode shapes for folding angle $\alpha = 135^0$, stacking sequence $[45^0/-45^0/45^0/-45^0/-45^0/45^0/-45^0/45^0]$ for different boundary conditions.

+ For FCFC boundary condition:

For the FCFC boundary condition, from Fig.13 we can see that modes (1, 2 and 3) are the bending modes of the corrugated plate according to different direction.

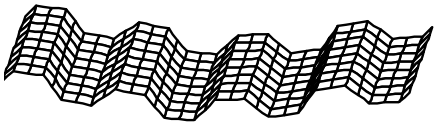

Mode 1, $\alpha = 135^0$: f_1= 12.51 Hz

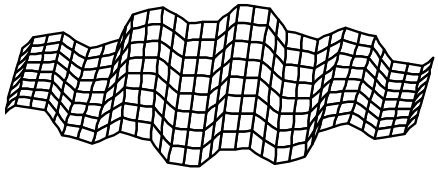

Mode 2, $\alpha = 135^0$: f_2= 23.17 Hz

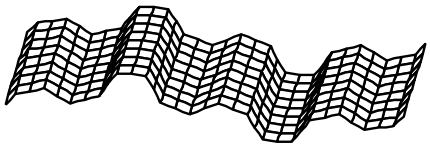

Mode 3, $\alpha = 135^0$: f_3= 34.88 Hz

Fig.13. First three mode shapes of FCFC case

+ For CFFF boundary condition:

For CFFF boundary condition, Fig.14 shows that modes 1 and 2 are bending modes of individual plates. Mode 3 is the bending mode of the corrugated plate.

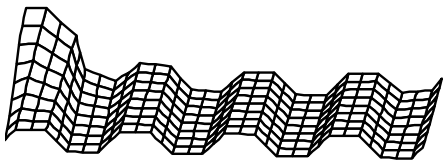

Mode 1, $\alpha = 135^0$: f_1= 90.76 Hz

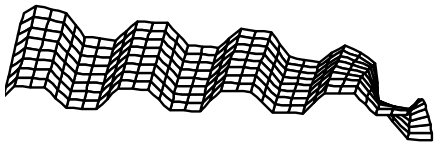

Mode 2, $\alpha = 135^0$: f_2= 92.23 Hz

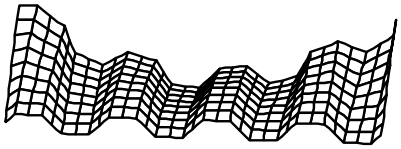

Mode 3, $\alpha = 135^0$: f_3= 138.19 Hz

Fig.14. First three mode shapes of CFFF case

+ For CCCC boundary condition:

Fig. 15 shows that modes (1, 2 and 3) of the CCCC case are bending modes of individual plates.

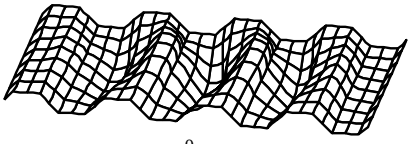

Mode 1, $\alpha = 135^0$: f_1= 438.26 Hz

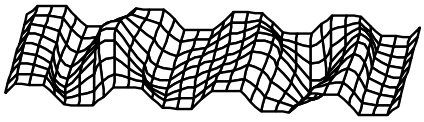

Mode 2, $\alpha = 135^0$: f_2= 478.15 Hz

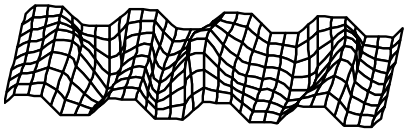

Mode 3, $\alpha = 135^0$: f_3= 539.86 Hz

Fig.15. First three mode shapes of FCFC case

Mode shapes make this study interesting, but any generalized recommendation is very difficult without undergoing numerical experiments.

Table 3 shows that all the obtained optimal frequencies are higher than those of the corrugated plates having typical stacking sequences (which chosen as reference configurations).

For FCFC condition, we found that the optimal configuration is $[0^0/0^0/0^0/0^0]_S$ for all studied folding angles. It give ω^1_{opt} = 16.11 Hz; 18.19 Hz and 26.31 Hz for $\alpha = 135^0$; 120^0 and 90^0, respectively.

For CFFF condition, we found that the optimal configuration is $[0^0/90^0/90^0/90^0]_S$ for all studied folding angles. It give ω^1_{opt} = 109.27 Hz; 133.34 Hz and 160,63 Hz for $\alpha = 135^0$; 120^0 and 90^0, respectively.

For CCCC condition, we found that the optimal configuration is $[0^0/0^0/90^0/90^0]_S$ for folding angles $\alpha = 135^0$; 120^0. It give ω^1_{opt} = 495.06 Hz; 545.77 Hz for $\alpha = 135^0$; 120^0, respectively. The optimal configuration of

$[85.5^0/-87.8^0/90^0/-89^0/-89^0/90^0/-87.8^0/85.5^0]$ for $\alpha = 90^0$ with corresponding frequency of $\omega^1_{opt} = 683.11$ Hz.

Table 3. Frequency optimization of the corrugated laminate plate with respect to fiber orientations.

Folding angle	BC's	Fiber orientations	Natural frequencies		
			f_1	f_2	f_3
$\alpha=135^0$	FCFC	$[45^0/-45^0/45^0/-45^0/-45^0/45^0/-45^0/45^0]$	12.51	23.17	34.88
		$[0^0/90^0/0^0/90^0/90^0/0^0/90^0/0^0]$	14.76	22.34	41.32
		$[0^0/0^0/0^0/0^0/0^0/0^0/0^0/0^0]$ (opt)	**16.11**	22.98	44.91
	CFFF	$[45^0/-45^0/45^0/-45^0/-45^0/45^0/-45^0/45^0]$	90.76	92.23	138.19
		$[0^0/90^0/0^0/90^0/90^0/0^0/90^0/0^0]$	101.72	103.41	153.34
		$[0^0/90^0/90^0/90^0/90^0/90^0/90^0/0^0]$ (opt)	**109.27**	109.54	165.14
	CCCC	$[45^0/-45^0/45^0/-45^0/-45^0/45^0/-45^0/45^0]$	438.26	478.15	539.86
		$[0^0/90^0/0^0/90^0/90^0/0^0/90^0/0^0]$	480.12	527.36	593.48
		$[0^0/0^0/90^0/90^0/90^0/90^0/0^0/0^0]$ (opt)	**495.06**	544.93	614.72
$\alpha=120^0$	FCFC	$[45^0/-45^0/45^0/-45^0/-45^0/45^0/-45^0/45^0]$	14.23	26.02	39.17
		$[0^0/90^0/0^0/90^0/90^0/0^0/90^0/0^0]$	16.81	24.73	45.97
		$[0^0/0^0/0^0/0^0/0^0/0^0/0^0/0^0]$ (opt)	**18.19**	25.81	49.95
	CFFF	$[45^0/-45^0/45^0/-45^0/-45^0/45^0/-45^0/45^0]$	110.01	112.13	168.21
		$[0^0/90^0/0^0/90^0/90^0/0^0/90^0/0^0]$	123.62	124.14	185.37
		$[0^0/90^0/90^0/90^0/90^0/90^0/90^0/0^0]$ (opt)	**133.34**	133.68	200.86
	CCCC	$[45^0/-45^0/45^0/-45^0/-45^0/45^0/-45^0/45^0]$	491.17	533.24	598.43
		$[0^0/90^0/0^0/90^0/90^0/0^0/90^0/0^0]$	534.37	581.45	653.19
		$[0^0/0^0/90^0/90^0/90^0/90^0/0^0/0^0]$ (opt)	**545.77**	596.56	671.81
$\alpha=90^0$	FCFC	$[45^0/-45^0/45^0/-45^0/-45^0/45^0/-45^0/45^0]$	20.58	36.75	52.87
		$[0^0/90^0/0^0/90^0/90^0/0^0/90^0/0^0]$	24.01	34.92	62.81
		$[0^0/0^0/0^0/0^0/0^0/0^0/0^0/0^0]$ (opt)	**26.31**	36.67	68.21
	CFFF	$[45^0/-45^0/45^0/-45^0/-45^0/45^0/-45^0/45^0]$	133.97	135.24	196.53
		$[0^0/90^0/0^0/90^0/90^0/0^0/90^0/0^0]$	149.11	151.32	217.41
		$[0^0/90^0/90^0/90^0/90^0/90^0/90^0/0^0]$ (opt)	**160.63**	161.51	220.15
	CCCC	$[45^0/-45^0/45^0/-45^0/-45^0/45^0/-45^0/45^0]$	596.38	641.63	711.54
		$[0^0/90^0/0^0/90^0/90^0/0^0/90^0/0^0]$	643.11	690.15	764.36
		$[85.5^0/-87.8^0/90^0/-89^0/-89^0/90^0/-87.8^0/85.5^0]$ (opt)	**683.11**	720.08	778.92

From Table 3 we can see that the effect of boundary condition is significant on natural frequencies and it optimal frequencies. The natural frequencies of corrugated laminate plates having CCCC condition are extremely higher than others.

3.2.2 Transient analysis

In the transient analysis, the same corrugated composite plates subjected to an exploded knife-edge loading condition scheme of q_0 = 10kN/m, which having t_1 = 1ms, t_2 = 2ms, t_3 = 50ms, illustrated in Fig. 16.

The load applied on four individual plates as shown in Fig.17.

The undamped displacement responses measured at point A (the center of an individual bottom face) are shown in Fig.17.

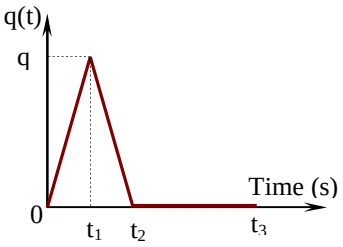

Fig.16. Exploded loading condition scheme.

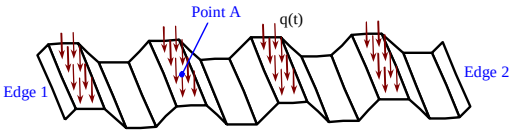

Fig. 17 The corrugated laminate plate subjected to uniformly distributed load of intensity q^0

To observe the effects of optimal fiber orientations on transient displacement response, the corrugated plates with folding angle $\alpha = 135^0$ which having lamination schemes $[45^0/-45^0/45^0/-45^0]_S$ and $[0^0/90^0/0^0/90^0]_S$ (denoted as $[45^0/-45^0]_4$ and $[0^0/90^0]_4$) are considered to compare with optimal fiber orientation plate. The imposed boundary conditions: FCFC and CFFF. The results presented in the Fig.18 and Fig.19 for FCFC and CFFF condition, respectively.

Fig. 20 shows the effect of folding angle α ($\alpha = 135^0, 120^0, 90^0$) on transient responses at point A of the plate which having lamination schemes $[45^0/-45^0/45^0/-45^0]_S$.

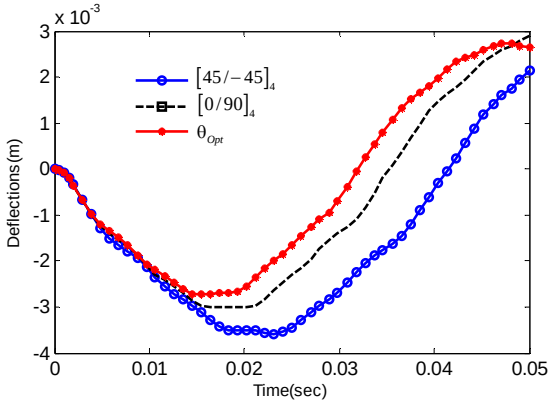

Fig.18. Effects of optimal fiber orientations on transient displacement responses of the corrugated composite plate, time step Δt=0.5(ms): FCFC condition, $\alpha = 135^0$.

From Fig. 18 and Fig.19 we can see that the effect of optimal fiber orientation on displacement responses of FCFC condition is significant than its effect on CFFF condition. As the folding angle decrease, the wave arrives at an earlier time and the frequencies of the wave increase. It can be concluded that a bigger folding angle reduce the bending stiffness.

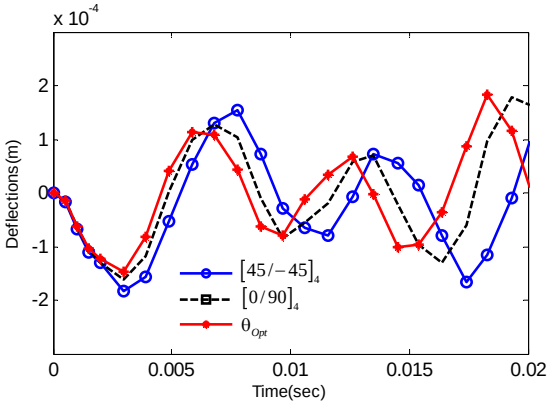

Fig.19. Effects of optimal fiber orientations on transient displacement responses of the corrugated composite plate, time step Δt=0.5(ms): CFFF condition, $\alpha = 135^0$.

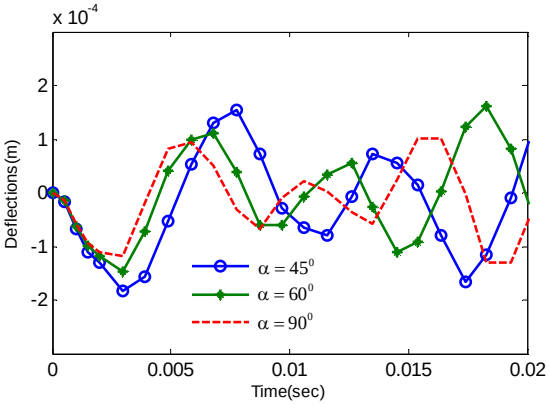

Fig.20. Effects of folding angle α on transient displacement responses, $[45^0/-45^0/45^0/-45^0]_S$: CFFF condition, $\alpha = 135^0$.

4. Conclusion

In this paper, a computer code has been developed for optimization of the corrugated laminate composite plate using genetic algorithm. The code has two distinct modules. First, based on the first order shear deformation theory and using eight-nodded isoparametric plate elements, a finite element code was built for calculating natural frequencies of the folded laminate composite plate. In this module, the transverse shear deformation, the rotary inertia of plate are

carried out. Second one is the GA module for solving optimization problem.

We conclude that GA can be successfully employed for optimal design the corrugated laminate composite plate with any number of design variables. The GA is guided random and exhaustive search process, hence the probability of finding the global optimum is high and the variables could be real.

By using more than one variables approach, the optimal results of stacking sequence can be modified to suit the designers' requirement.

Some set of new results are presented to see the effects of optimal fiber orientations on dynamic responses of corrugated laminate composite plates for different boundary conditions.

The applicability of the present approach covers a wide range of forced vibration problems, with varying material combinations, geometric features, and boundary conditions.

The results of this study will serve as a benchmark for future research for designing corrugated composite structures and sandwich structures made of composite materials, as it was extremely quick and reliable in producing design results.

Acknowledgments

"This research is funded by Vietnam National Foundation for Science and Technology Development (NAFOSTED) under grant number: ***107.02-2011.08***".

Reference

[1] Briassoulis D (1986). Equivalent orthotropic properties of corrugated sheets. *Computers and Structures*; 23(2):129-38.

[2] Abdel-Sayed G (1970). Critical shear loading of curved panels of corrugated sheets. *J. Engng Mech. Div. ASCE* ;96:895-911.

[3] Bryan RE, El-Dakhakhni MW (1968). Shear fexibility and strength of corrugated decks. *J. Struct. Div. ASCE* ; 94:2549-80.

[4] Davis JM (1978). Simplified diaphragm analysis. *J. Struct. Div. ASCE*; 103:2093-109.

[5] Easley TJ, McFarland ED (1969). Buckling of light gage corrugated metal shear diaphragms. *J. Struct. Div. ASCE*; 95:1497-516.

[6] Easley TJ (1975). Buckling formulas for corrugated metal shear diagphragms. *J. Struct. Div. ASCE*; 101:1403-17.

[7] Mangetal AH, Girya-Vallabhan VC, Smith HJ (1976). Finite element analysis of doubly corrugated shells. *J. Struct. Div. ASCE*; 102:2033-50.

[8] Easley JT, McFarland DE (1969). Buckling of light-gage corrugated metal shear diaphragms. Journal of the Structural Division- ASCE; 95:1497-516.

[9] Shimansky RA, Lele MM (1995). Transverse stiffness of a sinusoidally corrugated plate. *Mechanics of Structures and Machines*; 23(3):439-51.

[10] Semenyuk NP, Neskhodovskaya NA (2002). On design models in stability problems for corrugated cylindrical shells. *International Applied Mechanics*; 38(10):1245-52.

[11] Easley JT (1975). Buckling formulas for corrugated metal shear diaphragms. *Journal of the Structural Division- ASCE*; 101(7):1403-17.

[12] Machimdamrong C, Watanabe E, Utsunomiya T (2004). Shearbuckling of corrugated plates with edges elastically restrained against rotation. *International Journal of Structural Stability and Dynamics* (1): 891-04.

[13] M. Basher, N.E. Shanmugam, A.R. Khalim (2011). Horizontally curved composite plate girders with trapezoidally corrugated webs. *Journal of Constructional Steel Research, Volume 67, Issue 6, June 2011*, Pages 947-956.

[14] Vladimir S. Sokolinsky, Kyle C. Indermuehle, Juan A. Hurtado (2011). Numerical simulation of the crushing process of a corrugated composite plate. *Applied*

Science and Manufacturing, Volume 42, Issue 9, Pages 1119-1126.

[15] Bathe, K-J (1996), *Finite element procedures*. Prentice-Hall, Inc.

[16] Tran Ich Thinh (1994), *Composite Materials*. Viet Nam Education Publishing House.

[17] Tran Ich Thinh, Bui Van Binh, Tran Minh Tu (2012), Bending and Vibration analyses of multi-folding laminate composite plate using finite element method. *Vietnam Journal of Mechanics, VAST*, Vol.34, No.3.

[18] Hossein Ghiasi, Damiano Pasini, Larry Lessard (2009). Optimum stacking sequence design of composite materials-Review. *Composite Structures* 90 1–11.

[19] Ali Reza Tavakolpour, Intan Z. Mat Darus, Osman Tokhi, Musa Mailah (2010). Genetic algorithm-based identification of transfer function parameters for a rectangular. *Composite Structures;* 53 112–126.

[20] U. Topal, Ü. Uzman (2009). Frequency optimization of laminated folded composite plates. *Materials and Design* 30, 494–501.

The 2nd International Conference on Engineering Mechanics and Automation (ICEMA2)
Hanoi, August 16-17, 2012
ISBN: 978-604-913-097-7

On the Nonlinear Stability of Eccentrically Stiffened Functionally Graded Imperfect Plates Resting on Elastic Foundations.

Dao Van Dung[a] and Hoang Thi Thiem[b]

[a]*Vietnam National University, Ha Noi, dvdung@vnu.edu.vn*
[b]*Ha noi University of Mining and Geology.*

Abstract

In this study, the buckling and post-buckling behavior of eccentrically stiffened imperfect plates made of functionally graded materials subjected to in-plane compressive loads and resting on Winkler-Pasternak type elastic foundations are investigated. By using Galerkin's method, the close-form expressions of buckling loads and nonlinear post-buckling load-deflection curves of plates are determined. The effects of foundations and stiffeners on stability of plates are considered.

Key Words: Functionally graded materials, Plates, Elastic foundations, Stiffener, Buckling load.

1. Introduction

Functionally graded materials (FGMs), due to essential characteristics such as high stiffness, excellent temperature resistance capacity compared with ordinary materials, have been widely used for a variety of engineering applications [1]. The mechanical behavior of FGM plates and shells resting on foundations, such as bending, vibration, stability, buckling, etc., has attracted attention of many researchers. Cheng and Kitipornchai [2] proposed a membrane analogy to derive an exact explicit eigenvalues for compression buckling and vibration of FGM plates on a Winkler-Pasternak foundation based on the first-order shear deformation theory. Ait Atmane et al. [3] developed a new higher shear deformation theory to investigate the free vibration analysis of simply supported functionally graded plates resting on a Winkler-Pasternak elastic foundation. Based on the higher order shear deformation plate theory and general von Karman-type equation that includes the plate-foundation interaction and thermal effects, Shen and Wang [4] studied the nonlinear bending of FGM plates under combined loading by using two step perturbation technique to determine the load-deflection and load-bending moment curves. Duc et al.[5] presented an analytical approach to investigate buckling and post-buckling behavior of imperfect FGM plates subjected to in-plane compressive and thermal loads. The buckling of FGM truncated conical shells under axial compressive load and resting on Winkler-Pasternak foundations is presented by Sofiyev [6] according to the modified

Donnell type stability and compatibility equations with the linear strain-displacement relations. The vibration of FGM cylindrical shells resting on elastic foundations solved by the wave propagation approach is considered by Shah et al. [7] by using Love's first order thin shell theory. A hybrid semi-analytic and differential quadrature method based on the three-dimensional elasticity formulation proposed for free vibration analysis of initially stresses FGM cylindrical curved panels resting on two-parameter elastic foundation, subjected to thermal environment is investigated by Farid et al. [8]. The post-buckling, nonlinear bending and nonlinear vibration of stiff thin films on elastic foundations in thermal environments modeled as a non-local orthotropic plate are presented by Shen [9]. In that paper, the governing equation that includes plate-foundation interaction is solved by a two-step perturbation technique. Sofiyev et al.[10] studied the stability of FGM truncated circular conical shells subjected to combined loads with different edge conditions and resting on elastic foundations by applying Galerkin method. Bakhtiari-Nejad and Bideleh [11] obtained results on nonlinear free vibration analysis of pre-stressed circular cylindrical shells on the two-parameter foundation by Rayleigh-Ritz procedure and perturbation method.

However, there are very little researches on static and dynamic buckling of stiffened FGM structures. Recently, Najafizadeh et al. [12] studied static buckling behavior of axially compressed FGM stiffened cylindrical shells subjected. Bich et al. [13] and [14] investigated the nonlinear static and dynamic responses of eccentrically stiffened FGM plates, shells and panels by analytical approach.

As far as the authors' knowledge, the buckling behavior of stiffened plates and shells resting on an elastic foundation under combined loads have not been investigated, as yet. In the present study, the results of the papers [5] and [13] are developed for stiffened FGM plates resting on Winkler-Pasternak foundations. The nonlinear buckling and post-buckling of eccentrically stiffened FGM imperfect plates are considered. Applying Galerkin's method have been received the explicit equations for finding the critical buckling loads and post-buckling load-deflection curves. The effects of geometric parameters, volume fraction of constituent materials, Winkler and Pasternak foundation parameters on nonlinear buckling behavior of plates are shown by numerical method.

2. Fundamental relations

2.1. FGM plates and elastic foundations

Consider a thin FGM rectangular with length a, width b and uniform thickness h that rests on an elastic foundation. A Cartesian coordinate system (x, y, z) is chosen so that the (x y)-plane is taken to be the un-deformed middle surface of the plate and the axis z is in the thickness direction with $-h/2 \le z \le h/2$. Functionally graded materials are composite materials with the mechanical properties varying continuously through the thickness of structures. In this paper, FGM plates are assumed to be made from a mixture of ceramic and metal with the volume fraction given by a power law distribution as

$$V_c = V_c(z) = \left(\frac{z}{h} + \frac{1}{2}\right)^k$$
$$V_m = V_m(z) = 1 - V_c(z) \quad (1)$$

where k is the volume fraction index and takes only non-negative values, and subscripts m and c refer to the metal and ceramic constituents, respectively.

Effective properties of FGM plate are determined by linear ruler of mixture as

$$\mathrm{Pr}_{eff} = \mathrm{Pr}_m(z)V_m(z) + \mathrm{Pr}_c(z)V_c(z) \quad (2)$$

According to the mentioned laws (1) and (2), the Young modulus can be expressed by

$$E = E(z) = E_m V_m + E_c V_c$$
$$= E_m + E_{cm}\left(\frac{z}{h} + \frac{1}{2}\right)^K$$
$$E_{cm} = E_c - E_m \ ,$$

and the Poisson ratio is assumed to be a constant, i.e.

$$\nu(z) = \nu = const \tag{3}$$

The load-displacement relationship of the foundation is assumed as following

$$q_0 = K_1 w - K_2 \nabla^2 w \tag{4}$$

where $\nabla^2 = \frac{\partial^2}{\partial x^2} + \frac{\partial^2}{\partial y^2}$ is Laplace operator, w is the deflection of the plate, and K_1, K_2 are the Winkler foundation stiffness and shearing layer stiffness of the Pasternak foundation, respectively.

2.2. Eccentrically stiffened FGM plates (ES-FGM plates) on elastic foundations.

Assume that the plate is reinforced by eccentrically longitudinal and transversal homogeneous stiffeners with the elastic modulus E_0 and the mass density ρ_0.

The governing equations of ES-FGM plates according to the classical plate theory with von Karman geometrical nonlinearity and smeared stiffeners techniques have been established in [13] and are extended in the present study, for plates on elastic foundations. These include the compatibility equation

$$\begin{aligned}
&A_{11}^* \frac{\partial^4 \varphi}{\partial x^4} + (A_{66}^* - 2A_{12}^*) \frac{\partial^4 \varphi}{\partial x^2 \partial y^2} \\
&+A_{22}^* \frac{\partial^4 \varphi}{\partial y^4} + B_{21}^* \frac{\partial^4 \mathrm{w}}{\partial x^4} + B_{12}^* \frac{\partial^4 w}{\partial y^4} + \\
&+(B_{11}^* + B_{22}^* - 2B_{66}^*) \frac{\partial^4 \mathrm{w}}{\partial x^2 \partial y^2} \\
&= \left(\frac{\partial^2 \mathrm{w}}{\partial x \partial y} \right)^2 - \frac{\partial^2 \mathrm{w}}{\partial x^2} . \frac{\partial^2 \mathrm{w}}{\partial y^2},
\end{aligned} \tag{5}$$

and the equilibrium equation

$$\begin{aligned}
&D_{11}^* \frac{\partial^4 \mathrm{w}}{\partial x^4} + (D_{12}^* + D_{21}^* + 4D_{66}^*) \frac{\partial^4 \mathrm{w}}{\partial x^2 \partial y^2} \\
&+D_{22}^* \frac{\partial^4 \mathrm{w}}{\partial y^4} - B_{21}^* \frac{\partial^4 \varphi}{\partial x^4} \\
&-(B_{11}^* + B_{22}^* - 2B_{66}^*) \frac{\partial^4 \varphi}{\partial x^2 \partial y^2} \\
&-B_{12}^* \frac{\partial^4 \varphi}{\partial y^4} - \frac{\partial^2 \varphi}{\partial y^2} . \frac{\partial^2 \mathrm{w}}{\partial x^2} + 2 \frac{\partial^2 \varphi}{\partial x \partial y} . \frac{\partial^2 \mathrm{w}}{\partial x \partial y} \\
&- \frac{\partial^2 \varphi}{\partial x^2} . \frac{\partial^2 \mathrm{w}}{\partial y^2} + K_1 \mathrm{w} \\
&-K_2 \left(\frac{\partial^2 \mathrm{w}}{\partial x^2} + \frac{\partial^2 \mathrm{w}}{\partial y^2} \right) = 0
\end{aligned} \tag{6}$$

where φ= φ (x, y) is stress function, and

$$A_{11}^* = \frac{1}{\Delta} \left(A_{11} + \frac{E_0 A_1}{s_1} \right),$$

$$A_{22}^* = \frac{1}{\Delta} \left(A_{22} + \frac{E_0 A_2}{s_2} \right),$$

$$A_{12}^* = \frac{A_{12}}{\Delta}, \; A_{66}^* = \frac{1}{A_{66}},$$

$$\Delta = \left(A_{11} + \frac{E_0 A_1}{s_1} \right) \left(A_{22} + \frac{E_0 A_2}{s_2} \right) - A_{12}^{\;2},$$

$$\begin{aligned}
B_{11}^* &= A_{22}^* (B_{11} + C_1) - A_{12}^* B_{12}, \\
B_{22}^* &= A_{11}^* (B_{22} + C_2) - A_{12}^* B_{12}, \\
B_{12}^* &= A_{22}^* B_{12} - A_{12}^* (B_{22} + C_2), \\
B_{21}^* &= A_{11}^* B_{12} - A_{12}^* (B_{11} + C_1), \\
B_{66}^* &= \frac{B_{66}}{A_{66}}.
\end{aligned}$$

$$\begin{aligned}
D_{11}^* &= D_{11} + \frac{E_0 I_1}{s_1} - (B_{11} + C_1) B_{11}^* \\
&\quad - B_{12} B_{21}^*, \\
D_{22}^* &= D_{22} + \frac{E_0 I_2}{s_2} - B_{12} B_{12}^* \\
&\quad -(B_{22} + C_2) B_{22}^*, \\
D_{12}^* &= D_{12} - (B_{11} + C_1) B_{12}^* \\
&\quad -B_{12} . B_{22}^*, \\
D_{21}^* &= D_{12} - B_{12} B_{11}^* \\
&\quad -(B_{22} + C_2) B_{21}^*, \\
D_{66}^* &= D_{66} - B_{66} . B_{66}^*,
\end{aligned} \tag{7}$$

with

$$A_{11} = A_{22} = \frac{E_1}{1-\nu^2},\ A_{12} = \frac{E_1\nu}{1-\nu^2},$$
$$A_{66} = \frac{E_1}{2(1+\nu)},$$
$$B_{11} = B_{22} = \frac{E_2}{1-\nu^2}, \qquad B_{12} = \frac{E_2\nu}{1-\nu^2},$$
$$B_{66} = \frac{E_2}{2(1+\nu)},$$
$$D_{11} = D_{22} = \frac{E_3}{1-\nu^2},$$
$$D_{12} = \frac{E_3\nu}{1-\nu^2},\ D_{66} = \frac{E_3}{2(1+\nu)},$$
$$C_1 = \pm\frac{E_0 A_1 z_1}{s_1},\quad C_2 = \pm\frac{E_0 A_2 z_2}{s_2},$$
$$I_1 = \frac{1}{12}b_1 h_1^3 + A_1 z_1^2,$$
$$I_2 = \frac{1}{12}b_2 h_2^3 + A_2 z_2^2,$$
$$z_1 = \frac{h+h_1}{2},\ z_2 = \frac{h+h_2}{2},$$
$$E_1 = \left(E_m + \frac{E_c - E_m}{k+1}\right)h,$$
$$E_2 = \frac{(E_c - E_m)kh^2}{2(k+1)(k+2)},$$
$$E_3 = \frac{E_m}{12}h^3 + (E_c - E_m)\left(\frac{1}{k+3} - \frac{1}{k+2} + \frac{1}{4k+4}\right)h^3, \tag{8}$$

where s_1, s_2 are spacing of the longitudinal and transversal stiffeners; A_1, A_2 are the cross-section areas of stiffeners; h_1, b_1 and h_2, b_2 are the high and the width of longitudinal and transversal stiffeners respectively, and z_1, z_2 are the eccentricities of stiffeners with respect to the mid-surface of plate. In order to provide the continuity between the plate and stiffeners, thus E_0 and ρ_0 are taken the value $E_0 = E_m$, $\rho_0 = \rho_m$ if the full metal stiffeners are put at the metal-rich side of the plate and conversely $E_0 = E_c$, $\rho_0 = \rho_c$ if the full ceramic ones at the ceramic rich side.

For an imperfect ES-FGM plate, Eqs.(5) and (6) are modified into form as

$$A_{11}\frac{\partial^4\varphi}{\partial x^4} + (A_{66}^* - 2A_{12}^*)\frac{\partial^4\varphi}{\partial x^2\partial y^2} + A_{22}^*\frac{\partial^4\varphi}{\partial y^4} + B_{21}^*\frac{\partial^4 w}{\partial x^4} + (B_{11}^* + B_{22}^* - 2B_{66}^*)\frac{\partial^4 w}{\partial x^2\partial y^2} + B_{12}^*\frac{\partial^4 w}{\partial y^4} - \left(\frac{\partial^2 w}{\partial x\partial y}\right)^2 + \frac{\partial^2 w}{\partial x^2}\cdot\frac{\partial^2 w}{\partial y^2} - 2\frac{\partial^2 w}{\partial x\partial y}\cdot\frac{\partial^2 w_*}{\partial x\partial y} + \frac{\partial^2 w}{\partial x^2}\cdot\frac{\partial^2 w_*}{\partial y^2} + \frac{\partial^2 w}{\partial y^2}\cdot\frac{\partial^2 w_*}{\partial x^2} = 0, \tag{9}$$

$$D_{11}^*\frac{\partial^4 w}{\partial x^4} + (D_{12}^* + D_{21}^* + 4D_{66}^*)\frac{\partial^4 w}{\partial x^2\partial y^2} + D_{22}^*\frac{\partial^4 w}{\partial y^4} - B_{21}^*\frac{\partial^4\varphi}{\partial x^4} - (B_{11}^* + B_{22}^* - 2B_{66}^*)\frac{\partial^4\varphi}{\partial x^2\partial y^2} - B_{12}^*\frac{\partial^4\varphi}{\partial y^4} - \frac{\partial^2\varphi}{\partial y^2}\left(\frac{\partial^2 w}{\partial x^2} + \frac{\partial^2 w_*}{\partial x^2}\right) + 2\frac{\partial^2\varphi}{\partial x\partial y}\left(\frac{\partial^2 w}{\partial x\partial y} + \frac{\partial^2 w_*}{\partial x\partial y}\right) - \frac{\partial^2\varphi}{\partial x^2}\left(\frac{\partial^2 w}{\partial y^2} + \frac{\partial^2 w_*}{\partial y^2}\right) + K_1 w - K_2\left(\frac{\partial^2 w}{\partial x^2} + \frac{\partial^2 w}{\partial y^2}\right) = 0, \tag{10}$$

in which $w_* = w_*(x, y)$ is a known function representing initial small imperfection of the plate and w is additional deflection of plate.

The couple of nonlinear Eqs.(5) and (6) or Eqs.(9) and (10) in terms of two dependent unknown w and φ are used to investigate the

stability of in-plane compressed ES-FGM plates on elastic foundation.

3. Solution of basic equations

Consider an ES-FGM imperfect plate with simply supported and subject to in-plane compressive loads of intensities p_1 and p_2 respectively. In this case the boundary conditions are

$w=0,\ M_1=0,\ N_1 = N_{10} = -p_1 h,\ N_{12}=0$ tại $x=0, a$

$w=0,\ M_2=0,\ N_2 = N_{20} = -p_2 h,\ N_{12}=0$ tại $y=0, b$ (11)

The approximate solutions of Eqs.(9) and (10) satisfying the mentioned conditions (11) are chosen in the form as

$$w = f \sin \lambda_m x \sin \mu_n y,$$
$$w_* = \xi h \sin \lambda_m x \sin \mu_n y, \qquad (12)$$

where $\lambda_m = \frac{m\pi}{a}$, $\mu_n = \frac{n\pi}{b}$, m and n are the half-wave numbers along the x-axis and the y-axis, respectively, and ξ is a imperfection size of plate.

Substituting Eq. (12) into Eq. (9) and solving obtained equation for unknown φ, lead to

$$\varphi = \varphi_1 \cos 2\lambda_m x + \varphi_2 \cos 2\mu_n y + \varphi_3 \sin \lambda_m x \sin \mu_n y + \frac{1}{2} N_{10} y^2 + \frac{1}{2} N_{20} x^2 \qquad (13)$$

in which

$$\varphi_1 = \frac{\mu_n^2 f (f + 2\xi h)}{32 A_{11}^* \lambda_m^2},$$

$$\varphi_2 = \frac{\lambda_m^2 f (f + 2\xi h)}{32 A_{22}^* \mu_n^2},$$

$$\varphi_3 = \frac{-f\left[B_{21}^* \lambda_m^4 + (B_{11}^* + B_{22}^* - 2B_{66}^*)\lambda_m^2 \mu_n^2 + B_{12}^* \mu_n^4\right]}{A_{11}^* \lambda_m^4 + (A_{66}^* - 2A_{12}^*)\lambda_m^2 \mu_n^2 + A_{22}^* \mu_n^4} \qquad (14)$$

Substituting the expressions (12) and (13) into Eq. (10) and using Galerkin method for the resulting equation yield

$$\frac{ab}{4}\left(D^* + \frac{B^{*2}}{A^*} + D_k\right) f - \frac{2mn\pi^2 \delta_m \delta_n}{3ab} \cdot \frac{B^*}{A^*} \cdot f(f + \xi h) + \frac{mn\pi^2 \delta_m \delta_n}{6ab} \cdot H^* f(f + 2\xi h) + \frac{m^2 n^2 \pi^4}{64ab} L^* f(f + \xi h)(f + 2\xi h) + \frac{ab}{4}(N_{10}\lambda_m^2 + N_{20}\mu_n^2)(f + \xi h) = 0, \qquad (15)$$

where the coefficients are given by

$$D_k = K_1 + K_2(\lambda_m^2 + \mu_n^2),$$
$$D^* = D_{11}^* \lambda_m^4 + (D_{12}^* + D_{21}^* + 4D_{66}^*)\lambda_m^2 \mu_n^2 + D_{22}^* \mu_n^4,$$
$$B^* = B_{21}^* \lambda_m^4 + (B_{11}^* + B_{22}^* - 2B_{66}^*)\lambda_m^2 \mu_n^2 + B_{12}^* \mu_n^4,$$
$$A^* = A_{11}^* \lambda_m^4 + (A_{66}^* - 2A_{12}^*)\lambda_m^2 \mu_n^2 + A_{22}^* \mu_n^4,$$
$$H^* = \frac{B_{21}^*}{A_{11}^*} + \frac{B_{12}^*}{A_{22}^*},$$
$$L^* = \frac{\mu_n^2}{A_{11}^* \lambda_m^2} + \frac{\lambda_m^2}{A_{22}^* \mu_n^2},$$
$$\delta_m = 1 - (-1)^m,\ \delta_n = 1 - (-1)^n,$$
$$m, n = 1, 2, \ldots \qquad (16)$$

By introducing

$$D^* = \frac{\overline{D}}{h},\quad B^* = \frac{\overline{B}}{h^3},$$
$$A^* = \frac{\overline{A}}{h^5},\quad H^* = \overline{H} h^2,$$
$$L^* = \overline{L}.h,\quad f = \overline{f}.h,$$

Eq. (15) can be rewritten as

$$p_1 m^2 + p_2 \lambda^2 n^2 = \frac{1}{\pi^2}\left(\overline{D} + \frac{\overline{B}^2}{\overline{A}} + D_k h\right)\left(\frac{a}{h}\right)^2 . \frac{\overline{f}}{\overline{f}+\xi} - \frac{8}{3} mn\delta_m \delta_n \frac{\overline{B}}{\overline{A}}\left(\frac{h}{b}\right)^2 . \overline{f} + \frac{2mn\delta_m\delta_n}{3}\left(\frac{h}{b}\right)^2 . \overline{H} . \frac{\overline{f}(\overline{f}+2\xi)}{\overline{f}+\xi} + \frac{\pi^2 m^2 n^2}{16}\left(\frac{h}{b}\right)^2 \overline{L}.\overline{f}(\overline{f}+2\xi). \quad (17)$$

Eq. (17) is used to analyze the buckling and post-buckling of ES-FGM imperfect plates resting on elastic foundations and under the in-plane compressive loads.

Hereafter investigate the nonlinear buckling of ES-FGM plates in some cases of active loads.

3.1. Stiffened FGM plates acted on by only axial compressive load p_1

In this case, Eq. (17) is reduced to

$$p_1 = \frac{1}{\pi^2 m^2}\left(\overline{D} + \frac{\overline{B}^2}{\overline{A}} + D_k h\right)\left(\frac{a}{h}\right)^2 . \frac{\overline{f}}{\overline{f}+\xi} - \frac{8n\delta_m\delta_n}{3m} . \frac{\overline{B}}{\overline{A}} . \left(\frac{h}{b}\right)^2 . \overline{f} + \frac{2n\delta_m\delta_n}{3m}\left(\frac{h}{b}\right)^2 . \overline{H} . \frac{\overline{f}(\overline{f}+2\xi)}{\overline{f}+\xi} + \frac{\pi^2 n^2}{16}\left(\frac{h}{b}\right)^2 \overline{L}\,\overline{f}(\overline{f}+2\xi). \quad (18)$$

For perfect plates, ξ=0, Eq. (18) representing the load-deflection curve of plate, leads to

$$p_1 = \frac{1}{\pi^2 m^2}\left(\frac{a}{h}\right)^2 \left(\overline{D} + \frac{\overline{B}^2}{\overline{A}} + D_k h\right) - \left(\frac{2n\delta_m\delta_n}{3m}\right)\left(\frac{h}{b}\right)^2 \left[\frac{4\overline{B}}{\overline{A}} - \overline{H}\right] . \overline{f} + \frac{\pi^2 n^2}{16}\left(\frac{h}{b}\right)^2 . \overline{L} . \overline{f}^2 . \quad (19)$$

from which upper buckling load may be obtained with $\overline{f} \to 0$ as

$$p_{1upper} = \frac{1}{\pi^2 m^2}\left(\overline{D} + \frac{\overline{B}^2}{\overline{A}} + D_k h\right)\left(\frac{a}{h}\right)^2 . \quad (20)$$

As can be seen, the upper buckling load coincides with the linear buckling load.

The lower buckling load of ES-FGM plate can be found from Eq (19) by using the condition $\frac{dp_1}{d\overline{f}} = 0$ as

$$\overline{f} = \frac{16\delta_m\delta_n}{3mn\pi^2\overline{L}}\left(\frac{4\overline{B}}{\overline{A}} - \overline{H}.\right)$$

and is obtained the lower buckling load

$$p_{1lower} = \frac{1}{\pi^2 m^2}\left(\frac{a}{h}\right)^2 \left(\overline{D} + \frac{\overline{B}^2}{\overline{A}} + D_k h\right) - \frac{16\delta_m^2\delta_n^2}{9m^2\pi^2\overline{L}}\left(\frac{h}{b}\right)^2 \left(\frac{4\overline{B}}{\overline{A}} - \overline{H}\right)^2 \quad (21)$$

3.2. Un-stiffened FGM plates

In this case, $A_1=A_2=0$ and $I_1=I_2=0$, Eq. (17) becomes

$$p_1 m^2 + p_2 \lambda^2 n^2 = \frac{1}{\pi^2}\left[D\left(\lambda_m^2 + \mu_n^2\right)^2 h + D_k h\right]\left(\frac{a}{h}\right)^2 \frac{\overline{f}}{\overline{f}+\xi} + \frac{\pi^2 m^2 n^2}{16}\left(\frac{h}{b}\right)^2 \frac{E_1}{h}\left(\frac{\mu_n^2}{\lambda_m^2} + \frac{\lambda_m^2}{\mu_n^2}\right)\overline{f}\left(\overline{f}+2\xi\right). \quad (22)$$

If the plate is perfect, ξ=0, Eq. (22) leads to the result given by [13].

If the plate is acted on by only axial compressive load p_1 and $\xi = 0$, Eq. (22) leads to the upper buckling load presented by [5].

4. Numerical results and discussions

To validate the accuracy of the proposed approach, the obtained numerical results for un-stiffened FGM plate under uni-axial compression are compared with those in [5]. Computations have been carried out for the following material and the geometrical parameters of plate: E_m=70GPa; E_c=380GPa; ν=0.3; and a/b =1; b/h=40; k=1; m=n=1; K_2=0(GPa.m). Here, symbols □ and ○ are results of ref.[5], lines ─ ($\xi = 0$) and ··· ($\xi = 0.1$) are results of this paper.

It is seen that these results (in Fig.1) are in good agreement to these one of [5].

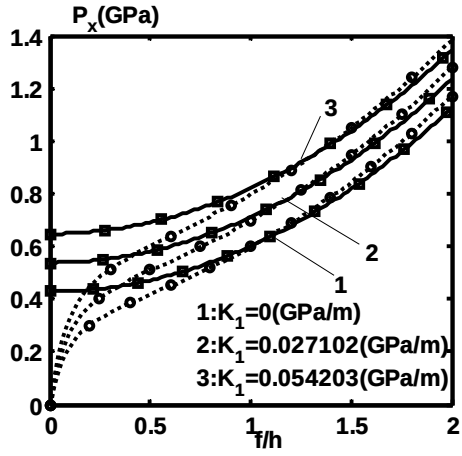

Fig.1.Comparision of postbuckling curves for un-stiffened FGM plates under uniaxial compression with the results of [5].

To illustrate the effects of stiffener and foundations on the post-buckling behavior of ES-FGM plates, three aspects are taken into consideration: uni-axially compressed plate resting on the Winkler foundation ($K_1 \neq 0$, $K_2=0$), on the Pasternak foundation ($K_1=0$, $K_2 \neq 0$), and on foundation with ($K_1 \neq 0$, $K_2 \neq 0$).

Consider an ES-FGM plate with a=b=1.50m; h=0.008m and stiffeners with h_1= h_2=0.03m; b_1= b_2=0.003m; s_1=s_2=0.15m; z_1=z_2=0.019m; and k=1; m=n=1. The combination of plate materials consists of aluminum E_m=70GPa and alumina E_c=380GPa and Poisson ratio ν=0.3. Elastic modulus of stiffeners are taken by E_0=380 GPa when stiffeners are put at surface z=h/2, and E_0=70 GPa when they are put at z=-h/2.

Figs.2a and 2b, shown that foundation parameter K_1 has considerable influence on the stability of plate. The buckling loads and post-buckling loading carrying capability of plate are increased with the increase of foundation modulus K_1.

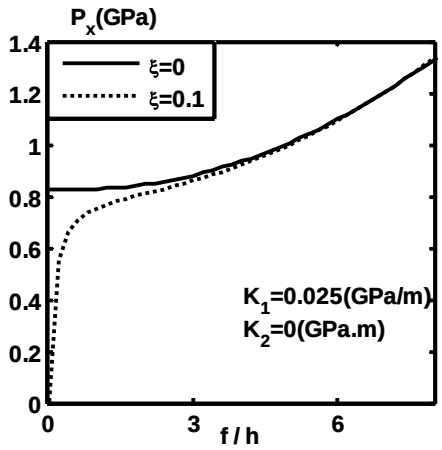

Fig.2a. FGM plate with ceramic stiffeners under uniaxial compression load.

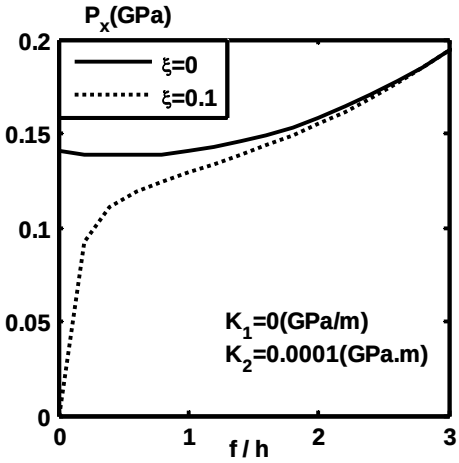

Fig.2b. FGM plate with metal stiffeners under uniaxial compression load.

Figs.3a and 3b estimates the effect of foundation shear parameter K_2. As can be seen, the shear parameter K_2 of the Pasternak foundation has beneficial influence on the buckling resistance and the improvement of capacity of post-buckling loading bearing of plate.

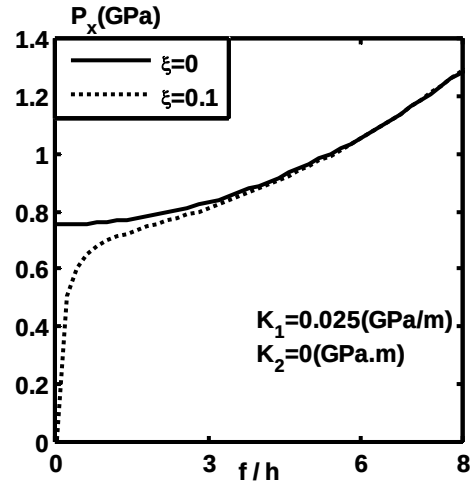

Fig.3a. FGM plate with ceramic stiffeners under uniaxial compression load

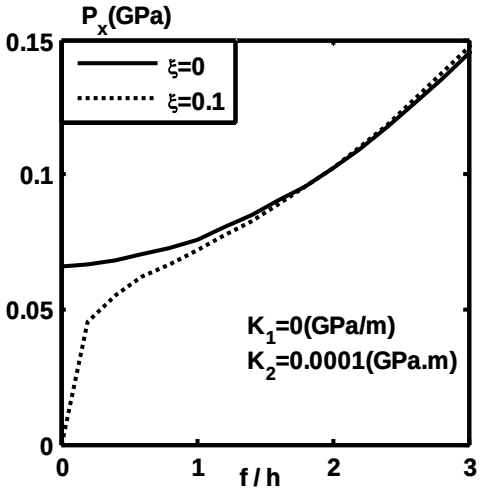

Fig.3b. FGM plate with metal stiffeners under uniaxial compression load.

Figs.4a and 4b gives the results for the plate subjected to uni-axial compressive loads resting on Winkler-Pasternak. As can be observed, the buckling loads and post-buckling loading carrying capacity of plate in this case are the best. The prime reason is that the presence of both foundation coefficient K_1 and K_2 makes the plate being more rigid.

Figs.5a and 5b also indicate that for a plate without foundation (K_1=K_2=0) the post-buckling load-deflection curves are lowest. So, the foundation influences beneficially on stability of plates.

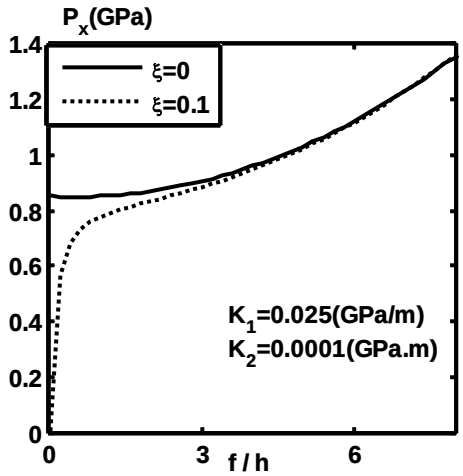

Fig.4a. FGM plate with ceramic stiffeners under uniaxial compression load.

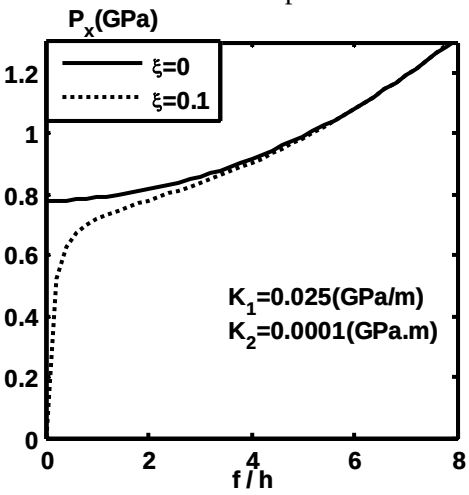

Fig.4b. FGM plate with metal stiffeners under uniaxial compression load.

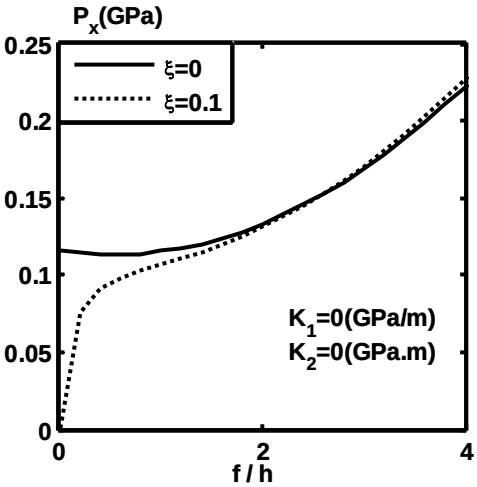

Fig.5a. FGM plate with ceramic stiffeners under uniaxial compression load without foundation.

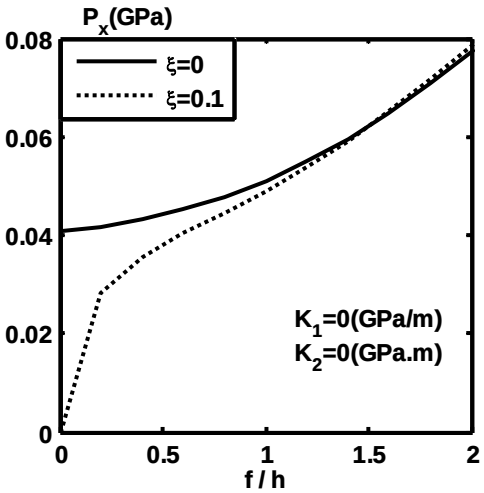

Fig.5b. FGM plate with metal stiffeners under uniaxial compression load without foundation.

5. Conclusions

An analytical approach has been developed in this paper for nonlinear buckling and post-buckling analysis of eccentrically stiffened FGM imperfect rectangular thin plates resting on two-parameter foundation and subjected to in-plane compressive loads. The close-form expressions of buckling loads and nonlinear post-buckling load-deflection curves of plates are determined. The influences of Winkler and Pasternak foundation and imperfection sensitivity on stability of plates are considered in detail.

A**cknowledgements**

This paper was supported by the National Foundation for Science and Technology Development of Vietnam-NAFOSTED. The authors are grateful for this financial support.

References

[1]. FGM Forum (1991*)*. Survey for application of FGM. Tokyo, Japan: The Society of Non Tradition Technology.

[2]. Cheng ZQ and Kitipornchai S (1999). Membrance analogy of buckling and vibration of inhomogeneous plates. ASCE. J Eng Mech; Vol 125, No 11: pp. 1293- 1297.

[3]. Ait Atmane H, Tounsi A, Mechab I and Adda Bedia EA (2010). Free vibration analysis of functionally graded plates resting on Winkler-Pasternak elastic foundation using a new shear deformation theory. Int J Mech Mater Des; Vol6, No2: pp. 113-121.

[4]. Shen HS and Wang XZ (2010). Nonlinear bending of FGM plates subjected to combined loading and resting on elastic foundations. Compos Struct; 92: pp. 2517-2524.

[5]. Duc ND, Nam D and Tung HV (2010). Effects of elastic foundation on nonlinear stability of FGM plates under compressive and thermal loads. Proceedings of the tenth National Conference in Deformable Solid Mechanics, Thai Nguyen, Viet Nam; pp. 191-197.

[6]. Sofiyev AH (2010). The buckling of FGM truncated conical shells subjected to axial compressive load and resting on Winkler-Pasternak foundations. Int J Pressure Vessels and Piping; 87: pp. 753-761.

[7]. Shah AG, Mahmood T, Naeem MN, Iqbal Z and Arshad SH (2010). Vibrations of functionally graded cylindrical shells based on elastic foundations. Acta Mech; 211: pp. 293-307.

[8]. Farid M, Zahedinejad P and Malekzadeh P (2010). Three-dimensional temperature dimensional free vibration analysis of functionally graded material curved panels resting on two-parameter elastic foundation using a hybrid semi-analytic, differential quadrature method. Material and Design; 31: pp. 2-13.

[9]. Shen SH (2011). Non-local plate model for nonlinear analysis of thin films on elastic foundations in thermal environments. Compos Struct; 93: pp. 1143-1152.

[10]. Sofiyev AH, Alizada AN, Akin O, Valiyev A, Avcar M and Adiguzel S (2012). On the stability of FGM shells subjected to combined loads with different edge

conditions and resting on elastic foundations. Acta Mech; 223: pp. 189-204.

[11]. Bakhtiari- Nejad F and Bideleh SMM (2012). Nonlinear free vibration analysis of prestressed circular cylindrical shells on the Winkler/Pasternak foundation. Thin-Walled struct; 53: pp. 26-39.

[12]. Najafizadeh MM, Hasani A and Khazaeinejad P (2009). Mechanical stability of functionally graded stiffened cylindrical shells. Appl Math Model; 33: pp. 1151-1157.

[13]. Bich DH, Nam VH and Phuong NT (2011). Nonlinear post-buckling of eccentrically stiffened functionally graded plates and shallow shells. Viet Nam J. Mech VAST Vol 33, No 3, pp. 131-147.

[14] Bich DH, Dung DV and Nam VH (2012). Nonlinear dynamical analysis of eccentrically stiffened functionally graded cylindrical panels. Compos Struct, 94: pp. 2465–2473.

The 2nd International Conference on Engineering Mechanics and Automation (ICEMA2)
Hanoi, August 16-17, 2012
ISBN: 978-604-913-097-7

Nonlinear Dynamic Buckling of Eccentrically Stiffened Functionally Graded Cylindrical Shells Subjected to Axial Compression

Dao Van Dung[a] and Vu Hoai Nam[b]

[a] *Vietnam National University, Ha Noi, Viet Nam, email: dvdung@vnu.edu.vn*
[b] *University of Transport Technology, Ha Noi, Viet Nam, email: hoainam.vu@utt.edu.vn*

Abstract

An analytical approach is presented to investigate the nonlinear buckling of eccentrically stiffened functionally graded cylindrical shells subjected to time-dependent axial compression. Based on the classical thin shell theory with the geometrical nonlinearity in von Karman–Donnell sense and the smeared stiffeners technique, the governing equations of motion of eccentrically stiffened functionally graded cylindrical shells with geometrically imperfection are derived. The simply supported functionally graded cylindrical shells are reinforced by ring and stringer stiffeners system on internal or external surface. The nonlinear dynamic critical buckling loads are found according to the Budiansky–Roth criterion. Numerical results are given for evaluate effects of reinforcement and input factors to the dynamic buckling of structure.

Key Words: Functionally graded material; Dynamical analysis; Critical dynamic buckling load; Cylindrical shell; Stiffener.

1. Introduction

With heat-resistant properties, functionally graded material (FGM) structures as plates and shells have became popular in engineering designs of coating of nuclear reactors and space shuttle. The static and dynamical behavior of FGM cylindrical shell attracts special attention of a lot of authors in the world.

In static analysis of FGM cylindrical shells, many studies have been focused on the buckling and post-buckling of shells under mechanic and thermal loading. Shen [1] presented nonlinear post-buckling of perfect and imperfect FGM cylindrical thin shells in thermal environments under lateral pressure by using the classical shell theory with the geometrical nonlinearity in von Karman–Donnell sense. By using higher order shear deformation theory, Shen [2] continued to investigate post-buckling of FGM hybrid cylindrical shells in thermal environments under axial loading. Huang and Han [3-5] studied buckling and post-buckling of FGM cylindrical shells under axial compression, radial pressure and combined axial compression and radial pressure base on the Donnell shell theory and the nonlinear strain-displacement relations of large deformation. Using the first-order shear

deformation shell theory and von Karman strains, Liew et al. [6] investigated post-buckling responses of functionally graded cylindrical shells under axial compression and thermal loads.

For dynamical analysis of FGM cylindrical shells, Ng et al. [7] and Darabi et al. [8] presented respectively linear and nonlinear parametric resonance analyses for FGM cylindrical shells. Sofiyev and Schnack [9] and Sofiyev [10] obtained critical parameters for cylindrical thin shells under linearly increasing dynamic torsional loading and under a periodic axial impulsive loading by using Galerkin technique together with Ritz type variation method. Shariyat [11] investigated nonlinear dynamic buckling problems of axially and laterally preloaded FGM cylindrical shells under transient thermal shocks. Geometrical imperfection effects were also included in his research. Using the similar method, he also presented a dynamic buckling analysis for FGM cylindrical shells under complex combinations of thermo–electro-mechanical loads [12]. Huang and Han [13] presented nonlinear dynamic buckling problems of functionally graded un-stiffened cylindrical shells subjected to time-dependent axial load by using Budiansky–Roth dynamic buckling criterion [14]. Various effects of the inhomogeneous parameter, loading speed, dimension parameters; environmental temperature rise and initial geometrical imperfection on nonlinear dynamic buckling were discussed.

Recently, static and dynamic analysis of eccentrically stiffened FGM structures has been attracted attention by researchers. Najafizadeh et al. [15] have studied static buckling behavior of FGM cylindrical shell under axial compressive load and reinforced by ring and stringer FGM stiffeners. By reinforcing an eccentrically homogeneous stiffener system, Bich et al. [16] have investigated the nonlinear static post-buckling of eccentrically stiffened functionally graded plates and shallow shells. The nonlinear dynamical buckling of functionally graded cylindrical panels reinforced by eccentrically homogeneous stiffeners considered by Bich et al. [17].

In this paper are developed the results of [13].The dynamic governing equations are established and nonlinear dynamic buckling of axially compressed imperfect eccentrically stiffened FGM circular cylindrical shells are investigated by analytical approach. It shows the influences of stiffener, volume-fractions index, initial imperfection, geometrical parameters and loading speed to the dynamic buckling of shells.

2. Eccentrically stiffened FGM cylindrical shells (ES-FGM cylindrical shells)

2.1. Functionally graded material

Functionally graded material in this paper, is assumed to be made from a mixture of ceramic and metal with the volume-fractions given by a power law

$$V_c = V_c(z) = \left(\frac{2z+h}{2h}\right)^k,$$

$$V_m = V_m(z) = 1 - V_c(z),$$

where h is the thickness of shell; $k \geq 0$ is the volume-fraction index; z is the thickness coordinate and varies from $-h/2$ *to* $h/2$; the subscripts m and c refer to the metal and ceramic constituents respectively.

Effective properties of FGM shell Pr_{eff} are determined by linear rule of mixture as

$$Pr_{eff} = Pr_m(z)V_m(z) + Pr_c(z)V_c(z)$$

According to the mentioned law, the Young modulus and the mass density can be expressed in the form

$$\begin{aligned} E(z) &= E_m V_m + E_c V_c = E_m + \\ &\quad + (E_c - E_m)\left(\frac{2z+h}{2h}\right)^k, \\ \rho(z) &= \rho_m V_m + \rho_c V_c = \rho_m + \\ &\quad + (\rho_c - \rho_m)\left(\frac{2z+h}{2h}\right)^k \end{aligned} \tag{1}$$

and the Poisson ratio ν is assumed to be constant.

2.2. Constitutive relations and governing equations.

Consider a functionally graded cylindrical thin shell with length L, mean radius R and reinforced by homogeneous ring and stringer stiffener systems (see Fig.1). Stiffener is pure-ceramic if it is located at ceramic-rich side and is pure-metal if is located at metal-rich side. The origin of the coordinate o locates on the middle plane and at the left end of the shell, x, $y=R\theta$, and z axes are in the axial, circumferential, and inward radial directions respectively.

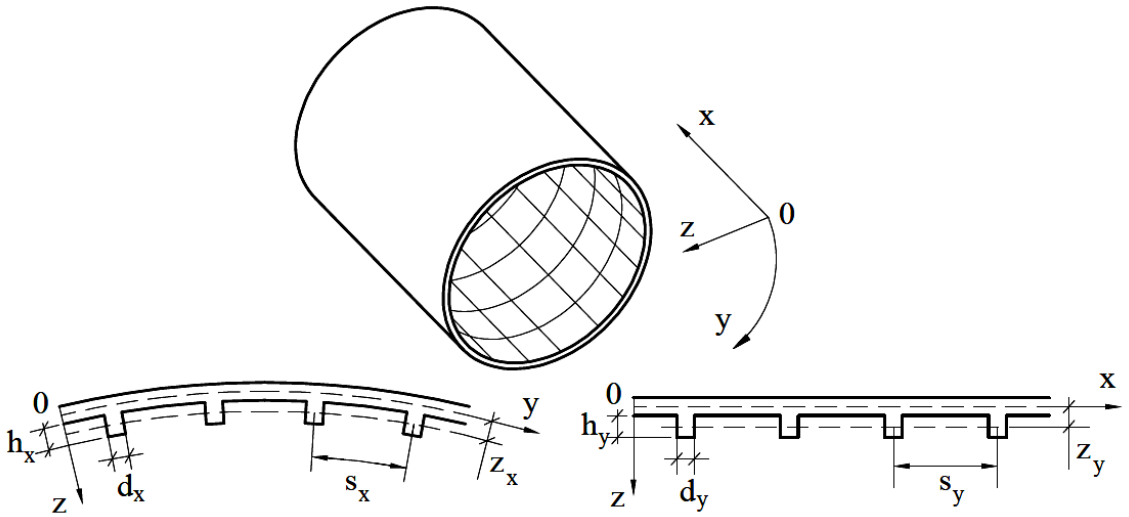

Fig.1. Configuration of an eccentrically stiffened cylindrical shell

According to the von Karman nonlinear strain–displacement relations [18], the strain components at the middle plane of imperfect circular cylindrical shells are of the form

$$\varepsilon_x^0 = \frac{\partial u}{\partial x} + \frac{1}{2}\left(\frac{\partial w}{\partial x}\right)^2 + \frac{\partial w}{\partial x}\frac{\partial w_0}{\partial x},$$

$$\varepsilon_y^0 = \frac{\partial v}{\partial y} - \frac{w}{R} + \frac{1}{2}\left(\frac{\partial w}{\partial y}\right)^2 + \frac{\partial w}{\partial y}\frac{\partial w_0}{\partial y},$$

$$\gamma_{xy}^0 = \frac{\partial u}{\partial y} + \frac{\partial v}{\partial x} + \frac{\partial w}{\partial x}\frac{\partial w}{\partial y} + \frac{\partial w}{\partial y}\frac{\partial w_0}{\partial x} + \frac{\partial w}{\partial x}\frac{\partial w_0}{\partial y}, \tag{2}$$

$$\chi_x = \frac{\partial^2 w}{\partial x^2},\ \chi_y = \frac{\partial^2 w}{\partial y^2},\ \chi_{xy} = \frac{\partial^2 w}{\partial x \partial y}.$$

where $u=u(x, y)$, $v=v(x, y)$ and $w=w(x, y)$ are displacements along x, y and z axes respectively and $w_0=w_0(x, y)$ denotes initial imperfection of shell and assumed to be small.

The strains across the shell thickness at a distance z from the mid-surface are represented by

$$\varepsilon_x = \varepsilon_x^0 - z\chi_x, \varepsilon_y = \varepsilon_y^0 - z\chi_y,$$
$$\gamma_{xy} = \gamma_{xy}^0 - 2z\chi_{xy}, \tag{3}$$

The deformation compatibility equation is deduced from Eq. (2) as [3]

$$\frac{\partial^2 \varepsilon_x^0}{\partial y^2} + \frac{\partial^2 \varepsilon_y^0}{\partial x^2} - \frac{\partial^2 \gamma_{xy}^0}{\partial x \partial y} = -\frac{1}{R}\frac{\partial^2 w}{\partial x^2} - \left(\frac{\partial^2 w_0}{\partial x \partial y}\right)^2 + \left(\frac{\partial^2 w}{\partial x \partial y} + \frac{\partial^2 w_0}{\partial x \partial y}\right)^2 + \frac{\partial^2 w_0}{\partial x^2}\frac{\partial^2 w_0}{\partial y^2} - \left(\frac{\partial^2 w}{\partial x^2} + \frac{\partial^2 w_0}{\partial x^2}\right)\left(\frac{\partial^2 w}{\partial y^2} + \frac{\partial^2 w_0}{\partial y^2}\right), \tag{4}$$

Hook's stress–strain relation is applied for the shell

$$\sigma_x^{sh} = \frac{E(z)}{1-\nu^2}\left(\varepsilon_x + \nu\varepsilon_y\right),$$
$$\sigma_y^{sh} = \frac{E(z)}{1-\nu^2}\left(\varepsilon_y + \nu\varepsilon_x\right), \tag{5}$$
$$\tau_{xy}^{sh} = \frac{E(z)}{2(1+\nu)}\gamma_{xy},$$

and for stiffeners[17]

$$\sigma_x^{st} = E_0\varepsilon_x,$$
$$\sigma_y^{st} = E_0\varepsilon_y. \tag{6}$$

where E_0 is Young's modulus of ring and stringer stiffeners

Taking into account the contribution of stiffeners by the smeared stiffeners technique and omitting the twist of stiffeners and integrating the stress – strain equations and their moments through the thickness of shell, the expressions for force and moment resultants of an ES-FGM cylindrical shell are of the form [16, 17]

$$\begin{aligned}
N_x &= \left(A_{11} + \frac{E_0 A_x}{s_x}\right)\varepsilon_x^0 + A_{12}\varepsilon_y^0 - \\
&\quad -(B_{11} + C_x)\chi_x - B_{12}\chi_y, \\
N_y &= A_{12}\varepsilon_x^0 + \left(A_{22} + \frac{E_0 A_y}{s_y}\right)\varepsilon_y^0 - B_{12}\chi_x - \\
&\quad -(B_{22} + C_y)\chi_y, \\
N_{xy} &= A_{66}\gamma_{xy}^0 - 2B_{66}\chi_{xy},
\end{aligned} \tag{7}$$

$$\begin{aligned}
M_x &= (B_{11} + C_x)\varepsilon_x^0 + B_{12}\varepsilon_y^0 - \\
&\quad -\left(D_{11} + \frac{E_0 I_x}{s_x}\right)\chi_x - D_{12}\chi_y, \\
M_y &= B_{12}\varepsilon_x^0 + (B_{22} + C_y)\varepsilon_y^0 - D_{12}\chi_x - \\
&\quad -\left(D_{22} + \frac{E_0 I_y}{s_y}\right)\chi_y, \\
M_{xy} &= B_{66}\gamma_{xy}^0 - 2D_{66}\chi_{xy},
\end{aligned} \tag{8}$$

where A_{ij}, B_{ij}, $D_{ij}\,(i,j=1,2,6)$ are extensional, coupling and bending stiffness of the un-stiffened FGM cylindrical shell.

$$\begin{aligned}
A_{11} &= A_{22} = \frac{E_1}{1-\nu^2}, A_{12} = \frac{E_1\nu}{1-\nu^2}, A_{66} = \frac{E_1}{2(1+\nu)}, \\
B_{11} &= B_{22} = \frac{E_2}{1-\nu^2}, B_{12} = \frac{E_2\nu}{1-\nu^2}, B_{66} = \frac{E_2}{2(1+\nu)}, \\
D_{11} &= D_{22} = \frac{E_3}{1-\nu^2}, D_{12} = \frac{E_3\nu}{1-\nu^2}, D_{66} = \frac{E_3}{2(1+\nu)},
\end{aligned} \tag{9}$$

with

$$\begin{aligned}
&C_x = \pm\frac{E_0 A_x z_x}{s_x}, C_y = \pm\frac{E_0 A_y z_y}{s_y}, \\
&z_x = \frac{h_x + h}{2}, \quad z_y = \frac{h_y + h}{2}. \\
&E_1 = \left(E_m + \frac{E_c - E_m}{k+1}\right)h, E_2 = \frac{(E_c - E_m)kh^2}{2(k+1)(k+2)}, \\
&E_3 = \left[\frac{E_m}{12} + (E_c - E_m)\left(\frac{1}{k+3} - \frac{1}{k+2} + \frac{1}{4k+4}\right)\right]h^3,
\end{aligned} \tag{10}$$

where the coupling parameters C_x and C_y are negative for outside stiffeners and positive for inside ones. The spacing of the longitudinal and transversal stiffeners are denoted by s_x and s_y respectively. The quantities A_x, A_y are the cross-section areas of stiffeners and I_x, I_y, z_x, z_y are the second moments of cross section areas and the eccentricities of stiffeners with respect to the middle surface of shell respectively. The quantity E_0 takes the value $E_0=E_m$ of the full metal stiffeners if they are put at the metal-rich side of the shell and conversely $E_0=E_c$ if the full ceramic ones are put at the ceramic-rich side.

From the constitutive relations (7), one can obtain inversely

$$\begin{aligned}
\varepsilon_x^0 &= A_{22}^* N_x - A_{12}^* N_y + B_{11}^*\chi_x + B_{12}^*\chi_y, \\
\varepsilon_y^0 &= A_{11}^* N_y - A_{12}^* N_x + B_{21}^*\chi_x + B_{22}^*\chi_y, \\
\gamma_{xy}^0 &= A_{66}^* + 2B_{66}^*\chi_{xy},
\end{aligned} \tag{11}$$

in which

$$\begin{aligned}
A_{11}^* &= \frac{1}{\Delta}\left(A_{11} + \frac{E_0 A_x}{s_x}\right), \quad A_{12}^* = \frac{A_{12}}{\Delta}, \\
A_{22}^* &= \frac{1}{\Delta}\left(A_{22} + \frac{E_0 A_y}{s_y}\right), \quad A_{66}^* = \frac{1}{A_{66}}, \\
\Delta &= \left(A_{11} + \frac{E_0 A_x}{s_x}\right)\left(A_{22} + \frac{E_0 A_y}{s_y}\right) - A_{12}^2, \\
B_{11}^* &= A_{22}^*(B_{11} + C_x) - A_{12}^* B_{12}, \\
B_{22}^* &= A_{11}^*(B_{22} + C_y) - A_{12}^* B_{12}, \\
B_{12}^* &= A_{22}^* B_{12} - A_{12}^*(B_{22} + C_y), \\
B_{21}^* &= A_{11}^* B_{12} - A_{12}^*(B_{11} + C_x), B_{66}^* = \frac{B_{66}}{A_{66}}.
\end{aligned} \tag{12}$$

Substituting Eq. (11) into Eq. (8) leads to

$$\begin{aligned} M_x &= B_{11}^* N_x + B_{21}^* N_y - D_{11}^* \chi_x - D_{12}^* \chi_y, \\ M_y &= B_{12}^* N_x + B_{22}^* N_y - D_{21}^* \chi_x - D_{22}^* \chi_y, \\ M_{xy} &= B_{66}^* N_{xy} - 2D_{66}^* \chi_{xy}, \end{aligned} \tag{13}$$

in which

$$\begin{aligned} D_{11}^* &= D_{11} + \frac{E_0 I_x}{s_x} - \left(B_{11} + C_x\right) B_{11}^* - B_{12} B_{21}^*, \\ D_{22}^* &= D_{22} + \frac{E_0 I_y}{s_y} - B_{12} B_{12}^* - \left(B_{22} + C_y\right) B_{22}^*, \\ D_{12}^* &= D_{12} - \left(B_{11} + C_y\right) B_{12}^* - B_{12} B_{22}^*, \\ D_{21}^* &= D_{12} - B_{12} B_{11}^* - \left(B_{22} + C_y\right) B_{21}^*, \\ D_{66}^* &= D_{66} - B_{66} B_{66}^*. \end{aligned} \tag{14}$$

The nonlinear equations of motion of a thin circular cylindrical shell based on the classical shell theory and the assumption (Refs [8, 9]) $u << w$ and $v << w$, $\rho_1 \frac{\partial^2 u}{\partial t^2} \to 0$, $\rho_1 \frac{\partial^2 v}{\partial t^2} \to 0$ are given by [3]

$$\begin{aligned} &\frac{\partial N_x}{\partial x} + \frac{\partial N_{xy}}{\partial y} = 0, \quad \frac{\partial N_{xy}}{\partial x} + \frac{\partial N_y}{\partial y} = 0, \\ &\frac{\partial^2 M_x}{\partial x^2} + 2\frac{\partial^2 M_{xy}}{\partial x \partial y} + \frac{\partial^2 M_y}{\partial y^2} + \\ &+ N_x \left(\frac{\partial^2 w}{\partial x^2} + \frac{\partial^2 w_0}{\partial x^2} \right) + 2N_{xy} \left(\frac{\partial^2 w}{\partial x \partial y} + \frac{\partial^2 w_0}{\partial x \partial y} \right) + \\ &+ N_y \left(\frac{\partial^2 w}{\partial y^2} + \frac{\partial^2 w_0}{\partial y^2} \right) + \frac{1}{R} N_y = \rho_1 \frac{\partial^2 w}{\partial t^2}, \end{aligned} \tag{15}$$

where

$$\begin{aligned} \rho_1 &= \int_{-h/2}^{h/2} \rho(z) dz + \rho_0 \left(\frac{A_x}{s_x} + \frac{A_y}{s_y} \right) = \\ &= \left(\rho_m + \frac{\rho_c - \rho_m}{k+1} \right) h + \rho_0 \left(\frac{A_x}{s_x} + \frac{A_y}{s_y} \right), \end{aligned} \tag{16}$$

with

$\rho_0 = \rho_m$ for metal stiffener,

$\rho_0 = \rho_c$ for ceramic stiffener.

Considering the first two of Eqs. (15), a stress function φ may be defined as

$$N_x = \frac{\partial^2 \varphi}{\partial y^2}, \; N_y = \frac{\partial^2 \varphi}{\partial x^2}, \; N_{xy} = -\frac{\partial^2 \varphi}{\partial x \partial y}. \tag{17}$$

Substituting Eq. (11) into the compatibility Eq. (4) and Eq. (13) into the third of Eqs. (15), taking into account Eqs. (2) and (17), yields

$$\begin{aligned} &A_{11}^* \frac{\partial^4 \varphi}{\partial x^4} + \left(A_{66}^* - 2A_{12}^* \right) \frac{\partial^4 \varphi}{\partial x^2 \partial y^2} + \\ &+ A_{22}^* \frac{\partial^4 \varphi}{\partial y^4} + B_{21}^* \frac{\partial^4 w}{\partial x^4} + B_{12}^* \frac{\partial^4 w}{\partial y^4} + \frac{1}{R} \frac{\partial^2 w}{\partial x^2} + \\ &+ \left(B_{11}^* + B_{22}^* - 2B_{66}^* \right) \frac{\partial^4 w}{\partial x^2 \partial y^2} - \\ &- \left[\left(\frac{\partial^2 w}{\partial x \partial y} \right)^2 - \frac{\partial^2 w}{\partial x^2} \frac{\partial^2 w}{\partial y^2} \right] - 2 \frac{\partial^2 w}{\partial x \partial y} \frac{\partial^2 w_0}{\partial x \partial y} + \\ &+ \frac{\partial^2 w}{\partial x^2} \frac{\partial^2 w_0}{\partial y^2} + \frac{\partial^2 w}{\partial y^2} \frac{\partial^2 w_0}{\partial x^2} = 0 \end{aligned} \tag{18}$$

$$\begin{aligned} &\rho_1 \frac{\partial^2 w}{\partial t^2} + D_{11}^* \frac{\partial^4 w}{\partial x^4} + D_{22}^* \frac{\partial^4 w}{\partial y^4} + \\ &+ \left(D_{12}^* + D_{21}^* + 4D_{66}^* \right) \frac{\partial^4 w}{\partial x^2 \partial y^2} - B_{21}^* \frac{\partial^4 \varphi}{\partial x^4} - \\ &- \left(B_{11}^* + B_{22}^* - 2B_{66}^* \right) \frac{\partial^4 \varphi}{\partial x^2 \partial y^2} - B_{12}^* \frac{\partial^4 \varphi}{\partial y^4} - \\ &- \frac{\partial^2 \varphi}{\partial y^2} \left(\frac{\partial^2 w}{\partial x^2} + \frac{\partial^2 w_0}{\partial x^2} \right) + \\ &+ 2 \frac{\partial^2 \varphi}{\partial x \partial y} \left(\frac{\partial^2 w}{\partial x \partial y} + \frac{\partial^2 w_0}{\partial x \partial y} \right) - \\ &- \frac{1}{R} \frac{\partial^2 \varphi}{\partial x^2} - \frac{\partial^2 \varphi}{\partial x^2} \left(\frac{\partial^2 w}{\partial y^2} + \frac{\partial^2 w_0}{\partial y^2} \right) = 0, \end{aligned} \tag{19}$$

Eqs.(18) and (19) are a nonlinear equation system in terms of two dependent unknowns w and φ. They are used to investigate the dynamic characteristics of imperfect ES-FGM shells.

3. Nonlinear dynamic buckling analysis

Suppose that an imperfect ES-FGM cylindrical shell is simply supported and subjected to compressive load of intensities

r_0 at its cross-section (in Pa). Thus the boundary conditions considered in the current study are as

$$w = 0, \quad M_x = 0, \quad N_x = -r_0 h, \quad N_{xy} = 0, \quad at \quad x = 0;\ L, \tag{20}$$

Assume the deflection of shell is composed of a pre-buckling uniform deflection f_* and a buckling defection $f(t)\sin\frac{m\pi x}{L}\sin\frac{ny}{R}$ satisfying the mentioned condition (20), the buckling mode shape is chosen by

$$w = f_* + f(t)\sin\frac{m\pi x}{L}\sin\frac{ny}{R}, \tag{21}$$

where $f(t)$ is time dependent buckling amplitude, f_* is pre-buckling uniform deflection and m, n are number of haft wave ,wave number in axial and circumferential directions, respectively.

The initial-imperfection w_0 is assumed to have similar form of the buckling deflection, i.e.

$$w_0 = f_0 \sin\frac{m\pi x}{L}\sin\frac{ny}{R}, \tag{22}$$

where f_0 is the known imperfect amplitude.

Substituting Eqs.(21) and (22) into Eq.(18) and solving obtained equation for unknown φ lead to

$$\varphi = \varphi_1 \cos\frac{2m\pi x}{L} + \varphi_2 \cos\frac{2ny}{R} - \\ -\varphi_3 \sin\frac{m\pi x}{L}\sin\frac{ny}{R} - r_0 h\frac{y^2}{2} \tag{23}$$

where

$$\varphi_1 = \frac{n^2\lambda^2}{32m^2\pi^2 A_{11}^*}\, f\left(f + 2f_0\right),$$

$$\varphi_2 = \frac{m^2\pi^2}{32n^2\lambda^2 A_{22}^*}\, f\left(f + 2f_0\right),$$

$$\varphi_3 = f\Big[B_{21}^* m^4\pi^4 + \\ + \left(B_{11}^* + B_{22}^* - 2B_{66}^*\right)m^2n^2\pi^2\lambda^2 + \\ + B_{12}^* n^4\lambda^4 - \frac{L^2}{R}m^2\pi^2\Big] \Big/ \Big[A_{11}^* m^4\pi^4 + \\ \left(A_{66}^* - 2A_{12}^*\right)m^2n^2\pi^2\lambda^2 + A_{22}^* n^4\lambda^4\Big]. \tag{24}$$

and $\lambda = \frac{L}{R}$,

Substituting the expressions (21-23) into Eq.(19) and applying Galerkin method to the resulting equation yield

$$\rho_1 L^4 \ddot{f} + \left(D + \frac{B^2}{A}\right) f + \\ + Kf\left(f + f_0\right)\left(f + 2f_0\right) - \\ - L^2 m^2\pi^2 h r_0 \left(f + f_0\right) = 0, \tag{25}$$

where

$$A = A_{11}^* m^4\pi^4 + A_{22}^* n^4\lambda^4 \\ + \left(A_{66}^* - 2A_{12}^*\right)m^2n^2\pi^2\lambda^2,$$

$$B = B_{21}^* m^4\pi^4 + B_{12}^* n^4\lambda^4 - \frac{L^2}{R}m^2\pi^2 \\ + \left(B_{11}^* + B_{22}^* - 2B_{66}^*\right)m^2n^2\pi^2\lambda^2, \tag{26}$$

$$D = D_{11}^* m^4\pi^4 + D_{22}^* n^4\lambda^4 \\ + \left(D_{12}^* + D_{21}^* + 4D_{66}^*\right)m^2n^2\pi^2\lambda^2,$$

$$K = \left(\frac{n^4\lambda^4}{16A_{11}^*} + \frac{m^4\pi^4}{16A_{22}^*}\right).$$

Omitting the term of inertia and putting $f_0 = 0$ in Eq. (25), yields an equation for determining the static critical load of ES-FGM cylindrical shells

$$L^2 m^2\pi^2 h r_0 f = \left(D + \frac{B^2}{A}\right) f + Kf^3, \tag{27}$$

Taking $f \neq 0$, i.e. considering the shell after the lost of stability leads to

$$L^2 m^2\pi^2 h r_0 = \left(D + \frac{B^2}{A}\right) + Kf^2, \tag{28}$$

From Eq.(28), the static buckling load can be determined by taking $f \to 0$

$$r_{scr} = \frac{1}{L^2 m^2\pi^2 h}\left(D + \frac{B^2}{A}\right). \tag{29}$$

Suppose that an axial load varying linearly on time $r_0 = ct$ (c (in Pa/s) is a loading speed) and introduce parameters:

$$\bar{D}=\frac{D}{h^3},\ \bar{B}=\frac{B}{h},\ \bar{A}=Ah,\ \bar{K}=\frac{K}{h},$$
$$\xi=\frac{f}{h},\ \xi_0=\frac{f_0}{h},\ \tau=\frac{r_0}{r_{scr}}=\frac{ct}{r_{scr}}, \tag{30}$$

The non-dimension form of Eq.(25) is rewritten as

$$\frac{1}{S_1}\frac{d^2\xi}{d\tau^2}+\frac{1}{r_{scr}}\left[\left(\bar{D}+\frac{\bar{B}^2}{\bar{A}}\right)\xi+ +\bar{K}\xi\left(\xi+\xi_0\right)\left(\xi+2\xi_0\right)\right]- -\left(\frac{L}{h}\right)^2 m^2\pi^2\left(f+f_0\right)\tau=0, \tag{31}$$

where

$$S_1=\frac{r_{scr}^3h^3}{L^4c^2\rho_1}. \tag{32}$$

Using the Runge–Kutta method and Budiansky-Roth dynamic buckling criterion, the responses of ES-FGM cylindrical shells can be determined from Eq. (31) with the critical condition taken as the first inflexion on the response curve satisfying $\left.\frac{d^2\xi}{d\tau^2}\right|_{\tau=\tau_{cr}}=0\cdot$

4. Numerical results and discussions

To validate the present formulation, the dynamic buckling of un-stiffened FGM cylindrical shells under axial compression is considered (see Table 1), which was also analyzed by Huang and Han [13] using the energy method and classical shell theory. It is evident that very good agreement is achieved in this comparison study.

To illustrate the proposed approach to eccentrically stiffened FGM cylindrical shells, the shells considered here are inwardly stiffened cylindrical thin shells with *R=0.5 m, h=0.005 m, $f_0=10^{-6}$ m.* The combination of materials consists of aluminum $E_m=70.10^9$ *N/m*^{2}, $\rho_m=2702$ *kg/m*^{3} and alumina $E_c=380.10^9$ *N/m*^{2}, $\rho_c=3800$ *kg/m*^{3}. The Poisson's ratio is chosen to be 0.3 for simplicity. Material of stiffeners has elastic modulus $E_0=380.10^9$ *N/m*^{2}, $\rho_0=3800$ *kg/m*^{3}. The height of stiffeners is equal to *12 mm*, its width *3 mm*, stiffener system includes 10 ring stiffeners and 10 stringer stiffeners distributed regularly in the axial and circumferential directions respectively. The eccentricities of stiffeners with respect to the middle surface of shell $z_x=z_y=0.0085$ *m.*

Table 1: Comparisons of dynamic buckling of un-stiffened FGM cylindrical shells under an axial compression load

	Present	Ref. [13]
R/h=500, L/R=2, ξ_0=0, c=100MPa/s		
k=0.2	194,94(2,11)	194,94(2,11)
k=1.0	169,94(2,11)	169,94(2,11)
k=5.0	149,98(2,11)	150,25(2,11)
R/h=500, L/R=2, ξ_0=0, k=0.5		
c=100MPa/s	181,68(2,11)	181,67(2,11)
c=50 MPa/s	179,38(2,11)	179,37(2,11)
c=10 MPa/s	177,02(2,11)	177,97(1,8)
L/R=2, ξ_0=0, k=0.2, c=100MPa/s		
R/h=800	124,67(2,12)	124,91(2,12)
R/h=600	162,18(3,14)	162,25(3,14)
R/h=400	239,56(5,15)	239,18(5,15)

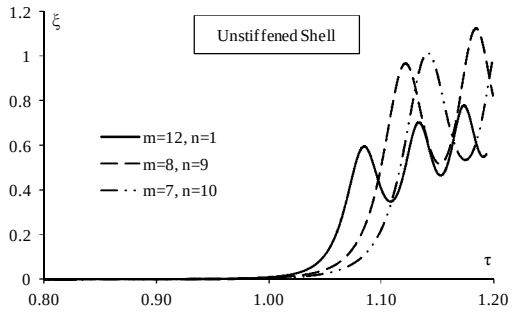

Fig. 2. Effect of buckling mode shapes on load – deflection curve of un-stiffened shell.

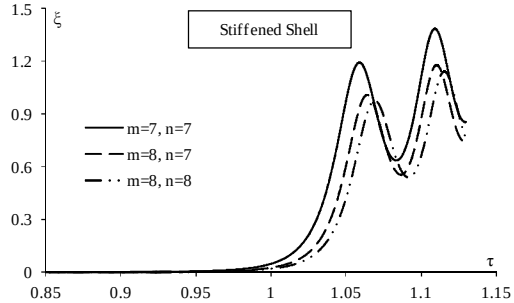

Fig. 3. Effect of buckling mode shapes on load – deflection curve of stiffened shell.

Figs. 2 and 3 show the effect of buckling mode shapes on load – deflection curve of stiffened and un-stiffened FGM cylindrical

shells subjected to an axial compressive load with the power law index *k=1, L=1* m and compressive load $r_0=10^{11}t$. Clearly, the smallest critical dynamic buckling load corresponds to the buckling mode shape *m=12, n=1* with un-stiffened shell and *m=7, n=7* with stiffened shell. This figure also shows that there is no definite point of instability as in static analysis. Rather, there is a region of instability where the slope of ξ vs. τ curve increases rapidly.

Table 2: Nonlinear critical buckling loads of the cylindrical shells under an axial compression $\left(\times 10^8\,\mathrm{N/m^2}\right)$

R/h	*k*	Un-stiffened			Stiffened		
		Static	Dynamic		Static	Dynamic	
			$c=10^{11}$	$c=2\times10^{11}$		$c=10^{11}$	$c=2\times10^{11}$
100	0.2	19,358(7,9)	20,214(12,1)	20.910(12,1)	24,324(7,8)	25,762(7,8)	26,890(7,8)
	1	12.494(8,9)	13,401(12,1)	14,122(12,1)	17,006(7,7)	18,534(7,7)	19,691(7,7)
	5	7.4635(6,9)	7,549(11,4)	9,243(12,1)	10,870(6,7)	12,697(7,7)	13,888(7,7)
	10	6.399(11,2)	7,512(11,2)	8,260(12,1)	9,6372(6,7)	11,533(7,7)	12,790(7,7)
125	0.2	15.486(5,10)	16.286(13,1)	16.950(13,1)	21,972(7,8)	23.809(8,8)	24.434(8,8)
	1	9.995(9,10)	10.829(14,1)	11.473(13,1)	15,879(7,8)	17.425(7,8)	18.593(7,8)
	5	5.971(12,5)	6.928(13,1)	7.645(13,1)	10.369(6,7)	12.203(7,7)	13.413(7,7)
	10	5.119(12,4)	6.119(13,1)	6.849(13,1)	9.199(6,7)	11.123(6,7)	12.511(6,7)
150	0.2	1.2905(9,11)	13.666(15,1)	14.262(15,1)	2.0971(7,8)	23.063(8,8)	23.402(8,8)
	1	8.329(5,11)	9.109(15,1)	9.727(15,1)	1.5504(7,8)	17.069(7,8)	18.252(7,8)
	5	4.976(10,10)	5.870(15,1)	6.516(15,1)	10.278(6,7)	12.154(7,7)	13.376(7,7)
	10	4.266(12,7)	5.210(14,1)	5.907(14,1)	9.136(6,7)	11.080(6,7)	12.479(6,7)

Table 2 shows the critical static and dynamic buckling loads of stiffened and un-stiffened cylindrical shells. The effects of input parameters on the dynamic responses of cylindrical shells under axial compressive load are obtained. With the same input parameters, the effectiveness of reinforcement is obviously proven, the critical buckling load of stiffened shell is greater than one of un-stiffened shell. Table 2 also shows that the dynamic critical buckling loads increases when the loading speed increases. In contract, the dynamic critical load decreases with the increase of the volume fraction index k or the ratio-to-thickness ratio R/h.

Table 3: *Effect of stiffener quantity and stiffener combination on nonlinear critical dynamic buckling loads* $\left(\times 10^8\,\mathrm{N/m^2}\right)$

Stiffeners quantity	Ring stiffeners	Stringer stiffeners	Ring & Stringer stiffeners
5	15.184(7,7)	15.098(5,9)	16.375(8,8)
10	16.285(7,8)	15.442(4,9)	18,534(7,7)
15	17.380(7,8)	15.727(4,9)	20.206(7,7)
20	17.982(7,8)	15.972(3,8)	21.843(7,7)

Effect of stiffener quantity and stiffener combination on nonlinear critical dynamic buckling loads is shown in Table 3. Effect of ring stiffeners seems stronger than stringer stiffeners. Especially, the combination of ring and stringer stiffeners has a large effect on the stability of shell. The dynamic critical buckling load in this case is greatest.

To investigate the imperfection effects in the critical dynamic buckling load, various

imperfection parameters $f_0 = 0, 10^{-5}, 10^{-6}$ are considered in Fig. 4. Clearly, the initial imperfection strongly influences on the critical dynamic buckling loads of ES-FGM cylindrical shells subjected to an axial compressive load.

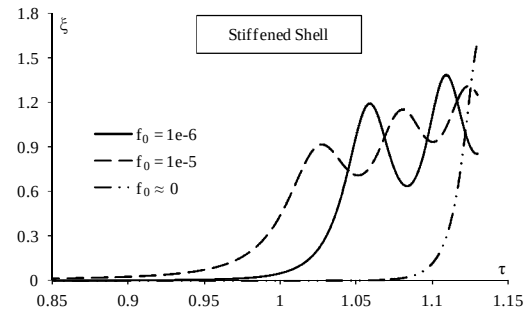

Fig. 4. Effect of initial imperfection on critical dynamic buckling of stiffened shell.

5. Conclusions

A formulation of governing equations of eccentrically stiffened functionally graded cylindrical thin shells based upon the classical shell theory and the smeared stiffeners technique with von Karman–Donnell nonlinear terms is presented in this paper. A nonlinear dynamic equation for analysis of dynamic buckling of ES-FGM cylindrical shells is obtained by using the Galerkin method. The dynamic critical buckling load is found by using the Runge-Kutta method and the Budiansky-Roth criterion.

Some conclusions can be obtained from the present analysis:

i). Stiffeners enhance the stability and load-carrying capacity of FGM cylindrical shells.

ii). Dynamic critical buckling load of stiffened shell is higher than one of un-stiffened shell.

iii). Initial geometrical imperfection, loading speed and the radius-to-thickness ratio are significantly influenced on dynamic stability of cylindrical shell.

Acknowledgements

This paper was supported by the National Foundation for Science and Technology Development of Vietnam-NAFOSTED. The authors are grateful for this financial support.

References

[1] Shen H.S (2003). Postbuckling analysis of pressure-loaded FGM cylindrical shells in thermal environments. *Eng Struct*, 25(4), pp. 487-97.

[2] Shen H.S (2005). Postbuckling of axially-loaded FGM hybrid cylindrical shells in thermal environments. *Compos Sci Technol*, 65(11-12), pp.1675–90.

[3] Huang H and Han Q (2008). Buckling of imperfect functionally graded cylindrical shells under axial compression. *Euro J Mech - A/Solids*, 27(6), pp. 1026–36.

[4] Huang H and Han Q (2009). Nonlinear buckling and postbuckling of heated functionally graded cylindrical shells under combined axial compression and radial pressure. *Int J Non-Linear Mech*, 44(2), pp. 209–18.

[5] Huang H and Han Q (2010). Research on nonlinear postbuckling of FGM cylindrical shells under radial loads. *Compos Struct*, 92(6), pp. 1352-57.

[6] Liew KM, Zhao X and Lee YY (2012). Post-buckling responses of functionally graded cylindrical shells under axial compression and thermal loads. *Composites Part B*: Engineering, 43(3), pp. 1621–30.

[7] Ng TY, Lam KY, Liew KM and Reddy JN (2001). Dynamic stability analysis of functionally graded cylindrical shells under periodic axial loading. *Int J Solids Struct*, 38(8), pp. 1295-309.

[8] Darabi M, Darvizeh M and Darvizeh A (2008). Non-linear analysis of dynamic stability for functionally graded cylindrical shells under periodic axial loading. *Compos Struct*, 83(2), pp. 201–11.

[9] Sofiyev AH and Schnack E (2004). The stability of functionally graded cylindrical shells under linearly increasing

dynamic torsional loading. *Eng Struct*, 26(10), pp. 1321–31.

[10] Sofiyev AH (2005). The stability of compositionally graded ceramic–metal cylindrical shells under aperiodic axial impulsive loading. *Compos Struct*, 69(2), pp. 247–57.

[11] Shariyat M (2008). Dynamic thermal buckling of suddenly heated temperature-dependent FGM cylindrical shells under combined axial compression and external pressure. *Int J Solids Struct*, 45, pp. 2598–612.

[12] Shariyat M (2008). Dynamic buckling of suddenly loaded imperfect hybrid FGM cylindrical with temperature-dependent material properties under thermo-electro-mechanical loads. *Int J Mech Sci*, 50(12), pp.1561–71.

[13] Huang H and Han Q (2010). Nonlinear dynamic buckling of functionally graded cylindrical shells subjected to a time-dependent axial load. *Compos Struct*, 92(2), pp. 593–8.

[14] Budiansky B and Roth RS (1962). Axisymmetric dynamic buckling of clamped shallow spherical shells. *NASA technical note, D_510*, pp. 597–609.

[15] Najafizadeh MM, Hasani A and Khazaeinejad P (2009). Mechanical stability of functionally graded stiffened cylindrical shells. *Appl Math Model*, 33(2), pp.1151–57.

[16] Bich DH, Nam VH and Phuong NT (2011). Nonlinear postbuckling of eccentrically stiffened functionally graded plates and shallow shells. *Vietnam J Mech*; 33(3), pp.132–47.

[17] Bich DH, Dung DV and Nam VH (2012). Nonlinear dynamical analysis of eccentrically stiffened functionally graded cylindrical panels. *Compos Struct*, 94(8), pp. 2465-73.

[18] Brush DD and Almroth BO (1975). *Buckling of bars, plates and shells*. Mc. Graw-Hill.

The 2nd International Conference on Engineering Mechanics and Automation (ICEMA2)
Hanoi, August 16-17, 2012
ISBN: 978-604-913-097-7

Response Evaluations of Linear Random Waves for Reliability Based Fatigue Analysis

Dao Nhu Mai[1,2], Le Thi Viet Anh[3] and Ha Van Sam[2]

[1] Institute of Mechanics, Vietnam Academy of Science and Technolog - 18, Hoang Quoc Viet, Cau Giay, Hanoi, Vietnam
[2] University of Engineering and Technology, VNU – 144, Xuan Thuy, Hanoi
Email: dnmai@imech.ac.vn, maidao.vco@gmail.com
[3] Water Resources University, - 175, Tay Son, Hanoi

Abstract

Offshore structures are more sensitive to fatigue damages than in land structures due to periodic wave loadings. In fact fatigue life may be modeled as a random variable because of the large uncertainty occurring in various main parameters. As a result safety against fatigue failures can be systematically evaluated in terms of probability. Ang A. H. – S. (1977) proposed a technical procedure for Reliability Based Fatigue Analysis. In this procedure the main assumptions are

- random loading can be modeled with beta distribution
- fatigue is characterized by an SN relationship
- and formulation of the reliability function using Weibull distribution

The procedure could be applied to an stress-range information. The key point is how to get the stress-range information, so the purpose of this study is evaluation response of Linear Random Waves acting on a jacket type structure. Then the fatigue analysis is carried out the obtained stress-range.

Keywords: *fatigue, reliability, S-N curves, beta distribution, Weibull distribution, stress-range.*

1 Introduction

Usually the fatigue analysis and reliability calculation are carried out in the design process, especially for dynamic sensitivity structures. When repeated cycling loading acting on structures, the fatigue analysis is performed for hot spot where the stress concentration is high (as welded joint). Reliability calculation is a probability approach to assure the structural safety when uncertainties occurring in design parameters.

Structures, which are subjected to repeated cyclic loading, are sensitive to accumulated fatigue damage. Offshore structures are more sensitive to fatigue damages than other structures, because of the wave loading. These damages frequently occur at the

welded joints or places where there is high-stress concentration. However, there is considerable uncertainty in the prediction of fatigue life of a welded joint and also uncertainty in the cyclic loadings that tend to induce fatigue damage.

Because of these uncertainties, fatigue life of a structure can be calculated only in terms of reliability (i.e., probability of no fatigue failure within a given life). Fatigue damage can be modeled as a random variable and safety against fatigue failures can be systematically evaluated in terms of probability. Ang A. H.–S. (1977) has developed a technical procedure for the Reliability based Fatigue Analysis (RBFA). The following concepts are accepted

- random loading can be modeled with Beta distribution
- fatigue is characterized by an S-N relationship (the experimental stress range and number of loadings cycle to failure curve)
- formulation of the reliability function using Weibull distribution.

This procedure could be applied to stress-range information. The key point is how to get the stress-range information. In Ang A. H.-S. et. al. (2001) study, the fatigue analysis procedure is applied to LNG tanker using a stress range obtained in two year measurement a segment of deck structure at the intersection with a transverse oil-tight bulkhead using a stress range obtained by spectral finite analysis. However

- the measurement is costly and complex
- spectral finite analysis can be performed only for linear systems.

An attempt to implement the RBFA to a jack up rig has demonstrated in the paper (Dao Nhu Mai et. al., 2010). The beta distribution of fatigue loading was established for a range of wave height and wave periods (41 cases). Dynamic analysis was carried out for each wave loading case to get a corresponding stress range.

In this study, the RBFA is carried out for the same rig but

- Taking into account the random property of wave, Linear Random Wave Simulation is used to calculate the wave loadings,
- Nonlinear Dynamic Analysis using the Newmark Technique to obtain the stress range,
- Ran-flow method to construct the beta distribution for stress range f(s),
- Accounting non linearity.

2 Backgrounds of Reliability based Fatigue Analysis

2.1 Physics of fatigue

The physics of fatigue process is very complicate. In practice, experimental S-N curves are used to define the fatigue life. The curves are developed from tests of specific welded joints under constant amplitude cyclic loadings. The relationship between fatigue life and stress range has the form

$$\ln \bar{n} = \ln c - m \ln s \tag{1}$$

or $$\bar{n} = c/s^m \tag{1a}$$

where $\bar{n}$ is predicted number of cycles to failure for stress *s*,

s is stress range,

m is negative inverse slope of S-N curve,

$\ln c$ is intercept of $\ln \bar{n}$-axis by S-N curve.

The cumulative fatigue damage is calculated using the linear Miner's rule when variable or random loadings are involved

$$D = \sum_{\forall i} \frac{n_i}{\bar{n}(s_i)} \tag{2}$$

where D is accumulated fatigue damage,

n_i is number of stress cycles in stress block i,

$\bar{n}(s_i)$ is number of cycles to failure at constant stress range s_i.

The failure occurs, when the expected value of D is 1

$$E(D) = E\left[\sum \frac{n_i}{\bar{n}(s_i)}\right] = 1 \tag{3}$$

where $E(D)$ is the expectation or mean of D.

When stress range S is random with the probability density function $f(s)$, the equation (3) has the form

$$E(D)=\int_0^\infty \frac{\bar{n} f_S(s)ds}{\bar{n}(s)} = \bar{n}\int_0^\infty \frac{s^m f_S(s)ds}{c} = 1.0, \quad (4)$$

from which

$$\bar{n} = \frac{c}{\int_0^\infty s^m f_S(s)ds} = \frac{c}{E(S^m)}, \quad (5)$$

where $E(S^m)$ is the m-th moment of S, (Ang A. H.-S., 1977).

2.2. Fatigue loadings

The PDF of all applied stress range S is very important to evaluate the fatigue life (eq. 5). Any loading with the amplitude larger a minimum limit can cause the damage to structures. On the other hand, an upper limit of stress range can be assumed. Considering all these issue, the *beta* distribution is selected to model fatigue loadings, because of following reasons

– it has finite lower and upper limits
– and is quite flexible for fitting any histogram of stress-range data.

With the zero lower limit and upper limit S_0, the PDF of the beta distribution is

$$f_s(s) = \frac{1}{B(q,r)} \frac{s^{q-1}(s_0-s)^{r-1}}{s_0^{q+r-1}}, 0 \le s \le s_0 \quad (6)$$

Where $B(q,r) = \frac{\Gamma(q)\Gamma(r)}{\Gamma(q+r)}$ is beta function,

q and r are the parameters of distribution, which can be expressed in term of the mean and COV of the applied stress range as follows

$$q = \frac{\mu}{s_0}\left[\Omega^{-2}\left(\frac{s_0}{\mu}-1\right)-1\right], \; r = \left(\frac{s_0}{\mu}-1\right)q. \quad (7)$$

Using beta distribution, the m-th moment of S can be expressed as

$$E(S^m) = s_0^m \frac{\Gamma(m+q)\Gamma(q+r)}{\Gamma(q)\Gamma(m+q+r)} \quad (8)$$

2.3 Reliability against fatigue

The hazard function should monotonically be increasing, because fatigue damage is cumulative so probability of fatigue failure will increase with the life spent

$$h(n) = \frac{k}{w-\varepsilon}\left(\frac{n-\varepsilon}{w-\varepsilon}\right)^{k-1}, \; k>1 \quad (9)$$

The corresponding reliability function is

$$L(n) = \exp\left[-\int_0^n h(n)dn\right] = \exp\left[-\left(\frac{n-\varepsilon}{w-\varepsilon}\right)k\right] \quad (10)$$

where

ε is the minimum life (conservatively ε is assumed zero),
w is the most probable life,
k is the shape parameter.

Two parameter, w and k, are expressed in term of the mean and standard deviation of the fatigue life as follows

$$\bar{n} = w\Gamma\left(1+\frac{1}{k}\right), \quad (11)$$

$$\sigma_N = w\left[\Gamma\left(1+\frac{2}{k}\right)+\Gamma^2\left(1+\frac{1}{k}\right)\right]^{1/2}. \quad (12)$$

Therefore the COV turn out to be

$$\Omega_N = \sigma_N / \bar{n} \cong k^{1.08}$$

and $k = \Omega_N^{-1.08}$. (13)

In consequence, the reliability function (10) can be rewritten as

$$L(n) = \exp\left[-\left\{\frac{n}{\bar{n}}\Gamma\left(1+\Omega^{1.08}\right)\right\}^{\Omega^{-1.08}}\right]. \quad (14)$$

2.4 Reliability-based design for fatigue resistance

The arm is to determination of the allowable stress range to insure a design life n_0 with a target reliability $L(n_0)$. Equating Eq. (14) to the target reliability, we obtain

$$L(n) = L(n_0) = 1 - p_F(n_0)$$

where $p_F(n_0)$ is the probability of failure within life n_0. Then, by inversion Eq. (14) and using the approximation

$\ln[1-p_F(n_0)] \cong -p_F(n_0)$,

we obtain the required mean life

$$\Rightarrow \bar{n} = -n_0 \frac{\Gamma(1+\Omega^{1.08})}{(p_F)^{\Omega^{1.08}}} = n_0 . \gamma_F \qquad (15)$$

where γ_F "scatter factor".

For beta distribution random loadings allowable stress range for design (Ang A.H. – S., 1977)

$$s_0 = \left(\frac{c}{n}\right)^{1/m} \left[\frac{\Gamma(q)\Gamma(m+q+r)}{\Gamma(m+q)\Gamma(q+r)}\right]^{1/m} \qquad (16)$$

3 Linear Random Wave Simulation

From a given wave energy spectrum a random instantaneous elevation of the sea surface can be numerically evaluated using the summation of a finite number of Fourier components. Tucker *et al.* suggest an alternative method where the amplitude components are themselves random

$$\eta(t) = \sum_{n=1}^{N/2} a_n \cos\omega_n t + b_n \sin\omega_n t \qquad (17)$$

where a_n and b_n are independent Gaussian random variables with zero mean and a variance simulation

$$a_n = rn_{a_n}\sqrt{S_{\eta\eta}(\omega_n)d\omega}\,, b_n = rn_{b_n}\sqrt{S_{\eta\eta}(\omega_n)d\omega} \qquad (18)$$

rn_{a_n} and rn_{b_n} - standardised normally distributed random variable

Wave energy spectrum shape differs with location and conditions, depending on variables such as the wind duration and fetch length. The Pierson-Moskowitz (Pierson and Moskowitz, 1964) and the JONSWAP (Hasselmann *et al.*, 1973) spectra are widely used examples. The sea-states are usually described by just two terms, the significant wave height H_s and the mean zero crossing period T_z.

$$S_{PM}(\omega) = \frac{5\pi^4 H_s^2}{T_p^4 \omega^5} \exp\left[-20\left(\frac{\pi}{T_p\omega}\right)^4\right] \qquad (19)$$

$$S_J(\omega) = \frac{5\pi^4 H_s^2 k_\gamma}{T_p^4 \omega^5} \exp\left[-20\left(\frac{\pi}{T_p\omega}\right)^4\right] \gamma^a \qquad (20)$$

4 Modelling of Structural Non-linearities

In this section, modelling of structural non-linearities is shortly described in form of two models. These models are presented in the form of stiffness/flexible matrix which can be implemented in any finite element codes.

4.1 Euler Beam-Column Model

The Euler Beam-column model takes into accounts effect of the axial force on. The load-deflection relationship are given in the form (Kassimali, A.; Abbasnia, R., 1991)

$$S_1 = N_1 = \frac{EF}{L}u$$

$$S_2 = V_1 = \frac{EI}{L^3}c_1 v_1 + \frac{EI}{L^2}c_2\theta_1 - \frac{EI}{L^3}c_1 v_2 + \frac{EI}{L^2}c_2\theta_2$$

$$S_3 = M_1 = \frac{EI}{L^2}c_2 v_1 + \frac{EI}{L}c_3\theta_1 - \frac{EI}{L^2}c_2 v_2 + \frac{EI}{L}c_4\theta_2$$

$$S_5 = V_2 = -\frac{EI}{L^3}c_1 v_1 - \frac{EI}{L^2}c_2\theta_1 + \frac{EI}{L^3}c_1 v_2 - \frac{EI}{L^2}c_2\theta_2$$

$$S_6 = M_2 = \frac{EI}{L^2}c_2 v_1 + \frac{EI}{L}c_4\theta_1 - \frac{EI}{L^2}c_2 v_2 + \frac{EI}{L}c_3\theta_2 \qquad (21)$$

where

$$c_1 = \frac{\phi^3 \sin\phi}{\Delta(\phi)},\ c_2 = \frac{\phi^2(1-\cos\phi)}{\Delta(\phi)},$$

$$c_3 = \frac{\phi(\sin\phi - \phi\cos\phi)}{\Delta(\phi)}, c_4 = \frac{\phi(\phi - \sin\phi)}{\Delta(\phi)} \qquad (22)$$

$$\Delta(\phi) = 2(1-\cos\phi) - \phi\sin\phi,\ \phi = L\sqrt{\frac{P}{EI}} \qquad (23)$$

The tangential stiffness matrix is derived using formula (Oran, C., 1973)

$$k_{tij} = \frac{\partial S_i}{\partial u_j} + \frac{\partial S_i}{\partial \phi}\frac{\partial \phi}{\partial u_j} \qquad (24)$$

and has the form

$$[K_{te}]=\begin{bmatrix} \frac{EF}{L} & & & & & \\ \frac{G_1}{H} & \frac{EI}{L^3}c_1 & & Sym & & \\ \frac{G_2}{H} & \frac{EI}{L^2}c_2 & \frac{EI}{L}c_3 & & & \\ \frac{G_3}{H} & -\frac{EI}{L^3}c_1 & -\frac{EI}{L^2}c_2 & \frac{EI}{L^3}c_1 & & \\ \frac{G_3}{H} & \frac{EI}{L^2}c_2 & \frac{EI}{L}c_4 & -\frac{EI}{L^2}c_2 & \frac{EI}{L}c_3 \end{bmatrix}, \quad (25)$$

where

$$G_1=\frac{EI}{L^3}\frac{\partial c_1}{\partial\varphi}v_1+\frac{EI}{L^2}\frac{\partial c_2}{\partial\varphi}\theta_1-\frac{EI}{L^3}\frac{\partial c_1}{\partial\varphi}v_2+\frac{EI}{L^2}\frac{\partial c_2}{\partial\varphi}\theta_2,$$

$$G_2=\frac{EI}{L^2}\frac{\partial c_2}{\partial\varphi}v_1+\frac{EI}{L}\frac{\partial c_3}{\partial\varphi}\theta_1-\frac{EI}{L^2}\frac{\partial c_2}{\partial\varphi}v_2+\frac{EI}{L}\frac{\partial c_4}{\partial\varphi}\theta_2,$$

$$G_3=-\frac{EI}{L^3}\frac{\partial c_1}{\partial\varphi}v_1-\frac{EI}{L^2}\frac{\partial c_2}{\partial\varphi}\theta_1+\frac{EI}{L^3}\frac{\partial c_1}{\partial\varphi}v_2-\frac{EI}{L^2}\frac{\partial c_2}{\partial\varphi}\theta_2,$$

$$G_4=\frac{EI}{L^2}\frac{\partial c_2}{\partial\varphi}v_1+\frac{EI}{L}\frac{\partial c_4}{\partial\varphi}\theta_1-\frac{EI}{L^2}\frac{\partial c_2}{\partial\varphi}v_2+\frac{EI}{L}\frac{\partial c_3}{\partial\varphi}\theta_2,$$

$$H=\frac{2I\varphi}{FL}. \quad (26)$$

4.2 Strain Hardening Plasticity Model

The Strain Hardening Plasticity Model is used to describe the behaviour of the spudcan. The model can be expressed in the term of a flexible matrix (Cassidy, M. J., 1999 and Houlsby, G. T.; Cassidy, M. J., 2001)

$$\left[\begin{array}{ccc|ccc|c} 1(0) & 0 & 0 & 0(1) & 0 & 0 & 0 \\ 0 & 1(0) & 0 & 0 & 0(1) & 0 & 0 \\ 0 & 0 & 1(0) & 0 & 0 & 0(1) & 0 \\ \hline C_1 & 0 & 0 & -1 & 0 & 0 & \frac{\partial g}{\partial P} \\ 0 & C_2 & C_4 & 0 & -1 & 0 & \frac{\partial g}{\partial V} \\ 0 & C_4 & C_3 & 0 & 0 & -1 & \frac{\partial g}{\partial M/2R} \\ \hline \frac{\partial f}{\partial P} & \frac{\partial f}{\partial V} & \frac{\partial f}{\partial M/2R} & 0 & 0 & 0 & B_{7,7} \end{array}\right] \left(\begin{array}{c} \Delta P \\ \Delta V \\ \frac{\Delta M/2R}{\Delta u} \\ \Delta v \\ \frac{2R\Delta\theta}{\lambda} \end{array}\right) = \left(\begin{array}{c} \Delta P(\Delta u) \\ \Delta V(\Delta v) \\ \frac{\Delta M/2R(2R\Delta\theta)}{0} \\ 0 \\ \frac{0}{0} \end{array}\right), \quad (27)$$

where $B_{7,7}=\frac{\partial g}{\partial P}\frac{\partial P_0}{\partial w_p}\frac{\partial f}{\partial P_0}$

This model has four components

– Elastic Behaviour (Bell, R. W., 1991).

$$C_1=\frac{1}{2GR}\frac{1}{k_v},\ C_2=\frac{1}{2GR}\frac{k_m}{k_hk_m-k_c^2},$$

$$C_3=\frac{1}{2GR}\frac{k_h}{k_hk_m-k_c^2},\ C_4=\frac{1}{2GR}\frac{k_c}{k_c^2-k_hk_m} \quad (28)$$

– Yield Surface

$$f=\left(\frac{v}{v_0}\right)^2+\left(\frac{m}{m_0}\right)^2-2a\frac{v}{v_0}\frac{m}{m_0}-\beta_{12}p^{2\beta_1}(1-p)^{2\beta_2}=0 \quad (29)$$

– Strain Hardening

$$P_0=\frac{cu_p+k_2u_p^2}{k_1+u_p} \quad (30)$$

– Flow rule

$$g=\left(\frac{V}{\alpha_v v_0 P_0'}\right)^2+\left(\frac{M/2R}{\alpha_m m_0 P_0'}\right)^2-\frac{2aVM/2R}{\alpha_v\alpha_m v_0 m_0 P_0'^2} \quad (31)$$
$$-\left[\frac{(\beta_1+\beta_2)^{(\beta_1+\beta_2)}}{\beta_1^{\beta_1}\beta_2^{\beta_2}}\right]^2\left(\frac{P}{P_0'}\right)^{2\beta_1}\left(1-\frac{P}{P_0'}\right)^{2\beta_2}=0$$

5 Numerical Illustration

5.1 Calculation Procedure

- Step 1. Linear Random wave Simulation
- Step 2. Non linear Dynamic Analysis using Newmark Algorithm to get Stress Range S
- Ran Flow to get the histogram of stress range S
- Building the Beta distribution

- Calculating

$$E(S^m) = s_0^m \frac{\Gamma(m+q)\Gamma(q+r)}{\Gamma(q)\Gamma(m+q+r)}$$

$$\Rightarrow \bar{n} = -n_0 \frac{\Gamma(1+\Omega^{1.08})}{(p_F)^{\Omega^{1.08}}} = n_0.\gamma_F$$

$$s_0 = \left(\frac{c}{n}\right)^{1/m} \left[\frac{\Gamma(q)\Gamma(m+q+r)}{\Gamma(m+q)\Gamma(q+r)}\right]^{1/m}$$

5.2 Example – Jackup Rig

An example of jack up rigs with the height of 90m is considered. The properties of equivalent beam element are E=2.108MPa, A= 0.2m2, I=4.84m4, J=9.68m4 Mhull=700Tone. A finite element model with 19 nodes, 12 beam-column elements and 3 simple beams is established for dynamic analysis. The "spudcan" element are connected to joints 1-3

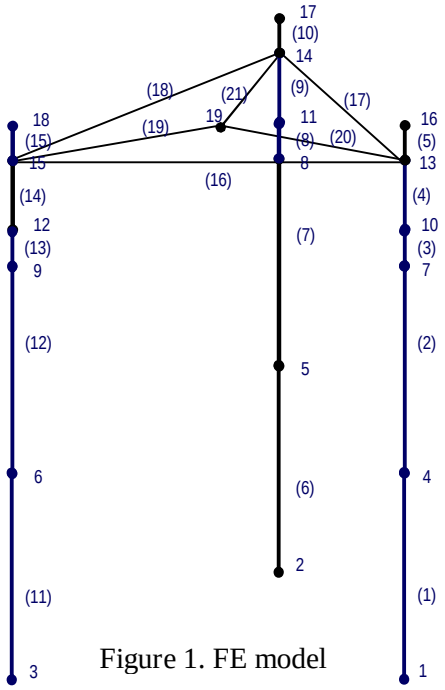

Figure 1. FE model

Wave Energy Spectrum Pierson Moskovitch is chosen. The 3 hours short–term wave state is simulated with the sea conditions:

– sea depth d=62m,
– sea water density ρ=1025kg/m3,
– force coefficients C_m=2, C_d=0.8,
– Significant height H_s=12m,
– Wave peak period T_z=5,5s.

S-N curve for the tubular beam is used to evaluate the fatigue damage with m=3.

The results of numerical illustration are presented in figures 2- 6.

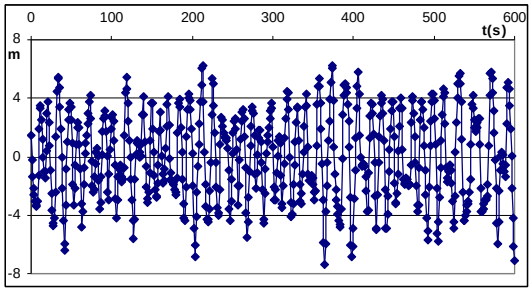

Figure 2. Wave surface elevation in the first 600s

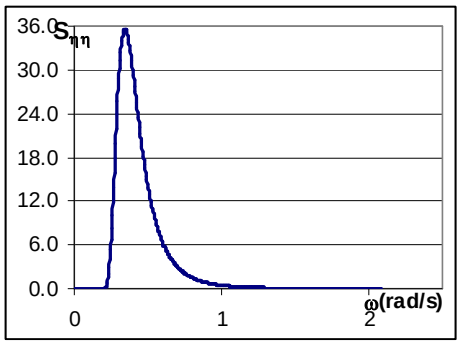

Figure 3. Wave energy spectrum

Figure 4. Wave number k

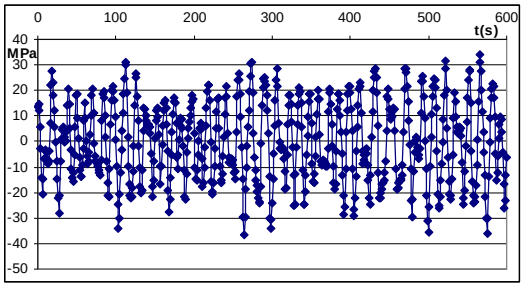

Figure 5. Stress range in the first 600s

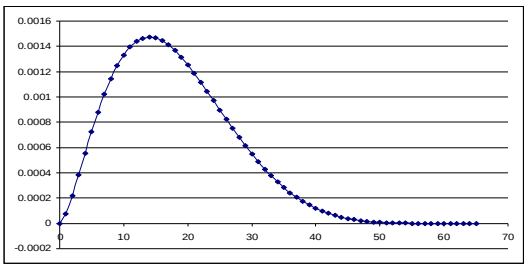

Figure 6. Probability Density Function f(s)

From the probability density function f(s) we obtain following data

s0=67MPa, μ=18.56, Ω=0.5

Parameters of beta distribution can be evaluated by expressions (7)

q=2.6149, r=6.8247

The m-th moment of stress range $E(S_m)$ can be calculated using equation (8). Fatigue life is estimated by equation (15), the reliability is obtained by (14) and the allowable stress range is calculated by equation. (16)

n=30 years, R=0.875, [s]=123.848MN/m^2

Conclusion

Reliability Based Fatigue Analysis is carried out for a structures accounting non linearities and random loadings to obtain the fatigue life and allowable stress range. The main contributions are

- using the Linear Random Wave Simulation for Pierson-Moskovitch wave spectrum to calculate the wave loading.
- nonlinear dynamic analysis using the Newmark technique to obtain the stress range
- Ran-flow method to construct the beta distribution for stress range f(s)

References

1. Ang AHS. Bases for reliability approach to structural fatigue. Proceedings of ICOSSAR '77, Munich, September 1977. pp. 97}114.
2. A.H.-S. Ang, M.C. Cheung, T.A. Shugar, J.D. Fernie (2001), "Reliability-based fatigue analysis and design of floating structures", *Marine Structures 14*, pp:25-36
3. Bell, R. W., (1991). The analysis of offshore foundations subjected to combined loading. M.Sc. Thesis. University of Oxford, Department of Engineering Science.
4. Cassidy, M. J., (1999). Non-linear analysis of jack-up structures subjected to random waves. DPhil thesis, Oxford University.
5. Đào Như Mai, Nguyễn Việt Khoa and Nguyễn Hữu Cường (2010). "Reliability Based Fatigue Analysis". Proceedings of the 10th National Conference on Mechanics of Solids, Thai Nguyen, Nov. 2010, pp 484-491
6. DNV-RP-C203.(2008) *Recommended Practice Det Norske Veritas* . Fatigue Design Of Offshore Steel Structures
7. Hasselmann, K., Barnett, T.P., Bouws, E., Carlson, H., Cartwright, D.E., Enke, K., Ewing, J.A., Gienapp, H., Hasselmann, D.E., Kruseman, P., Meerburgh, A., Muller, P., Olbers, D.J., Richter, K., Sell, W. and Walden, H. (1973). Measurements of wind wave growth and swell decay during the JONSWAP project. *Deutsches Hydrographisches Zeitschrift Reihe*, Suppl. A., 8, No 12.
8. Houlsby, G. T.; Cassidy, M. J., (2001). "A plasticity model for the behaviour of footings on sand under combined loading". *Geotechnique*, 52(2), pp. 117–129.
9. Kassimali, A.; Abbasnia, R., (1991). "Large deformation analysis of elastic space frames". *J. Struct. Engng ASCE*, 117(7), pp. 2069-2087.
10. Oran, C., (1973). "Tangent stiffness in space frames". *J. Struct. Div. ASCE*, 99(6), pp. 987-1001.
11. Pierson, W.J. and Moskowitz, L. (1964). A proposed spectral form for fully developed wind seas based on the similarity theory of S.A. Kitaigorodskii. *J. Geophys. Res.*, Vol. 69, No. 24, pp. 5181-90.

The 2nd International Conference on Engineering Mechanics and Automation (ICEMA2)
Hanoi, August 16-17, 2012
ISBN: 978-604-913-097-7

Dynamic Response of a Functionally Graded Bernoulli Beam to a Moving Load

Le Thi Ha[a] and Nguyen Dinh Kien[b]

[a] *Theoretical Mechanics Group, University of Transport and Communications, E-mail: lethiha@yahoo.com.vn*
[b] *Department of Solid Mechanics, Institute of Mechanics, Vietnam Academy of Science and Technology. E-mail: ndkien@imech.ac.vn*

Abstract

The dynamic response of a functionally graded Bernoulli beam to a moving point load is investigated by the finite element method. The beam material is assumed to be graded in the thickness direction by a power law distribution. The shift in the beam neutral axis position which arose from the non-symmetric material distribution in the thickness direction is taken into consideration. The numerical results show that the maximum dynamic deflections of the beam are underestimated by ignoring the change in the neutral axis position. The dynamic axial stress at the mid-span of the beam is also altered and the stress is not vanished at the mid-plane when taking the shift in the neutral axis into account. The influence of the moving speed on the mid-span axial stress distribution is also examined

Key Words: Functionally graded material, Bernoulli beam, neutral axis, finite element method, moving load, dynamic response.

1. Introduction

Analysis of beams subjected to moving loads is an important topic in structural mechanics and it plays an important role in practical application. Many efforts have been made by both the analytical and numerical methods in investigating the dynamic response of beams under different types of moving loads. A large number of publications on the topic can be found in the literature, only the main contributions are briefly discussed herein. The early and excellent reference is the monograph of Frýba (1972), in which a number of closed-form solutions for the moving load problems has been derived by using Fourier and Laplace transforms. Hino et al. (1984, 1985) analyzed moving load problems of bridge engineering by using the Galerkin finite element method. Lin and Trethewey (1990) derived the finite element equations for a Bernoulli beam subjected to different types of moving load, and then solved the obtained governing equation by Runge-Kutta integration method. Thambiratnam and Zhuge (1996) computed the dynamic deflection of beams on a Winkler elastic foundation subjected to a constant speed moving load by using the traditional planar Bernoulli beam element. Also using the finite element method, Nguyen and his colleagues (Nguyen and Tran, 2006; Nguyen, 2008; Nguyen and Le, 2011) computed dynamic response of beams subjected to moving

harmonic load by taking the effect of the elastic foundation support, axial load into consideration.

Functionally graded materials firstly initiated by Japanese scientists in 1984 have received great interest in recent years. By varying volume percentage of material constitutes in a desired direction, the specific physical and mechanical properties of the formed material can be obtained, and with the unique feature, functionally graded materials offer a great potential for use as structural material. A comprehensive list of publications on static, dynamic as well as buckling analyses of functionally graded (FG) structures subjected different loadings is given in the review paper by Birman and Byrd (2007), the contributions that are most relevan to the present work are briefly discussed herein.

Kang and Li derived the expression for determining the position of neutral axis of FG beam with material property continuously varies in thickness direction, and then derived solution for large displacements of the beam subjected to a tip load and tip moment (Kang and Li, 2009; Kang and Li, 2010). Li (2008) presented a unified approach for analyzing static and dynamic behavior of FG beams with the power-law gradient and a laminated beam. Ying et al. (2008) proposed the two-dimensional elasticity solutions for FG beams resting on an elastic foundation with the exponential-law graduation through the thickness for material property. Based on the two new beam theories, Sina et al. (2009) presented an analytical method for studying the free vibration of FG beams with material property graded in the thickness direction by a power law. Alshorbagy et al. (2011) investigated the free vibration characteristics of FG Bernoulli beams by the finite element method. The free vibration of FG beams was studied by Gunda et al. (2011) by using the hierarchical beam theory. Adopting polynomials as trail functions for the displacements, Şimşek and Kocatürk (2009) investigated dynamic response of FG Bernoulli beam subjected to a moving concentrated harmonic load. Also using the same approach, Şimşek investigated the dynamic response of linear and nonlinear Timoshenko FG beams under a moving mass and a moving harmonic load (Şimşek, 2010a; Şimşek, 2010b).

In the present paper, the dynamic response of a FG Bernoulli beam to a moving point load is investigated by the finite element method. The material properties are assumed to vary continuously in the thickness direction by a simple power law. The shift in the neutral axis position which resulted from the non-symmetry of the elastic modulus is taken into consideration. The effect of the material non-homogeneity, neutral axis position on the dynamic response, including the dynamic amplification factor and stress distribution is examined in detail.

2. Functionally graded beam

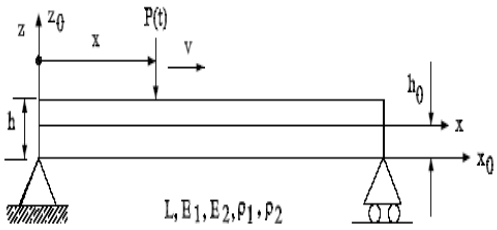

Figure 1. A simply supported FG beam under a moving load

Figure 1 shows a simply supported FG beam with length of L and height of h, subjected to a moving point load P. The coordinate system (x_0,z_0) is chosen as that the x_0 axis is on the bottom surface. The beam is assumed to be formed from two material components with the Young's modulus and mass density vary continuously in the thickness direction according to the power law as

$$E(z_0) = (E_1 - E_2)\left(\frac{z_0}{h}\right)^n + E_2$$
$$\rho(z_0) = (\rho_1 - \rho_2)\left(\frac{z_0}{h}\right)^n + \rho_2 \quad (1)$$

where n is the nonnegative power law index, defined the distribution of the material components through the thickness. As seen from equations (1), the bottom surface ($z_0=0$) contains only material 1, whereas the upper surface ($z_0=h$) is pure material 2.

Since the Young's modulus varies non-symmetrically through the thickness, the neutral axis of the beam is no longer at the mid-plan, but shifted from the mid-plane unless for the case of symmetric Young's modulus. The position of the neutral axis for a cross section can be determined by solving the following equation (Kang and Li, 2009; Kang and Li, 2010)

$$\frac{E_2-E_1}{E_1}\int_0^1(1+\beta)^n\,tdt+\frac{(1+\beta)^n}{2}\left(1-\frac{1}{\beta^2}\right)$$

$$=\frac{E_t-E_b}{E_b}\frac{\Gamma(n+1)}{\beta^2\Gamma(n+3)} \qquad (2)$$

where $\Gamma(*)$ is the Gamma function with its value can readily be defined for a given power law index; $\beta=(h-h_0)/h_0$, where h_0 denotes the distance from the bottom surface to the neutral axis as shown in Figure1.

The solution of equation (2), namely β, and thus the position of the neutral axis h_0, depends on the ratio between the Young's modulus of the material components, E_2/E_1, and the power law index n. Figure 1 shows the position of the neutral axis as a function of the power law index n of the FG beam formed from steel and alumina (Al_2O_3). The Young's modulus of steel is 210 GPa, and that of alumina is 390 GPa (Şimşek, 2009).

3. Governing equation

Considering a simply supported FG beam with length of L in a co-ordinate system (x,z) as shown in Figure 2, where x axis is coincident with the neutral axis of the beam. Based on Bernoulli beam theory, the displacements at a point of the beam are given by

$$u(x,z,t)=-z\frac{\partial w(x,t)}{\partial x}$$
$$w(x,z,t)=w(x,t) \qquad (3)$$

where u(x,t) and w(x,t) denote the axial and transverse displacement of a point on the beam axis, respectively; z is distance from the considering point to the neural axis; t denotes the time variable.

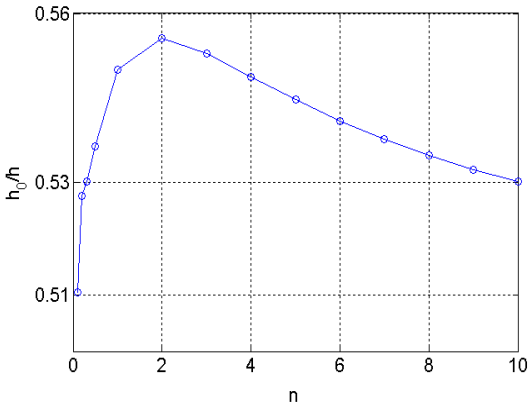

Figure 2. Effect of the gradient index on the position of the neutral axial of the FG beam formed from alumina and steel

Assuming linear elastic behavior for the beam material, the axial train and axial stress is given by

$$\varepsilon_x=-z\frac{\partial^2 w(x,t)}{\partial x^2}=z\chi$$
$$\sigma_x=E(z)\varepsilon_x=zE(z)\chi \qquad (4)$$

where $\chi=-\dfrac{\partial^2 w(x,t)}{\partial x^2}$ is the beam curvature.

Assuming the beam is being divided into a number of two-node elements, (i, j), with length of l. The train energy for e element can be written as

$$U=\frac{1}{2}\int_0^l\int_A E(z)\varepsilon_x^2\,dA\,dx=\frac{1}{2}\int_0^l D_{xx}\chi^2\,dx \qquad (5)$$

where

$$D_{xx} = \int_A z^2 E(z) dA = b\int_0^{h-h_0} z^2 E(h_0 + z) dz + b\int_0^{h_0} z^2 E(h_0 - z) dz \quad (6)$$

is the bending stiffness of the beam. It is noted that E*(z)* in equation (6) is defined by equation (1) with $z=z_0-h_0$, and h_0 is the distance from the bottom surface to the x axis. It is easy to verify that when $E=constant$, equation (6) deduces to $Ebh^3/12$ – the bending stiffness of a homogeneous beam. In a similar way, we can write the kinetic energy for the beam element in the following form

$$T = \frac{1}{2}\int_0^l \left[I_A \dot{w}^2 + I_D \left(\frac{\partial \dot{w}}{\partial x} \right)^2 \right] dx \quad (7)$$

Where a dot symbol is used to denote the derivative with respective to time, and

$$(I_A, I_B) = \int_A (1, z^2) \rho(z) dA \quad (8)$$

The potential energy for the moving load is given by

$$V = -Pw(x,t)\delta(x - vt) \quad (9)$$

where $\delta(*)$ is the Delta-Diract function, and v is the speed of the moving load, which assumes to be constant in the present work.

An interpolation scheme is now adopted for the transverse displacement w as

$$w = \mathbf{N}^T \mathbf{d} = N_1 w_i + N_2 \theta_i + N_3 w_j + N_4 \theta_j \quad (10)$$

where $\mathbf{d} = \{w_i, \theta_i, w_j, \theta_j\}^T$ is the nodal displacement vector for the element, and $\mathbf{N} = \{N_1, N_2, N_3, N_4\}^T$ is the vector of interpolating functions. Present work uses Hermite polynomials to interpolate the transverse displacement. From equations (4), (5), (7), (9) and (10), one can write the strain energy, kinetic energy and potential of the moving load in the forms

$$U = \frac{1}{2}\mathbf{d}^{\mathrm{T}}\mathbf{k}\mathbf{d}, \quad T = \frac{1}{2}\dot{\mathbf{d}}^{\mathrm{T}}\mathbf{k}\dot{\mathbf{d}}, \quad V = -Pd^T \mathbf{N}\delta(x - vt) \quad (13)$$

where **k, m** are respectively the element stiffness matrices for the element, and they are having the following forms

$$\mathbf{k} = \int_0^l \left(\frac{\partial^2 \mathbf{N}}{\partial x^2} \right) D_{xx} \left(\frac{\partial^2 \mathbf{N}}{\partial x^2} \right)^T dx$$

$$\mathbf{m} = \int_0^l \left[\mathbf{N} I_A \mathbf{N}^T + \left(\frac{\partial \mathbf{N}}{\partial x} \right) I_D \left(\frac{\partial \mathbf{N}}{\partial x} \right)^T \right] dx \quad (14)$$

Applying Hamilton's principle and then assembling over the elements, one get the equations of motion for the discrete beam in the form

$$\mathbf{M}\ddot{\mathbf{D}} + \mathbf{K}\mathbf{D} = \mathbf{F}_{ex} \quad (15)$$

where **D, M, K** are the structural nodal load vector, mass and stiffness matrices. $\mathbf{F}_{ex}$ is the structural vector of the external load given by

$$\mathbf{F}_{ex} = P\left\{ 000...\underbrace{N_1, N_2, N_3, N_4}_{\text{element under loading}}...000 \right\}^T \quad (16)$$

where the interpolating functions N_1, .., N_4 are evaluated at the current position of the moving load, that is at the point $x=vt$. Equation (16) can be solved by the direct integral method (Géradin and Rixen, 1997; Cook et al., 1989). The implicit Newmark method based on the average constant acceleration method which ensures the unconditional stability is adopted in the present work.

4. Numerical results

A simply supported FG beam form from steel and alumina as above mentioned is used in the analysis. The geometry data for the beam are adopted from the work by Şimşek and Kocatürk (2009) as follows: b=0.4 m,

h=0.9 m, L=20 m, where b, h, L denote the width, height and length of the beam, respectively. In addition to the Young's modulus of the constitutes stated in Section 2, the mass density for steel and alumina are 7800 kg/m^3 and 3960 kg/m^3, respectively. The beam is discretized by ten equal elements, and 400 time steps are used in the Newmark method.

Figure 3 shows the relation between the moving speed v and the maximum deflection at the mid-span of the beam for different values of the power law index n. In the figure, the deflection is normalized by the static deflection of the steel beam under a load P at the beam center, $D = PL^3/48E_sI$.

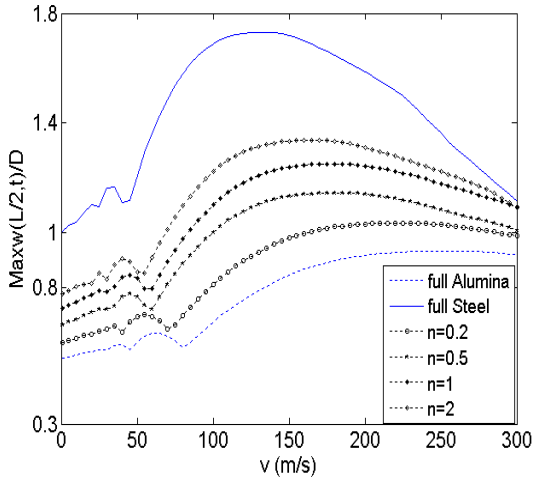

Figure 3. Variation of the mid-span maximum normalized dynamic deflections with the speed of moving load

It is seen from the figure that the maximum deflection of the beam increases when raising the speed of the moving load until a certain value, and it then decreases beyond this value. The maximum deflection also increases with an increase in the power law index n. This phenomenon is expected since the elastic modulus of the beam, as seen from equation (1), is lower for a higher index n, and thus the bending stiffness of the beam is lower for a higher index n. The peak values of the maximum dynamic deflection in Figure 3 and the corresponding moving speed are listed in Table 1, where the peak values of the maximum deflection computed by Şimşek and Kocatürk (2009) are also listed. To study the effect of the shift in the neutral axis, the numerical results computed by the element with $h_0=h/2$ are also listed in the Table.

Table 1. Maximum normalized deflections at the center, max($w(L=2;\ t)$)/D), and corresponding speed in Figure 3

Index n	Şimsek (2009)	$h_0=h/2$	Present $h_0\neq h/2$	Speed (m/s)
0.2	1.0344	1.0296	1.0341	222
0.5	1.1444	1.1360	1.1398	198
1	1.2503	1.2121	1.2496	179
2	1.3376	1.2895	1.3369	164
Al_20_3	0.9328	0.9324		252
Steel	1.7324	1.7316		132

As seen from the table, the numerical results of the present work are in god agreement with that of Şimşek and Kocatürk (2009). In addition, the dynamic deflection of the beam is somehow underestimated by ignoring the shift in the neutral axis.

Figure 4 shows the relation between the maximum normalized deflection at the mid-span and the power law index n for two values of the moving load speed, v = 50 m/s and v = 100 m/s. The figure shows an increase in the maximum dynamic deflection when raising the power law index n regardless of the moving speed. As seen from equation (1), the elastic modulus of the FGM beam reduces when raising the power law index n, and thus the increase in maximum dynamic deflection when raising the index n is expected.

To study the influence of the neutral axis position, the computation is also performed for the case $h_0=h/2$, and the results are depicted in the figure by the dashes lines. The effect of the shift in the neutral axis on the maximum deflection is clearly observed from the figure, where the maximum dynamic deflection of the beam is under estimated when ignoring the shift in the neutral axis position, regardless of the power law index n and the moving speed. The difference in the deflections is somehow larger for the case v=100 m/s.

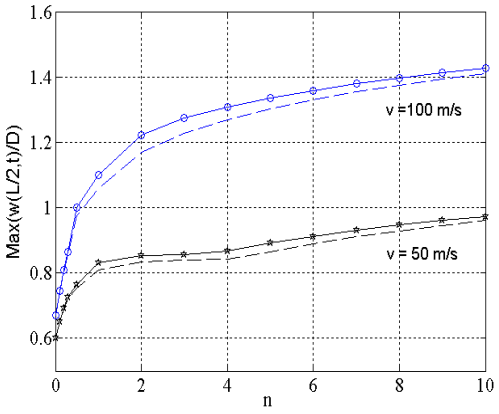

Figure 4. Relation between maximum normalized deflection and index n; solid lines: $h_0 \neq h/2$, dashed lines: $h_0 = h/2$

The time-histories for the mid-span deflection of the beam corresponding to moving speeds of 50 m/s and 100 m/s are depicted in Figures 5 and 6, respectively. In the figures, ΔT is the total time which is necessary for the load to travel completely through the beam. The figures also show the influence of the power law index n and the shift in the neutral axis position on the dynamic response of the beam. The underestimation of the maximum dynamic deflection is again clearly observed from the figures, regardless of the moving speed and the power law index. Moreover, the beam tends to execute more vibration circles for the case of the smaller power law index, regardless of the moving speed.

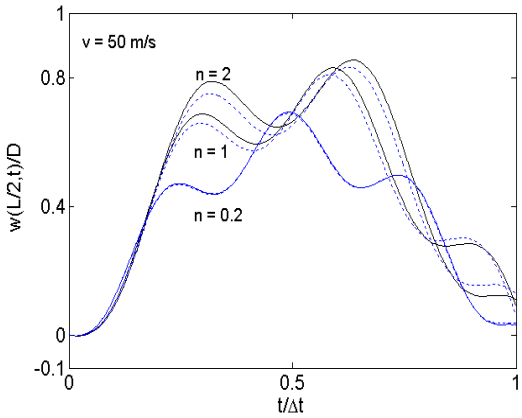

Figure 5. Time-histories for normalized mid-span deflections with $v = 50$ m/s; solid lines: $h_0 \neq h/2$, dotted lines: $h_0 = h/2$

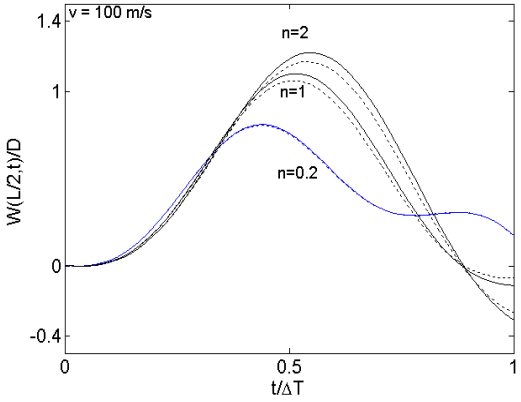

Figure 6. Time-histories for normalized mid-span deflections with $v = 100$ m/s: solid lines: $h_0 \neq h/2$, dotted lines: $h_0 = h/2$

Figure 7 shows the distribution of the mid-span normalized axial stress through the beam thickness. In the figure, the stress is normalized by the maximum static stress of the beam under the load P acting at the beam center. While the axial stress of the homogeneous beam (steel and alumina) vanishes at the mid-plane, that of the FG beam does not. The axial stress of the FG beam intersects the lines $\sigma_x = 0$ at the position of the neutral axis, that is a distance h_0 measured from the lower surface. Thus, when taking the effect of the shift in the neutral axis into consideration, the axial stress curve slightly shifts to the right direction. As a result, the tensile stress increases somehow, and the compressive stress reduces the same amount at the same time.

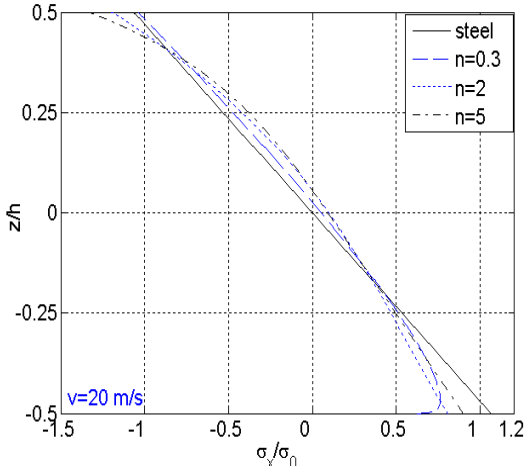

Figure 7. Thickness distribution of mid-span normalized axial stress (v = 20 m/s)

The effect of the moving speed on the thickness distribution of the mid-span axial stress is depicted in Figure 8 for the case n=0.3. As seen from the figure, the maximum tensile and compressive stresses are steadily increased when raising the moving speed. However, the increase in the maximum stresses will soon reach peak values, and they then start to decrease. The maximum tensile and compressive stresses corresponding a moving speed v=200 m/s, as seen from Figure 8, is much lower the maximum stresses corresponding v=100 m/s and v=150 m/s. This behavior of the maximum stresses is similar to that of the dynamic magnification factors, and it can be explained by the fact that when the moving speed is high, the maximum response of the beam may be occurred after the moving load have left the beam.

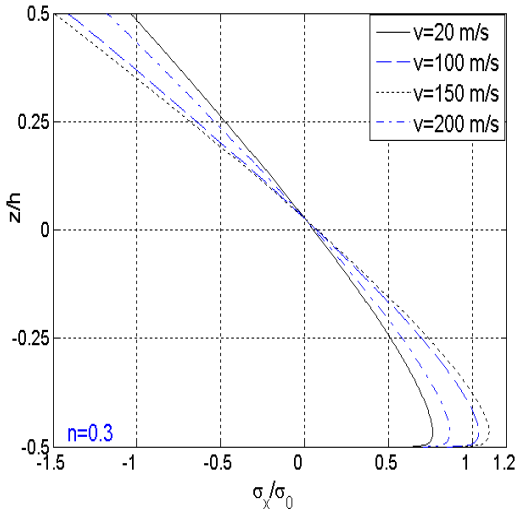

Figure 8. Effect of moving speed on thickness distribution of mid-span normalized axial stress (n = 0.3)

5. Conclusions

In this paper, the dynamic response of a FG Bernoulli beam subjected to a moving point load has been investigated by the finite element method. A two-node conventional beam element taking the shift in the beam neutral axis position into account was formulated and employed in the investigation. The dynamic response of the beam, including the dynamic magnification factor and the time-histories for mid-span deflection have been computed by using the implicit Newmark method. The numerical investigation has shown that, in addition to the loading parameter as in case of homogeneous beam, the dynamic response of the FG beam is clearly affected by the material distribution. The maximum dynamic deflection and the axial stress at the mid-span of the beam are altered when taking the shift in the neutral axis into consideration. The maximum mid-span deflection and maximum axial tensile stress are underestimated by ignoring the shift in the beam neutral axis. The effect of the moving speed on the mid-span stress distribution through the beam thickness has also examined and discussed.

6. References

Alshorbagy, A.E., M.A. Eltaher and F.F. Mahmoud (2011). Free vibration characteristics of a functionally graded beam by finite element method. *Applied Mathematical Modelling*, 35, pp. 412-425.

Birman. V and L.W. Byrd (2007). Modeling and analysis of functionally graded materials and structures. *Applied Mechanics Reviews*, 60, pp. 195-216.

Cook, R.D., D.S. Malkus and M.E. Plesha (1989). *Concepts and applications of finite element analysis*, John Willey & Sons, New York.

Frýba, L. (1972). *Vibration of solids and structures under moving loads*. Academia, Prague.

Géradin M. and R. Rixen (1997). *Mechanical vibrations. Theory and application to structural dynamics*. John Wiley and Sons, Chichester, second edition.

Gunda, J.B., R.K. Gupta, G.R. Janardhan and G.V. Rao (2011). Large amplitude vibration analysis of composite beams: Simple closed-form solutions. *Composite Structures*, 93, pp. 870-879.

Hino, J., T. Yoshimura, K. Konihi and N. Ananthanarayana (1984). A finite element method prediction of the vibration of a bridge subjected to a moving vehicle load. *Journal of Sound and Vibration*, 96, pp. 54-53.

Hino, J., T. Yoshimura, and N. Ananthanarayana (1985). Vibration analysis of non-linear beams subjected to a moving load using the finite element method. *Journal of Sound and Vibration*, 100, pp. 477-491.

Kang, Y.A. and X.F. Li (2009). Bending of functionally graded cantilever beam with power-law nonlinearity subjected to an end force. *Non-linear Mechanics*, 44, pp. 696-703.

Kang, Y.A. and X.F. Li (2010). Large deflection of a non-linear cantilever functionally graded beam. *Journal of Reinforced Plastics Composites*, 29, pp. 1761-1774.

Koizumi. M. (1997). FGM activities in Japan. *Composites:* part B, 28, pp. 1-4.

Li, X.F. (2008). A unified approach for analyzing static and dynamic behaviors of functionally graded Timoshenko and Euler-Bernoulli beams. *Journal of Sound and Vibration*, 318, pp.1210-1229.

Lin. W. H and M. W. Trethewey (1990). Finite element analysis of elastic beams subjected to moving dynamic loads. *Journal of Sound and Vibration*, 136, pp. 323-342.

Nguyen Dinh Kien and Tran Thanh Hai (2006). Dynamic analysis of prestressed Bernoulli beams resting on two-parameter foundation under moving harmonic load. *Vietnam Journal of Mechanics*, 28, pp. 176-188.

Nguyen Dinh Kien (2008). Dynamic response of prestressed Timoshenko beams resting on two-parameter foundation to moving harmonic load. *Technische Mechanik*, 28, pp. 237-258.

Nguyen Dinh Kien and Le Thi Ha (2011). Dynamic characteristics of elastically supported beam subjected to a compressive axial force and a moving load. *Vietnam Journal of Mechanics*, 33, pp. 113-131.

Olsson, M. (1991). On the fundamental moving load problem. *Journal of Sound and Vibration*, 145, pp. 299-307.

Şimşek, M. and T. Kocatürk (2009). Free and forced vibration of a functionally graded beam subjected to a concentrated moving harmonic load. *Composite Structures*, 90, pp. 465-473.

Şimşek, M. (2010a). Vibration analysis of a functionally graded beam under a moving mass by using different beam theory. *Composite Structures*, 92, pp. 904-917.

Şimşek, M. (2010b). Non-linear vibration analysis of a functionally graded Timoshenko beam under action of a moving harmonic load. *Composite Structures*, 92, pp. 2532-2546.

Sina, S.A., H.M. Navizi and H. Haddadpour (2009). An analytical method for free vibration analysis of functionally graded beams. Materials & Design, 30, pp. 741-747.

Thambiratnam, D. and Y. Zhuge (1996). Dynamic analysis of beams on elastic foundation subjected to moving loads. *Journal of Sound and Vibration*, 198, pp. 149-161.

Ying, J., C.F. Lu and W.Q. Chen (2008). Two-dimensional elasticity solutions for functionally graded beams resting on elastic foundation. *Composite Structures*, 84, pp. 209-219.

The 2nd International Conference on Engineering Mechanics and Automation (ICEMA2)
Hanoi, August 16-17, 2012
ISBN: 978-604-913-097-7

Free Vibration Analysis of Mindlin Plates on Elastic Foundation by Continuous Element Method

Nguyen Manh Cuong[a] and Tran Ich Thinh[b]

[a] *Hanoi University of Science and Technology, nguyenmanhcuong@hotmail.fr*
[b] *Hanoi University of Science and Technology, tranichthinh@yahoo.com*

Abstract

This research investigates the vibration behavior of Mindlin plates resting on elastic foundations by continuous element method. The dynamic stiffness matrix is constructed from analytical solutions of Mindlin plate on Winkler foundation equation. Obtained frequencies and harmonic responses for various types of boundary conditions are validated by comparing to the international articles and to the FEM. The influences of the foundation stiffness, the length ratio and the plate thickness ratio on the frequencies of thick plates are discussed. Numerical results confirms many advantages of continuous element model: less discretization, higher precision, volume of data storage and computing time saved, suitable for medium and high frequency range

Key Words: vibration Mindlin plate, elastic foundation, continuous element method, dynamic stiffness matrix, plate on elastic foundation

1. Introduction

Thick plate structures or Mindlin plates have been widely used in various engineering fields, and their dynamic response behaviors are well studied in a large number of publications Leissa (1973), Dawe (1982), Lim S.P. (1989), Liew (1998)… However, when they are resting on an elastic foundation the foundation–structure effects plays significant role in their behaviors and modifies the dynamic responses of the structures compared to those in the absence of foundation. Hence, the vibration of Mindlin plates on elastic foundation is of great importance in structural, aerospace, civil, mechanical and marine engineering applications.

Laura and Gutierrez (1985) studied the vibration of rectangular plates supported by a non-homogenous elastic foundation by the Rayleigh–Ritz method. Takahashi and Sonoda (1992) computed buckling and vibration solutions for rectangular plates supported by a Pasternak foundation. Lee and Lin (1993) examined the vibration of rectangular plates resting on a non-uniform elastic Winkler foundation using Levy series and the Green's functions. Using the same approach Lam et al. (2000) obtained the vibration solutions for a rectangular plate resting on a two-parameter foundation. Cheung et al. (2000) employed the finite strip method to study the buckling and vibration of plates with changes in thickness and

resting on a non-homogenous Winkler elastic foundation. More recently, Shen et al. (2001) studied the free and forced vibration of Reissner–Mindlin plates with four free edges resting on a Pasternak-type elastic foundation.

Nowadays, FEM is widely used for analyzing the vibration of plates on elastic foundation. Nevertheless, FEM is an approximate method and it generally converges to the exact solution with increasing number of elements. However, the accuracy of results cannot be always guaranteed. This is particularly true in dynamic analysis at high frequencies when the FEM may become unreliable. Thus, there is, and there will always be a need to use analytical methods based on classical theories, to validate the FEM and to assure confidence in design. One such method is the dynamic stiffness method (DSM) or continuous element method (CEM) which gives exact results that are independent of the number of elements used in the analysis. For instance, one or two single structural elements in the DSM are enough to compute any number of natural frequencies to any desired accuracy, which is impossible in the FEM. Especially, with increasing mode number in the medium and high frequency range, significant differences can arise in both response and stability analyses.

The DSM is based on the exact closed form solution of their governing differential equations of motion which lead to the dynamic stiffness matrix relating a state vector of loads to the corresponding state vector of responses at the sides of the structure. Several industrial computer codes using CEM have been developed such as BUNVIS-RG (Anderson, 1987), VICONOPT (William, 1991) and PFVIBAT (Akkeson, 1976).

At present CEM has been developed mainly for one-dimensional elements such as bars and beams (Leung, 1993), (Lunden, 1983), (Banejee, 1992). Recently, CE models for thick plate and thick shells of revolution have also been presented (Nguyen Manh Cuong, 2003), (Casimir, 2007).

Despite all the aforementioned works on DSM and on vibration of plates resting on elastic foundations, to the author's best knowledge, there exist no dynamic stiffness matrix in open literature for free vibration of Mindlin plates resting on an elastic foundation. This paper aims to fill the apparent gap in this area by providing the dynamic stiffness matrix for the vibration of Mindlin plates on a elastic foundation. Our model is validated by comparisons to different international researches and to FEM. CEM gives excellent accuracy, especially in the range of medium and high frequencies. Results on natural frequencies of Mindlin plate without or on elastic foundation and harmonic responses confirm advantages of the method: better precision of solution, size of model and computing time reduced. The presented CE model in this paper can be used as benchmarks for researchers to verify their numerical methods and are also important for engineers to design plates supported by elastic foundations.

2. Theoretical formulation

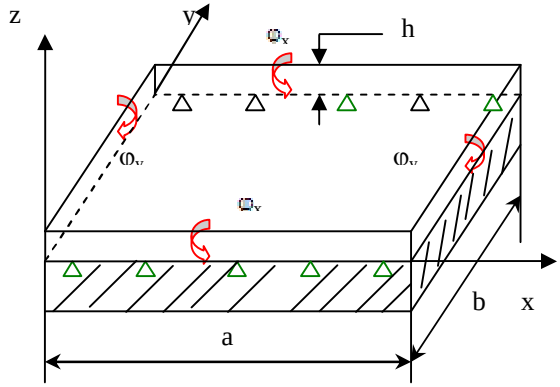

Figure 1. Mindlin plate on elastic foundation

with:

E: Young modulus υ:Poisson coefficient

ρ: mass density h: thickness of plate

a, b: dimensions of plate

G: shear modulus D: bending modulus

$$G = \frac{E}{2(1+\upsilon)} \qquad D = \frac{Eh^3}{12(1-\upsilon^2)}$$

w: bending displacement

φ_x, φ_y: rotations of the middle section

K: shear correction factor, *K = 5/6*

k: stiffness of Winkler foundation

A thick plate is assumed to rest on Winkler-type elastic foundations in the z direction (see Figure 1). The two edges of the plate parallel to the x-axis are simply supported and the two remaining edges may have any combinations of free, simply supported or clamped conditions.

2.1. Governing differential equations

The displacement field of Mindlin theory, assuming no motion in the membrane mode ($u_0 = v_0 = 0$) is given by Equation (1) where the symbols are defined in Figure 1:

$$\begin{aligned} u(x,y,z) &= z\varphi_y \\ v(x,y,z) &= z\varphi_x \\ W(x,y,z) &= w(x,y) \end{aligned} \tag{1}$$

Strain-displacement relationships of the problem are determined by Liu (2000):

$$Q_x = KGh(\frac{\partial w}{\partial x} + \varphi_x) \qquad Q_y = KGh(\frac{\partial w}{\partial y} + \varphi_y)$$

$$M_x = D(\frac{\partial \varphi_x}{\partial x} + \nu\frac{\partial \varphi_y}{\partial y}) \quad M_y = D(\frac{\partial \varphi_y}{\partial y} + \nu\frac{\partial \varphi_x}{\partial x})$$

$$M_{xy} = \frac{1-\nu}{2} D(\frac{\partial \varphi_y}{\partial x} + \frac{\partial \varphi_x}{\partial y}) \tag{2}$$

2.2. Equations of motion

The equation of motion of Minlin plate on elastic foundation can be expressed as Liu (2000):

$$\begin{cases} \dfrac{\partial M_x}{\partial x} + \dfrac{\partial M_{xy}}{\partial y} - Q_x = \dfrac{\rho h^3}{12}\dfrac{\partial^2 \varphi_x}{\partial t^2} \\ \dfrac{\partial M_{xy}}{\partial x} + \dfrac{\partial M_y}{\partial y} - Q_y = \dfrac{\rho h^3}{12}\dfrac{\partial^2 \varphi_y}{\partial t^2} \\ \dfrac{\partial Q_x}{\partial x} + \dfrac{\partial Q_y}{\partial y} - kw = \rho h \dfrac{\partial^2 w}{\partial t^2} \end{cases} \tag{3}$$

From Hamilton principle, boundary conditions of thick plate on elastic foundation are determined by Liu (2000):

- Simply supported (S): $w=\varphi_y=M_x=0$
- Clamped (C) : $w=\varphi_x=\varphi_y=0$ (4)
- Free (F): $Q_x=M_x=M_{xy}=0$

2.3. Dynamic stiffness matrix [K (ω)]$_m$

The solution of the free vibration problem is developed by Levy series expansions as follow:

$$\begin{Bmatrix} w(x,y,t) \\ \varphi_x(x,y,t) \\ \varphi_y(x,y,t) \end{Bmatrix} = \sum_{m=0}^{\infty} \begin{Bmatrix} w_m(x)\sin(\alpha y) \\ \varphi_{xm}(x)\sin(\alpha y) \\ \varphi_{ym}(x)\cos(\alpha y) \end{Bmatrix} e^{i\omega t}$$

$$\begin{Bmatrix} Q_x \\ M_x \\ M_{xy} \end{Bmatrix} = \sum_{m=0}^{\infty} \begin{Bmatrix} Q_{xm}\cos(\alpha y) \\ M_{xm}\sin(\alpha y) \\ M_{xym}\sin(\alpha y) \end{Bmatrix} e^{j\omega t} \text{ with: } \alpha = \frac{m\pi}{b} \tag{5}$$

The vector $\{y\}^T=\{w,\varphi_x, \varphi_y, Q_x, M_x, M_{xy}\}_m{}^T$ is called state-solution vector corresponding to the mth vibration mode.

In order to construct the Continuous element of thick plate on elastic foundation, the following expressions need to be calculated from equations (2), (3) and (5). Here the index 'm' is omitted for the sake of simplification

$$\begin{aligned} \frac{dw}{dx} &= \frac{h^2}{6K(1-\upsilon)} Q_x - \varphi_x \\ \frac{d\varphi_x}{dx} &= M_x + \upsilon\alpha\varphi_y \\ \frac{d\varphi_y}{dx} &= \frac{2}{(1-\upsilon)} M_{xy} - \alpha\varphi_x \\ \frac{dQ_x}{dx} &= \left[\frac{k-\rho h\omega^2}{D} + \frac{6\alpha^2 K(1-\upsilon)}{h^2}\right] w \\ &+ \frac{6\alpha K(1-\upsilon)}{h^2}\varphi_y \\ \frac{dM_x}{dx} &= \frac{-\rho h^3\omega^2}{12D}\varphi_x + \alpha M_{xy} + Q_x \\ \frac{dM_{xy}}{dx} &= \frac{6\alpha K(1-\upsilon)}{h^2} w \\ &+ \left[\frac{-\rho h^3\omega^2}{12D} + \frac{6K(1-\upsilon)}{h^2} + \alpha^2(1-\upsilon^2)\right]\varphi_y - \upsilon\alpha M_x \end{aligned} \tag{6}$$

The equations (6) are written into matrix form as: $\dfrac{d\{y\}^T}{dx} = [A]_m\{y\}^T$, where $[A]_m$ is a 6x6 matrix:

$$[A]_m=\begin{bmatrix} & \begin{matrix}0&-1&0\\0&0&\upsilon\alpha\\0&-\alpha&0\end{matrix} & & \begin{matrix}\frac{h^2}{6K(1-\upsilon)}&0&0\\0&1&0\\0&0&\frac{2}{1-\upsilon}\end{matrix} \\ \frac{k-\rho h\omega^2}{D}+\frac{\alpha^2 6K(1-\upsilon)}{h^2} & 0 & \frac{\alpha 6K(1-\upsilon)}{h^2} & \begin{matrix}0&0&0\\1&0&\alpha\\0&-\upsilon\alpha&0\end{matrix} \\ 0 & \frac{-\rho h\omega^2}{D} & 0 & \\ \frac{\alpha 6K(1-\upsilon)}{h^2} & 0 & \alpha^2(1-\upsilon^2)+\frac{\alpha 6K(1-\upsilon)}{h^2}\frac{\rho h\omega^2}{12D} & \end{bmatrix} \quad (7)$$

The transfer matrix $[T]_m$ is determined by:

$$[T]_m = e^{[A]_m a} = \begin{bmatrix} T_{11} & T_{12} \\ T_{21} & T_{22} \end{bmatrix} \quad (8)$$

Then the dynamic stiffness matrix $[K(\omega)]_m$ will be calculated by :

$$[K(\omega)]_m = \begin{bmatrix} T_{12}^{-1}T_{11} & -T_{12}^{-1} \\ T_{21}-T_{22}T_{12}^{-1}T_{11} & T_{22}T_{12}^{-1} \end{bmatrix}_m \quad (9)$$

The natural frequencies and harmonic responses of thick plate on elastic foundation ($k\neq 0$) and without elastic foundation ($k=0$) will be computed from this DSM.

3. Numerical results and discussions

This part of research is dedicated to validate CE model by comparing to results from available literature and to the FEM (Ansys). First, natural frequencies by CEM of thick plate without elastic foundation ($k=0$) but sumited to different boundary conditions will be compared to solutions of international researches Dawe (1982), Lim S.P. (1989), Leissa (1973) and to the FEM. A Matlab computer program using CE formulation is developed to resolve the vibration analysis of Mindlin plates. Next, obtained results by using DSM for Mindlin plate on elastic foundation will be validated by comparing to Leissa (1973) [4] and Xiang (2003) [5]. At last, the comparison of harmonic responses by DSM and by FEM will be carried out in order to demonstrate advantages of our model in the medium and high frequency range.

3.1. Validation of the CEM for Mindlin plate without elastic foundation (k=0)

Let's examine a Mindlin plate with the following properties: E=200 GPa, υ=0.3, ρ=2700 kg/m^3, h=0.0254m, a=b=10h. Natural frequencies of the structure calculated by CEM will be compared to results obtained by J. Dawe, SPLim and AW.Leissa and by FEM (Ansys).

The validation of our model is done by comparing a dimensionless parameter Ω calculated by: $\Omega = \omega\sqrt{2(1+\nu)\rho a^2/E}$

Table 1. Dimensionless parameter Ω calculated by different methods for thick SCSC plate

Mode	Leissa	Dawe	Lim	CEM
1	1.413	1.302	1.328	1.3012
2	2.671	2.398	2.433	2.3962
3	3.383	2.888	2.978	2.8892
4	4.615	3.852	3.960	3.8457
5	4.988	4.237	4.272	4.2376
6	6.299	4.939	5.100	4.9463

Table 1 and Table 2 demonstrate the comparison of Ω by CEM for SCSC and SSSS thick plate with researches of J. Dawe, SP. Lim and AW. Leissa.

Table 2. Dimensionless parameter Ω calculated by different methods for thick SSSS plate

Mode	Leissa	Dawe	Lim	CEM
1	0.9632	0.9300	0.9303	0.9301
2	2.4080	2.2180	2.2200	2.2194
3	3.8530	3.4020	3.4060	3.4055
4	4.8160	4.1440	4.1510	4.1494

CE model gives excellent results compared to those of Dawe using Rayleigh-Ritz method and those of SP. Lim using 3D Finite Element. The errors of the comparison don't exceed 3%.

Next, CE model for thick plate is validated by comparing to FEM using Ansys. The Ansys SHELL181 element taking into account both the rotatory inertia and shear deformations effects is used for modeling the plate. To validate the convergence of FEM model, tree different meshes (8x8, 10x10, 12x12) will be carried out to evaluate the

vibration of the plate. Table 3 illustrates the natural frequencies of thick SFSF and SCSF plates computed by DSM and by FEM.

Table 3. Natural frequencies (Hz) of thick plates by CEM and by FEM

BC	Mode	Ansys (8x8)	Ansys (10x10)	Ansys (12x12)	CEM	Errors (%)
FF	1	1546.9	1546.8	1546.8	1541	0.42
	2	2532.9	2532.9	2532.8	2511	0.93
	3	5644.7	5643.6	5643.2	5526	2.20
	4	6019.6	6016.2	6014.9	5933	1.45
	5	7109.5	7106.1	7104.8	6984	1.85
	6	10421	10416	10414	10142	2.81
	7	11228	11213	11208	10803	3.85
CF	1	2009.8	2009.7	2009.7	1999	0.80
	2	5034.2	5033.5	5033.2	4963	1.40
	3	6402.0	6398.6	6397.3	6305	3.12
	4	9299.8	9295.8	9294.3	9107	2.33
	5	10515	10504	10500	10237	3.65
	6	12903	12840	12838	12815	0.82
	7	13191	13157	13145	14017	2.29

Obtained results confirm the precision of our formulation. For the first seven vibration modes, the errors vary only from 0.42% to 3.85%. It is interesting to remark that FEM results converge towards those of CEM when the size of the elements decreases. FEM is an approximate method and it requires a very important number of elements to reach the values of CEM which is based on analytical solution of the thick plate equations. It is also important to note that using the minimum of elements but CE gives better solutions in all low, medium or high range of frequencies meanwhile FEM meets difficulties to deal with medium or high frequencies. This problem is demonstrated by the discrepancies between CE and FE models since the 6^{th} and 7^{th} vibration modes. Moreover, these differences become more and more important when the frequency increases.

Thus, CEM is an interesting approach to examine the free vibration of thick plate with many advantages: minimum size of model, higher precision, computing time reduced, having no difficulties to get good results in the medium and high range of frequencies.

3.2.CEM for Mindlin plate on elastic foundation ($k \neq 0$)

After the validation of our formulation for thick plate in absence of elastic foundation, this section concerns the vibration analysis of Mindlin plate on elastic foundation with different boundary conditions and with various values of k. Obtained results are compared to works of Leissa (1973) and Xiang (2003). The foundation effect is introduced by the foundation parameter kb^4/D which takes tree different values: 0, 10^2 and 10^3.

Consider a Mindlin plate on elastic foundation with the following properties: h=0.0254m, a/b=1, h/b = 0.005, E = 200 GPa, $\upsilon = 0.3$, $\rho = 2700$ kg/m^3.

Table 4 demonstrates the comparison of dimensionless parameter $\Omega = \omega b^2\sqrt{\rho h/D}$ calculated by CEM and by researches of Leissa and Xiang for thick plate on elastic foundation submitted to various types of boundary conditions and different values of k.

Table 4. Comparison of Ω for Mindlin plate on elastic foundation with different boundary conditions

kb^4 /D	Ref	Boundary condition SS	CC	FF	SC	CF	SF
0	Leissa	19.74	28.95	9.63	23.65	12.69	11.68
	Xiang	19.74	28.94	9.63	23.64	12.68	11.68
	CE	19.73	28.94	9.63	23.63	12.67	11.69
10^2	Xiang	22.13	30.63	13.88	25.67	16.15	15.38
	CE	22.13	30.61	13.87	25.66	16.15	15.37
10^3	Xiang	37.28	42.87	31.62	39.49	34.07	33.71
	CE	37.28	42.86	33.65	39.48	34.07	33.70

The errors of results are very small which confirms the reliability of our formulation. Among the boundary conditions, the SSSS gives better results because the real boundary condition of the plate is well simulated. The increasing of the foundation stiffness k leads to a bigger discrepancy of results of the two methods.

3.3.Harmonic responses

In order to demonstrate the major advantages of CE model, a comparison of harmonic responses by CEM and by FEM of a SFSF Mindlin plate resting on elastic foundation is conducted. The same plate as in the 3.2 section resting on the elastic

foundation with the stiffness $kb^4/D = 100$ is considered. A distributed load q = 1 N/m is applied to the edge x = a and the response point is situated on the middle point of the same edge. Two types of meshes: 10x10 and 30x30 and SHELL63 element are used for computing the harmonic response of plate by Ansys. The special form of continuous element relationship *{F} = [K(ω)] {U}* allows a direct acquisition of bending response of plate whereas a modal analysis procedure is needed for the calculation of response of plate by FEM. Figure 2 illustrates tree response curves obtained by using CEM and FEM.

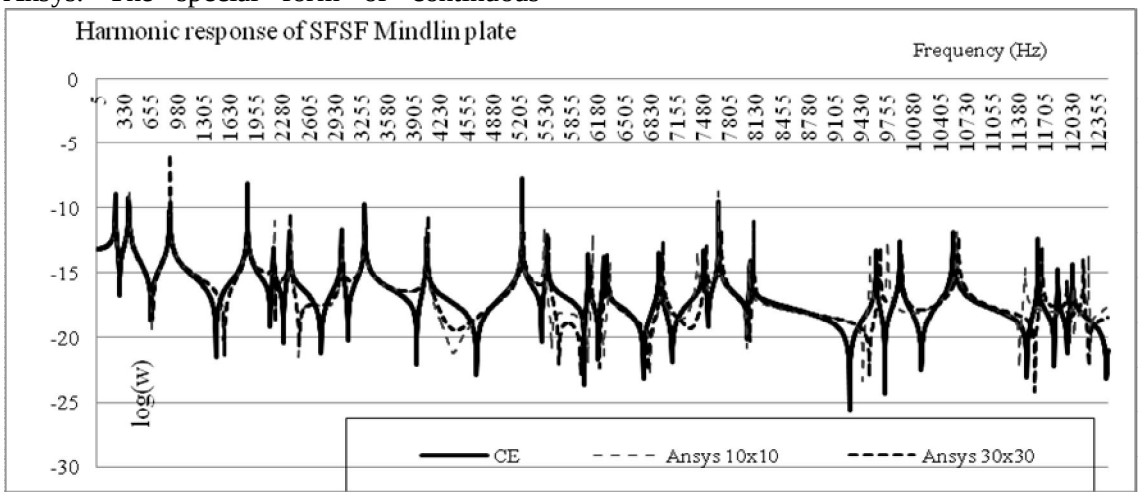

Figure 2. Harmonic responses of SFSF thick plate by CEM and by FEM

By studying this diagram, the following remarks are reveals:

- All the curves are coincided until 5190 Hz. That means all CE and FE models work well to predict the low vibration frequencies of the plate on elastic foundation.
- The gaps between CE and FE curves become larger from 5495 Hz. This is explained by the fact that FEM is an approximate method whose precision depends on the number of elements. The very fine mesh 30x30 isn't sill enough to meet the accuracy of CE model basing on the exact solution of the Mindlin plate equations. This phenomenon in medium and high frequency analysis causes a wrong response of FEM but it doesn't affect the CE results.
- Results of FEM converge towards those of CEM when the mesh is finer. This can be explained by the choice of the mesh and the shape of the functional chosen which more or less take into account the transverse shear and rotational inertia.
- The computing time by CEM is economized. Using a minimum number of elements leading to a less data storage and combining with the direct acquisition of response without modal analysis, CE model accelerates the calculating time.

In conclusion, the developed model demonstrates many advantages for the vibration analysis of thick plate resting on elastic foundation. In particularly, the reduction of the size of model and the precision of results in medium and high frequency range make CEM an interesting approach to overcome the actual problem of FEM.

4. Parameters effects on Mindlin plate resting on elastic foundation

Next, the variations of k, h/a ratio and a/b ratio will be studied by CEM in order to determine the influences of the foundation stiffness, the plate thickness and the plate dimensions on natural vibrations of the Mindlin plate on elastic foundation.

4.1.Effect of the foundation stiffness k

The same plate is again considered. The stiffness foundation parameter kb^4/D takes

3 different values: 0 (absence of elastic foundation), 10^2 and 10^3 representing various types of elastic foundation. Table 5 shows the variation of the dimensionless parameter Ω of plates submitted to SSSS, SCSC, SFSF, SSSC, SCSF and SSSF boundary conditions.

Table 5. Influences of the foundation stiffness k on the frequency parameter Ω of Mindlin plate on elastic foundation

BC	kb^4/D	f_1	f_2	f_3	f_4	f_5
SS	0	8.05	20.13	32.2	40.25	52.32
	10^2	9.03	20.54	32.46	40.45	52.47
	10^3	15.21	23.91	34.69	42.27	53.88
CC	0	11.81	22.33	28.27	38.57	41.68
	10^2	12.49	22.7	28.56	38.78	41.88
	10^3	17.49	25.79	31.08	40.67	43.63
FF	0	3.93	6.58	14.96	38.57	19.05
	10^2	5.66	7.74	15.51	38.78	19.48
	10^3	13.49	14.48	19.76	40.67	23.01
SC	0	9.64	21.08	23.92	35.13	40.89
	10^2	10.47	21.47	24.26	35.36	41.09
	10^3	16.11	24.71	27.18	37.42	42.88
CF	0	5.17	13.48	17.01	25.69	29.51
	10^2	6.59	14.08	17.49	26.01	29.79
	10^3	13.9	18.66	21.35	28.74	32.21
SF	0	4.77	11.31	16.8	24.08	25.22
	10^2	6.27	12.03	17.29	24.42	25.55
	10^3	13.75	17.16	21.18	27.32	28.33

Figure 3 illustrates the graphical representation of the influence of k on the fundamental frequency of the structure.

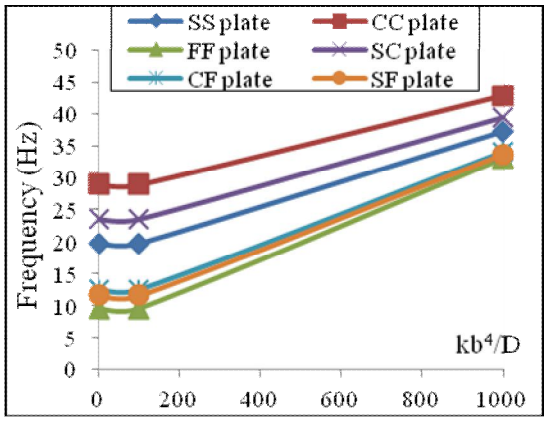

Figure 3. Fundamental frequency parameter of Mindlin plate with different values of k

It is easy to note that the increasing of the foundation stiffness causes the raise of natural frequencies of the structure i.e. this reinforces the stiffness of the plate. Nevertheless, the speed of accession of frequencies is not equal between the boundary conditions. The rate of speed rising can be classed as follows: SFSF>SSSF>SCSF>SSSS>SSSC>SCSC.

4.2.Effect of plate thickness

Now a study on the influence of plate thickness on the natural frequency is carried out in order to determine the role of the rotatory inertia and shear deformations effects. The characteristics of the plate on elastic foundation are: h=0.0254 m, a/b=1, E=200 GPa, υ=0.3, ρ=2700 kg/m^3.The h/b ratio varies from 0.02 to 0.1 with a step of 0.02. There are two types of foundations: $kb^4/D=10^2$ and $kb^4/D=10^3$. Tree kinds of boundary condition: SSSS, SCSC and SFSF are considered. Obtained results are summarized in the Figure 4.

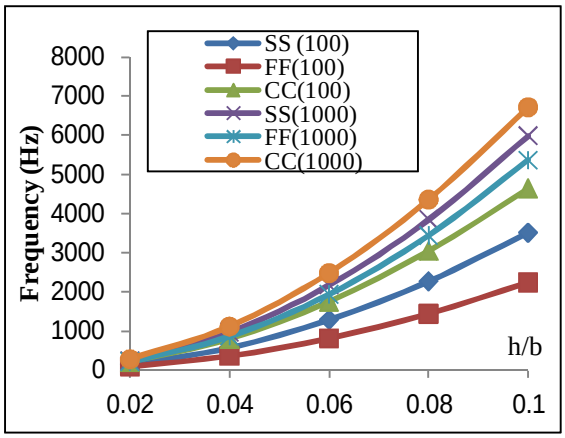

Figure 4. Effect of h/b ratio on fundamental frequency of thick plate on elastic foundation

It is clearly to observe a rise of frequencies when the plate's thickness increases. However, the frequencies of SCSC plate grow more rapidly than other boundary conditions. In addition, the augmentation of the foundation stiffness makes the plate frequencies higher.

4.3.Effect of plate dimensions

In this section, the a/b ratio will be varied from 0.2 to 1 by a step of 0.2. The properties of plate on elastic foundation are: h=0.0254 m, h/b=0.1, E=200 GPa, υ=0.3, ρ=2700 kg/m^3. Two types of foundations:

$kb^4/D=10^2$ and $kb^4/D=10^3$ and tree kinds of boundary condition: SSSS, SCSC and SFSF are also considered. Figure 5 shows the comparison of fundamental frequencies of the plate.

It is seen that the frequencies of SFSF plate does almost not vary when the a/b ratio changes. For the case of SSSS and SCSC plates, as the a/b increases, the frequencies decreases.

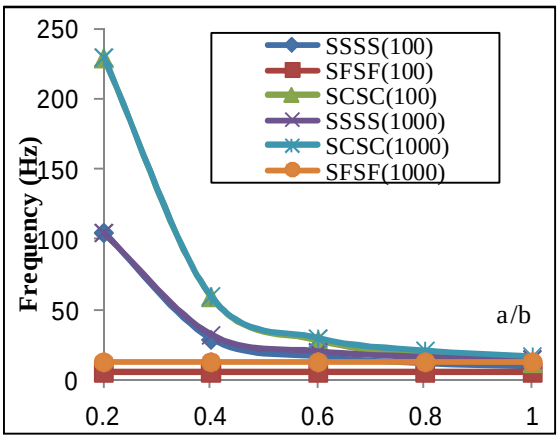

Figure 5. Influence of a/b ratio on fundamental frequency of thick plate on elastic foundation

5. Conclusions

This research has succeeded in building a dynamic stiffness matrix for a continuous element of thick isotropic plate resting on Winkler foundation and taking into account the rotational inertia and transverse shear. By applying the presented formulas, a Matlab program has been built and obtained results are in perfect agreement with the finite element method and with international researches. The precision of the CE solution are validated throughout numerous examples. Numerical test cases and harmonic responses confirm the advantages of our model: less data storage, computing time saved, high precision, suitable for medium and high frequency analysis.

The FEM can be used for modeling Mindlin plate on elastic foundation but it meets difficulty to determine a response of the structure on the range of medium frequencies due to a large number of elements for meshing. In this case, the calculation exceeds the capacity of storage and precision machinery. Therefore, CEM is a high efficient way to deal with these problems.

This study can be extended to analyze the vibration of plates resting on Pasternak foundation, composite plates, plates with damping, plates reinforced by stiffness, plates in contact with fluid.

6. References

Laura PAA, Gutierrez RH (1985). *Vibrating nonuniform plates on elastic foundation.* Journal of Engineering Mechanics American Society of Civil Engineers;111:1185–96.

Takahashi K, Sonoda T (1992). *Dynamic stability of a rectangular plate on Pasternak foundation subjected to sinusoidally time-varying in-plane load*. Theoretical and Applied Mechanics;41:55–62.

Lee SY, Lin SM (1993). *Levy-type solution for the analysis of non-uniform plates.* Computers and Structures;49:931–9.

Lam KY, Wang CM, He XQ (2000). *Canonical exact solutions for Levy-plates on two-parameter foundation using Green's functions.* Engineering Structures,22,364–78.

Cheung YK, Au FTK, Zheng DY (2000). *Finite stripmethod for the free vibration and buckling analysis of plates with abrupt changes in thickness and complex support conditions.* Thin-Walled Structures;36:89–110.

Shen HS, Yang J, Zhang L (2001). *Free and forced vibration of Reissner–Mindlin plates with free edges resting on elastic foundations*. Journal of Sound and Vibration;244:299–320.

Nguyen Manh Cuong (2003), *Eléments Continus de plaques et coques avec prise en compte du cisaillement transverse. Application à l'interaction fluide-structure*, Thèse de Doctorat, Université Paris VI.

J.B.Casimir, Manh Cuong Nguyen (2007). *Thick shells of revolution: Derivation of the dynamic stiffness matrix of continuous elements and application to a tested cylinder*, Computers & structures, 85(23-24), 1845-1857

Lunden R, Akesson B (1983). *Damped second order Rayleigh Timoshenko beam vibrationin space –an exact complex dynamic member stiffness matrix*. Int J Numer Methods Eng;19:431–49.

Leung AYT (1993). *Dynamic stiffness and substructures.* New-York: Springer.

Banerjee JR, Williams FW (1992). *Coupled bending-torsional dynamic stiffness matrix for Timoshenko beam elements*, Comput Struct;42:301–10.

Anderson MS, Williams FW (1987). *BUNVIS-RG: exact frame buckling and vibration program, with repetitive geometry and substructuring.* J Spacecraft Rockets; 24:353–61.

Akkeson B (1976). *A computer program for plane frame vibration analysis by an exact method*. Int J Numer Methods Eng; 10:1221–31.

Williams FW, Kennedy D, Butler R, Anderson MS (1991). *VICONOPT: program for exact vibration and buckling analysis or design of prismatic plate assemblies*. AIAA J;29:1927–8.

Leissa AW (1969). *Vibration of plates.* NASA SP-169. OOce of Technology Utilization, Washington.

F.-L. Liu (2000). *Rectangular thick plates on Winkler foundation: differential quadrature element solution.* International Journal of Solids and Structures 37 1743-1763

Dawe D.J. and Roufaiel O.L (1982). *Vibration analysis of rectangular Mindlin's plates subjected to membrane streses.* Journal of Sound and Vibration, 85, 263-275

Lim S.P., Lee K.H. and Senthilnathan N.R (1989). *Linear and non-linear bending of shear deformable plates.* Journal of Sound and Vibration, Vol. 130, N°1, 150-166

Leissa A.W (1973). *The free vibration of rectangular plates.* Journal of Sound and Vibration, 31, 257-293

Y. Xiang (2003), *Vibration of rectangular Mindlin plates resting on non-homogenous elastic foundations*, International Journal of Mechanical Sciences 45, 1229–1244

The 2nd International Conference on Engineering Mechanics and Automation (ICEMA2)
Hanoi, August 16-17, 2012
ISBN: 978-604-913-097-7

Structural Analysis of Three Phase Composite Plate under Bending Loads

Nguyen Dinh Duc[(1)] and Bui Duc Tiep[(2)]

[(1)]*University of Engineering and Technology - Vietnam National University, Hanoi*
[(2)]*Institute of Mechanics, Vietnam Academy of Science and Technology*

Abstract

Composite materials are widely used in Vietnam now. To improve the physical and mechanical characteristics of composites structures, polymer- matrixes are usually reinforced by fibers and particles. This paper presents an optimization for laminated three phase polymer composite under bending loads. Using finite element method, the paper investigated effects of material and geometrical properties, fibers and particles on bending of the composite plate. Based on obtained results, suitable volume ratios of particles, fibers and their orientations of three phase composite plate under bending loads is proposed and discussed.

Keywords: structural analysis, three phase composite plate, bending.

1. Introduction

Today composite materials are widely applied in Vietnam. Researches have shown that adding particle to fiber reinforced composite improves bending resistance [1], thermal resistance [2], waterproofing [3] and reduces inelastic strains [4].

The physic-mechanical properties of 3-phase composite depend on the volume ratio and the allocation of the component materials [5]. Thus to study the effect of fiber and particle volume ratios, fiber orientation, and plate geometry on the bending deflection is very important [5,6]. In Vietnam there have been several authors concerning with this problem, such as the bending analysis of 3-phase composite lamina based on classical plate theory [3], or bending of 3-phase laminated composite plate base on shear strain theory [1,3]. However, the commonly used 3-phase composites are laminated and the common simulation programs are mainly constructed based on the classical strain theory. Thus, in this paper we aim to achieve an optimization of 3-phase laminated composite plate for bending based on the classical strain theory. A numerical analysis is performed to obtain the optimal design for fiber and particle volume ratios, fiber orientation and geometrical properties.

The elastic moduli of unidirectional fiber composite are determined as in Vanin's [7]. The moduli for 3-phase composite are calculated as in [1-3]:

Here

$$G_j = \frac{E_j}{2\left(1+\nu_j\right)}; K_j = \frac{E_j}{3\left(1-2\nu_j\right)}$$

$j = m, a, c$

$$E_{11} = \xi_a E_a + (1-\xi_a)\bar{E} + \frac{8\bar{G}\xi_a(1-\xi_a)(\nu_a - \bar{\nu})}{2-\xi_a + \bar{x}\xi_a + (1-\xi_a)(x_a - 1)\frac{\bar{G}}{G_a}}$$

$$E_{22} = \left\{ -\frac{\nu_{21}^2}{E_{11}} + \frac{1}{8\bar{G}} \left[2\frac{(1-\xi_a)\bar{x} + (1+\xi_a\bar{x})\frac{\bar{G}}{G_a}}{\bar{x} + \xi_a + (1-\xi_a)\frac{\bar{G}}{G_a}} + 2\frac{\bar{x}(1-\xi_a) + (1+\xi_a\bar{x})\frac{\bar{G}}{G_a}}{\bar{x} + \xi_a + (1-\xi_a)\frac{\bar{G}}{G_a}} \right] \right\}^{-1}$$

$$\nu_{12} = \bar{\nu} - \frac{(\bar{x}+1)(\bar{\nu} - \nu_a)\xi_a}{2-\xi_a + \bar{x}\xi_a + (1-\xi_a)(x_a - 1)\frac{\bar{G}}{G_a}}$$

$$\nu_{23} = -\frac{E_{22}\nu_{21}^2}{E_{11}} + \frac{E_{22}}{8\bar{G}} \left[2\frac{(1-\xi_a)\bar{x} + (1+\xi_a\bar{x})\frac{\bar{G}}{G_a}}{\bar{x} + \xi_a + (1-\xi_a)\frac{\bar{G}}{G_a}} - \frac{2(1-\xi_a)(\bar{x}-1) + (x_a - 1)(\bar{x} - 1 + 2\xi_a)\frac{\bar{G}}{G_a}}{2-\xi_a + \bar{x}\xi_a + (1-\xi_a)(x_a - 1)\frac{\bar{G}}{G_a}} \right]$$

$$G_{23} = \frac{E_{22}}{2(1+\nu_{23})} = \bar{G}\frac{\bar{x} + \xi_a + (1-\xi_a)\frac{\bar{G}}{G_a}}{(1-\xi_a)\bar{x} + (1+\bar{x}\xi_a)\frac{\bar{G}}{G_a}}$$

$$G_{12} = \bar{G}\frac{1+\xi_a + (1-\xi_a)\frac{\bar{G}}{G_a}}{1-\xi_a + (1+\xi_a)\frac{\bar{G}}{G_a}}$$

In which the index $j = m,a,c$ belongs to matrix, fiber and particle respectively.

$$\bar{G} = G_m \frac{1-\xi_c(7-5\nu_m)H}{1+\xi_c(8-10\nu_m)H}$$

$$H = \frac{G_m/G_c - 1}{8-10\nu_m + (7-5\nu_m)\frac{G_m}{G_c}}$$

$$\bar{E} = \frac{9\bar{K}\bar{G}}{3\bar{K} + \bar{G}}; \qquad \bar{\nu} = \frac{3\bar{K} - 2\bar{G}}{6\bar{K} - 2\bar{G}}$$

$$x_a = 3 - 4\nu_a$$

$$\bar{K} = K_m \frac{1 + 4\xi_c G_m L(3K_m)^{-1}}{1 - 4\xi_c G_m L(3K_m)^{-1}}$$

$$L = \frac{K_c - K_m}{K_c + \frac{4G_m}{3}} \qquad \bar{x} = 3 - 4\bar{\nu}$$

2. Bending analysis for 3-phase laminated composite plate

2.1. The generally orthotropic lamina

According to Kirchhoff theory, the normal vector of the midplane is still perpendicular to it after deformation, and then the expression for strains are [5-8]:

Stress components are calculated from Hooke's law:

$$\varepsilon_{11} = -z\frac{\partial^2 w}{\partial x^2} \qquad \sigma_{11} = -z\left(A_{11}\frac{\partial^2 w}{\partial x^2} + A_{12}\frac{\partial^2 w}{\partial y^2}\right)$$

$$\varepsilon_{22} = -z\frac{\partial^2 w}{\partial y^2} \quad (1) \qquad \sigma_{22} = -z\left(A_{22}\frac{\partial^2 w}{\partial y^2} + A_{12}\frac{\partial^2 w}{\partial x^2}\right) \quad (2)$$

$$\varepsilon_{12} = -2z\frac{\partial^2 w}{\partial x \partial y} \qquad \sigma_{12} = 2A_{66}z\frac{\partial^2 w}{\partial x \partial y}$$

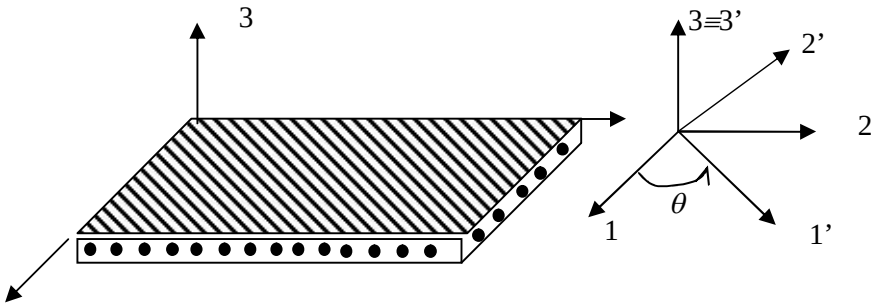

Figure 1. The generally orthotropic lamina

Bending and twisting moments are:

$$M_x = \int_{-0,5h}^{0,5h} \sigma_{11} z dz = -\left(D_x\frac{\partial^2 w}{\partial x^2} + D_1\frac{\partial^2 w}{\partial y^2}\right)$$

$$M_y = \int_{-0,5h}^{0,5h} \sigma_{22} z dz = -\left(D_y\frac{\partial^2 w}{\partial y^2} + D_1\frac{\partial^2 w}{\partial x^2}\right) \quad (3)$$

$$H = \int_{-0,5h}^{0,5h} \sigma_{12} z dz = -2D_{xy}\frac{\partial^2 w}{\partial x \partial y}$$

Here

$$D_x = \frac{A_{11}h^3}{12} = \frac{E_{11}h^3}{12\left(1-\nu_{12}\nu_{23}\right)}$$

$$D_y = \frac{A_{22}h^3}{12} = \frac{E_{22}h^3}{12\left(1-\nu_{12}\nu_{23}\right)} \quad (4)$$

$$D_1 = \frac{A_{12}h^3}{12} = \frac{E_{11}\nu_{23}h^3}{12\left(1-\nu_{12}\nu_{23}\right)}$$

$$D_{xy} = \frac{A_{66}h^3}{12} = \frac{G_{23}h^3}{12}$$

$$D = D_1 + 2D_{xy} = \frac{h^3}{12}\left(\frac{E_{11}\nu_{23}}{1-\nu_{12}\nu_{23}} + 2G_{23}\right)$$

From the equilibrium equation for a plate element [6,8], we obtain

$$\frac{\partial Q_x}{\partial x} + \frac{\partial Q_y}{\partial y} + q = 0; \qquad \sum_z = 0$$

$$\frac{\partial H}{\partial x} + \frac{\partial M_y}{\partial y} - Q_y = 0; \qquad \sum M_x = 0 \quad (5)$$

$$\frac{\partial H}{\partial y} + \frac{\partial M_x}{\partial x} - Q_x = 0; \qquad \sum M_y = 0$$

Thus

$$\frac{\partial^2 M_x}{\partial x^2} + \frac{\partial^2 M_y}{\partial y^2} + 2\frac{\partial^2 H}{\partial x \partial y} = -q(x,y) \quad (6)$$

Here

$M_x; M_y$ - bending moment

H - twisting moment

Q - surface load

Introducing (3), (4) into (6), we get the expression for the bending deflection of orthotropic 3-phase composite plate:

$$D_x\frac{\partial^4 w}{\partial x^4} + 2\left(D_1 + 2D_{xy}\right)\frac{\partial^4 w}{\partial x^2 \partial y^2} + D_y\frac{\partial^4 w}{\partial y^4} = q(x,y)$$

$$D_x\frac{\partial^4 w}{\partial x^4} + 2D\frac{\partial^4 w}{\partial x^2 \partial y^2} + D_y\frac{\partial^4 w}{\partial y^4} = q(x,y) \quad (7)$$

The maximum bending deflection can be calculated with distributed load having the form as follow:

$$q(x,y)=\sum_{m=1}^{\infty}\sum_{n=1}^{\infty}q_0\sin\frac{m\pi x}{a}\sin\frac{n\pi y}{b} \qquad (8)$$

When $q(x,y)=q_0$ it's easy to obtain (7) from:

The bending flection then has the form

$$w=\sum_{m=1,3,5}^{\infty}\sum_{n=1,3,5}^{\infty}a_{mn}\sin\frac{m\pi x}{a}\sin\frac{n\pi y}{b} \qquad (10)$$

Here

$$a_{mn}=\frac{16q_o}{\pi^6}\frac{1}{mn\left[\frac{m^4}{a^4}D_x+\frac{2m^2n^2}{a^2b^2}D+\frac{n^4}{b^4}D_y\right]} \qquad (11)$$

In the principal coordinates, the stiffness matrix has the following form [6]

$$Q=\begin{bmatrix}Q_{11} & Q_{12} & 0\\ Q_{12} & Q_{22} & 0\\ 0 & 0 & Q_{66}\end{bmatrix}$$

Here

$$\begin{aligned}Q_{11}&=\frac{E_{11}}{1-\frac{E_{22}}{E_{11}}\nu_{12}^2}\\ Q_{12}&=\frac{\nu_{12}E_{22}}{1-\nu_{12}\nu_{21}}=\nu_{12}Q_{22}\\ Q_{22}&=\frac{E_{22}}{1-\frac{E_{22}}{E_{11}}\nu_{12}^2}=\frac{E_{22}}{E_{11}}Q_{11}\\ Q_{66}&=G_{12}\end{aligned} \qquad (12)$$

In the non-principal coordinates [6,8]

$$\begin{aligned}Q'_{11}&=Q_{11}\cos^4\theta+Q_{22}\sin^4\theta\\ &\quad+2\left(Q_{12}+2Q_{66}\right)\sin^2\theta\cos^2\theta\\ Q'_{12}&=Q_{12}(\cos^4\theta+\sin^4\theta)\\ &\quad+\left(Q_{11}+Q_{22}-4Q_{66}\right)\sin^2\theta\cos^2\theta\end{aligned}$$

$$\begin{aligned}&D_x\frac{\partial^4 w}{\partial x^4}+2D\frac{\partial^4 w}{\partial x^2\partial y^2}+D_y\frac{\partial^4 w}{\partial y^4}\\ &=\frac{16q_0}{\pi^2}\sum_{m}^{\infty}\sum_{n}^{\infty}\frac{1}{mn}\sin\frac{m\pi x}{a}\sin\frac{n\pi y}{b}\end{aligned} \qquad (9)$$

$$\begin{aligned}Q'_{22}&=Q_{22}\cos^4\theta+Q_{11}\sin^4\theta\\ &\quad+2\left(Q_{12}+2Q_{66}\right)\sin^2\theta\cos^2\theta\\ Q'_{66}&=Q_{66}(\cos^4\theta+\sin^4\theta)\\ &+\left(Q_{11}+Q_{22}-2\left(Q_{12}+2Q_{66}\right)\right)\sin^2\theta\cos^2\theta\end{aligned} \qquad (13)$$

The laminate bending stiffness matrix is

$$D=\begin{bmatrix}D_{11} & D_{12} & 0\\ D_{12} & D_{22} & 0\\ 0 & 0 & D_{66}\end{bmatrix}$$

In which

$$\begin{aligned}D_{11}&=Q'_{11}\frac{e^3}{12} & D_{12}&=Q'_{12}\frac{e^3}{12}\\ D_{22}&=Q'_{22}\frac{e^3}{12} & D_{66}&=Q'_{66}\frac{e^3}{12}\end{aligned} \qquad (14)$$

Or: $D_{ij}=\frac{e^3}{12}Q'_{ij}$

Here, *e* is the plate thickness.

The plate's bending equation is [1,3,6]

$$D_{11}\frac{\partial^2 w_0}{\partial x^4}+2(D_{12}+2D_{66})\frac{\partial^4 w_0}{\partial x^2\partial y^2}+D_{22}\frac{\partial^2 w_0}{\partial y^4}=q_0 \qquad (15)$$

D_{ij} are calculated from (12), (13), (14). Introducing them into (15), we can get the equation of bending deflection of the plate.

2.2. The laminated 3-phase composite plate

An orthotropic laminate under distributed transverse load $q=q(x,y)$ has the equilibrium equation of the form:

$$A_{11}\frac{\partial^2 u_0}{\partial x^2}+A_{66}\frac{\partial^2 u_0}{\partial y^2}+(A_{12}+A_{66})\frac{\partial^2 v_0}{\partial x\partial y}=0 \quad (16)$$

$$(A_{12}+A_{66})\frac{\partial^2 u_0}{\partial x\partial y}+A_{66}\frac{\partial^2 v_0}{\partial x^2}+A_{22}\frac{\partial^2 v_0}{\partial y^2}=0 \quad (17)$$

$$D_{11}\frac{\partial^2 w_0}{\partial x^4}+2(D_{12}+2D_{66})\frac{\partial^4 w_0}{\partial x^2\partial y^2}+D_{22}\frac{\partial^2 w_0}{\partial y^4}=q(x,y) \quad (18)$$

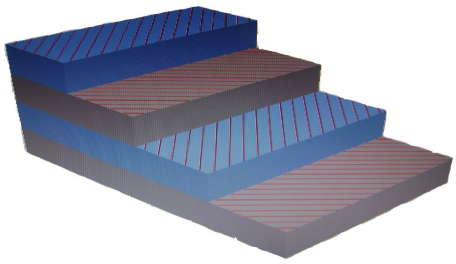

Figure 2. The laminated composite plate

In general, the distributed load can be represented using double Fourier serie

$$q(x,y)=\sum_{m=1}^{\infty}\sum_{n=1}^{\infty}q_{mn}\sin\frac{m\pi x}{a}\sin\frac{n\pi y}{b} \quad (19)$$

In which q_{mn} are coefficients that can be calculated from

$$q_{mn}=\frac{4}{ab}\int_0^b\int_0^a q(x,y)\sin\frac{m\pi x}{a}\sin\frac{n\pi y}{b}dxdy \quad (20)$$

The solution of the bending problem can be expressed as displacement functions using double Fourier series which satisfy the boundary conditions:

$$u_0(x,y)=\sum_{m=1}^{\infty}\sum_{n=1}^{\infty}A_{mn}\cos\frac{m\pi x}{a}\cos\frac{n\pi y}{b} \quad (21)$$

$$v_0(x,y)=\sum_{m=1}^{\infty}\sum_{n=1}^{\infty}B_{mn}\cos\frac{m\pi x}{a}\cos\frac{n\pi y}{b} \quad (22)$$

$$w_0(x,y)=\sum_{m=1}^{\infty}\sum_{n=1}^{\infty}C_{mn}\sin\frac{m\pi x}{a}\sin\frac{n\pi y}{b} \quad (23)$$

Substitution of u_0 and v_0 in equations (16) and (17) yields that $A_{mn}=0$ and $B_{mn}=0$. The membrance displacements are also zero: $u_0=v_0=0$.

Introduce (23) into (18) and rewrite q(x,y) as in (19), we get the expression of C_{mn}

$$C_{mn}=\frac{\frac{q_{mn}}{\pi^4}}{D_{11}\left(\frac{m}{a}\right)^4+2(D_{12}+2D_{66})\left(\frac{m}{a}\right)^2\left(\frac{n}{b}\right)^2+D_{22}\left(\frac{n}{b}\right)^4} \quad (24)$$

The bending deflection of a point (x,y)

$$w_0(x,y)=\frac{a^4}{\pi^4}\sum_{m=1}^{\infty}\sum_{n=1}^{\infty}\frac{q_{mn}}{D_{mn}}\sin\frac{m\pi x}{a}\sin\frac{n\pi y}{b} \quad (25)$$

Here

$$D_{mn}=D_{11}m^4+2(D_{12}+2D_{66})(mnR)^2+D_{22}(nR)^4$$
$$R=a/b \quad (26)$$

3. NUMERICAL RESULTS

The following part will present a numerical analysis using finite element method and commercial software ABAQUS.

A 3-phase composite laminated plate has the component materials' properties:

Epoxy matrix: E_m = 2.75 GP_a , $\nu_m=0.35$

Glass fiber: E_a = 72.38 GP_a , $\nu_a=0.2$

Glass particle: E_c = 740GP_a $\nu_c=0.21$

The plate is 40x120mm, has 4 laminae . The lamina thickness is 1mm.

3.1. Effect of fiber and particle volume ratios

First, we keep the fiber volume ratio $\xi_a=0.2$ and let the particle volume ratio vary from 0.1-0.5; then we keep the particle volume ratio $\xi_c=0.25$ and let the fiber volume ratio vary from 0.1-0.5. The bending deflection is calculated in three cases of boundary conditions: four clamped edges, one clamped edge, and two opposite clamped edges. The results are given in Table 1

The dependence of the bending deflection on the fiber and particle volume ratios is shown in Fig. 3.

From Fig.3, we can see that the bending deflection is in inverse ratio to the fiber and

particle volume ratios. However, the effect of fiber volume ratio is stronger than that of particle volume ratio.

Table 1. The plate bending deflection of different boundary conditions cases and materials volume ratios

Particle volume ratios	**Four clamped edges**	**One clamped edge**	**Two clamped edges**
0.1	6.19E-04	2.59	5.26E-02
0.2	5.67E-04	2.313	4.85E-02
0.3	5.13E-04	2.109	4.43E-02
0.4	4.58E-04	1.896	3.98E-02
0.5	4.02E-04	1.673	3.51E-02
Fiber volume ratios	**Four clamped edges**	**One clamped edge**	**Two clamped edges**
0.1	7.56E-04	3.159	6.64E-02
0.2	5.40E-04	2.212	4.64E-02
0.3	4.15E-04	1.686	3.54E-02
0.4	3.33E-04	1.349	2.82E-02
0.5	2.75E-04	1.109	2.32E-02

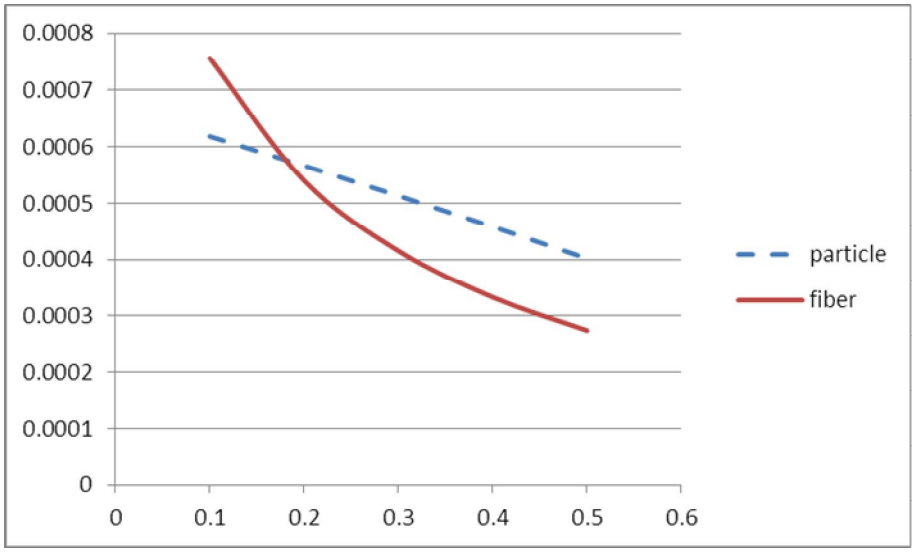

Figure 3. The effect of fiber and particle volume ratios on bending deflection

3.2. Effect of fiber orientation

Consider 3 symmetry plates having 4 lamina with different fiber orientation: 30/-30/30/-30, 45/-45/45/-45, 60/-60/60/-60.

Alternatively, we keep the fiber volume ratio $\xi_a = 0.2$ and let the particle volume ratio vary from 0.1-0.5; then we keep the particle volume ratio $\xi_c = 0.25$ and let the fiber volume ratio vary from 0.1-0.5. The result for bending deflection is shown in Table 2.

The dependence of the bending deflection on the fiber orientation is shown in Fig.4 and Fig. 5. Fig. 4 and Fig.5 show that the fiber orientation 60/-60/60/-60 provides the smallest bending deflection in both cases.

Table 3 and Fig.7 and Fig.8 show that for the one clamped edge case, the 30/-30/30/-30 plate has the smallest bending deflection

The results for the two opposite clamped edges case are given in Table 4 and presented in Fig.9. and Fig.10. Fig. 10 and Fig.11 show that for the two opposite clamped edges case, the 30/-30/30/-30 plate has the smallest bending deflection.

Table 2. The dependence of bending deflection on fiber orientation (four clamped edges)

Four clamped edges			
Particle volume ratios	**45/-45/45/-45**	**30/-30/30/-30**	**60/-60/60/-60**
0.1	7.90E-04	1.16E-03	5.32E-04
0.2	6.97E-04	9.78E-04	4.90E-04
0.3	6.08E-04	8.14E-04	4.46E-04
0.4	5.23E-04	6.69E-04	4.02E-04
0.5	4.42E-04	5.41E-04	3.56E-04
Fiber volume ratios	**45/-45/45/-45**	**30/-30/30/-30**	**60/-60/60/-60**
0.1	8.51E-04	1.07E-03	6.65E-04
0.2	6.52E-04	8.93E-04	4.68E-04
0.3	5.18E-04	7.41E-04	3.58E-04
0.4	4.22E-04	6.13E-04	2.87E-04
0.5	3.47E-04	5.04E-04	2.36E-04

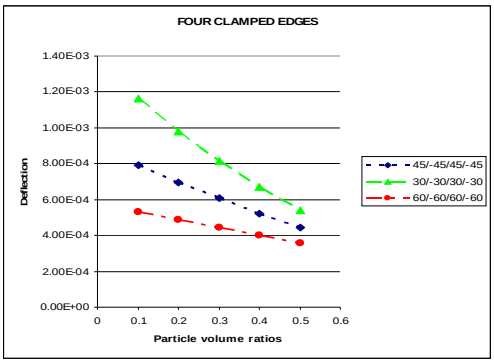

Figure 4. Effect of fiber orientation and particle volume ratio (four clamped edges)

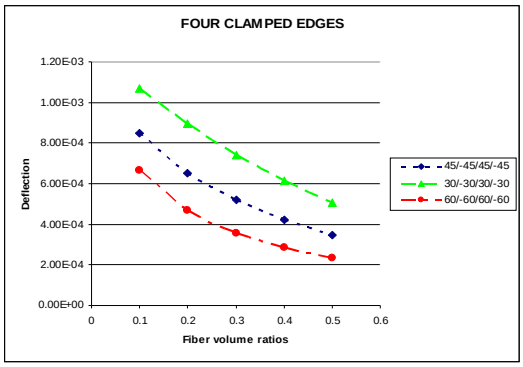

Figure 5. Effect of fiber orientation and fiber volume ratio (four clamped edges)

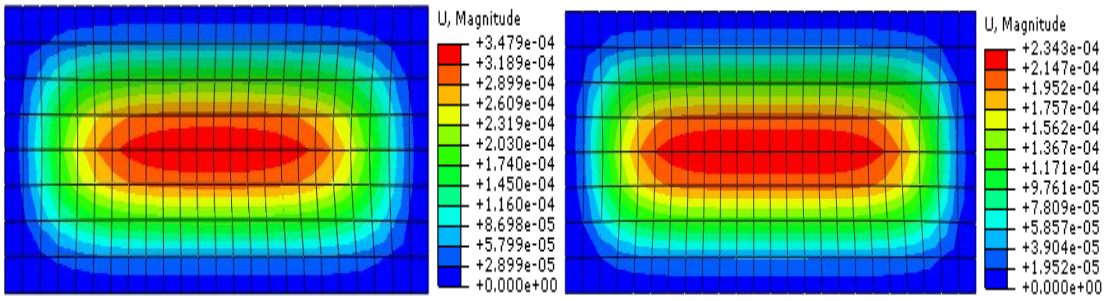

Figure 6. The bending deflection of 45/-45/45/-45 and 60/-60/60/-60 plate (four clamped edges)

Table 3. The dependence of bending deflection on fiber orientation (one clamped edge)

One clamped edge			
Particle volume ratios	**45/-45/45/-45**	**30/-30/30/-30**	**60/-60/60/-60**
0.1	3.872	2.41E+00	5.54E+00
0.2	3.318	2.191	4.539
0.3	2.82	1.973	3.699
0.4	2.369	1.756	2.985
0.5	1.958	1.538	2.372
Fiber volume ratios	**45/-45/45/-45**	**30/-30/30/-30**	**60/-60/60/-60**
0.1	3.885	2.934	4.822
0.2	3.063	2.082	4.102
0.3	2.469	1.598	3.439
0.4	2.015	1.28E+00	2.85E+00
0.5	1.648	1.05E+00	2.33E+00

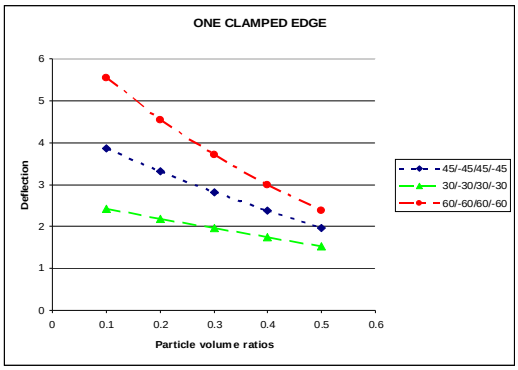

Figure 7. Effect of fiber orientation and particle volume ratio (one clamped edge)

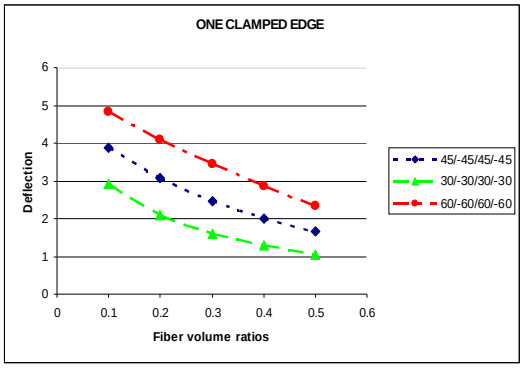

Figure 8. Effect of fiber orientation and fiber volume ratio (one clamped edge)

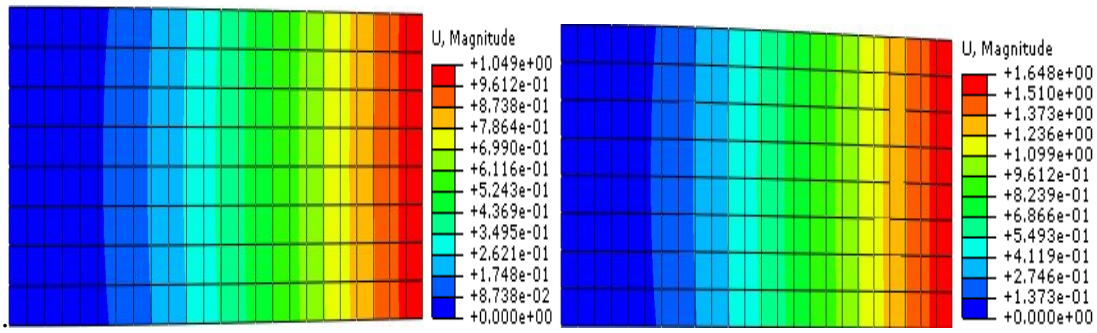

Figure 9. The bending deflection of 30/-30/30/-30 and 45/-45/-45/-45 plate (one clamped edge)

Table 4. The dependence of bending deflection on fiber orientation (two opposite clamped edges)

Two opposite clamped edges			
Particle volume ratios	**45/-45/45/-45**	**30/-30/30/-30**	**60/-60/60/-60**
0.1	7.93E-02	5.08E-02	1.14E-01
0.2	6.85E-02	4.62E-02	9.37E-02
0.3	5.85E-02	4.16E-02	7.67E-02
0.4	4.94E-02	3.70E-02	6.21E-02
0.5	4.10E-02	3.24E-02	4.95E-02
Fibre volume ratios	**45/-45/45/-45**	**30/-30/30/-30**	**60/-60/60/-60**
0.1	8.10E-02	6.18E-02	1.00E-01
0.2	6.34E-02	4.39E-02	8.47E-02
0.3	5.09E-02	3.37E-02	7.10E-02
0.4	4.15E-02	2.70E-02	5.88E-02
0.5	3.40E-02	2.21E-02	4.81E-02

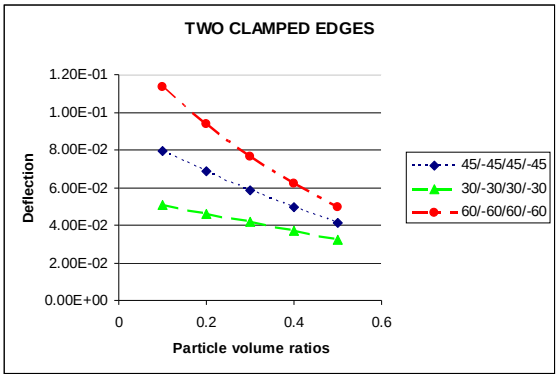

Figure 10. Effect of fiber orientation and particle volume ratio (two opposite clamped edges)

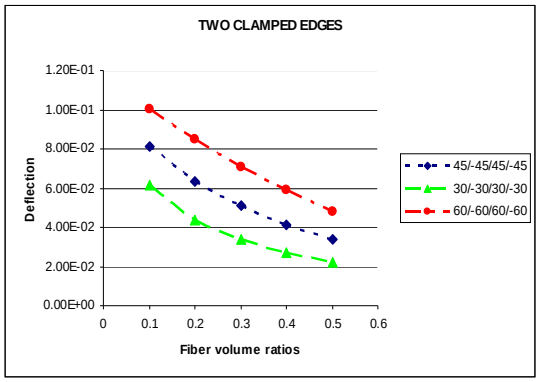

Figure 11. Effect of fiber orientation and fiber volume ratio (two opposite clamped edges)

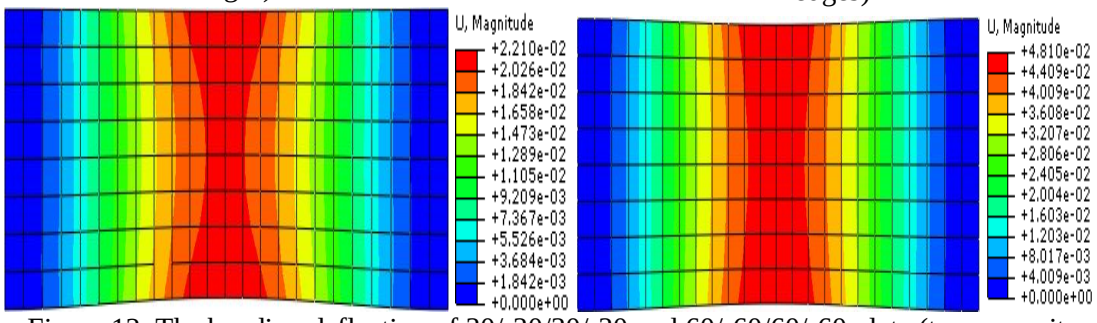

Figure 12. The bending deflection of 30/-30/30/-30 and 60/-60/60/-60 plate (two opposite clamped edges)

From the obtained results in this section, we can come to a conclusion: the plate bending deflection strongly depends on the fiber orientation. There are different optimal fiber orientation for different boundary condition cases. The 45/-45/45/-45 plate has average bending deflection in all cases. Thus, when the boundary condition is undetermined, the 45/-45/45/-45 plate is the best for ready manufacture.

3.3. Effect of symmetry and asymmetry

Consider two plates having 4 laminas, the fiber orientations are 45/-45/45/-45 and 45/45/-45/-45, respectively. Again we first keep the fiber volume ratio $\xi_a = 0.2$ and let the particle volume ratio vary from 0.1-0.5; then we keep the particle volume ratio $\xi_c = 0.25$ and let the fiber volume ratio vary from 0.1-0.5. The calculation is done for 3 boundary condition case: four clamped edges, one clamped edge and two opposite clamped edges. The result for bending deflection is shown in Table5.

Fig. 13 shows the effect of symmetry and asymmetry on bending deflection (two opposite clamped edges) when changing fiber and particle volume ratios. Figure 13. Effect of stacking sequence

From the results in Table 5 and Fig.13, we realize that, with the same thickness, same number of laminas, same fiber and particle volume ratios, symmetric plate provides smaller bending deflection than non symmetric plate. In the symmetry case, the effect of fiber volume ratio is stronger than that of particle volume ratio. However, for the asymmetry case, they are nearly the same.

Table 5. Bending deflection of symmetric and non symmetry plate

	Four clamped edges		**One clamped edge**		**Two opposite clamped edges**	
Particle volume ratios	**45/-45/45/-45**	**45/45/-45/-45**	**45/-45/45/-45**	**45/45/-45/-45**	**45/-45/45/-45**	**45/45/-45/-45**
0.1	7.90E-04	9.87E-04	3.872	4.477	7.93E-02	9.33E-02
0.2	6.97E-04	8.31E-04	3.318	3.729	6.85E-02	7.78E-02
0.3	6.08E-04	6.96E-04	2.82	3.089	5.85E-02	6.46E-02
0.4	5.23E-04	5.77E-04	2.369	2.535	4.94E-02	5.31E-02
0.5	4.42E-04	4.73E-04	1.958	2.052	4.10E-02	4.30E-02
Fiber volume ratios	**45/-45/45/-45**	**45/45/-45/-45**	**45/-45/45/-45**	**45/45/-45/-45**	**45/-45/45/-45**	**45/45/-45/-45**
0.1	8.51E-04	9.31E-04	3.885	4.128	8.10E-02	8.64E-02
0.2	6.52E-04	7.61E-04	3.063	3.397	6.34E-02	7.10E-02
0.3	5.18E-04	6.27E-04	2.469	2.804	5.09E-02	5.85E-02
0.4	4.22E-04	5.17E-04	2.015	2.309	4.15E-02	4.82E-02
0.5	3.47E-04	4.25E-04	1.648	1.887	3.40E-02	3.94E-02

4. CONCLUSION

From the presented results, we can yield some remarks on the bending of 3-phase composite plate made of epoxy matrix, glass fiber and glass particle:

1. The fiber and particle volume ratio both have effect on the bending deflection of the plate. The effect of fiber volume ratio is stronger than that of particle volume ratio when the plate is symmetric. For the asymmetry case, they are nearly the same.

2. The fiber orientations also influence the bending deflection. There are different suitable fiber orientations for different boundary conditions. The 45/-45/45/-45 plate provide average bending deflection in all cases, thus it is the best choice for ready manufacture.

3. With the same number of laminas and thickness, symmetric plate is better than non symmetric plate for bending.

Acknowledgment: This work was supported by Project QGDA.12.03 of Found for Science and Technology Development of Vietnam National University, Hanoi. The authors are grateful for this financial support.

References

[1]. Nguyen Dinh Duc, Dinh Khac Minh. Bending analysis of three-phase polymer composite plates reinforced by glass fibers and Titanium oxide particles. J. Computational Materials Sciencs, 2010, vol. 49, N4, p.194-198

[2]. Nguyen Dinh Duc, Luu Van Boi, Nguyen Tien Dac (2008). Determining thermal expansion coefficients of three-phase fiber composite material reinforced by spherical particles. Journal of Science, Mathematics- Physics, VNU, Vol. 24, No2, p.57-65.

[3]. Dinh Khac Minh, Bending of three-phase composite laminated plates in shipbuilding industry. PhD thesis in Engineering. Maritime University, Hai Phong, 2011.

[4]. Nguyen Dinh Duc, Dinh Khac Minh, Pham Van Thu. The bending analysis of three phase polymer composite plate reinforced glass fiber and titanium oxide particles including creep effect. International Journal of Aeronautical and Space Sciences , 2010, 11(4), p.361–366.

[5]. Nguyen Hoa Thinh, Nguyen Dinh Duc. Composite materials: Mechanics and Technology of manufacture. Publisher “Science and Technology”, Hanoi, 2002.

[6]. Tran Ich Thinh. Composite materials: Mechanics and calculating for structures. Publisher “Education”, Hanoi, 1994.

[7]. G.A. Vanin. Micro-Mechanics of composite materials, “Nauka dumka”, Kiev, 1985.

[8]. Reddy J.N. - Mechanics of Laminated Composite Plates and Shells: Theory and Analysys, CRC Press, 2004.

The 2nd International Conference on Engineering Mechanics and Automation (ICEMA2)
Hanoi, August 16-17, 2012
ISBN: 978-604-913-097-7

Nonlinear Dynamic Response of S-FGM Plate

Nguyen Dinh Duc and Pham Hong Cong

Vietnam National University, Hanoi; ducnd@vnu.edu.vn, congph_54@vnu.edu.vn

Abstract:

This paper presents an analytical investigation on the nonlinear dynamic response of S-FGM plate resting on elastic foundation and subjected to mechanical loads. The formulations use classical theory taking into account geometrical nonlinearity, initial geometrical imperfection of the S-FGM plate and stress function. The volume fractions of metal and ceramic is applied by Sigmoi-law distribution (S-FGM). The non-linear equations are solved by the Runge-Kutta and Bubnov-Galerkin methods. Obtained results show effects of material, imperfection and elastic foundations on the dynamical response of S-FGM plate.

Key Words: Nonlinear dynamic response, S-FGM plate, imperfection, elastic foundation

1. Introduction

Functionally Graded Materials (FGMs), which are microscopically composites and made from mixture of metal and ceramic constituents, have received considerable attention in recent years due to their high performance heat resistance capacity and excellent characteristics in comparison with conventional composites. By continuously and gradually varying the volume fraction of constituent materials through a specific direction, FGMs are capable of withstanding ultrahigh temperature environments and extremely large thermal gradients. Therefore, these novel materials are chosen to use in temperature shielding structure components of aircraft, aerospace vehicles, nuclear plants and engineering structures in various industries. As a result, many investigations have been carried out on the dynamic and vibration of FGM plates and shells. Here, we only mention some publications about dynamic analysis of FGM plates and shells recently.

Bich et al. investigated nonlinear dynamic of imperfect FGM shallow shell [1]. In [2] Hui-Shen Shen studied stability and free vibration of unsymmetrical FGM plates using first order shear deformation theory. Based on first order shear deformation theory, Najafizadeh and Eslami investigated buckling and post-buckling of FGM plates subjected to mechanical [3] and thermal loads [4]. Eslami and Wu [5] also used analytical approach and first order shear deformation theory for determining static critical buckling thermal

loads for thick FGM plates while materials properties didn't depended on temperatures. In [6] Duc and Tung used first order shear deformation theory and analytical approach to investigating the static stability of imperfect FGM plates with temperature-dependent properties.

Despite its complexity, the third order shear deformation theory was used by some researchers to investigate the static stability of FGM plates: in [7], Duc and Tung studied static buckling and post-buckling of imperfect FGM plate on elastic foundation using stress function; Samsam and Eslami investigated static buckling of FGM plates under mechanical and thermal loads using displacement field [8]. Mohammad and Singh studied static response and free vibration of P-FGM plates using first order shear deformation theory with finite element method in [9].

Up to date, dynamic analysis of FGM plates and shells has received comparatively great attention. This paper presents an analytical approach to investigate the nonlinear dynamic response of imperfect S-FGM symmetrical plates on elastic foundation using classical theory of plate. Numerical results for dynamic response of the FGM plate are obtained by Rugge-Kutta method.

2. Nonlinear dynamic of imperfect S-FGM plate

In the modern engineering and technology, there are many structures usually working in a very high heat resistance environment. To increase the ability to adjust to a high temperature, structures with the top and bottom surfaces are made of ceramic and the core of the structure is made of metal. The S-FGM plate considered in this paper is the one example of these structures.

Consider a rectangular FGM plate that consists of functionally graded ceramic- metal- ceramic materials and is midplane-symmetric (S-FGM). The outer surface layers of the plate are ceramic-rich, but the midplane layer is purely metallic.

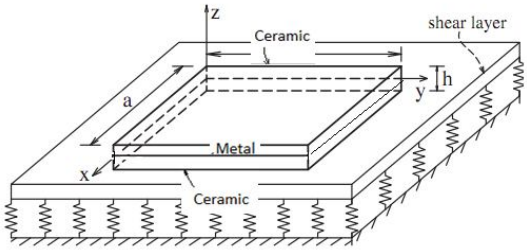

Fig. 1. S-FGM plate on elastic foundation

The plate is referred to a Cartesian coordinate system x,y,z, where xy is the midplane of the plate and z is the thickness coordinator, $-h/2 \le z \le h/2$. The length, width , and total thickness of the plate are a, b and h, respectively (Fig.1).

By applying a simple Sigmoi -law distribution, the volume fractions of metal and ceramic, V_m and V_c, are assumed as [6]:

$$V_m(z) = \begin{cases} \left(\dfrac{2z+h}{h}\right)^N, & -h/2 \le z \le 0 \\ \left(\dfrac{-2z+h}{h}\right)^N, & 0 \le z \le h/2 \end{cases}$$

$$V_c(z) = 1 - V_m(z) \quad (2.1)$$

where the volume fraction index N is a nonnegative number that defines the material distribution and can be chosen to optimize the structural response.

It is assumed that the effective properties P_{eff} of the functionally graded plate, such as the modulus of elasticity E and ρ, vary in the thickness direction z and can be determined by the linear rule of mixture as

$$P_{eff} = Pr_m V_m(z) + Pr_c V_c(z) \quad (2.2)$$

where Pr denotes a material property, and subscripts m and c stand for the metal and ceramic constituents, respectively.

From Eqs. (2.1) and (2.2), the effective properties of the S-FGM plate can be written as follows:

$$[E,\rho]=[E_c,\rho_c]+[E_{mc},\rho_{mc}]\begin{cases}\left(\dfrac{2z+h}{h}\right)^N, -h/2\le z\le 0\\ \left(\dfrac{-2z+h}{h}\right)^N, 0\le z\le h/2\end{cases} \tag{2.3}$$

Where; $E_{mc}=E_m-E_c,\ \rho_{mc}=\rho_m-\rho_c$ (2.4)

and the Poisson ratio ν is assumed constant $\nu(z)=\nu$

Suppose that the symmetrical FGM plate is subjected to a transverse load of intensity q_0. In the present study, the classical theory of plates is used to obtain the motion and compatibility equations, as well as expression for determining the dynamic response of the FGM plate.

The train-displacement relations taking into account the von Karman nonlinear terms are

$$\varepsilon_x=\varepsilon_x^0+z\chi_x,\ \varepsilon_y=\varepsilon_y^0+z\chi_y,\ \gamma_{xy}=\gamma_{xy}^0+2z\chi_{xy} \tag{2.5}$$

With

$$\begin{aligned}&\varepsilon_x^0=u_{,x}+w_{,x}^2/2;\ \varepsilon_y^0=v_{,y}+w_{,y}^2/2\\ &\gamma_{xy}^0=u_{,y}+v_{,x}+w_{,x}w_{,y}\\ &\chi_x=-w_{,yy};\ \chi_y=-w_{,yy};\ \chi_{xy}=-w_{,xy}\end{aligned} \tag{2.6}$$

where ε_x^0 and ε_y^0 are the normal strains, γ_{xy}^0 is the shear strain on the midplane of the plate, and γ_{xz} and γ_{yz} are the transverse shear strains; u,v, and w are the midplane displacement components along the x,y, and z axes $(,)$ indicates a partial derivative.

The strains are related in the compatibility equation

$$\frac{\partial^2\varepsilon_x^0}{\partial y^2}+\frac{\partial^2\varepsilon_y^0}{\partial x^2}-\frac{\partial^2\gamma_{xy}^0}{\partial x\partial y}=\left(\frac{\partial^2 w}{\partial x\partial y}\right)^2-\frac{\partial^2 w}{\partial x^2}\frac{\partial^2 w}{\partial y^2} \tag{2.7}$$

Hooke law for an FGM plate is defined as

$$\begin{aligned}&\sigma_x=\frac{E}{1-\nu^2}\left(\varepsilon_x+\nu\varepsilon_y\right);\ \sigma_y=\frac{E}{1-\nu^2}\left(\varepsilon_y+\nu\varepsilon_x\right)\\ &\sigma_{xy}=\frac{E}{2(1+\nu)}\gamma_{xy}\end{aligned} \tag{2.8}$$

The force and moment resultants of the plate can be expressed in terms of stress components across the plate thickness as

$$\left(N_i,M_i\right)=\int_{-h/2}^{h/2}\sigma_i\left(1,z\right)dz, i=x,y,xy \tag{2.9}$$

Inserting Eqs. (2.5), (2.8) into Eq. (2.9) gives the constitutive relations as

$$\begin{aligned}&\left(N_x,M_x\right)=\frac{1}{1-\nu^2}[\left(E_1,E_2\right)\left(\varepsilon_x^0+\nu\varepsilon_y^0\right)+\\ &\left(E_2,E_3\right)\left(\chi_x+\nu\chi_y\right)]\\ &\left(N_y,M_y\right)=\frac{1}{1-\nu^2}[\left(E_1,E_2\right)\left(\varepsilon_y^0+\nu\varepsilon_x^0\right)\\ &+\left(E_2,E_3\right)\left(\chi_y+\nu\chi_x\right)]\\ &N_{xy}=\frac{E_1}{2\left(1+\nu\right)}\gamma_{xy}^0+\frac{E_2}{1+\nu}\chi_{xy}\\ &M_{xy}=\frac{E_2}{2\left(1+\nu\right)}\gamma_{xy}^0+\frac{E_3}{1+\nu}\chi_{xy}\end{aligned} \tag{2.10}$$

Where:

$$\begin{aligned}&E_1=E_ch+E_{mc}h/(N+1);E_2=0\\ &E_3=\frac{E_ch^3}{12}+\frac{E_{mc}h^3}{2(N+1)(N+2)(N+3)}\end{aligned} \tag{2.11}$$

For using late, the reverse relations are obtained from Eq. (2.10)

$$\varepsilon_x^0 = \frac{1}{E_1}\left(N_x - \nu N_y\right); \varepsilon_y^0 = \frac{1}{E_1}\left(N_y - \nu N_x\right)$$
$$\gamma_{xy}^0 = \frac{2}{E_1} N_{xy}\left(1+\nu\right) \quad (2.12)$$

The equations of motion for a FGM plate based on the Classical Plate Theory (CPT) can be written as [10]:

$$\frac{\partial N_x}{\partial x} + \frac{\partial N_{xy}}{\partial y} = J_0 \frac{\partial^2 u}{\partial t^2} - J_1 \frac{\partial^3 \mathrm{w}}{\partial x \partial t^2}$$
$$\frac{\partial N_{xy}}{\partial x} + \frac{\partial N_y}{\partial y} = J_0 \frac{\partial^2 v}{\partial t^2} - J_1 \frac{\partial^3 \mathrm{w}}{\partial y \partial t^2}$$
$$\frac{\partial^2 M_x}{\partial x^2} + 2\frac{\partial^2 M_{xy}}{\partial x \partial y} + \frac{\partial^2 M_y}{\partial y^2} + N_x \frac{\partial^2 \mathrm{w}}{\partial x^2}$$
$$+2N_{xy}\frac{\partial^2 \mathrm{w}}{\partial x \partial y} + N_y \frac{\partial^2 \mathrm{w}}{\partial y^2} - k_1 w + k_2 \nabla^2 w + q_0 = \quad (2.13)$$
$$J_0 \frac{\partial^2 \mathrm{w}}{\partial t^2} + J_1\left(\frac{\partial^3 u}{\partial x \partial t^2} + \frac{\partial^3 v}{\partial y \partial t^2}\right) -$$
$$J_2\left(\frac{\partial^4 \mathrm{w}}{\partial x^2 \partial t^2} + \frac{\partial^4 \mathrm{w}}{\partial y^2 \partial t^2}\right)$$

Where

$$J_i = \int_{-h/2}^{h/2} z^i \rho(z) dz \ \left(i = 0,1,2\right)$$

k_1 is Winkler foundation modulus and k_2 is the shear layer foundation stiffness of Pasternak model.

with

$$J_0 = \rho_c h + \frac{\rho_{mc} h}{N+1}; \ J_1 = 0$$
$$J_2 = \frac{\rho_c h^3}{12} + \frac{\rho_{mc} h^3}{2(N+1)(N+2)(N+3)} \quad (2.14)$$

The substitution Eq. (2.10) into Eq. (2.13) leads to:

$$\frac{\partial N_x}{\partial x} + \frac{\partial N_{xy}}{\partial y} = J_0 \frac{\partial^2 u}{\partial t^2}; \frac{\partial N_{xy}}{\partial x} + \frac{\partial N_y}{\partial y} = J_0 \frac{\partial^2 v}{\partial t^2} \quad (2.15)$$

$$D\Delta^2 \mathrm{w} - \left(\begin{array}{l} N_x \frac{\partial^2 \mathrm{w}}{\partial x^2} + 2N_{xy}\frac{\partial^2 \mathrm{w}}{\partial x \partial y} + \\ N_y \frac{\partial^2 \mathrm{w}}{\partial y^2} - k_1 w + k_2 \nabla^2 w \end{array}\right) + \quad (2.16)$$
$$J_0 \frac{\partial^2 \mathrm{w}}{\partial t^2} - J_2\left(\frac{\partial^4 \mathrm{w}}{\partial x^2 \partial t^2} + \frac{\partial^4 \mathrm{w}}{\partial y^2 \partial t^2}\right) = q_0$$

Where $\Delta = \partial^2 / \partial x^2 + \partial^2 / \partial y^2$ and $D = \frac{E_3}{1-\nu^2}$

For solving Esq. (2.15) and (2.16) we introduce Airy's stress function $\varphi = \varphi(x, y)$ so that

$$N_x = \frac{\partial^2 \varphi}{\partial y^2}; N_y = \frac{\partial^2 \varphi}{\partial x^2}; N_{xy} = -\frac{\partial^2 \varphi}{\partial x \partial y} \quad (2.17)$$

The Volmir's assumption can be used in the dynamical analysis [11]: By taking the inertia $J_0 \frac{\partial^2 u}{\partial t^2} \to 0$ and $J_0 \frac{\partial^2 v}{\partial t^2} \to 0$ into consideration because $u \ll \mathrm{w}, v \ll \mathrm{w}$, equations (2.15) are satisfied. Inserting Eq. (2.17) into the Eq. (2.16) for prefect plate leads to

$$D\Delta^2 \mathrm{w} - \left(\begin{array}{l} \frac{\partial^2 \varphi}{\partial y^2}\frac{\partial^2 \mathrm{w}}{\partial x^2} - 2\frac{\partial^2 \varphi}{\partial x \partial y}\frac{\partial^2 \mathrm{w}}{\partial x \partial y} + \\ \frac{\partial^2 \varphi}{\partial x^2}\frac{\partial^2 \mathrm{w}}{\partial y^2} - k_1 w + k_2 \nabla^2 w \end{array}\right) + \quad (2.18)$$
$$J_0 \frac{\partial^2 \mathrm{w}}{\partial t^2} - J_2\left(\frac{\partial^4 \mathrm{w}}{\partial x^2 \partial t^2} + \frac{\partial^4 \mathrm{w}}{\partial y^2 \partial t^2}\right) = q_0$$

Equation (2.18) includes two dependent unknowns w and φ. To obtain a second equation, relating the unknowns, the geometrical compatibility for an imperfect plate can be used :

$$\varepsilon_{xm,yy}^0 + \varepsilon_{ym,xx}^0 - \gamma_{xym,xy}^0 =$$
$$w_{,xy}^2 - w_{,xx} w_{,yy} - \left(\left(w_{,xy}^*\right)^2 - w_{,xx}^* w_{,yy}^*\right) \quad (2.19)$$

in which w^* is a known function representing initial small imperfection of the FGM plate.

Setting Eqs. (2.12) and (2.17) into Eq. (2.19) gives the compatibility equation of an imperfect FGM plate as

$$\frac{1}{E_1}\left(\frac{\partial^4\varphi}{\partial x^4}+2\frac{\partial^4\varphi}{\partial x^2\partial y^2}+\frac{\partial^4\varphi}{\partial y^4}\right)= \left[\left(\frac{\partial^2\mathrm{w}}{\partial x\partial y}\right)^2-\frac{\partial^2\mathrm{w}}{\partial x^2}\frac{\partial^2\mathrm{w}}{\partial y^2}\right]-\left[\left(\frac{\partial^2\mathrm{w}^*}{\partial x\partial y}\right)^2-\frac{\partial^2\mathrm{w}^*}{\partial x^2}\frac{\partial^2\mathrm{w}^*}{\partial y^2}\right] \tag{2.20}$$

For an imperfect FGM plate, following to the Volmir's approach [11] for an imperfect plate, Eq. (2.18) is modified into form as

$$D\Delta^2\left(\mathrm{w}-\mathrm{w}^*\right)-\left(\begin{array}{l}\dfrac{\partial^2\varphi}{\partial y^2}\dfrac{\partial^2\mathrm{w}}{\partial x^2}-2\dfrac{\partial^2\varphi}{\partial x\partial y}\dfrac{\partial^2\mathrm{w}}{\partial x\partial y}\\ +\dfrac{\partial^2\varphi}{\partial x^2}\dfrac{\partial^2\mathrm{w}}{\partial y^2}-k_1w+k_2\nabla^2w\end{array}\right)$$
$$+J_0\frac{\partial^2\mathrm{w}}{\partial t^2}-J_2\left(\frac{\partial^4\mathrm{w}}{\partial x^2\partial t^2}+\frac{\partial^4\mathrm{w}}{\partial y^2\partial t^2}\right)=q_0 \tag{2.21}$$

Equations (2.20) and (2.21) are the basic relations used to investigate the dynamic response of imperfect S-FGM plate on elastic foundations. They are nonlinear in the dependent unknowns w and φ.

Suppose that the S-FGM plate is simply supported at its edges and subjected to q transverse loads $q_0(t)$. The boundary conditions can be expressed as

$$\begin{array}{l}\mathrm{w}=0, M_x=0, N_x=0, N_{xy}=0; \quad at \quad x=0,a\\ \mathrm{w}=0, M_y=0, N_y=0, N_{xy}=0; \quad at \quad y=0,b\end{array} \tag{2.22}$$

The mentioned conditions (2.22) can be satisfied if the deflection w and the stress function φ are represented by:

$$\begin{array}{l}\mathrm{w}=f(t).\sin\dfrac{m\pi x}{a}.\sin\dfrac{n\pi y}{b}\\ \varphi=g(t).\sin\dfrac{m\pi x}{a}.\sin\dfrac{n\pi y}{b}\\ w^*(x,y)=f_0\sin\dfrac{m\pi x}{a}\sin\dfrac{n\pi y}{b}\end{array} \tag{2.23}$$

in which $m,n=1,2,...$ are natural numbers representing the number of half waves in the x and y directions respectively; f is the deflection amplitude; $f_0=const$, varying between 0 and 1, represents the size of the imperfections.

The introduction of Eq. (2.23) into Eqs. (2.20) and (2.21) and applying the Galerkin method gives

$$m_1=\frac{A_5}{A_3};\ m_2=\frac{A_6}{A_3};\ m_3=\frac{A_4}{A_3};\ m_4=\frac{4ab}{A_3mn\pi^2}$$
$$\frac{1}{E_1}\left(\frac{m^2}{a^2}+\frac{n^2}{b^2}\right)^2\pi^2\frac{ab}{4}g(t)=-\frac{4}{3}\frac{mn}{ab}\left(f^2(t)-f_0^2\right) \tag{2.24}$$

$$\begin{array}{l}D\left(f(t)-f_0\right)\left(\dfrac{m^2}{a^2}+\dfrac{n^2}{b^2}\right)^2\pi^4\dfrac{ab}{4}-\dfrac{8}{3}\dfrac{mn\pi^2}{ab}g(t)f(t)\\ +\dfrac{ab}{4}\left[K_1\dfrac{D}{a^4}+K_2\dfrac{D}{a^2}\left(\dfrac{m^2}{a^2}+\dfrac{n^2}{b^2}\right)\pi^2\right]f(t)\\ J_0\dfrac{ab}{4}\ddot{f}(t)+J_2\left(\dfrac{m^2}{a^2}+\dfrac{n^2}{b^2}\right)\pi^2\dfrac{ab}{4}\ddot{f}(t)=p\dfrac{4ab}{mn\pi^2}\end{array} \tag{2.25}$$

where $K_1=\frac{k_1a^4}{D};\ K_2=\frac{k_2a^2}{D}$; m,n - odd numbers.

Eqs. (2.24) and (2.25) can be simplified as follow:

$$g(t)=\frac{A_2}{A_1}\left(f^2(t)-f_0^2\right) \tag{2.26}$$

$$A_3\ddot{f}(t)+A_5f(t)+A_6f^3(t)+A_4f_0=q_0\frac{4ab}{mn\pi^2} \tag{2.27}$$

where:

$$A_1=\frac{1}{E_1}\left(\frac{m^2}{a^2}+\frac{n^2}{b^2}\right)^2\pi^2\frac{ab}{4};A_2=-\frac{4}{3}\frac{mn}{ab}$$

$$A_3 = J_0\frac{ab}{4} + J_2\left(\frac{m^2}{a^2}+\frac{n^2}{b^2}\right)\pi^2\frac{ab}{4};$$

$$A_4 = -D\left(\frac{m^2}{a^2}+\frac{n^2}{b^2}\right)^2\pi^4\frac{ab}{4}$$

$$A_5 = D\left(\frac{m^2}{a^2}+\frac{n^2}{b^2}\right)^2\pi^4\frac{ab}{4} + \frac{8}{3}\frac{mn\pi^2}{ab}\frac{A_2}{A_1}f_0^2$$

$$+\frac{ab}{4}\left[K_1\frac{D}{a^4} + K_2\frac{D}{a^2}\left(\frac{m^2}{a^2}+\frac{n^2}{b^2}\right)\pi^2\right]$$

$$A_6 = -\frac{8}{3}\frac{mn\pi^2}{ab}\frac{A_2}{A_1}$$

The Eq. (2.27) can be written as:

$$\ddot{f}(t) + m_1 f(t) + m_2 f^3(t) + m_3 f_0 = m_4 q_0 \quad (2.28)$$

in which:

The equation (2.28) for obtaining the nonlinear dynamic response the initial conditions are assumed as $f(0) = f_0, \dot{f}(0) = 0$. The applied loads are varying as function of time. The nonlinear equation (2.28) can be solved by the Newmark's numerical integration method or by the Runge-Kutta method.

3. Numerical results and Discussion

The imperfect symmetrical FGM plate considered here a square plate: $a = b = 1m$, $h = 0.01m$. The plates are simply supported at all its edges. The combination of materials consists of aluminum ($E_m = 70.10^9 N/m^2$, $\rho_m = 2702kg/m^3$) and alumina ($E_c = 380.10^9 N/m^2$, $\rho_c = 3800kg/m^3$) . The Poisson ration ν is chosen to be 0.3 for simplicity. The plate subjected by an uniformly distributed excited transverse load $q_0(t) = p\sin\Omega t$.

The nonlinear dynamic response of the FGM plate acted on by the harmonic uniformly excited transverse load $q_0(t) = p\sin\Omega t$ are obtained by solving Eq. (2.28) combined with the initial conditions and by use of the Runge-Kutta method.

Fig. 2 shows the graph of maximum deflection of 36 periods; Fig.3 shows nonlinear response of the FGM plate of long period with different intensity of loads:

$p = 1500N/m^2$ and $p = 2000N/m^2$; $\Omega = 500$.

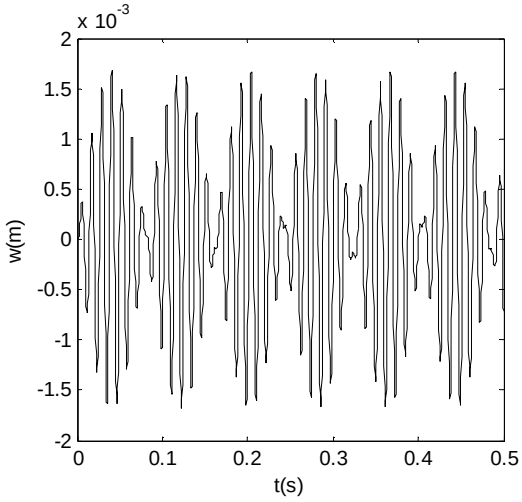

Fig. 2: Dynamic response of the FGM plate ($N = 1,\ q_0(t) = 1500\sin(500t)$)

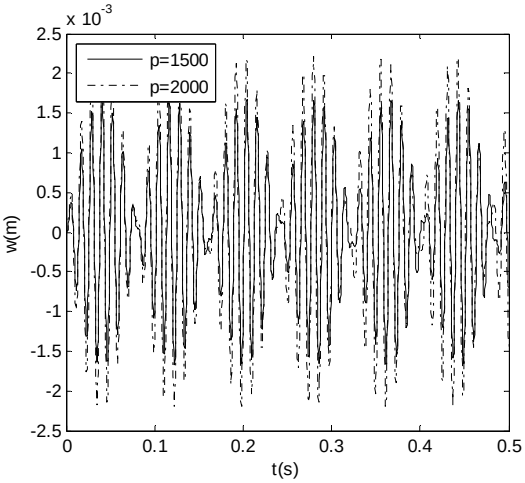

Fig. 3. Dynamic response with different intensity of loads

Relation of maximum deflection and velocity of maximum deflection when $(\mathrm{N}=1)$ and $q_0(t)=1500\sin(500t)$ is presented in Fig.4.

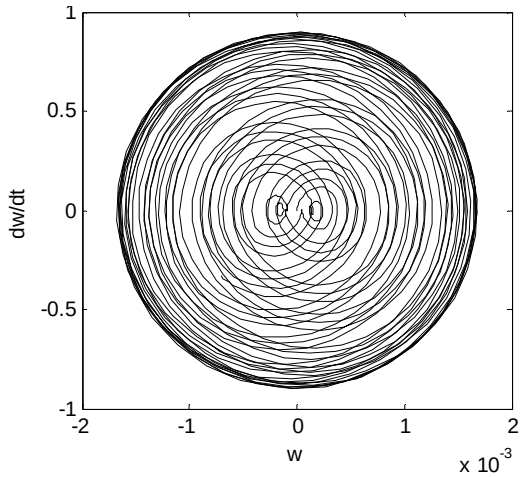

Fig.4. Deflection-velocity relation

Fig. 5 shows the influence of power law indices on nonlinear dynamic responses of the FGM plate ($N=1,2,3;\ q_0(t)=1500\sin(500t)$). Fig.6 shows the effect of the imperfection ($f_0=0.003$) on nonlinear dynamic responses of the FGM plate. Fig.6 is chosen with $q_0(t)=75000\sin(500t)$ and $N=1$.

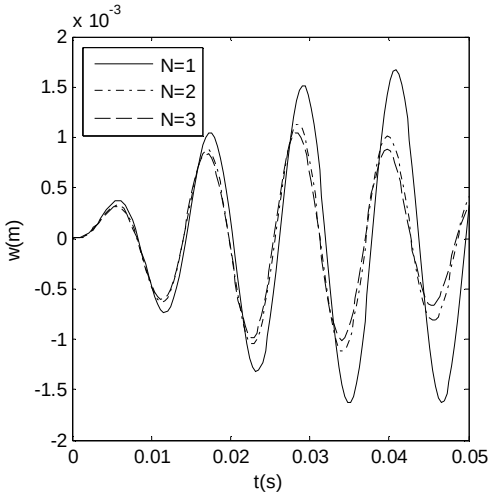

Fig.5. Nonlinear response of FGM plate with various N

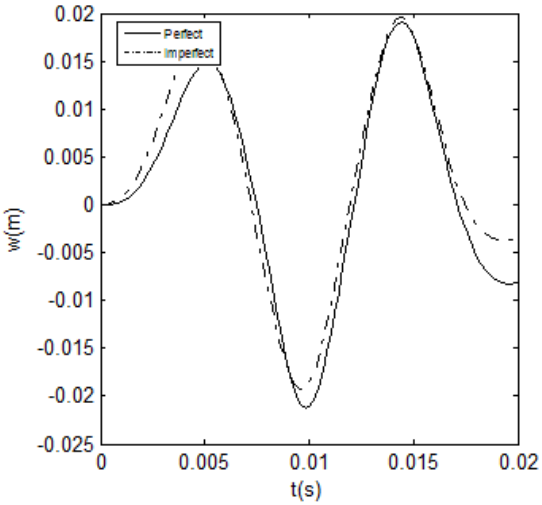

Fig.6. Influence of imperfection on nonlinear dynamic response of FGM plate

Fig.7 shows the influence of elastic foundations on nonlinear dynamic responses of the FGM plate with $q_0(t)=1500\sin(500t)$ and $N=1$

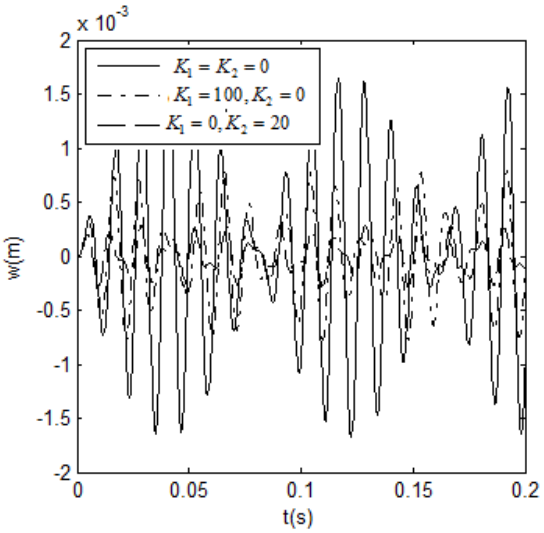

Fig. 7: influence of elastic foundations on nonlinear dynamic responses of the FGM plate

Fig. 7 illustrates the effect of the elastic coefficient k_1, k_2 on the nonlinear dynamic response of the FGM plate. We conclude that these elastic foundations have a strong effect on

the nonlinear dynamic response of the FGM plates. Compared to the case corresponding to the coefficient k_1, the Pasternak type elastic foundation with the coefficient k_2 has a stronger effect.

4. Conclusions

This paper presents an analytical approach to investigate the nonlinear dynamic response of imperfect S-FGM plate resting on elastic foundation. Numerical results for dynamic response of the FGM plate are obtained by Rugge-Kutta method and stress function. The paper shows eeffects of material, imperfection and elastic foundations on the dynamical response of S-FGM plates.

References

[1] D.H.Bich, V.D.Long (2010), Non-linear dynamical analysis of imperfect functionally graded material shallow shells, *Vietnam Journal of Mechanics*, VAST, 32 (1), pp. 1-14.

[2] Hui-Shen Shen, (2009), Functionally Graded materials, Non linear Analysis of plates and shells, *CRC Press, Taylor & Francis Group, London, New York*.

[3] Najafizadeh M.M., Eslami M.R. (2002), Buckling analysis of circular plates of functionally graded materials under uniform radial compression, *Int. J. Mech. Sci;* 44, pp. 2479-2493.

[4] Najafizadeh M.M., Eslami M.R. (2002), First-order theory-based thermoelastic stability of functionally graded material circular plates, *AIAA J;* 40 (7), pp. 1444-1449.

[5] Wu Lanhe (2004), Thermal buckling of a simply supported moderately thick rectangular FGM plate. *Composite structures*; 64, pp. 211-218.

[6] N.D.Duc, H.V. Tung (2010), Mechanical and thermal post-buckling of shear-deformable FGM plates with temperature-dependent properties. *J. Mechanics of Composite Materials*, 46 (5), pp. 461-476.

[7] N.D.Duc, H.V.Tung (2011), Mechanical and thermal postbuckling of higher order shear deformable functionally graded plates on elastic foundations. *J. Composite Structures*, Vol. 93, pp. 2874-2881.

[8] B.A.Samsam Shariat, M.R. Eslami (2007), Buckling of thick functionally graded plates under mechanical and thermal loads. *J. Composite Structures*, 78, pp.433-439.

[9] Mohammad Talha, B.N. Singh (2010), Static response and free vibration analysis of FGM plates using higher order shear deformation theory. *Applied Mathematical Modeling, Elsevier*, pp.3991-4011.

[10] Nayfeh A.H., Pai P.F. (2004), *Linear and nonlinear structural mechanics.* New Jersey: Wiley-Interscience.

[11] A. S. Volmir (1972), *Non-linear dynamics of plates and shells*, Science Edition, M.

The 2nd International Conference on Engineering Mechanics and Automation (ICEMA2)
Hanoi, August 16-17, 2012
ISBN: 978-604-913-097-7

Nonlinear Stability Analysis of Imperfect Three Phase Polymer Composite Plate Resting on Elastic Foundations

Nguyen Dinh Duc, Tran Quoc Quan and Nguyen Xuan Tu

University of Engineering and Technology - Vietnam National University, Hanoi
ducnd@vnu.edu.vn, quantq_530@vnu.edu.vn, nguyenxuantu121984@gmail.com

Abstract

Polymer composites are widely used in Vietnam now. To improve the physical and mechanical characteristics of materials, polymer- matrixes are usually reinforced by fibers and particles. This paper presents an analytical investigation on the nonlinear response of thick imperfect three phase polymer composite plate resting on elastic foundations and subjected to some mechanical loads. The formulations are based on the classical plate theory taking into account geometrical nonlinearity, initial geometrical imperfection and Pasternak type elastic foundation. By applying Galerkin method, explicit relations of load-deflection curves are determined. Effects of fibers and particles, material and geometrical properties, foundation stiffness and imperfection on the buckling and postbuckling loading capacity of the three phase composite plate are analyzed and discussed..

Keywords: Nonlinear stability, three phase composite plate, imperfection, elastic foundation

1. Introduction

Composite material is made from two or more different component materials, to create a new material having better physic-mechanical properties [1]. One of the most distinguished characteristic of composite is anisotropy, with more than 2 elastic moduli. Thus, doing analysis with composite is often more complicated than conventional materials [1,2].

Plate, shell and panel are basic structures used in engineering and industry. These structures play an important role as main supporting component in all kind of structure in machinery, civil engineering, ship building, flight vehicle manufacturing…The stability of composite plate and shell is the first and most important problem in optimal design. Thus, many researchers are interested in this problem. The general view of composite plate and shell can be found in [3, 9, 10] .

One of the most classic references is Brush D.O., Almroth B.O. [5]. This book contains the most basic equations for orthotropic composite plate and shell. Laminated composite with reinforced fibers is orthotropic and can be calculated with these equations. Some research on the stability of laminated composite can be obtained in [5,10].

Functional graded materials (FGMs) is a new generation of composite which was first studied by a group from Sendai, Japan in 1984 [11]. The birth of this new material

came from the need of an advanced material which possesses intelligent properties and high load resistance. The most common FGM is the one that consists of ceramic and metal. Ceramic has large elastic moduli and small thermal expansion coefficient and heat transfer coefficient makes the FGM touch and independent from thermal load. On the other hand, metal makes the FGM ductile and prevents it from crack. The effective properties of FGM are varied (graded) through the material thickness from ceramic-rich surface to metal-rich surface to accommodate with the role (function) of each component. The most important properties of FGM are high stiffness and high temperature resistance. Thus, FGM is the best choice for structures in ultra high temperature environments such as air craft, rocket, petroleum equipment, metallurgy, nuclear pile…In recent years, the stability of FGM has gain more and more attention from domestic and international researchers. Several of the studies concerning the stability of FGM can be found in [12-21].

Another attractive research trend is 3-phase polymer composite, which consist of matrix, reinforced fibers and particles. The main role of reinforced fibers is to improve the strength, while that of the particles is to prevent cracks and plasticity. However, recent publications concerning 3-phase composite are mainly about experimental studies, manufacturing process. The general view of 3-phase composite can be found in [4]. There are indigenous studies dealing with calculating thermal expansion coefficient [22], bending [23], and creep [24] of 3-phase composite. These researches show that optimal 3-phase composite can be obtained by controlling the volume ratios of fiber and particle.

In the present paper, we studied the stability of 3-phase polymer composite with imperfection on elastic foundation. The paper focuses on deriving the algorithm for calculating the stability of 3-phase composite by analyzing the load-deflection relationship base on the basic equations of laminated composite, while also studies the effect of component material properties, geometrical properties, imperfection and elastic foundation on the stability of 3-phase polymer composite plate.

2. Determine the elastic moduli of 3-phase composite

The elastic modules of 3-phase composites are estimated using two theoretical models of the 2-phase composite consecutively: $nD_m = O_m + nD$ [1]. This paper considers 3-phase composite reinforced with particles and unidirectional fibers, so the problem's model will be : $1D_m=O_m +1D$. Firstly, the modules of the effective matrix O_m which called "effective modules" are calculated. In this step, the effective matrix consists of the original matrix and particles, it is considered to be homogeneous, isotropic and have two elastic modules. The next step is estimating the elastic modules for a composite material consists of the effective matrix and unidirectional reinforced fibers.

Assume that all the component phases (matrix, fiber and particle) are homogeneous and isotropic, we will use $E_m, E_{a,} E_c; \nu_m, \nu_a, \nu_c; \psi_m, \psi_a; \psi_c$ to denote Young modulus and Poisson ratio and volume ratio for matrix, fiber and particle, respectively. According to [1, 22-24], we can obtain the modules for the effective composite as below :

$$\bar{G} = G_m \frac{1-\psi_c\left(7-5\nu_m\right)H}{1+\psi_c\left(8-10\nu_m\right)H} \quad (1)$$

$$\bar{K} = K_m \frac{1+4\psi_c G_m L\left(3K_m\right)^{-1}}{1-4\psi_c G_m L\left(3K_m\right)^{-1}} \quad (2)$$

Here: $L = \dfrac{K_c - K_m}{K_c + \dfrac{4G_m}{3}}$;

$$H = \frac{G_m/G_c - 1}{8-10\nu_m + \left(7-5\nu_m\right)\dfrac{G_m}{G_c}} \quad (3)$$

$\bar{E}, \bar{\nu}$ can be calculate from ($\bar{G}, \bar{K}$) as below

$$\overline{E} = \frac{9\overline{K}\overline{G}}{3\overline{K}+\overline{G}};\ \overline{\nu} = \frac{3\overline{K}-2\overline{G}}{6\overline{K}-2\overline{G}} \quad (4)$$

The elastic moduli for 3-phase composite reinforced with unidirectional fiber are chosen to be calculated using Vanin's formulas [25]:

$$E_{11} = \psi_a E_a + (1-\psi_a)\overline{E} + \frac{8\overline{G}\psi_a(1-\psi_a)(\nu_a-\overline{\nu})}{2-\psi_a+\overline{x}\psi_a+(1-\psi_a)(x_a-1)\frac{\overline{G}}{G_a}}$$

$$E_{22} = \left\{\frac{\nu_{21}^2}{E_{11}} + \frac{1}{8\overline{G}}\times \left[\frac{2(1-\xi_a)(\overline{\chi}-1)+(\chi_a-1)(\overline{\chi}-1+2\xi_a)\frac{\overline{G}}{G_a}}{2-\xi_a+\overline{\chi}\xi_a+(1-\xi_a)(\chi_a-1)\frac{\overline{G}}{G_a}}\right]^{-1} + 2\frac{\overline{\chi}(1-\xi_a)+(1+\xi_a\overline{\chi})\frac{\overline{G}}{G_a}}{\overline{\chi}+\xi_a+(1-\xi_a)\frac{\overline{G}}{G_a}}\right\}^{-1}$$

$$G_{12} = \overline{G}\frac{1+\xi_a+(1-\xi_a)\frac{\overline{G}}{G_a}}{1-\xi_a+(1+\xi_a)\frac{\overline{G}}{G_a}}$$

$$G_{23} = \overline{G}\frac{\overline{\chi}+\xi_a+(1-\xi_a)\frac{\overline{G}}{G_a}}{(1-\xi_a)\overline{\chi}+(1+\overline{\chi}\xi_a)\frac{\overline{G}}{G_a}}$$

$$\frac{\nu_{23}}{E_{22}} = -\frac{\nu_{21}^2}{E_{11}} + \frac{1}{8\overline{G}}\left[2\frac{(1-\xi_a)\overline{x}+(1+\xi_a\overline{x})\frac{\overline{G}}{G_a}}{\overline{x}+\xi_a+(1-\xi_a)\frac{\overline{G}}{G_a}} - \frac{2(1-\xi_a)(\overline{x}-1)+(x_a-1)(\overline{x}-1+2\xi_a)\frac{\overline{G}}{G_a}}{2-\xi_a+\overline{x}\xi_a+(1-\xi_a)(x_a-1)\frac{\overline{G}}{G_a}}\right]$$

$$\nu_{21} = \overline{\nu} - \frac{(\overline{\chi}+1)(\overline{\nu}-\nu_a)\xi_a}{2-\xi_a+\overline{\chi}\xi_a+(1-\xi_a)(\chi_a-1)\frac{\overline{G}}{G_a}} \quad (5)$$

In which : $\overline{x} = 3-4\overline{\nu}$

To numerical calculating, we chosen three phase composite polymer made of polyester AKAVINA (made in Vietnam), fibers (made in Korea) and titanium oxide (made in Australia) with the properties as in Table 1.

Table 1. Properties of the component phases for 3-phase composite

Component phase	**Young modulus E**	**Poisson ratio ν**
Matrix polyester AKAVINA (Vietnam)	1,43 GPa	0.345
Glass fiber (Korea)	22 GPa	0.24
Titanium oxide TiO_2 (Australia)	5,58 GPa	0.20

The results of elastic moduli of composite materials for different volume ratios of component materials are given in Table 2.

In which 14 variant cases of different volume ratios of component three phase composite materials are given in Table 3.

3. Theoretical formulation

The three- phase composite plates – foundation interaction is represented by Pasternak model as

$$q_e = k_1 w - k_2 \nabla^2 w \quad (6)$$

where $\nabla^2 = \partial^2/\partial x^2 + \partial^2/\partial y^2$, w is the deflection of the plate, k_1 is Winkler foundation modulus and k_2 is the shear layer foundation stiffness of Pasternak model.

In this study, the classical shell theory is used to establish governing equations and determine the nonlinear response of composite plates.

$$\begin{pmatrix}\varepsilon_x\\ \varepsilon_y\\ \gamma_{xy}\end{pmatrix}=\begin{pmatrix}\varepsilon_x^0\\ \varepsilon_y^0\\ \gamma_{xy}^0\end{pmatrix}+z\begin{pmatrix}k_x\\ k_y\\ 2k_{xy}\end{pmatrix} \quad (7) \qquad \begin{pmatrix}k_x\\ k_y\\ k_{xy}\end{pmatrix}=\begin{pmatrix}-w_{,xx}\\ -w_{,yy}\\ -w_{,xy}\end{pmatrix} \quad (8)$$

where

$$\begin{pmatrix}\varepsilon_x^0\\ \varepsilon_y^0\\ \gamma_{xy}^0\end{pmatrix}=\begin{pmatrix}u_{,x}+w_{,x}^2/2\\ v_{,y}+w_{,y}^2/2\\ u_{,y}+v_{,x}+w_{,x}w_{,y}\end{pmatrix}$$

In which u, v are the displacement components along the x, y directions, respectively.

Table 2. Elastic moduli for three phase composite materials

	$\psi_a = const$, ψ_c - Particle's ratio increase						$\psi_c = const$, ψ_a - Fiber's ratio increase				
	E_1 (GPa)	**E_2 (GPa)**	**ν_{12}**	**G_{12} (GPa)**	**G_{23} (GPa)**		**E_1 (GPa)**	**E_2 (GPa)**	**ν_{12}**	**G_{12} (GPa)**	**G_{23} (GPa)**
Case 1	18.2019	8.0967	0.8043	1.8616	2.7174	Case 8	24.2929	7.9971	1.0513	1.4840	2.6771
Case 2	17.8415	7.4411	0.8722	1.6747	2.4451	Case 9	20.9035	7.3880	1.0116	1.4974	2.4247
Case 3	17.5209	6.8385	0.9457	1.5093	2.2044	Case 10	17.5209	6.8385	0.9457	1.5093	2.2044
Case 4	17.2338	6.2829	1.0256	1.3618	1.9900	Case 11	14.1451	6.3402	0.8496	1.5199	2.0103
Case 5	16.9751	5.7687	1.1132	1.2296	1.7978	Case 12	10.7762	5.8860	0.7190	1.5295	1.8382
Case 6	16.7404	5.2916	1.2097	1.1103	1.6244	Case 13	7.4144	5.4702	0.5486	1.5382	1.6843
Case 7	16.5273	4.8474	1.3167	1.0021	1.4672	Case 14	4.0598	5.0880	0.3327	1.5461	1.5461

Table 3. Variant cases of different volume ratios of fibers and particles

Case	**1**	**2**	**3**	**4**	**5**	**6**	**7**
ψ_m	0.5	0.55	0.6	0.65	0.7	0.75	0.8
ψ_a	0.2	0.2	0.2	0.2	0.2	0.2	0.2
ψ_c	0.3	0.25	0.2	0.15	0.1	0.05	0.0
Case	**8**	**9**	**10**	**11**	**12**	**13**	**14**
ψ_m	0.5	0.55	0.6	0.65	0.7	0.75	0.8
ψ_a	0.3	0.25	0.2	0.15	0.1	0.05	0.0
ψ_c	0.2	0.2	0.2	0.2	0.2	0.2	0.2

Hooke law for a composite plate is defined as

$$\begin{pmatrix}\sigma_x\\ \sigma_y\\ \sigma_{xy}\end{pmatrix}=\begin{pmatrix}Q_{11} & Q_{12} & 0\\ Q_{12} & Q_{22} & 0\\ 0 & 0 & Q_{66}\end{pmatrix}\begin{pmatrix}\varepsilon_x\\ \varepsilon_y\\ \gamma_{xy}\end{pmatrix} \quad (9)$$

in which:

$$Q_{11}=\frac{E_1}{1-\frac{E_2}{E_1}\nu_{12}^2}=\frac{E_1}{1-\nu_{12}\nu_{21}},$$

$$Q_{22}=\frac{E_2}{1-\frac{E_2}{E_1}\nu_{12}^2}=\frac{E_2}{E_1}Q_{11},$$

$$Q_{12}=\frac{E_1}{1-\frac{E_2}{E_1}\nu_{12}^2}=\frac{\nu_{12}}{Q_{22}},\ Q_{66}=G_{12}.$$

The force and moment resultants of the composite plates are determined by

$$(N_i, M_i)=\int_{-h/2}^{h/2}\sigma_i(1,z)dz \qquad i=x,y,xy \quad (10)$$

Substitution of Eqs. (7), (9) into Eq. (10) and the result into Eq. (10) give the constitutive relations as

$$\left(N_x, N_y\right) = h\left[(Q_{11}, Q_{12})\varepsilon_x^0 + (Q_{12}, Q_{22})\varepsilon_y^0\right]$$
$$N_{xy} = hQ_{66}\gamma_{xy}^0$$
$$\left(M_x, M_y\right) = \frac{h^3}{12}\left[(Q_{11}, Q_{12})k_x + (Q_{12}, Q_{22})k_y\right]$$
$$M_{xy} = \frac{h^3}{6}Q_{66}k_{xy} \qquad (11)$$

The nonlinear equilibrium equations of a composite plate based on the classical theory are :

$$N_{x,x} + N_{xy,y} = 0 \qquad (12a)$$

$$N_{xy,x} + N_{y,y} = 0 \qquad (12b)$$

$$M_{x,xx} + 2M_{xy,xy} + M_{y,yy} + \\ + N_x w_{,xx} + 2N_{xy}w_{,xy} + N_y w_{,yy} + \qquad (12c) \\ + q - k_1 w + k_2 \nabla^2 w = 0$$

Calculated from Eq. (11):

$$\varepsilon_{0x} = \frac{1}{h}D_1(Q_{12}N_y - Q_{22}N_x)$$
$$\varepsilon_{0y} = \frac{1}{h}D_1(Q_{12}N_x - Q_{11}N_y) \qquad (13)$$
$$\gamma_{0xy} = \frac{1}{h}D_2 N_{xy}$$

where

$$D_1 = \frac{1}{Q_{12}{}^2 - Q_{11}Q_{22}}, D_2 = \frac{1}{Q_{66}} \quad (14)$$

Substituting once again Eq. (13) into the expression of M_{ij} in (10), then M_{ij} into the Eq. (12c) leads to:

$$N_{x,x} + N_{xy,y} = 0$$
$$N_{xy,x} + N_{y,y} = 0 \qquad (15)$$
$$P_1 w_{,xxxx} + P_2 w_{,xxyy} + P_3 w_{,yyyy} + \\ + N_x w_{,xx} + 2N_{xy}w_{,xy} + N_y w_{,yy} + \\ + q - k_1 w + k_2 \nabla^2 w = 0$$

where

$$P_1 = -\frac{h^3}{12}Q_{11}, \quad P_2 = -\frac{h^3}{6}(Q_{12} + 2Q_{66}) \quad (16)$$
$$P_3 = -\frac{h^3}{12}Q_{22} \qquad (16$$

f(x,y) is stress function defined by

$$N_x = f_{,yy},\ N_y = f_{,xx},\ N_{xy} = -f_{,xy} \quad (17)$$

For an imperfect composite plate, Eq. (15) are modified into form as

$$P_1 w_{,xxxx} + P_2 w_{,xxyy} + P_3 w_{,yyyy} + \\ + f_{,yy}\left(w_{,xx} + w^*_{,xx}\right) - 2f_{,xy}\left(w_{,xy} + w^*_{,xy}\right) + \\ + f_{,xx}\left(w_{,yy} + w^*_{,yy}\right) + q - k_1 w + k_2 \nabla^2 w = 0 \qquad (18)$$

which $w^*(x, y)$ is a known function representing initial small imperfection of the plate. The geometrical compatibility equation for an imperfect composite plate is written as

$$\varepsilon^0_{x,yy} + \varepsilon^0_{y,xx} - \gamma^0_{xy,xy} = w^2_{,xy} - w_{,xx}w_{,yy} + \\ + 2w_{,xy}w^*_{,xy} - w_{,xx}w^*_{,yy} - w_{,yy}w^*_{,xx} \qquad (19)$$

From the constitutive relations (13) in conjunction with Eq. (17) one can write

$$\varepsilon_{0x} = \frac{1}{h}D_1(Q_{12}f_{,xx} - Q_{22}f_{,yy})$$
$$\varepsilon_{0y} = \frac{1}{h}D_1(Q_{12}f_{,yy} - Q_{11}f_{,xx}) \quad (20)$$
$$\gamma_{0xy} = -\frac{1}{h}D_2 f_{,xy}$$

Setting Eq. (20) into Eq. (19) gives the compatibility equation of an imperfect composite plate as

$$\frac{1}{h}\left[-D_1Q_{11}f_{,xxxx} + \left(2D_1Q_{12} + D_2\right)f_{,xxyy} - \right. \\ \left. --D_1Q_{22}f_{,yyyy}\right] - w^2_{,xy} - w_{,xx}w_{,yy} + \\ + 2w_{,xy}w^*_{,xy} - w_{,xx}w^*_{,yy} - w_{,yy}w^*_{,xx} = 0$$

Eqs. (18) and (21) are nonlinear equations in terms of variables w and f and used to

investigate the stability of thin composite plates on elastic foundations subjected to mechanical loads.

In the present study, the edges of composite plates are assumed to be simply supported. Depending on the in-plane restraint at the edges, three cases of boundary conditions, labeled as Cases 1, 2 and 3 will be considered [26-30].

Case 1. Four edges of the plate are simply supported and freely movable (FM). The associated boundary conditions are

$$w = N_{xy} = M_x = 0 \ , \ N_x = N_{x0}$$

at $x = 0, a$

$$w = N_{xy} = M_y = 0 \, , \ N_y = N_{y0}$$

at $y = 0, b$. (22)

Case 2. Four edges of the plate are simply supported and immovable (IM). In this case, boundary conditions are

$$w = u = M_x = 0 \ , \ N_x = N_{x0}$$

at $x = 0, a$

$$w = v = M_y = 0 \ , \ N_y = N_{y0}$$

at $y = 0, b$. (23)

Case 3. All edges are simply supported. Two edges $x = 0, a$ are freely movable, whereas the remaining two edges $y = 0, b$ are immovable. For this case, the boundary conditions are defined as

$$w = N_{xy} = M_x = 0 \ , \ N_x = N_{x0}$$

at $x = 0, a$

$$w = v = M_y = 0 \ , \ N_y = N_{y0}$$

at $y = 0, b$ (24)

where N_{x0}, N_{y0} are in-plane compressive loads at movable edges (i.e. Case 1 and the first of Case 3) or are fictitious compressive edge loads at immovable edges (i.e. Case 2 and the second of Case 3).

The approximate solutions of w and f satisfying boundary conditions (22)-(24) are assumed to be:

$$\left(w, w^*\right) = \left(W, \mu h\right) \sin \lambda_m x \sin \delta_n y \quad (25a)$$

$$f = A_1 \cos 2\lambda_m x + A_2 \cos 2\delta_n y + \\ + A_3 \sin \lambda_m x \sin \delta_n y + \frac{1}{2} N_{x0} y^2 + \frac{1}{2} N_{y0} x^2 \quad (25b)$$

$\lambda_m = m\pi / a \quad , \delta_n = n\pi / b \quad W$ is amplitude of the deflection and μ is imperfection parameter. The coefficients $A_i \ (i = 1 \div 3)$ are determined by substitution of Eqs. (25a, 25b) into Eq. (21) as

$$A_1 = \frac{P_4 \delta_n^2}{\lambda_m^2} W(W + 2\mu h) \quad ,$$

$$A_2 = \frac{P_5 \lambda_m^2}{\delta_n^2} W(W + 2\mu h) \, , \ A_3 = 0 \, . \quad (26)$$

where

$$P_4 = -\frac{h}{32 D_1 Q_{11}} ,$$

$$P_5 = -\frac{h}{32 D_1 Q_{22}}$$

Subsequently, substitution of Eqs. (25a, 25b) into Eq. (18) and applying the Galerkin procedure for the resulting equation yield

$$\frac{ab}{4}[P_1 \lambda_m^4 + P_2 \lambda_m^2 \delta_n^2 + P_3 \delta_n^4 - k_2 \left(\lambda_m^2 + \delta_n^2\right) - k_1]W - \\ - \frac{ab}{2}\left(P_5 \lambda_m^4 + P_4 \delta_n^4\right) W \left(W + \mu h\right)\left(W + 2\mu h\right) - \\ - \frac{ab}{4}\left(N_{x0} \lambda_m^2 + N_{y0} \delta_n^2\right)\left(W + \mu h\right) + \frac{4q}{\lambda_m \delta_n} = 0 \quad (27)$$

where m, n are odd numbers. This is basic equation governing the nonlinear response of

thick three-phase polymer composite plates under mechanical loading conditions.

4. Nonlinear stability analysis

Consider a simply supported polymer composite plates with all movable edges is rested on elastic foundations. Two cases of mechanical loads will be analyzed.

4.1. Polymer composite plates under axial compressive loads

Consider a polymer composite plates supported by elastic foundations and subjected to axial compressive loads F_x uniformly distributed at two curved edges $x = 0,\ a$ in the absence of external pressure loads. In this case, $q = 0,\ N_{y0} = 0,\ N_{x0} = -F_x h$, and Eq. (27) leads to

$$F_x = b_1^2 \frac{\bar{W}}{\bar{W} + \mu} + b_2^2 \bar{W}\left(\bar{W} + 2\mu\right)$$

$$b_1^2 = \frac{\pi^2 m^2 \left(-\bar{P} B_a^2 - \bar{P}_2 \frac{n^2}{m^2} - \frac{\bar{P}_3 n^4}{B_a^2 m^4} \right)}{B_h^2} + \frac{\bar{P}_2 \left(m^2 B_a^2 + n^2 \right) K_2}{m^2 B_h^2} + \frac{B_a^2 \bar{P}_2 K_1}{m^2 \pi^2 B_h^2} \tag{28}$$

$$b_2^2 = \frac{2\pi^2 \left(\bar{P}_5 m^4 B_a^4 + \bar{P}_4 n^4 \right)}{m^2 B_a^2 B_h^2}$$

And

$$\bar{P}_1 = \frac{P_1}{h^3}, \bar{P}_2 = \frac{P_2}{h^3}, \bar{P}_3 = \frac{P_3}{h^3},$$

$$\bar{P}_4 = \frac{P_4}{h}, \bar{P}_5 = \frac{P_5}{h}$$

For a perfect composite plate $(\mu = 0)$ only subjected to axial compressive load F_x, Eq. (32) leads to:

$$F_x = b_1^2 + b_2^2 \bar{W}^2 \tag{29}$$

From which upper buckling compressive load may be obtained with $W \to 0$ as

$$F_x = b_1^2 = \frac{\pi^2 m^2 \left(-\bar{P} B_a^2 - \bar{P}_2 \frac{n^2}{m^2} - \frac{\bar{P}_3 n^4}{B_a^2 m^4} \right)}{B_h^2} + \frac{\bar{P}_2 \left(m^2 B_a^2 + n^2 \right) K_2}{m^2 B_h^2} + \frac{B_a^2 \bar{P}_2 K_1}{m^2 \pi^2 B_h^2} \tag{30}$$

4.2. Numerical results and discussion for an three phase composite plate

In addition, the results presented in this section from Eq. (32) correspond to deformation mode with half-wave numbers $m = n = 1$

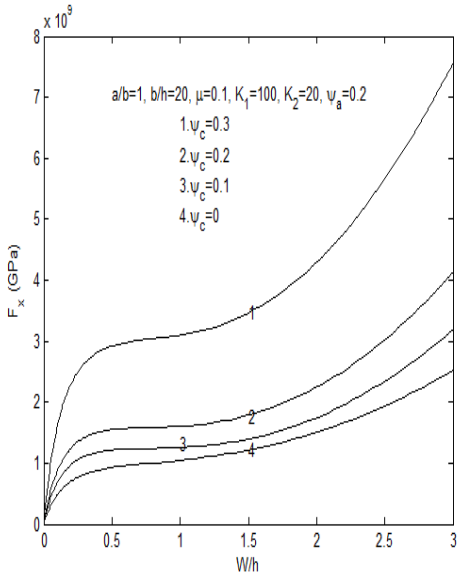

Fig. 1. Effects of ratio ψ_c on the pressure-deflection curves of three-phase polymer composite plate

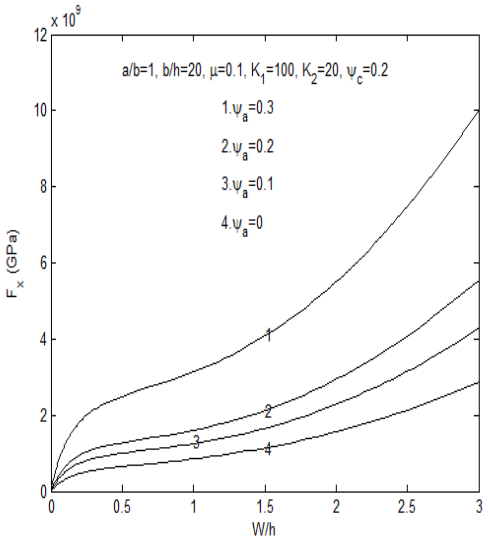

Fig. 2. Effects of ratio ψ_a on the pressure-deflection curves of three-phase polymer composite plates

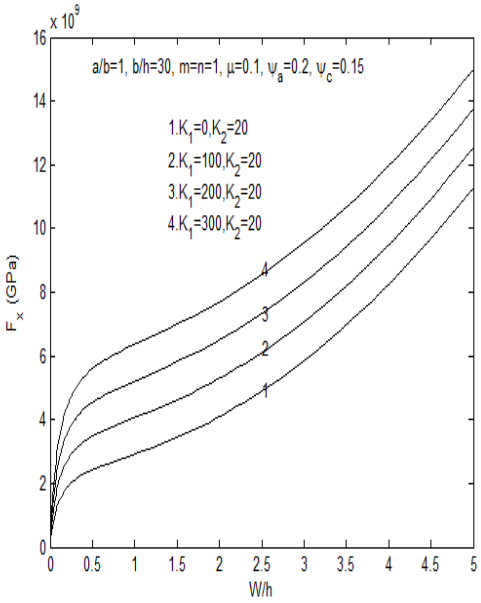

Fig. 3. Effects of elastic foundations on the postbuckling curves of three-phase polymer composite plate under axial compression

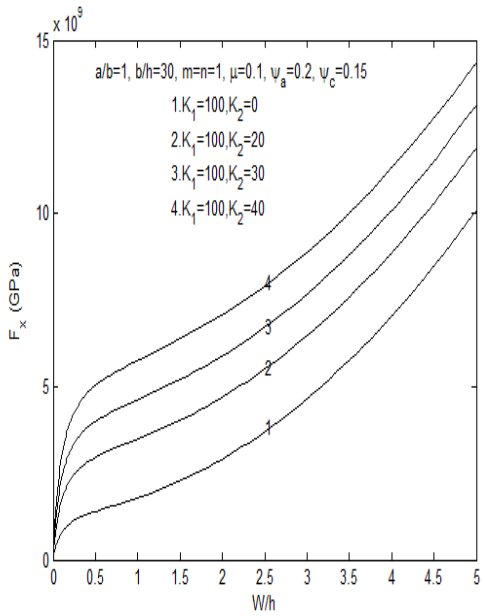

Fig. 4. Effects of elastic foundations on the postbuckling curves of three-phase polymer composite plate under axial compression

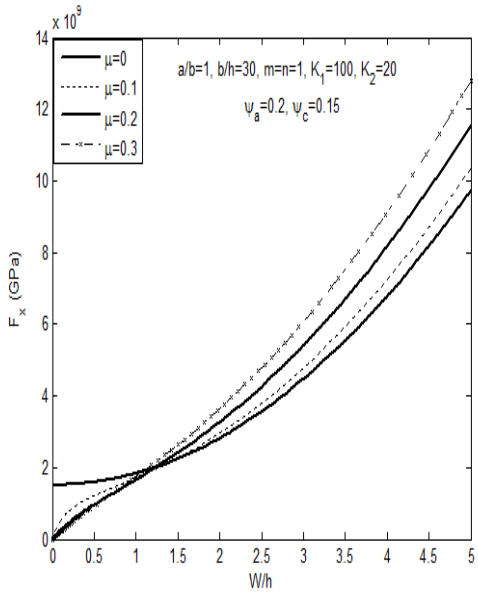

Fig. 5. Effects of imperfection on postbuckling load-deflection curves for simply supported polymer composite plate

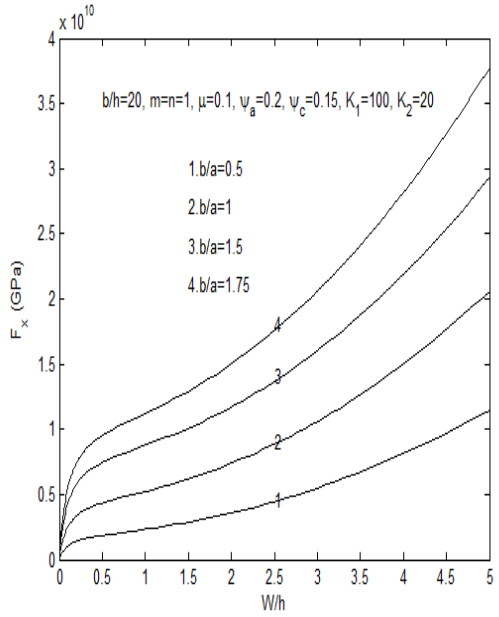

Fig. 6. Effects of ratio b/a on the pressure-deflection curves of three-phase polymer composite plate

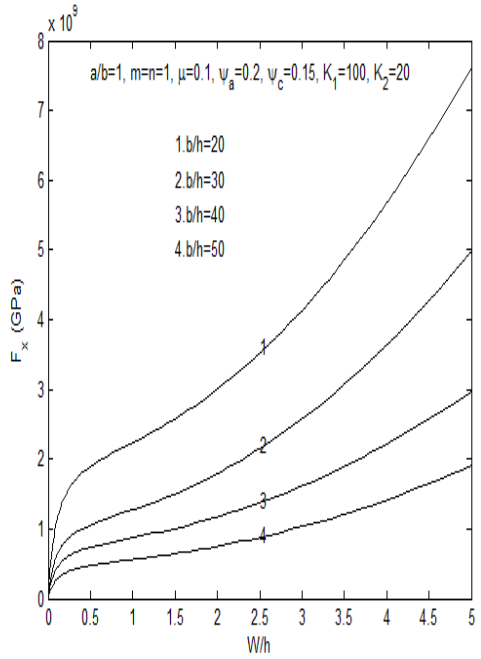

Fig. 7. Effects of ratio b/h on the pressure-deflection curves of three-phase polymer composite plate

5. Concluding remarks

The paper presents an analytical investigation on the nonlinear response of three-phase polymer composite plates resting on elastic foundations and subjected to mechanical conditions. The formulations are based on the classical theory of plates taking into account geometrical nonlinearity, initial imperfection and elastic foundations. Galerkin method is used to obtain explicit expressions of load-deflection curves. The results show that elastic media, especially Pasternak type foundations have a beneficial influence on the buckling loads and postbuckling load carrying capacity of three-phase polymer composite plates. The study also shows the effects of fibers and particles, geometrical parameters, imperfection on the nonlinear response of three-phase polymer composite plates.

Acknowledgment

This work was supported by Project QGDA.12.03 of Found for Science and Technology Development of Vietnam National University, Hanoi. The authors are grateful for this financial support.

References

[1]. Nguyen Hoa Thinh, Nguyen Dinh Duc. Composite materials: Mechanics and Technology of manufacture. Publisher "Science and Technology", Hanoi, 2002.

[2]. Tran Ich Thinh. Composite materials: Mechanics and calculating for structures. Publisher "Education", Hanoi, 1994.

[3]. Hoang Van Tung, Elastic stability for FGM Plates and Shells. PhD thesis in Mechanics. University of Sciences – Vietnam National University, Hanoi, 2011.

[4]. Dinh Khac Minh, Bending of three-phase composite laminated plates in shipbuilding industry. PhD thesis in Engineering. Maritime University, Hai Phong, 2011.

[5]. Brush D.O., Almroth B.O., Buckling of Bars, Plates and Shells, McGraw-Hill, New York, 1975.

[6]. Brunelle EJ Oyibo GA (1983). Generic buckling curves for specially orthotropic

rectangular plates. AIAA Journal 1983;21:1150-6

[7]. Bank LC, Yin J (1996). Buckling of orthotropic plates with free and rotationally restrained edges.Thin-Walled Structures;24: 83-96.

[8]. Christian Mittelstedt (2007). Stability behaviour of arbitrarily laminated compositeplates with free and elastically restrained unloaded edges. Int. Journal of Mech Sciences 49, 819-833.

[9]. Dao Huy Bich (2002), Non-linear analysis of laminated plates, Vietnam Journal of Mech, vol 24 (4), 197-208.

[10]. Dao Huy Bich, Vu Hoai Nam, Nguyen Thi Phuong (2011) Nonlinear postbuckling of eccentrically stiffened functionally graded plates and shallow shells. Vietnam Journal of Mech, vol 33 (3), 131-147.

[11]. Koizumi M. (1997), "FGM activities in Japan", Composites Part B 28, pp. 1-4.

[12]. Praveen G.N., Reddy J.N. (1998), "Nonlinear transient thermoelastic analysis of functionally graded ceramic-metal plates", Int. J. Solids Struct. 35(33), pp. 4457-4476.

[13]. Reddy J.N. (2000), "Analysis of functionally graded plates", Int. J. Numer. Meth. Engrg. 47, pp. 663-684.

[14]. Feldman E., Aboudi J. (1997), "Buckling analysis of functionally graded plates subjected to uniaxial loading", Compos. Struct. 38, pp. 29-36.

[15]. Javaheri R., Eslami M.R. (2002), "Buckling of functionally graded plates under in-plane compressive loading", ZAMM 82(4), pp. 277-283.

[16]. Javaheri R., Eslami M.R. (2002), "Thermal buckling of functionally graded plates based on higher order theory", J. Thermal Stresses 25(1), pp. 603-625.

[17]. Samsam Shariat B.A., Eslami M.R. (2007), " Buckling of thick functionally graded plates under mechanical and thermal loads", Compos. Struct. 78, pp. 433-439.

[18]. Liew K.M., Yang J., Kitipornchai S. (2003), "Postbuckling of piezoelectric FGM plates subjected to thermo-electro-mechanical loading", Int. J. Solids Struct. 40, pp. 3869-3892.

[19]. Hui-Shen Shen, (2009) "Functionally Graded materials, Non linear Analysis of plates and shells", CRC Press, Taylor & Francis Group, London, Newyork.

[20]. Nguyen Dinh Duc, Hoang Van Tung (2010), Mechanical and thermal postbuckling of shear deformable FGM plates with temperature-dependent properties. J. Mechanics of Composite Materials, 2010, Vol.46, Issue 5, Page 461- 476.

[21]. Nguyen Dinh Duc, Hoang Van Tung (2011), Mechanical and thermal postbuckling of higher order shear deformable functionally graded plates on elastic foundations. J. Composite Structures, Vol. 93, 2011, p2874-2881

[22]. Nguyen Dinh Duc, Luu Van Boi, Nguyen Tien Dac (2008). Determining thermal expansion coefficients of three-phase fiber composite material reinforced by spherical particles. Journal of Science, Mathematics- Physics, VNU, Vol. 24, No2, p.57-65.

[23]. Nguyen Dinh Duc, Dinh Khac Minh. Beending analysis of three-phase polymer composite plates reinforced by glass fibers and Titanium oxide particles. J. Computational Materials Sciencs, 2010, vol. 49, N4, p.194-198

[24]. Nguyen Dinh Duc, Dinh Khac Minh, Pham Van Thu. The bending analysis of three phase polyme composite plate reinforced glass fiber and titanium oxide particles including creep effect. International Journal of Aeronautical and Space Sciences , 2010, 11(4), p.361–366.

[25]. G.A. Vanin. Micro-Mechanics of composite materials, "Nauka Dumka", Kiev, 1985.

The 2nd International Conference on Engineering Mechanics and Automation (ICEMA2)
Hanoi, August 16-17, 2012
ISBN: 978-604-913-097-7

A Fibre Beam-Column Element for Cyclic Response Analysis of Reinforced Concrete Structure

Nguyen Xuan Huy[a], and Pham Thi Thanh Thuy[b]

[a] *University of Transport and Communications, nguyenxuanhuy@utc.edu.vn*
[b] *University of Transport and Communications, phamthuykc@gmail.com*

Abstract

This paper presents a fibre beam- column element for the non-linear analysis of reinforced concrete structure. The formulations of this fibre element and its use for modelling the non linear behaviour of reinforced concrete structures are detailed. The non-linear hysteretic behaviour of the element derives from the constitutive relations of concrete and reinforcing steel fibres into which each section is divided. Comparison with experimental results of a reinforced concrete structure submitted to cyclic loading shows the performance of the approach.

Key Words: fibre beam- column element, non-linear, cyclic, reinforced concrete

1. Introduction

Simulating the non-linear behaviour of reinforced concrete structure under cyclic loading is an important problem for the engineering community. Non-linear analysis of complex civil engineering structures based on a detailed finite element model requires large-scale computations and handles delicate solution techniques. The necessity to perform parametric studies simplified numerical modelling that reduces computational cost. This paper presents a fibre beam- column element for the non-linear analysis of reinforced concrete structure. The formulations of this fibre element and its use for modelling the non-linear behaviour of reinforced concrete structures are detailed.

2. Fibre beam- column element

Fibre beam elements have been developed since about twenty years ago. They are based on the cross section discretization of fibers. Working at section level with simple uniaxial constitutive models, the 3D behaviour under axial and bending forces is recovered through integration of fibre stresses over the cross-section. In the following sections, a summary of the formulations for beam-column elements is introduced. These formulations are then further described with reference to their implementation in a fibre section model (Spacone et al., 1996).

2.1. Beam-column element

The beam-column element is shown in Figure 1. The reference frame for element is the local coordinate system x, y, z, while

X, Y, Z denote the global reference system. The longitudinal axis x is the union of geometric of each section.

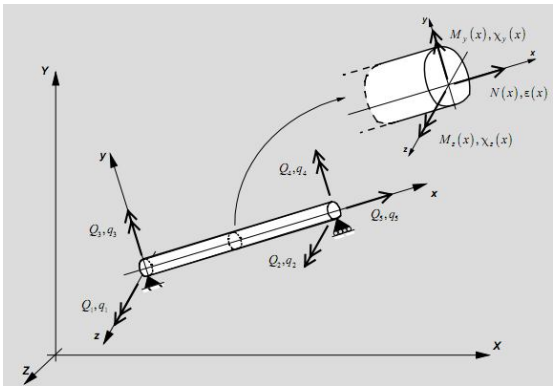

Figure 1. Beam-column element

The element has 5 degrees of freedom: one axial extension q_5 and two rotations relative to the chord at each end node q_1, q_3 and q_2, q_4 respectively. For the sake of clarity these are called element generalized deformation. Q_1, Q_3 and Q_2, Q_4 are the bending moments at each end node respecively. Q_5 is the axial force. The end roration and corresponding moments refer two arbitrary, orthogonal axes x and y. The element generalized forces and deformations are grouped in the following vectors:

$$Q = \begin{Bmatrix} Q_1 \\ Q_2 \\ Q_3 \\ Q_4 \\ Q_5 \end{Bmatrix} \tag{1}$$

$$q = \begin{Bmatrix} q_1 \\ q_2 \\ q_3 \\ q_4 \\ q_5 \end{Bmatrix} \tag{2}$$

Section deformation are represented by three strain resultant: the axial strain $\varepsilon(x)$ along the longitudibal axis and two curvatures $\chi_z(x), \chi_y(x)$ about two arbitrary, orthogonal axes z, y respectively. The corresponding force resultants are the axial force $N(x)$ and two bending moments $M_z(x)$ and $M_y(x)$. The section generalized forces and deformations are grouped in the following vectors:

$$D(x) = \begin{Bmatrix} M_z(x) \\ M_y(x) \\ N(x) \end{Bmatrix} = \begin{Bmatrix} D_1(x) \\ D_2(x) \\ D_3(x) \end{Bmatrix} \tag{3}$$

$$d(x) = \begin{Bmatrix} \chi_z(x) \\ \chi_y(x) \\ \varepsilon(x) \end{Bmatrix} = \begin{Bmatrix} d_1(x) \\ d_2(x) \\ d_3(x) \end{Bmatrix} \tag{4}$$

2.2. Fibre beam-column element

The fibre beam-column element is presented in the local reference system x, y, z (Figure 2).

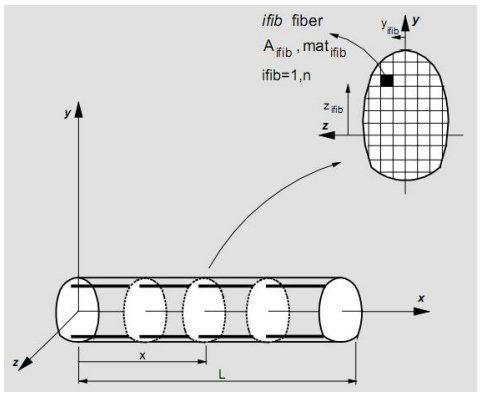

Figure 2. Fibre beam- column element

It is divided into a discrete number of cross section. These are located at the control points of the numerical integration scheme used in element formulation. Each section is subdivided into $n(x)$ fibres where n is a function of x. The generalized element forces and deformations and corresponding section forces and deformations are those defined in section 2.1. Two more vectors are introduced to describe the state of the fibres at each section. These contain the strain and stress of the fibres are written in the following form:

$$e(x)=\begin{Bmatrix}\varepsilon_1(x,y_1,z_1)\\ \dots\\ \varepsilon_{ifib}(x,y_{ifib},z_{ifib})\\ \dots\\ \varepsilon_n(x,y_n,z_n)\end{Bmatrix} \quad (5)$$

$$E(x)=\begin{Bmatrix}\sigma_1(x,y_1,z_1)\\ \dots\\ \sigma_i(x,y_{ifib},z_{ifib})\\ \dots\\ \sigma_n(x,y_n,z_n)\end{Bmatrix} \quad (6)$$

In the fibre state vectors x describes the position of the section along the longitudinal reference axis and y_{ifib}, z_{ifib} refer to the fibre position in the cross section. Following the hypothesis that plane sections remain plane and normal to the longitudinal axis, the fibre strain and the section deformation vector are related by the simple matrix relation:

$$e(x)=l(x).d(x) \quad (7)$$

Where $l(x)$ is a linear geometric matrix as follow:

$$l(x)=\begin{bmatrix}-y_1 & z_1 & 1\\ \dots & \dots & \dots\\ -y_{ifib} & z_{ifib} & 1\\ \dots & \dots & \dots\\ -y_n & z_n & 1\end{bmatrix} \quad (8)$$

3. Constitutive models

In this work, the Kent and Park concrete model is adopted for modelling the material behaviour of concrete under compression. The formulations of the stress-strain relations of confined and unconfined concrete of the model are summarized in (Kent et al., 1971). This model consists of an ascending branch represented by a second-degree parabolic curve and a descending linear part.

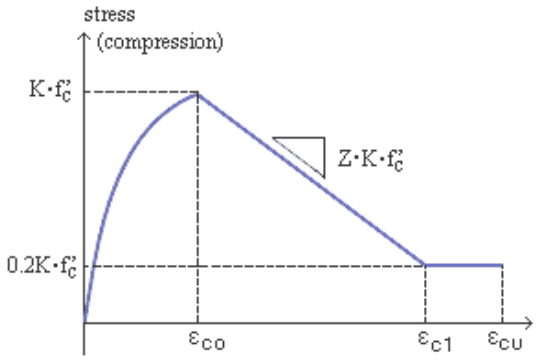

Figure 3. Kent and Park Model

Where,

ε_{co} - Concrete strain at maximum stress

K - Strength increase factor due to confinement

Z - Strain softening slope

f_c' - Concrete compressive cylinder strength [MPa]

ε_{cu} - Ultimate compressive strain of concrete confined by stirrup-ties suggested by Scott et al.

A modified Menegotto and Pinto (Menegotto et al., 1973) hysteretic model with a 3-stage monotonic curve (linear, plateau and hardening) is instead used to describe steel behaviour.

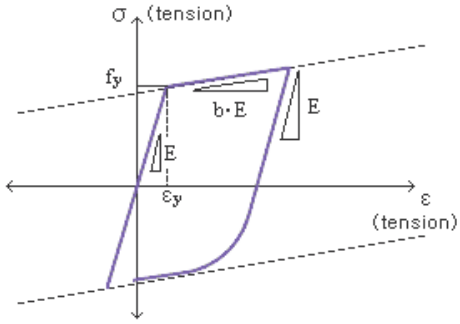

Figure 4. Menegotto and Pinto Model

Where,

f_y - Yield Strength

E - Young's Modulus

b - Stiffness Reduction Ratio

4. Application

In order to validate the performance of the proposed numerical strategy, the beam-

column element is used hereafter to simulate the non-linear behaviour of a reinforced concrete structure submitted cyclic loading, tested in the National Laboratory of Civil Engineering- Portugal (Figure 5).

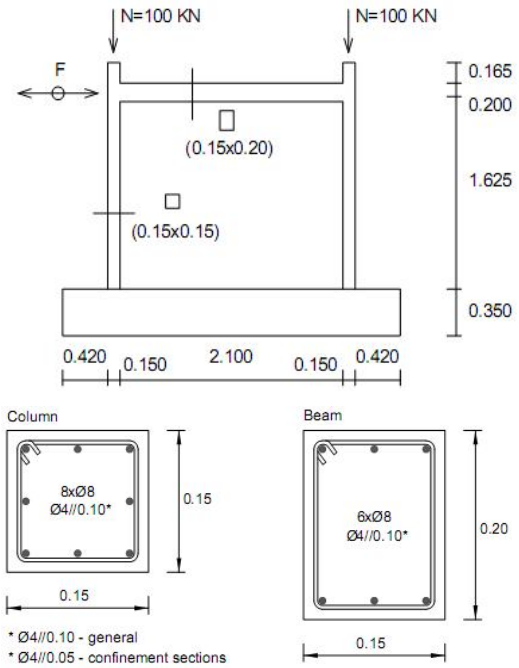

Figure 5. Experimental RC frame

A constant vertical load (P=100 kN) at the top of each column and a lateral increasing cyclical load/displacement pattern at the beam level were applied.

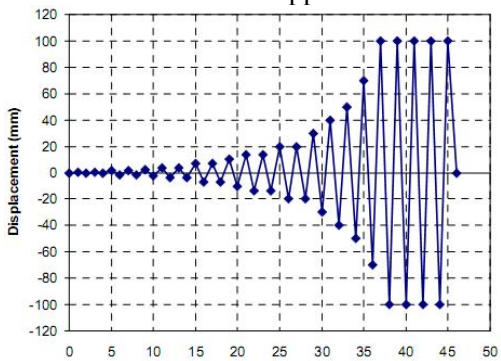

Figure 6. Lateral displacement

The materials used in the reinforced concrete frame structure were: C20/25 concrete; S400 for longitudinal reinforcement and S500 for the stirrups.

The structure shows a smooth evolution with a maximum obtained just before the complete concrete cracking at the top and bottom columns ends (Figure 7). After this point a soft stiffness decrease occurwithout collapse but with significant columns damage and inelastic hinge spread.

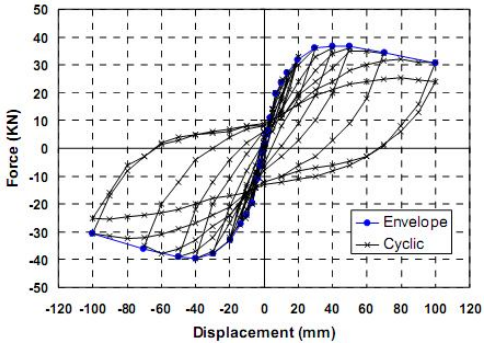

Figure 7. Experimental results

The fibre beam-column element presented in section 2 is used to simulate the behaviour of RC frame structure. This element is implemented in the finite element code Midas Civil (figure 8).

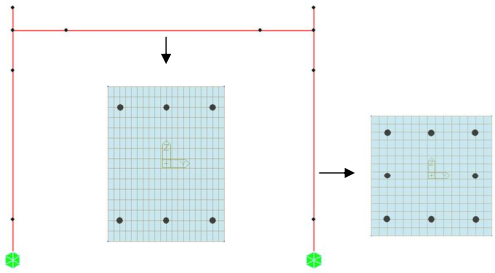

Figure 8. Finite element mesh

The model results is represented in Figure 9. As shown in this figure, the models simulate correctly the global behaviour of the structure in terms of displacement and forces.

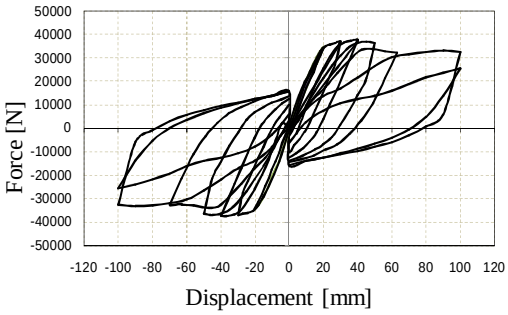

Figure 9. Model results

5. Conclusions

This paper presents the simplified modelling strategy to simulate non linear behaviour of reinforced concrete structures. The simulation is performed using Bernoulli fiber beam-column elements that provide a compromise between numerical cost, quality of results and facility of modelling.

As demonstrated by the results presented, the model was able to reproduce with good approximation the response of the structures. This confirms that the level of the discretization and the type of numerical elements adopted in model are sufficient to describe the non linear behaviour of the reinforced concrete structures.

This research is funded by Vietnam National Foundation for Science and Technology Development (NAFOSTED) under grant number 107.01-2011.11.

6. References

X.H. Nguyen. Vulnérabilité des structures en béton armé à voiles porteurs: expérimentation et modélisation (2006). PhD thesis, Institut National Polytechnique de Grenoble, France.

X.H. Nguyen, J. Mazars, P. Kotronis (2006). Modélisation simplifiée 3D du comportement dynamique de structures en béton armé. *Revue Européenne de Génie Civil* ; 10(3): 361-374.

E. Spacone, F.C. Filippou, F.F Taucer (1996). Fiber Beam-Column Model for Nonlinear Analysis of reinforced concrete Frames. I: Formulation. *Earthquake Engineering and Structural Dynamics*; 25(7): 711-725.

MIDAS finite element code official web site: http://www.midasuser.com/

Fabio Taucer, et al., (1991)“A Fiber Beam-Column Element for Seismic Response Analysis of Reinforced Concrete Structures”, EERC-91/17, College of Engineering, University of California at Berkeley.

Kent, D.C., Park, T. (1975)Flexural Members with Confined Concrete. *ASCE Journal of Structural Division* 97:7, 1969-1190.

Menegotto, M. and Pinto, P.E., (1973) “Method of Analysis for Cyclically Loaded Reinforced Concrete Plane Frames Including Changes in Geometry and Non-Elastic Behavior of Elements under Combined Normal Force and Bending”, Proceedings, IABSE Symposium on Resistance and Ultimate Deformability of Structures Acted on by Well Defined Repeated Loads”, Lisbon, pp.15-22.

The 2nd International Conference on Engineering Mechanics and Automation (ICEMA2)
Hanoi, August 16-17, 2012
ISBN: 978-604-913-097-7

Postbuckling of Stiffened Functionally Graded Cylindrical Shells Subjected to Axial Loading

Nguyen Thi Phuong

University of Transport Technology, Ha Noi, Viet Nam, email: nguyenthiphuong85@gmail.com

Abstract

This paper deals with the nonlinear buckling analysis of stiffened functionally graded cylindrical shells subjected to axial compression loading. The material properties are assumed to be temperature-independent and vary smoothly through the thickness direction according to a simple power law distribution in terms of the volume fraction of constituents. The cylindrical shell is reinforced by internal and external stiffeners made of full metal or full ceramic depending on the material of the surface reinforced. The fundamental equations for cylindrical shells are obtained basing on the classical shell theory with the smeared stiffeners technique taking into account geometrical nonlinearity. By use of the Galerkin's method an approximated analytical solution to the nonlinear stability problem of reinforced FGM cylindrical shells are obtained. The postbuckling load – deflection curves of the shells are investigated and explicit analytical expressions of the upper and lower buckling loads are presented. Comparison of obtained results with those in the literature is produced.

Key Words: Functionally graded material. Buckling. Stiffeners cylindrical shells. Upper and lower buckling loads. Postbuckling.

1. Introduction

Functionally graded materials (FGM) are widely used in many fields such as civil, engineering aviation, aerospace and nuclear reactors based on their remarkable features such as high temperature resistant, lightweight, durable, resistant to chemical corrosion [1].... These advantages occur due to the properties of material varying smoothly through the thickness by changing continuously in the volume fractions of their constituents.

To increase the load – carrying static and dynamic capability for structural FGM structures, which are reinforced by stiffeners. Thus the study of these problems of reinforced FGM cylindrical shells with geometrical nonlinearity are of significant practical interest.

In recent years, many studies concerned with stability and vibration of FGM cylindrical shells without stiffeners are researched. The buckling and postbuckling behavior of perfect and imperfect cylindrical shells subject to combined loading of external pressure and axial compression are considered by Shen and Chen [2], based on the boundary layer theory. While Huang and Han [3] used the nonlinear large deflection theory and the Ritz energy method to study the nonlinear buckling and postbuckling of FGM cylindrical shells. In the works [4] Huang and Han investigated the buckling behavior of axially compressed FGM

cylindrical shells with geometrical imperfections using Donnell shell theory and the nonlinear strain-displacement relations of large deformation. Shen [5, 6] presented the postbuckling of FGM cylindrical shells under complex combinations of mechamic and thermal load. Liew, Zhao and Lee [7] aslo mentioned this problem using the element-free kp-Ritz method. The general elastic buckling of FGM plates and shells is investigated by Tung [8].

In the field of dynamic buckling, Ng et al [9], Sofyev [10, 11], Darabi [12] investigated dynamic buckling analysis of FGM cylindrical shells under various loading. Huang and Han [13] presented nonlinear dynamic buckling problems of FGM cylindrical shells subjected to time-dependent axial load by using Budiansky-Roth criterion. Dynamic thermal buckling of suddenly heated temperature-dependent FGM cylindrical shells under mechanical load also is interested in the works [14] by Shariyat.

On the buckling and postbuckling of stiffened cylindrical shells under mechanical load are studied [15, 16]. However, for the stiffened FGM cylindrical shells, there are very little researches. Recently, Najafizadeh et al. [17] studied statical buckling behaviors of FGM cylindrical shell with the stiffeners made of FGM, but the effect was not really high because ignoring the continuity within shell and stiffeners. Bich et al. [18] have studied the nonlinear statical postbuckling of eccentrically stiffened functionally graded plates and shallow shells.

The fundamental equations for cylindrical shells based on the classical shell theory with the smeared stiffeners technique taking into account geometrical nonlinearity in Donnell's theory are obtained in this paper. Stiffener made of ceramic and metal are reinforced internal and external of cylindrical shell respectively. The resulting equations are solved by Garlekin's method to obtain closed – form expressions of the upper and lower critical loads and nonlinear post-buckling load – deflection curves. Comparing results with those in the literature validates the present analysis.

2. Governing equations

2.1. Functionally graded materials (FGMs)

Suppose that cylindrical shells are made from a mixture of ceramic and metal, and the material composition varies continuously and smoothly along the thickness following a power law [9]:

$$V_m + V_c = 1,$$

$$V_c(z) = \left(\frac{2z+h}{2h}\right)^k$$

where V_m and V_c being volume – fractions of metal and ceramic phases respectively,
h is the thickness of thin-walled structure,
k is the volume – fraction exponent ($k \geq 0$).

According to this distribution, the elasticity modulus of cylindrical shells change in the thickness direction z can be determined by the linear rule of mixture as

$$E(z) = E_m V_m + E_c V_c = E_m + (E_c - E_m)\left(\frac{2z+h}{2h}\right)^k \qquad (1)$$

in which E_c, E_m are modulus of elasticity of ceramic and metal constituents respectively, $E_{cm} = E_c - E_m$, and Poisson ratio is assumed to be constant.

2.2. Fundamental equations

Consider a cylindrical shell of thickness h, length L, radius R and reinforced by internal and external stiffeners. The shell is referred to a coordinate system (x, y, z), in which x and y are in the axial and circumferential directions of the shell and z is in the direction of the inward normal to the middle surface (Type B [6]).

In the present study, the classical shell theory and the Lekhnitsky smeared stiffeners technique are used to obtain the equilibrium and compatibility equations as well as expressions of buckling loads and nonlinear load – deflection curves of eccentrically stiffened FGM cylindrical shells.

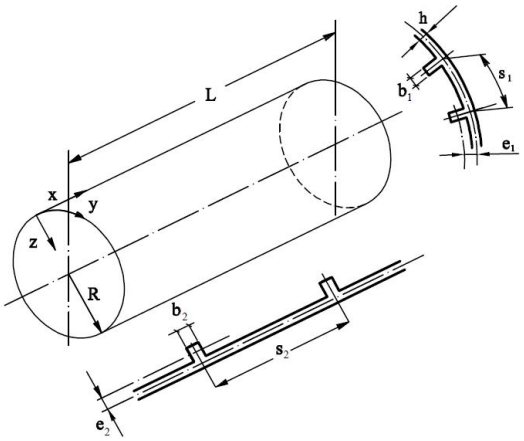

Fig.1. Configuration of an eccentrically stiffened cylindrical shell

The strains across the shell thickness at a distance z from the mid-surface are

$$\varepsilon_x = \varepsilon_x^0 - z\chi_1, \quad \varepsilon_y = \varepsilon_y^0 - z\chi_y, \quad \gamma_{xy} = \gamma_{xy}^0 - 2z\chi_{xy}, \tag{2}$$

where ε_x^0 and ε_y^0 are normal strains, γ_{xy}^0 is the shear strain at the middle surface of the shell and χ_{ij} are the curvatures.

According to the Donnell's shell theory, the strains at the middle surface and curvatures are related to the displacement components u, v, w in the x, y, z coordinate directions as [19]:

$$\varepsilon_x^0 = \frac{\partial u}{\partial x} + \frac{1}{2}\left(\frac{\partial w}{\partial x}\right)^2, \quad \chi_x = \frac{\partial^2 w}{\partial x^2},$$

$$\varepsilon_y^0 = \frac{\partial v}{\partial y} - \frac{w}{R} + \frac{1}{2}\left(\frac{\partial w}{\partial y}\right)^2, \quad \chi_y = \frac{\partial^2 w}{\partial y^2}, \tag{3}$$

$$\gamma_{xy}^0 = \frac{\partial u}{\partial y} + \frac{\partial v}{\partial x} + \frac{\partial w}{\partial x}\frac{\partial w}{\partial y}, \quad \chi_{xy} = \frac{\partial^2 w}{\partial x \partial y},$$

From Eqs. (3) the strains must be relative in the deformation compatibility equation

$$\frac{\partial^2 \varepsilon_x^0}{\partial y^2} + \frac{\partial^2 \varepsilon_y^0}{\partial x^2} - \frac{\partial^2 \gamma_{xy}^0}{\partial x\, \partial y} = \left(\frac{\partial^2 w}{\partial x \partial y}\right)^2 - \frac{\partial^2 w}{\partial x^2}\frac{\partial^2 w}{\partial y^2} - \frac{1}{R}\frac{\partial^2 w}{\partial x^2} \tag{4}$$

The constitutive stress – strain equations by Hooke law for the shell material are omitted here for brevity. The contribution of stiffeners can be accounted for using the Lekhnitsky smeared stiffeners technique. Then integrating the stress – strain equations and their moments through the thickness of the shell, the expressions for force and moment resultants of stiffened FGM cylindrical shell are obtained.

$$N_x = \left(A_{11} + \frac{E_0 A_1}{s_1}\right)\varepsilon_x^0 + A_{12}\varepsilon_y^0 - \left(B_{11} + C_1\right)\chi_x - B_{12}\chi_y,$$

$$N_y = A_{12}\varepsilon_x^0 + \left(A_{22} + \frac{E_0 A_2}{s_2}\right)\varepsilon_y^0 - B_{12}\chi_x - \left(B_{22} + C_2\right)\chi_y, \tag{5}$$

$$N_{xy} = A_{66}\gamma_{xy}^0 - 2B_{66}\chi_{xy},$$

$$M_x = \left(B_{11} + C_1\right)\varepsilon_x^0 + B_{12}\varepsilon_y^0 - \left(D_{11} + \frac{E_0 I_1}{s_1}\right)\chi_x - D_{12}\chi_y,$$

$$M_y = B_{12}\varepsilon_x^0 + \left(B_{22} + C_2\right)\varepsilon_y^0 - D_{12}\chi_x - \left(D_{22} + \frac{E_0 I_2}{s_2}\right)\chi_y, \tag{6}$$

$$M_{xy} = B_{66}\gamma_{xy}^0 - 2D_{66}\chi_{xy},$$

where A_{ij}, B_{ij}, $D_{ij}\,(i,j = 1,2,6)$ are extensional, coupling and bending stiffenesses of the shell without stiffeners.

$$A_{11} = A_{22} = \frac{E_1}{1-\nu^2}, \quad A_{12} = \frac{E_1 \nu}{1-\nu^2},$$

$$A_{66} = \frac{E_1}{2(1+\nu)}, \quad B_{11} = B_{22} = \frac{E_2}{1-\nu^2},$$

$$B_{12} = \frac{E_2 \nu}{1-\nu^2}, \quad B_{66} = \frac{E_2}{2(1+\nu)},$$

$$D_{11} = D_{22} = \frac{E_3}{1-\nu^2}, D_{12} = \frac{E_3 \nu}{1-\nu^2}, D_{66} = \frac{E_3}{2(1+\nu)}, \tag{7}$$

with

$$E_1 = \int_{-h/2}^{h/2} E(z)\,dz = \left(E_m + \frac{E_c - E_m}{k+1}\right)h,$$

$$E_2=\int_{-h/2}^{h/2}E(z)zdz=\frac{(E_c-E_m)kh^2}{2(k+1)(k+2)},$$

$$E_3=\int_{-h/2}^{h/2}E(z)z^2dz=\left[\frac{E_m}{12}+(E_c-E_m)\times\right.$$

$$\left.\times\left(\frac{1}{k+3}-\frac{1}{k+2}+\frac{1}{4k+4}\right)\right]h^3,$$

and

$$C_1=\pm\frac{E_0A_1z_1}{s_1},\quad C_2=\pm\frac{E_0A_2z_2}{s_2}. \tag{8}$$

in which s_1, s_2: Spacing of longitudinal and transversal stiffeners respectively.

A_1, A_2 : Cross section areas of stiffeners.

I_1, I_2: Moment interties of cross section areas.

z_1, z_2: Eccentricities of stiffeners to the middle surface of the shell respectively.

In order to provide continuity between the shell and stiffeners, the stiffeners are made of full metal if putting them at the metal-rich side of the shell and conversely full ceramic stiffeners at the ceramic rich side of the shell, consequently $E_0=E_m$ for full metal stiffeners and $E_0=E_c$ for full ceramic ones.

The sign plus or minus of C_1, C_2 depends on internal or external stiffeners.

The strain-force resultant relations are obtained reversely from Eqs.(5)

$$\begin{aligned}\varepsilon_x^0&=A_{22}^*N_x-A_{12}^*N_y+B_{11}^*\chi_x+B_{12}^*\chi_y,\\ \varepsilon_y^0&=A_{11}^*N_y-A_{12}^*N_x+B_{21}^*\chi_x+B_{22}^*\chi_y,\\ \gamma_{xy}^0&=A_{66}^*N_{xy}+2B_{66}^*\chi_{xy},\end{aligned} \tag{9}$$

Where

$$A_{11}^*=\frac{1}{\Delta}\left(A_{11}+\frac{E_0A_1}{s_1}\right),A_{12}^*=\frac{A_{12}}{\Delta},$$

$$A_{66}^*=\frac{1}{A_{66}},A_{22}^*=\frac{1}{\Delta}\left(A_{22}+\frac{E_0A_2}{s_2}\right)$$

$$\Delta=\left(A_{11}+\frac{E_0A_1}{s_1}\right)\left(A_{22}+\frac{E_0A_2}{s_2}\right)-A_{12}^2;$$

$$\begin{aligned}B_{11}^*&=A_{22}^*(B_{11}+C_1)-A_{12}^*B_{12},\\ B_{22}^*&=A_{11}^*(B_{22}+C_2)-A_{12}^*B_{12},\\ B_{12}^*&=A_{22}^*B_{12}-A_{12}^*(B_{22}+C_2),\\ B_{21}^*&=A_{11}^*B_{12}-A_{12}^*(B_{11}+C_1),B_{66}^*=\frac{B_{66}}{A_{66}}.\end{aligned} \tag{10}$$

Substituting Eqs. (9) into Eqs. (6) yeilds

$$\begin{aligned}M_x&=B_{11}^*N_x+B_{21}^*N_y-D_{11}^*\chi_x-D_{12}^*\chi_y,\\ M_y&=B_{12}^*N_x+B_{22}^*N_y-D_{21}^*\chi_x-D_{22}^*\chi_y,\\ M_{xy}&=B_{66}^*N_{xy}-2D_{66}^*\chi_{xy},\end{aligned} \tag{11}$$

where

$$\begin{aligned}D_{11}^*&=\left(D_{11}+\frac{E_0I_1}{s_1}\right)-(B_{11}+C_1)B_{11}^*-B_{12}B_{21}^*,\\ D_{22}^*&=\left(D_{22}+\frac{E_0I_2}{s_2}\right)-B_{12}B_{12}^*-(B_{22}+C_2)B_{22}^*,\\ D_{12}^*&=D_{12}-(B_{11}+C_1)B_{12}^*-B_{12}B_{22}^*,\\ D_{21}^*&=D_{12}-B_{12}B_{11}^*-(B_{22}+C_2)B_{21}^*,\\ D_{66}^*&=D_{66}-B_{66}B_{66}^*.\end{aligned} \tag{12}$$

The nonlinear equilibrium equations of a cylindrical shell based on the classical shell theory are given by

$$\begin{aligned}&\frac{\partial N_x}{\partial x}+\frac{\partial N_{xy}}{\partial y}=0,\\ &\frac{\partial N_{xy}}{\partial x}+\frac{\partial N_y}{\partial y}=0,\\ &\frac{\partial^2M_x}{\partial x^2}+2\frac{\partial^2M_{xy}}{\partial x\partial y}+\frac{\partial^2M_y}{\partial y^2}+N_x\frac{\partial^2w}{\partial x^2}+\\ &\quad+2N_{xy}\frac{\partial^2w}{\partial x\partial y}+N_y\frac{\partial^2w}{\partial y^2}+\frac{1}{R}N_y=0.\end{aligned} \tag{13}$$

Considering the first two of Eqs.(13), a stress function may be defined as

$$N_x=\frac{\partial^2\varphi}{\partial y^2},\ N_y=\frac{\partial^2\varphi}{\partial x^2},\ N_{xy}=-\frac{\partial^2\varphi}{\partial x\partial y}. \tag{14}$$

Substituting of Eqs.(9) into the compatibility Eqs.(4) and Eqs.(11) into

Eqs.(13), taking into account expressions (3) and (14), yields a system of equations

$$A_{11}^{*}\frac{\partial^4\varphi}{\partial x^4}+\left(A_{66}^{*}-2A_{12}^{*}\right)\frac{\partial^4\varphi}{\partial x^2\partial y^2}+A_{22}^{*}\frac{\partial^4\varphi}{\partial y^4}+$$
$$+B_{21}^{*}\frac{\partial^4 w}{\partial x^4}+\left(B_{11}^{*}+B_{22}^{*}-2B_{66}^{*}\right)\frac{\partial^4 w}{\partial x^2\partial y^2}+$$
$$+B_{12}^{*}\frac{\partial^4 w}{\partial y^4}+\frac{1}{R}\frac{\partial^2 w}{\partial x^2}=\left(\frac{\partial^2 w}{\partial x\partial y}\right)^2-\frac{\partial^2 w}{\partial x^2}\frac{\partial^2 w}{\partial y^2}, \tag{15}$$

$$D_{11}^{*}\frac{\partial^4 w}{\partial x^4}+\left(D_{12}^{*}+D_{21}^{*}+4D_{66}^{*}\right)\frac{\partial^4 w}{\partial x^2\partial y^2}+$$
$$+D_{22}^{*}\frac{\partial^4 w}{\partial y^4}-B_{21}^{*}\frac{\partial^4\varphi}{\partial x^4}-B_{12}^{*}\frac{\partial^4\varphi}{\partial y^4}-$$
$$-\left(B_{11}^{*}+B_{22}^{*}-2B_{66}^{*}\right)\frac{\partial^4\varphi}{\partial x^2\partial y^2}-\frac{1}{R}\frac{\partial^2\varphi}{\partial x^2}-$$
$$-\frac{\partial^2\varphi}{\partial x^2}\frac{\partial^2 w}{\partial y^2}+2\frac{\partial^2\varphi}{\partial x\partial y}\frac{\partial^2 w}{\partial x\partial y}-\frac{\partial^2\varphi}{\partial y^2}\frac{\partial^2 w}{\partial x^2}=0. \tag{16}$$

Eqs.(15) and (16) are the basic equations used to investigate the stability of eccentrically stiffened functionally graded cylindrical shells. They are nonlinear equations in terms of two dependent unknowns w and φ.

3. Buckling analysis of functionally graded reinforced cylindrical shells subjected to axial compressive load.

Consider a functionally graded cylindrical shell subjected to an axial compressive load N_0. The pre-buckling state of the cylindrical shell can be obtained as $N_x^0=-N_0=-r_0h$, $N_y^0=0$, $N_{xy}^0=0$ where N_x^0, N_y^0, N_{xy}^0 are membrane forces for the condition with zero initial moments respectively.

The linear stability equations may be derived by application of the adjacent equilibrium criterion. It is assumed that equilibrium state of the FGM cylindrical shells under applied load is represented by displacement components u_0, v_0 and w_0. The state of adjacent equilibrium differs that of stable equilibrium by δu, δv and δw and the total displacement components of neighboring configuration are

$$u=u_0+\delta u,\quad v=v_0+\delta v,\quad w=w_0+\delta w. \tag{17}$$

Similarly, the force and moment resultants of the neighboring state are represented by

$$N_x=N_x^0+\delta N_x,\quad M_x=M_x^0+\delta M_x,$$
$$N_y=N_y^0+\delta N_y,\quad M_y=M_y^0+\delta M_y,$$
$$N_{xy}=N_{xy}^0+\delta N_{xy},\quad M_{xy}=M_{xy}^0+\delta M_{xy} \tag{18}$$

Substitution of Eqs. (17) and (18) into Eqs. (15) and (16), subtracting from the resulting equations terms relating to stable equilibrium state, neglecting nonlinear terms in governing equations for increments we obtain

$$A_{11}^{*}\frac{\partial^4(\delta\varphi)}{\partial x^4}+\left(A_{66}^{*}-2A_{12}^{*}\right)\frac{\partial^4(\delta\varphi)}{\partial x^2\partial y^2}+$$
$$+A_{22}^{*}\frac{\partial^4(\delta\varphi)}{\partial y^4}+B_{21}^{*}\frac{\partial^4(\delta w)}{\partial x^4}+$$
$$+\left(B_{11}^{*}+B_{22}^{*}-2B_{66}^{*}\right)\frac{\partial^4(\delta w)}{\partial x^2\partial y^2}+$$
$$+B_{12}^{*}\frac{\partial^4(\delta w)}{\partial y^4}+\frac{1}{R}\frac{\partial^2(\delta w)}{\partial x^2}=0 \tag{19}$$

$$D_{11}^{*}\frac{\partial^4(\delta w)}{\partial x^4}+\left(D_{12}^{*}+D_{21}^{*}+4D_{66}^{*}\right)\frac{\partial^4(\delta w)}{\partial x^2\partial y^2}+$$
$$+D_{22}^{*}\frac{\partial^4(\delta w)}{\partial y^4}-B_{21}^{*}\frac{\partial^4(\delta\varphi)}{\partial x^4}-$$
$$-\left(B_{11}^{*}+B_{22}^{*}-2B_{66}^{*}\right)\frac{\partial^4(\delta\varphi)}{\partial x^2\partial y^2}-$$
$$-B_{12}^{*}\frac{\partial^4(\delta\varphi)}{\partial y^4}-\frac{1}{R}\frac{\partial^2(\delta\varphi)}{\partial x^2}+N_0\frac{\partial^2(\delta w)}{\partial x^2}=0, \tag{20}$$

Suppose that the boundary is simple support at the ends: $x=0,\ L$, boundary conditions for increments are

$$\delta w = 0,\ \frac{\partial^2(\delta w)}{\partial x^2} = 0,\ \delta N_x = 0,$$
$$\delta N_{xy} = 0,\ at\ x = 0,\ L \tag{21}$$

The conditions (21) are satisfied when choosing

$$\delta w = \sum_{m,n} f_{mn} \sin\frac{m\pi x}{L}\sin\frac{ny}{R},$$
$$\delta\varphi = \sum_{m,n} \eta_{mn} \sin\frac{m\pi x}{L}\sin\frac{ny}{R} \tag{22}$$

Substituting Eq. (22) into equations (20), (21) yields

$$\eta_{mn} A + f_{mn} B = 0 \tag{23}$$
$$f_{mn} D - \eta_{mn} B - m^2\pi^2 L^2 r_0 h f_{mn} = 0 \tag{24}$$

where

$$A = m^4\pi^4 A_{11}^* + n^4\lambda^4 A_{22}^* + $$
$$+ m^2 n^2\pi^2\lambda^2\left(A_{66}^* - 2A_{12}^*\right),$$
$$B = m^4\pi^4 B_{21}^* + n^4\lambda^4 B_{12}^* - Rm^2\pi^2\lambda^2 + $$
$$+ m^2 n^2\pi^2\lambda^2\left(B_{11}^* + B_{22}^* - 2B_{66}^*\right), \tag{25}$$
$$D = m^4\pi^4 D_{11}^* + n^4\lambda^4 D_{22}^* + $$
$$+ m^2 n^2\pi^2\lambda^2\left(D_{12}^* + D_{21}^* + 4D_{66}^*\right),$$
$$\lambda = \frac{L}{R}.$$

Eliminating η_{mn} from Eqs.(23-24) leads to

$$\left(D + \frac{B^2}{A}\right) f_{mn} - m^2\pi^2 L^2 h r_0 f_{mn} = 0 \tag{26}$$

Because of $f_{mn} \neq 0$

$$r_0 = \frac{1}{m^2\pi^2 L^2 h}\left(D + \frac{B^2}{A}\right) \tag{27}$$

Eq. (27) is used for determining the buckling loads of FGM cylindrical shells under axial compressive load. For given values of the material and geometrical properties of the FGM shell, critical buckling loads are determined by minimizing loads with respect to values of *m, n*.

4. Postbuckling analysis of functionally graded reinforced cylindrical shells subjected to axial compressive load.

Taking into consideration geometrical non-linearity the system of governing equations has of the form (15), (16) with simply supported boundary condition

$$w = 0,\ \frac{\partial^2 w}{\partial x^2} = 0,\ N_x = -N_0 = -r_0 h,$$
$$N_{xy} = 0,\ at\ x = 0,\ L \tag{28}$$

The boundary conditions (28) can be satisfied if the buckling mode shape is represented by

$$w = f \sin\frac{m\pi x}{L}\sin\frac{ny}{R} \tag{29}$$

where f is a maximum deflection. Substituting (29) into Eqs.(15) and solving obtained equation for unknown φ leads to

$$\varphi = \frac{n^2\lambda^2 f^2}{32m^2\pi^2 A_{11}^*}\cos\frac{2m\pi x_1}{a} + $$
$$+ \frac{m^2\pi^2 f^2}{32n^2\lambda^2 A_{22}^*}\cos\frac{2n\pi x_2}{b} - \tag{30}$$
$$- \frac{B}{A} f \sin\frac{m\pi x_1}{a}\sin\frac{n\pi x_2}{b} - N_o\frac{y^2}{2}$$

Introduction of expressions (29) and (30) into Eqs. (15), (16) and application of Galerkin's method for the resulting equation yield

$$\left(D + \frac{B^2}{A}\right) f + Hf^2 + Kf^3 - m^2\pi^2 L^2 r_0 h f = 0 \tag{31}$$

where denote

$$H = \frac{8mn\Delta_1\Delta_2\lambda^2}{3}\frac{B}{A} - \frac{Rn\Delta_1\Delta_2\lambda^4}{6m\pi^2 A_{11}^*} + $$
$$+ \frac{2mn\Delta_1\Delta_2\lambda^2}{3}\left(\frac{B_{21}^*}{A_{11}^*} + \frac{B_{12}^*}{A_{22}^*}\right),$$
$$K = \frac{1}{16}\left(\frac{m^4\pi^4}{A_{22}^*} + \frac{n^4\lambda^4}{A_{11}^*}\right),\ \lambda = \frac{L}{R},$$
$$\Delta_1 = (-1)^m - 1,\ \Delta_2 = (-1)^n - 1.$$

Introducing the parameters

$$\overline{D}=\frac{D}{h^3},\ \overline{B}=\frac{B}{h},\ \overline{A}=Ah,\ \overline{H}=\frac{H}{h^2},$$
$$\overline{K}=\frac{K}{h},\ \overline{f}=\frac{f}{h},\overline{E}_1=\frac{E_1}{h},\ \overline{E}_2=\frac{E_2}{h^2},\quad (32)$$
$$\overline{E}_3=\frac{E_3}{h^3},$$

the Eq.(31) can be rewritten by

$$\left(\overline{D}+\frac{\overline{B}^2}{\overline{A}}\right)\overline{f}+\overline{H}\,\overline{f}^2+\overline{K}\,\overline{f}^3-$$
$$-m^2\pi^2\left(\frac{L}{h}\right)^2 r_0\,\overline{f}=0 \quad (33)$$

Because of $\overline{f}\neq 0$, i.e. considering the shell after the loss of stability we obtain

$$r_0=\frac{h^2}{m^2\pi^2L^2}\left[\left(\overline{D}+\frac{\overline{B}^2}{\overline{A}}\right)+\overline{H}\,\overline{f}+\overline{K}\,\overline{f}^2\right] \quad (34)$$

Substituting $\overline{f}\to 0$ in Eq. (36) yields the value of critical load

$$r_{upper}=\frac{1}{m^2\pi^2L^2h}\left(D+\frac{B^2}{A}\right)$$

The lower buckling load of the eccentrically stiffened FGM cylindrical shell can be obtained from equation (33) using the condition $\frac{dr^*}{df}=\overline{H}+2\overline{K}\,\overline{f}=0$ which yields $\overline{f}=-\frac{\overline{H}}{2\overline{K}}$ and the lower buckling load is found as

$$r_{lower}=\frac{h^2}{m^2\pi^2L^2}\left(\overline{D}+\frac{\overline{B}^2}{\overline{A}}-\frac{\overline{H}^2}{4\overline{K}}\right) \quad (36)$$

As can be seen that Eq.(35) coincides with Eq.(27),i.e. the critical load in linear stability problem is equal to the upper critical load in nonlinear stability problem of FGM stiffened cylindrical shell.

For a cylindrical shell without stiffeners Eq. (35) reduces to

$$r_{upper}=\left[\frac{\overline{E}_1\overline{E}_3-\overline{E}_2^2}{\overline{E}_1\left(1-\upsilon^2\right)}\left(m^2\pi^2+n^2\left(\frac{L}{R}\right)^2\right)^2+\right.$$
$$\left.+\frac{m^4\pi^4\overline{E}_1\left(\frac{L}{R}\right)^2\left(\frac{L}{h}\right)^2}{\left(m^2\pi^2+n^2\left(\frac{L}{R}\right)^2\right)^2}\right]\frac{1}{m^2\pi^2\left(\frac{L}{h}\right)^2} \quad (37)$$

From this equation, minimizing r_{upper} with respect to $\frac{1}{m^2\pi^2}\left(m^2\pi^2+n^2\left(\frac{L}{R}\right)^2\right)^2$, the critical axial compression of FGM cylindrical shells is obtained as

$$r_{upper}=\frac{2h}{R}\sqrt{\frac{\overline{E}_1\overline{E}_3-\overline{E}_2^2}{\left(1-\upsilon^2\right)}} \quad (38)$$

By setting *k=0*, Eq. (37) degenerates into the classic critical load of axially loaded isotropic shells [20]:

(35)

4. Numerical examples

To validate the present formulation in buckling and post-buckling of reinforced FGM cylindrical shells under mechanical loads, the postbuckling of a simply supported FGM cylindrical shells without stiffeners under uniaxial compression is considered,

Numerical results will be given for a cylindrical shells made of Zirconia (ZrO_2) and Titanium (Ti-6Al-4V). The elasticity moduli of Zirconia and Titanium at the initial temperature T_o = 300K may be calculate be 168.08 GPa and 105.69 GPa, the Poisson's ratio is chosen to be 0.3.

Obtained results are compared with those of Huang and Han [13] using the energy method. As shown in Table 1, a good agreement is obtained in this comparison study.

To validate the buckling results of the present, the comparison is made with the results of Tung [8]. The cylindrical shells are

made of FGM that consist of Alumina and aluminum: $E_c = 380\ GPa$ and $E_m = 70\ GPa$, the Poisson's ratio is chosen to be 0.3.

Table 1: Comparison of the present critical load (MPa) with theoretical results reported by Huang and Han (T_o=300K, $L/R = 2$)

	Huang and Han ($\sigma_{scr} = \sigma_{dcr}/\tau_{cr}$)	Present	Difference (%)
Critical load versus k			
$R/h = 500$			
k =0.2	189.262 (2, 11)	189.324 (2, 11)	0.033
k= 1.0	164.352 (2, 11)	164.386 (2, 11)	0.021
k= 5.0	144.471 (2, 11)	144.504 (2, 11)	0.023
Critical load versus R/h			
k=0.2			
$R/h = 400$	236.578 (5, 15)	236.464 (5, 15)	-0.048
$R/h = 600$	157.984 (3, 14)	158.022 (3, 14)	0.024
$R/h = 800$	118.849 (2, 12)	118.898 (2, 12)	0.041

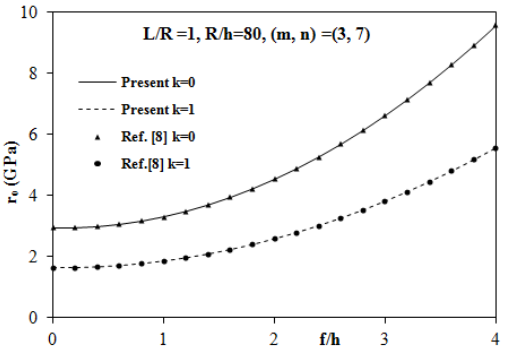

Fig. 2. Comparison of non-linear postbuckling curve

As shown in Fig. 2, the present results have good agreement with the above mentioned results.

The effect of stiffeners, material parameter and geometric ratio on the buckling of Al/ Al_2O_3 cylindrical shells is examined in this section.

Table 2 shows the values of critical buckling loads of unreinforced and reinforced cylindrical shells respectively under uniaxial compressive load with four different values of volume fraction index $k = (0.2,\ 1,\ 5,\ 10)$; geometric parameters of cylindrical shell and stiffeners considered here are: $h = 0.005m$, $R = 0.5m$, $L = 1.0m$, 10 inside stiffeners and 10 outside stiffeners of cylindrical, width and eccentricities of stiffeners $b_1 = b_2 = 0.003$ and $z_1 = z_2 = 0.0125(m)$ respectively.

Table 2: Critical buckling loads (GPa) of FGM cylindrical shells under axial compressive load

k	Un-reinforced	Reinforced					
		Inside stiffeners			Outside stiffeners		
		Stringer stiffeners	Ring stiffeners	Ring and Stringer stiffeners	Stringer stiffeners	Ring stiffeners	Ring and Stringer stiffeners
0.2	1.936 (7, 9)	1.953 (1,5)	1.956 (11,5)	3.453 (6,6)	1.969 (1,5)	1.963 (12,1)	2.488 (9,6)
1	1.250 (8, 9)	1.273 (1,5)	1.271 (11,5)	2.582 (5,6)	1.289 (1,5)	1.274 (12,1)	1.830 (9,5)
5	0.746 (6, 9)	0.755 (1,5)	0.769 (11,5)	1.751 (5,5)	0.771 (1,5)	0.774 (12,1)	1.254 (8,5)
10	0.640 (1, 5)	0.647 (1,5)	0.662 (10,5)	1.525 (4,5)	0.663 (1,5)	0.669 (11,1)	1.110 (8,4)

The critical buckling loads of unreinforced and reinforced FGM cylindrical shells are observed to be dependent on the constituent volume fractions, they decrease when increasing the power index k, furthermore with greater value k the effect of stiffeners is observed to be stronger. This is completely reasonable because the lower value occurs with the elasticity modulus of the metal constituent.

The results in table 2 show that the reinforcement by stiffeners has large effect in the stability of cylindrical shells under axial compression. Clearly, the variances of critical buckling of inside ring or stringer stiffeners and outside ones aren't considerable but the effect of combination of inside ring and stringer stiffeners is much greater than that of outside ones.

Figs. 3-4 represent the postbuckling curves of FGM cylindrical shells reinforced by internal and external stiffeners under axial compressive load.

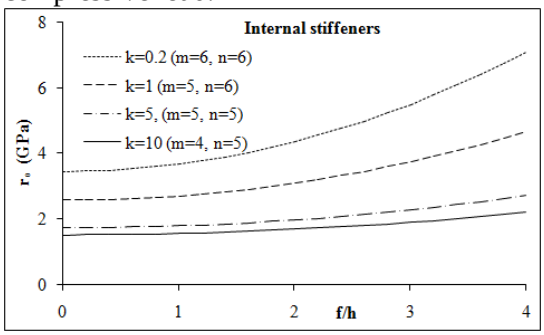

Fig.3: Effect of volume fraction index on the nonlinear of FGM cylindrical shells reinforced by internal stiffeners.

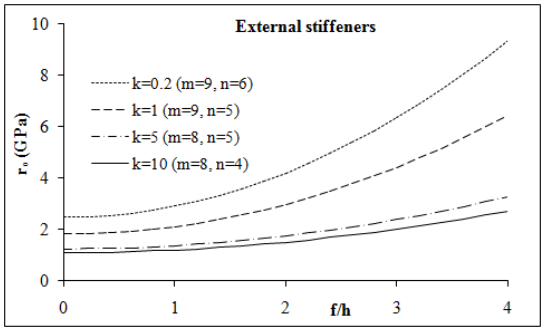

Fig.4. Effect of volume fraction index on the nonlinear of FGM cylindrical shells reinforced by external stiffeners.

Clearly, the postbuckling load-carrying capability of cylindrical shells decreases considerably when value of volume fraction index k increases. The influence of volume fraction index k to the postbuckling load-carying capability of outside stiffeners cylindrical shells is greater than that of inside ones.

Postbuckling curves of reinforced FGM cylindrical shells with various ratio R/h and L/R are shown in Fig.5 and Fig.6.

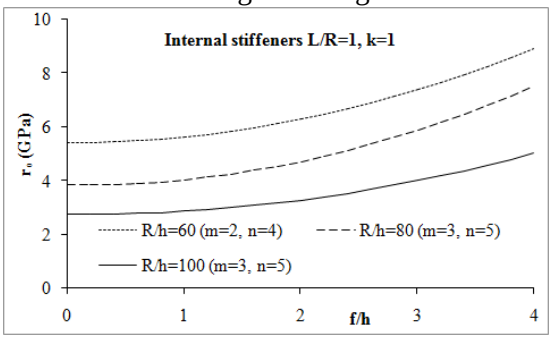

Fig.5. Effect of the ratio R/h on the nonlinear of FGM cylindrical shells reinforced by internal stiffeners under axial compressive load.

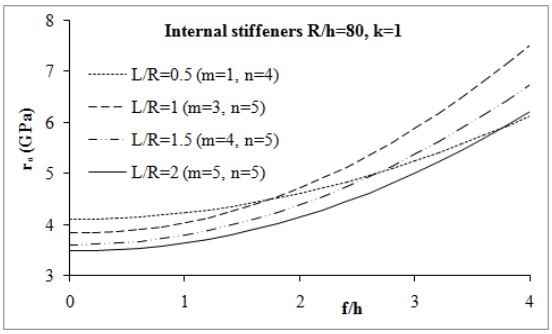

Fig.6. Effect of the ratio L/R on the nonlinear of FGM cylindrical shells reinforced by internal stiffeners under axial compressive load.

Fig.5 and Fig.6 show the postbuckling load-carrying capacity of reinforced FGM cylindrical shell decrease as the ratio R/h and L/R increase.

5. Conclutions

A formulation of the governing equations of eccentrically reinforced functionally graded plates and shallow shells under axial compression based upon the classical shell

theory and the smeared stiffeners technique with von Karman- Donnell nonlinear terms has been presented in this paper.

By using of Galerkin method, the explicit expressions for analysis of buckling loads and postbuckling of eccentrically stiffened FGM cylindrical shells are obtained.

The nonlinear response of cylindrical shells is complex and significantly influenced by material parameters. Stiffeners enhance the stability and load-carrying capacity of cylindrical shells.

Effects of ring or stringer stiffeners seem to be not considerable but those of combination of ring and stringer ones strong enhance the stability and load-carrying capacity of FGM cylindrical shells. Effects of material geometrical parameters are also investigated in this paper.

Acknowledgement

The author would like to thank Professor Dao Huy Bich for helping her to complete this work. This publication was partly supported by National Foundation for Science and Technology Development of Vietnam-NAFOSTED.

Reference

[1] Kozumi M. The concept of FGM. Ceram Trans Funct Grad Master **34**(1993) 3-10.

[2] Hui-shen Shen, Tie-yun Chen, Buckling and postbuckling behavior of cylindrical shells under combined external pressure and axial compression. *Thin-Walled Struct*. **12** (1991) 321 – 334.

[3] Huaiwei Huang, QiangHan. Nonlinear buckling and postbuckling of heated functionally graded cylindrical shells under combined axial compression and radial pressure. *International Journal of Non-Linear Mechanics* **44** (2009) 209–218.

[3] Li S.I., Batra R.C. Buckling of axially compressed thin cylindrical shells with FGM middle layer. *Thin Wall Struct.* **44** (2006) 1039-1047.

[4] Huaiwei Huang, Qiang Han. Buckling of imperfect functionally graded cylindrical shells under axial compression. *European Journal of Mechanics - A/Solids* **27**(2008) 1026–1036.

[5] Shen H.S. Postbuckling analysis of axially-loaded FGM hybrid cylindrical shells in thermal environments. *Composites Science and Technology* **65** (2005) 1675–1690.

[6] Shen H.S. Postbuckling analysis of pressure-loaded FGM cylindrical shells in thermal environments. *Engineering Structures* **25** (2003) 487-497.

[7] Liew K.M., Zhao X., Lee Y.Y. Postbuckling responses of functionally graded cylindrical shells under axial compression and thermal loads. *Composites Part B: Engineering* **43** (2012) 1621–1630.

[8] Tung H. V., Elastic buckling of functionally graded plates and shells. Ph.D. thesis, Vietnam National University, Hanoi.

[9] Ng T.Y., Lam K.Y. et al. Dynamic stability analysis of FGM cylindrical shells under periodic axial loading. *Int. J. Solids Struct.* **38** (2001) 1295-1309.

[10] Sofiyev A.H. The stability of FGM ceramic-metal cylindrical shells under a periodic axial impulse loading. *Composite Structures* **69** (2005) 247-257.

[11] Sofiyev A.H., Schnack E., The stability of functionally graded cylindrical shells under linearly increasing dynamic torsional loading. *Engineering Structures* **26**(2004) 1321–1331

[12] Darabi M., Darvizeh M., Darvizeh A., Non-linear analysis of dynamic stability for functionally graded cylindrical shells under periodic axial loading. *Composite Structures* **83** (2008) 201–211

[13] Huaiwei Huang, Qiang Han, Nonlinear dynamic buckling of functionally graded cylindrical shells subjected to time dependent axial load. *Composite Structures* **92** (2010) 593-598.

[14] Shariyat M. Dynamic thermal buckling of suddenly heated temperature-dependent

FGM cylindrical shells, under combined axial compression and external pressure. *International Journal of Solids and Structures* **45** (2008) 2598–2612.

[15] Chen XingHua, Long LianChun, Buckling Analysis and Optimization of Stiffened Cylindrical Shells under Uniform Axial Compression. *Engineering Materials* **462-463 (**2011) 88-93.

[16] Hui-shen Shen, Pin Zhou, Tie-yun Chen, Postbuckling analysis of stiffened cylindrical shells under combined external pressure and axial compression. *Thin-Walled Struct*. 15 (1993) 43 - 63.

[17] Najafizadeh MM, Hasani A, Khazaeinejad P. Mechanical stability of functionally graded stiffened cylindrical shells. *Appl Math Model* **54** (2009) 179–307.

[18] Dao Huy Bich, Vu Hoai Nam, Nguyen Thi Phuong, Nonlinear postbuckling of eccentrically stiffened functionally graded plates and shallow shells, *Vietnam Journal of Mechanics* **33 (**2011) 132–147.

[19] Brush D. D., Almroth B.O. *Buckling of bars, plates and shells* .Mc. Graw- Hill 1975.

[20] Timoshenko SP, Gere JM. Theory of elastic stability. 2rd Ed. McGraw-Hill 1961.

The 2nd International Conference on Engineering Mechanics and Automation (ICEMA2)
Hanoi, August 16-17, 2012
ISBN: 978-604-913-097-7

Plastic Collapse Limits of Axis-Symmetric Circular Disks under Variable Thermo-Mechanical Loading

Nguyen Minh Tuan [a], Pham Duc Chinh [a] and Sergei Alexandrov [b]

[a] *Institute of Mechanics, 264 Doi Can, Hanoi, Vietnam*
[b] *Institute for Problems in Mechanics, 101-1 Prospect Vernadskogo, 119526, Moscow, Russia*

Abstract

Axis-symmetric problem for elastic- plastic circular hollow disks subjected to variable internal pressure and uniform temperature field is considered. The outer radius of the disk is fixed, and the disk is supposed to satisfy Misses yield condition. Application of Pham's reduced shakedown kinematical theorem reveals two possible collapse modes: incremental and alternating plascity ones. Another plastic limit mode is when the plastic deformation occurs over the whole disk. Numerical illustrations for disks of different sizes are provided.

Key words: elastic- plastic disk, thermo-mechanical loading, shakedown, plastic limit

1. Introduction

Determination of plastic limit states for thin plates and disks subjected to various kinds of loads has been pursued in many works [1-4]. Thermal loading of thin disks under various kinds of constraints was studied in [5-7]. Various rigid and elasto-plastic solutions for thin plates with cylindrical hole have been provided in [8-10]. The closed form solutions are necessary for studying qualitative effects and verifying numerical methods. In plane stress problems one often encounters singular plastic strain rate fields, which are difficult to treat numerically [11].

Under variable loading, additional collapse modes arise such as incremental collapse and alternating plasticity collapse determined by shakedown theory [12,13]. Reduced shakedown kinematical theorem has been constructed in [14-16] to help solving many practical problems, including those under dynamic loading.

In this paper, the plastic limit states of the circular hollow disks subjected to variable internal pressure and homogeneous temperature are investigated. The outer radius of the disk is presumed to be fixed.

2. Shakedown limits for circular disks

Consider an axis-symmetric problem for thin circular hollow disk of internal and external radii r_0 and R_0, subjected to internal pressure P and homogeneous temperature difference over the reference environment temperature field T, that vary over the ranges (see Fig.1).

$$0 \le P \le P^+; \quad 0 \le T \le T^+ \tag{1}$$

The outer radius of the disk is presumed to be fixed, i.e. $u_r(R_0)=0$.

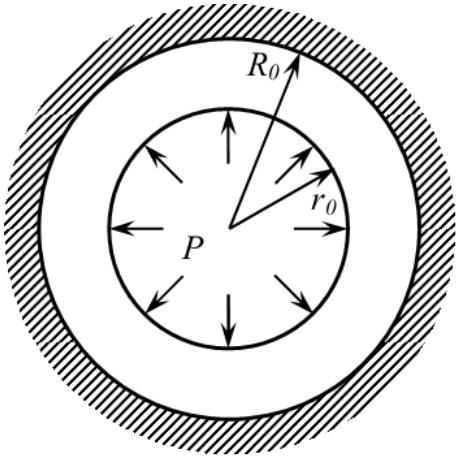

Fig. 1. A circular disk

The fictitious elastic stress field in the disk, under presumption of it's perfectly elastic behavior, has the particular form in cylindrical coordinates:

$$\sigma_r^e=\frac{A_e}{r^2}+B_e;\ \sigma_\theta^e=-\frac{A_e}{r^2}+B_e;\ \sigma_z^e=0 \quad (2)$$

where:

$$A_e=\frac{r_0^2\left[\alpha ET-P(1-\nu)\right]}{r_0^2(1+\nu)+(1-\nu)R_0^2}$$

$$B_e=\frac{-(1+\nu)Pr_0^2+\alpha ETR_0^2}{(1+\nu)r_0^2+(1-\nu)R_0^2} \quad (3)$$

where E,ν are elastic constants, α - thermal expansion coefficient.

Let k_s denote the shakedown safety factor, that is at $k_s>1$ the structure will shakedown, while it will not at $k_s<1$, and $k_s=1$ defines the boundary of the shakedown domain. The reduced shakedown kinematical theorem [14-16] applied to the problem can be given as (Mises yield condition is presumed):

$$k_s^{-1}=max\{I,A\} \quad (4)$$

$$I=\sup_{\varepsilon^p,0\le P\le P^u,0\le T\le T^u}$$

$$\frac{\int_{r_0}^{R_0}\max_{t_r}\left[\sigma_r^e(r,t_r)\varepsilon_r^e(r)+\sigma_\theta^e(r,t_r)\varepsilon_\theta^e(r)\right]r\,dr}{\frac{2}{\sqrt{3}}\sigma_y\int_{r_0}^{R_0}\left\{\left[\varepsilon_\rho^p(r)\right]^2+\left[\varepsilon_\theta^p(r)\right]^2+\varepsilon_r^p(r)\varepsilon_\theta^p(r)\right\}^{1/2}r\,dr} \quad (5)$$

$$A=\max_{r,t,t'}\frac{1}{2\sigma_y}$$

$$\left[\left[\bar\sigma_r^e(r,t)-\bar\sigma_r^e(r,t')\right]^2-\left[\bar\sigma_\theta^e(r,t)-\bar\sigma_\theta^e(r,t')\right]^2\right.$$

$$\left.-\left[\bar\sigma_\theta^e(r,t)-\bar\sigma_\theta^e(r,t')\right]^2.\left[\bar\sigma_\theta^e(r,t)-\bar\sigma_\theta^e(r,t')\right]^2\right]^2 \quad (6)$$

where σ_y - the yield stress; $\left\{\varepsilon_r^p(r),\varepsilon_\theta^p(r),\varepsilon_z^p(r)\right\}$ - the plastic strain increment (over a cycle), which should be compatible (expressible through a displacement field) and incompressible:

$$\varepsilon_r^p(r)+\varepsilon_\theta^p(r)+\varepsilon_z^p(r)=0 \quad (7)$$

Introduce the dimensionless variables:

$$p=P/\sigma_y;\rho=r/R_0$$

$$\rho_0=r_0/R_0;\tau=\alpha ET/\sigma_y$$

$$\bar\sigma_\rho^e=\sigma_r^e/\sigma_Y=a/\rho^2+b$$

$$\bar\sigma_\theta^e=\sigma_\theta^e/\sigma_Y=-a/\rho^2$$

$$a=\frac{\rho_0^2\left[\tau-(1-\nu)p\right]}{\rho_0^2(1+\nu)+1-\nu}$$

$$b=\frac{(1+\nu)\rho_0^2p+\tau}{(1+\nu)\rho_0^2+1-\nu} \quad (8)$$

$$\rho_0\le\rho\le1;\ 0\le p\le p^+;\ 0\le\tau\le\tau^+$$

$$p^+=P^+/\sigma_y;\tau^+=\alpha ET^+/\sigma$$

$$I=\sup_{\varepsilon^p,0\le p\le p^+,0\le\tau\le\tau^+}$$

$$\frac{\int_{\rho_0}^{1} \max_{t_\rho} \left[\bar{\sigma}_\rho^e(\rho,t_\rho)\varepsilon_\rho^e(\rho) + \bar{\sigma}_\theta^e(\rho,t_\rho)\varepsilon_\theta^e(\rho) \right] \rho \, d\rho}{\frac{2}{\sqrt{3}} \int_{\rho_0}^{1} \left\{ \left[\varepsilon_\rho^p(\rho)\right]^2 + \left[\varepsilon_\theta^p(\rho)\right]^2 + \varepsilon_\rho^p(\rho)\varepsilon_\theta^p(\rho) \right\}^{1/2} \rho \, d\rho} \tag{9}$$

$$A = \max_{\rho,t,t'} \frac{1}{2} \left[\left[\bar{\sigma}_\rho^e(\rho,t) - \bar{\sigma}_\rho^e(\rho,t') \right]^2 + \left[\bar{\sigma}_\theta^e(\rho,t) - \bar{\sigma}_\theta^e(\rho,t') \right]^2 - \left[\bar{\sigma}_\rho^e(\rho,t) - \bar{\sigma}_\rho^e(\rho,t') \right] \cdot \left[\bar{\sigma}_\theta^e(\rho,t) - \bar{\sigma}_\theta^e(\rho,t') \right] \right]^{1/2} \tag{10}$$

Equation $I = 1$ defines the incremental collapse mode in the loading space $\{\tau, p\}$ (mode I), while $A = 1$ - the alternating plasticity collapse mode (mode II). The lower envelope of them defines the shakedown boundary $k_s = 1$.

The alternating plasticity collapse curve $A = 1$ from (10) and (8) can be solved directly. To solve (9) and (8), we substitute into (9) the admissible kinematical field:

$$\varepsilon_\theta^p = 0; \varepsilon_r^p = -\varepsilon_z^p = \delta(\rho - \bar{\rho})$$

$$\rho_0 \le \bar{\rho} \le 1 \tag{11}$$

and optimize it over $\rho_0 \le \bar{\rho} \le 1$ (called the collapse mode I).

3. Applications

For numerical illustrations, we take $\nu = 0.3$. The incremental plasticity collapse curve ($I = 1$) and the alternating plasticity collapse curve $A = 1$ (mode II) are projected in Figs 2, 3, and 4 for three cases $r_0 = 0.25R_0$ $(\rho_0 = 0.25)$, $r_0 = 0.5R_0$ $(\rho_0 = 0.5)$ and $r_0 = 0.75R_0$ $(\rho_0 = 0.75)$. The shakedown domain lies under all those collapse curves.

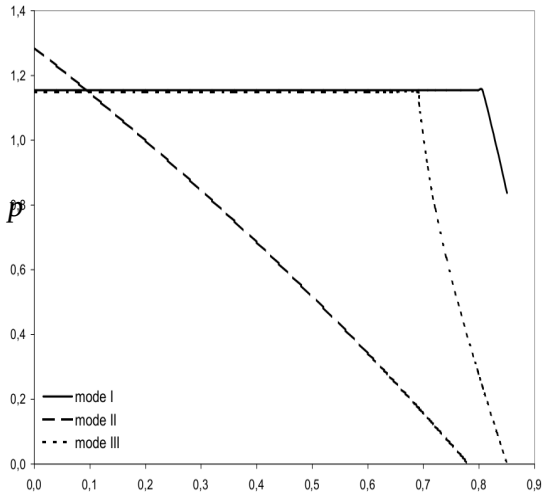

Fig. 2. $r_0 = 0.25R_0$ $(\rho_0 = 0.25)$

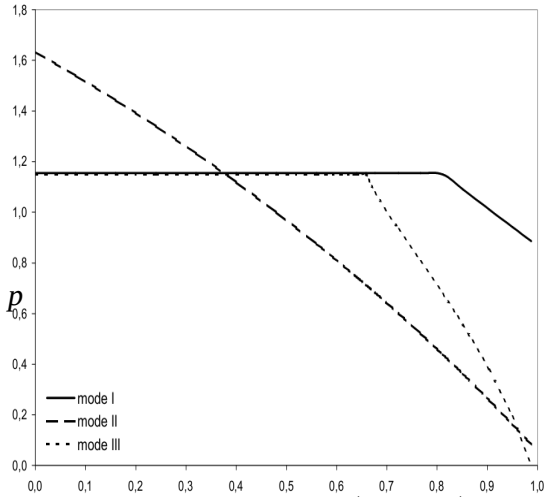

Fig. 3. $r_0 = 0.5R_0$ $(\rho_0 = 0.5)$

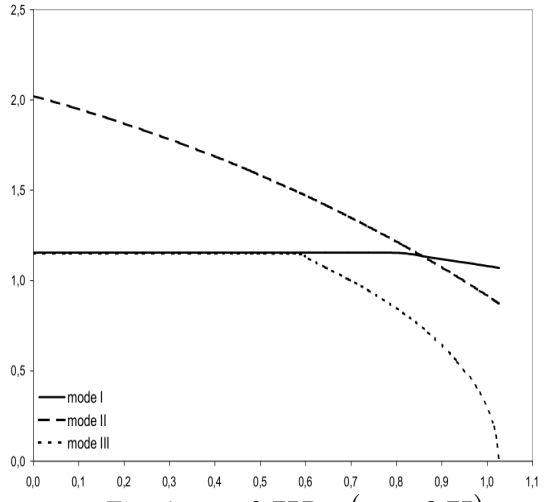

Fig. 4. $r_0 = 0.75R_0$ $(\rho_0 = 0.75)$

In [10], a special plastic limit state for the disk, at which the plastic yielding occurs over the whole disk (but the disk can still sustain higher loads), has been constructed, as the solution of equations:

$$\frac{2\cos\varphi}{\sqrt{3}} = -P; 1 = \rho_0 . exp\left[\int_{\varphi_0}^{\varphi_m} \frac{d\beta}{\sqrt{3}\cos(\beta)}\right]$$

$$(1-\nu)B - (1+\nu)A + \tau = 0$$

$$A + B = \frac{2\cos\varphi_m}{\sqrt{3}}$$

$$B - A = \frac{\cos\varphi_m}{\sqrt{3}} + \sin\varphi_m \qquad (12)$$

Equations (12) should determine the respective plastic limit curves (plastic limit mode III) in Figs. 2, 3 and 4.

4. Conclusion

In summary, applications of a plastic limit analysis and reduced shakedown kinematical theorem for axis-symmetric thermo-mechanical loading of circular hollow disks reveal 3 possible plastic limit (collapse) modes in the loading space. The domains under those curves are the safe domains with respect to the corresponding limit modes.

p

Acknowledgement

This work is supported by VAST (Vietnam) and RFBR (Russia).

References

τ

[1] G. Ma, S. Iwasaki, Y. Myiamoto, H. Deto. Plastic limit analysis of circular plates with respect to the unified yield criterion. *Int. J. Mech. Sci. 40, 963-976 (1998).*

[2] G. Ma, H. Hao, Y. Myiamoto. Llimit angular velocity of rorating disc with unified yield criterion. *Int. J. Mech. Sci. 43, 1137-11536 (2001).*

[3] R. Debski, M. Zyczkowski. On de-cohesive carrying capacity of variable-thickness annular perfectly plastic disks. *Z. Angew. Math. Mech. 82, 655-669 (2002).*

[4] S.E. Alexandrov, E.V. Lomakin, I.R. Dzeng. *Dok. RAS 435, 610-612 (2010).*

[5] H. Lippman. The effect of a temperature cycle on the stress distribution in a shrink fit. *Int. J. Plast. 8, 567-582 (1992).*

[6] W. Mark. Thermal assembly of an elastic plastic hub and a solid shaft. *Arch. Appl. Mech. 63, 42050 (1993).*

[7] S. Alexandrov, N. Alexandrova, Thermal effect on the development of plastic zones in thin axis-symmetric plates. *J. Strain Anal. Eng. Design 36, 169-176 (2001).*

[8] Y.C. Hsu, R.G. Forman. Elastic-plastic analysis of an infinite sheet having a circular hole under pressure. *ASME J. Appl. Mech. 42, 347-352 (1975).*

[9] R. Masri, T. Cohen D. Durban. Enlargement of a circular hole in a thin plastic sheet: Taylor-Bethe controversy in retrospect. *Q. J. Mech. Appl. Math 63, 589-616 (2010).*

[10] S. Alexandrov, E.A. Liamina: Plastic limit state of thin hollow disks under thermo-mechanical loading. *Preprint.*

[11] M. Kleiber and, P. Kowalczyk: Sensitivity analysis in plane stress elasto– plasticity and elasto – viscoplasticity. *Computer Methods in Applied Mechanics and Engineering 137, 395–409 (1996).*

[12] W.T. Koiter: General theorems for elastic-plastic solids. *In Progress in solids mechanics (Ed. I.N. Sneddon & R. Hill), North-Holland, Amsterdam, 165-221 (1963).*

[13] A. König: Shakedown of elastic-plastic structures. *Elsevier (1987.), Amsterdam.*

[14] D.C. Pham , Stumpf, H.: Kinematical approach to shakedown analysis of some structures. *Q. Appl. Math. LII, 707-719 (1994).*

[15] D.C. Pham: Shakedown theory for elastic-perfectly plastic bodies revisited. *Int. J. Mech. Sci. 45, 1011-1027 (2003).*

[16] D.C. Pham: On shakedown theory for elastic-plastic materials and extensions. *J. Mech. Phys. Solids 56, 1905-1915 (2008).*

The 2nd International Conference on Engineering Mechanics and Automation (ICEMA2)
Hanoi, August 16-17, 2012
ISBN: 978-604-913-097-7

Dynamic Stiffness Matrix of Continuous Element for Free Vibration Analysis of Laminated Composite Plates Using FSDT

Ta Thi Hien[a], Tran Ich Thinh[b], Nguyen Manh Cuong[c] and Dinh Gia Ninh[d]

[a]*University of Transport and Communications, Hanoi, Vietnam; hiengt79@yahoo.com*
[b]*Hanoi University of Science & Technology, Hanoi, Vietnam; tranichthinh@yahoo.com*
[c]*Hanoi University of Science & Technology, Hanoi, Vietnam; nguyenmanhcuong@hotmail.fr*
[d]*Hanoi University of Science & Technology, Hanoi, Vietnam; ninhdinhgia@gmail.com*

Abstract

This research presents the vibration analysis of thick laminated composite plates by the Continuous Element Method (CEM). Based on the analytical solutions of the FSDT differential equations of thick composite plate taking into account the shear deformation effects, the dynamic transfer matrix has been built from which natural frequencies and harmonic responses are easily calculated. A computer program is developed for performing the numerical calculations and natural frequencies of plates with various types of boundary conditions are presented. Obtained results are validated to published analytical and Finite Element Method (FEM) results. Through different numerical examples, advantages of CEM are confirmed: reduced size of model, higher precision, reduced time of computation and larger range of studied frequencies.

Key Words: thick laminated plate, vibration of composite plate, continuous element method, dynamic stiffness matrix, vibration analysis.

1. Introduction

Composite materials are increasingly being used in structural design, particularly in the transport, naval, petroleum and aerospace industry. This is mainly due to the benefits derivable from their high specific strength and from their directional properties. For an efficient and optimum design of composite structures an accurate knowledge of their static and dynamic behavior is important. In particular, the free vibration strongly influenced by the number of elements.

In order to reduce discretization errors and to improve computational efficiency compared to the traditional methods, the analysis of composite structures is an important consideration in design.

Many computational methods are used in structural dynamic, in which two most popular methods are: finite element method (FEM) and boundary element methods (BEM). However, limitations appear when the frequency band widens. Indeed, the main disadvantage of these two methods resides in a discretization of the domain or of its boundary. When the excitation frequency increases, the accuracy of the results is continuous element method (CEM)[1,2] based on the dynamic stiffness matrix (DSM) of structural elements is developed. This method is an attractive alternative to the finite element method for the analysis of

harmonic response of complex structures that are made up of simple structural elements.

The continuous element method constitutes a third class of methods, which have been the focus of attention of many researchers in Europe since 1970th, particularly in aeronautical and naval engineering. Continuous element-based computer codes were elaborated by R. Lunden et all [3], C. Duforet [4], the M. S. Andreson and et all [5,6] and P. H. Kulla [7]. For submarine structures, the CEM finds its application in the acoustical frequency range.

Continuous elements are mainly used to describe the dynamic behavior of assemblies composed of straight or curved beams [8,9]. For such structures, the meshing of the domain is given by its topology. Beam elements are not discretized. Continuous plate elements are directly deduced from the theory of vibrations of plates having simple geometries such as triangles or rectangles. This domain in elasto-dynamics has been largely studied during the last 50 years since Mindlin's famous equations. There is an abundant literature on this subject and it exceeds the scope of this paper to cover all the publications in this domain. Leissa [10] gathered all possible approximate solutions for vibrations for various plate geometries and for various boundary conditions. Kulla [7] was the first to present applicable solutions in plate continuous elements.

The development of a dynamic stiffness (DS) matrix for a plate element presents considerable difficulties. Wittrick and Williams [11,12] are probably the earliest investigators who developed DSM for simply supported (SS) plates using classical plate theory (CPT). The inadequacy of CPT when investigating the free vibration characteristics of thick plates is well known and any method based on CPT will no-doubt incur errors in modal analysis, particularly at high frequencies. Anderson and Kennedy [13,14] advanced VICONOPT by including the effect of shear deformation in their DS development. Recently, Nguyen Manh Cuong [17] and Casimir [18] have succeeded in building the DSM for thick isotropic plate and shells of revolution.

This paper presents a continuous element model based on the first-order shear deformation theory which takes into account both the rotator inertia and shear deformations effects for the free vibration analysis of anti-symmetric angle-ply thick laminated composite plates. The method is based on a series expansion of the displacement of the cross-section's middle line and an integration of the dynamic transfer matrix. The accuracy of the present model is numerically evaluated by comparing the frequencies and harmonic responses with those obtained by using the conventional FEM or analytical method.

2. Formulation of laminated anti-symmetrical angle-ply composite plate

2.1. Kinematics of plates.

Consider a thick composite laminated rectangular plate with side lengths a and b as shown in figure 1. The laminate is of uniform thickness h, and in general is made up of a number of laminate, each consisting of unidirectional fiber reinforced composite material. The fiber angle, θ, is measured from the x-axis in the counterclockwise direction. Based on the first-order shear deformation theory [15], the displacement field at the point in the laminated plates is express as

$$\begin{aligned} u &= u_0(x,y) + z\varphi_x(x,y) \\ v &= v_0(x,y) + z\varphi_y(x,y) \\ w &= w_0(x,y) \end{aligned} \tag{1}$$

where: u_0, v_0 are the in-plane displacements and w_0 is the transverse displacement of a point (x,y) on the middle plane. θ_x, θ_y are rotations of the normal to the middle plane about y, x axes respectively. The strains are related to the displacements given in (1) and can be written as

$$\varepsilon_x = \frac{\partial u}{\partial x} = \frac{\partial u_0}{\partial x} + z.\frac{\partial \varphi_x}{\partial x};\ \varepsilon_y = \frac{\partial v}{\partial y} = \frac{\partial v_0}{\partial y} + z.\frac{\partial \varphi_y}{\partial y}$$

$$\gamma_{xy}=\frac{\partial u}{\partial y}+\frac{\partial v}{\partial x}=\frac{\partial u_0}{\partial y}+\frac{\partial v_0}{\partial x}+z.\left(\frac{\partial \varphi_x}{\partial y}+\frac{\partial \varphi_y}{\partial x}\right) \quad (2)$$

$$\gamma_{xz}=\frac{\partial u}{\partial z}+\frac{\partial w}{\partial x}=\frac{\partial w_0}{\partial x}+\varphi_x$$

$$\gamma_{yz}=\frac{\partial v}{\partial z}+\frac{\partial w}{\partial y}=\frac{\partial w_0}{\partial y}+\varphi_y$$

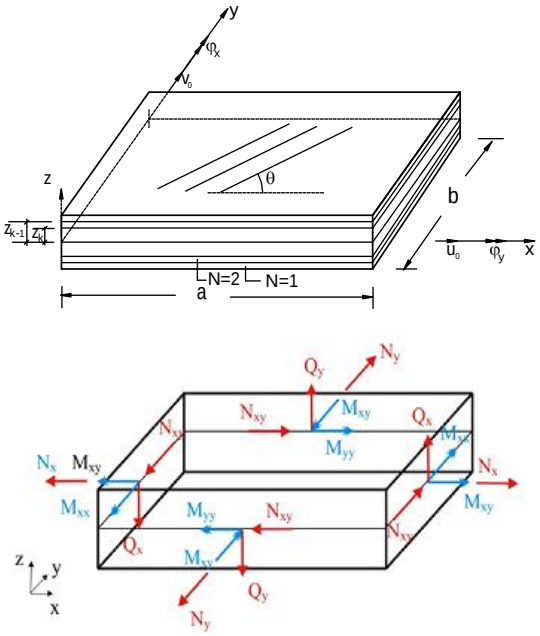

Fig. 1. Laminate geometry with positive set of lamina/laminate reference axes, displacement components, stress resultants, and fiber orientation

2.2. Lamina constitutive relations

The stress-strain relationships, accounting for transverse shear deformation, in the plate coordinate for the k-th layer can be expressed as:

$$\begin{bmatrix}\sigma_{xx}\\ \sigma_{yy}\\ \sigma_{xy}\\ \sigma_{yz}\\ \sigma_{xz}\end{bmatrix}_k=\begin{pmatrix}\bar{Q}_{11} & \bar{Q}_{12} & \bar{Q}_{16} & 0 & 0\\ \bar{Q}_{12} & \bar{Q}_{22} & \bar{Q}_{26} & 0 & 0\\ \bar{Q}_{16} & \bar{Q}_{26} & \bar{Q}_{66} & 0 & 0\\ 0 & 0 & 0 & \bar{Q}_{44} & \bar{Q}_{45}\\ 0 & 0 & 0 & \bar{Q}_{45} & \bar{Q}_{55}\end{pmatrix}_k.\begin{bmatrix}\varepsilon_x\\ \varepsilon_y\\ \gamma_{xy}\\ \gamma_{yz}\\ \gamma_{xz}\end{bmatrix}_k \quad (3)$$

where $\bar{Q}_{ij}$ are transformed elastic coefficient, and related to the coefficients Q_{ij} in the material principal directions [15].

$$\left[Q_{ij}^{'}\right]_k=\left[T_1\right]_k^{-1}\left[Q_{ij}\right]_k\left[T_1\right]_k \quad (i,j=1,2,6)$$

$$\left[Q_{ij}^{'}\right]_k=\left[T_2\right]_k^{-1}\left[Q_{ij}\right]_k\left[T_2\right]_k \quad (i,j=4,5) \quad (4a)$$

with:

$$\left[T_1\right]_k=\begin{bmatrix}\cos^2\theta_k & \sin^2\theta_k & 2\sin\theta_k\cos\theta_k\\ \sin^2\theta_k & \cos^2\theta_k & -2\sin\theta_k\cos\theta_k\\ -\sin\theta_k\cos\theta_k & \sin\theta_k\cos\theta_k & \cos^2\theta_k-\sin^2\theta_k\end{bmatrix}$$

$$\left[T_2\right]_k=\begin{bmatrix}\cos\theta_k & -\sin\theta_k\\ \sin\theta_k & \cos\theta_k\end{bmatrix} \quad (4b)$$

2.3. Stress and moment resultants

The stress and moment resultants of laminated composite plates can be obtained by integrating (3) over the thickness, and are given by:

$$\begin{bmatrix}N_x\\ N_y\\ N_{xy}\\ Q_x\\ Q_y\end{bmatrix}=\int_{-h/2}^{+h/2}\begin{pmatrix}\sigma_{xx}\\ \sigma_{yy}\\ \sigma_{xy}\\ \sigma_{xz}\\ \sigma_{yz}\end{pmatrix}dz\,,\quad\begin{bmatrix}M_x\\ M_y\\ M_{xy}\end{bmatrix}=\int_{-h/2}^{+h/2}\begin{pmatrix}\sigma_x\\ \sigma_y\\ \sigma_{xy}\end{pmatrix}zdz \quad (5)$$

The constitutive equations for the composite laminate plate are given by:

$$\begin{bmatrix}N_x\\ N_y\\ N_{xy}\\ M_x\\ M_y\\ M_{xy}\end{bmatrix}=\begin{bmatrix}A_{11} & A_{12} & A_{16} & B_{11} & B_{12} & B_{16}\\ A_{12} & A_{22} & A_{26} & B_{12} & B_{22} & B_{26}\\ A_{16} & A_{26} & A_{66} & B_{16} & B_{26} & B_{66}\\ B_{11} & B_{12} & B_{16} & D_{11} & D_{12} & D_{16}\\ B_{12} & B_{22} & B_{26} & D_{12} & D_{22} & D_{26}\\ B_{16} & B_{26} & B_{66} & D_{16} & D_{26} & D_{66}\end{bmatrix}.\begin{bmatrix}\varepsilon_x^0\\ \varepsilon_y^0\\ \gamma_{xy}^0\\ k_x\\ k_y\\ k_{xy}\end{bmatrix} \quad (6a)$$

$$\begin{bmatrix}Q_x\\ Q_y\end{bmatrix}=\begin{bmatrix}A_{55} & A_{45}\\ A_{45} & A_{44}\end{bmatrix}\begin{bmatrix}\gamma_{xz}^0\\ \gamma_{yz}^0\end{bmatrix} \quad (6b)$$

The reduce stiffness coefficients in above equations is defined as

$$A_{ij}=\sum_{k=1}^{N}\left(\bar{Q}_{ij}\right)_k\left[z_k-z_{k-1}\right], \quad (i, j = 1, 2, 6)$$

$$B_{ij}=\frac{1}{2}\sum_{k=1}^{N}\left(\bar{Q}_{ij}\right)_k\left[z_k^2-z_{k-1}^2\right], \quad (i, j = 1, 2, 6)$$

$$D_{ij}=\frac{1}{3}\sum_{k=1}^{N}\left(\bar{Q}_{ij}\right)_k\left[z_k^3-z_{k-1}^3\right], \quad (i, j =1, 2, 6)$$

$$A_{ij}=k\sum_{k=1}^{N}\left(\bar{Q}_{ij}\right)_k\left[z_k-z_{k-1}\right], \quad (i, j = 4,5)$$

and the strain resultants are defined as:

$$\varepsilon_x^0 = \frac{\partial u_0}{\partial x};\ \varepsilon_y^0 = \frac{\partial v_0}{\partial y};\ \gamma_{xy}^0 = \frac{\partial u_0}{\partial y} + \frac{\partial v_0}{\partial x};$$

$$k_x = \frac{\partial \varphi_x}{\partial x};\ k_y = \frac{\partial \varphi_y}{\partial y};\ k_{xy} = \frac{\partial \varphi_x}{\partial y} + \frac{\partial \varphi_y}{\partial x}; \quad (7)$$

$$\gamma_{yz}^0 = \varphi_y + \frac{\partial w_0}{\partial y};\ \gamma_{xz}^0 = \varphi_x + \frac{\partial w_0}{\partial x}$$

with k=5/6: the shear correction factor, *N*: number of layers, z_{k-1}, z_k : the position of the top and bottom faces of the k^{th} layer.

For general angle-ply composite laminated plates, forces and moment resultants are determined by [15]:

$$N_{xx} = A_{11}\frac{\partial U_o}{\partial x} + A_{12}\frac{\partial V_o}{\partial y} + B_{16}\left(\frac{\partial \varphi_x}{\partial y} + \frac{\partial \varphi_y}{\partial x}\right)$$

$$N_{yy} = A_{12}\frac{\partial U_o}{\partial x} + A_{22}\frac{\partial V_o}{\partial y} + B_{26}\left(\frac{\partial \varphi_x}{\partial y} + \frac{\partial \varphi_y}{\partial x}\right)$$

$$N_{xy} = A_{66}\left(\frac{\partial U_o}{\partial y} + \frac{\partial V_o}{\partial x}\right) + B_{11}\frac{\partial \varphi_x}{\partial x} + B_{26}\frac{\partial \varphi_y}{\partial y}$$

$$M_{xx} = B_{16}\left(\frac{\partial U_o}{\partial y} + \frac{\partial V_o}{\partial x}\right) + D_{11}\frac{\partial \varphi_x}{\partial x} + D_{12}\frac{\partial \varphi_y}{\partial y}$$

$$M_{yy} = B_{26}\left(\frac{\partial U_o}{\partial y} + \frac{\partial V_o}{\partial x}\right) + D_{12}\frac{\partial \varphi_x}{\partial x} + D_{22}\frac{\partial \varphi_y}{\partial y}$$

$$M_{xy} = B_{16}\frac{\partial U_o}{\partial x} + B_{26}\frac{\partial \varphi_y}{\partial y} + D_{66}\left(\frac{\partial \varphi_x}{\partial y} + \frac{\partial \varphi_x}{\partial x}\right)$$

$$Q_x = kA_{55}\left(\frac{\partial W_o}{\partial x} + \varphi_x\right)$$

$$Q_y = kA_{44}\left(\frac{\partial W_o}{\partial y} + \varphi_y\right) \quad (8)$$

2.4. Equation of motions

The governing equations of equilibrium can be derived using the principle of virtual displacements. The equilibrium equations associated with the present first-order shear deformation theory are:

$$\frac{\partial N_{xx}}{\partial x} + \frac{\partial N_{xy}}{\partial y} = I_0\frac{\partial^2 W_o}{\partial t^2} + I_1\frac{\partial^2 \varphi_x}{\partial t^2}$$

$$\frac{\partial N_{xy}}{\partial x} + \frac{\partial N_{yy}}{\partial y} = I_o\frac{\partial^2 V_o}{\partial t^2} + I_1\frac{\partial^2 \varphi_y}{\partial t^2}$$

$$\frac{\partial Q_x}{\partial x} + \frac{\partial Q_y}{\partial y} = I_o\frac{\partial^2 W_o}{\partial t^2} \quad (9)$$

$$\frac{\partial M_{xx}}{\partial x} + \frac{\partial M_{xy}}{\partial y} - Q_x = I_2\frac{\partial^2 \varphi_x}{\partial t^2} + I_1\frac{\partial^2 U_o}{\partial t^2}$$

$$\frac{\partial M_{xy}}{\partial x} + \frac{\partial M_{yy}}{\partial y} - Q_y = I_2\frac{\partial^2 \varphi_y}{\partial t^2} + I_1\frac{\partial^2 V_o}{\partial t^2}$$

where:

$$I_i = \sum_{k=1}^{N}\int_{z_k}^{z_{k+1}} \rho^{(k)} z^i dz, \quad (\mathrm{i} = 0,1,2) \quad (10)$$

in which $\rho^{(k)}$ is the material mass density of the k^{th} layer.

3. Continuous element method for vibration analysis of thick laminated composite plate

3.1. Strong formulation

For natural vibration of the plate, displacements and forces resultants can be expressed by series of Levy [15].

$$U_0(x,y) = \sum_{m=1}^{\infty} U_m(x)\cos\alpha y$$

$$N_{xx}(x,y) = \sum_{m=1}^{\infty} N_{xxm}(x)\cos\alpha y$$

$$V_0(x,y) = \sum_{m=1}^{\infty} V_m(x)\sin\alpha y$$

$$N_{xy}(x,y) = \sum_{m=1}^{\infty} N_{xym}(x)\sin\alpha y$$

$$W_0(x,y) = \sum_{m=1}^{\infty} W_m(x)\sin\alpha y$$

$$Q_x(x,y) = \sum_{m=1}^{\infty} Q_{xm}(x)\sin\alpha y \quad (11)$$

$$\phi_x(x,y) = \sum_{m=1}^{\infty} \phi_{xm}(x)\sin\alpha y$$

$$M_x(x,y) = \sum_{m=1}^{\infty} M_{xm}(x)\sin\alpha y$$

$$\phi_y(x,y)=\sum_{m=1}^{\infty}\phi_{ym}(x)\cos\alpha y$$

$$M_{xy}(x,y)=\sum_{m=1}^{\infty}N_{xym}(x)\cos\alpha y$$

The vector $\{y\}_m{}^T = \{U_m, V_m, W_m, \varphi_m, \varphi_{ym}, N_{xxm}, N_{xym}, Q_{xm}, M_{xxm}, M_{xym}\}^T$ is called state vector. By replacing expressions (11) into (8) and (9), 13 equations depending only on variable x will be obtained. Next, N_{yym}, M_{yym} and Q_{ym} will be expressed as functions of u_m, v_m, w_m, φ_{xm}, φ_{ym}, N_{xxm}, N_{xym}, Q_{xm}, M_{xxm}, M_{xym} by using relation (8). Then, the derivations of state vector with respect to variable x are calculated from equations (8) and (9), after some manipulations:

$$\frac{dU_m}{dx}=\alpha c_2 V_m+\frac{D_{66}}{C_1}N_{xxm}-\frac{B_{16}}{C_1}M_{xym}$$

$$\frac{dV_m}{dx}=\alpha U_m+\alpha c_5\varphi_y-\frac{D_{11}}{C_4}N_{xym}-\frac{B_{16}}{C_4}M_{xxm}$$

$$\frac{dW_m}{dx}=\frac{1}{kA_{55}}Q_{xm}-\varphi_{xm}$$

$$\frac{d\varphi_{xm}}{dx}=-\alpha c_6\varphi_{ym}-\frac{B_{16}}{c_4}N_{xym}+\frac{A_{66}}{c_4}M_{xxm}$$

$$\frac{d\varphi_{ym}}{dx}=\alpha c_3 V_m-\alpha\varphi_{xm}-\frac{B_{16}}{c_1}N_{xx\theta}+\frac{A_{11}}{c_1}M_{xym}$$

$$\frac{dN_{xxm}}{dx}=-I_o\omega^2U_m-\alpha N_{xym} \qquad (12)$$

$$\frac{dN_{xym}}{dx}=\left(-I_0\omega^2+\alpha^2c_7\right)V_m-\alpha c_2N_{xxm}-\alpha c_3M_{xym}$$

$$\frac{dM_{xm}}{dx}=-I_2\omega^2\varphi_{xm}+\alpha M_{xym}+Q_{xm}$$

$$\frac{dM_{xym}}{dx}=kA_{44}\alpha W_m+(-I_2\omega^2+\alpha^2c_8+kA_{44})\varphi_{ym}+\alpha c_5N_{xym}+\alpha c_6M_{xxm}$$

$$\frac{dQ_{xm}}{dx}=\left(-I_o\omega^2+kA_{44}\alpha^2\right)W_m+\alpha kA_{44}\varphi_{ym}$$

With:

$$c_1=A_{11}D_{66}-B_{16}B_{16},\quad c_2=\frac{B_{16}B_{26}-A_{12}D_{66}}{c_1}$$

$$c_3=\frac{B_{16}A_{12}-A_{11}B_{26}}{c_1},\quad c_4=A_{66}D_{11}-B_{16}B_{16}$$

$$c_5=\frac{B_{16}D_{12}-D_{11}B_{26}}{c_4},\quad c_6=\frac{B_{16}B_{26}-D_{12}A_{66}}{c_4}$$

$$c_7=A_{12}c_2+A_{22}+B_{26}c_3$$

$$c_8=B_{26}c_5+D_{22}+D_{12}c_6$$

Equations (12) are written in the matrix form for each mode m:

$$\frac{d\{y\}_m^T}{dx}=[A]_m\{y\}_m^T \qquad (13)$$

where $[A]_m$ is a 10x10 matrix.

3.2. Dynamic transfer matrix, dynamic stiffness matrix [K(ω)]

The dynamic transfer matrix $[T]_m$ is given by :

$$[T]_m=e^{[A]_m L} \qquad (14)$$

Then $[T]_m$ is separated into four blocks:

$$[T]_m=\begin{bmatrix}T_{11} & T_{12}\\ T_{21} & T_{22}\end{bmatrix} \qquad (15)$$

Finally, the dynamic stiffness matrix $[K(\omega)]_m$ is determined by [32]:

$$[K(\omega)]_m=\begin{bmatrix}T_{12}^{-1}T_{11} & -T_{12}^{-1}\\ T_{21}-T_{22}T_{12}^{-1}T_{11} & T_{22}T_{12}^{-1}\end{bmatrix}_m \qquad (16)$$

The natural frequencies is calculated from the determinant of the dynamic stiffness matrix $[K(\omega)]_m$. For example:

Free-free boundary condition:

$\det(K)=0$

Clamped-clamped boundary condition:

$\det(T_{12})=0$

3.3. Assembly of dynamic stiffness matrices

The dynamic stiffness matrix can be easily assembled with other element matrices in order to model a long plate structure, plate with portions of different properties or to overcome the problem of numerical

instability relating to the too long length of the element.

The assembly procedure of the finite element method is used here. Fig 2 illustrates an example of assembly for two dynamic stiffness matrices. The global dynamic stiffness matrix $[K(\omega)]_m$ of a composite plate structure is constructed from two elements $[K_1(\omega)]_m$ and $[K_2(\omega)]_m$ assembled along a common edge.

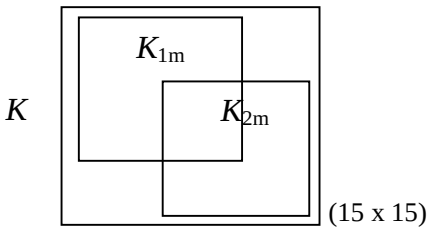

Fig. 2. Assembly of two plate continuous elements.

4. Numerical results and discussion

A Matlab's code has been developed based on the foregoing theoretical formulation for calculating free vibrations of composite laminated plates with different boundary conditions.

Material properties (typical of graphite/ epoxy) using for all examples.
$E_1=40E_2$; $E_2=6.96$ GPa; $G_{12} = G_{13} = 0.6E_2$; $G_{23} = 0.5E_2$; $\upsilon_{12} = 0.25$; $\rho=1600$ kg/m^3.

4.1. Validation of present study

Consider a square laminated angle-ply plate made by above material subjected to simply supported boundary condition on all edges. The non-dimensionalized natural frequencies are defined as: $\varpi = (\omega \times a^2/h)\sqrt{\rho / E_2}$

The comparison of dimensionless fundamental natural frequencies for different number of layers, different thickness ratios (a/h) calculating by CEM (present) and by FEM (Ansys) and by higher-order theory [Kant-16] are shown in the Table 1. Results of first five vibration modes for angle-ply [45^0, -45^0, 45^0, -45^0] laminated composite square plate comparing with analytical Reddy's results can be seen from Table 2.

Table 1: Non-dimensionalized fundamental natural frequencies of simply supported angle – ply laminated composite square plate.

	[45°/ - 45°]					[45° / - 45°]$_4$				
a/h	Kant [16]	Ansys (30x30)		CEM		Kant [16]	Ansys (30x30)		CEM	
5	10.692	10.491	(1.916)*	10.475	(2.072)	12.967	12.922	(0.348)	12.894	(0.566)
10	13.207	13.306	(0.744)	13.367	(1.197)	19.274	19.346	(0.372)	19.292	(0.093)
20	14.228	14.480	(1.740)	14.611	(2.621)	23.236	23.302	(0.283)	23.267	(0.133)
50	14.568	14.881	(2.103)	14.964	(2.646)	24.901	24.909	(0.032)	24.940	(0.156)
100	14.619	14.941	(2.155)	14.636	(0.116)	25.173	25.190	(0.067)	25.324	(0.596)

*: Number in parentheses are error percentage with respect to the results of [16]

Table 2. Non-dimensionalized natural frequency for angle-ply [45^0, -45^0, 45^0, -45^0] simply supported laminated composite square plate

m	Reddy [15]	Ansys (30x30)		CEM	
1	18.46	18.53	(0.38)*	18.48	(0.11)
2	34.87	34.41	(1.34)	33.43	(4.31)
3	54.27	54.48	(0.39)	54.23	(0.07)
4	75.58	75.97	(0.51)	77.10	(1.97)
5	97.56	95.80	(1.84)	97.49	(0.07)

*: Number in parentheses are error percentage with respect to the results of [15]

It can be shown from Tables 1-2 that the frequencies obtained by CEM of composite laminated plates with simply supported boundary conditions are in a good agreement with those of Kant and ANSYS, and with analytical Reddy results. The errors of comparison do not exceed 4.31%.

4.2. Effect of boundary conditions, thickness ratio, aspect ratio, fiber orientation

In Table 3, the fundamental natural frequencies calculated by CEM are compared with results by Kant [16] with different boundary conditions (S- simply supported, C- clamped, F – free) and different angle of fiber orientation. It is easily to note that the agreement among the two approaches is very satisfied. The fundamental frequencies increase with the increased number of layers; the fundamental frequencies with angle of fiber orientation $\theta = 30^0$ are higher than with $\theta = 45^0$. Natural frequencies of square plates with the boundary condition SSSS are highest.

Table 3. Dimensionless fundamental natural frequencies with the different boundary conditions and the different angles of fiber orientation of square laminated composite plate (a/h =10)

θ	Ref	FSFS	FSCS	SSSS
[30/-30]	Kant [16]	6.950	8.650	12.680
	CEM	6.950	8.479	12.002
	Error (%)	0.000	2.017	5.649
$[30/-30]_2$	Kant [16]	9.610	11.880	17.630
	CEM	9.590	11.894	17.611
	Error (%)	0.209	0.118	0.108
[45/-45]	Kant [16]	4.760	7.520	13.040
	CEM	4.757	7.612	13.360
	Error (%)	0.063	1.209	2.395
$[45/-45]_2$	Kant [16]	6.260	10.360	18.460
	CEM	6.261	10.360	18.486
	Error (%)	0.016	0.000	0.141

Table 4 displays the fundamental natural frequencies obtained by CEM and by higher order theory ([16]-Kant) including the percentage errors for different plate thickness ratios, aspect ratios with different angles of fiber orientation. The table shows very good agreement between results.

Dimensionless fundamental frequencies of rectangular composite plates with different thickness ratios for angle of fiber orientation $\theta = 45^0$ and different number of layer are plotted in Fig.3. It can be observed from Figure 3 that a/h ratio increases, the fundamental frequency increases.

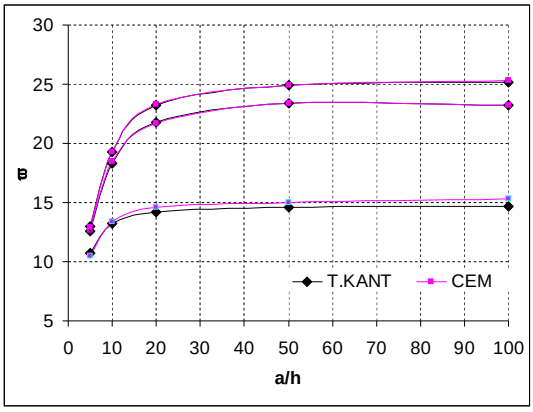

Fig. 3. Effect of thickness ratio on dimensionless natural frequencies of simply supported anti- symmetric angle- ply square plate; stacking sequence [θ/-θ]

Fig. 4 shows the effect of the aspect ratio a/b on dimensionless natural frequencies with different number of layers. It can be seen that the fundamental frequencies increase with the increased aspect ratio and number of layers.

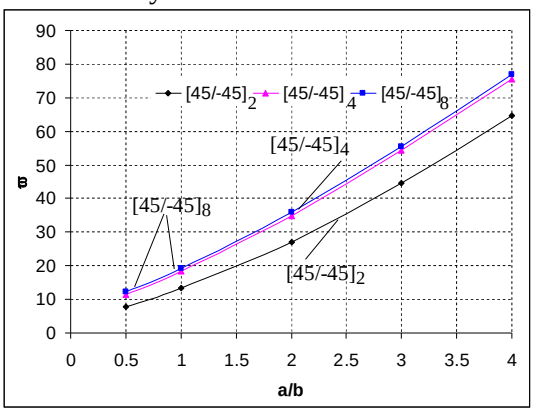

Fig. 4. The effect of aspect ratio on dimensionless natural frequencies of simply supported rectangular plate, staking sequence (θ,- θ, θ,- θ); a/h=10

Effect of anisotropy of composite materials and number of layers on natural frequencies can be observed from Fig. 5-6, and it can be said that the natural frequencies increase when anisotropy of composite materials and number of layers increase.

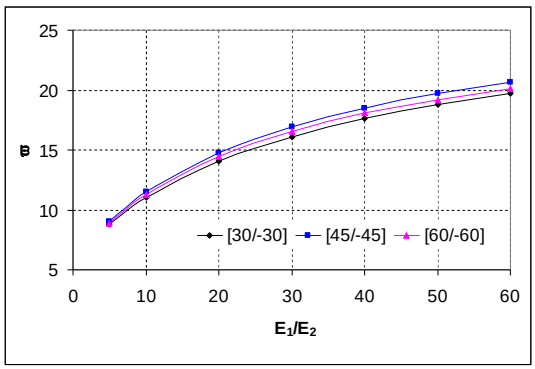

Fig 5: The effect of anisotropy of composite materials (E_1/E_2) on dimensionless natural frequencies of simply supported rectangular plate, staking sequence $[\theta,-\theta]_4$; a/h=10

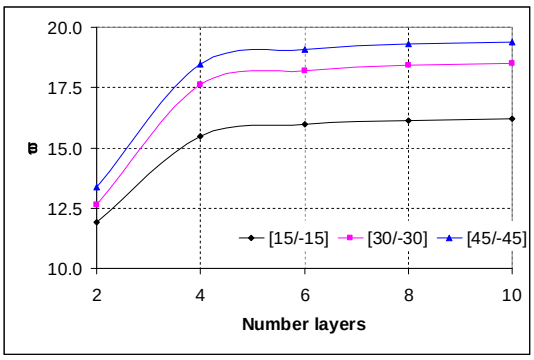

Fig. 6. The effect layer number on non-dimensional natural frequencies of simply supported square plate, a/h=10

Table 4: Dimensionless fundamental natural frequencies of simply supported laminated composite rectangular plates with different aspect ratio (a/b), thickness ratio (a/h), lamination angle and staking sequence $[\theta,-\theta,\theta,-\theta]$

a/h	θ	Ref	a/b			
			0.5	1	2	4
5	30	Kant [16]	3.749	4.855	7.522	15.314
		CEM	3.765	4.957	7.527	15.373
		Error (%)	0.43	2.09	0.07	0.39
	45	Kant [16]	3.459	5.018	8.540	17.053
		CEM	3.484	5.049	8.491	17.102
		Error (%)	0.71	0.62	0.58	0.29
	60	Kant [16]	2.936	4.855	8.988	11.652
		CEM	2.965	4.851	8.979	11.662
		Error (%)	1.00	0.09	0.09	0.09
10	30	Kant [16]	1.283	1.751	2.936	6.182
		CEM	1.286	1.761	2.957	6.202
		Error (%)	0.25	0.55	0.73	0.33
	45	Kant [16]	1.150	1.833	3.459	7.537
		CEM	1.156	1.849	3.482	7.557
		Error (%)	0.49	0.87	0.65	0.27
	60	Kant [16]	0.938	1.751	3.745	5.929
		CEM	0.948	1.803	3.783	5.903
		Error (%)	1.11	2.97	1.01	0.44
20	30	Kant [16]	0.365	0.517	0.938	2.146
		CEM	0.372	0.518	0.928	2.193
		Error (%)	2.03	0.19	1.05	2.19
	45	Kant [16]	0.321	0.545	1.150	2.879
		CEM	0.322	0.545	1.202	2.913
		Error (%)	0.31	0.00	4.52	1.21
	60	Kant [16]	0.256	0.517	1.283	2.979
		CEM	0.256	0.516	1.297	2.996
		Error (%)	0.04	0.04	1.08	0.57

4.3. Harmonic responses of composite plate

In order to demonstrate the advantages of CE model, a comparison of harmonic response for a SFSF laminate angle-ply plate

will be carried out. The properties of plate are: h=0.054m, a = b = 10h. The plate is submitted by a distributed force on the x=a edge and the response point is situated in the middle of the same edge.

The harmonic response obtained with 3 continuous elements is compared with those obtained with 100 (10x10 mesh) and 900 finite elements (30x30 mesh) of ANSYS SHELL 99 for SFSF (45^o/-45^o/45^o/-45^o) anti-symmetric angle-ply laminated composite plate. Results are given in Fig. 7

With 10x10 mesh, there is a convergence of results obtained with CEM and FEM up to 567.6 Hz. Beyond this limit, there is a discrepancy which can be explained by the fact that the meshing in FE idealization is not fine enough. An excellent convergence is noted for CEM and FEM with 900 elements (30x30 mesh).

It is obvious to remark important differences between CE and FE curves from 2975 Hz. FEM is an approximate method and the very fine mesh 30x30 is not still enough to reach the precision of CEM which is based on exact solution of FSDT equations. By using the minimum of elements, CEM gives good results in all low, medium and high frequency. Thus, CEM is a very interesting approach to overcome the difficulty of FEM in high frequency range.

A good similarity can be observed between the three curves of harmonic responses of CSFS (45^o/-45^o/45^o/-45^o) angle-ply plate by CEM and by FEM with 10x10 and 30x30 meshes can be seen in Fig.8

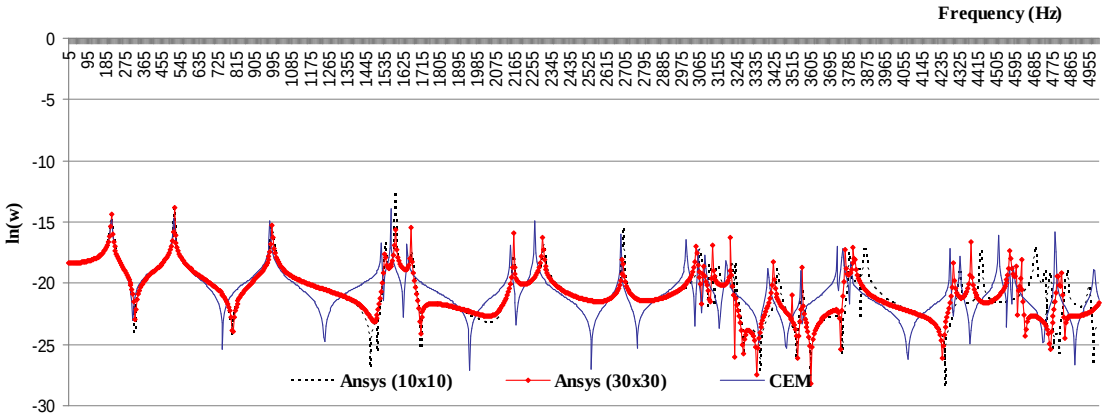

Fig. 7. Comparison of harmonic responses of SFSF angle-ply composite plate (45^o/-45^o/45^o/-45^o) by CEM and by FEM with different mesh (h=0.1m, a=b=10h)

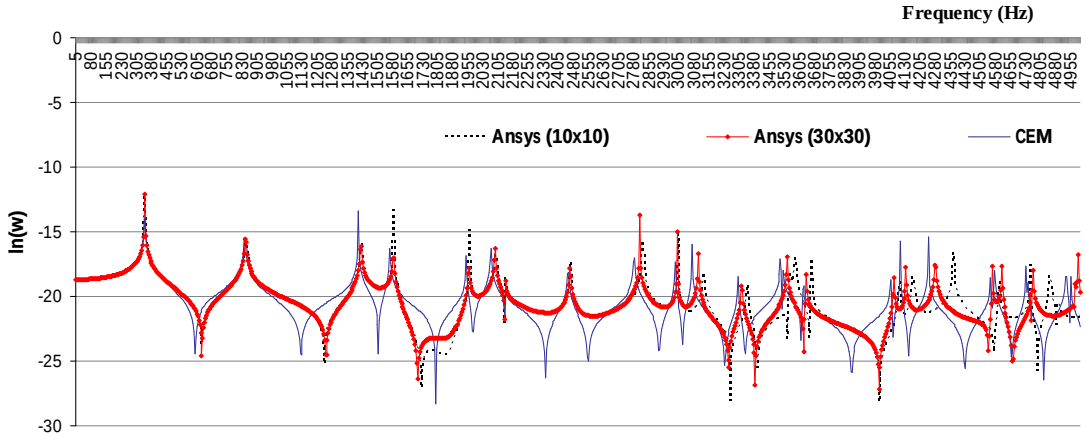

Fig. 8. Comparison of harmonic responses of CSFS (45^o/-45^o/45^o/-45^o) angle-ply by CEM and by FEM with different meshes, (h=0.1m, a=b=10h)

5. Conclusions

A simple method to deal with the construction of the dynamic stiffness matrix of angle-ply moderately thick laminated composite plates is presented. This method has been successfully used to develop a plate continuous element that takes into account rotational inertia and shear deformation effects. Through different comparisons with the published results and with the other numerical methods, the obtained results are very satisfied

The effect of boundary conditions, anisotropy of composite materials, number of layers, dimension ratio, thickness ratio on natural frequencies were investigated. Natural frequencies and harmonic response obtained with this kind of formulation are in close agreement with finite element solutions. The main advantage is the reduction of the size of the model thus allowing high precision in the results for a large frequency range.

The research can be extended to solve the vibration of composite plate on elastic foundation, damped composite plate, composite plate with stiffeners, composite plate in contact with fluid.

Acknowledgements

This research is funded by Vietnam National Foundation for Science and Technology Development (NAFOSTED) under grant number : ***107.02-2011.08*** .

6. References

[1] P.H. Kulla, The continuous elements method, ESA International Conference on Spacecraft Structures and Mechanical Testing, ESTEC, Noodwijk, The Netherlands, 1991.

[2] A. Y. T. Leung. Dynamic Stiffness and Substructures, Springer, London, 1993.

[3] R. Lunden, B. Akesson, Damped second order Rayleigh Timoshenko beam vibration in space — an exact complex dynamic member stiffness matrix, International Journal for Numerical Methods in Engineering 19 (1983) 431–449.

[4] C. Duforet, Dynamic study of an assembling of rods in medium and higher frequency ranges—Computer code ETAPE, in: Proceedings of the Third Colloquiium on New Trends in Structure Calculations, Bastia, Corsica, 1985, pp. 229–246 (in French).

[5] M.S. Anderson, F.W. Williams, J.R. Banerjee, B.J. Durling, C.L. Herstorm, D. Kennedy, D.B. Warnaar, User Manual for BUNVIS-RG: an exact buckling and vibration program for lattice structures, with repetitive geometry and substructuring options, NASA Technical Memorandum 87669, 1986.

[6] F.W. Williams, D. Kennedy, R. Butler, M.S. Anderson, VICONOPT: program for exact vibration and bucklinganalysis or design of prismatic plate assemblies, American Institute of Aernautics and Astronautics Journal 29 (1991) 1927–1928.

[7] P.H. Kulla, Continuous elements, some practical examples. In: Proceedings of the ESTEC Workshop on Continuum Methods for Flexible Structures, Noordw.yk, The Netherlands, June 1989.

[8] J.B. Casimir, Ele´ments Continus de Type Poutre (Etude Statique et Dynamique d'Assemblages de Poutres Planes ou Gauches), Thesis in French, CNAM, 1997.

[9] J.B. Casimir, C. Duforet, T. Vinh, Dynamic behaviour of structures in large frequency range by continuous element methods, Journal of Sound and Vibration 267 (2003) 1085–1106.

[10] A.W. Leissa, Vibration of Plates, NASA SP160 Publications, 1968.

[11] Wittrick WH, Williams FW. A general algorithm for computing natural frequencies of elastic structures. Quarterly J Mech Appl Math 1970;24(3):263–84.

[12] Wittrick WH, Williams FW. Buckling and vibration of anisotropic or isotropic plate assemblies under combined loadings. Int J Mech Sci 1974;16(4):209–39.

[13] Anderson MS, Kennedy D. Inclusion of transverse shear deformation in exact buckling and vibration of composite plate assemblies. Tech. Rep. NASA/CR-1993-4510, Langley, Hampton; 1993.

[14] Anderson MS, Kennedy D. Transverse shear deformation in exact buckling and vibration of composite plate assemblies. AIAA J 1993;31(10):1963–5.

[15] Reddy J.N, Mechanics of laminated composite plates and shells, Theory and Analysis.2004, CRC Press.

[16] T.Kant, Mallikarjuna, A higher-order theory for free vibration of unsymmetrically laminated composite and sandwich plates-finite element evaluations. Computer and Structures 1988.

[17] Nguyen Manh Cuong, Eléments Continus de plaques et coques avec prise en compte du cisaillement transverse. Application à l'interaction fluide-structure, Thèse de Doctorat, Université Paris VI, 2003.

[18] J.B.Casimir, Nguyen Manh Cuong. Thick shells of revolution: Derivation of the dynamic stiffness matrix of continuous elements and application to a tested cylinder, Computers & structures, 85(23-24), 1845-1857, 2007.

The 2nd International Conference on Engineering Mechanics and Automation (ICEMA2)
Hanoi, August 16-17, 2012
ISBN: 978-604-913-097-7

Mechanical Properties of Jute Fiber Reinforced Poly(Butylene Succinate) Biodegradable Composites

Tran Huu Nam

Department of Fundamental Sciences, Petrovietnam University, 173 Trung Kinh, Ha Noi, Viet Nam
E-mail: namth@pvu.edu.vn and thnam.hut@gmail.com

Abstract

In present research, the poly(butylene succinate) (PBS) biodegradable composites reinforced with unidirectional jute fibers were developed. The unidirectional jute/PBS biodegradable composites were fabricated by compression molding method. The effect of fiber content from 10 to 60 wt% on the mechanical properties of jute/PBS biodegradable composites was studied. The influence of alkali and silane treatment on the fiber surface and mechanical properties of jute/PBS biodegradable composites was also investigated. The reinforcement of jute fibers improved mechanical properties of PBS resin. In this study, the best mechanical properties of jute/PBS biodegradable composite were achieved at 50 wt% fiber content. The mechanical properties of surface treated jute/PBS composites were significantly higher than those of PBS resin and untreated ones. Alkali and silane treated jute/PBS biodegradable composite at 50 wt% fiber content exhibited an increase in tensile strength by 42.6% and 33.5%, in tensile modulus by 20.6% and 16.7%, in fracture strain by 18.6% and 16.2%, in flexural strength by 5.5% and 2.7%, and in flexural modulus by 17.5% and 14.5% compared with untreated one, respectively. Compared with silane treatment, alkali treatment showed better mechanical properties of jute/PBS biodegradable composites. Fractured surface morphologies of composite specimens exhibited an improvement of interfacial fiber–matrix adhesion in the composites reinforced with surface treated jute fibers.

Key Words: Natural fiber biodegradable composites, mechanical properties, surface treatments.

1. Introduction

Biodegradable green composites made of biodegradable polymers and natural fibers have attracted great interests in recent years due to their environment-friendly properties and potential applications in biomedical and bioengineering fields (Cheung et al., 2009). Natural fiber biodegradable composites have some major advantages over conventional composites as eco–friendliness, low cost, lightweight, high specific properties and biodegradability (Zhang et al., 2005 and Monteiro et al., 2009). Among the biodegradable polymers, poly(butylene succinate) (PBS) is increasing commercial interest. PBS is thermoplastic aliphatic polyester which can be naturally degraded into the environment by bacteria and fungi (Kim and Rhee, 2003). PBS has excellent biodegradability in nature, such as in soil,

lake, sea, and compost (Hirotsu et al., 2000). It can be completely combustible by fire without evolving toxic gases (Lee et al., 2005). As a result, PBS can be a good candidate material for the matrix of biodegradable composites.

The natural fibers such as, hemp, jute, kenaf, flax, coir, ramie, sisal, bamboo, and, etc. offer specific benefits such as low cost, low density, low pollutant emissions, acceptable specific properties, renewability and biodegradability (Mohanty et al., 2000b and Satyanarayana et al., 2009). Among natural fibers, jute is the second most important bast fiber after cotton because of its easy availability at low cost. Jute has inherent advantages, including its renewable nature, biodegradability, moderate moisture regain, and good thermal and acoustic insulation properties that make it a wise choice in home furnishings and in high performance technical textiles. However, a major drawback of using jute fiber as reinforcing material is its hydrophilic nature and responsible for moisture absorption. To be an effective reinforcing constituent for jute fiber, it is essential to improve compatibility and bonding between the fiber and the matrix. To make them suitable reinforcing candidates with adequate bond characteristics for general applications, various chemical modifications of jute fibers have been attempted (Xue and Tabil, 2007). In present work, the unidirectional jute/PBS composites were developed by compression molding method. The effect of fiber content on mechanical properties of jute/PBS composites was studied. The influence of alkali and silane treatment on mechanical properties of jute/PBS composites was investigated. The fiber surface morphologies and fractured surfaces of composite specimens were investigated by scanning electron microscope (SEM) providing the information to evaluate the interfacial fiber-matrix adhesion.

2. Experimental

2.1. Materials

The raw jutes were supplied by Hung Yen Jute and Garment JSC (Viet Nam). Biodegradable PBS pellets (#1001) with melting temperature of 115^{o}C were supplied by Showa High Polymers Ltd. (Japan). The density of jute fiber and PBS are 1.4 g/cm^3 and 1.26 g/cm^3, respectively.

2.2. Surface treatment of jute fibers

Two different methods were used to treat the jute fibers before composite fabrication, including (i) alkali treatment (AT) and (ii) silane treatment (ST). For AT method, first untreated (UT) jute fibers were treated with 2% NaOH solution in a glass beaker for 3 h at room temperature (RT). Next, the fibers were taken out of the solution, then washed several times with fresh water and subsequently with distilled water until pH of the solution was equal to 7. Finally, the jute fibers were air-dried for two days.

For ST method, UT jutes were treated with γ-Methacryloxypropyltrimethoxysinale (γ-MPS) which was supplied by Shin-Etsu Chemical Co., Ltd. (Tokyo, Japan). First, the aqueous solution was prepared by dissolving liquid 0.3 wt% of γ-MPS in acidified water (the pH of the solution was adjusted to 4.5 with acetic acid). Next, UT jute fibers were immersed in the solution for 1 h at RT. Last, the fibers were air-dried for two days.

2.3. Composite fabrication

The composite plates made from PBS and different UT, AT and ST jute fiber content from 10 to 60 wt% were fabricated by hot press equipment (Imoto Corp., Kyoto, Japan). To begin with, jute fibers were dried at 60^{o}C in a vacuum oven for 24 hours. Next, dried jute fibers were cut into the segments with the length of 150 mm, weighed, aligned in a parallel array and placed in the mold between the PBS sheets as described by Nam et al. (2011). Finally, composite plates were pressed in a stainless steel mold with a thickness of 2 mm under 12 MPa pressure for 10 minutes at 150^{o}C and quickly cooled by fan. Both PBS sheets and composite plates were prepared with the same thermal history.

2.4. Tensile and flexural test

The tensile specimens were cut out from pure PBS and composite plates by cutting machine AC-300CF (MARUTO Co., Tokyo, Japan). The both clamped ends of tensile specimens (Figure 1) were glued by two glass fiber reinforced plastic (GFRP) tabs. Tensile properties were measured according to JIS K7113 using a universal testing machine RTF–1350 (JTT Inc., Tokyo, Japan). Tensile tests were carried out at RT with a crosshead speed of 0.5 mm/min.

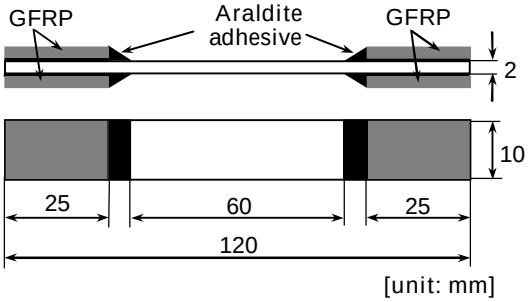

Figure 1. Tensile specimen

The flexural properties were measured by a three-point bending method according to JIS K7171 using universal testing machine Senstar SC-5H (JTT Inc., Tokyo, Japan). The dimension of flexural specimens was 50 mm x 25 mm x 2 mm. The flexural test was carried out at RT with a crosshead speed of 2 mm/min. The flexural strength (σ_f) and modulus (E_f) were calculated using the following equations:

$$\sigma_f = \frac{3FL}{2bh^2} \quad (1)$$

$$E_f = \frac{L^3 m}{4bh^3} \quad (2)$$

where F is the maximal applied force, L is the length of support span, m is the slope of the force-deflection curve, b and h are the width and thickness of the specimen, respectively. Tensile and flexural properties of PBS and the composites were obtained from seven specimens.

2.5. Morphological characterization

The jute surface morphologies and fractured surface of the composites after tensile tests were examined using SEM (VE-7800, Keyence Inc., Osaka, Japan).

3. Results and discussion

3.1. Surface modification of jute fibers

Figure 2 showed SEM micrographs of jute fiber surface before and after treatments.

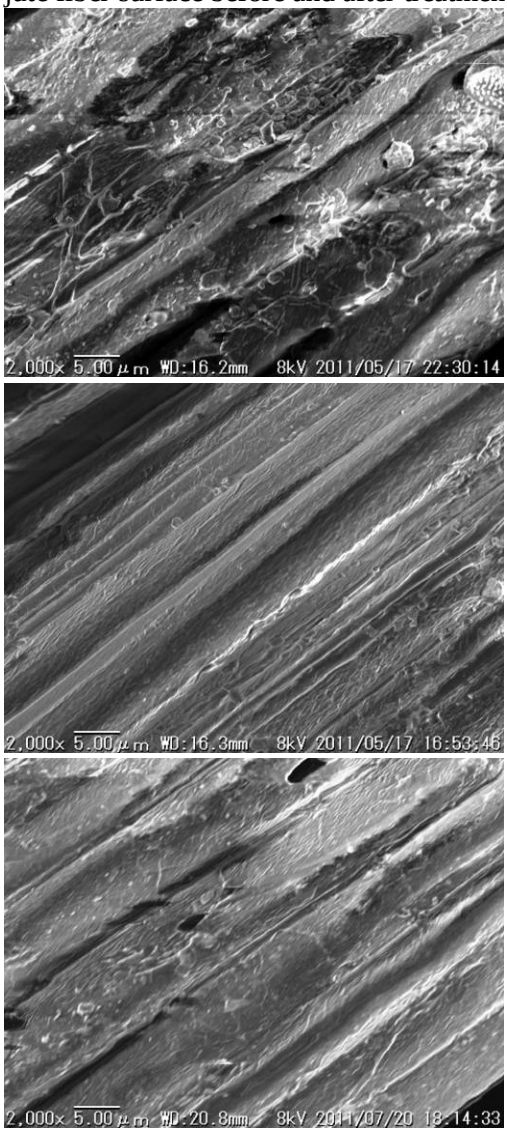

Figure 2. SEM micrographs of jute fiber surface: a. UT, b. AT and c. ST jute.

It is observed that jute fibers after treatment have some changes in their surface structure. Natural and artificial impurities

were found on the UT jute fiber surface (Figure 2a). However, these impurities on jute fiber surface were removed after AT making the fiber cleaner and rougher than before (Figure 2b). Moreover, a rougher surface morphology was typical for the treated jute fibers, because of the removal of lignin and hemicelluloses in comparison with UT fibers (Gassan and Bledzki, 1999). It can be realized that AT increases the surface roughness and exposes the cellulose on the fiber surface. Furthermore, the hydrophilic behavior of jute fiber induced by predominance of –OH groups will thus be weakened, and its compatibility with hydrophobic PBS will accordingly be improved (Lee and Wang, 2006).

For ST, jute fibers were treated with hydrolyzed silane solution to allow silane penetrates into the fiber lumina and further diffuse into the cell walls. As a result, after ST jute fiber surfaces were modified as observed in Figure 2c. This can be explained that when hydrolyzed silane solutions are mixed with natural fibers, the reactive silanol groups have a high affinity for each other, forming –Si–O–Si– bonds and also for the hydroxyl sites of fibers via hydrogen bonds (Hill et al., 2004 and Donath et al., 2006). The silanols of γ-MPS firstly form a monolayer on the fiber, and then are further adsorbed resulting in the formation of a rigid polysiloxane layer on the fiber surface (Xie et al., 2010). In general, the main defects of natural fibers as reinforcing fillers, such as high moisture absorption, poor wettability, and incompatibility with hydrophobic polymer, can be improved by surface modification. This shows that surface modification of jute fiber can improve the properties of its composites.

3.2. Effect of fiber content on mechanical properties of UT jute/PBS composites

Mechanical properties of PBS resin and UT jute/PBS composites with different fiber weight content were given in Table 1. As seen in Table 1, the incorporation of jute fibers improved mechanical strength and modulus of PBS resin. It can be realized that tensile and flexural strength gradually increased with increasing the fiber content from 0 to 50 wt%, but decreased with upper fiber content. Tensile modulus of the composites gradually increased with increasing the fiber content up to 60 wt% while flexural modulus increased with increasing the fiber content to 50 wt%, but it decreased at 60 wt% fiber content. The increase in mechanical strength and modulus of the composites is due to the reinforcement of jute fibers in PBS matrix, because the strength and modulus of jute fiber are higher than those of PBS matrix. The decrease in mechanical strength and flexural modulus at 60 wt% fiber content probably resulted from incomplete fiber wetting, because PBS content is not sufficient to wet all fiber surfaces. The high mechanical strength at 50 wt% fiber content might be due to adequate fiber content in the composites, which leads to greater wetting. Compared with PBS, UT jute/PBS biodegradable composite at 50 wt% fiber content showed an increase in tensile strength by 320%, tensile modulus by 2594%, flexural strength by 274.7% and flexural modulus by 1577.1%. The best mechanical properties of UT jute/PBS biodegradable composite obtained at the fiber content of 50 wt% in this study.

The incorporation of high fiber content reduced fracture strain of the composites, because increasing the amount of reinforced fibers will lead to the decrease in the amount of polymeric matrix available for the elongation. The decrease in fracture strain, as shown in Table 1, is mainly due to the structural integrity of PBS being destroyed by jute fiber loading, and increasing fiber content imply poor interfacial fiber–matrix bonding leading to quicker fracture than pure PBS (Liu et al., 2009). Compared with PBS, fracture strain of UT jute/PBS composite with 10 wt% fiber content significantly reduces to 89%. After such initial drop, the percent fracture strain decreases inconsiderably with increasing the fiber content. This can be explained due to lower fracture strain of jute than that of PBS resin. The fracture strain of jute/PBS biodegradable

composites indicated that the ductile nature of PBS resin strongly decreases with the addition of jute fibers.

Table 1. Mechanical properties of PBS and UT jute/PBS biodegradable composites.

Fiber content (wt%)	Tensile strength (MPa)	Tensile modulus (GPa)	Fracture strain (%)	Flexural strength (MPa)	Flexural modulus (GPa)
PBS	37.5 ± 1.1	1.0 ± 0.06	9.0 ± 0.91	49.4 ± 2.4	0.9 ± 0.2
10	66.6 ± 5.3	10.2 ± 1.6	0.97 ± 0.07	70.3 ± 4.8	2.9 ± 0.5
20	98.0 ± 6.5	13.2 ± 2.0	0.86 ± 0.05	115.9 ± 6.9	7.4 ± 0.6
30	131.1 ± 10.5	20.5 ± 2.2	0.85 ± 0.06	137.2 ± 8.9	9.0 ± 0.7
40	143.3 ± 11.3	23.2 ± 2.3	0.79 ± 0.07	161.1 ± 8.7	11.6 ± 0.9
50	157.7 ± 10.5	27.0 ± 2.4	0.75 ± 0.08	185.1 ± 8.6	14.4 ± 0.8
60	147.5 ± 9.90	30.8 ± 2.8	0.63 ± 0.08	150.1 ± 9.5	12.7 ± 0.8

3.3 Effect of fiber surface treatment on mechanical properties of the composites

AT improves the fiber–matrix adhesion due to the removal of natural and artificial impurities from the fiber surface as well as changing in the arrangement of units in the cellulose macromolecule (Gonzalez et al., 1999). As described above, AT increases the surface roughness, and the amount of cellulose exposed on the fiber surface resulting in better mechanical interlocking. This was well depicted in Figure 2 by comparing the SEM micrograph of alkali treated fiber with the UT fiber. Thus, the development of a rough surface tomography and enhancement in aspect ratio offer better fiber–matrix interfacial bond resulting in increasing the mechanical properties. ST is a chemical which functions at the interface to create a chemical bridge between the reinforcement and matrix. It improves the interfacial adhesion when one end of the molecule is tethered to the reinforcement surface and the functionality at the other end reacts with the polymer phase (Xie et al., 2010).

The effect of fiber surface treatment and fiber content on the mechanical properties of jute/PBS composites was shown in Figures 3-4. The mean tensile strength, modulus and fracture strain of jute/PBS composite at 50 wt% fiber content range from 157.7 to 231.9 MPa, 26.9 to 36.3 GPa and 0.8 to 0.93%, respectively. As seen in Figure 3, surface modifications of jute fibers by AT and ST improved tensile properties of jute/PBS biodegradable composites. Compared with UT jute, AT and ST jute/PBS composite at 50 wt% fiber content exhibited an increase in tensile strength by 42.6% and 33.5%, in tensile modulus by 20.6% and 16.7%, in fracture strain by 18.6% and 16.2%, respectively. Moreover, as shown in Figure 4, surface treatment of jute fibers improved also the flexural properties of jute fiber reinforced PBS biodegradable composites. The mean flexural properties of AT and ST jute/PBS composites yielded higher than those of UT one. This reflects the contribution of alkali or silane in terms of changes of fiber properties and the enhancement of interfacial fiber–matrix adhesion. The flexural strength and modulus of jute/PBS biodegradable composite at 50 wt% fiber content range from 185.1 to 198.9 MPa and 14.4 to 17.6 GPa, respectively. AT and ST jute/PBS composite at 50 wt% fiber content showed an increase in flexural strength by 5.5% and 2.7%, and flexural modulus by 17.5% and 14.5% compared with UT jute/PBS biodegradable composite,

respectively. It is interesting to note that flexural strength has the same trend as tensile strength with increasing the fiber content.

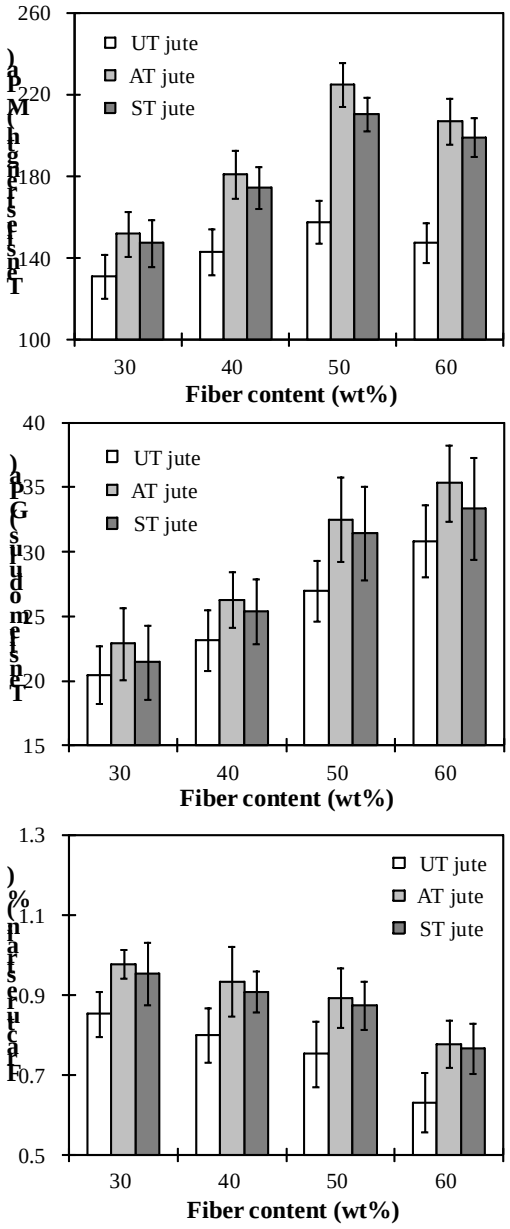

Figure 3. Effect of fiber surface treatment on: (a) tensile strength, (b) tensile modulus and (c) fracture strain of jute/PBS composites with different fiber weight content.

The increase in mechanical properties of surface treated jute/PBS biodegradable composites may be due to greater fiber–matrix interfacial and physical bonding. As described above, surface treatment can improve the compatibility between jute fiber and PBS matrix leading to less interfacial fiber–matrix debonding.

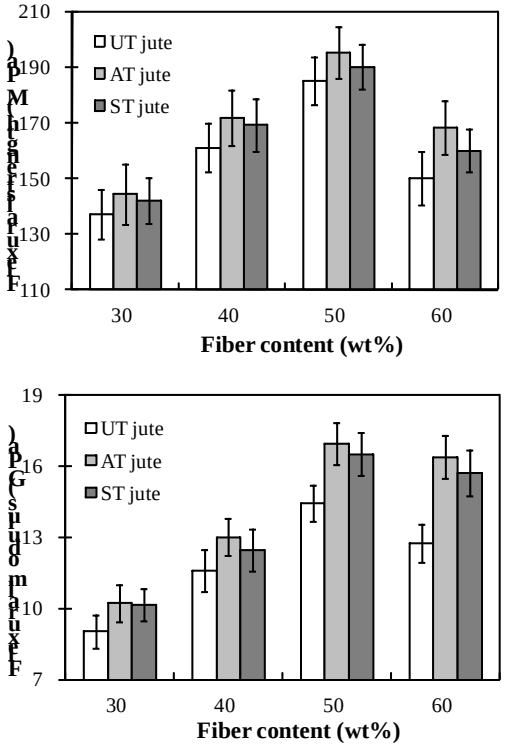

Figure 4. Effect of fiber surface treatment on: (a) flexural strength and (b) flexural modulus of jute/PBS composites with different fiber weight content

As shown in Figure 5a, the pulled-out fibers can be found on the fracture surface of UT jute/PBS, suggesting poor interfacial fiber-matrix adhesion. It is obvious that UT jute fiber can be easily pulled-out from the interfacial region with poor compatibility resulting in rapid partial-collapse of PBS composite. For the ST jute/PBS composite (Figure 5b), several jute fibers were pulled-out and broken to some extent during the fracture process, and a little PBS matrix remained and adhered to the surface of the jute fibers. Nevertheless, lots of pulled-out fibers disappeared in the case of AT jute (Figure 5c), proving good compatibility being formed in PBS composites. In general, surface treated jute fiber having a good adhesion with PBS matrix can effectively disperse and transfer stress, leading to the improvement in mechanical properties of surface treated jute/PBS composites.

Consequently, surface treatment of jute fiber is necessary to enhance the interfacial fiber–matrix adhesion prior to composite processing.

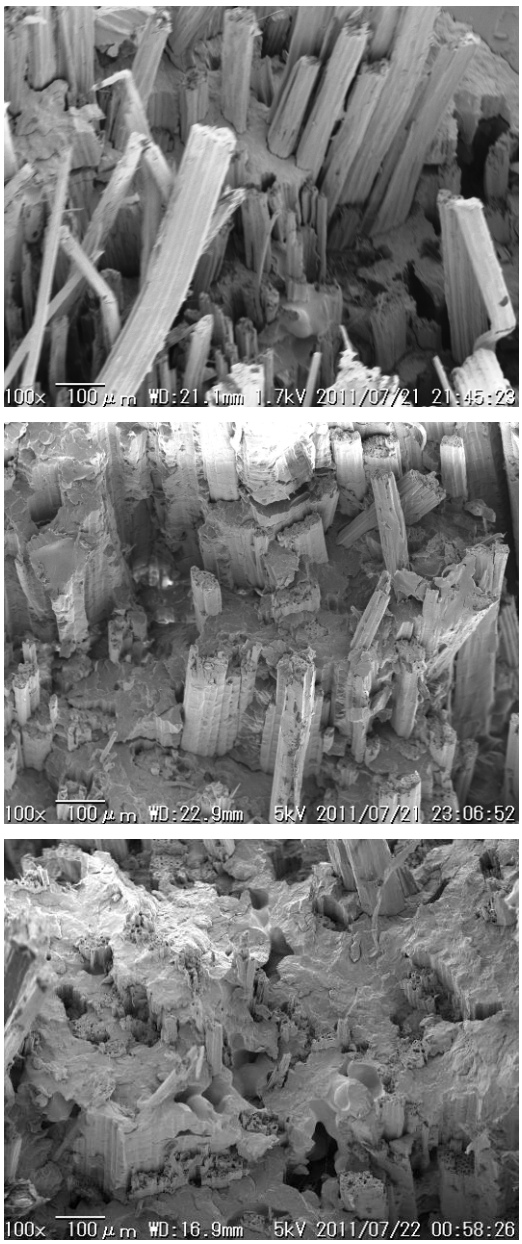

Figure 5. SEM micrographs of fractured surface of PBS biodegradable composite reinforced with 30 wt% fiber content of: (a) UT jute, (b) ST jute and (d) AT jute.

The mechanical strength and modulus of unidirectional jute/PBS composites showed an optimum fiber content. The optimum fiber content varies with the nature of both fiber and matrix, fiber aspect ratio, fiber–matrix interfacial adhesion, fiber agglomeration, processing technique, end etc (Liu et al., 2009). Similar investigations have also been reported by Mohanty et al. (2000a) for jute fabrics/polyester composites in which the optimum fiber content is 32 wt% and by Roe and Ansell (1985) for jute/polyester composites is about 60 vol. %. In this study, the addition of 50 wt% fiber content showed the best mechanical properties of jute/PBS composites. In short, the results of mechanical properties point out the importance by using the right amount of fiber as reinforcement in the composites.

4. Conclusions

Mechanical properties of unidirectional jute fibers reinforced PBS biodegradable composites have been studied. Effect of AT and ST on the mechanical properties of jute/PBS biodegradable composites has been investigated. The mechanical properties of surface treated jute/PBS composites are significantly higher than those of PBS resin and UT ones. Mechanical strength of jute/PBS biodegradable composites increased with increasing fiber content up to 50 wt%, but decreased with upper fiber content. The authors propose that the 50 wt% jute fiber content reinforced PBS biodegradable composites have the best mechanical properties in this study. Surface modification by AT and ST increased mechanical properties of jute/PBS composites, in which AT method showed highest mechanical properties of jute/PBS composites. AT increased the fiber surface roughness and exposed the cellulose on jute surface leading to the increase of mechanical interlocking and interfacial bonding. The present results suggest that a useful composite with good properties could be successfully developed based on jute fiber and PBS matrix.

5. References

Cheung H. Y., M. P. Ho, K. T. Lau, F. Cardona and D. Hui (2009). Natural fibre–reinforced composites for bioengineering and environmental

engineering applications. *Composites Part B*, 40, pp. 655-663.

Donath S., H. Militz and C. Mai (2006). Creating water-repellent effects on wood by treatment with silanes. *Holzforschung*, 60, pp. 40-46.

Gassan J. and A. K. Bledzki (1999). Alkali treatment of jute fibers: Relationship between structure and mechanical properties. *Journal of Applied Polymer Science*, 71, pp. 623-629.

Gonzalez A. V., J. M. Cervantes-Uc, R. Olayo and P. J. Herrera-Franco (1999). Effect of fiber surface treatment on the fiber–matrix bond strength of natural fiber reinforced composites. *Composites Part B*, 30, pp. 309-320.

Hill C. A. S., M. R. M. Farahani and M.D.C. Hale (2004). The use of organo alkoxysilane coupling agents for wood preservation. *Holzforschung*, 58, pp. 316-325.

Hirotsu T., T. Tsujisaka, T. Masuda and K. Nakayama (2000). Plasma surface treatments and biodegradation of poly (butylene succinate) sheets. *Journal of Applied Polymer Science*, 78, pp. 1121-1129.

Kim D. Y. and Y. H. Rhee (2003). Biodegradation of microbial and synthetic polyesters by fungi. *Applied Microbiology and Biotechnology*, 61(4), pp. 300-308.

Lee S. H. and A. Wang (2006). Biodegradable polymers/bamboo fiber biocomposite with bio-based coupling agent. *Composites Part A*, 37, pp. 80-91.

Lee S. M., D. Choa, W. H. Park, S. G. Lee, S. O. Han and L. T. Drzal (2005). Novel silk/poly(butylene succinate) biocomposites: the effect of short fibre content on their mechanical and thermal properties. *Composites Science and Technology*, 65, pp. 647–657.

Liu L., J. Yu, L. Cheng and W. Yu (2009). Mechanical properties of poly(butylene succinate) (PBS) biocomposite reinforced with surface modified jute fibre. *Composites Part A*, 40, pp. 669-674.

Mohanty A. K., M. A. Khan and G. Hinrichsen (2000a). Influence of chemical surface modification on the properties of biodegradable jute fabrics-polyester amide composites. *Composites Part A*, 31, pp. 143-150.

Mohanty A. K., M. Misra and G. Hinrichsen (2000b), Biofibres, biodegradable polymers and biocomposites: An overview. *Macromolecular Materials and Engineering*, 276/277, pp. 1-24.

Monteiro S. N., F. P. D Lopes, A. S. Ferreira and D.C.O. Nascimento (2009). Natural–fiber polymer–matrix composites: cheaper, tougher, and environmentally friendly. *JOM*, 61, pp. 17-22.

Nam T. H., S. Ogihara, N. H. Tung and S. Kobayashi (2011). Effect of alkali treatment on interfacial and mechanical properties of coir fiber reinforced poly(butylene succinate) biodegradable composites. *Composites Part B*, 42(6), pp. 1648-1656.

Roe P. J. and M. P. Ansell (1985). Jute-reinforced polyester composites. *Journal of Materials Science*, 20, pp. 4015-4020.

Satyanarayana K. G., G. G. C. Arizaga and F. Wypych (2009). Biodegradable composites based on lignocellulosic fibers – an overview. *Progress in Polymer Science*, 34(9), pp. 982-1021.

Xie Y., C. A. S. Hill, Z. Xia, H. Militz and C. Mai (2010). Silane coupling agents used for natural fiber/polymer composites: A review. *Composites Part A*, 41, pp. 806-819.

Xue L. and L.G. Tabil (2007). Chemical treatments of natural fibre for natural fibre reinforced composites: a review. *Journal of Polymers and the Environment*, 15, pp. 25-33.

Zhang M. Q., M. Z. Rong and X. Lu (2005)., Fully biodegradable natural fiber composites from renewable resources: All plant fiber composites. *Composites Science and Technology*. 65, pp. 2514-2525.

The 2nd International Conference on Engineering Mechanics and Automation (ICEMA2)
Hanoi, August 16-17, 2012
ISBN: 978-604-913-097-7

Experimental and Numerical Studies on Free Vibration of Folded Laminate Composite Plate with and without Stiffeners

Tran Ich Thinh[a], Bui Van Binh[b] and Tran Minh Tu[c]

[a] *Hanoi University of Science & Technology, Dai Co Viet Str. 1, Hai Ba Trung Dist. Hanoi, Vietnam; tranichthinh@yahoo.com*
[b] *University of Power Electric, Hoang Quoc Viet Str. 235, Tu Liem Dist. Hanoi, Vietnam; binhphuongduc@yahoo.com*
[c] *University of Civil Engineering, Giai Phong Str. 55, Hai Ba Trung Dist. Hanoi, Vietnam; tpnt2002@yahoo.com*

Abstract

In this paper, free vibration of folded laminate composite plate with and without stiffeners is studied by finite element and experiment method. Based on the first order shear deformation theory, an 8-noded isoparametric element with 5-degrees of freedom per node is developed for both of plate and stiffener. In experiment, the natural frequencies of the plates are determined by Dewebook and Dasylab software. It is shown good agreement between two sets of experimental results and numerical results under different boundary conditions.

Key Words: experimental frequency, folded laminate composite plate, finite element method, Mindlin theory.

1. Introduction

Folded laminate composite plates are very useful in engineering. Applications for them have been found almost everywhere in various branches of engineering, such as in roofs, ship hulls, sandwich plate cores and cooling towers, etc. Because of their high strength-to-weight ratio, easy to form, economical, and have much higher load carrying capacities than at plates, which ensures their popularity and has attracted constant research interest since they were introduced.

For folded isotropic plates, Goldberg and Leve [1] used both the two-dimensional theory of elasticity and the two-way slab theory to derive the stiffness of the individual slab of a folded plate. Yitzhaki and Reiss [2] chose the moments along the joints of the folded plates as variables and applied the slope deflection method to analyze the folded plates. Cheung [3] was the first author developed the finite strip method for analyzing isotropic folded plates. Additional works in the finite strip method have been presented. The difficulties encountered with the intermediate supports in the finite strip method [4] were overcome and subsequently Maleki [5] proposed a new method, known as compound strip method. The compound strip method which is basically the finite strip method with the provision for including the effect of an intermediate support by taking an additional stiffness matrix for the support element. A finite strip based on a mixed-hybrid formulation was developed by

Lavy et al. [6]. Irie et al. [7] used Ritz method for the analysis of free vibration of an isotropic cantilever folded plate. Perry et al. [8] presented a rectangular hybrid stress element for analyzing an isotropic folded plate structures in bending cases. In this, they used a four-node element, which is based on the classical hybrid stress method, is called the hybrid coupling element and is generated by a combination of a hybrid plane stress element and a hybrid plate bending element.

However, few studies of laminated composite folded plates are available. Niyogi et al. in [9] reported the analysis of unstiffened and stiffened symmetric cross-ply laminate composite folded plates using first-order transverse shear deformation theory and nine nodes elements. Haldar and Sheikh [10] presented a free vibration analysis of isotropic and composite folded plate by using a sixteen nodes triangular element. L.X.Peng et al. [11] presented a analysis of folded plates subjected to bending load by the first-order shear deformation theory (FSDT) and meshless method.

In the previous works [12-15], we presented a finite element method to analyze the bending, free vibration and time displacement response of V-shape; W-shape sections and multi-folding laminate plate (which having trapezoidal corrugate plate). In these studies, the effects of folding angles, fiber orientations, loading conditions, boundary condition have been investigated.

In this study, finite element model and experiment on free vibration of unstiffened and stiffened folded plates under various boundary conditions are investigated. In the finite element model, based on FSDT, the transverse shear deformation, the rotary inertia of plate and stiffeners are considered. Both of stiffener and folded plates are modeled by eight-noded isoparametric rectangular plate elements. The membrane and bending terms are coupled to present 3D-structure for the folded laminate plates with and without stiffeners. According to our presented technique, we did not use any assumption of eccentricity between plate and stiffeners. The natural frequencies measured by our experiment are compared with the results calculated by our finite element model. It is shown that concordance between the two sets of results.

2. Theoretical formulations

2.1 Displacement and strain field

According to the Reissner-Mindlin plate theory, the displacements (u, v, w) are referred to those of the mid-plane (u_0, v_0, w_0) as:

$$\begin{Bmatrix} u \\ v \\ w \end{Bmatrix} = \begin{Bmatrix} u_0 + z\theta_x \\ v_0 + z\theta_y \\ w_0 \end{Bmatrix} \text{ and } \begin{Bmatrix} \theta_x \\ \theta_y \end{Bmatrix} = \begin{Bmatrix} \frac{\partial w}{\partial x} + \phi_x \\ \frac{\partial w}{\partial y} + \phi_y \end{Bmatrix} \quad (1)$$

Here, θ_x and θ_y are the total rotations, ϕ_x and ϕ_y are the constant average shear deformations about the y and x-axes, respectively.

The z-axis is normal to the xy-plane that coincides with the mid-plane of the laminate positive downward and clockwise with x and y.

The generalized displacement vector at the mid- plane can thus be defined as

$$\{d\} = \{u_0, v_0, w_0, \theta_x, \theta_y\}^T$$

The strain-displacement relations can be taken as:

$$\begin{Bmatrix} \varepsilon_{xx} \\ \varepsilon_{yy} \\ \varepsilon_{zz} \\ \gamma_{xy} \\ \gamma_{yz} \\ \gamma_{xz} \end{Bmatrix} = \begin{Bmatrix} \frac{\partial u_0}{\partial x} + z\frac{\partial \theta_x}{\partial x} \\ \frac{\partial v_0}{\partial y} + z\frac{\partial \theta_y}{\partial y} \\ 0 \\ \left(\frac{\partial u_0}{\partial y} + \frac{\partial v_0}{\partial x}\right) + z\left(\frac{\partial \theta_x}{\partial y} + \frac{\partial \theta_y}{\partial x}\right) \\ \frac{\partial w_0}{\partial y} + \theta_y \\ \frac{\partial w_0}{\partial x} + \theta_x \end{Bmatrix} \quad (2)$$

2.2 Finite element formulations

The Hamilton variation principle is used here to derive the laminate equations of motion. The mathematical statement of the Hamilton principle in the absence of damping can be written as [16]:

$$\int_{t_1}^{t_2}\delta\left(\begin{array}{l}\frac{1}{2}\int_V \rho\{\dot{u}\}^T\{\dot{u}\}dV-\frac{1}{2}\int_V\{\varepsilon\}^T\{\sigma\}dV- \\ -\left(\begin{array}{l}\int_V\{u\}^T\{f_b\}dV+ \\ +\int_S\{u\}^T\{f_s\}dS+\{u\}^T\{f_c\}\end{array}\right)\end{array}\right)dt=0 \quad (3)$$

in which:

$$T=\frac{1}{2}\int_V\rho\{\dot{u}\}^T\{\dot{u}\}dV\ ;\ U=\frac{1}{2}\int_V\{\varepsilon\}^T\{\sigma\}dV\ ;$$

$$W=\int_V\{u\}^T\{f_b\}dV+\int_S\{u\}^T\{f_s\}dS+\{u\}^T\{f_c\}$$

U, T are the potential energy, kinetic energy; W is the work done by externally applied forces.

$u=[u,v,w]^T$ is the displacement of any generic point (x, y, z) in space.

In laminated plate theories, the membrane $\{N\}$, bending moment $\{M\}$ and shear stress $\{Q\}$ resultants can be obtained by integration of stresses over the laminate thickness.

The stress resultants-strain relations can be expressed in the form:

$$\left\{\begin{array}{c}\{N\}\\ \{M\}\\ \{Q\}\end{array}\right\}=\left[\begin{array}{ccc}[A_{ij}] & [B_{ij}] & [0]\\ [B_{ij}] & [D_{ij}] & [0]\\ [0] & [0] & [F_{ij}]\end{array}\right]\left\{\begin{array}{c}\{\varepsilon^0\}\\ \{\kappa\}\\ \{\gamma^0\}\end{array}\right\} \quad (4)$$

where

$$\left([A_{ij}],[B_{ij}],[D_{ij}]\right)=\sum_{k=1}^{n}\int_{h_{k-1}}^{h_k}\left([Q'_{ij}]_k\right)\left(1,z,z^2\right)dz$$

$$i,j = 1, 2, 6 \quad (5)$$

$$[F_{ij}]=\sum_{k=1}^{n} f\int_{h_{k-1}}^{h_k}\left([C'_{ij}]_k\right)dz;\quad f = 5/6;\ i,j = 4, 5 \quad (6)$$

n: number of layers, h_{k-1}, h_k : the position of the top and bottom faces of the k^{th} layer.

$[Q'_{ij}]_k$ and $[C'_{ij}]_k$: reduced stiffness matrices of the k^{th} layer (see [17]).

In the present work, eight nodded isoparametric quadrilateral element with five degrees of freedom per nodes is used. The displacement field of any point on the mid-plane given by:

$$u_0=\sum_{i=1}^{8}N_i(\xi,\eta).u_i\ ;\ v_0=\sum_{i=1}^{8}N_i(\xi,\eta).v_i\ ;$$

$$w_0=\sum_{i=1}^{8}N_i(\xi,\eta).w_i\ ;\ \theta_x=\sum_{i=1}^{8}N_i(\xi,\eta).\theta_{xi}\ ;$$

$$\theta_y=\sum_{i=1}^{8}N_i(\xi,\eta).\theta_{yi} \quad (7)$$

where: $N_i(\xi,\eta)$ are the shape function associated with node i in terms of natural coordinates (ξ,η).

The element stiffness matrix given by equation:

$$[k]_{e(40\times40)}=\int_{A_e}\left([B]^T\right)_{40\times8}[H]_{8\times8}[B]_{8\times40}\,tdA_e \quad (8)$$

where $[H]$ is the material stiffness matrix given by: $[H]=\left[\begin{array}{ccc}[A_{ij}] & [B_{ij}] & 0\\ [B_{ij}] & [D_{ij}] & 0\\ 0 & 0 & [F_{ij}]\end{array}\right]$

The element mass matrix given by:

$$[m]_e=\int_{A_e}\rho[N_i]^T[\overline{m}][N_i]dA_e \quad (9)$$

with ρ is mass density of material.

The strain field so that can be expressed as:

$$\{\varepsilon^0\} = \begin{Bmatrix} \varepsilon_{xx}^0 \\ \varepsilon_{yy}^0 \\ \varepsilon_{xy}^0 \\ \kappa_x \\ \kappa_y \\ \kappa_{xy} \\ \gamma_{yz}^0 \\ \gamma_{xz}^0 \end{Bmatrix} = \begin{bmatrix} \frac{\partial}{\partial x} & 0 & 0 & 0 & 0 \\ 0 & \frac{\partial}{\partial y} & 0 & 0 & 0 \\ \frac{\partial}{\partial y} & \frac{\partial}{\partial x} & 0 & 0 & 0 \\ 0 & 0 & 0 & z\frac{\partial}{\partial x} & 0 \\ 0 & 0 & 0 & 0 & z\frac{\partial}{\partial y} \\ 0 & 0 & 0 & z\frac{\partial}{\partial y} & z\frac{\partial}{\partial x} \\ 0 & 0 & \frac{\partial}{\partial y} & 0 & 1 \\ 0 & 0 & \frac{\partial}{\partial x} & 1 & 0 \end{bmatrix} \begin{Bmatrix} u^0 \\ v^0 \\ w^0 \\ \theta_x \\ \theta_y \end{Bmatrix} =$$

$$= [\partial] \begin{Bmatrix} u^0 \\ v^0 \\ w^0 \\ \theta_x \\ \theta_y \end{Bmatrix} = [\partial][N_i]\{q_e\} = [B]_{8\times 40}\{q_e\}$$

in which:
$$[\overline{m}] = \begin{bmatrix} I_0 & 0 & 0 & I_1 & 0 \\ 0 & I_0 & 0 & 0 & I_1 \\ 0 & 0 & I_0 & 0 & 0 \\ I_1 & 0 & 0 & I_2 & 0 \\ 0 & I_1 & 0 & 0 & I_2 \end{bmatrix}$$

and $I_i = \sum_{1}^{8}\int_{h_k}^{h_{k+1}} z^i \rho \mathrm{d}z$, i=0,1,2

Nodal force vector is expressed as:

$$\{f\}_e = \int_{A_e} [N_i]^{\mathrm{T}} q dA_e \qquad (10)$$

where q is the intensity of the applied load.

For free vibration analysis, the damping effect is neglected; the governing equations are [16]:

$$[M]\{\ddot{u}\} + [K]\{u\} = \{0\} \text{ or}$$
$$\left\{[M] - \omega^2[K]\right\} = \{0\} \qquad (11)$$

in which $\{u\}, \{\ddot{u}\}$ are the global vectors of unknown nodal displacement, acceleration, respectively.

$[M], [K], f(t)$ are the global mass matrix, stiffness matrix, applied load vectors, respectively.

Where

$$[M] = \sum_{1}^{n}[m^*]_e ; [K] = \sum_{1}^{n}[k^*]_e ;$$
$$\{f(t)\} = \sum_{1}^{n}\{f_e^*(t)\} \qquad (12)$$

in which:
$$[m^*]_e = [T]^T[m]_e[T]; [k^*]_e = [T]^T[k]_e[T];$$
$$[f^*]_e = [T]^T\{f\}_e$$

with n is the number of element.

For the Reissner–Mindlin model, it is necessary to introduce a new unknown for the in-plane rotation called drilling degree of freedom, θ_z. The rotation θ_z at a node is not measured and does not contribute to the strain energy stored in the element.

The technique is used here: Before applying the transformation, the 40×40 stiffness and mass matrices are expanded to 48×48 sizes, to insert sixth θ_z drilling degrees of freedom at each node of a finite element. The off-diagonal terms corresponding to the θ_z terms are zeroes, while a very small positive number, we taken the θ_z equal to 10^{-4} times smaller than the smallest leading diagonal, is introduced at the corresponding leading diagonal term. The load vector is similarly expanded by using zero elements at corresponding locations. So that, for a folded element, the displacement vector of each node [12-15]:

$$\{u\} = [T]\{u'\} \qquad (13)$$

in which:

$u' = [u', v', w']^T$ is the displacement of any generic point in local coordinate system (x',y',z').

$$[T] = \begin{bmatrix} l_{x'x} & l_{y'x} & l_{z'x} & 0 & 0 & 0 \\ l_{x'y} & l_{y'y} & l_{z'y} & 0 & 0 & 0 \\ l_{x'z} & l_{y'z} & l_{z'z} & 0 & 0 & 0 \\ 0 & 0 & 0 & l_{y'y} & -l_{x'y} & l_{z'y} \\ 0 & 0 & 0 & -l_{y'x} & l_{x'x} & -l_{z'x} \\ 0 & 0 & 0 & l_{y'z} & -l_{x'z} & l_{z'z} \end{bmatrix}$$ is the transformation matrix.

l_{ij} : are the direction cosines between the global and local coordinates (see 15).

3. Numerical results

3.1. Validation Example.

In order to validate the presented finite element code and our model, the first five natural frequencies of a cantilever two folded composite plate studied by Guha Niyogi [9] are recalculated.

The layout of the plate is shown in Fig.1 with the dimension L=1.5m, total thickness t=0.03m, physical and mechanical properties of material: E_1 = 60.7GPa, E_2=24.8 GPa, G_{12} =G_{13}= 12.0 GPa, υ_{12}=0.23, ρ = 1300 kg/m^3.

Three case are considered for different folding angle α= 90^0, 120^0, 150^0 with fiber orientation [90^o/90^o/90^o].

These results have been compared with published results given by Guha Niyogi [9] and presented in Table 1.

Table1. Comparison first five natural frequencies (Hz) of two folded composite plates for different folding angle, (90^o/90^o/90^o), thickness t=3cm, error $(\%) = \left|\frac{\text{Present} - [9]}{[9]}\right| 100\%$.

Folding angle α	Source	f_1	f_2	f_3	f_4	f_5
90^o	**Present**	**63.3**(0.47%)	**69.7**(0.14%)	**150.5**(1.44%)	**156.7**(0.47%)	**204.0**(1.04%)
	[9]	63.6	69.8	152.7	158.3	201.9
120^o	**Present**	**59.5**(0.34%)	**63.1**(0.47%)	**150.3**(1.44%)	**153.9**(0.71%)	**193.5**(1.36%)
	[9]	59.3	63.4	152.5	155.0	190.9
150^o	**Present**	**42.3**(0%)	**60.7**(0.16%)	**133.8**(1.75%)	**144.9**(0.48%)	**149.9**(1.25%)
	[9]	42.3	60.8	131.5	145.6	151.8

Table 1 is shown that the five natural frequencies are in excellent agreement with the percentage difference of peak values less than 1.75% of each other.

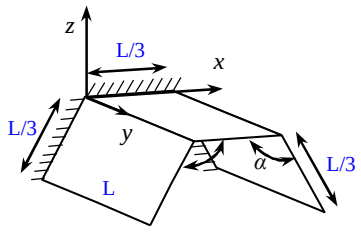

Fig 1- Two folded composite plate.

In the following section, several new numerical and experiment examples have been analyzed.

3.2. Free vibration of folded laminate glass fiber/polyester composite plate

In this section, a detailed finite element calculation of the natural modes and frequencies of a group of folded laminate plates were carried out. And some experimental tests on free vibration were performed. A one fold-, two folds- and five folds folded laminate plate models were chosen for the purpose of this study.

The composite material in ship building is used for all s models and experimental specimens: E-glass fibers and polyester resin. Material properties of the folded plate and stiffeners are determined by our experiment for all cases: E_1=10.58 GPa; E_2=2.64 GPa; G_{12}=G_{13}= 1.02 GPa; υ_{12}=0.17; ρ=1600 kg/m^3.

The plate made of symmetric off-axis configuration [45^0/-45^0/45^0/-45^0] and in-axis configuration [0^0/90^0/0^0/90^0] are taken for s models and experimental specimens.

In s experimental study, various folding angles α were considered. Within the limited length of the paper we can't explain all studies cases.

So that we only presented the results for folding angle $\alpha = 120^0$. However, we could like to point that the natural frequencies of the plates extremely depend on folding angle α.

All specimens made of the same material properties and geometrical dimensions.

The boundary conditions are:

+ Cantilever plate (CFFF): clamped all edges at $x = 0$: $u = v = w = \theta_x = \theta_y = \theta_z = 0$.

+ Clamped two ends of the plates (CFCF): at $x = 0$ and at x= L: $u = v = w = \theta_x = \theta_y = \theta_z = 0$.

+ Clamped two edges running along the length (y-direction) (FCFC): $u = v = w = \theta_x = \theta_y = \theta_z = 0$.

The specimens are divided in four groups with folding angle $\alpha = 120^0$:

1) Unstiffened two folds folded laminate composite plate (without stiffeners):

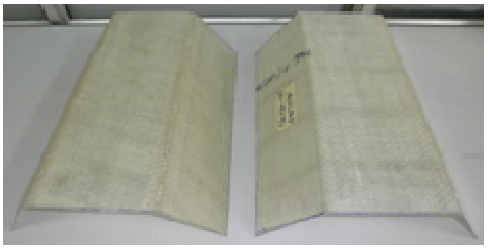

Folding angle α=120

2) Two folds folded laminate composite plate with three stiffeners attached below the folded plate running along the length of the folded edges and one stiffener attached below the folded plate along transverse direction:

Folding angle α=120

3) One fold folded laminate composite plate with two stiffeners attached below the folded plate running along the length of the folded edges and one stiffener attached below the folded plate along transverse direction:

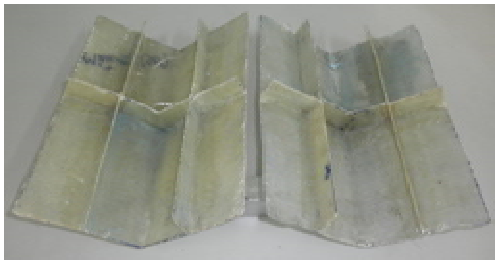

Folding angle α=120

4) Five folds folded laminate composite plate with five stiffeners attached below the folded plate running along the length of the folded edges and one stiffener attached below the folded plate along transverse direction:

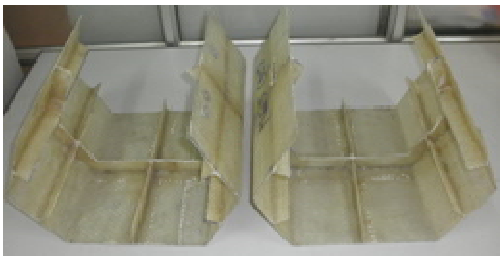

Folding angle α=120

Three first natural frequencies of those specimens were measured by using a Multi-vibration measuring machines (DEWE BOOK - DASYLab 5.61.10); 3 measurement points, confirm frequency $f_N = 5000$ Hz ($\Delta t = 0.0002$ sec), duration T=2768 (frequency resolution $\Delta f = 0.1526$ Hz).

+ Free vibration of unstiffened two folds folded laminate plate.

In this subsection, natural frequencies and mode shapes of the unstiffened two folds folded laminate plate were determined by finite element solution and experimental measurement.

The geometry of the folded plate plotted in Fig. 2

The finite element results of three natural frequencies are compared with experimental ones in Table 2 for different boundary conditions and folding angle $\alpha=120^0$.s

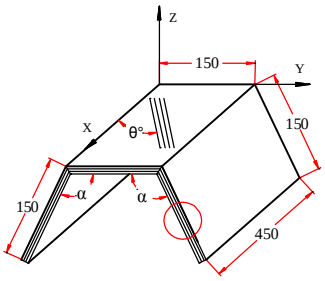

Fig.2.Unstiffened two folds folded laminate plate.

Fig.3. Experimental set-up for cantilever unstiffened two folds folded laminate plate

Table 2. Natural frequencies (Hz) of unstiffened glass fiber/polyester two folded plates, $\alpha=120^0$

Boundary Condition	$[0^0/90^0/0^0/90^0]$		$[45^0/-45^0/45^0/-45^0]$	
	FEM	Experiment	FEM	Experiment
CFFF	(f_1) 18.13	18.62 (2.70%)	17.96	18.31 (1.95%)
	(f_2) 22.64	23.19 (2.43%)	20.99	22.58 (7.58%)
	(f_3) 33.59	31.0 (7.71%)	40.37	40.28 (0.22%)
CFCF	(f_1) 29.31	27.47 (6.28%)	31.36	32.04 (2.17%)
	(f_2) 33.17	35.71 (7.66%)	33.94	34.79 (2.50%)
	(f_3) 63.68	67.44 (5.9 %)	64.87	72.33 (11.5%)
FCFC	(f_1) 37.73	39.98 (5.96%)	31.58	33.26 (5.32%)
	(f_2) 101.62	97.74 (3.82%)	83.49	76.3 (8.61%)
	(f_3) 104.44	107.12 (2.57%)	92.34	94.3 (2.12%)

The first three mode shapes of the plate having folding angle $\alpha = 120^0$ are plotted in Fig.4 for different boundary conditions. From the Table 2, it is seen that natural frequencies obtained from numerical calculation are in good agreements with those of the experimental investigation, the percentage difference of values less than 11.5% of each other.

The natural frequencies of CFFF cases are lowest and the natural frequencies of FCFC cases are highest for both of considered configurations and folding angle α.

For folding angle $\alpha = 120^o$, the natural frequencies depend on the boundary conditions in significance. Fig.4 shown that mode shapes of the plates also depend on the boundary conditions.

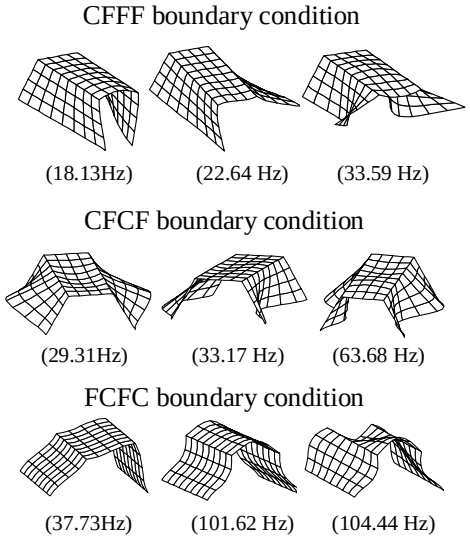

Fig.4. The first three mode shapes of the unstiffened two folds folded laminate plate

+ Free vibration of stiffened two folds folded laminate plate.

In this subsection, natural frequencies and mode shapes of the stiffened two folds folded laminate plate were investigated.

The geometry of the plate plotted in Fig. 5 and the experimental set-up for CFFF case plotted in Fig.6.

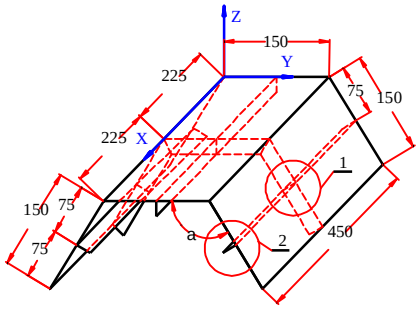

Fig.5.Stiffened two folds folded laminate plate.

Fig.6. Experimental set-up for cantilever stiffened two folds folded laminate plate

The finite element results of three natural frequencies are compared with experimental ones in Table 3 for two boundary conditions (CFFF and CFCF). The first three mode shapes of the plate having folding angle α =120^0 are available in Fig. 7.

CFFF boundary condition

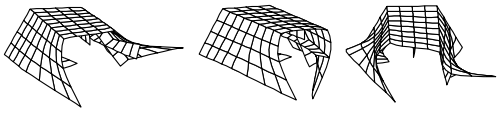

(47.94 Hz) (54.32 Hz) (103.19 Hz)

CFCF boundary condition

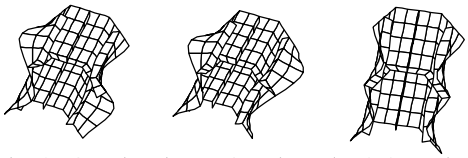

(110.73 Hz) (111.53 Hz) (118.61 Hz)

Fig.7. The first three mode shapes of the stiffened two folds folded laminate plate

From the Table 3, it is seen that natural frequencies obtained from numerical calculation are in good agreements with those of the experimental investigation.

The difference ranges from 4.68% to 9.69% in case CFFF and from 6.94% to 12.65% in case CFCF with folding angle α=120^0.

The natural frequencies of CFCF cases are extremely higher than corresponding frequencies of CFFF cases.

Table 3. Natural frequencies (Hz) of stiffened glass fiber/polyester two folded plates, α = 120^0

Boundary Condition	[0^0/90^0/0^0/90^0]		[45^0/-45^0/45^0/-45^0]	
	FEM	Experiment	FEM	Experiment
CFFF	(f_1) 47.94	45.16 (5.80%)	42.92	38.76 (9.69%)
	(f_2) 54.32	50.12 (7.73%)	50.18	47.83 (4.68%)
	(f_3) 103.19	95.1 (7.84%)	94.62	87.94 (7.06%)
CFCF	(f_1) 110.73	118.41 (6.94%)	120.15	133.1 (10.78%)
	(f_2) 111.53	122.36 (9.71%)	122.06	137.5 (12.65%)
	(f_3) 118.61	128.17 (8.06%)	122.97	138.23(12.41%)

For CFFF boundary condition, the natural frequencies of the plate having in-axis configuration are higher than the natural frequencies of the off-axis plates. However, for CFCF case they are lower than natural frequencies of off-axis plate. This

phenomenon can explained that the effect of mode shape of the plate.

Fig.7 shown that the first three mode shapes of the stiffened plates are seemed bending modes of individual plates and they depended on its boundary conditions.

From table 2 and table 3, we can see that natural frequencies of the stiffened composite plate are much higher than corresponding frequencies of the unstiffened plates.

+ Free vibration of one fold folded laminate composite plate with stiffeners

In this subsection, natural frequencies and mode shapes of the stiffened one fold folded laminate plate were calculated by finite element modeling and compared with experimental ones in Table 4 for cantilever boundary conditions (CFFF case). The plates have folding angle $\alpha = 120^0$.

The geometry of the plate plotted in Fig. 8 and the experimental set-up for CFFF case plotted in Fig. 9.

The first three mode shapes of the plate having folding angle $\alpha = 120^0$ are available in Fig. 10.

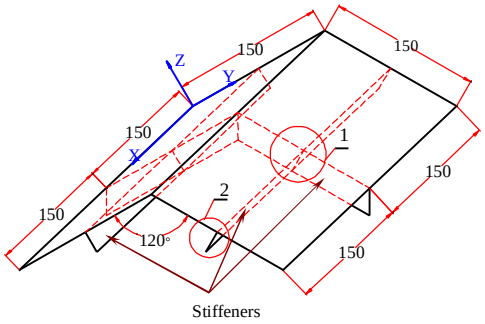

Fig.8.The stiffened one fold folded laminate plate.

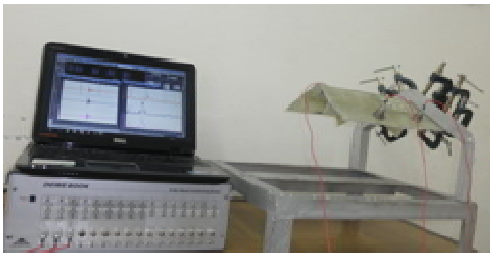

Fig.9. Experimental set-up for cantilever stiffened one fold folded laminate plate

CFCF boundary condition

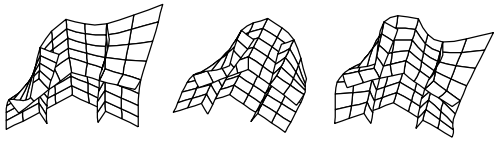

(60.42 Hz) (80.16 Hz) (132.13 Hz)

Fig.10. The first three mode shapes of stiffened one fold folded laminate plate

Table 4. Natural frequencies (Hz) of stiffened glass fiber/polyester one folded plates, $\alpha = 120^0$

Boundary Condition	$[0^0/90^0/0^0/90^0]$		$[45^0/-45^0/45^0/-45^0]$	
	FEM	Experiment	FEM	Experiment
CFFF	(f_1) 60.42	66.62 (10.23%)	54.36	50.15 (7.74%)
	(f_2) 80.16	78.74 (1.77%)	83.17	78.91 (5.12%)
	(f_3) 132.13	121.8 (7.82%)	133.23	121.5 (8.81%)

From the Table 4 we can see that natural frequencies obtained from numerical calculation are in good agreements with those of the experimental measurements. The difference ranges from 1.77% to 10.23% in this case for folding angle $\alpha = 120^0$.

For the cantilever one folded composite plate, natural frequencies of the plate having in-axis configuration are higher than corresponding ones of the plate made of off-axis configuration.

This phenomenon could explain that the mode shapes depend on the stacking scheme

on direction flexural rigidity.The finite element results of three natural frequencies are compared with experimental ones in Table 5 for the boundary condition CFFF (cantilever plate). The plates multi-folded with folding angle $\alpha = 120^0$.

The geometry of the plate plotted in Fig.11 and the experimental set-up for CFFF case plotted in Fig.12.

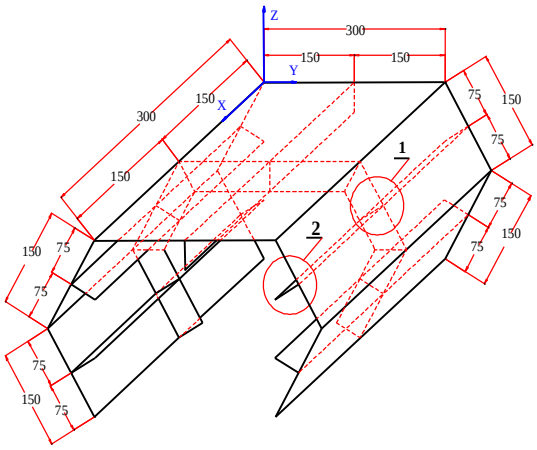

Fig.11.Stiffened one fold folded laminate plate

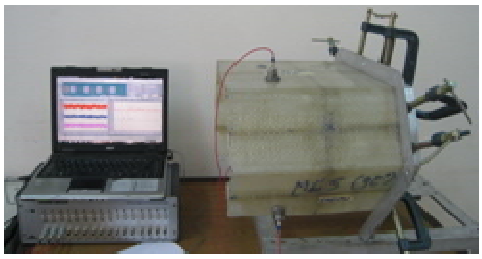

Fig.12. Experimental set-up for cantilever stiffened five folds folded laminate plate

The first three mode shapes of the plate having folding angle $\alpha = 120^0$ are available in Fig. 13.

CFFF boundary condition

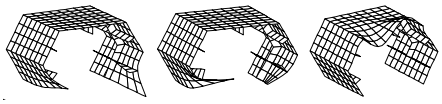

74.36 Hz 75.49 Hz 112.23Hz

Fig.13. The first three mode shapes of stiffened five folds folded laminate plate

Table 5. Natural frequencies (Hz) of stiffened glass fiber/polyester five folded plates, $\alpha = 120^0$

Boundary Condition	$[0^0/90^0/0^0/90^0]$		$[45^0/-45^0/45^0/-45^0]$	
	FEM	Experiment	FEM	Experiment
CFFF	(f_1) 74.36	76.3 (2.61 %)	75.16	80.26 (6.78%)
	(f_2) 75.49	76.6 (1.47%)	76.24	84.5 (10.83%)
	(f_3) 112.23	116.6 (3.89 %)	98.44	106.7 (8.39%)

Table 5 shown that natural frequencies obtained from experimental measurements are closed with those of the numerical calculations.

The difference ranges from 1.47% to 10.83% in case CFFF for both of considered stacking sequences.

Natural frequencies obtained by experiment are higher than the others of numerical solutions.

The first mode and the second mode of the folded plate is symmetric mode

4. Conclusion

In the present paper, a finite element algorithm and home-made Matlab computer code based on the first-order shear deformation theory developed to study a free vibration analysis of the folded composite plates with and without stiffeners. In which, an eight nodded isoparametric quadrilateral element with five degrees of freedom per nodes is used for both of the plates and stiffeners. Experimental studies on vibration of the folded composite plates with various type of geometry are also performed. On the

basis of the obtained numerical and experimental results in this study, some following conclusions are drawn:

- Experimental natural frequencies are in good agreement with those calculated by finite element models.

- For studied glass/polyester two folds folded plates, the folded laminate plate which reinforced by stiffeners show bigger frequencies than unstiffened folded plate. Mode shapes of stiffened folded plates are different with those of unstiffened folded plate.

- With each boundary condition, the mode shapes of studies folded plate are different for all studies cases. The folded geometry is significant on natural mode shapes of the plates. And the mode shapes obtained by numerical simulations can predict the excited method for vibration measurement. It is shown that the feasibility of numerical predictions in experimental natural frequencies measurement.

Acknowledgments

"This research is funded by Vietnam National Foundation for Science and Technology Development (NAFOSTED) under grant number: ***107.02-2011.08***".

5. References

[1] J. E. Goldberg and H.L.Leve (1957), *Theory of prismatic folded structures*. Int. Assoc. *Bridge and Structural Engng 17*, 58-86.

[2] Yitzhaki D and Reiss M (1962). Analysis of folded plates. *J Struct Div, ASCE*, 88, pp. 107-142.

[3] Y. K. Cheung (1968), Finite strip method of elastic slabs. *Proc.ASCE* 94, 1365-1378.

[4] Y.K. Cheung (1969), Folded-plate structures by finite strip method, *J.Struct. Div., ASCE*12 2963-2979.

[5] S.Maleki (1991), Compound strip method for Box Girders and folded plates, *Comput Struct.* 40 527-538.

[6] Y. Lavy, P. Bar-Yoseph and G.Rosenhouse (1992), Mixed-hybrid finite strip method for folded plate structures. *Comput. Struct.* 42, 433-46.

[7] T.Irie, G.Yamada, Y. Kobayashi (1984), Free vibration of a cantilever folded plate, *J Acoust. Soc. Am.* 76(6) 1743-1748.

[8] Perry B, Bar-Yoseph P, Rosenhouse G (1992), Rectangular hybrid shell element for analysing folded plate structures. *Computers and Structures* 44:177–83.

[9] Sreyashi Pal and Guha Niyogi (2008), Application of folded formulation in analyzing stiffened laminated composite and sandwich folded plate vibration. *Journal of Reinforced Plastics and composites*, 27: 692-710.

[10] S. Haldar, A.H. Sheikh (2005), Free vibration analysis of isotropic and composite folded plates using a shear flexible element. *Finite Elem. Anal. Des*. 42: 208–226.

[11] L. X. Peng, K. M. Liew and S. Kitipornchai (2011), Bending Analysis of Folded Laminated Plates by the FSDT Meshfree Method. *Procedia Engineering* 14 2714–2721.

[12] Bui van Binh, Tran Ich thinh, Tran Minh Tu (2011), Analysis of bending folded laminated composite plate by finite element method. *International conference on Science and Technology*, Science and Technics Publishing House, Session 6: 711-723.

[13] Tran Ich Thinh, Bui Van Binh, Tran Minh Tu (2011), Vibration of folded laminate composite plate. *International conference on Science and Technology*, Science and Technics Publishing House, Session 6: 659-670.

[14] Tran Ich Thinh, Bui Van Binh, Tran Minh Tu (2011), Static and free vibration of laminated composite folded plate using finite element method. *Journal of Science and Technology*, Vol.49, No.2.

[15] Tran Ich Thinh, Bui Van Binh, Tran Minh Tu (2012), Bending and Vibration analyses of multi-folding laminate composite plate using finite element method. *Vietnam Journal of Mechanics, VAST*, Vol.34, No.3.

[16] Bathe, K-J (1996), *Finite element procedures*. Prentice-Hall, Inc.

[17] Tran Ich Thinh (1994), *Composite Materials*. Viet Nam Education Publishing House.

[18] Nguyen Van Dat (2005), Study on designing bilge machine platform of composite ship in vibration suppression, *Ph.D. Thesis*. Nha Trang University.

The 2nd International Conference on Engineering Mechanics and Automation (ICEMA2)
Hanoi, August 16-17, 2012
ISBN: 978-604-913-097-7

Free Vibration Characteristics of Functionally Graded Beams Resting on Elastic Foundation

Trinh Thanh Huong[a] and Nguyen Dinh Kien[b]

[a] *Department of Solid Mechanics, Institute of Mechanics, Vietnam Academy of Science and Technology. E-mail: thanhhuong31@gmail.com*
[b] *Department of Solid Mechanics, Institute of Mechanics, Vietnam Academy of Science and Technology. E-mail: ndkien@imech.ac.vn*

Abstract

The free vibration characteristics of functionally graded beams resting on a Winkler elastic foundation are investigated by the finite element method. The material properties of the beams are assumed to be graded in the thickness direction by a simple power law. A shear deformable beam element using the exact polynomials as interpolating functions for the kinematic variables and taking the effect of the shift in the neutral axis into account is formulated and employed in computing the natural frequencies and mode shapes. The numerical results show that the formulated element is capable to give the accurate vibration characteristics of the beams by using just several elements. The influence of the material non-homogeneity, foundation support as well as the aspect ratio on the vibration characteristics of the beams is examined and highlighted in detail.

Key Words: Functionally graded beam, neutral axis, Winkler foundation, finite element method, free vibration

1. Introduction

Functionally graded materials (FGMs) initiated by Japanese scientists in Sendai in 1984 (Koizumi, 1997) have received great interest from engineers and researchers. FGMs are formed by varying percentage of material components in a desired direction, and as a results, the specific physical and mechanical properties of the formed material can be obtained. With the unique feature, FGMs offer a great potential for use as structural material, and analysis of structures made of FGMs has become a main topic in the field of structural mechanics. A comprehensive list of publications on static, dynamic as well as buckling analyses of functionally graded structures subjected different loadings is given in the work by Şimşek and Kocatür (2009) and Şimşek (2010). Contributions that are most relevant to the problem addressed of the present work are briefly discussed herein.

The free vibration frequencies and mode shapes of a simply supported FGM beam were studied by Adopting et al. (2007) by using the first order, parabolic and exponential shear deformation beam theories Using the rotational spring model, Yang and Chen (2008) derived the analytical solutions

of natural frequencies, buckling loads and mode shapes of cracked FGM Bernoulli beams. Li (2008) presented a unified approach for analyzing static and dynamic behavior of FGM beams with the power-law gradient and a laminated beam. Ying et al. (2008) proposed the two-dimensional elasticity solutions for FGM beams resting on an elastic foundation with the exponential-law graduation through the thickness for material property. Employing two new beam theories denoted as FSDBT1 and FSDBT2, Sina et al. (2009) presented an analytical method for studying the free vibration of FGM beams with material property graded in the thickness direction by a power law. Alshorbagy et al. (2011) investigated the free vibration characteristics of FGM Bernoulli beams by the finite element method. The free vibration of FGM beams was studied by Gunda et al. (2011) by using the hierarchical beam theory. Adopting the exact polynomials obtained from the solutions of differential uniform homogeneous Timoshenko beam element, Shahba et al. (2011) derived the finite element formulation for studying the natural frequencies, buckling loads of tapered Timoshenko beam made of axially functionally graded material. To improve the accuracy and convergence, the exact variation of the cross section profile has been employed in computing the mass and stiffness matrices in the work by Shahba et al. (2011).

The objective of the present paper is to investigate the free vibration characteristics of functionally graded beams resting on a Winkler elastic foundation by the finite element method. The material distribution of the beams is assumed to vary in the thickness direction by a simple power law. A beam element taking the effect of the shear deformation and foundation support into account is formulated by using exact polynomials as interpolation functions for transverse displacement and rotation. The effect of the shift in the neutral axis position, which arose from the material inhomogeneity is also taken into consideration. The influence of the material inhomogeneity, foundation support on the frequencies and mode shapes of the beams are investigated. The effect of the length to height ratio is also examined and highlighted.

2. Functionally graded beams

Figure 1 shows a uniform FGM beam with length of L and height of h, resting on an elastic foundation. The coordinate system (x_0, z_0) is chosen as that the x_0 axis is on the bottom surface. The beam is assumed to be formed from two material components with the property P varies continuously in the thickness direction according to the power law as

$$P(z_0) = (P_t - P_b)\left(\frac{z_0}{h}\right)^n + P_b \tag{1}$$

where n is the nonnegative power law index, defined the distribution of the material components through the thickness; P_b, P_t denote the material property such as Young's modulus, shear modulus or mass density of the material at the bottom and top surfaces, respectively. As seen from equation (1), the bottom and top surfaces corresponding to $z_0 = 0$ and $z_0 = h$, contain pure one material component. Due to the variation of Young's modulus through the thickness of the beam, the neutral axis is no longer at the mid-plane, but shifted from the mid-plane unless for the case of symmetric Young's modulus. The position of the neutral axis for a cross section can be determined by solving the following equation (Kang and Li, 2009; Kang and Li, 2010)

$$\frac{E_t - E_b}{E_b}\int_0^1 (1+\beta)^n t\,dt + \frac{(1+\beta)^n}{2}\left(1 - \frac{1}{\beta^2}\right) = \frac{E_t - E_b}{E_b}\frac{\Gamma(n+1)}{\beta^2\Gamma(n+3)} \tag{2}$$

where E_b, E_t are Young's modulus of the material on the bottom and top surfaces, respectively; $\Gamma(*)$ is the Gamma function with its value can readily be defined for a

given power law index; $\beta = (h - h_0)/h_0$, where h_0 denotes the distance from the bottom surface to the neutral axis (confirm Figure 1).

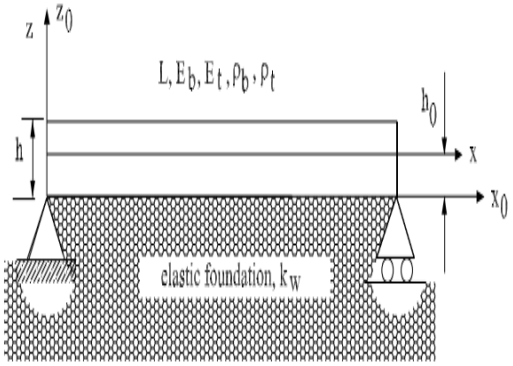

Figure 1. Simply supported FGM beam resting on elastic foundation

The solution of equation (2), namely β, and thus the position of the neutral axis h_0, depends on the ratio between the Young's modulus of the material components, $\frac{E_t}{E_b}$, and the power law index n. Figure 2 shows the effect of the power law index n on the position of the neutral for the FGM beam formed from Aluminum (Al) and Alumina (Al_2O_3). The Young's modulus of aluminum is $E_b = 70GPa$, and that of alumina is $E_t = 390GPa$ (Şimşek, 2010).

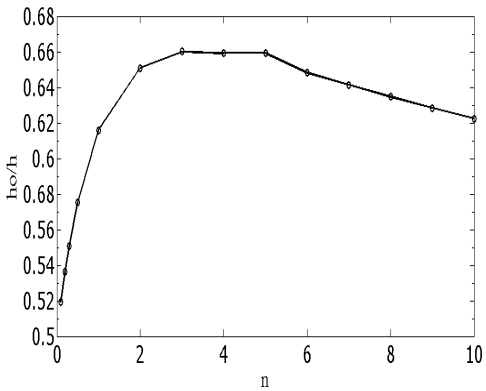

Figure 2. Effect of power law index on position of the neutral axis of the FGM beam

3. Finite element formulation

Considering a FGM beam in a coordinate system (x, z) as shown in Figure 1, where the x axis coincides with the beam neutral axis. Adopting the Timoshenko beam, the axial and transverse displacements at any point of the beam are given by

$$\begin{aligned} u(x,z,t) &= -z\theta(x,t), \\ w(x,z,t) &= w(x,t) \end{aligned} \tag{3}$$

where $w(x,t)$ and $\theta(x,t)$ are the transverse displacement and cross sectional rotation correspond to a point with abscissa x on the neutral axis, respectively; z is the distance from the considering point to the x axis. Assuming the linearly elastic behavior, the strains and stresses associated with the displacement field (3) are given by

$$\begin{aligned} &\varepsilon_x = -z\frac{\partial\theta}{\partial x},\ \gamma_{xz} = \frac{\partial w}{\partial x} - \theta \\ &\sigma_x = E(z)\varepsilon_x,\ \tau_{xz} = \psi G(z)\gamma_{xz} \end{aligned} \tag{4}$$

where ψ is the correction factor, and its value depends on the geometry of the beam cross section. Following the finite element method procedure, the beam assumed to be divided into NE elements with length of l. From equation (4), the strain energy for an element can be written in the form

$$\begin{aligned} U = \frac{1}{2}\int_0^l\int_A \left[E(z)\varepsilon_x{}^2 + \psi G(z)\gamma_{xz}{}^2\right]dAdx \\ + \frac{1}{2}\int_0^l k_W w^2 dx \end{aligned} \tag{5}$$

where A and k_W denote the cross section area and foundation stiffness modulus, respectively. In equation (5), the first term stemming from the bending and shear deformation of the beam, and the second one is from the foundation deformation. It is noted that the elastic moduli in equation (5) is written in term of z coordinate, where $z = z_0 - h_0$. Using the expressions of the trains, one can rewrite the strain energy as

$$U=\frac{1}{2}\int_0^l\left[D_{xx}\left(\frac{\partial\theta}{\partial x}\right)^2+\psi A_{xz}\left(\frac{\partial w}{\partial x}-\theta\right)^2\right]dx$$
$$+\frac{1}{2}\int_0^l k_W w^2 dx \quad (6)$$

where the bending and shear rigidities are given by

$$D_{xx}=\int_A z^2E(z)dA,\ A_{xz}=\int_A G(z)dA \quad (7)$$

In a similar way, the kinetic energy for the element can be written in the form

$$T=\frac{1}{2}\int_0^l\left(I_A\dot{w}^2+I_D\dot{\theta}^2\right)dx \quad (8)$$

where

$$I_A=\int_A\rho(z)dA,\ I_D=\int_A z^2\rho(z)dA \quad (9)$$

To this point, interpolation schemes for $w(x,t)$ and $\theta(x,t)$ are necessary to introduce. The exact polynomials derived by Kosmatka (1995) and Yokoyama (1996) by solving the equilibrium different equations of a homogeneous Timoshenko beam segment are adopted in the present work

$$\begin{aligned}w(x,t)&=\mathbf{N}_w^T\mathbf{d}\\&=N_{w1}w_1+N_{w2}\theta_1+N_{w3}w_2+N_{w4}\theta_2\\\theta(x,t)&=\mathbf{N}_\theta^T\mathbf{d}\\&=N_{\theta1}w_1+N_{\theta2}\theta_1+N_{\theta3}w_2+N_{\theta4}\theta_2\end{aligned} \quad (10)$$

where $\mathbf{d}=\{w_1\quad\theta_1\quad w_2\quad\theta_2\}^T$ is the element vector of the nodal displacements; $\mathbf{N}_w$ and $\mathbf{N}_\theta$ respectively are the matrices of interpolation functions for the transverse displacement and rotation, and having the following forms (Kosmatka, 1995; Yokoyama, 1996)

$$N_{w1}=\frac{1}{1+\lambda}\cdot\left[2\left(\frac{x}{l}\right)^3-3\left(\frac{x}{l}\right)^2-\lambda\left(\frac{x}{l}\right)+(1+\lambda)\right]$$

$$N_{w2}=\frac{l}{1+\lambda}\cdot\left[\left(\frac{x}{l}\right)^3-\left(2+\frac{\lambda}{2}\right)\left(\frac{x}{l}\right)^2+\left(1+\frac{\lambda}{2}\right)\left(\frac{x}{l}\right)\right]$$

$$N_{w3}=-\frac{1}{1+\lambda}\cdot\left[2\left(\frac{x}{l}\right)^3-3\left(\frac{x}{l}\right)^2-\lambda\left(\frac{x}{l}\right)\right]$$

$$N_{w4}=\frac{l}{1+\lambda}\cdot\left[\left(\frac{x}{l}\right)^3-\left(1-\frac{\lambda}{2}\right)\left(\frac{x}{l}\right)^2-\frac{\lambda}{2}\left(\frac{x}{l}\right)\right] \quad (11)$$

and

$$N_{\theta1}=\frac{6}{(1+\lambda)l}\left[\left(\frac{x}{l}\right)^2-\left(\frac{x}{l}\right)\right]$$

$$N_{\theta2}=\frac{1}{1+\lambda}\cdot\left[3\left(\frac{x}{l}\right)^2-(4+\lambda)\left(\frac{x}{l}\right)+(1+\lambda)\right]$$

$$N_{\theta3}=-\frac{6}{(1+\lambda)l}\left[\left(\frac{x}{l}\right)^2-\left(\frac{x}{l}\right)\right] \quad (12)$$

$$N_{\theta4}=\frac{1}{1+\lambda}\cdot\left[3\left(\frac{x}{l}\right)^2-(2-\lambda)\left(\frac{x}{l}\right)\right]$$

In equations (11) and (12), λ is the shear deformation parameter defined as

$$\lambda=\frac{12}{l^2}\frac{E_0I}{\psi G_0A} \quad (13)$$

where E_0 and G_0 respectively are the Young and shear moduli of the homogeneous beam. In the numerical computation performed in Section 4, E_b and G_b are assigned as E_0 and G_0, respectively. Using the interpolation schemes, the strain and kinetic energies for the element can be written in the forms

$$U = \frac{1}{2}\mathbf{d}^{\mathbf{T}}(\mathbf{k_b} + \mathbf{k_s} + \mathbf{k_f})\mathbf{d}$$
$$T = \frac{1}{2}\dot{\mathbf{d}}^{\mathbf{T}}(\mathbf{m_w} + \mathbf{m_\theta})\dot{\mathbf{d}} \quad (14)$$

where $\mathbf{k}_b$, $\mathbf{k}_s$, $\mathbf{k}_f$ respectively are the element stiffness matrices stemming from the bending, shear deformation of the beam, and the foundation deformation, and having the forms

$$\mathbf{k}_b = \int_0^l \frac{\partial \mathbf{N}_\theta}{\partial x} D_{xx} \frac{\partial \mathbf{N}_\theta^T}{\partial x} dx$$
$$\mathbf{k}_s = \int_0^l \left(\frac{\partial \mathbf{N}_w}{\partial x} - \mathbf{N}_\theta \right) A_{xz} \left(\frac{\partial \mathbf{N}_w}{\partial x} - \mathbf{N}_\theta \right)^T dx$$
$$\mathbf{k}_f = \int_0^l \mathbf{N}_w k_W \mathbf{N}_w^T dx \quad (15)$$

The mass matrices $\mathbf{m}_w$ and $\mathbf{m}_\theta$ in equation (14) are resulted from the transverse displacement and section rotation, and having the forms

$$\mathbf{m}_w = \int_0^l \mathbf{N}_w I_w \mathbf{N}_w^T dx, \mathbf{m}_\theta = \int_0^l \mathbf{N}_\theta I_\theta \mathbf{N}_\theta^T dx \quad (16)$$

With the strain and kinetic energies given by equation (14), Hamilton's principle for free vibration analysis reads

$$\delta \int_{t_1}^{t_2} \left(\frac{1}{2}\dot{\mathbf{d}}^{\mathbf{T}}\mathbf{m}\dot{\mathbf{d}} + \frac{1}{2}\mathbf{d}^T\mathbf{k}\mathbf{d} \right) dt \quad (17)$$

where $\mathbf{m} = \mathbf{m}_w + \mathbf{m}_\theta$, $\mathbf{k} = \mathbf{k}_b + \mathbf{k}_s + \mathbf{k}_f$ are the element mass and stiffness matrices, respectively. Equation (17) gives the equations of motion for the element, and after assembling over the number of elements, they can be written in the form

$$\mathbf{M}\ddot{\mathbf{D}} + \mathbf{K}\mathbf{D} = \mathbf{0} \quad (18)$$

where $\mathbf{M} = \sum^{NE} \mathbf{m}$, $\mathbf{K} = \sum^{NE} \mathbf{k}$ are the structural mass and stiffness matrices, respectively; $\mathbf{D}$ is the structural vector of the nodal displacements. A harmonic vibration can be assumed for the free vibration, $\mathbf{D} = \mathbf{V}\sin\omega t$, so that equation (18) can be written in the form

$$(\mathbf{K} - \omega^2\mathbf{M})\mathbf{V} = \mathbf{0} \quad (19)$$

where ω is the natural frequency, and $\mathbf{V}$ is the mode shape, which can be obtained by the standard way of solving eigenvalue problem described in the structủal text books (Géradin and Rixen , 1997; Hughes, 2000).

4. Numerical results

The FGM beams formed from Al and Al_2O_3 are used to compute the free vibration characteristics presented in this Section. In addition to the Young's modulus given in Section 2, the mass density of the Al and Al_2O_3 are 2702 kg/m^3 and 3960 kg/m^3, respectively. A Poisson ratio $\nu = 0.3$ is used for both the material components. Following the work by Sina et al. (2009), the dimensionless natural frequency parameter for is introduce as

$$\mu = \omega L^2 \sqrt{\frac{I_A}{h^2 \int_{-h_0}^{h-h_0} E(z)dz}} \quad (20)$$

where ω denotes the natural frequency of the FGM beam. A dimensionless foundation stiffness parameter k is also introduced as

$$k = k_W \frac{L^4}{E_b I} \quad (21)$$

Two types of boundary conditions, namely simply supported (SS) and clamped at one end and free at the other (CF), are considered herewith. Otherwise stated, the beam with a length to height ratio of 100 is used in the analysis.

4.1. Fundamental frequency

Table 1 lists the non-dimensional frequencies for the unsupported FGM beam having different values of the length to height ratio obtained by using eight elements for the case $n = 3$. For the purpose of comparison, the analytical solutions derived

by Sina et al. (2009) based on the two different shear deformation beam theories, FSDBT1 and FDDBT2, are also listed in the table. The FSDBT1 ignored the lateral stresses and all derivatives with respect to lateral coordinate in the plate equations of motion while the FSDBT2 assumed that the stress and moment resultants in the lateral direction are zero (Sina et al., 2009). It is seen that the fundamental frequency obtained in the present work is very good in agreement with that of Sina et al. (2009), regardless of the boundary conditions and the length to height ratio.

Table 1. Non-dimensional fundamental frequency of FGM beam

B.C.'s	L/h	10	30	100
SS	FSDBT1 Ref. [8]	2.774	2.813	2.817
	FSDBT2 Ref. [8]	2.695	2.737	2.742
	Present	2.6992	2.7368	2.7412
CF	FSDBT1 Ref. [8]	0.996	1.003	1.003
	FSDBT2 Ref. [8]	0.969	0.976	0.977
	Present	0.9695	0.9759	0.9766

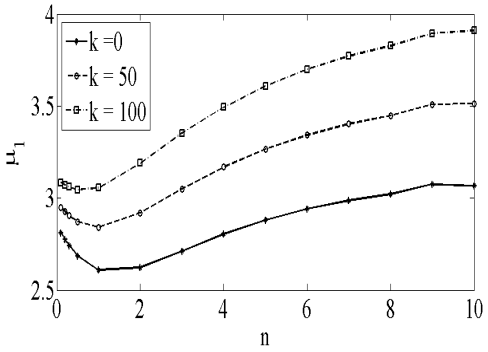

Figure 3. Effect of power law index n on non-dimensional fundamental frequency of SS beam resting on elastic foundation

The effect of the power law index n on the non-dimensional fundamental frequency of the FGM simply supported and clamped free beams resting on the elastic foundation are shown in Figure 3 and Figure 4, respectively. As seen from the figures, the fundamental frequency reduces and reaches a minimum value when steady raising the index n, and it then gradually increases, regardless of the foundation stiffness and the boundary conditions. The foundation support increases the fundamental frequency of the beams, but hardly changes the relationship between the power law index and the frequency.

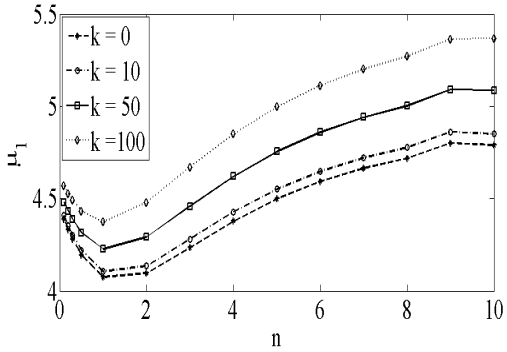

Figure 4. Effect of power law index n on non-dimensional fundamental frequency of CF beam resting on elastic foundation

4.2. Mode shapes

The lowest two mode shapes for the transverse displacement of the simply supported FGM beam resting on the elastic foundation with a foundation stiffness $(k = 50)$ computed with different values of the power law index n are depicted in Figure 5. The corresponding mode shapes for the clamped free FMG beam are shown in Figure 6. As seen from the figures, the mode shapes of the beams are greatly affected by the power law index n, and the deflection of the beam increase when raising the index n, regardless of the mode shape and the boundary conditions. This is due to the fact that, as seen from equation (1), the elastic modulus, and thus the bending stiffness of the beam is lower for a higher index n. As a result, the beam is weaker for a higher index. It is noted that the computation has been performed with different values of the foundation parameter k, and it is found that the mode shapes of the beams are not influenced by the foundation stiffness.

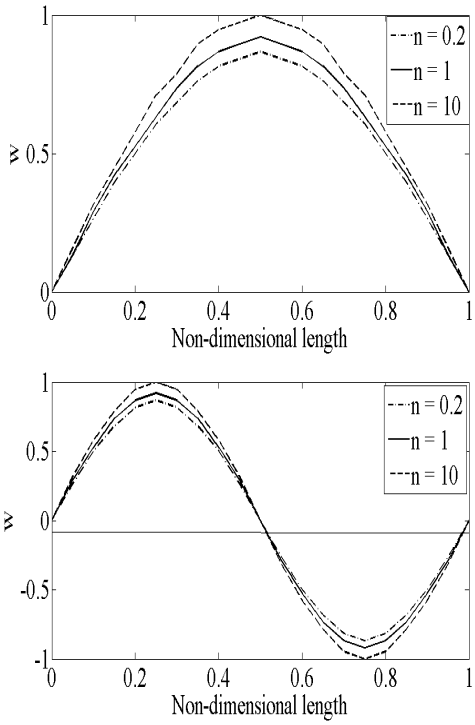

Figure 5. The lowest two mode shapes for SS beam (k=50, L/h=100)

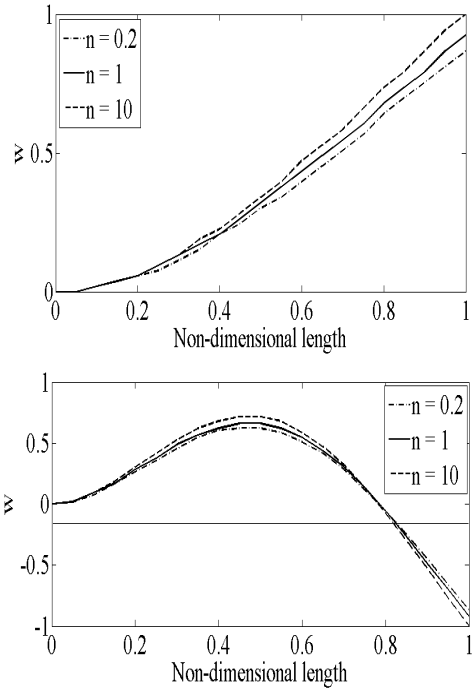

Figure 6. The lowest two mode shapes for CF beam (k=50, L/h=100)

4.3. Effect of aspect ratio

The vibration characteristics of beams having different values of length to height ratio (also known as the aspect ratio) are computed in this sub-section. The relation between the power law index n and the fundamental frequency of simply supported and clamped free beams with different values of the length to height ratio and with $n = 3, k = 50$ are depicted in Figure 7 and Figure 8, respectively. The lowest two mode shapes of the beams having different length to height ratios are depicted in Figure 9 and Figure 10.

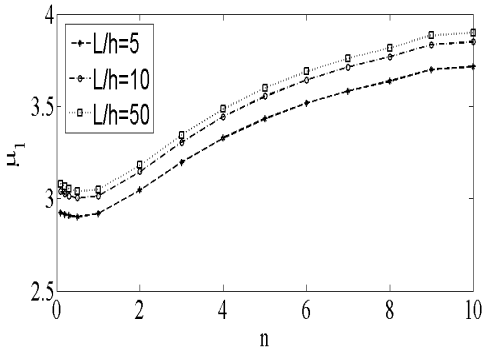

Figure 7. Non-dimensional fundamental frequency of SS beam with different values of L/h ($n = 3, k = 50$)

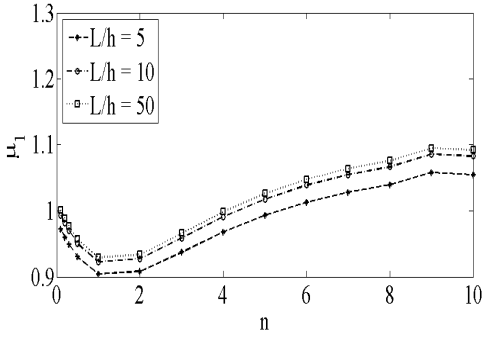

Figure 8. Non-dimensional fundamental frequency of CF beam with different values of L/h ($n = 3, k = 50$)

Figure 7 and Figure 8 show a reduction in the fundamental frequency of the beams when the length to height ratio is lower, regardless of the power law index. By examining Figure 7 and Figure 8 with Figures 3 and 4, one can se that the effect of the aspect ratio on the fundamental of the

beams is very similar to that of the foundation stiffness.

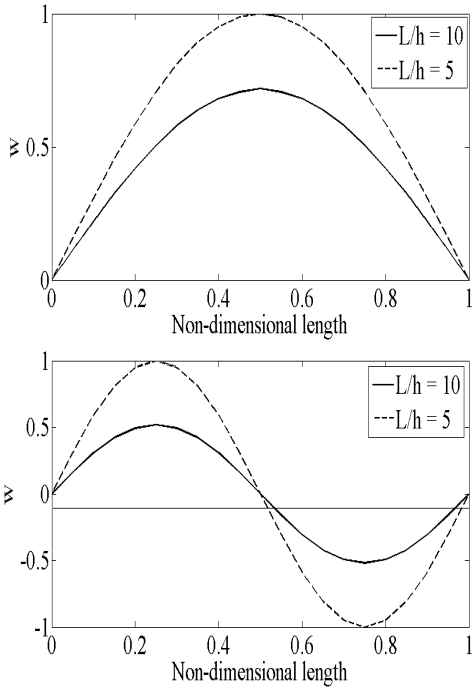

Figure 9. Mode shapes of simply supported FGM beam with different L/h ratios ($n = 3, k = 50$)

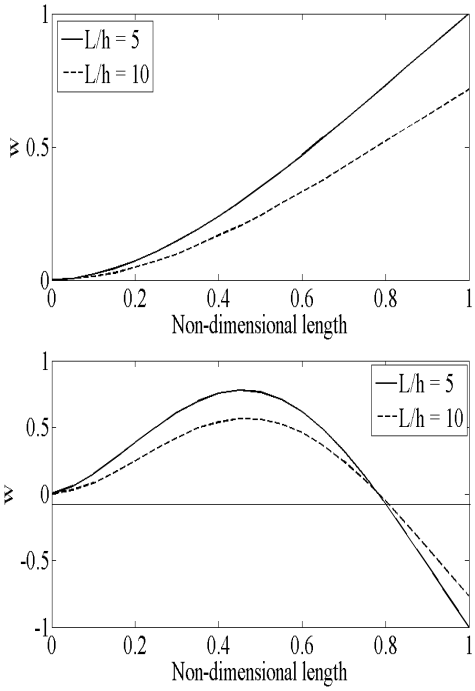

Figure 10. The lowest two mode shapes for clamped free FGM beam ($n = 3, k = 50$)

For the mode shapes, as seen from Figure 9 and Figure 10, the deflection of the beams is larger for the beam having a lower length to height ratio. Thus, the shear deformation which cannot be ignored for the stubby beam reduces the fundamental frequency and increases the deflection of the beam. The numerical results show the ability of the formulated element in modeling the shear effect of the beams.

5. Conclusions

A finite element formulation for study the free vibration of the FGM beams resting on a Winkler elastic foundation has been presented. A beam element taking the effects of the shear deformation and the shift in the neutral axis into account has been formulated by using the exact polynomials as interpolation functions for the transverse displacement and rotation.

The vibration characteristics of the simply supported and clamped free beams resting on the elastic foundation have been computed. The influence of the non-homogeneous material, the length to height ratio on the fundamental frequencies and mode shapes of the beam has been numerically examined in detail. The numerical results have shown that the vibration characteristics of the FGM beam are greatly influenced by material inhomogeneity defined through the power law index and the foundation stiffness. The influence of the length to heigh ratio on the free vibration characteristics of the beams has also investigated and highlighted.

References

Alshorbagy, A.E., M.A. Eltaher and F.F. Mahmoud (2011). Free vibration characteristics of a functionally graded beam by finite element method. *Applied Mathematical Modelling*, 35, pp. 412-425.

Aydogdu, M. and V. Taskin (2007). Free vibration analysis of functionally graded beams with simply supported edges. *Materials & Design*, 28, pp. 1651-1656.

Géradin M. and R. Rixen (1997). *Mechanical vibrations: Theory and application to structural dynamics.* John Wiley and Sons, Chichester, second edition.

Gunda, J.B., R.K. Gupta, G.R. Janardhan and G.V. Rao (2011). Large amplitude vibration analysis of composite beams: Simple closed-form solutions. *Composite Structures*, 93, pp.870-879.

Hughes, T.J.R. (2000). *The finite element method: Linear static and dynamic finite element analysis.* Dover publication Inc., Mineola .

Kang, Y.A. and X.F. Li (2009). Bending of functionally graded cantilever beam with power-law nonlinearity subjected to an end force. *Non-linear Mechanics*, 44, pp. 696-703.

Kang, Y.A. and X.F. Li (2010). Large deflection of a non-linear cantilever functionally graded beam. *Journal of Reinforced Plastics Composites*, 29, pp. 1761-1774.

Koizumi, M. (1997). FGM activities in Japan. *Composites*, part B, 28, pp.1-4.

Li, X.F. (2008). A unified approach for analyzing static and dynamic behaviors of functionally graded Timoshenko and Euler-Bernoulli beams. *Journal of Sound and Vibration*, 318, pp.1210-1229.

Shahba, A., R. Attarnejad, M.T. Marvi, and S. Hajilar (2011). Free vibration and stability analysis of axially functionally graded tapered Timoshenko beams with conditions. *Composites*, part B, 42, pp. 801-808.

Şimşek, M. and T. Kocatürk (2009). Free and forced vibration of a functionally graded beam subjected to a concentrated moving harmonic load. *Composite Structures*, 90, pp. 465-473.

Şimşek, M. (2010). Vibration analysis of a functionally graded beam under a moving mass by using different beam theory. *Composite Structures*, 92, pp. 904-917.

Sina, S.A., H.M. Navizi and H. Haddadpour (2009). An analytical method for free vibration analysis of functionally graded beams. Materials & Design, 30, pp. 741-747.

Yang, J. and Y. Chen (2008). Free vibration and buckling analysis of functionally graded beams with edge cracks. *Composite Structures*, 83, pp. 48-60.

Ying, J., C.F. Lu and W.Q. Chen (2008). Two-dimensional elasticity solutions for functionally graded beams resting on elastic foundation. *Composite Structures*, 84, pp. 209-219.

Authors Index

PUBLISHING HOUSE FOR SCIENCE AND TECHNOLOGY

Address: 18, Hoang Quoc Viet, Cau Giay, Hanoi

Tel: 04.22149034/40/41 Fax: 04 37910147

Email: nxb@vap.ac.vn; Website: http:// www.vap.ac.vn

Responsible for Publication

Director: Prof. Dr. Sc. Nguyen Khoa Son

Editors in Chief: Prof. Dr. Sc. Nguyen Khoa Son

Technical Editors: Dao Nhu Mai

Cover Designer: Dao Nhu Mai

PROCEEDINGS OF THE INTERNATIONAL CONFERENCE ON ENGINEERING MECHANICS AND AUTOMATION - ICEMA 2012

ISBN: 978-604-913-097-7

Printing 150 copies, size 19 x 27cm, printed in Publishing House for Science and Technology

Registered number for Publication:

Printing completed and Copyright deposited on December 2012.

ISBN: 978-604-913-097-7